A Molecular View on Alzheimer's Disease by Cryo Electron Microscopy

Inaugural-Dissertation

zur Erlangung des Doktorgrades
der Mathematisch-Naturwissenschaftlichen Fakultät
der Heinrich-Heine Universität Düsseldorf

Vorgelegt von

Mara Zielinski
aus Weener

Jülich, August 2023

aus dem Institut für Biologische Informationsprozesse: Strukturbiochemie (IBI-7)
des Forschungszentrums Jülich

Gedruckt mit der Genehmigung der
Mathematisch-Naturwissenschaftlichen Fakultät der
Heinrich-Heine-Universität Düsseldorf

Berichterstatter:

1. Prof. Dr. Gunnar Schröder

2. Prof. Dr. Carsten Sachse

3. Prof. Dr. Henning Stahlberg

Tag der mündlichen Prüfung: 05.02.2024

Eidesstattliche Erklärung

Ich versichere an Eides Statt, dass die Dissertation von mir selbständig und ohne unzulässige fremde Hilfe unter Beachtung der "Grundsätze zur Sicherung guter wissenschaftlicher Praxis an der Heinrich-Heine-Universität Düsseldorf" erstellt worden ist. Weiterhin erkläre ich, dass diese Dissertation an keiner anderen Fakultät eingereicht wurde. Ich habe bislang keine erfolglosen oder erfolgreichen Promotionsversuche unternommen.

Düsseldorf, am ....

(Unterschrift)

Abstract

According to the World Health Organization, 55 million people worldwide live with dementia in 2023. This number is expected to rise to over 130 million cases by 2050. The most common form of dementia is Alzheimer's disease, which accounts for 60-70% of all dementia cases. A hallmark of Alzheimer's disease is the aggregation of amyloid-β into insoluble fibrils and their subsequent accumulation into extracellular plaques. However, the polymorphic nature of amyloid-β fibrils has long posed a challenge to structural studies. But recent advances in the field of cryogenic electron microscopy have led to tremendous progress in the structural elucidation of amyloid fibrils and amyloid-β fibrils in particular. The aim of this study is to gain further molecular insights on amyloid-β fibrils that play an important role in Alzheimer's disease. Further, it provides an outlook on how structural investigations could contribute to the development of novel therapeutics and imaging tracers.

In this thesis, Alzheimer's disease is investigated at the molecular level within the framework of the following four projects.

(1) A common tool for studying Alzheimer's disease are animal models, particularly transgenic mice. In this study, the structures of nine amyloid-β fibrils extracted from brain tissue of six transgenic mice were determined. Five of the determined fibril structures observed in three different mice present novel amyloid-β fibril folds. Furthermore, amyloid-β fibrils similar to those found in humans, mostly in familial cases of Alzheimer's disease, were observed in three mice. Finally, one mouse showed amyloid-β fibrils similar to human amyloid-β fibrils, that are mostly observed in sporadic Alzheimer's disease cases.

(2) The study of *in vitro* amyloid-β fibrils under different fibrillisation conditions is key to finding a suitable laboratory model system for Alzheimer's disease. In this chapter, the *in vitro* fibril structures of synthetic amyloid-β42 fibrillised at neutral pH are presented. Of the nine polymorphs observed in the data set, a reconstruction was possible for six polymorphs. The medium-resolution maps did not allow for *de novo* atomic model, but a schematic C_α-backbone trace could be generated for all polymorphs, allowing comparison with other published amyloid-β fibril structures.

(3) Mutations in the amyloid precursor protein gene can cause early-onset familial Alzheimer's disease. This is also the case for the Uppsala mutation, a multi-codon deletion that results in the deletion of six amino acids within the amyloid-β sequence. In this work, first the structure of *in vitro* amyloid-βUpp(1-42)$_{\Delta 19\text{-}24}$ fibrils was determined. Afterwards, the structure of murine amyloid-βUpp(1-42)$_{\Delta 19\text{-}24}$ fibrils, which is different from both determined *in vitro* polymorphs, is presented. Finally, cryogenic electron microscopy data of amyloid-βUpp(1-42)$_{\Delta 19\text{-}24}$ fibrils purified from human brain tissue has been collected. Helical reconstruction yielded a high-resolution map for Tau paired helical filaments as well as medium resolution maps of Tau straight filaments and likely wild-type amyloid-β fibrils.

(4) The Icelandic mutation in the amyloid precursor protein gene is the only intra-amyloid-β APP mutation that is not associated with a familial form of Alzheimer's disease, but is protective against amyloid pathology and Alzheimer's disease. In this study, we first investigated whether A2T amyloid-β42 can form fibrils *in vitro*. Subsequently, A2T amyloid-β fibrils were studied by cryogenic electron microscopy and the structures of the two most abundant polymorphs were solved to high resolution. Interestingly, one polymorph is identical to a cryogenic electron microscopy structure of *in vitro* wild-type amyloid-β42 fibrils.

Zusammenfassung

Nach Angaben der World Health Organisation, leben im Jahr 2023 weltweit 55 Millionen Menschen mit Demenz. Es wird erwartet, dass diese Zahl bis zum Jahr 2050 auf über 130 Millionen Fälle ansteigen wird. Die häufigste Form der Demenz ist die Alzheimer Krankheit, die 60-70% aller Demenzfälle ausmacht. Ein charakteristisches Merkmal der Alzheimer Krankheit ist die Aggregation von Amyloid-β in unlösliche Fibrillen und deren anschließende Ansammlung in extrazellulären Plaques. Die polymorphe Natur der Amyloid-β Fibrillen hat jedoch lange Zeit eine Herausforderung für die Untersuchungen derer Struktur dargestellt. Die jüngsten Fortschritte auf dem Gebiet der Kryoelektronenmikroskopie haben allerdings zu enormen Fortschritten bei der Strukturaufklärung von Amyloidfibrillen und insbesondere von Amyloid-β Fibrillen geführt. Ziel dieser Arbeit ist es, weitere molekulare Erkenntnisse über Amyloid-β Fibrillen zu gewinnen, die bei der Alzheimer Krankheit eine wichtige Rolle spielen. Darüber hinaus gibt sie einen Ausblick darauf, wie strukturelle Untersuchungen zur Entwicklung neuer Therapeutika und bildgebender Tracer beitragen könnten.

In dieser Arbeit wird die Alzheimer Krankheit im Rahmen der folgenden vier Projekte auf molekularer Ebene untersucht.

(1) Ein gängiges Instrument zur Untersuchung der Alzheimer Krankheit sind Tiermodelle, insbesondere transgene Mäuse. In dieser Studie wurden die Strukturen von neun Amyloid-β Fibrillen bestimmt, die aus dem Gehirngewebe von sechs transgenen Mäusen extrahiert wurden. Fünf der ermittelten Fibrillenstrukturen, die in drei verschiedenen Mäusen beobachtet wurden, weisen neuartige Fibrillenfaltungen von Amyloid-β auf. Des Weiteren wurden in drei Mäusen Amyloid-β Fibrillen beobachtet, die denen ähneln, die im Menschen, insbesondere bei fa-

miliären Fällen der Alzheimer Krankheit, gefunden wurden. Zudem wies eine Maus Amyloid-β Fibrillen auf, die menschlichen Amyloid-β Fibrillen ähneln, die vor allem bei sporadischen Fällen der Alzheimer Krankheit beobachtet werden.

(2) Die Untersuchung von *in vitro* Amyloid-β Fibrillen bei verschiedenen Fibrillisationbedingungen ist ein wichtiger Schritt auf der Suche nach einem geeigneten Modellsystem für die Alzheimer Krankheit. In diesem Kapitel wird die *in vitro* Fibrillenstruktur von synthetischem Amyloid-β42, das bei neutralem pH-Wert fibrillisiert ist, vorgestellt. Von den neun im Datensatz beobachteten Polymorphen konnte eine Rekonstruktion für sechs Polymorphe berechnet werden. Die Dichtekarten bei mittlerer Auflösung ließen die *de novo* Erstellung eines atomaren Modells nicht zu, aber für alle Polymorphe konnte eine schematische Darstellung des C_α-Rückgrats erstellt werden, welches einen Vergleich mit anderen veröffentlichten Amyloid-β Fibrillenstrukturen ermöglichte.

(3) Mutationen im Amyloid-Precursor-Protein Gen können eine früh auftretende Form der familiären Alzheimer Krankheit verursachen. Dies gilt auch für die Uppsala-Mutation, eine Multi-Codon Deletion, die zur Entfernung von sechs Aminosäuren innerhalb der Sequenz von Amyloid-β führt. Im Rahmen dieser Arbeit wurde zunächst die Struktur von *in vitro* Amyloid-βUpp(1-42)$_{\Delta 19\text{-}24}$ Fibrillen bestimmt. Anschließend wird die Struktur von murinen Amyloid-βUpp(1-42)$_{\Delta 19\text{-}24}$ Fibrillen vorgestellt, die sich von beiden berechneten *in vitro*-Polymorphen unterscheidet. Zudem wurden kryoelektronenmikroskopische Daten von Amyloid-βUpp(1-42)$_{\Delta 19\text{-}24}$ Fibrillen gesammelt, die aus menschlichem Gehirngewebe aufgereinigt wurden. Die helikale Rekonstruktion ergab eine hochaufgelöste Dichtekarte von Tau "paired helical" Filamenten sowie Dichtekarten von Tau "straight" Filamenten und Amyloid-β Fibrillen, vermutlich Wildtyp, bei mittlerer Auflösung.

(4) Die isländische Mutation im Amyloid-Precursor-Protein Gen ist die einzige intra-Amyloid-β APP Mutation, die nicht mit einer familiären Form der Alzheimer-Krankheit assoziiert ist, sondern schützend gegen Amyloid-Pathologie und die Alzheimer Krankheit wirkt. In dieser Studie haben wir zunächst unter-

sucht, ob A2T Amyloid-β42 *in vitro* Fibrillen bilden kann. Anschließend wurden A2T Amyloid-β Fibrillen mit Hilfe der Kryoelektronenmikroskopie untersucht und die Strukturen der beiden häufigsten Polymorphe mit hoher Auflösung gelöst. Interessanterweise ist ein Polymorph identisch zu einer kryoelektronenmikroskopischen Struktur von *in vitro* Wildtyp-Amyloid-β42 Fibrillen.

During the course of my work at the Institute of Biological Information Processing - Structural Biochemistry (IBI-7) at Forschungszentrum Jülich from October 2019 to August 2023, the following manuscripts have been published or submitted to scientific journals:

Included in this thesis:

- **Publication I:**
  Zielinski, M.*, Röder, C.*, Schröder, G.F. Challenges in sample preparation and structure determination of amyloids by cryo-EM. *Journal of Biological Chemistry* 297.2 (2021).

  Received: 03 February 2021, Accepted: 28 June 2021, Published: 03 July 2021

- **Manuscript I:**
  Zielinski, M.*, Peralta Reyes, F.S.*, Gremer, L., Schemmert, S., Frieg, B., Willuweit, A., Donner, L., Elvers, M., Nilsson, L.N.G., Syvänen, S., Sehlin, D., Ingelsson, M., Willbold, D., Schröder, G.F. Cryo-EM Structures of Amyloid-β Fibrils from Alzheimer's Disease Mouse Models.

  Submitted to Nature Neuroscience: 18 June 2023.

  This manuscript was accepted (06 October 2023) and published (16 November 2023) in Nature Neuroscience as: **Zielinski, M.***, Peralta Reyes, F.S.*, Gremer, L., Schemmert, S., Frieg, B., Schäfer, L., Willuweit, A., Donner, L., Elvers, M., Nilsson, L.N.G., Syvänen, S., Sehlin, D., Ingelsson, M., Willbold, D., Schröder, G.F. Cryo-EM of Aβ fibrils from mouse models find tg-APP$_{\text{ArcSwe}}$ fibrils resemble those found in patients with sporadic Alzheimer's disease.

- **Publication II:**
  Pagnon de la Vega, M., Giedraitis, V., Michno, W., Kilander, L., Güner, G., **Zielinski, M.**, Löwenmark, M, Brundin, R.M., Danfors, T., Söderberg, L., Alafuzoff, I., Nilsson, L.N.G., Erlandsson, A., Willbold, D. Müller, S.A., Schröder, G.F., Hanrieder, J., Lichtenthaler, S.F., Lannfelt, L., Sehlin, D.,

Ingelsson, M. The Uppsala APP deletion causes early onset autosomal dominant Alzheimers disease by altering APP processing and increasing amyloid β fibril formation. *Science translational medicine*, 13.606 (2021).

Received: 05 May 2020, Accepted: 22 June 2021, Published: 11 August 2021

* These authors contributed equally

Not included in this thesis:

- **Publication III:**
  Schützmann, M.P.*, Hasecke, F.*, Bachmann, S., **Zielinski, M**, Hänsch, S, Schröder, G.F., Zempel, H, Hoyer, W. Endo-lysosomal Aβ concentration and pH trigger formation of Aβ oligomers that potently induce Tau missorting. *Nature Communications* 12.1 (2021).

  Received: 01 July 2020, Accepted: 14 July 2021, Published: 30 July 2021

- **Publication IV:**
  Cukkemane, A., Becker, N., **Zielinski, M.**, Frieg, B., Lakomek, N.-A., Heise, H., Schröder, G.F., Willbold, D., Weiergräber, O. H. Conformational heterogeneity coupled with β-fibril formation of a scaffold protein involved in chronic mental illnesses. *Translational Psychiatry* 11, 639 (2021)

  Received: 03 June 2021, Accepted: 07 December 2021, Published: 17 December 2021

  * These authors contributed equally

Contents

1. Introduction and Theoretical Background

1.1. Amyloids

1.1.1. History of Amyloid Research

The following section 1.1.1 has been adapted from Publication I: "Challenges in sample preparation and structure determination of amyloids by cryo-EM." [1]

Protein folding has long been explained exclusively by the Anfinsen dogma, which states that the folding of a protein is determined only by its primary sequence [2]. Nowadays, we know that there are exceptions to this rule. One major exception is the amyloid fold, which is an alternative fold that almost all proteins can adopt independent from their primary sequence [3, 4]. Rudolf Virchow considered the main building blocks of amyloids to be starch and therefore coined the term amyloid in the 19th century in reference to the Greek word for starch [5–7]. Shortly thereafter, amyloid deposits were found to be proteinaceous [5, 8]. Amyloid fibrils are formed by the aggregation of proteins into stacks of β-sheets, resulting in the so-called cross-β pattern, which is a major characteristic of the amyloid fold [3, 4, 9, 10]. Another important characteristics of the amyloid fold are enhanced birefringence through Congo Red staining [5, 11, 12] and the binding of Thioflavin T (ThT) [13]. More than 50 amyloids [3, 14, 15] are currently associated with protein misfolding diseases such as Alzheimer's Disease (AD) [16], Parkinson's Disease (PD) [17, 18], and Type II Diabetes (T2D) [19]. Such diseases, that involve the accumulation of amyloid fibrils in tissue, have been combined under the term amyloidosis [20]. The proteins that are involved in these diseases,

like Amyloid-β (Aβ) (from AD) or α-synuclein (from PD), are often intrinsically disordered proteins (IDPs). However, functional amyloids found mainly in fungi or bacteria have also been described [21–24]. Here, they often act as defense mechanism against other species. To date, it is still unclear why such a variety of proteins are able to adopt the fibrillar fold, either functional or pathogenic. Neither is the mechanism behind protein aggregation from an IDP or globular fold into an amyloid understood.

1.1.2. Alzheimer's Disease

According to the World Health Organisation (WHO), dementia is the seventh leading cause of death worldwide and one of the leading causes of disability in the elderly population [25]. In 2020, more than 55 million people worldwide were living with dementia, with the proportion of German dementia patients over 65 years of age at about 1.7 million in 2021 [26, 27]. Globally, this number is expected to increase by 20 million annually and, consequently, 113 million cases are expected to be counted in 2050 [28]. The resulting high socioeconomic burden of dementia makes finding a treatment or prevention one of the most imperative public health challenges [29]. The most common form of dementia is AD, which accounts for about 60-70% of all dementia cases [25]. AD is a genetic neurodegenerative disease clinically characterized by progressive memory loss and cognitive impairment [30]. Alois Alzheimer was the first to describe the "eigenartige Erkrankung der Hirnrinde" (translated freely: peculiar disease of the cerebral cortex) in 1906 when he found protein deposits, namely neurofibrillary tangles (NFTs) and senile plaques, in and between nerve cells in the brain tissue of his patient [31, 32]. Today we know that in addition to these pathological hallmarks, other neuropathological characteristics of AD include the presence of neuropil threads and the loss of specific neurons and synapses [16].

The main component of extracellular neuritic plaques, that can be found in the cerebral cortex, is aggregated Aβ [30]. Additionally, Aβ can accumulate in the blood vessels of the meninges, damaging the vascular wall [30, 33]. The resulting cerebral amyloid angiopathy (CAA) leads to microhaemorrhages in the brain [30, 33]. Intra-cellular NFTs consist mainly of tau, a microtubule-associated protein

(MAP) whose physiological function is to stabilise microtubules [34, 35]. Phosphorylation of tau, which is possible at many different phosphorylation sites, can control physiological, but also pathological function and therefore also the ability to self-assemble into neuronal filaments [36].

1.1.3. Amyloid-β and its link to Alzheimer's disease

Parts of the following section 1.1.3 have been adapted from Publication I: "Challenges in sample preparation and structure determination of amyloids by cryo-EM." [1].

Production of Aβ Aβ is a 4.2 kDa peptide derived from the amyloid precursor protein (APP) [37]. The single-pass transmembrane protein APP is localized on chromosome 21 in humans [38] and while the physiological function of APP ist not entirely understood, it is suggested to be involved in brain development, synaptic plasticity, memory, and neuroprotection [38, 39].

APP can be processed in two different ways, the non-amyloidogenic pathway (Figure 1.1 A) and the amyloidogenic pathway (Figure 1.1 B), involving the three proteases α- β- and γ-secretase [40].

In the non-amyloidogenic pathway, APP is first cleaved by the α-secretase A Disintegrin And Metalloprotease 10 (ADAM10) resulting in the production of sAPPα (extracellularly released) and the C83 fragment, which is retained in the membrane [41, 42]. Subsequently, the cleavage of C83 by γ-secretase produces the soluble P3 (extracellularly released) peptide and the APP intracellular domain (AICD) [41, 42]. γ-secretase is made of four protein subunits: presenilin (PSEN) (PSEN1 or PSEN2), presenilin enhancer (PEN), APH (APH-1a or APH-1b) and Nicastrin [43].

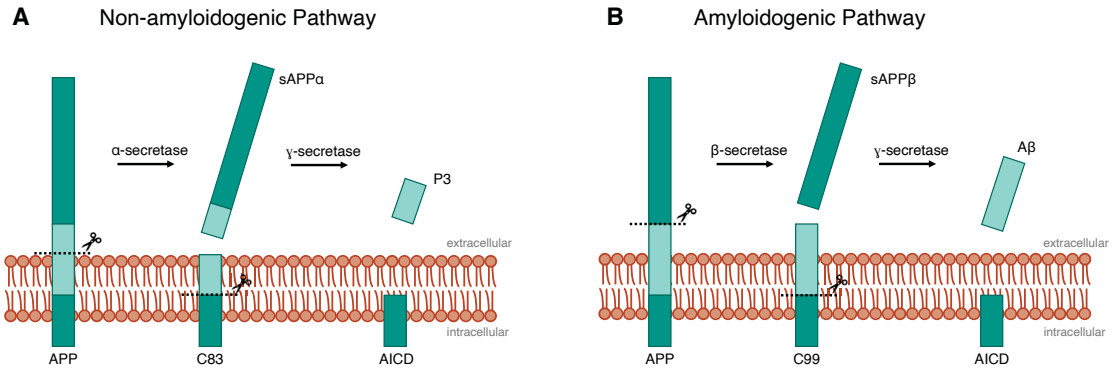

Figure 1.1.: APP processing. (A) In the non-amyloidogenic pathway, APP is first cleaved by α-secretase, leading to the production of the C83 and the sAPPα-fragment. Subsequent cleavage by γ-secretase leads to the formation of AICD and the P3 peptide. (B) In the amyloidogenic pathway, APP is first cleaved by β-secretase, leading to the formation of the C99 fragment and the sAPPβ fragment. Subsequent cleavage by γ-secretase leads to the formation of Aβ and AICD. (Adapted and modified from Hampel et al. [44])

In contrast, in the amyloidogenic pathway, APP is first cleaved by the β-secretase BACE1 producing the extracellularly released sAPPβ fragment and the C99 fragment remaining in the membrane [37]. The subsequent cleavage of the latter by γ-secretase results in the production of the Aβ peptide [37].

Typically, depending on γ-secretase cleavage, monomers with a length of 37 to 43 residues are generated [45]. The most abundant peptides are 40 (Aβ(1-40)) residues in length, however, the more hydrophobic 42 residue long Aβ42 is assumed to drive aggregation and in a consequence also plaque deposition [46].

Aggregation of Aβ Aβ self-aggregates into various assemblies (Figure 1.2). This aggregation is presumed to follow two major pathways leading to either Aβ fibrils (on-pathway) or other aggregates, such as oligomers or protofibrils (off-pathway).

On-pathway (Figure 1.2, solid arrows), disordered monomers aggregate into fibrillar oligomers that serve as precursors for the formation of insoluble mature fibrils. Insoluble plaques found in brain tissue of AD patients [47, 48] form from accumulation of mature Aβ fibrils along with other cellular components. The initial formation of fibrillar oligomers, also referred to as primary nucleation, is considered a rare event since it requires multiple monomers to arrange into the

fibril fold that allows for hydrogen bonding and steric interactions [49]. However, once a fibrillar oligomer has formed, the attachment of monomers to the ends of an existing fibril (elongation) can occur at a higher rate [49]. And although the exact pathway of Aβ fibril formation remains elusive, there are studies suggesting a conformational conversion of fibrillar oligomers into fibrils [50]. Additionally, fibrils can form through (cross-)seeding [51] and secondary processes like fragmentation of existing fibrils or secondary nucleation (Figure 1.2, bottom) [52].

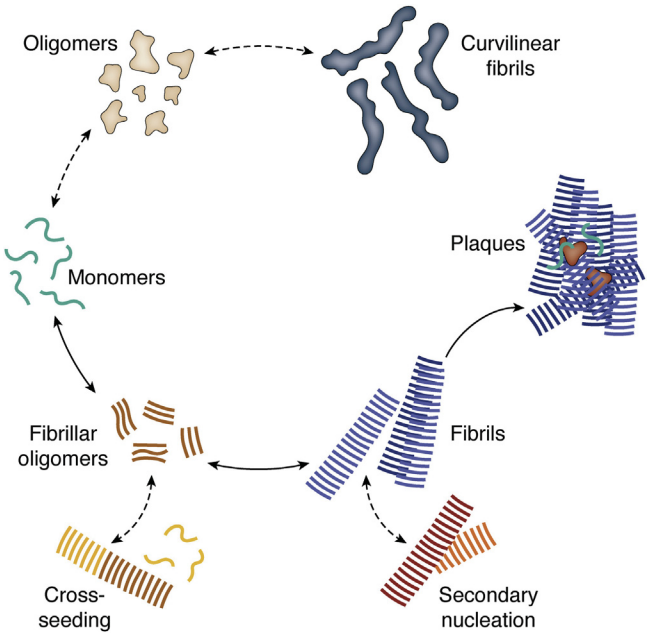

Figure 1.2.: Amyloidogenic proteins aggregate into structurally distinct species via different pathways. Monomeric proteins (green) can follow the on-pathway (solid arrows) and aggregate into fibrillar oligomers (brown), which in turn grow into mature fibrils (blue) that can eventually, together with other cellular components, be deposited as plaques. Fibrillar oligomers could seed the formation of fibrils with monomers of a different protein (yellow, cross-seeding). In addition, monomers can attach to one fibril, leading to the growth of a mature fibril on the surface of another, which is called secondary nucleation (red). Off-pathway (dotted arrows), monomers aggregate into soluble aggregates of intermediate size, such as oligomers (beige), which can serve as precursors for the formation of curved fibrils (dark blue). (adapted from Zielinski et al. [1]).

In secondary nucleation, monomers attach to a mature fibril and form a new fibril (Figure 1.2, red/orange) that eventually detaches from the original fibril [53]. In addition, during cross-seeding, fibrillar oligomers or mature fibrils of one protein

can be a seed for the formation of fibrils with monomers of another protein (Figure 1.2, brown/yellow) [54, 55].

Off-pathway (Figure 1.2, dashed arrows) aggregation of Aβ monomers leads to the formation of soluble Aβ oligomers, which might eventually aggregate into curvilinear fibrils [56–61]. The aggregation mechanism of on- and off-pathway oligomers and amyloid fibrils and their role in pathology remains unclear [62–64], but evidence is accumulating that not amyloid fibrils but amyloid oligomers, especially those following the off-pathway, constitute the pathogenic species in amyloidoses (compare *"The Amyloid Cascade Hypothesis"*) [65–68].

Two forms of Alzheimer's Disease AD can be divided into two classes according to the age of symptom onset and genetic predisposition. For late-onset AD (LOAD) or sporadic AD (sAD), which accounts for more than 95% of all AD cases, symptoms usually appear after the age of 65. In contrast, for early-onset AD (EOAD) or familial AD (fAD), which affects less than 5% of all AD patients accordingly, symptoms start before the age of 65. [69]

The exact cause of sAD is not fully understood, but it is thought to be a combination of genetic risk factors and environmental influences, with age being the greatest risk factor [30, 70, 71]. The presence of the ϵ4 allele in Apolipoprotein E (APOE), a protein involved in lipid metabolism, is the only confirmed genetic risk factor for sAD [71, 72]. APOE is thought to regulate Aβ clearance in the brain and exists in three forms: ϵ2, ϵ3, and ϵ4 with ϵ3 being the most common form among the general population [72, 73]. While carriers of the rather rare APOE ϵ2 allele have a decreased risk of developing AD, the risk is increased three- to 12-fold for carriers of one or two copies of the APOE ϵ4 allele in comparison to APOE ϵ3 [30, 71, 74].

In contrast, fAD is caused by familial mutations in the APP, PSEN1, and PSEN2 genes, with mutations in PSEN1 responsible for most fAD cases [46, 71]. Additionally, trisomy 21 (Down syndrome) causes fAD, most likely due to the fact that individuals with down syndrome have a supernumerary chromosome 21 and therefore, also an additional copy of APP [75–77]. Mutations in PSEN1 alter γ-secretase cleavage and therefore, cause an increase in the production of more aggregation prone Aβ42 over Aβ40 [78]. Mutations in APP are responsible for 10-15% of all

fAD cases [79]. Today, 70 APP mutations are known, 22 of which lie within the sequence of Aβ [80].

The *Swedish* mutation adjacent to the β-secretase cleavage site, is a pathogenic double mutation with residues K670 and M671 being replaced by N670 and L671, respectively, which results in an overall increased production of Aβ (Figure 1.3) [81].

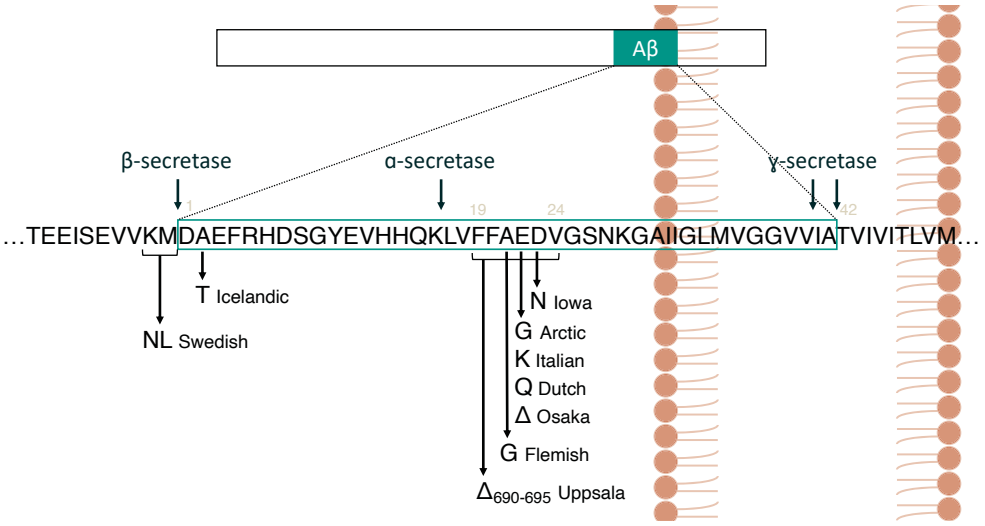

Figure 1.3.: A selection of fAD causing APP mutations close to or within the Aβ sequence. The Aβ sequence is outlined in green. The β, α and γ secretase cleavage sites are marked. (modified from Pagnon de la Vega et al. [82]).

In contrast, one of the first mutations within the sequence of Aβ, the *Icelandic* mutation A2T (A673T in APP), is not pathogenic but results in a reduced production of Aβ and is the only known mutation that protects against AD [83].

The region around residues F19-V24 harbours several pathogenic Aβ mutations. The *Flemish* mutation A21G (A692G in APP) was first reported in a Dutch family in which family members from four generations suffered from AD or cerebral hemorrhages associated with CAA [84]. Here, *in vitro* studies show increased secretion of Aβ40 and Aβ42 [85], but a decreased aggregation propensity of Aβ [86]. The *Italian* mutation E22K (E693K in APP) and the *Dutch* E22Q (E693Q in APP) mutation both cause a severe hereditary form of CAA in mutation carriers [87–89]. In contrast, the *Arctic* mutation E22G (E693G in APP) does not result in CAA, but instead is characterized by increased Aβ40 protofibril formation [90]. All mis-

sense mutations at residue 22 (Italian, Dutch, Arctic) have in common that they lead to lower levels of Aβ42 and consequently to a reduced Aβ42/Aβ40 ratio, and to an accelerated aggregation of Aβ into protofibrils and/or fibrils *in vitro* [90, 91]. Furthermore, these mutations show autosomal dominant inheritance. The *Osaka* mutation E22Δ (E693Δ in APP) is the only known intra-Aβ single point deletion and, in contrast to missense mutations at position 22, this mutation leads to a recessive inheritance pattern [92]. Interestingly, the mutation leads to an overall decreased production of Aβ and an unchanged Aβ42/Aβ40 ratio. In addition, increased oligomerisation, but no fibrillisation, was observed for Aβ mutants *in vitro*. The *Iowa* mutation D23N (D694N in APP) has been found to cause autosomal dominant inherited vascular dementia with an enhanced fibrillogenesis and a greater pathogenicity in cell assays compared to wild-type Aβ40 [93, 94].

The *Uppsala* mutation (690-695Δ) is the first known multi-codon deletion mutation in APP leading to AD [82]. The mutation, which was found in three individuals of one family from Uppsala (Sweden), causes an autosomal dominantly inherited form of early onset fAD. For all three mutation carriers, an early symptom onset around age 40 as well as a rapidly progressing disease course was reported. Computed Tomography (CT) scans show typical characteristics of AD, however, positron emission tomography (PET) imaging with the amyloid dye [^{11}C]-labeled Pittsburgh Compound B (PIB) shows only a slightly pathological pattern. Analysis of postmortem brain tissue fit typical AD pathology, showing abundant deposition of extra-cellular Aβ plaques, mainly consisting of AβUpp(1-42)$_{\Delta 19-24}$ or an N-terminal truncated form, as well as intracellular NFTs. Moreover, it was found that the mutation leads mainly to Aβ42 pathology while it also alters APP processing resulting in an increased production of Aβ. In addition, *in vitro* aggregation experiments confirm a faster aggregation of AβUpp(1-42)$_{\Delta 19-24}$ into fibrils. [82]

The Amyloid Cascade Hypothesis

Hardy and Higgins formulated the first theory on the neurodegenerative cause of AD in 1992 [95], after Alois Alzheimer first described the neuropathological hallmarks (senile plaques and NFTs) of AD in 1906. They state: *"Our hypothesis is that deposition of amyloid β protein (AβP), the main component of plaques, is*

the causative agent of Alzheimer's pathology and that the neurofibrillary tangles, cell loss, vascular damage, and dementia follow as a direct result of the deposition" [95].

The fact that patients suffering from Down syndrome have a higher risk of developing AD supports their theory [76, 95]. In addition, mutations in PSEN1 and PSEN2 that cause an increased production of longer over shorter Aβ peptide lead to severe forms of fAD [96]. Moreover, carriers of the APOE ϵ4 allele, which promotes Aβ clearance with a decreased efficiency, have been shown to have a higher risk of developing AD [97]. Furthermore, several studies confirm a synaptotoxic effect of Aβ aggregates *in vitro* and in *in vivo* models [96]. However, it has been shown that amyloid plaques can also be found in patients who do not show AD-associated cognitive impairment [98, 99], which contradicts the hypothesis of Hardy and Higgins. Moreover, recent studies suggest that soluble Aβ aggregates such as oligomers rather than insoluble fibrils are the toxic species in AD, as they correlate more strongly with symptoms and severity [96, 100].

Nevertheless, the amyloid cascade hypothesis as well as other proposed theories shed some additional light on this versatile disease and might help developing efficient therapeutics and imaging tracers in the future [101, 102].

Post Translational Modifications Proteins can undergo chemical modifications after their biosynthesis [103, 104]. Among other things, such Post Translational Modifications (PTMs) influence the activity, structure and stability of proteins and are hence responsible for many biological processes [103, 105]. However, some PTMs are also associated with diseases, including Alzheimer's disease, where common PTMs of APP, secretases, tau and Aβ include phosphorylation, glycosylation, ubiquitination, SUMOylation, and acetylation [105, 106]. Such PTMs are thought to play an important role in the development and progression of the disease, and therefore structural studies of PTMs of Aβ, comparable to those already conducted for tau [107, 108], α-synuclein [109], and AL amyloid fibrils [110], could be a key element in identifying novel biomarkers and drug targets [105].

1.1.4. Alzheimer's Disease - Research models and Therapeutics

To date, there is no cure for AD, however, more than 400 therapeutic candidates have been assessed in AD trials between 2002 and 2012 [111]. Therapeutic approaches tested include inhibitors of β-secretase [112, 113], γ-secretase [114, 115], and monoclonal antibodies (mAb) against Aβ [116]. In 2022, four mAbs were in late-phase clinical development [117]: aducanumab [118], donanemab [119], gantenerumab [120], and lecanemab [121]. Two of them, aducanemab and lecanemab, have been approved by the US Food and Drug Administration (FDA) in 2021 and 2023, respectively [117, 122]. While aducanemab binds with higher selectivity to Aβ fibrils than to protofibrils, lecanemab was designed to bind mainly soluble oligomers and protofibrils [117, 123]. However, recent studies also suggest interactions between lecanemab and *"diffusible Aβ fibrils"* that were present *"in ultracentrifugal supernatants of aqueous extracts from AD brains"* and that are structurally identical to insoluble Aβ fibrils found in plaques [124]. Nevertheless, developing therapeutics against AD is a challenging task with a drug development failure rate of almost 100% [111]. The preclinical screening of novel therapeutics and the study of the pathogenesis of AD are often carried out in animal models [125]. The most commonly used animal models are genetically modified transgenic mice, which mimic some of the clinical hallmarks of the disease such as the accumulation of amyloid by expressing human APP (alone or in combination with PSEN1) and human MAPT resulting in the formation of amyloid plaques and NFTs, respectively [126]. For some time, however, it has been questioned whether mouse models mimic human AD pathology sufficiently well. In particular, the fact that transgenic mice carry fAD mutations raises the question of how well these models describe sAD pathology, which accounts for more than 95% of all AD cases [96, 127].

1.2. Cryogenic Electron Microscopy

Structural biology aims to understand the molecular composition of biological macromolecules in order to elucidate their function and interaction with their environment [128]. There are three major analytical techniques to determine a proteins

structure: X-ray crystallography, Nuclear Magnetic Resonance (NMR) spectroscopy and Electron Microscopy (EM) (Figure 1.4) [129]. In NMR-spectroscopy structural information is extracted from the detection of the chemical environment of atomic nuclei [130] and while this method works well for small proteins, it becomes complicated for larger protein complexes. In X-ray crystallography the X-ray diffraction pattern of protein crystals is used to determine the high-resolution three dimensional (3D) structure of proteins [131]. And even though protein structures determined by X-ray crystallography usually reach high resolution, this technique requires the protein of interest to crystallise. In 2017 Jacques Dubochet, Joachim Frank and Richard Henderson received the Nobel Prize in Chemistry "for developing cryo-electron microscopy for the high-resolution structure determination of biomolecules in solution" [132].

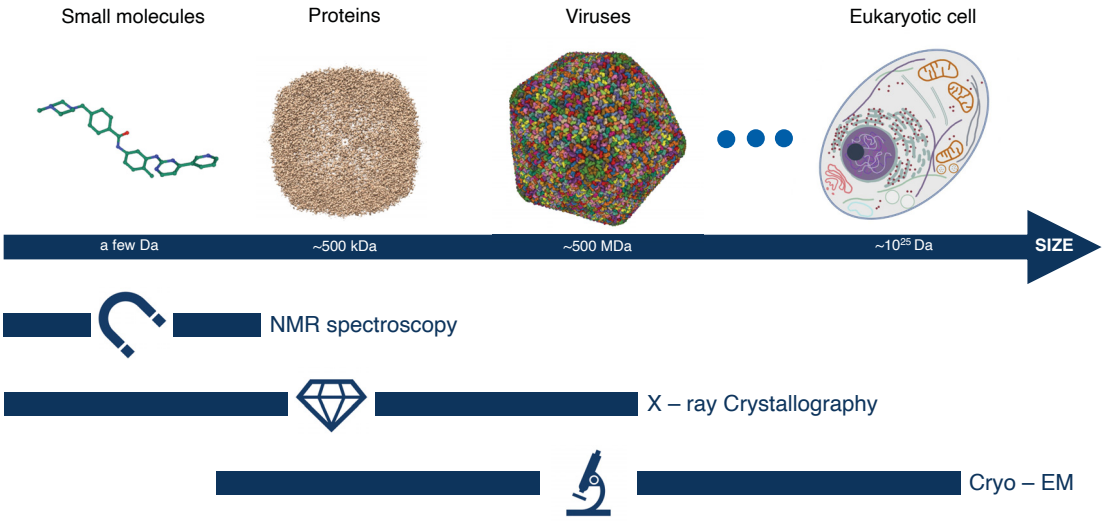

Figure 1.4.: Overview of the analytical techniques used in structural biology. While NMR spectroscopy is suited for the structure determination of peptides and small proteins, X-ray crystallography technically has no size limitation to protein structure determination, but requires the protein of interest to crystallize. The smallest published cryo-EM structure is from a 43 kDa protein [133]. Cryo-electron tomography enables the *in situ* investigation of a protein in its cellular context. The following PDB entries were used for this illustration: 2HYY (ligand; small molecule), 6Z6U (protein), 6NCL (virus).

Cryogenic Electron Microscopy (cryo-EM) is a microscopy technique that is based on Transmission Electron Microscopy (TEM) and is used to image radiation

sensitive specimens under cryogenic conditions.

This section includes a brief overview on the development of cryo-EM followed by a theoretical introduction into the architecture of a typical TEM and image formation and finally, an overview on a typical cryo-EM workflow.

1.2.1. A short history on the development of Cryo-EM

Parts of the following section 1.2.1 have been adapted from Publication I: "Challenges in sample preparation and structure determination of amyloids by cryo-EM." [1]

In 1929 Louis de Broglie was awarded the Nobel Prize for Physics "for his discovery of the wave nature of electrons" [134]. The so-called wave-particle duality found its first practical application when Ernst Ruska together with Max Knoll developed the first EM in 1931 [135]. The wavelength of electrons depends on their velocity and therefore, can be significantly smaller than the wavelength of visible light. Thus, when transferring the discoveries of Ernst Abbe in 1873 [136] to matter waves of electrons, the resolution that can be achieved in an EM is much higher than the resolution of a light microscope. And although, Ruska's first prototype could not achieve a higher resolution than a light microscope [137], it eventually, after some improvements, significantly influenced the development of modern science. Ruska was awarded with the Nobel Prize in Physics in 1986 "for his fundamental work in electron optics, and for the design of the first electron microscope" [138].

However, in order to image biological samples in an EM, some technical difficulties had to be overcome initially. Firstly, the high-energy electrons used for imaging can easily destroy biological samples. In addition, EMs operate in ultra-high vacuum to avoid scattering of the electron beam by air molecules. However, this can damage or destroy biological macromolecules because they are largely composed of water, which would evaporate immediately when exposed to the vacuum. [139, 140]

The development of shadowing [141] and negative stain EM [142] enabled ima-

ging of biological samples in an EM for the first time, leading to the first 3D structure of the extended tail of a T4 bacteriophage [143, 144]. In negative stain EM, the accessible sample surface is coated with electron-dense solutions, such as uranyl acetate, phospho-tungstates, ammonium molybdate or lanthanide-based stains, that are less sensitive to radiation damage [142, 145]. Nowadays, negative stain is still used as a first step to investigate sample concentration and quality, however, the resolution is limited to a maximum of ~20 Å and therefore, high-resolution structural information cannot be extracted from negative stain images [145].

Jacques Dubochet developed cryo-EM by devising a technique to create a thin layer of amorphous ice by placing a thin film of water in liquid ethane, thus finding a way to preserve biological specimens in an EM [146, 147]. However, the number of electrons that can be scattered from a biological sample before it gets destroyed is limited [139]. The first successful application of cryo-EM was the determination of the atomic structure of bacteriorhodopsin by Richard Henderson, who recorded low-dose EM images of its protein crystal [148]. However, in the beginning, cryo-EM did not routinely deliver high-resolution structures and thus, has often been referred to as "blobology". The acquisition of images on photographic film and the challenging reconstruction process made a structure determination project time-consuming and complex. The development of Charged-Coupled Device (CCD) cameras and later Direct Electron Detector (DED)'s as a replacement for photographic film has been one major step forward in the field, firstly speeding up data acquisition and secondly providing a better Signal-to-Noise Ratio (SNR) [149–152]. Another important factor that has contributed to cryo-EM becoming a powerful and widely used tool in structural biology has been computational development, such as the Single Particle Reconstruction (SPR), based on the work of Joachim Frank [153, 154]. Frank and Penczek [155] developed a technique called "projection matching", in which experimental projection images of the protein of interest in different orientations are compared with projection images from an initial reference, allowing for the assignment of orientations to the experimental projection images. These techniques, along with Marin van Heel's reconstitution method [156], which made sample tilting redundant, form the basis for today's software packages [157].

1.2.2. Architecture of a Transmission Electron Microscope

Unless otherwise stated, the following descriptions are based on [158], [159] and [160].

A typical TEM column (Figure 1.5) can be divided into five parts: the electron gun, the condenser lens system, the objective lens system, the projector lens system and the detector. In the following, the major components along the microscope column are described and their function is briefly explained.

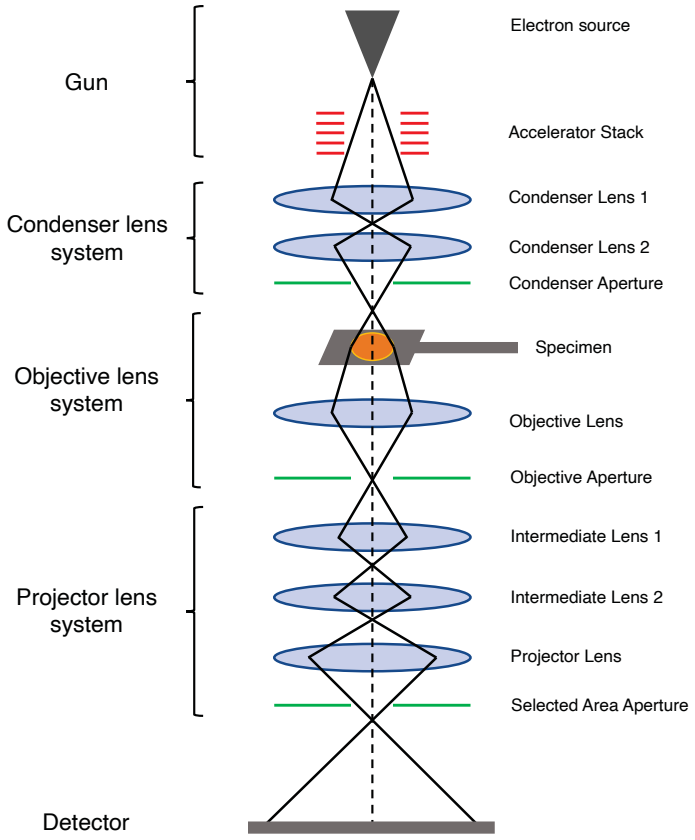

Figure 1.5.: Schematic of a typical TEM architecture. Electrons are emitted from the electron source and and accelerated by the accelerator stack. The condenser lens system focuses the electron beam onto the specimen. Afterwards, the image is magnified by the objective lens system and the projector lens system. The magnified image is recorded on the detector. (Inspired by [160])

The electron gun is located at the very top of the column and in a modern TEM

consists of an electron source and an accelerator stack. Nowadays, a Field Emission Gun (FEG) is usually used as electron source. In short, an electric field below the tip causes the electrons to tunnel out of it, which results in a more monochromatic and coherent electron beam. Emitted electrons are then accelerated down the microscope column by the accelerator stack and focused onto the specimen by the condenser lens system, which typically consists of two condenser lenses, that control the spot size (C1) and the beam intensity (C2), and a condenser aperture. The objective lens below the specimen produces a magnified image of the sample. The objective aperture ensures that only unscattered electrons and electrons scattered at a small angle pass through the adjacent projector lens system, where the image is further magnified.

In an EM, electromagnetic lenses are used to focus the coherent high-energy electrons. In order to compensate for a number of imperfections, these lenses are usually part of a lens system. Firstly, an electromagnetic lens typically does not produce a perfectly symmetrical magnetic field, which results in an oval-shaped beam. This so-called lens astigmatism is corrected by stigmators in the microscope. In addition, the lenses exhibit Spherical Aberration (C_s) and Chromatic Aberration (C_c). C_s arises from electrons passing the lens closer to its center are exposed to a weaker force than those passing it closer to the coils. To overcome this problem, small opening angles, coma free alignment and a C_s corrector are used. C_c occurs because electrons with lower energy are more strongly focused than electrons with higher energy. A monochromator and an energy filter can be used to overcome C_c.

Finally, the magnified image is recorded on photographic film, a CCD camera or a DED. Until a few years ago, photographic film was commonly used in EM, however, the process of developing and digitising the images is very time consuming and lacks the possibility of feedback during imaging. Detector quality can be measured by the Detective Quantum Efficiency (DQE), which measures how the SNR is further decreased by errors in the detection process. Accordingly, an ideal detector would not add any noise to the image and therefore, have a DQE=1. An alternative to photographic film are CCD cameras, that enable the automatic collection of data. In a CCD camera, incoming electrons hit a scintillator material and thereby generate photons, which then generate counts on the CCD chip. However, the thickness of the device causes undesired scattering events that blur

the signal on the detector. The DQE of a CCD camera is therefore, comparably low. A major contribution to the resolution revolution in cryo-EM has been the introduction of DED's. In a DED the electrons get directly detected when hitting a Complementary metal-oxide-semiconductor (CMOS) detector. Image blurring is further reduced by the thin detection layer that makes back-scattering of electrons less likely. Moreover, the recording speed is increased due to a faster readout of the CMOS detector. DED's can be operated in integration and counting mode. In integration mode, the incoming electrons built up charges over the exposure time. In contrast, in counting mode, individual electrons are detected. In addition, rapid processing of a DED allows for the tracking of beam-induced sample motion and the incorporation of radiation damage to the sample by recording movies instead of images. Finally, DED's achieve much higher DQE's than CCD cameras [161].

The Nyquist-Shannon sampling theorem defines the maximal achievable resolution to be twice the detector pixel size. In practice, however, this resolution, often referred to as the Nyquist limit in the field of cryo-EM, is not achievable due to aliasing and the properties of the detector [162, 163]. Aliasing decreases the achievable resolution by introducing artifacts when the generated image on the detector contains frequencies above the Nyquist limit, while the detector limits the resolution due to the decreasing DQE at higher frequencies close to the Nyquist limit [163].

1.2.3. Image Formation in Cryo-EM

Unless otherwise stated, the following descriptions are based on [158], [159] and [160].

In a TEM, the electrons can interact with the sample in three different ways. Most electrons pass through the sample without interaction and thus hit the detector as unscattered electrons. Next, the electrons could interact with the sample, depositing energy in the sample, resulting in a decrease in energy. These inelastically scattered electrons are usually deflected at a small angle from their incident path. The deposition of energy in the sample by inelastic scattering events causes radiation damage, which is one major resolution limitation in cryo-EM. The last

possible interaction is that the electrons interact with the atomic Coulomb potential of the sample and are scattered, but without losing energy. These elastically scattered electrons are usually scattered at a higher angle.

There are two types of image contrast in a TEM: amplitude and phase contrast. Amplitude contrast is generated by the effect that not all electrons that interact with the sample eventually contribute to the image formation on the detector. Electrons that get scattered at a high angle and inelastically scattered electrons are removed by the objective aperture and the energy filter, respectively. In dense areas of the sample, electrons get scattered more strongly and therefore, less electrons get detected at this area of the sample. Only unscattered electrons and electrons that are elastically scattered under a small angle reach the detector. Phase contrast results from the fact that electrons are scattered at different angles, which causes phase shifts. The interference of all elastically scattered electrons with the unscattered ones produces phase contrast. However, in biological samples, which are mainly composed of light atoms, the scattering angle is usually small resulting in only small phase shifts. Additionally, the amplitude of the scattered electrons is very small. This results in a weak contrast in the focused image. Therefore, phase contrast is usually generated by imaging out of focus, which causes a phase shift of the scattered electrons. In combination with the effect of the C_s of the objective lens, this can be described in Fourier Space by the Contrast Transfer Function (CTF). Equivalently, this effect is described in real space by the Point Spread Function (PSF), which accordingly describes the blurring effect in the image caused by missing, attenuated and inverted Fourier components. The CTF can be estimated and corrected for during image processing, however, the information close to $CTF \approx 0$ can not be recovered and therefore, it is necessary to collect images at different defocus values. The effect of the defocus on an image and the CTF is visualised in Figure 1.6.

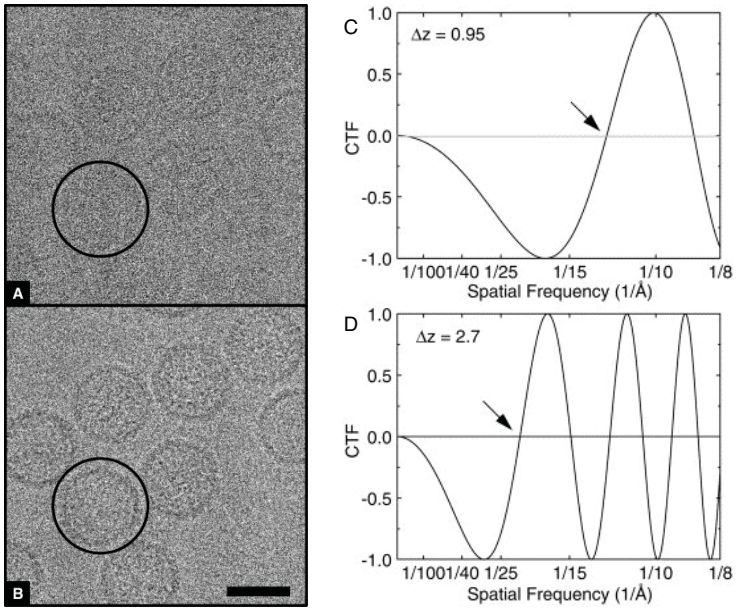

Figure 1.6.: Cryo-EM images of bacteriophage P22 procapsid at a defocus value of (A) 0.95 μm and (B) 2.7 μm and simulations of the corresponding CTF's for a defocus of (C) 0.95 μm and (D) 2.7 μm (adapted from Thuman-Commike and Chiu [164]).

Mathematically, the CTF can be modeled as given in equation 1.2.1

$$CTF = \sin(-\pi \Delta z \lambda_e k^2 + \frac{\pi}{2} C_s \lambda_e^3 k^4 + \phi) \tag{1.2.1}$$

with defocus Δz, the wavelength of the incident electrons λ_e, the spherical aberration C_s, and the spatial frequency k. ϕ is a phase shift factor, that is introduced e.g. when a phase plate is used for imaging.

1.2.4. Cryo-EM Workflow

Parts of the following section 1.2.4 have been adapted from Publication I: "Challenges in sample preparation and structure determination of amyloids by cryo-EM." [1]

A typical cryo-EM workflow consists of four steps (Figure 1.7): Sample preparation including protein purification and plunge freezing (Figure 1.7 A), Microscope data acquisition (Figure 1.7 B), Image Processing with the major steps of particle

selection, 2D classification as well as 3D reconstruction and density refinement (Figure 1.7 C) and finally, Model building and refinement (Figure 1.7 D).

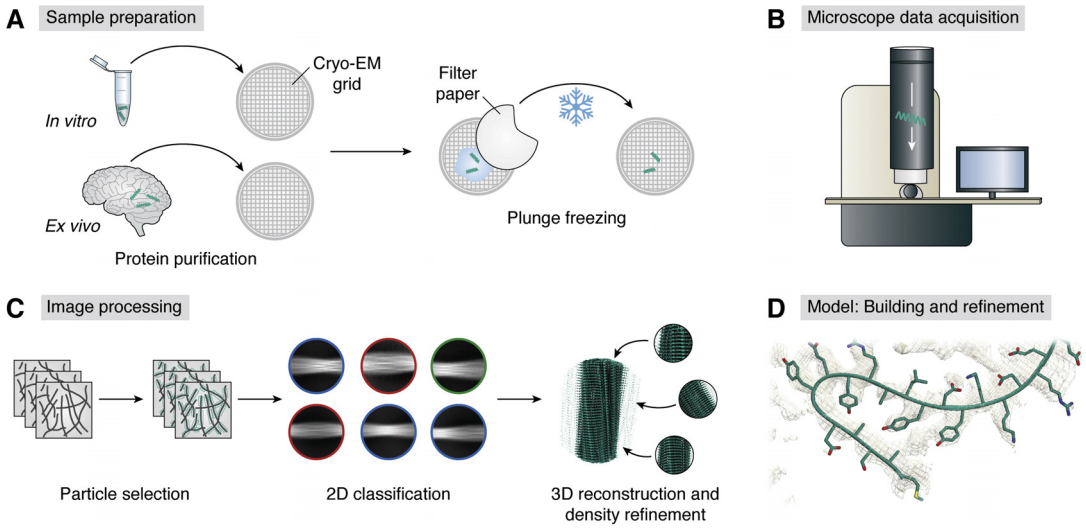

Figure 1.7.: Cryo-EM Workflow. (A) The first step of a cryo-EM structure determination project is the sample preparation including the steps of sample purification and the cryo-EM grid preparation. In the latter the sample is applied onto an EM grid, excess liquid is blotted off using filter paper and the grid is plunged in liquid ethane to create a thin film of vitreous ice. (B) Afterwards the prepared cryo-EM grids are screened and a dataset is collected on a microscope equipped with a DED. (C) The following image processing of the recorded data includes the major steps of particle selection, 2D classification, 3D reconstruction and density refinement. (D) As soon as the reconstructed map reaches high enough resolution, an atomic model can be built and refined. (Adapted from Zielinski et al. [1]).

In the following each step is described in more detail.

Sample Preparation To produce a usable sample for cryo-EM, the sample protein does not need to be isotopically labeled (NMR) or crystallised and treated with a crystallisation screening solution (X-ray). However, also for cryo-EM, sample preparation must be optimised to find conditions that yield thin ice and a sufficient particle concentration (50 nM - 5 μM) [165]. Therefore, biochemical assays are a first step to investigate the quality of a sample in terms of protein composition and homogeneity to find the optimal imaging conditions [166]. When the protein is embedded in a thin film, which is required for cryo-EM imaging, the resulting

high surface-to-volume ratio can affect the stability of the protein complex causing preferred orientation, denaturation or aggregation of the protein [167, 168]. This problem can be addressed by adjusting buffer conditions (e.g. salt concentration, pH value, additives, detergents) [166]. Finally, after biochemical assessment of the sample, negative stain EM is usually used as a fast screening method to visually evaluate sample concentration and homogeneity and, additionally, to determine if the buffer conditions need to be adjusted [168, 169].

Vitrification After successful purification of the protein of interest, a few microliters (~2 - 5 μL) of the sample solution are applied to an EM grid (Figure 1.8 A). During this process, the grid is typically kept in a humidity and temperature controlled environment [166].

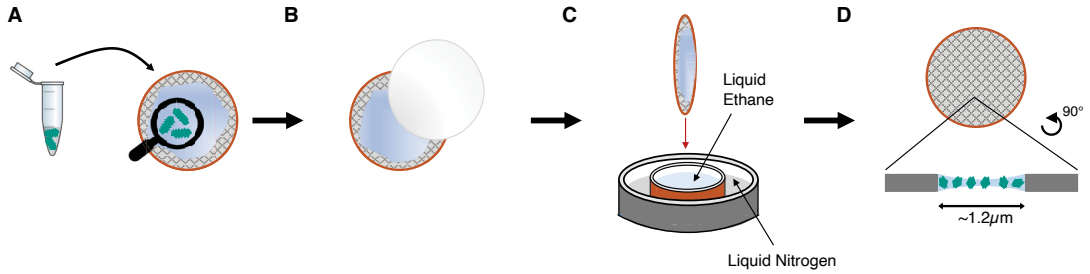

Figure 1.8.: Typical Cryo-EM Sample Vitrification Workflow: (A) The sample solution is applied onto a grid and (B) the excess liquid is blotted off using filter paper. (C) Afterwards the grid is plunge frozen in liquid ethane at approximately -170°, (D) leaving the sample in a thin film of vitreous ice.

EM grids usually are ~3 mm in diameter and consist of a mesh base made of copper, gold or nickel and a thin foil attached to it [168]. The foil can have regularly arranged holes of constant size (Quantifoil, Figure 1.9 A) or irregular arranged holes of various size (Lacey, Figure 1.9 B).

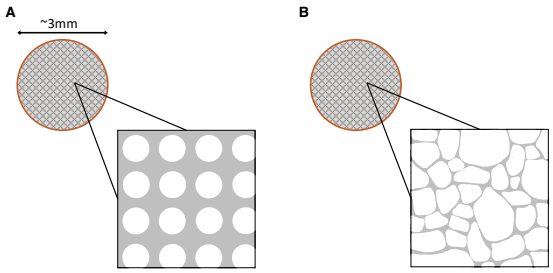

Figure 1.9.: Typical grid types used in cryo-EM. (A) Quantifoil grids have a foil with regularly sized and shaped holes, whereas (B) the film of lacey grids shows irregular holes.

Additionally, grids made of gold mesh and gold foil (UltraAuFoil grids) can reduce specimen movement [170, 171]. After deposition of the sample droplet on a cryo-EM grid, the excess liquid is blotted away with filter paper (Figure 1.8 B) to produce a 10 - 100 nm thin layer of sample solution in the holes. The grid is then rapidly immersed into a cryogen such as liquid propane or ethane at approximately -170°C (Figure 1.8 C) [146]. This process, called plunge freezing, produces a thin film of the protein solution with the protein in its native and hydrated state embedded in non-crystalline amorphous ice (Figure 1.8 D) [166, 168]. The grids afterwards need to be stored below -137°C until imaging in the cryo-EM [168].

Initially, plunge freezing was introduced as a manual technique [172, 173]. More automated and commercial vitrification equipment (e.g. the Vitrobot [174]) was introduced later to obtain reproducible good ice thickness, less contamination and homogeneous vitrification of the sample. As a crucial and resolution-determining step in the cryo-EM structure determination process, it is not surprising that several new developments of grid preparation techniques and devices have been introduced since then [175–198]. Most of them replace the process of blotting with filter paper, which is difficult to control and therefore often leads to high variability of ice thickness at constant parameter settings.

Microscope Data Acquisition Subsequently, the plunged cryo-EM grid needs to be screened to evaluate ice quality on the grid and to confirm a sufficiently high sample concentration and distribution [166].

Several tools exist to support cryo-EM data acquisition, with Thermo Fisher Scientific EPU software [199] and SerialEM [200] being the most common. For screening of a grid, an overview image of the entire grid is usually created by stitching together multiple low magnification images of the grid. This so-called atlas provides an overview of the ice thickness and accelerates the screening process. After selecting a grid of sufficient quality, the acquisition locations on the grid are determined based on the atlas. The software then automatically collects multiple so-called micrographs on the grid in the from of movies, where the total electron dose is distributed over the movie frames, at a rate of ~500 movies/hour on modern microscopes. However, evaluating overall grid and ice quality as well as the selection of gridsquares suitable for data collection can be challenging and time consuming. There are several approaches to automating this step using machine learning, which could make data collection even faster and potentially lead to higher quality datasets [201, 202].

Image Processing and Density Reconstruction The image processing can be divided into four major steps (Figure 1.7 C): Image Pre-Processing, including motion correction and CTF estimation, particle selection, 2D classification, 3D reconstruction, and refinement. As soon as the determined map reaches high enough resolution, the map can be interpreted by building an atomic model (Figure 1.7 D). These steps will be described in more detail in the following.

During the acquisition of a movie, the sample undergoes some motion induced by the electron beam [203, 204]. This so-called beam-induced motion causes blurring of the acquired images and thus a loss of high-resolution signal [203, 204]. Therefore, in the first step of image processing, a so-called motion correction is pearformed, in which individual movie frames are aligned and averaged [205–208]. Motion correction is the first step of the data pre-processing. The second step is the CTF estimation (compare Section 1.2.3), in which the CTF parameters are determined to enable CTF correction during image processing [209, 210].

The motion-corrected micrographs show the protein under investigation in different orientations. In order to compute a 3D map from 2D cryo-EM projection

images, the micrographs need to be inspected (Figure 1.10 A) and protein positions need to be marked on the micrograph (Figure 1.10 B, 1.11 A). This process is referred to as particle picking and forms an important basis for a high-resolution reconstruction. After protein positions are marked, the micrograph gets segmented into smaller particle images in a process that is called particle extraction (Figure 1.10 C, 1.11 B). The extracted particle images are used as input for the SPR.

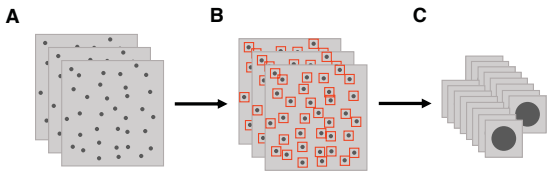

Figure 1.10.: During particle picking, (A) the raw micrographs are inspected and (B) the protein positions are marked. (C) Afterwards, the selected proteins are cut out of the micrograph to generate smaller images.

Manual particle picking is considered the most accurate approach, but is very time consuming especially in case of large datasets. Several software tools that implement an approach to (semi-) automatic particle picking are available. First automated approaches were based on template matching [211–214], more modern ones use a Convolutional neural network (CNN) [215–219]. Regardless of the type of implementation, a small subset of the entire dataset is first manually picked and subsequently used either to generate template images or to train the CNN. Automatic particle picking is then performed for the entire data set.

Following particle picking and extraction, reference-free two dimensional (2D) class averaging, also referred to as 2D classification, of the segmented images is performed to increase the SNR. The particle images are first aligned by determination and application of their in-plane rotation and x- and y-translation (Figure 1.11 C). Afterwards, aligned particle images can be classified into different orientations (Figure 1.11 D). In addition, 2D classification is a useful tool to discard non-optimal particles and to split a set of heterogeneous particles into several homogeneous subgroups that are reconstructed separately.

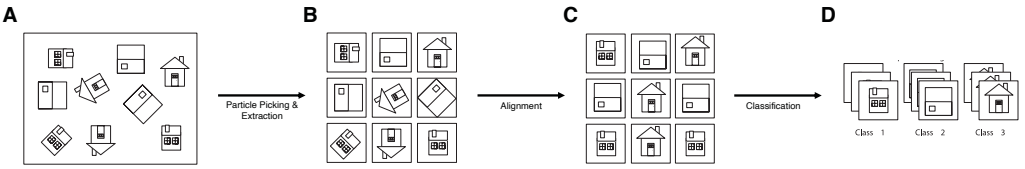

Figure 1.11.: Process of 2D class averaging. (A) Particle positions are detected on a micrograph and (B) particle images are extracted. (C) The particle images are aligned and (D) classified into different views. (Adapted from [220])

Most available methods for computing a 3D reconstruction from a set of 2D projection images are based on the Fourier slice theorem, which states that the Fourier Transform (FT) of different 2D projection images of a 3D object correspond to slices through the 3D FT of the 3D object. Hence, by determining the orientations of the 2D projection images, an inverse FT can be used to create a 3D map of the object. [221]

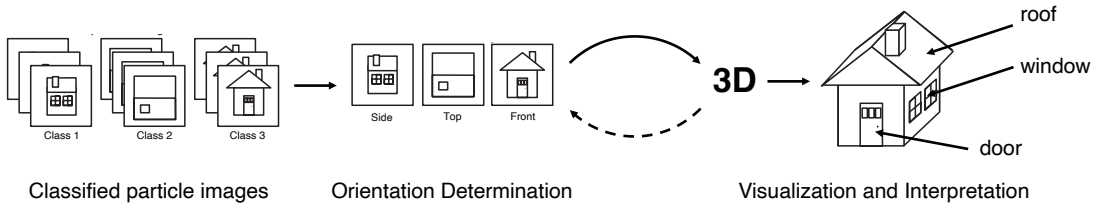

Figure 1.12.: Process of 3D reconstruction. The classified particles are used as input for iterative projection matching. Orientations are determined based on a comparison of the experimental images with computed projection images of a reference. The process is repeated iteratively until convergence. Eventually, the resulting 3D map can be visualised and interpreted. (Adapted from [220])

The orientation of individual projection images is generally determined by projection matching (Figure 1.12) [155].

Here, first projection images of an initial model are created computationally for different projection directions. These projection images are then used as reference images, which are compared with the experimental projection images of the protein. The orientation of the best-matching computed projection image is assigned to the experimental projection image. In this way, all images are assigned an initial orientation and a 3D map is calculated. This process is repeated iteratively, replacing the initial model with the map calculated in the previous step, until the

orientation assignments converge and the generated 3D map of the protein can be interpreted. [222]

Implementations of projection matching often use statistical weighting of the assigned orientations and thereby make the reconstruction process more robust to errors in the assignment of orientations [222]. RELION [223], which is the most used software package contributing to ~60% of all released maps according to Electron Microscopy Data Bank (EMDB) statistics [224], implements a Bayesian approach to structure determination [225]. In the Bayesian formalism, prior information can be incorporated in the likelihood function (the weighted orientations), resulting in improved maps and lower risk of overfitting [225]. A similar approach is implemented in cryoSPARC [226], which has recently gained popularity, particularly because of the possibility to perform structure determination during data collection, maximising feedback during acquisition.

Resolution The resolution of the final map is assessed by evaluating its consistency using the Fourier Shell Correlation (FSC). For this purpose, the data set is divided into two halves, from which two independent 3D reconstructions are calculated. Then, the cross-correlation between the two 3D reconstructions is calculated as a function of spatial frequency over corresponding shells in Fourier space. [227]

The FSC measures up to which spatial frequency the calculated map can be considered accurate, and therefore the FSC curve decreases with increasing spatial frequency. The final resolution of a map is derived from the spatial frequency, where the FSC curve passes a certain value. A cutoff value of 0.143 is typically used [228, 229], however, other cutoff values have been proposed too [230, 231].

It is important to note however, that the resolution of a cryo-EM map usually is not uniform, and therefore, might not be well described by a single resolution value determined by the FSC criterion. An approach to include local variations of the resolution in the map is to additionally determine local resolution values. [232]

Typically, the reconstructed cryo-EM map is sharpened in a final step to increase its interpretability by compensating for missing high-resolution details due to contrast loss, e.g. as a consequence of radiation damage and sample movement during imaging, as well as errors in image processing [228].

Atomic Model Building When the reconstructed density map reaches sufficient resolution to identify the main chain of the protein as well as side chain densities (~3.5 Å and better), a *de novo* atomic model can be build manually into the density map [233]. Manual model building is usually performed using software packages like Coot [234]. In addition, computational tools for automatic modeling are available [235–238], which become particularly useful for medium resolution maps. Once an initial atomic model is built it can be refined using software packages like PHENIX [239].

1.3. Cryo-EM of Amyloid Fibrils

Parts of the following section 1.3 have been adapted from Publication I: "Challenges in sample preparation and structure determination of amyloids by cryo-EM." [1]

1.3.1. Structure and Properties of Amyloid Fibrils

Amyloid fibrils are helical aggregates that usually consist of several subunits, called protofilaments, that wind around each other to form a mature fibril (Figure 1.13 A, B) [240]. Each protofilament consists of several stacked copies of the monomeric amyloid protein folded into its fibrillar arrangement (Figure 1.13 B, C). This repetitive stacking leads to the cross-β pattern that is the main feature of amyloid fibrils. An amyloid fibril can be described by its helical symmetry: the rise, which describes the stacking distance of the monomeric subunits in a protofilament, and the twist, which indicates the degree of rotation between one monomeric subunit and the neighbouring one. The twist is deduced from the crossover distance of the fibril or the pitch, the latter being twice the crossover distance. The contact between two protofilaments, also referred to as the interface, stabilises the dimerisation (in case of two protofilaments as depicted in 1.13) and is best visualised in the fibril cross-section (Figure 1.13 B).

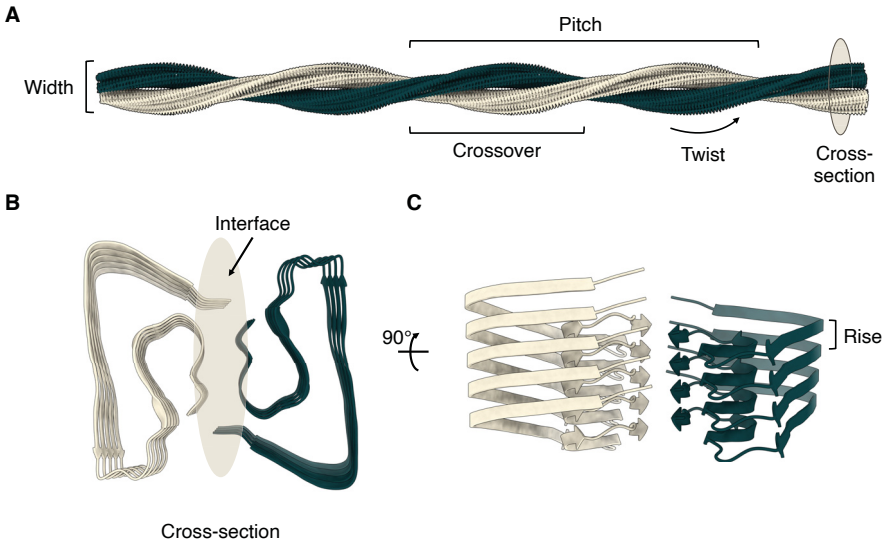

Figure 1.13.: Characteristics of an amyloid fibril, which is typically described by its (A) width, crossover distance or pitch, twist and cross-section. (B) The cross-section of a fibril reveals the protofilament interface. (C) The side view of a fibril along the helical axis. The monomeric subunits are one rise apart. In amyloid fibrils, this rise is typically 4.75 Å, resulting in the characteristic cross-β pattern.

Polymorphism Interestingly, amyloid fibrils composed of the same protein can look different even under the same conditions. This phenomenon is called polymorphism (Figure 1.14).

Polymorphism in amyloid fibrils can be divided into two different classes (Figure 1.14 A): protofilament polymorphism and ultrastructural polymorphism. Protofilament polymorphism, that refers mainly to differences in the secondary structure arrangement, can be subdivided into segmental polymorphism and packing polymorphism. While the latter describes differences in the β-sheet bending of one monomer or protofilament, segmental polymorphism describes differences in β-sheet annotation [241, 242] (Figure 1.14 B). Ultrastructural polymorphism describes the different assembly of structurally identical protofilaments into different fibrils that have different and/or multiple interfaces (Figure 1.14 C). Ultrastructural polymorphism is primarily based on the intermolecular interactions of mature fibrils or protofilaments [243]. It may also include the characteristic parameters of amyloid fibrils such as helical rise, helical twist, width and cross-over distance (Figure 1.13 A, C). Furthermore, Radamaker et al. [244] recently described an ad-

ditional level of polymorphism when they observed different monomer structures in a single fibril structure. This observation further increases the complexity of polymorphism in amyloid fibrils.

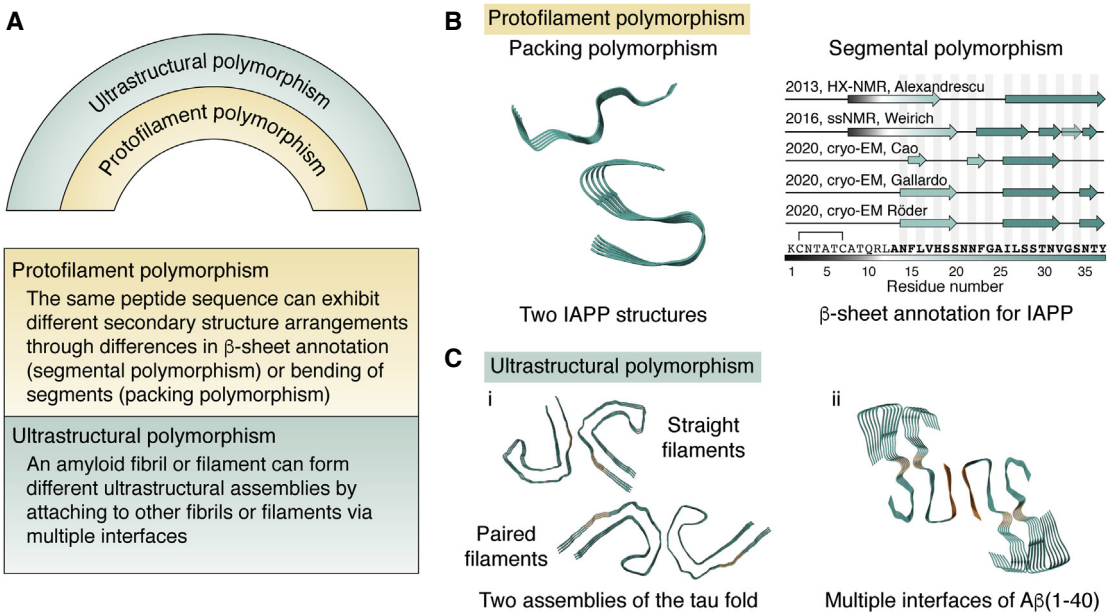

Figure 1.14.: Polymorphism in amyloid fibrils. (A) Polymorphism can be roughly divided into two classes: protofilament polymorphism, which can be subdivided into segmental and packing polymorphism, and ultrastructural polymorphism. (B) Examples of protofilament polymorphism. Packing polymorphism is exemplified by the islet amyloid polypeptide structures whose segments bend differently depending on pH. Segmental polymorphism was also found for the islet amyloid polypeptide, as the assignment of β-sheets is different ([245–249]). (C) Examples of ultrastructural polymorphism: (i) the general tau fold can show different interfaces leading to straight (top) or paired (bottom) helical filaments and (ii) Aβ(1-40) shows multiple interfaces (beige and orange) leading to double fibrils ([241]). Structures shown: (B) PDB 6Y1A ([249]), PDB 6VW2 ([246]); (C) PDB 6HRF, 6HRE ([250]) (C(i)); PDB 6SHS ([251]) (C(ii)).(adapted from Zielinski et al. [1]).

The degree of polymorphism in Aβ appears to be higher *in vitro* [252–258] than *in vivo*, but different *ex vivo* folds have also been described [251, 259–261]. Here, the different polymorphs of Aβ seem to be characteristic for the disease phenotype (sAD vs fAD) [261] and/or the brain region [251, 261] the fibrils were extracted from. For tau it is indeed an established fact that different folds are characteristic for different diseases, including AD, chronic traumatic encephalopathy (CTE) and

Pick's disease [107, 108, 250, 262–265]. This makes the structural study of different amyloid fibril polymorphs and their role in different diseases or disease phenotypes an interesting and potentially very insightful area of research.

1.3.2. Amyloid Structure Determination - Helical Reconstruction

It is no great surprise that the first 3D structure of a biological sample, the extended tail of the T4 bacteriophage, exhibits helical symmetry [143, 144]. Helical samples have two significant advantages over globular proteins: First, all information needed for a successful 3D reconstruction is provided by one single image of the fibril, and second, the repeating asymmetrical units in a helical filament have fixed orientations that can be deduced from the helical symmetry parameters twist and rise (Figure 1.13) [266]. The determination of the helical symmetry of an amyloid fibril is facilitated by the cross-β arrangement, which fixes the rise to a value around 4.75 Å [267]. This, however, does not only benefit the reconstruction process, but also potentially complicates the image alignment, since this is almost exclusively based on the 4.75 Å (meridian) signal caused by the cross-β pattern and a 10 Å (equatorial) signal due to the horizontal inter-strand distances within a molecule [268]. Consequently, the dominance of the 4.75 Å signal and the absence of larger structural features can complicate the high-resolution structure determination of amyloid fibrils [267].

The implementation of Fourier-Bessel principles to compute 3D models [143] as well as the development of the iterative helical real-space reconstruction (IHRSR) method [269], which is implemented in most commonly used software packages today [226, 270–273], were major breakthroughs in the field of helical reconstruction. The IHRSR as implemented in most software packages follows the normal single-particle reconstruction pipeline, it is therefore also often referred to as single-particle approach to helical reconstruction. Instead of picking individual particles, the start- and end-position of each fibril is marked on a micrograph (Figure 1.15 A, B).

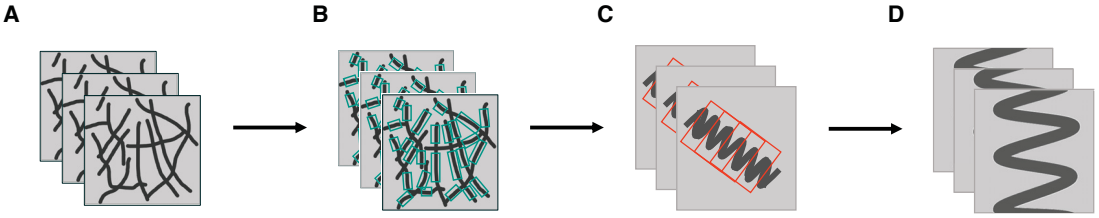

Figure 1.15.: Adapted picking procedure for amyloid fibrils. During particle picking, (A) the raw micrographs are inspected and (B) the fibril positions are selected, by selecting start- and end-position. Afterwards, (C) the selected fibril is segmented and (D) cut into smaller images.

Picking for amyloid fibrils can also be carried out both manually and automatically. However, some additional challenges, such as the need to avoid fibril crossings and overlappings during picking, while at the same time a fibril should ideally be picked in one piece from its beginning to its end, require approaches specifically designed for automatic filament selection [274–277]. After picking, the image of a helical protein is divided into equally sized, overlapping filament segments during particle extraction (Figure 1.15 C). These segments are then treated as individual images analogous to single particles (Figure 1.15 D). Their relative orientation is determined by iterative projection matching. In-between iterations, the helical symmetry is imposed onto the reconstructed volume, which is then used as reference in the next iteration.

Helical Symmetry In most software packages that implement a single-particle approach to helical reconstruction, helical symmetry is described by the helical rise and the helical twist. Additionally, point group symmetry may be present and can be applied during reconstruction. A C_n point group symmetry is an n-fold rotational symmetry in which n symmetry elements located at the same height along the helical axis are rotated by 360/n° with respect to each other. Most structurally described amyloid fibrils consist of two symmetrical protofilaments and therefore, oftentimes exhibit a C_2 point group symmetry (Figure 1.16 A). [267]

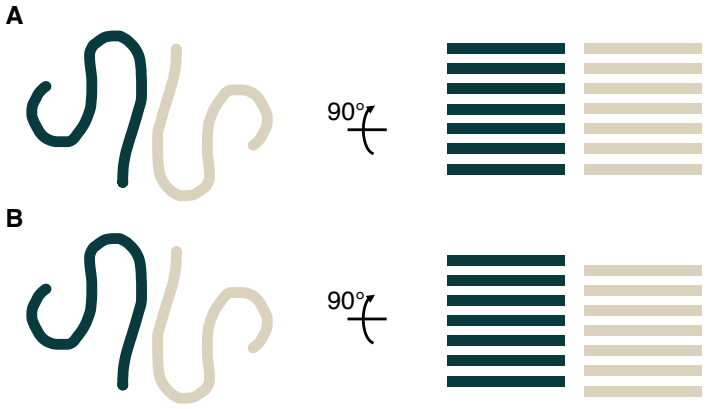

Figure 1.16.: Point group symmetry in amyloid fibrils. (A) Cross-section of an amyloid fibril with two symmetric protofilaments (left) that exhibits a C_2 symmetry (right). (B) Cross-section of an amyloid fibril with two symmetric protofilaments (left) that exhibits a pseudo-2_1 screw symmetry (right).

In some cases, however, the symmetry elements are not at the same height along the helical axis, but rather exhibit a staggered arrangement with a pseudo-2_1 screw axis (Figure 1.16 B) [267].

1.3.3. Cryo-EM Structures of Amyloid Fibrils

Although there is much knowledge about both the diversity of amyloid fibrils as well as their common architecture, the structural details at the atomic level are still limited today. The first high-resolution structures of amyloid fibrils were determined in the 2000s using solid-state NMR spectroscopy supported by X-ray fiber diffraction and transmission electron microscopy [9, 278, 279]. However, a high degree of polymorphism and the fact that crystallisation of mature fibrils is not possible make it difficult to determine the structure of amyloid fibrils by solid-state NMR or X-ray crystallography. The "resolution revolution" in cryo-EM has thus ushered in a new era in our understanding of the molecular structure of amyloidogenic proteins and amyloid fibrils in particular. The first high-resolution cryo-EM fibril structures of two disease-associated amyloids, tau and Aβ42, were solved in 2017 by Fitzpatrick et al. [262] and Gremer et al. [252], respectively. For the first time, it was possible to generate atomic models from cryo-EM data at the achieved resolutions of 3.4, 3.5 Å (tau) and 4.0 Å (Aβ42). Since then, more than 70

cryo-EM structures of amyloid fibrils have been published, the majority of which achieve a resolution of 3 to 4 Å [258]. Although these resolutions are sufficient for atomic model building in most cases, higher resolutions will be needed for the investigation of PTMs, involved cofactors, and for the understanding of secondary nucleation mechanisms, among other things. The first cryo-EM structure to reach the atomic resolution limit, which is assumed to be 1.2 Å [280], was the single-particle cryo-EM structure of a large globular protein complex published in 2020 [281, 282]. In the field of cryo-EM structure determination of amyloid fibrils, the highest resolution achieved so far is 1.86 Å [283].

Structural knowledge of Aβ fibrils Besides the first *in vitro* cryo-EM structure of a recombinant Aβ fibril in 2017 [252], a number of other publications on NMR spectroscopy and cryo-EM structures of Aβ fibrils revealed the high degree of polymorphism of Aβ *in vitro* (Figure 1.17 J - P) [253–257]. However, these fibrils neither resemble Aβ40 and Aβ42 fibrils obtained from AD brain tissue by seeded fibril growth [259, 260] (Figure 1.17 G - I), nor Aβ40 and Aβ42 fibrils obtained from the meninges (Figure 1.17 A) [251] and parenchyma (Figure 1.17 B, C) [261] of AD brain tissue, respectively. Yang et al. [261] described two human polymorphs characteristic for the disease phenotype: *'type I filaments'* are mainly found in sAD patients and *'type II filaments'* are mainly found in fAD patients and patients with other neurodegenerative conditions. Human type II filaments are also found in APP^{NL-F} knock-in mice (Figure 1.17E), a mouse model used in AD research. These mouse line harbours the Swedish double mutation (KM670/671NL) and the Beyreuther/Iberian mutation (I716F) in APP to express humanized Aβ [261]. Another commonly used mouse model are APP^{NL-G-F} knock-in mice, that additionally carry the Arctic mutation E693G and therefore, produce mutant human E22G Aβ [284, 285]. Their Aβ structure, however, differs from human Aβ fibrils (Figure 1.17 F). The structure of Aβ fibrils extracted from AD patients with the Arctic mutation was determined recently as well (Figure 1.17 D) [285]. The human Arctic Aβ fibril is made of four protofilaments in total, two copies of a protofilament A-B pair and also differs from all other previously determined Aβ fibrils [285].

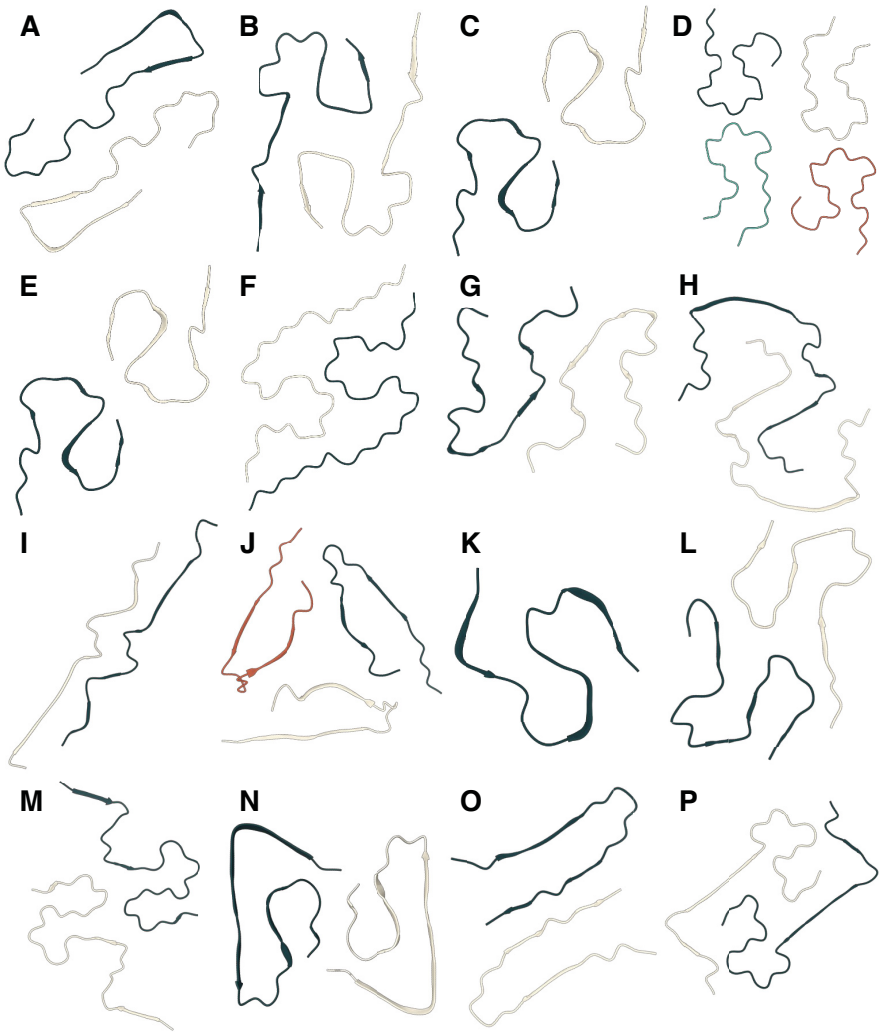

Figure 1.17.: Overview on structures of Aβ fibrils determined by NMR spectroscopy and cryo-EM. (A) Aβ40 fibril purified from AD brain meninges (PDB code: 6SHS, [251]). (B) Type I Aβ42 filaments from human brain parenchyma (PDB code: 7Q4B, [261]). (C) Type II Aβ42 filaments from human brain parenchyma (PDB code: 7Q4M, [261]). (D) E22G Aβ40 filaments extracted from AD brain tissue (PDB code: 8BG0, [285]). (E) Type II Aβ42 filaments from APP^{NL-F} mouse brain (PDB code: 7Q4M, [261]). (F) Murine E22G Aβ filaments from APP^{NL-G-F} mouse brains (PDB code: 8BG9, [285]). (G) Brain-derived seeded Aβ42 fibril type A (PDB code: 8EZD, [260]). (H) Brain-derived seeded Aβ42 fibril type B (PDB code: 8EZE, [260]). (I) Aβ40 fibril derived from Alzheimer's disease cortical tissue by seeded fibril growth (PDB code: 6W0O, [259]). (J) NMR structure of recombinant Aβ40 fibrils (PDB code: 2LMQ, [256]). (K) NMR structure of recombinant Aβ42 fibrils (PDB code: 2MXU, [257]). (L) NMR structure of recombinant Aβ42 fibrils (PDB code: 5KK3, [254]). (M) NMR structure of recombinant Aβ42 fibrils (PDB code: 2NAO, [255]). (N) Cryo-EM structure of recombinant Aβ42 fibrils (PDB code: 5OQV, [252]). (O) NMR structure of recombinant Aβ42 fibrils (PDB code: 6TI6, [253]). (P) NMR structure of recombinant E22Δ Aβ fibrils (PDB code: 2MVX, [286]).

Interestingly, a common C-terminal motif can be observed in a number of Aβ fibrils regardless of whether they are *in vitro* or *ex vivo* structures. However, apart from this common motif, *in vitro* Aβ fibrils are structurally different from *ex vivo* fibrils. The cause for these structural discrepancies between *in vitro* and *ex vivo* fibrils remains elusive, but could be related to the presence of co-factors, as so far the *in vitro* condition to produce *ex vivo* fibrils has not been found.

2. Objective and Outline

AD, which leads to loss of memory and other cognitive abilities, is the most common form of dementia [25]. It is a major cause of disability and dependency in the elderly, and the socioeconomic burden is expected to increase in the coming years [25]. Aggregation of Aβ into insoluble fibrils and their accumulation into extracellular plaques is a hallmark of AD [16]. Structural investigations of Aβ fibrils by X-ray crystallography and NMR-spectroscopy turned out to be tricky due to a high degree of polymorphism [1]. However, the resolution revolution in the field of cryo-EM around 2015 also marked the beginning of a new era for our understanding of Aβ fibrils on a structural level with the first cryo-EM structure of an Aβ fibril published in *Science* in 2017 [1, 252].

The aim of this work is to investigate AD on a molecular level in order to deepen our understanding of the disease pathogenesis, develop suitable laboratory model systems and support the development of new therapeutics.

One important tool to study the pathology of AD and to conduct preclinical screening of novel plaque-targeting therapeutics are animal models, especially transgenic mice showing Aβ brain pathology. However, the structure of Aβ fibrils in these mouse models has not yet been systematically studied, so that the structure of murine Aβ fibrils could not be adequately compared to the structure of fibrils found in humans. In Chapter 3 and Manuscript I, the cryo-EM structure of nine Aβ fibrils purified from brain tissue of six different mouse models is presented.

Another key element to study AD and its molecular mechanisms are laboratory model systems. But it is essential that the model system actually represents the studied aspect of the disease as well as possible. Therefore, when studying Aβ fibrils on a molecular level, finding the *in vitro* condition that leads to the aggregation of recombinant or synthetic Aβ into fibrils similar to those observed in

humans is of major importance. Therefore, the subject of chapter 4 is the cryo-EM structure determination of six *in vitro* Aβ42 polymorphs at neutral pH and their comparison to structures of *ex vivo* Aβ42 fibrils.

Mutations in the APP gene can cause early-onset familial AD. This is also true for the novel Uppsala mutation, in which six amino acids are removed from the middle of the Aβ sequence, resulting in a truncated peptide of only 36 residues in length. Chapter 5 and 6 contain structural studies of *in vitro* and *ex vivo* purified AβUpp(1-42)$_{\Delta 19\text{-}24}$ fibrils performed using cryo-EM.

In contrast, another mutation in the APP gene, the A673T or so-called Icelandic mutation, is the only known mutation that is not pathological but protective against AD. This makes the Icelandic mutation an important research topic, as its influence on pathogenesis is, among other things, an argument for the influential role of APP-derived Aβ at an early stage of AD. In Chapter 7 the cryo-EM structure of *in vitro* aggregated mutant A2T Aβ fibrils is presented.

The presented results are briefly summarized and their significance as well as resulting perspectives and possible future projects are discussed in chapter 8.

The study of amyloid fibrils at the structural level offers insights into the pathogenesis of AD. In addition, the findings presented will help to identify suitable *in vitro* and *in vivo* model systems of the disease. These are essential for the development of novel therapeutics that will eventually halt the progression of the disease or perhaps even cure it completely.

3. Manuscript I: Cryo-EM Structures of Amyloid-β Fibrils from Alzheimer's Disease Mouse Models

In collaboration with Sarah Schemmert, Benedikt Frieg, Luisa Schäfer, Antje Willuweit, Lili Donner, Margitta Elvers, Lars N.G. Nilsson, Stina Syvänen, Dag Sehlin, and Martin Ingelsson, we investigated the structure of Aβ fibrils purified from mouse brain tissue via cryo-EM. We solved the structure of nine fibrils from six mouse models, that are commonly used in AD research: APP/PS1, ARTE10, tg-SwDI, tg-APP$_{\text{Swe}}$, APP23 and tg-APP$_{\text{ArcSwe}}$ mice. The resulting article has been submitted to *Nature Neuroscience* on 18 June 2023. I summarized the article below. The article as published on the pre-print server bioRxiv as well as all the complete supplementary information can be found in the Appendix: *B Manuscript I*

This manuscript was accepted (06 October 2023) and published (16 November 2023) in Nature Neuroscience as: **Zielinski, M.***, Peralta Reyes, F.S.*, Gremer, L., Schemmert, S., Frieg, B., Schäfer, L., Willuweit, A., Donner, L., Elvers, M., Nilsson, L.N.G., Syvänen, S., Sehlin, D., Ingelsson, M., Willbold, D., Schröder, G.F. Cryo-EM of Aβ fibrils from mouse models find tg-APP$_{\text{ArcSwe}}$ fibrils resemble those found in patients with sporadic Alzheimer's disease. Ref. [287].

3.1. Summary

The following text was adapted from Manuscript I.

Mouse models, oftentimes transgenic mice, are widely used in AD research to study the pathogenesis of the disease, but also play an important role in the development of novel therapeutics and imaging tracers [125, 126]. However, the high failure rate in AD drug development [111] is potentially linked to the absence of the correct molecular targets in transgenic mice used for preclinical testing of novel therapeutics. In particular, a discrepancy in efficacy of a plaque targeting drug in mice and in humans could be explained by structural differences. Additionally, such structural differences might help to understand why PET imaging tracers fail to detect Aβ deposits in some patients [288].

For this study, Fernanda Salome Peralta Reyes extracted Aβ filaments from the brains of six different mouse models (APP/PS1, ARTE10, tg-SwDI, tg-APP$_{\mathrm{Swe}}$, APP23 and tg-APP$_{\mathrm{ArcSwe}}$). Immunogold negative stain EM confirms the presence of Aβ fibrils in the samples. I performed cryo-EM data acquisition for all samples and could determine the structure of nine Aβ fibrils.

A novel Aβ fibril fold, murine type III fibrils, was observed in APP/PS1 and ARTE10 mice. Interestingly, APP/PS1 murine type III fibrils are mainly composed of Aβ42, whereas ARTE10 murine type III fibrils are mainly composed of Aβ40. Murine type III Aβ fibrils have not been observed in humans yet, but show some structural similarity to human Arctic Aβ fibrils [285]. Patients with the Arctic mutation show massive Aβ deposits *post mortem* [289, 290] but were negative in PET imaging [288]. Interestingly, the PET tracer [^{11}C]PiB also does not work effectively in APP/PS1 mice, where murine type III fibrils account for 100% of all fibrils in the dataset. In contrast, ARTE10 mice are "PET-positive", but here also only 4% of all fibrils were of murine type III. Furthermore, it was shown that the [^{18}F]-labelled amyloid PET tracer florbetaben (FBB) works more effectively in ARTE10 mice than in APP/PS1 mice, because of congophilic dense-cored plaques and higher plaque load in ARTE10 mice [291].

We observed three novel Aβ polymorphs in tg-SwDI mouse. The mouse model harbors the Swedish double mutation, the Dutch (E22Q), and the Iowa (D23N) mutation and therefore, deposits mutant Aβ [292, 293]. The Dutch and Iowa

mutation have been observed in fAD families [87, 88, 93], but the combination of these cannot be found in humans. Moreover, the tg-SwDI mouse model is used to study CAA. We observed three novel polymorphs: DI1, DI2, and DI3. The dominant DI1 polymorph is the only dimeric Aβ fibril extracted from tg-SwDI mouse. All three polymorphs differ from other *in vitro* and murine/human *ex vivo* structures, however, the abundant DI1 Aβ fibril overlays in its N-terminal domain with Aβ40 fibrils purified from vascular deposits in the brain meninges associated with CAA [251]. This suggests that the tg-SwDI mouse line may indeed be well suited to studying CAA.

ARTE10, tg-APP$_{\text{Swe}}$, and APP23 show an Aβ42 fibril (murine type II) that is identical to previously described human type II filaments purified from fAD brain tissue [261]. All three models can therefore, together with the previously described APP$^{\text{NL-F}}$ knock-in mouse line [261], be used to study fAD. The efficacy of different aducanemab analogues was tested in APP23 mice and showed positive results [294]. Based on our results, the preclinical tests in the mouse model may have predicted efficacy of the drug in fAD rather than sAD. Additionally, given a high total brain Aβ level, all three mouse models also are "PET-positive", which is consistent with the finding that the dominant fibril type in all three mouse models is identical to human type II filaments.

Murine$_{\text{Arc}}$ type I fibrils extracted from tg-APP$_{\text{ArcSwe}}$ mouse are made of mutant E22G Aβ40. We observed at least two additional polymorphs in the dataset, however, surface bound additional densities prevented structure determination. Murine$_{\text{Arc}}$ type I Aβ40 fibrils resemble human type I Aβ42 filaments [261]. Extra densities in the fibril cavity of the murine$_{\text{Arc}}$ type I fibril shift the C-terminus slightly, however, the solvent-accessible surface is almost identical. Remarkably, murine$_{\text{Arc}}$ type I fibrils are structurally different from Aβ fibrils purified from APP$^{\text{NL-G-F}}$ knock-in mouse brain tissue, although here also mutant E22G Aβ is deposited [284, 285]. Interestingly, the NMR structure of Aβ40 fibrils with the Osaka mutation (E22Δ) [286] is structurally similar to murine$_{\text{Arc}}$ type I fibrils. In both cases the residue E22 is mutated. Human type I filaments are associated with sAD, which accounts for 95% of all AD cases. Tg-APP$_{\text{ArcSwe}}$ were used in therapeutic research and treated with the monoclonal antibody mAb158. The humanized version BAN2401 is known as lecanemab, which showed deceleration of

cognitive decline and a reduction of amyloid plaque burden in AD patients [117, 295–297]. The Aβ-directed antibody lecanemab is the most successful treatment for AD to date. It was developed primarily against intermediately sized soluble Aβ aggregates like oligomers and protofibrils [121, 123]. Although the structure of these aggregates is not yet known, lecanemab has also been shown to interact with "diffusible Aβ fibrils" found in "ultracentrifugal supernatants of aqueous extract from AD brains" and whose structure is identical to that of Aβ fibrils found in insoluble plaques [124]. Moreover, PET imaging of tg-APP$_{\text{ArcSwe}}$ mice with [^{11}C]PiB shows amyloid pathology [123] with a higher [^{11}C]PiB binding in tg-APP$_{\text{ArcSwe}}$ than in APP$^{\text{NL-G-F}}$ knock-in mouse [298]. As a consequence, tg-APP$_{\text{ArcSwe}}$ mice might indeed be predictive for the efficacy of a drug candidate in sAD.

The results of this study give an indication of how suitable the mouse models investigated are for AD research. In addition, it also shows how important it is to investigate the molecular targets of a drug candidate or imaging tracer also on a structural level in order to avoid drawing false conclusions from efficacy tests in mice with regard to efficacy in humans and to explain why PET imaging does not work reliably in all patients.

3.2. Contribution

For this study, I performed TEM screening of negative stain grids and immunogold negative stain grids that were prepared by Fernanda Salome Peralta Reyes and myself. I performed sample vitrification and cryo-EM data acquisition for all samples. I processed the images of all collected datasets and generated the final maps for Aβ fibrils from APP/PS1, ARTE10, tg-SwDI, tg-APP$_{\text{Swe}}$, and APP23 mice. Additionally, I participated in writing the original manuscript draft, prepared most figures, and discussed the paper with my co-authors. I am a shared first author of this article.

3.3. Further observations

3.3.1. Immunogold labelling of tg-APP$_{\text{ArcSwe}}$ Aβ fibrils with Lecanemab

As previously described, murine$_{\text{Arc}}$ type I fibrils purified from tg-APP$_{\text{ArcSwe}}$ mouse brain tissue resemble human type I fibrils, mainly observed in individuals with sAD. These structural similarities are one possible explanation for the clinical success of lecanemab. To address the question of whether lecanemab indeed binds to Aβ fibrils purified from tg-APP$_{\text{ArcSwe}}$ mouse brain tissue, we performed immunogold negative stain EM with lecanemab. For this, immunogold negative stain grids were prepared following [299]. Briefly, 2 µL of the final pellet were placed on a glow-discharged 300 mesh carbon-coated copper grid (EM Sciences, ECF300-CU) for 2 min. The sample was washed once with dH_2O and placed in blocking buffer for 15 min, following incubation with humanized lecanemab as primary antibody diluted in blocking buffer at a concentration of 2 µg/mL for 1.5 h. Afterwards, the grid was washed with washing buffer and was incubated with a mixture of 6 nm gold-conjugated anti-mouse and 10 nm gold-conjugated anti-human secondary antibody (each diluted 1:20 in blocking buffer and mixed 1:1, Abcam) for 1 h. The grid was washed five times with washing buffer and three times with dH_2O before staining with 1% (w/v) uranyl acetate (UrAc) for 1 min. The sample was air-dried, and TEM images were acquired using a ThermoFisher Scientific Talos 120C at an acceleration voltage of 120 kV. Images were collected on a 4k x 4k Ceta 16M CMOS camera using Thermo Scientific Velox Software. Figure 3.1 visualizes the results of the lecanemab immunogold labelling. It can be seen, that the Aβ fibrils are labelled with lecanemab confirming that lecanemab indeed binds to Aβ fibrils purified from tg-APP$_{\text{ArcSwe}}$ mouse brain tissue.

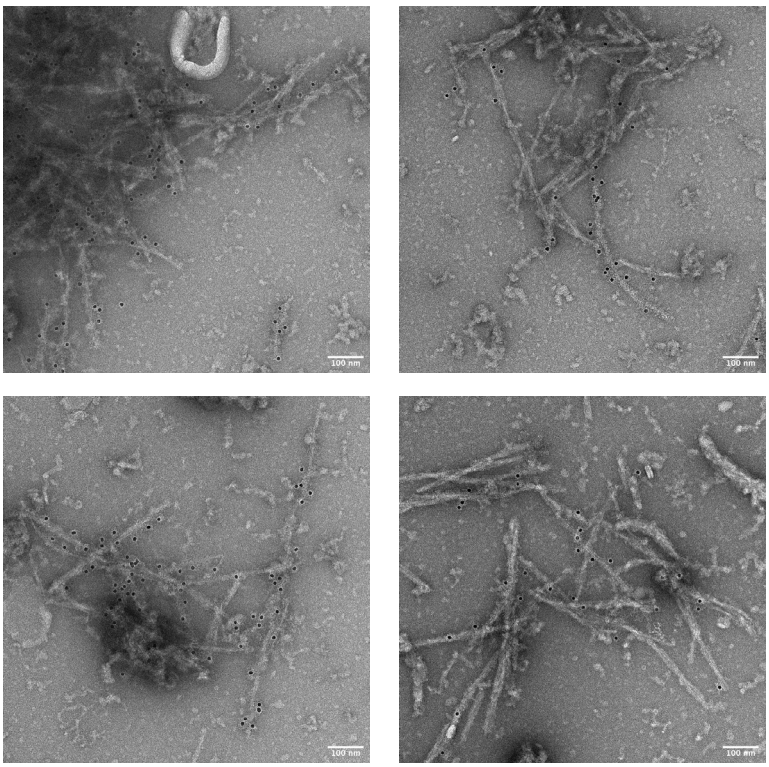

Figure 3.1.: Immunogold negative-stain EM image of the purified Aβ fibrils from tg-APP_{ArcSwe} mouse brain tissue labelled with lecanemab.

3.3.2. Additional proteins found in murine samples

Murine Aβ fibril samples were not entirely pure and therefore, additional proteins could be observed. An overview is shown in Figure 3.2. The Vault protein complex, a ribonucleoprotein that can be found in eukaryotic cells, could be identified directly from the recorded micrographs due to its characteristic shape (Figure 3.2 A,C)[300, 301].

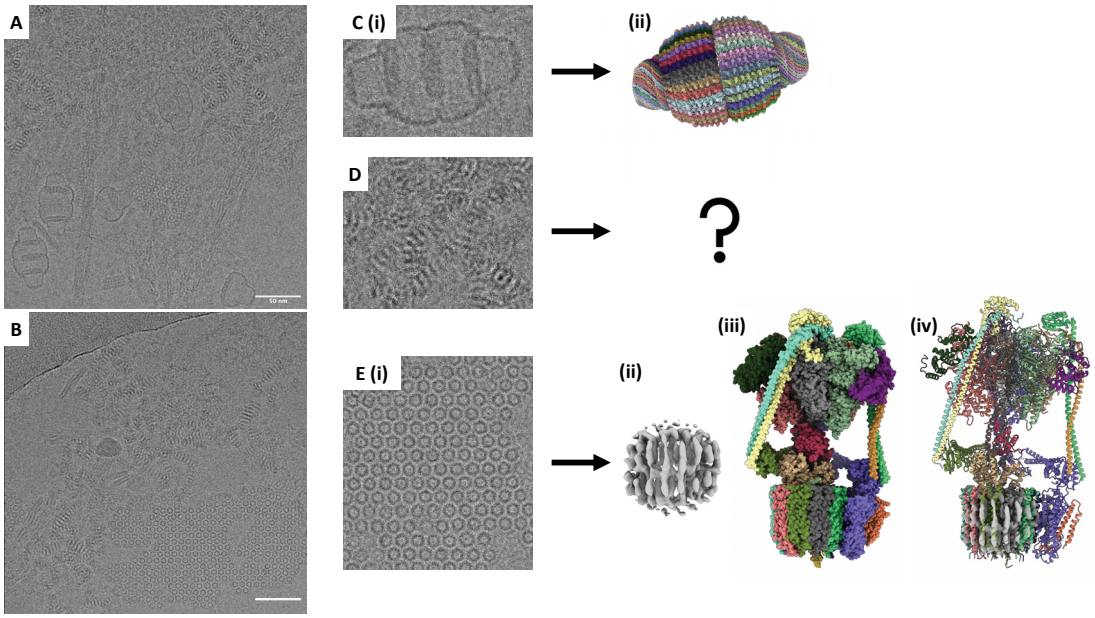

Figure 3.2.: Additional (identified and unidentified) cellular components present in murine Aβ fibril samples. (A,B) Two exemplary cryo-EM micrographs taken from the cryo-EM dataset of Aβ fibrils from tg-APP$_{\text{ArcSwe}}$ mouse brain tissue. (C) Vault Protein (i) as visible on a recorded cryo-EM images and (ii) its structure determined by cryo-EM [301] taken from the PDB (PDB 7PKZ). (D) Rod-shaped unidentified structure of varying length and approximately 80 Å in width on most images. (E) A globular protein of approximately 60 Å in width arranged in a lattice (i) as visible on a recorded cryo-EM image.(ii)-(iv) This protein was identified by single particle reconstruction to most likely be the C-ring of an ATPase. The displayed density map (ii) was computed and provided by Janus Lammert. The shown structure of the V-ATPase [302] was taken from the PDB (PDB 6VQ6).

Furthermore, we have observed a rod-shaped structure (Figure 3.2 A,D) that has repeating units that are ~40 Å apart (Figure 3.3). The length and width of this unknown structure varies, but most are ~80 Å wide. This rod-shaped structure was also observed in the cryo-EM dataset of Aβ fibrils extracted from human brain tissue (data not shown, compare Appendix D.0.1). Although the observed structure could consist of proteins, the distance of about 4 nm between the electron-dense repeating units indicates that it consists of lipids, with 4 nm being the thickness of a lipid bilayer.

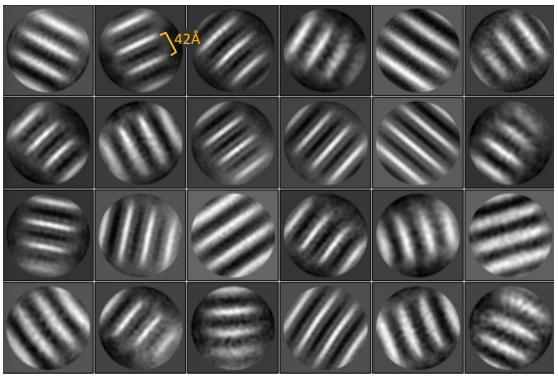

Figure 3.3.: Exemplary 2D classes of the unidentified rod-shaped structure found in murine and human Aβ fibril samples. The classes shown were computed from a cryo-EM dataset of Aβ fibrils purified from human brain tissue.

Finally, we observed a globular protein with a diameter of ~60 Å that arranges into a regular lattice on negative stain (Figure 3.4) and on cryo-EM grids (Figure 3.2 B, E).

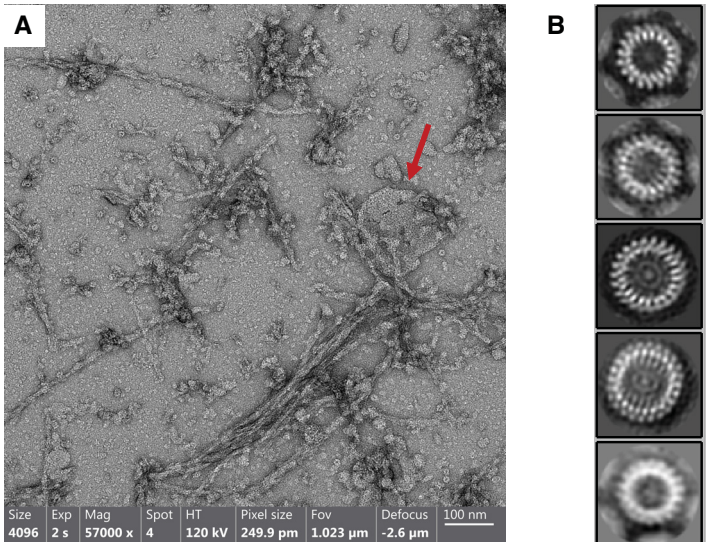

Figure 3.4.: Globular Protein observed in murine samples. (A) Negative stain EM images of a sample of Aβ fibrils purified from tg-APP$_{\mathrm{ArcSwe}}$ mouse brain tissue. (B) 2D classes computed from a cryo-EM dataset of Aβ fibrils purified from tg-APP$_{\mathrm{ArcSwe}}$ mouse brain tissue.

Janus Lammert performed the single-particle reconstruction from the merged cryo-EM datasets of all murine samples. Despite difficulties in reconstruction due

to a preferred orientation caused by the lattice arrangement of the protein, we were able to identify the protein likely to be the C-ring of a V-ATPase, which are ATP-dependent proton pumps that can be found in eukaryotic cells (Figure 3.2 E (ii)-(iv)) [303].

4. The cryo-EM structures of *in vitro* Aβ(1-42) fibrils at neutral pH

When studying Alzheimer's disease and its molecular mechanisms *in vitro*, suitable laboratory model systems that reflect the studied aspect of the disease as well as possible are essential. For Aβ, however, it is not yet known under what conditions synthetic or recombinant Aβ peptide aggregates *in vitro* into fibrils identical to those found in AD patients.

In collaboration with Raimond Ravelli at Maastricht University, we investigated the structure of synthetic Aβ(1-42) fibrils at neutral pH by cryo-EM. For this project, Raimond Ravelli prepared the Aβ fibril sample and collected cryo-EM datasets on a Titan Krios at the Netherlands Centre for Electron Nanoscopy (NeCEN) in Leiden.

4.1. Results and Discussion

Negative Stain EM of a neutral pH Aβ fibril sample, identical to the one prepared by Raimond Ravelli for cryo-EM, showed a high fibril concentration with large fibril clusters after 146 h of incubation (Figure 4.1 A).

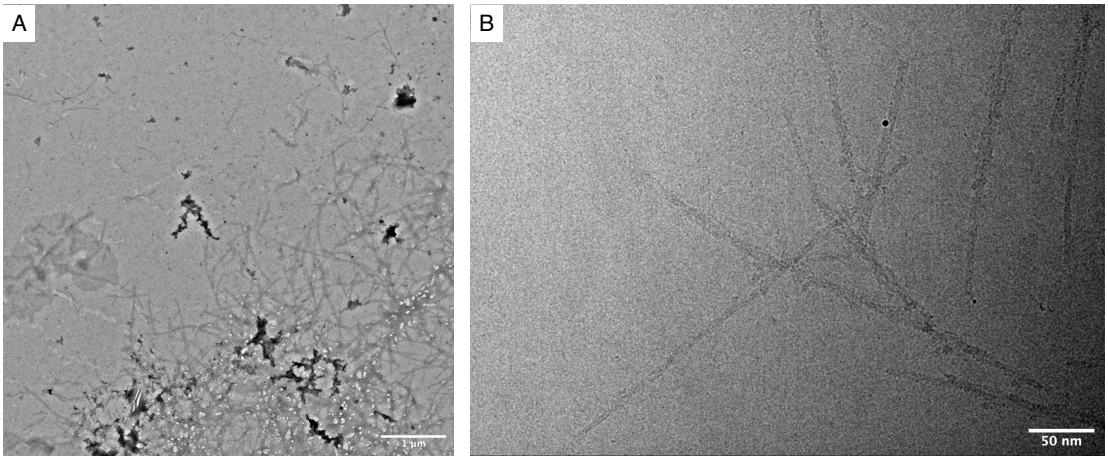

Figure 4.1.: EM images of Aβ42 fibrils at pH7.4. (A) Negative stain image after 146 h of incubation. (B) Cryo-EM image after 21 h of incubation. The image was low-pass filtered to 10 Å to enhance contrast.

To ensure isolated, unbranched fibrils in cryo-EM, the fibril sample was frozen already after 21 h of incubation. One representative cryo-EM micrograph showing straight fibrils at sufficient concentration is displayed in Figure 4.1 B. Moreover, it can be seen that the sample contains different Aβ fibril polymorphs. Fibrils were picked manually on the acquired micrographs, but due to the low contrast, polymorphs were not separated during picking. Instead, overlapping fibrils segments were extracted at a box size of 900 pix (downscaled to 300 pix) and 2D classification was performed to separate different polymorphs (Figure 4.2 A). A high degree of polymorphism can be observed in the dataset with at least nine different polymorphs. Six polymorphs could be identified during the first 2D classification run (Figure 4.2 A). All unidentified polymorphs were selected for a second 2D classification run, which resulted in the identification of three additional polymorphs (Figure 4.2 B).

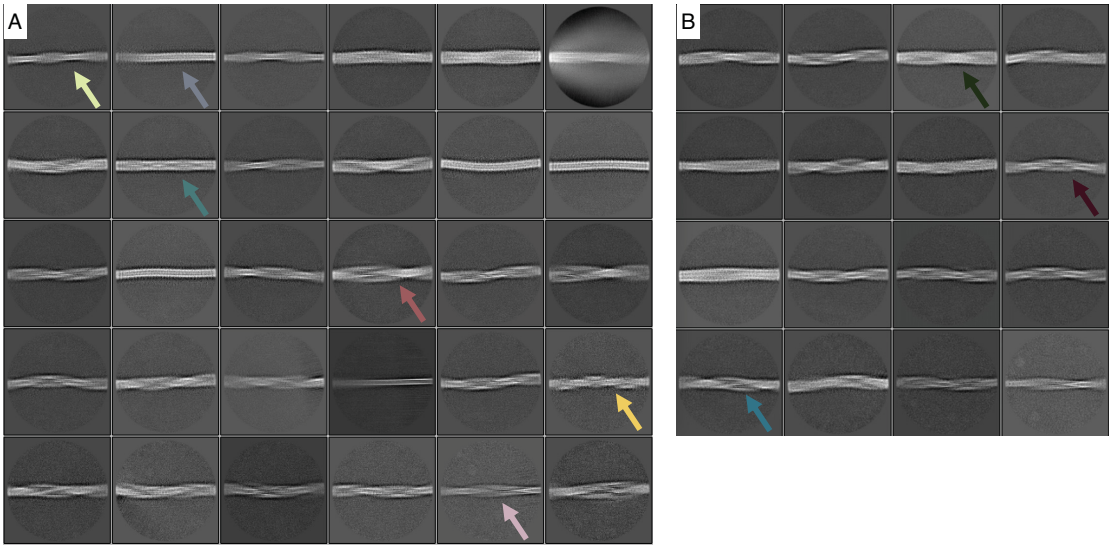

Figure 4.2.: Representative 2D class averages of pH 7.4 Aβ fibrils. (A) First 2D classification of all fibril segments at a box size of 900 pix (downscaled to 300 pix). (B) 2D class averages of all thicker fibrils after a second classification run.

From the pie chart in Figure 4.3 it can be seen that the most dominant polymorph, that accounts for 20.7% of all fibrils in the dataset is straight and therefore, a high-resolution reconstruction was not possible.

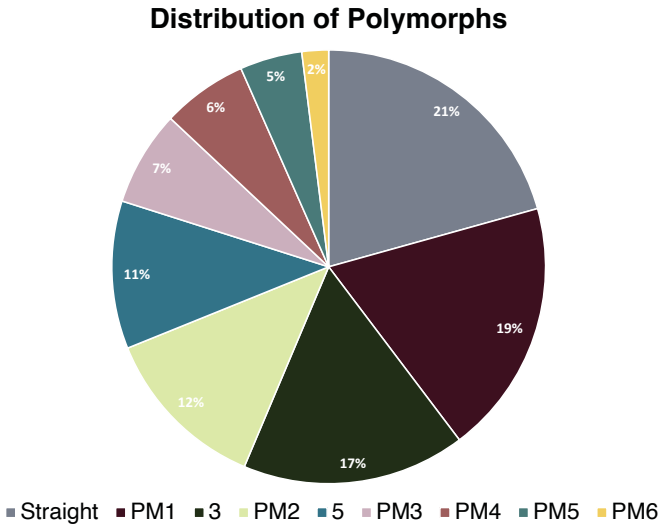

Figure 4.3.: Distribution of Polymorphs in the dataset of *in vitro* Aβ42 fibrils at neutral pH.

As indicated by the legend in Figure 4.3, structure determination was possible for six of the nine polymorphs observed in the 2D class averages shown in Figure 4.2. In addition to the most abundant yet straight polymorph, no structures could be determined for the third and fifth most dominant polymorphs, which account for 16.7% and 11% of all fibrils in the dataset, respectively.

An overview on the determined structures is given in Figure 4.4.

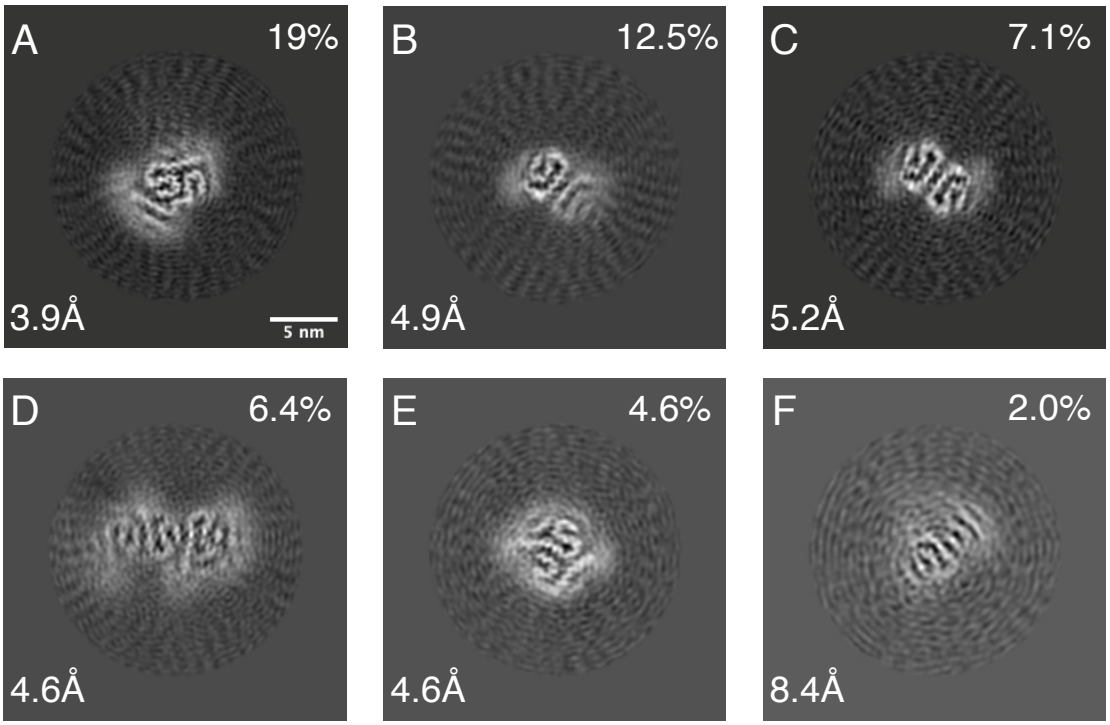

Figure 4.4.: Cryo-EM structures of *in vitro* Aβ42 fibrils at neutral pH (A-F). For each map, a projection of the reconstructed density including approximately one β-rung is shown. The scalebar in (A) applies to all panels. The percentage of a particular polymorph among all Aβ fibrils in the dataset is shown in the upper right corner. The resolution of the map is given in the lower left corner.

4.1.1. Cryo-EM Structure of Polymorph 1

The first Polymorph (PM1), that accounts for ~19% of all fibrils in the dataset, consists of two non-identical protofilaments (Figure 4.4 A). Both protofilaments are surrounded by a weak density, and additionally, a third protein fragment can be observed adjacent to one protofilament. Figure 4.5 shows the last 3D refinement

prior to 3D auto-refinement (Figure 4.5 A, B) as well as the post-processed map sharpened in different ways (Figure 4.5 C-H).

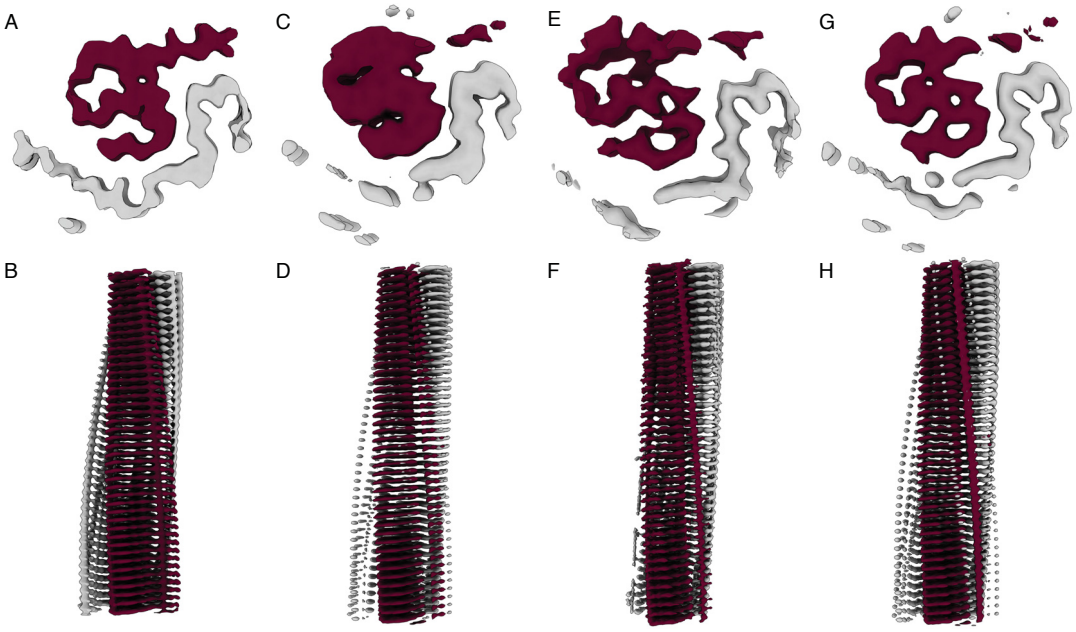

Figure 4.5.: Cryo-EM reconstructions of *in vitro* neutral pH Aβ42 PM1 fibrils. (A, B) 3D refined map sharpened with VISDEM [304] (resolution 3.9 Å). (C, D) Post-processed map sharpened with an automatically estimated B-factor of -133.7. (E, F) Post-processed map sharpened first with an automatically estimated B-factor of -133.7 and subsequently with VISDEM (resolution 2 Å). (G, H) Post-processed map sharpened with VISDEM (resolution 3.9 Å).

Although a global resolution of 3.9 Å (based on the gold-standard FSC 0.143 criterion; Figure 4.6 A) usually allows for *de novo* atomic model building, the post-processed map shows several structural breaks and only a few side chain densities (Figure 4.5). Of all four maps displayed, the output of the 3D refinement job prior to auto-refinement and post-processing produces the map with the highest visual resolution (Figure 4.5 A, B). Nevertheless, all displayed maps clearly lack high-resolution features, with even only one protofilament being resolved well enough to allow tracing of the backbone (Figure 4.5, A, C, E, and G, gray). Overestimation of the global resolution as well as bumps in the FSC curve, as seen in Figure 4.6 A, are usually associated with artefacts due to too tight masking. However, the applied soft-edge mask, extended by 8 pixels and further extended by a soft-edge

of 12 pixels, seems to fit the density (Figure 4.6 B).

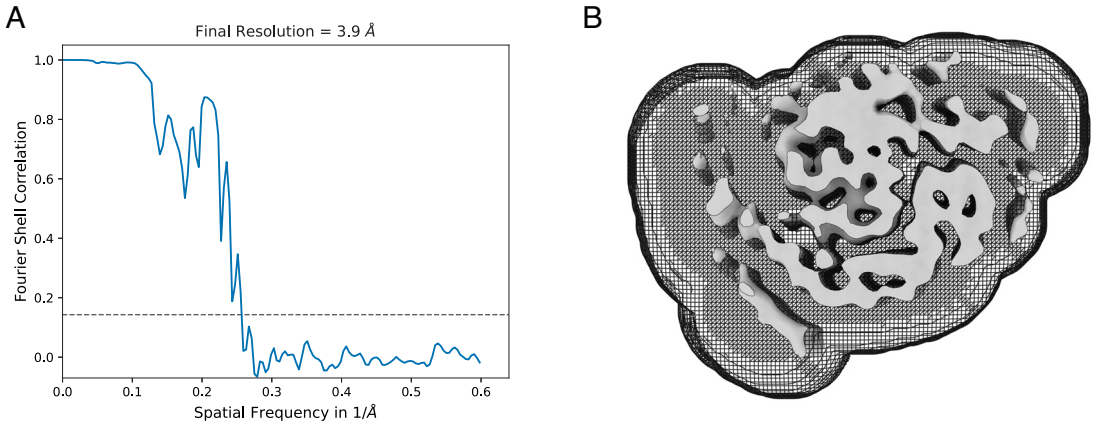

Figure 4.6.: Postprocessing and masking of *in vitro* neutral pH Aβ42 PM1 fibrils. (A) FSC curve from the gold-standard refinement of the cryo-EM map of PM1 yields a resolution of 3.9 Å (using the 0.143 criterion). (B) The post-processed map of PM1 and the applied mask during post-processing.

To evaluate the true resolution of the map, the local resolution was calculated for the 3D auto-refined map using the same mask as for the estimation of the global resolution (Figure 4.7). And indeed, calculation of the local resolution shows that the true resolution of the calculated map is ~4.1 Å.

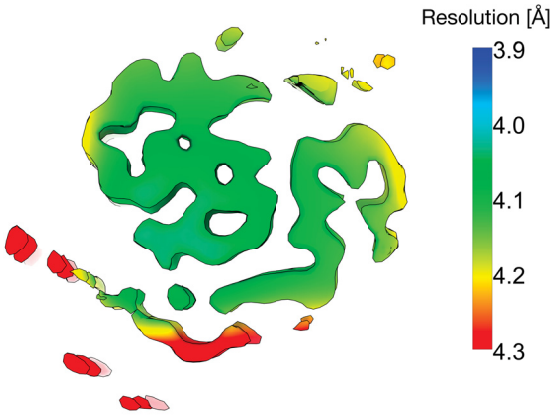

Figure 4.7.: Local resolution plot for *in vitro* neutral pH Aβ42 PM1 fibrils.

The cause of the overestimation of the global resolution remains unclear. At 4.1 Å, the map does not allow for *de novo* atomic model building.

Further 3D classification (K = 3) of the particle set, that was used to compute the final map shown above (Figure 4.4 A), reveals the presence of additional subpolymorphs (Figure 4.8).

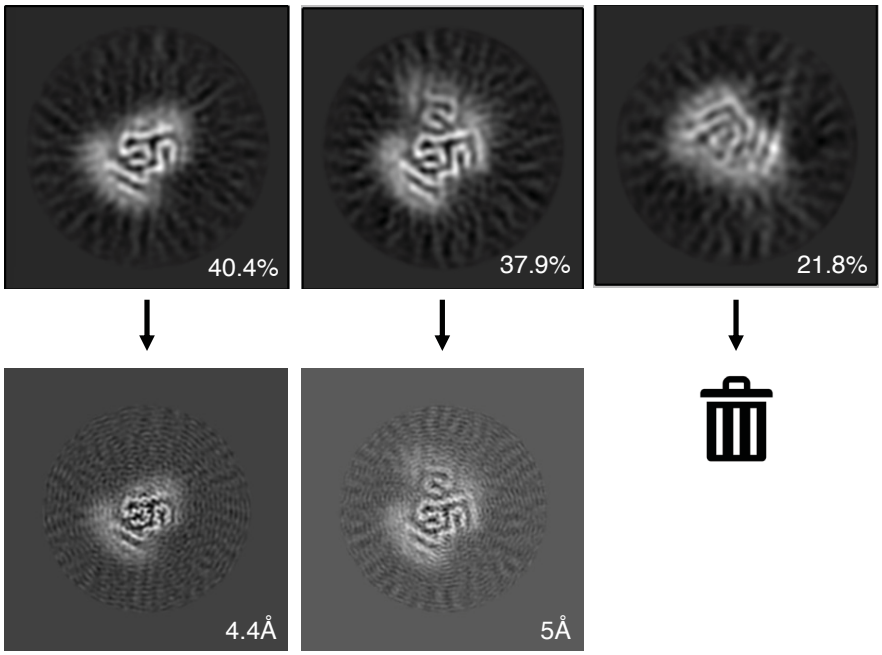

Figure 4.8.: 3D classification of the *in vitro* neutral pH Aβ42 PM1 particle set using three classes.

Two out of three calculated classes contain particles that lead to a reasonable reconstruction of the two subpolymorphs PM1.1 and PM1.2. PM1.1 resembles the two protofilament fibril displayed in Figure 4.4 A. PM1.2, on the other hand, consists of a PM1.1 fibril with an additional protofilament. Both polymorphs, PM1.1 and PM1.2, were refined individually (Figure 4.8, bottom) leading to final maps at resolutions of 4.4 Å and 5 Å (based on the gold-standard FSC 0.143 criterion; Figure 4.9), respectively.

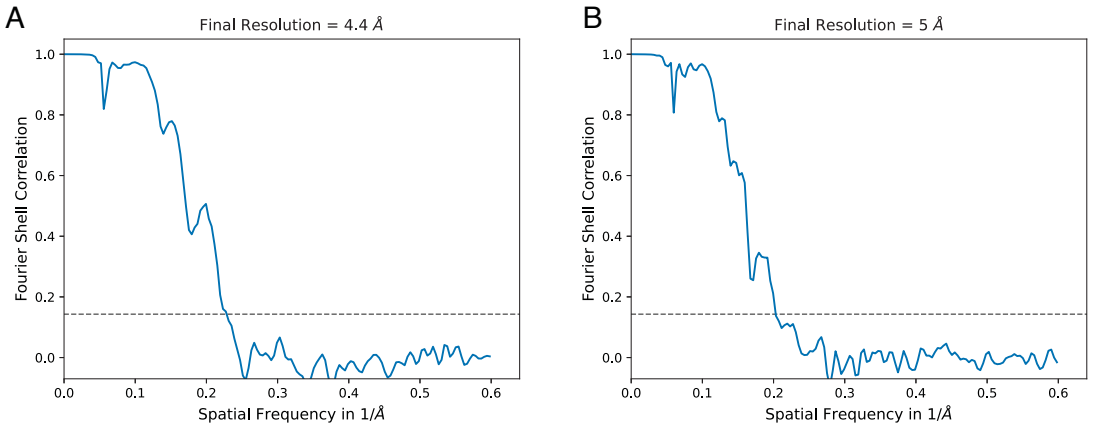

Figure 4.9.: FSC curves from the gold-standard refinement of the cryo-EM map of *in vitro* neutral pH Aβ42 (A) PM1.1 fibrils yields a resolution of 4.4 Å, and (B) PM1.2 fibrils yields a resolution of 5 Å (using the 0.143 criterion).

While the cross-section of PM1.1 shows more structural detail than the cross-section of PM1 (Figure 4.10 A, Figure 4.5), the resolution along the helical axis is limited due to lack of separation of individual layers (Figure 4.10 B). At a resolution of 5 Å, the side chains are not visible in the cryo-EM map of PM1.2 fibrils (Figure 4.10 C). Furthermore, the additional protofilament that is visible in Figure 4.8 is not well resolved and, as for PM1.1, the individual layers are not separated (Figure 4.10 D).

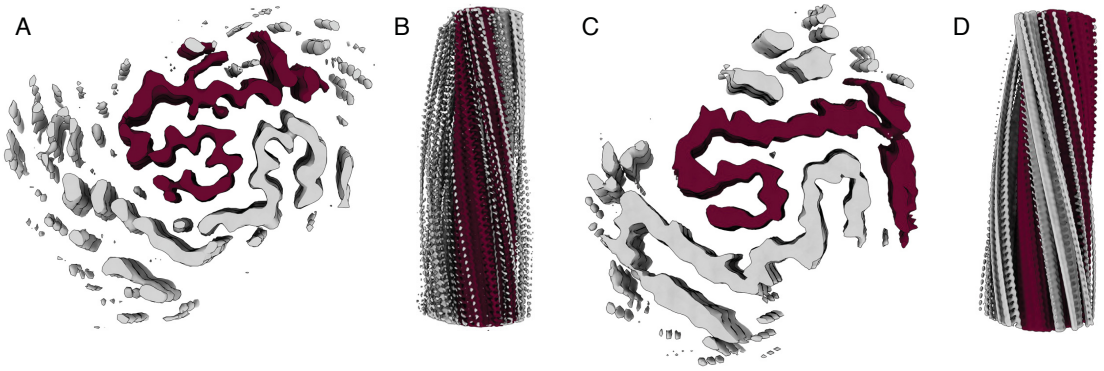

Figure 4.10.: Cryo-EM Maps of *in vitro* neutral pH Aβ42 PM1 sub-polymorphs. (A) Cross-section of the cryo-EM map of PM1.1. (B) Cryo-EM map of PM1.1 along the helical axis. (C) Cross-section of the cryo-EM map of PM1.2. (D) Cryo-EM map of PM1.2 along the helical axis.

Although *de novo* atomic model building is not possible for both polymorphs, PM1.1 allows for tentative backbone tracing and an initial sequence assignment (Figure 4.11 A, B).

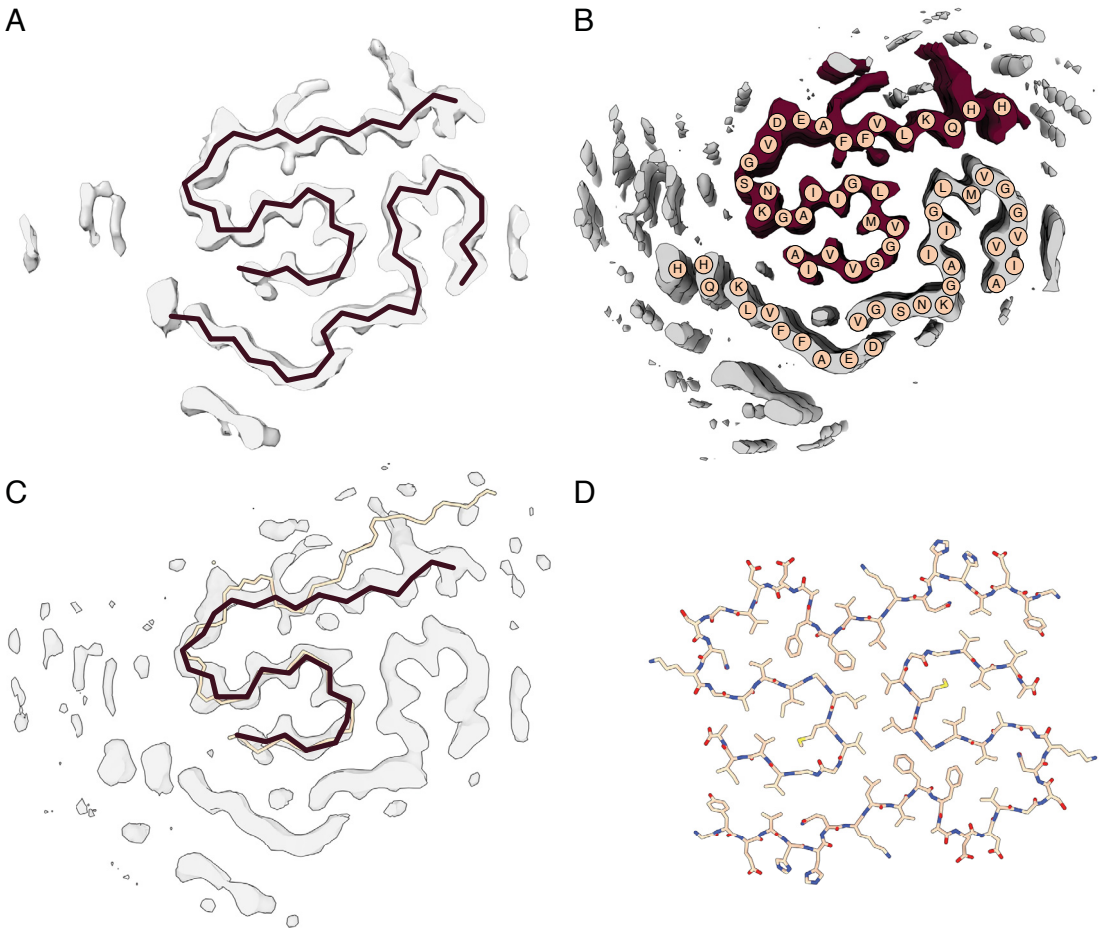

Figure 4.11.: Structure of *in vitro* neutral pH Aβ42 PM1.1 fibrils. (A) Schematic backbone trace of PM1.1 (burgundy) and the reconstructed cryo-EM map (gray). (B) Possible sequence assignment for PM1.1 (peach) and the reconstructed cryo-EM map (gray, burgundy). (C) Overlay of the cryo-EM map of PM1.1 (gray) with the atomic model of a human brain extracted type I Aβ42 protofilament ([261], PDB 7Q4B, peach) and the schematic of the PM1.1 backbone trace (burgundy). (D) Human type I filaments (PDB 7Q4B).

Moreover, one PM1.1 protofilament shows some structural similarity to one protofilament of type I filaments purified from human brain tissue [261] (Figure 4.11 C). Both protofilaments adopt an extended S-conformation, with the interface

between the protofilaments partially formed by the interaction of the C-terminal domain with the C-terminal domain of the neighbouring protofilament. However, in the symmetric type I filaments, L34 - V36 come into contact with L34 - V36 of the neighbouring protofilament (Figure 4.11 D), whereas in PM1.1 fibrils, a rotation of the C-terminal domain by approximately 90° compared to type I filaments, L34 - V36 come in contact with I31-L34. This rotation leads to a slightly shifted N-terminus of the type I-like protofilament in PM1.1 fibrils.

4.1.2. Cryo-EM Structure of Polymorph 2 and Polymorph 3

Polymorph 2 (PM2) and polymorph 3 (PM3) that account for 12.5% and 7.1% of all fibrils in the dataset, respectively, share a similar protofilament fold (Figure 4.4 B, C). In contrast to PM3, which consists of two LS-shaped protofilaments, PM2 consists of only one LS-shaped protofilament, with an additional weak density suggesting the presence of a second protofilament in some fibril segments. This second protofilament in PM2 becomes better visible in the cross-section of an intermediate 3D refinement step (Figure 4.12 A).

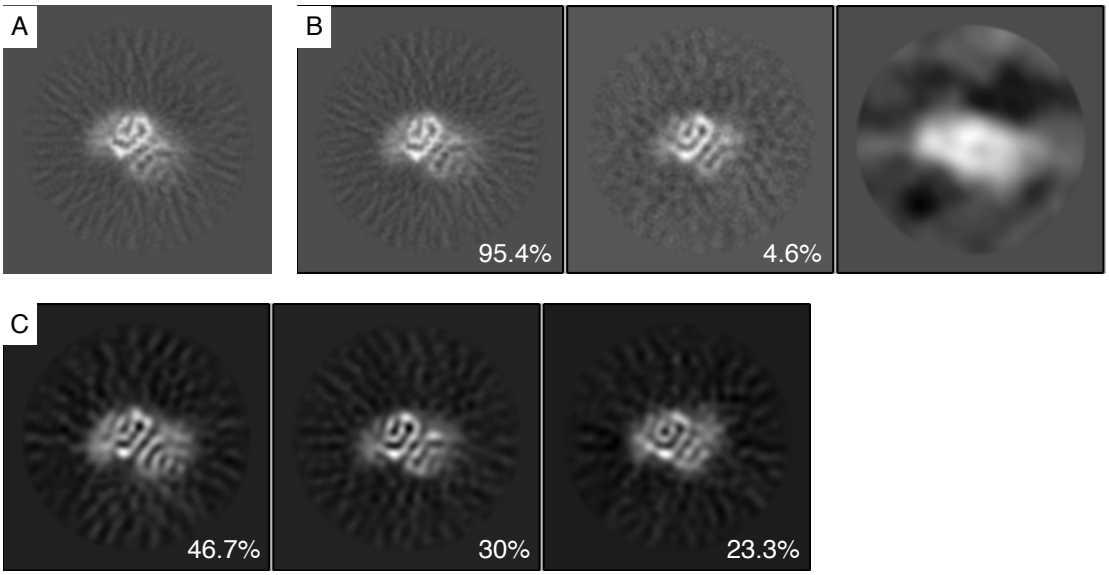

Figure 4.12.: Cryo-EM reconstruction of *in vitro* neutral pH Aβ42 PM2 fibrils. (A) Cross-section of the PM2 reconstruction after an intermediate 3D refinement step. (B) 3D classification result of the PM2 particle set with three classes and without image alignment. (C) 3D classification result of the PM2 particle set with three classes and with image alignment.

Separation of PM2 particles containing two protofilaments from those containing only one protofilament by 3D classification with or without alignment was not successful (Figure 4.12 B,C). Figure 4.13 shows the final post-processed map of PM2 and PM3.

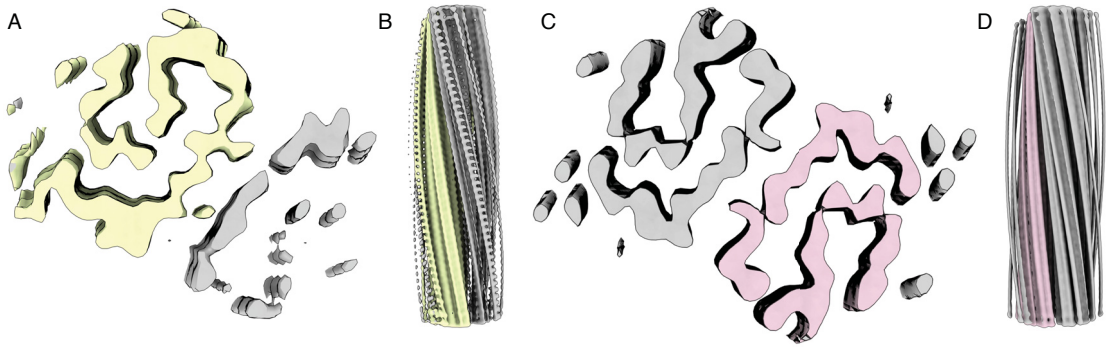

Figure 4.13.: Cryo-EM maps of *in vitro* neutral pH Aβ42 PM2 and PM3 fibrils. (A) Cross-section of the cryo-EM map of PM2. (B) Cryo-EM map of PM2 along the helical axis. (C) Cross-section of the cryo-EM map of PM3. (D) Cryo-EM map of PM3 along the helical axis.

For both polymorphs, *de novo* atomic model building is not possible at resolutions of 4.9 Å (PM2) and 5.2 Å (PM3) (based on the gold-standard FSC 0.143 criterion; Figure 4.14), however, the LS-shaped protofilament of both neutral pH polymorphs is reminiscent of the LS-shaped protofilament of *in vitro* Aβ42 fibrils formed at acidic pH [252].

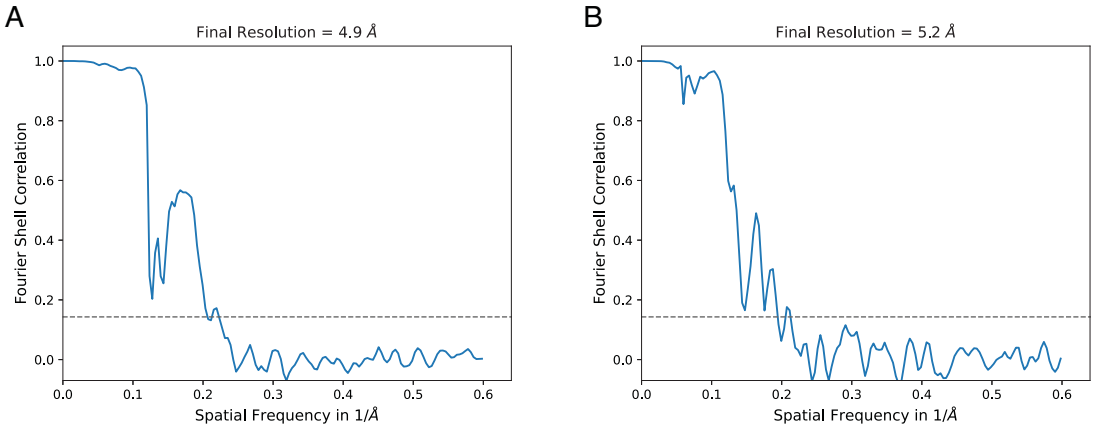

Figure 4.14.: FSC curves from the gold-standard refinement of the cryo-EM map of *in vitro* neutral pH Aβ42 (A) PM2 fibrils yields a resolution of 4.9 Å, and (B) PM3 fibrils yields a resolution of 5.2 Å (using the 0.143 criterion).

And indeed the LS-shaped protofilament of *in vitro* Aβ42 fibrils formed at acidic pH fits the cryo-EM map of PM2 and PM3 for most parts (Figure 4.15 A, B). With a similar LS-shaped protofilament, the major difference between acidic pH Aβ42 and neutral pH Aβ42 fibrils seems to be given by the protofilament dimerization (Figure 4.15 C). In acidic pH Aβ42 fibrils the interface is formed by hydrophobic interactions of the C-terminus and a salt bridge between D1 and K28. In contrast, the displacement of the protofilaments in neutral pH PM2 and PM3 Aβ42 fibrils results in an interface formed between residues Y10-E22.

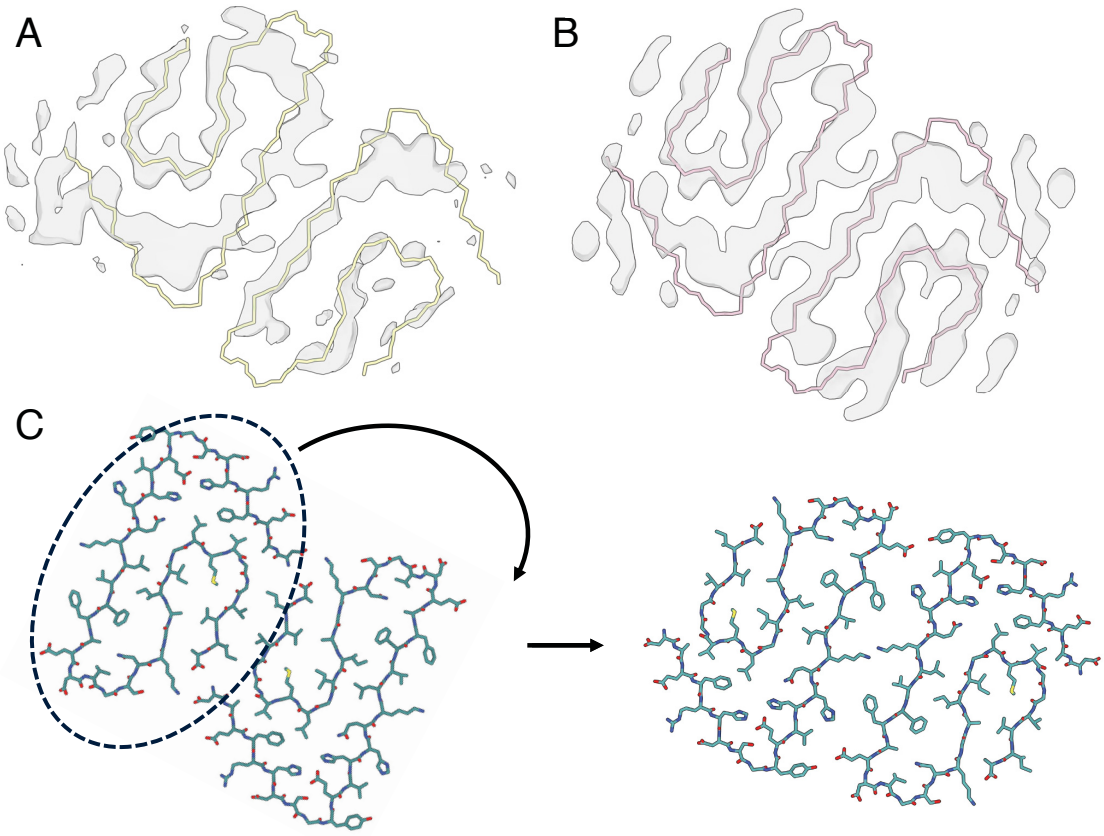

Figure 4.15.: Structural Interpretation of *in vitro* neutral pH Aβ42 PM2 and PM3 fibrils. (A) Overlay of the cryo-EM map of PM2 with the atomic model of two protofilaments of *in vitro* Aβ42 fibrils formed at acidic pH ([252], PDB 5OQV). (B) Overlay of the cryo-EM map of PM3 with the atomic model of two protofilaments of *in vitro* Aβ42 fibrils formed at acidic pH (PDB 5OQV). (C) Schematic representation of the displacement of the protofilaments required to produce the possible arrangement of protofilament arrangement in PM2 and PM3 Aβ42 fibrils from acidic Aβ42 fibrils (PDB 5OQV).

4.1.3. Cryo-EM Structure of Polymorph 4

Polymorph 4 (PM4), that accounts for 6.4% of all fibrils in the dataset, consists of two identical or non-identical protofilaments (Figure 4.4 D). In addition, a third protofilament appears to bind to the fibril less regularly but at a discrete site, as indicated by a faint density (Figure 4.16 A, pink arrow).

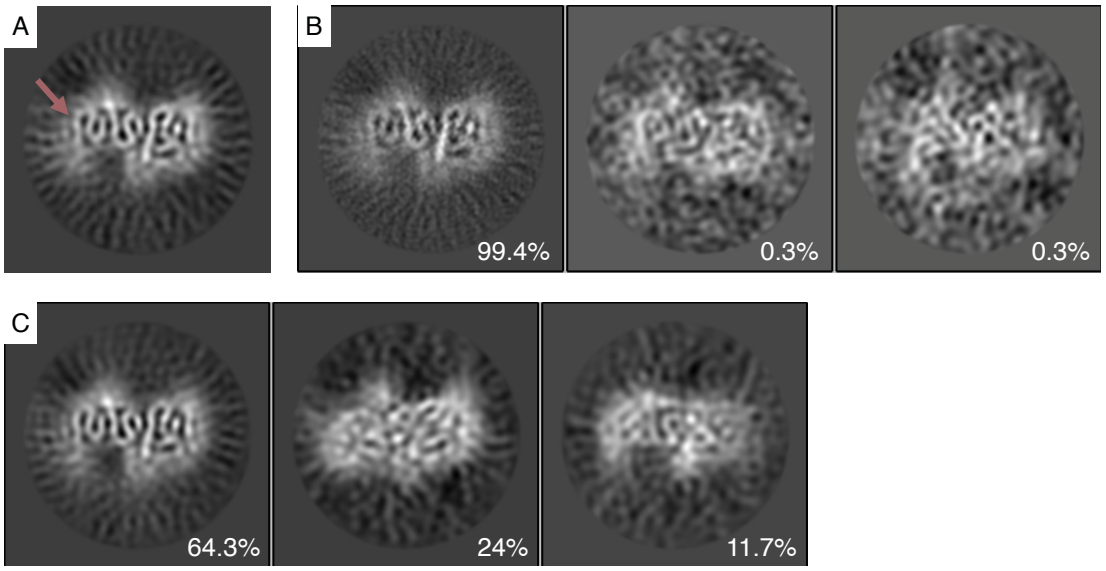

Figure 4.16.: Cryo-EM reconstruction of *in vitro* neutral pH Aβ42 PM4 fibrils. (A) Cross-section of the PM4 reconstruction after an intermediate 3D refinement step. (B) 3D classification result of the PM4 particle set with three classes and without image alignment. (C) 3D classification result of the PM4 particle set with three classes and with image alignment.

Similar to PM2, the separation of the fibril segments containing two protofilaments from those containing three protofilaments by 3D classification with or without alignment of individual fibril segments was not successful (Figure 4.16 B, C). The final map displayed in Figure 4.17 was solved to 4.6 Å resolution (based on the gold-standard FSC 0.143 criterion; Figure 4.18).

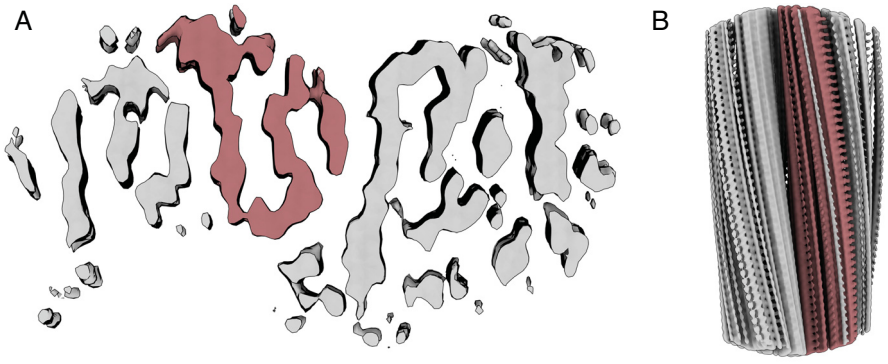

Figure 4.17.: Cryo-EM map of *in vitro* neutral pH Aβ42 PM4 fibrils. (A) Cross-section of the cryo-EM map of PM4. (B) Cryo-EM map of PM4 along the helical axis.

However, as for PM1, visual inspection of the density map indicates an overestimation of the actual resolution, as the map does not show higher-resolution features such as side-chain densities or layer separation. Therefore, *de novo* atomic model building was not possible.

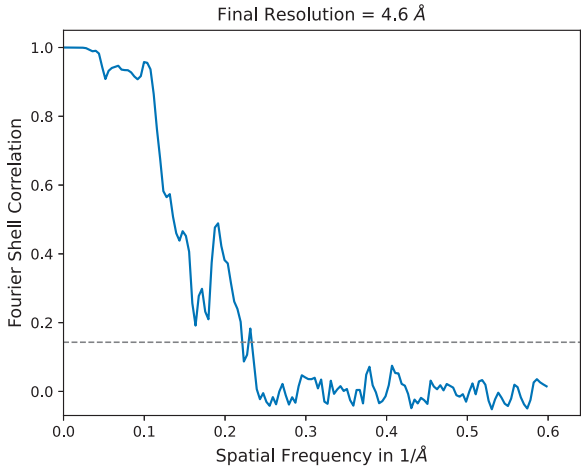

Figure 4.18.: FSC curve from the gold-standard refinement of the cryo-EM map of *in vitro* neutral pH Aβ42 PM4 fibrils yields a resolution of 4.6 Å (using the 0.143 criterion).

Nevertheless, a schematic of the tentative backbone trace suggests that the individual protofilaments of PM4 are connected via interactions between the C-termini around A42-G38 and the extended section around E22 to Y10 (Figure 4.19).

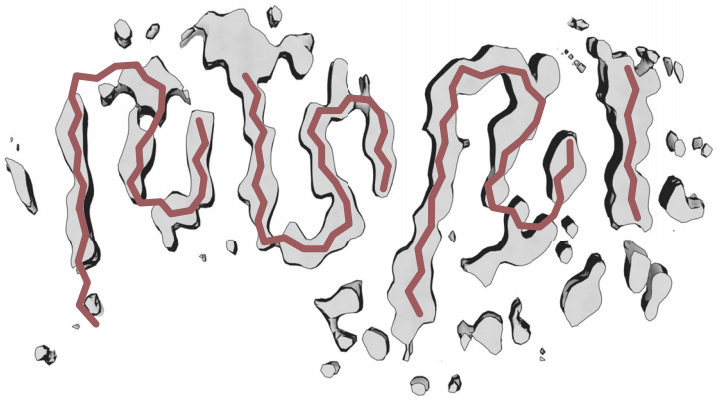

Figure 4.19.: Schematic of the preliminary backbone trace of *in vitro* neutral pH Aβ42 PM4 fibrils.

Moreover, the schematic representation of the backbone shows that all three protofilaments of PM4 probably share a common fold. And although both maps are only solved to medium resolution, the same fold can also be observed in the type I like protofilament of PM1.

4.1.4. Cryo-EM Structure of Polymorph 5

Polymorph 5 (PM5), solved to a resolution of 4.6 Å (based on the gold-standard FSC 0.143 criterion; Figure 4.20 A), is made of two non-identical protofilaments (Figure 4.20 B, C). As previously described for the other polymorphs, additional protein density can be observed adjacent to both protofilaments.

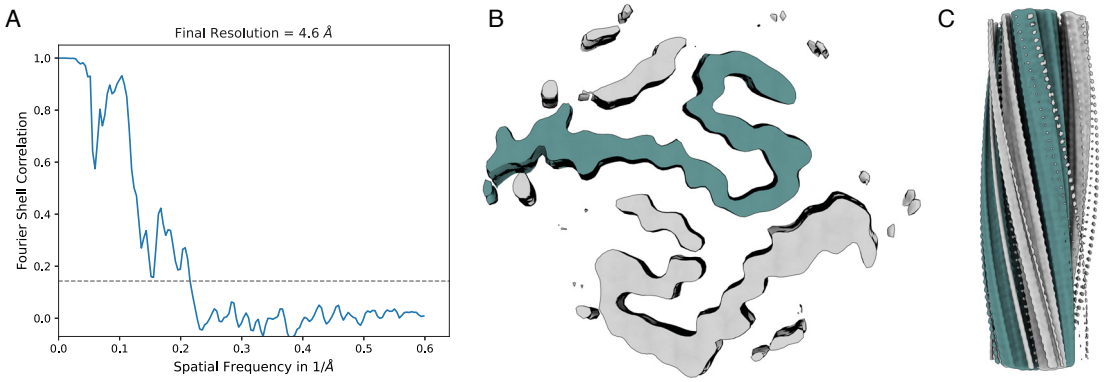

Figure 4.20.: Reconstruction of *in vitro* neutral pH Aβ42 PM5 fibrils. (A) FSC curve from the gold-standard refinement of the cryo-EM map of PM5 yields a resolution of 4.6 Å (using the 0.143 criterion). (B) Cross-section of the cryo-EM map of PM5. (C) Cryo-EM map of PM5 along the helical axis.

Although *de novo* atomic model building is not possible, a schematic of the fold shows that one PM5 protofilament bears some structural similarity to protofilaments observed in PM1 and PM4, as well as to a protofilament of type I filaments purified from human brain [261]. Moreover, the protofilament interface between the C-terminus and the extended backbone approximately between residues E22 and Y10 is likely identical to the protofilament interface observed in PM4.

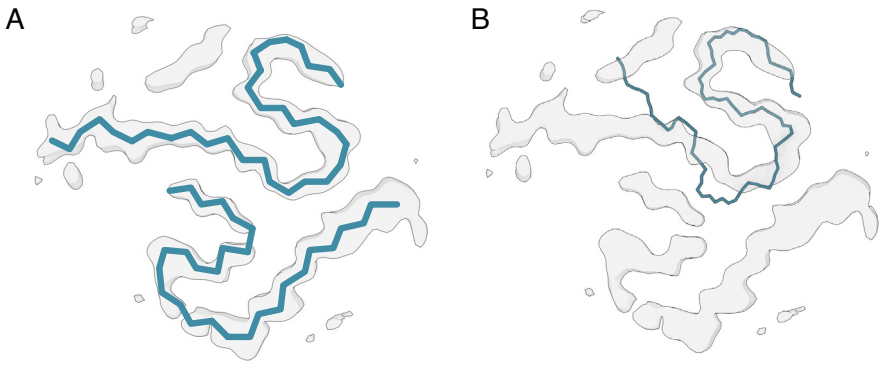

Figure 4.21.: Structure of *in vitro* neutral pH Aβ42 PM5 fibrils. (A) Schematic of the backbone trace of PM5. (B) Overlay of the cryo-EM map of PM5 with the atomic model of a human brain extracted type I Aβ42 protofilament ([261], PDB 7Q4B, teal).

4.1.5. Cryo-EM Structure of Polymorph 6

The least abundant polymorph 6 (PM6), which accounts for only 2% of all fibrils in the dataset, consists of an LS-shaped protofilament. Due to the limited number of fibril segments, PM6 could only be solved to a resolution of 8.4 Å (based on the gold-standard FSC 0.143 criterion; Figure 4.22 A; Cryo-EM map not shown.).

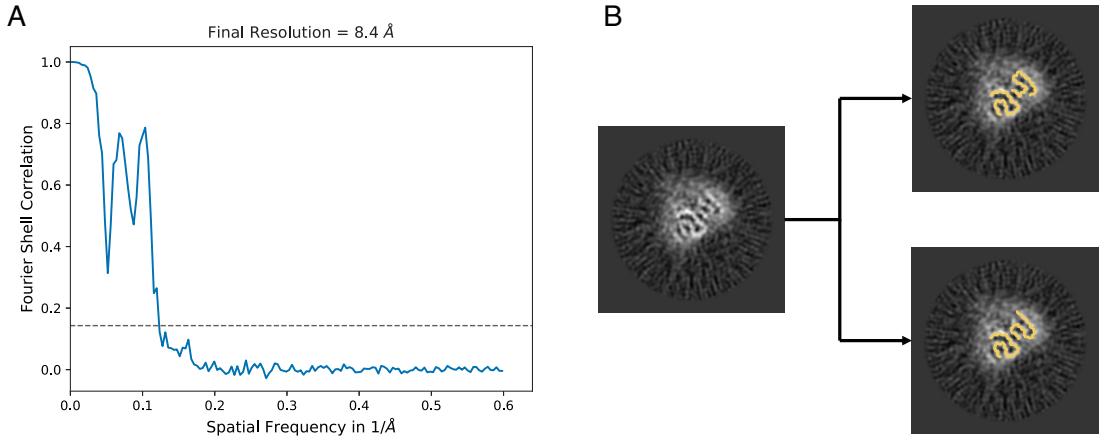

Figure 4.22.: Reconstruction of *in vitro* neutral pH Aβ42 PM6 fibrils. (A) FSC curve from the gold-standard refinement of the cryo-EM map of PM6 yields a resolution of 8.4 Å (using the 0.143 criterion). (B) Cross-section of the cryo-EM map of PM6 and possible backbone traces.

As previously described for other polymorphs of *in vitro* neutral pH Aβ42, faint

density can be observed next to LS-shaped protofilament suggesting the presence of a second protofilament. Figure 4.22 B shows two possible backbone conformations for PM6. In both possible conformations, the two protofilaments are possibly connected through interactions between the C-terminus and the extended backbone, likely between residues E22 and Y10.

4.1.6. Discussion

Aβ42 fibrils formed *in vitro* at neutral pH exhibit a high degree of polymorphism with at least nine different polymorphs present in the dataset. Structure determination was possible for six of the nine polymorphs. All six polymorphs present novel Aβ folds or protofilament interfaces. Interestingly, individual protofilaments can be observed in different polymorphs where they are connected by different interfaces, leading to the formation of distinct fibril polymorphs. All six fibrils formed *in vitro* differ from fibrils purified from human brain tissue, probably due to the absence of cofactors required for the formation of human Aβ fibrils. A faint density can be observed in PM1, PM2, PM4, and PM6, indicating the presence of another protofilament that appears to bind irregularly but at a discrete binding site. PM2 and PM3 both consist of two LS-shaped protofilaments that are connected through an identical interface. However, in PM2 fibrils, the second protofilament is only accounted for by faint density. After an incubation of only 21 hours, the sample solution could still contain on-pathway oligomers or monomers that are not yet bound, suggesting that PM2 fibrils are only an intermediate step and will eventually develop into PM3 fibrils. Accordingly, the presence of PM2 fibrils in this dataset could be an observation of secondary nucleation processes. It would therefore be interesting to study the structure of *in vitro* Aβ42 fibrils formed at neutral pH after a longer incubation period and, in particular, to investigate whether the distribution of individual polymorphs changes over time.

4.2. Methods

4.2.1. Sample Preparation

Synthetic peptide was purchased from Bachem and purified via RP-HPLC by Lothar Gremer. The sample was then HFIP treated and lyophilized (CHECK EPPI Label). 20 µL of 5 mM NaOH was added onto one lyophilized aliquot of Aβ42 (36 µg, i.e. 8 nmol). The sample was shortly vortexed and centrifuged to dissolve the lyophilized peptide. After an incubation time of 40 min at room temperature, 60 µL of dH_2O and subsequently, 120 µL 50 mM NaPi, pH 7.4, were added to the solution. The sample was stored at 4°C.

This sample was only used for negative stain EM. The sample used for cryo-EM was prepared in a similar way by Raimond Ravelli at Maastricht University.

4.2.2. Negative Stain EM

For negative stain EM, 3 µL of the Aβ42 fibril sample after an incubation time of 146 h was applied onto a glow-discharged 300 mesh carbon-coated copper grid (EM Sciences, ECF300-CU). The sample was incubated on the grid for 2 min and excess liquid was blotted off with filter paper. Afterwards, 3 µL of 2% (w/v) UrAc were applied onto the grid and incubated for 1min. The UrAc was removed with filter paper and the grid was air-dried. TEM images were acquired using a ThermoFisher Scientific Talos 120C at an accelerating voltage of 120 kV. Images were collected on a 4k x4k Ceta 16M CMOS camera using EPU data collection software.

4.2.3. Cryo-EM Data Acquisition

Sample vitrification was performed by Hans Duimel at Maastricht University. 2.5 µL of Aβ42 fibrils in NaPi buffer at pH 7.4 after 21 h incubation time was applied to holey gold grids (UltraAuFoil 1.2/1.3, 300 mesh), blotted with filter paper for 3 s and plunge frozen in liquid ethane using a Vitrobot (FEI), set at 95% humidity and 4°C temperature. Two cryo-EM datasets was collected by Raimond Ravelli at NeCEN in Leiden and joined for image processing (Table 4.1).

	First Dataset	Second Dataset
Data collection		
Microscope	Titan Krios	Titan Krios
Voltage [kV]	300	300
Detector	K3	K3
Energy filter slit width [eV]	20	20
Magnification	105,000	105,000
Pixel size [Å]	0.836	0.836
Defocus range [µm]	-1.2 to -2.2	-1.2 to -2.2
Exposure time [s]	2.52	2.52
Number of frames	50	50
Total dose [$e^-/Å^2$]	50	50

Table 4.1.: Cryo-EM data collection statistics of *in vitro* Aβ(1-42) fibrils at neutral pH.

4.2.4. Image processing and helical reconstruction

Prior to helical reconstruction, movie frames were gain-corrected, binned by a factor of two, aligned, and summed into single micrographs using RELION's implementation of MotionCor2 [208]. CTF estimation was performed using CTFFIND4.1 [209]. Helical reconstruction was performed using the helical reconstruction methods implemented in RELION [223, 272]. Fibrils were picked manually and polymorphs were separated using reference-free 2D class classification at a larger box size of 900 pix (downscaled to a box size of 300 pix). A featureless cylinder was lowpass filtered to 40 Å and used as initial model for 3D refinement. Several rounds of classification and refinement were used to increase the resolution by finding the optimal particle set, refining angular assignments and helical parameters. The initial helical rise was set to 4.75 Å and the twist was calculated from the cross-over distance measured from the larger box 2D class averages. 3D auto-refinement and subsequent post-processing was performed to compute the final B-factor sharpened map. The resolution as stated in Table 4.2 was calculated during post-processing according to gold-standard Fourier Shell Correlations at 0.143 applying a soft-edged solvent mask. ChimeraX [305] was used for molecular graphics and analyses. Further information on image processing can be found in Table 4.2.

	PM1	PM1.1	PM1.2	PM2	PM3	PM4	PM5	PM6
Micrographs	3,946	3,946	3,946	3,946	3,946	3,946	3,946	3,946
Box width [pix]	300	300	300	300	300	300	300	300
Initial particle images [no.]	453,373	453,373	453,373	453,373	453,373	453,373	453,373	453,373
Final particle images [no.]	76,289	31,558	29,011	48,072	10,797	25,570	9,944	7,994
Symmetry imposed	C1	C1	C1	C1	C2	C1	C1	C1
Helical rise [Å]	4.76	4.76	4.76	4.76	4.75	4.81	4.77	4.75
Helical twist [°]	-2.15	-2.17	-2.16	-2.37	-1.85	-1.42	-2.28	-3.78
Map resolution [Å]	3.9	4.4	5.0	4.9	5.2	4.6	4.6	8.4
FSC threshold	0.143	0.143	0.143	0.143	0.143	0.143	0.143	0.143
Applied B-factor [Å^2]	-134	-189	-179	-191	-200	-167	-142	-476

Table 4.2.: Structure determination statistics of *in vitro* Aβ(1-42) fibrils at neutral pH.

4.3. Contribution

For this project, I performed negative stain EM screening of a sample similar to the one used for cryo-EM. I performed image processing of the dataset and determined the structures of six polymorphs.

5. Publication II: The Uppsala APP deletion causes early onset autosomal dominant Alzheimers disease by altering APP processing and increasing amyloid β fibril formation.

Our collaboration partners in Uppsala, Sweden identified a multi-codon APP deletion mutation that causes early onset AD in three individuals in a family from Uppsala. The effects of this mutation along with a first structural idea of the resulting synthetic mutant Aβ fibrils were published in *Science Translational Medicine* in 2021 [82]. The following summary gives a brief overview of the most important results of Publication II. Subsequently, my contribution to this study is presented in more detail in a separate section. Both the article as well as its supplementary information can be found in the Appendix: *C Publication II*

5.1. Summary

The following text was adapted from Publication II.

The Uppsala mutation is the first reported multi-codon APP deletion (Δ690-695) that causes an autosomal-dominant inherited form of early-onset AD. All three mutation carriers (sibling 1, sibling 2, cousin) show an early symptom onset

at age 43 (sibling 1), 40 (sibling 2) and 41 (cousin) and a rapidly progressing disease course. Analyses of the cerebrospinal fluid (CSF) revealed Aβ42 concentrations comparable to those of non-AD controls, but pathologically elevated concentrations of total tau and phospho-tau. Additionally, amyloid-PET imaging with [^{11}C]PIB was performed for two carriers, showing only a slightly positive pattern. However, brain autopsy of one patient brain shows a widespread tau pathology and abundant and widespread Aβ plaques, consisting mainly of full-length and N-terminally truncated AβUpp42$_{\Delta 19\text{-}24}$. Mutation carriers have lower levels of Aβ oligomers and protofibrils than sAD patients, comparable to healthy controls. Cell culture experiments showed that the mutation increases β-secretase cleavage and thus the production of Aβ and alters α-secretase cleavage. Furthermore, *in vitro* aggregation experiments suggest a higher propensity of AβUpp42$_{\Delta 19\text{-}24}$ to aggregate into fibrils and an accelerated deposition of these fibrils into amyloid plaques.

5.2. Results - TEM analysis

The following text was adapted from Publication II.

For structural investigations, Martin Ingelsson provided synthetic AβUpp(1-42)$_{\Delta 19\text{-}24}$ peptide. Christine Röder performed sample purification by reversed phase-high performance liquid chromatography (RP-HPLC) and set up the fibrillisation at low pH fibrillisation conditions (30% (v/v) acetonitrile (AcN), 0.1% (v/v) trifluoroacetic acid (TFA)) [306]. The fibrils formed during several weeks of incubation at room temperature under quiescent conditions. EM screening of negatively stained fibrils revealed the presence of several µm long, well-ordered fibrils and a high degree of polymorphism. Out of four polymorphs that could be identified on negative stain EM images, two were present in sufficient concentration in the cryo-EM dataset to perform image processing. The structures of the dominant polymorphs were determined to resolutions of 5.7 Å and 5.1 Å for the first and second polymorph, respectively. Both polymorphs consist of two symmetrical protofilaments. Initial estimates for the helical symmetry reveal a pseudo 2_1 symmetry for both polymorphs with a helical rise of 2.41 Å and a helical twist of 178.45° for the first polymorph and a helical rise of 2.29 Å and a helical twist of 179.45° for the second polymorph. Atomic model building was not possible due

to the medium resolution of the reconstructions. However, a preliminary backbone trace confirms that for both polymorphs all 36 residues could potentially be accommodated in the density. Moreover, the double S-shaped polymorph 1 resembles to some degree a medium resolution cryo-EM structure of a wild-type Aβ(1-42) fibrils [307]. Here, the protofilament interface as well as the fibril core could be identical. The G-shaped fold of polymorph 2 seems to be novel, however, some vague similarity to a previously described cryo-EM structure of wild-type Aβ(1-42) fibrils can be observed [252]. In particular, the salt bridge between D1 in one protofilament and K28 in the opposite protofilament might also be present in polymorph 2. However, the C-terminal protofilament interface in the fibril core more closely resembles the interface in two solid-state NMR structures of wild-type Aβ(1-42) [254, 255].

5.3. Contribution

For this study, I performed negative stain EM sample screening, cryo-EM grid preparation, data acquisition and image processing. Additionally, I incorporated my results into the manuscript. I am a co-author of this article.

6. Cryo-EM Structures of AβUpp(1-42)$_{\triangle 19\text{-}24}$ Fibrils

For a brief introduction to the Uppsala deletion mutation, which causes a dominantly inherited form of early-onset AD, the reader is referred to Chapter 5. A first insight into the structure of AβUpp(1-42)$_{\Delta 19\text{-}24}$ fibrils was already presented within publication II (Chapter 5, Appendix: *C Publication II*).

During the course of this project, the structure of *in vitro* AβUpp(1-42)$_{\Delta 19\text{-}24}$ fibrils was determined at higher resolution using cryo-EM (Chapter 6.1.1). For this, Martin Ingelsson provided synthetic peptide, which was purified by RP-HPLC by Christine Röder and fibrillised under low pH conditions as described in *Publication II*.

Subsequently, the cryo-EM structure of murine AβUpp(1-42)$_{\Delta 19\text{-}24}$ fibrils has been determined (Chapter 6.1.2). The fibrils were purified from tg-UppSwe mouse brain tissue by Fernanda Salome Peralta Reyes following a previously described sarkosyl extraction protocol [261]. The mouse model was developed by María Pagnon de la Vega [308] and the tissue material was provided by Martin Ingelsson. Transgenic tg-UppSwe mice express human APP with the Uppsala mutation and the Swedish mutation [308]. The latter increases Aβ production [308].

Lastly, cryo-EM data of AβUpp(1-42)$_{\Delta 19\text{-}24}$ fibrils purified by Fernanda Salome Peralta Reyes (following a previously described sarkosyl extraction protocol [261]) from human brain tissue provided by Martin Ingelsson, was collected and the data was processed (Chapter 6.1.3). The latter is an ongoing project with further experiments being conducted by Simon Sommerhage.

6.1. Results and Discussion

6.1.1. The *in vitro* structure of AβUpp(1-42)$_{\Delta 19-24}$ fibrils

The sample of *in vitro* AβUpp(1-42)$_{\Delta 19-24}$ fibrils was prepared as previously described (Chapter 5, Appendix: *C Publication II*, Chapter 6.2.1). A first screening of the AβUpp(1-42)$_{\Delta 19\text{-}24}$ fibril sample after 46 days of incubation by atomic force microscopy (AFM) and negative-stain EM revealed straight and long fibrils with at least four different polymorphs present in the sample (Figure 6.1).

In the acquired cryo-EM micrographs (Figure 6.2 A), a predominance of two fibril polymorphs (Figure 6.2 B,C) could be observed. The first and second polymorph account for 50% and 38% of all fibrils in the dataset, respectively (Figure 6.2 D). Hence, image reconstruction from the cryo-EM images was possible for these two dominant polymorphs. In agreement with previous findings [82], visual inspection of the cryo-EM micrographs as well as 2D classification confirm that both filament types consist of two intertwined protofilaments (Figure 6.2 A,B,C).

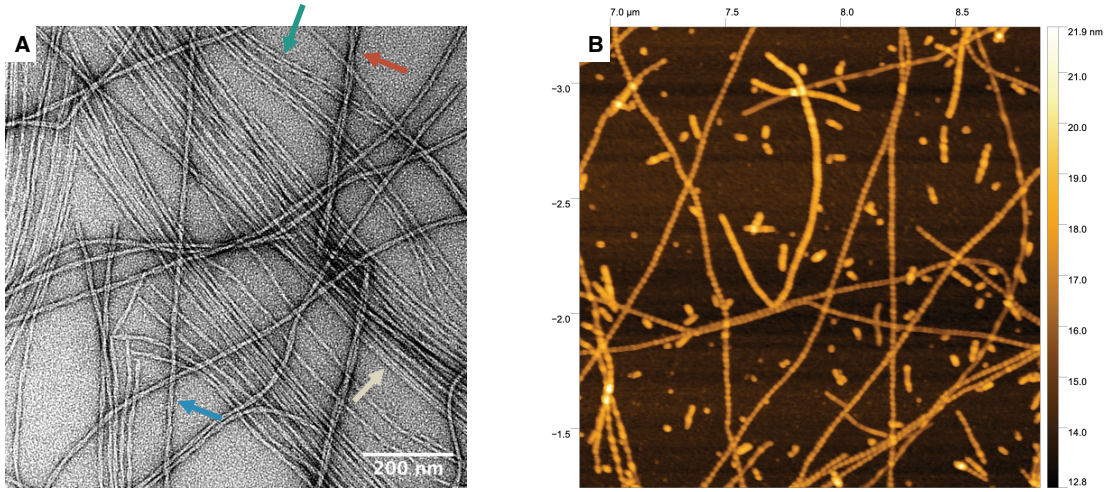

Figure 6.1.: (A) Negative stain EM and (B) AFM images of *in vitro* AβUpp(1-42)$_{\Delta 19\text{-}24}$ fibrils.

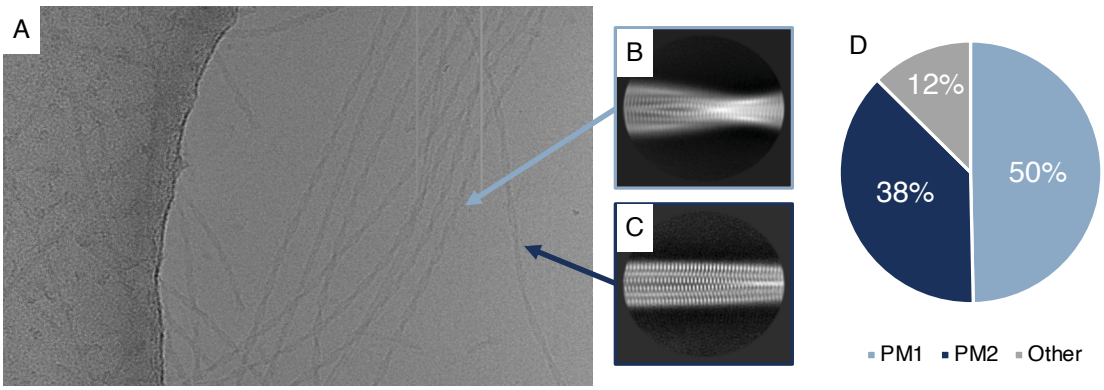

Figure 6.2.: Overview on the Cryo-EM Data Acquisition of *in vitro* AβUpp(1-42)$_{\Delta 19\text{-}24}$ fibrils. (A) One exemplary micrograph collected on a Talos Arctica. (B,C) Exemplary 2D class of the first (B) and second (C) polymorph. (D) Distribution of fibril polymorphs in the dataset.

AβUpp(1-42)$_{\Delta 19-24}$ Polymorph 1 In the recorded dataset of *in vitro* AβUpp(1-42)$_{\Delta 19\text{-}24}$ fibrils, a dominance of the rather fast twisting polymorph 1 with a corresponding small crossover distance of ~260 Å was observed. The width of the fibrils in the 2D projection images ranges from 4 - 8 nm (Figure 6.3 B). The 3D Cryo-EM map, that was determined to a resolution of 3.3 Å (based on the gold-standard FSC 0.143 criterion; Figure 6.4) shows clear sheet separation along the helical axis with a layer spacing of ~4.75 Å (Figure 6.3 C). 2D class averages already revealed a staggered arrangement of the layers of both protofilaments (Figure 6.2 B). 3D reconstruction confirms that the two protofilaments are related by a pseudo-2_1 screw symmetry assuming a right-handed twist with a helical rise of 2.37 Å and a helical twist of -178.4° (Figure 6.3 C). It should be noted, however, that the determination of the handedness by AFM was inconclusive, so a left-handed twist cannot be excluded. The cross-section reveals two identical monomeric subunits, which fold into an extended S-shape with a large inter-protofilament interface (Figure 6.3 D,E). The visibility of clear side chain densities in the reconstructed map allowed for *de novo* atomic model building of amino acids G9-A42 (Δ19-24). The missing nine amino acids D1-S8, which are located in the N-terminal part of the peptide, are likely flexible and therefore, cannot be clearly resolved in the cryo-EM map. We observed one β-sheet on the secondary structure level from residues K16-S26 (Δ19-24) (Figure 6.3 A).

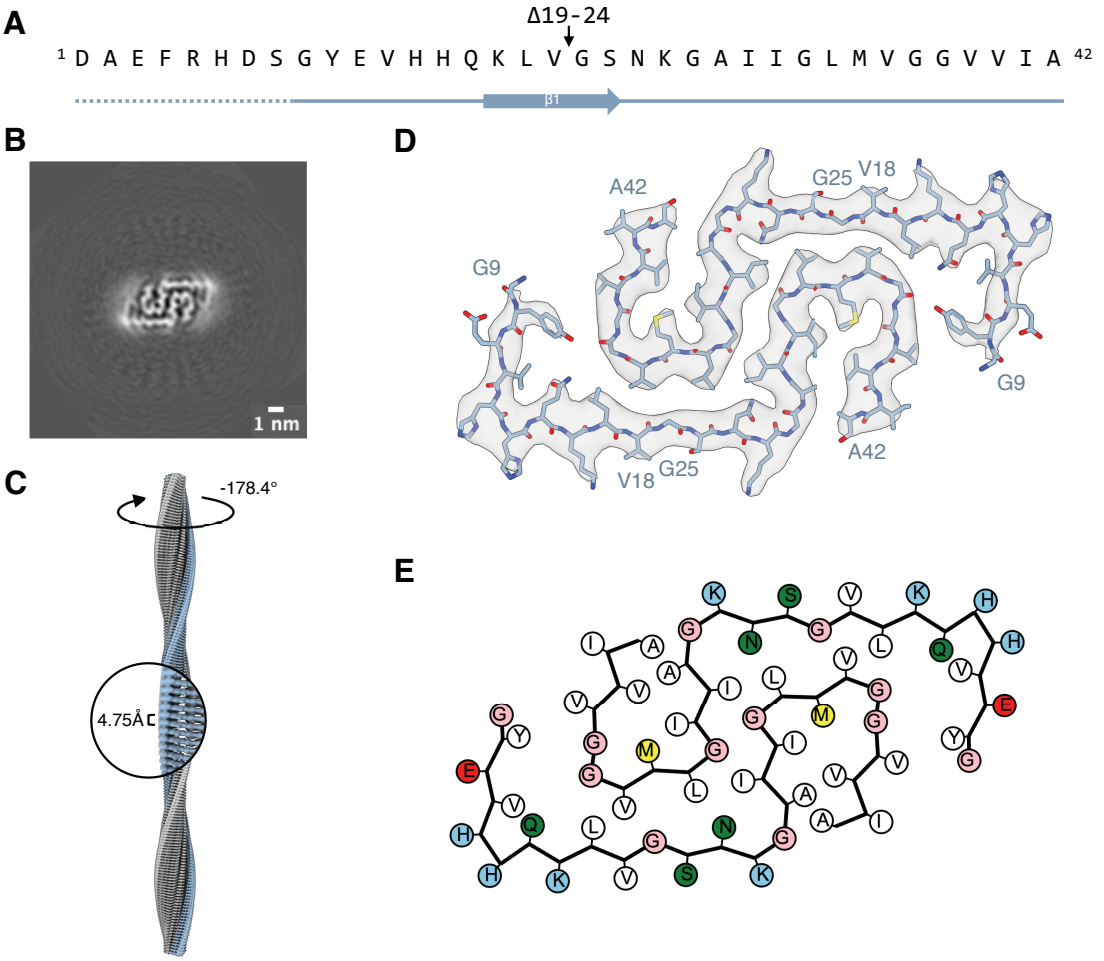

Figure 6.3.: Reconstruction of *in vitro* AβUpp(1-42)$_{\Delta 19-24}$ polymorph 1 fibrils. (A) Amino acid sequence of AβUpp(1-42)$_{\Delta 19-24}$. Solid lines indicate for which part of the sequence the atomic model was built (accordingly, dotted lines indicate for which part of the sequence atomic model building was not possible). Arrows indicate β-strands. (B) Projection of the reconstructed density including approximately one β-rung. (C) Reconstructed cryo-EM density along the helical axis with a close-up and labels denoting the helical twist and rise. (D) The cryo-EM density map (in transparent gray) with the atomic model (light blue). (E) A schematic of the fold, produced with atom2svg.py [309] (red: acidic side chain; blue: basic side chain; green: hydrophilic side chain; white: hydrophobic side chain; pink: glycine; yellow: sulfur containing)

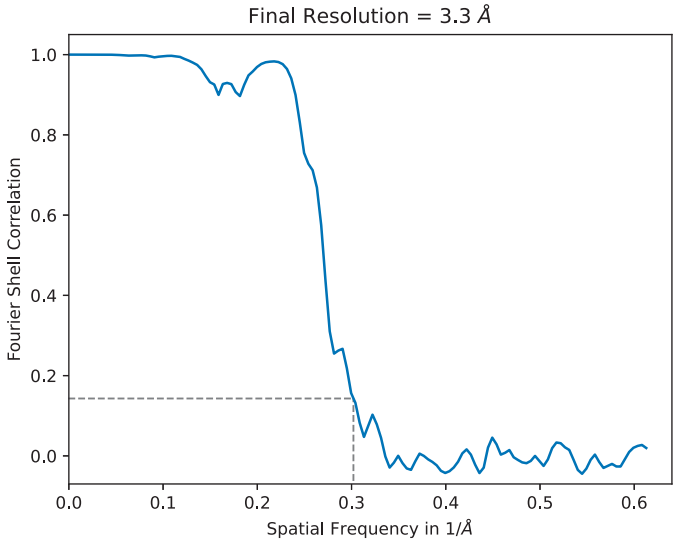

Figure 6.4.: FSC curve from the gold-standard refinement of the cryo-EM map of *in vitro* AβUpp(1-42)$_{\Delta 19-24}$ polymorph 1 fibrils yields a resolution of 3.3 Å (using the 0.143 criterion).

The first S-turn is formed by amino acids G9-G29, while the C-terminus of each monomeric subunit, that consists of a non-polar block of amino acids G29-A42, forms the second smaller S-turn. The first kink located around residues V12 and Q15 evolves around the two solvent-exposed polar residues H13 and H14. A hydrogen bond between Y10 and G37', where aa' denotes an amino acid in the respective other monomeric subunit, fixes the N-terminal part in its position and stabilizes the interface between the two protofilaments. The second S-turn of each monomeric subunit is stabilized by one hydrophobic cluster involving amino acids G29, A30, I32, M35, G38, V40 and A42. The kink of the second S-turn around N27 and I31 is stabilized by a hydrogen bond between N27 and G29^{i-1} in the neighbouring layer within the same protofilament (denoted by the index i-1). Another structural characteristic of polymorph 1 is the large inter-protofilament interface, which stabilises the dimer fold. The interface consists of two hydrophobic clusters around amino acids: (i) I31, G33, I31', G33' and (ii) G25, V36', L34'. The deletion of amino acids F19-V24 lies within the observed β-sheet between amino acids K16 to S26 on a straight, surface exposed stretch between residues H14 and K28.

AβUpp(1-42)$_{\Delta 19-24}$ Polymorph 2 The second most dominant polymorph 2 accounts for ~38% of all fibrils in the dataset (Figure 6.2 D). It has an almost constant width of 7 nm, but a high flexibility in its helical parameters resulting in observed crossover distances of ~350 - 700 Å. The observation of high helical flexibility was confirmed by 2D class averaging, where the same 2D projection could be observed for segments from fibrils with varying crossover distances. As for the first polymorph, 2D class averages of polymorph 2 show a staggered arrangement of β-strands perpendicular to the fibril axis (Figure 6.2 C). The 3.7 Å cryo-EM map (resolution estimate according to the gold-standard FSC 0.143 criterion; Figure 6.5) shows clear layer separation along the helical axis as well as visible side chain densities (Figure 6.6).

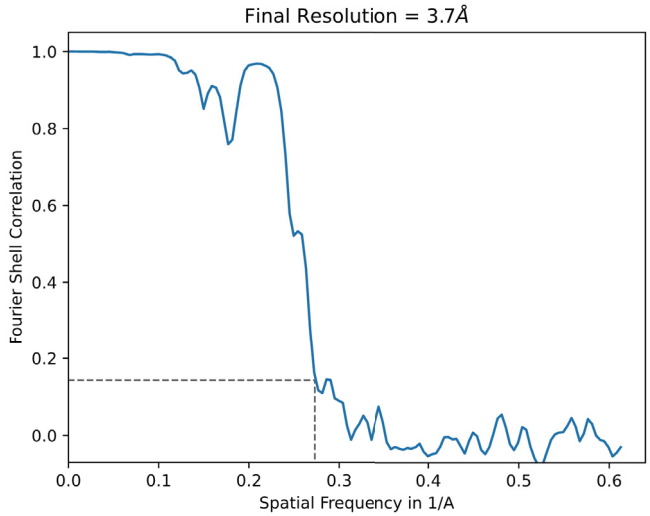

Figure 6.5.: FSC curve from the gold-standard refinement of the cryo-EM map of *in vitro* AβUpp(1-42)$_{\Delta 19-24}$ polymorph 2 fibrils yields a resolution of 3.7 Å (using the 0.143 criterion).

The two protofilaments are related by a pseudo-2_1 screw symmetry assuming a left-handed twist with a helical rise of 2.39 Å and a helical twist of 179.4°, which corresponds to a crossover distance of 690 Å (Figure 6.6 C). The cross-section of polymorph 2 reveals two identical G-shaped protofilaments (Figure 6.6 B,D). The G-fold results in a large intra-protofilament interface while the inter-protofilament interface is rather small in comparison to polymorph 1.

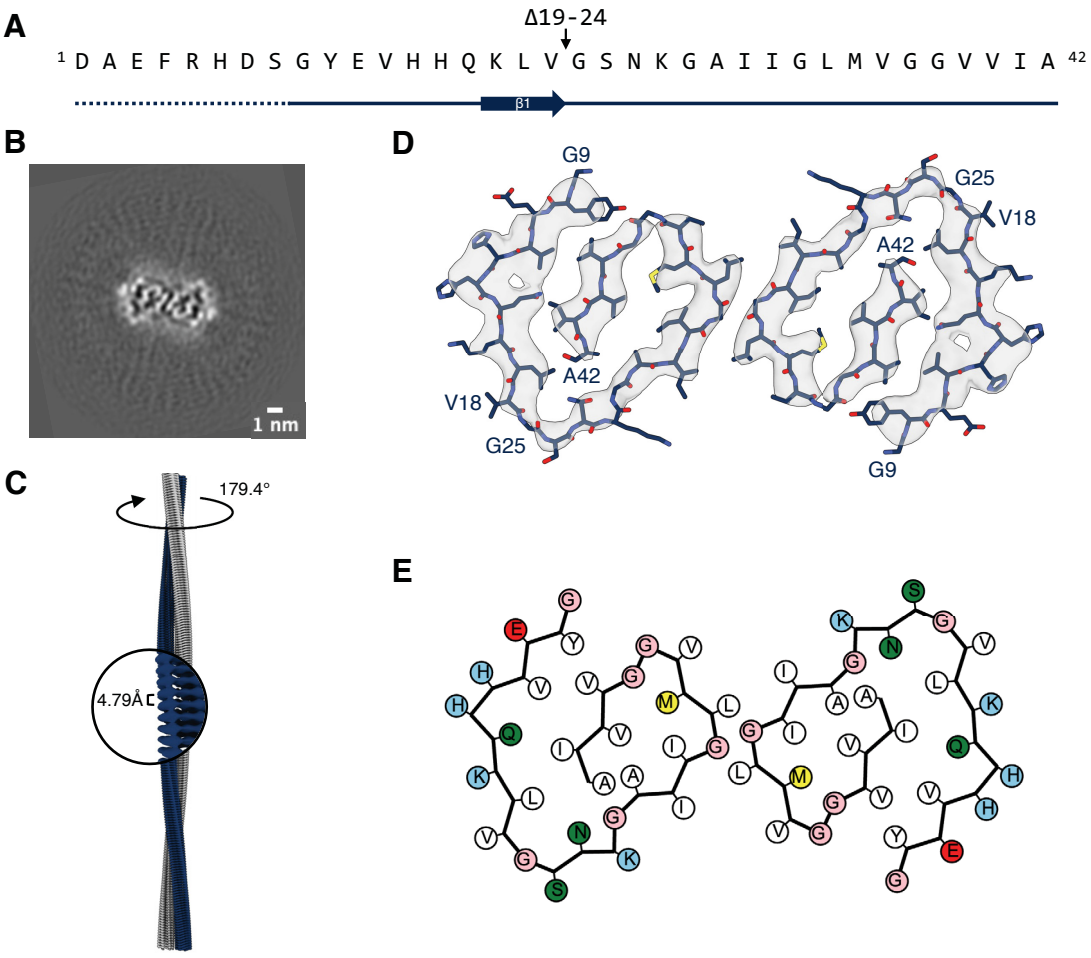

Figure 6.6.: Reconstruction of *in vitro* AβUpp(1-42)$_{\Delta 19-24}$ polymorph 2 fibrils. (A) Amino acid sequence of AβUpp(1-42)$_{\Delta 19-24}$. Solid lines indicate for which part of the sequence the atomic model was built (accordingly, dotted lines indicate for which part of the sequence atomic model building was not possible). Arrows indicate β-strands. (B) Projection of the reconstructed density including approximately one β-rung. (C) Reconstructed cryo-EM density along the helical axis with a close-up and labels denoting the helical twist and rise. (D) The cryo-EM density map (in transparent gray) with the atomic model (light blue). (E) A schematic of the fold, produced with atom2svg.py [309] (red: acidic side chain; blue: basic side chain; green: hydrophilic side chain; white: hydrophobic side chain; pink: glycine; yellow: sulfur containing)

Visible side chain densities allowed for *de novo* building of an atomic model into the reconstructed density map. The atomic model spans from amino acids G9-A42 (Δ19-24) (Figure 6.6 A). As previously discussed for polymorph 1, the missing nine N-terminal residues D1-S8 are likely flexible and therefore not resolved in the cryo-

EM map. One β-sheet was observed on the secondary structure level from residues K16-V18. The C-terminus of each monomeric subunit, that consists of a non-polar block of residues G29-A42, forms the inner curve of the G-shape, while the larger curve is formed by amino acids G9-G29. The overall G-shape is stabilized by two hydrophobic clusters involving residues: (i) G9, Y10, V12, Q15, L17, I41, V39, and G37, and (ii) G29, A30, I32, M35, G38, V40, and A42 (Figure 6.6 D,E). A hydrogen bond between N27 and G29 stabilizes the kink between the inner and the outer G-curve. The hydrophobic interface between both G-shaped monomeric subunits is rather small and involves only three amino acids: I31, G33, and L34.

Comparison with known structures The determined structures of both dominant AβUpp(1-42)$_{\Delta 19-24}$ polymorphs are novel and therefore, differ from all other Aβ fibril structures known to date. Polymorph 1 is made of two identical extended S-shaped protofilaments while polymorph 2 consists of two G-shaped protofilaments. In both cases, the protofilaments are connected by a pseudo-2_1 symmetry. The two S-shaped protofilaments of polymorph 1 are connected by a large inter-protofilament interface comprising 14 amino acids of each monomeric subunit. In contrast, the protofilament interface of polymorph 2 is rather small and comprises only three residues. However, the intra-protofilament interface is large and comprises 11 amino acids. A comparison of the fold of one monomeric subunit of both polymorphs shows that the structures differ between G9 and K28, but overlay quite well in the C-terminal domain between residues K28 and A42 (Figure 6.7 A). In polymorph 1, amino acids G9 to K28 form the large interface to the opposing protofilament, whereas these residues contribute to the intra-protofilament interface in polymorph 2. Both structures differ from a cryo-EM structure of wild-type Aβ(1-42) fibrils [252], where fibrils were formed using identical fibrillisation conditions (Figure 6.7 B). The structures of all three fibrils overlap from K28-A42, close to the introduced deletion mutation of residues F19-V24. The deleted amino acids, especially the negatively charged and solvent-exposed residues E22 and D23, are involved in a main chain kink in the wild-type Aβ(1-42) fibril. In contrast, in the dominant AβUpp(1-42)$_{\Delta 19-24}$ polymorph 1 the deletion is located on a straight part of the main chain.

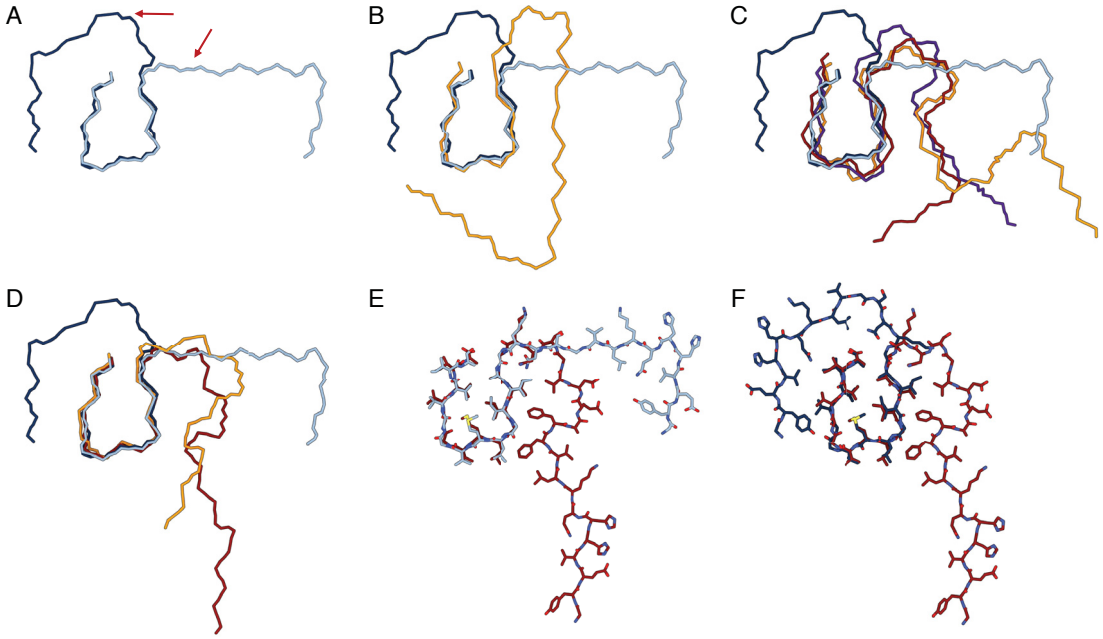

Figure 6.7.: Comparison of the *de novo* built atomic models of the two dominant *in vitro* AβUpp(1-42)$_{\Delta 19-24}$ polymorphs with other published structures of Aβ fibrils. (A) Comparison of AβUpp(1-42)$_{\Delta 19-24}$ polymorph 1 protofilaments (light blue) and AβUpp(1-42)$_{\Delta 19-24}$ polymorph 2 protofilaments (dark blue). Red arrows indicate the position of the deletion Δ19-24. (B) Comparison of AβUpp(1-42)$_{\Delta 19-24}$ polymorph 1 protofilaments (light blue) and AβUpp(1-42)$_{\Delta 19-24}$ polymorph 2 protofilaments (dark blue) with the cryo-EM structure of recombinant Aβ42 protofilaments formed using the same fibrillisation conditions (orange, PDB 5OQV). (C) Comparison of AβUpp(1-42)$_{\Delta 19-24}$ polymorph 1 protofilaments (light blue) and AβUpp(1-42)$_{\Delta 19-24}$ polymorph 2 protofilaments (dark blue) with NMR structures of Aβ42 protofilaments: PDB 2NAO (orange), PDB 2MXU (red) and PDB 5KK3 (purple). (D) Comparison of AβUpp(1-42)$_{\Delta 19-24}$ polymorph 1 protofilaments (light blue) and AβUpp(1-42)$_{\Delta 19-24}$ polymorph 2 protofilaments (dark blue) with cryo-EM structures of brain extracted Aβ42 protofilaments: PDB 7Q4B (red) and PDB 7Q4M (orange). (E) Comparison of AβUpp(1-42)$_{\Delta 19-24}$ polymorph 1 protofilaments (light blue) with one protofilament of human brain extracted Aβ42 type I filaments (PDB 7Q4B, red). (F) Comparison of AβUpp(1-42)$_{\Delta 19-24}$ polymorph 2 protofilaments (dark blue) with one protofilament of human brain extracted Aβ42 type I filaments (PDB 7Q4B, red).

The kink around E22 and D23 is also found in NMR structures of recombinant Aβ42 fibrils [254, 255, 257] (Figure 6.7 C). These NMR structures also show a similar C-terminal fold and thus, overlay with the obtained structures of AβUpp(1-42)$_{\Delta 19-24}$ fibrils from amino acids K28-A42. This common structural motif can

also be found in cryo-EM structures of Aβ(1-42) filaments purified from human brain tissue (Figure 6.7 D) [261]. Interestingly, the rather untypical orientation of side chains Y10-H14 is similar in AβUpp(1-42)$_{\Delta 19-24}$ polymorph 1 and polymorph 2 and *ex vivo* Aβ42 type I filaments (Figure 6.7 E,F).

6.1.2. The structure of murine AβUpp(1-42)$_{\Delta 19-24}$ fibrils

The sample of AβUpp(1-42)$_{\Delta 19-24}$ fibrils extracted from tg-UppSwe mouse brain tissue shows only one fibril polymorph in contrast to the *in vitro* preparation. A representative micrograph and 2D classes are shown in Figure 6.8. The 2D class averages already indicate the presence of additional density bound to the fibril surface (Figure 6.8 B).

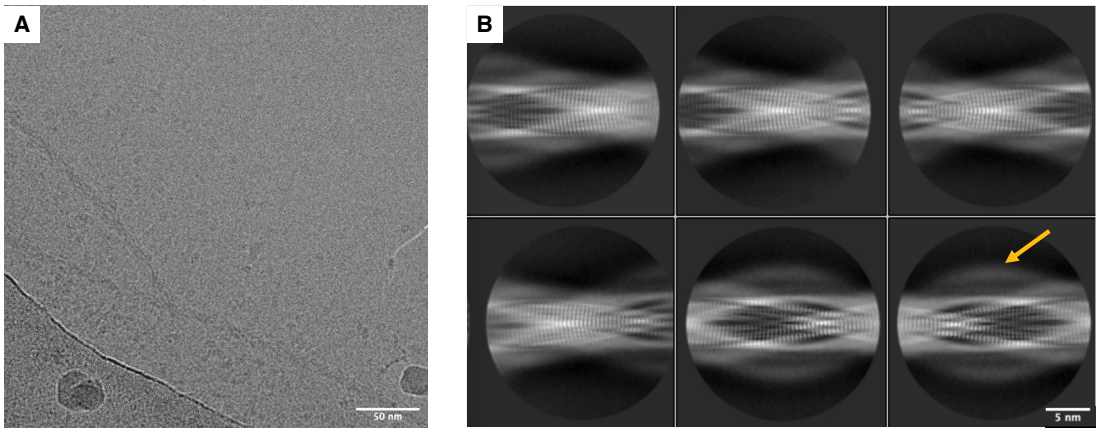

Figure 6.8.: (A) One representative cryo-EM mirograph of murine AβUpp(1-42)$_{\Delta 19-24}$ fibrils. (B) Six representative 2D classes of murine AβUpp(1-42)$_{\Delta 19-24}$ fibrils. The arrow indicates additional density that surrounds the fibril.

Immunogold negative stain EM with the Aβ monoclonal antibody Nab228 confirms that the fibrils visible in Figure 6.8 are indeed Aβ fibrils (Figure 6.9).

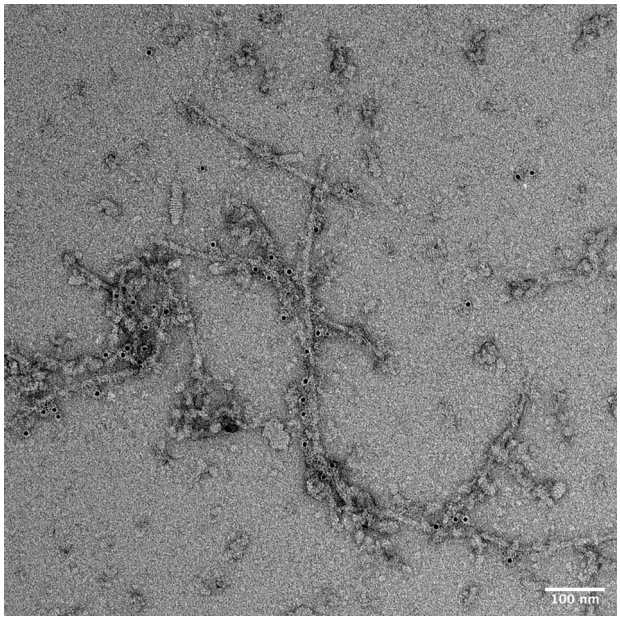

Figure 6.9.: Immunogold negative-stain EM image of the purified Aβ fibrils from tg-UppSwe mouse brain tissue labelled with Nab228 as primary antibody.

The cryo-EM structure of murine AβUpp(1-42)$_{\Delta 19-24}$ fibrils was determined to a resolution of 3.2 Å (based on the gold-standard FSC 0.143 criterion; Figure 6.10).

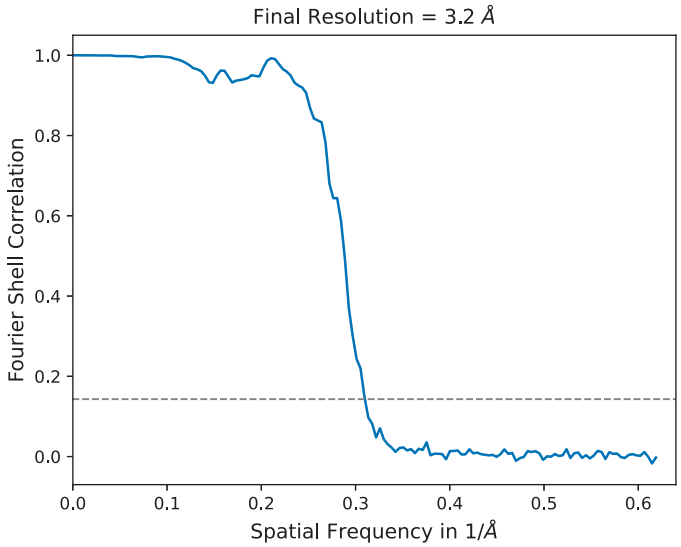

Figure 6.10.: FSC curve from the gold-standard refinement of the cryo-EM map of murine AβUpp(1-42)$_{\Delta 19-24}$ fibrils yields a resolution of 3.2Å (using the 0.143 criterion).

Murine AβUpp(1-42)$_{\Delta 19-24}$ fibrils are made of two symmetrical S-shaped protofilaments (Figure 6.11 B) that are related by a pseudo-2_1 screw symmetry with a refined helical twist of 178.3° and a helical rise of 2.36 Å (Figure 6.11 C).

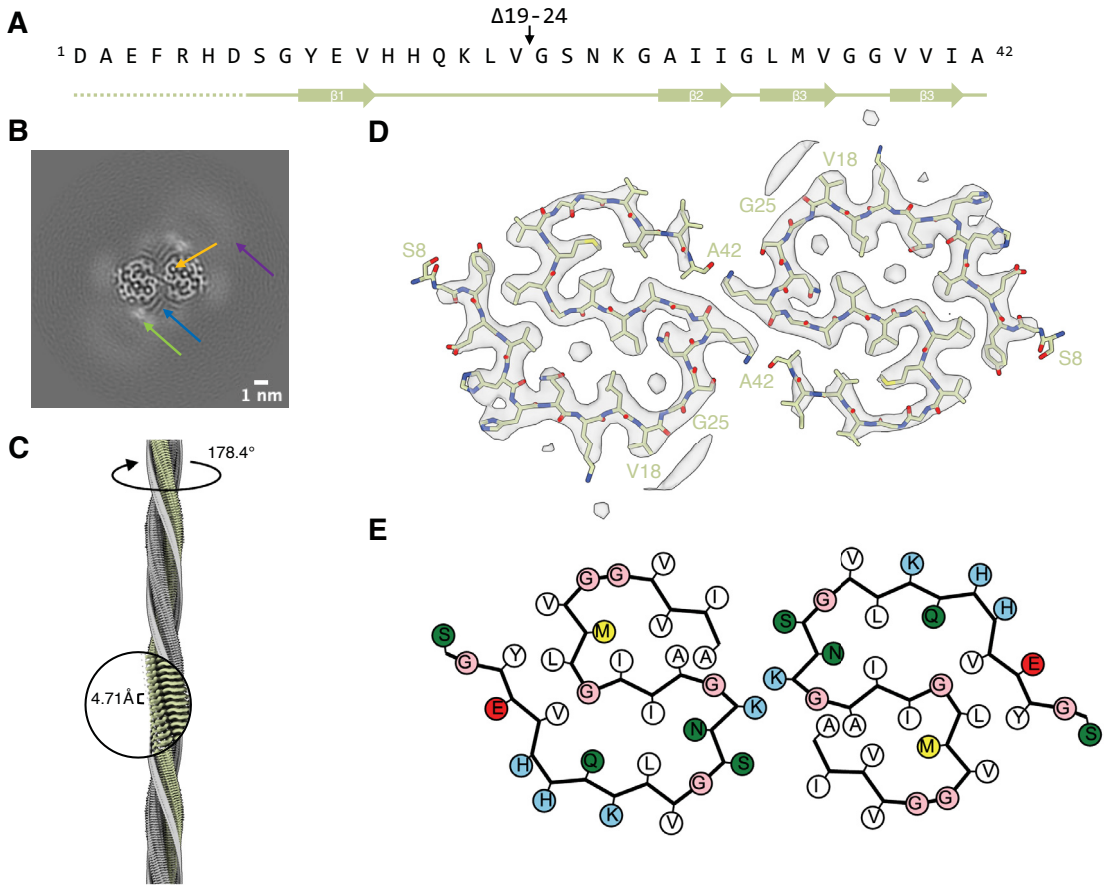

Figure 6.11.: The tg-UppSwe murine Uppsala fold of Aβ. (A) Amino acid sequence of AβUpp(1-42)$_{\Delta 19-24}$. Solid lines indicate for which part of the sequence the atomic model was built (accordingly, dotted lines indicate for which part of the sequence atomic model building was not possible). Arrows indicate β-strands. (B) Projection of the reconstructed density including approximately one β-rung. Arrows indicate bound additional densities: small, localized density (yellow), larger, localized density (green), micelle-like, weaker density (purple), and rod-like density (blue). (C) Reconstructed cryo-EM density along the helical axis with a close-up and labels denoting the helical twist and rise. (D) The cryo-EM density map (in transparent gray) with the atomic model (light green). (E) a schematic of the fold, produced with atom2svg.py [309] (red: acidic side chain; blue: basic side chain; green: hydrophilic side chain; white: hydrophobic side chain; pink: glycine; yellow: sulfur containing)

Model building was possible for the ordered fibril core that extends from residues S8 to A42 (Δ19 - 24) (Figure 6.11 A,C,D). Four β-sheets can be observed in each protofilament, extending over the following residues: (i) Y10 - V12, (ii) A30 - I32, (iii) L34 - V36 and (iv) V39 - I41 (Figure 6.11 A). Two hydrophobic cluster around residues (i) Y10, V12, Q15, L17, N27, I31, and L34, and (ii) A30, I32, M35, V40, and A42 stabilize the S-fold of each protofilament. In addition, a hydrogen bond between Q15 and the carbonyl group at H13 in the same protofilament stabilises the first, larger S-turn. The protofilament interface is stabilised by two symmetrical hydrogen bonds between A42 and K28 of the opposing protofilament.

Additional surface-bound densities as well as two smaller, localised densities harboured in the intraprotofilament interface can be observed (Figure 6.11 B, yellow arrow). The densities in the protofilament cavity and a surface-bound density between residues H14 and K16 indicate the presence of additional hydrophobic and hydrophilic molecules, respectively, whose identity remains unknown. Additionally, a larger, strong density can be observed close to K16 (Figure 6.11 B, green arrow). Similar densities were previously observed in Aβ fibrils extracted from other mouse models (compare Chapter 3). Moreover, as also previously described for other murine Aβ fibrils (compare Chapter 3), weaker, micelle-like densities can be observed on the fibril surface (Figure 6.11 B, purple arrow). Finally, rod-shaped densities are located close to residues V18 - S26 (Δ19 - 24) and V39 - A42 (Figure 6.11 B, blue arrow).

Murine AβUpp(1-42)$_{\Delta 19-24}$ fibrils and *in vitro* AβUpp(1-42)$_{\Delta 19-24}$ fibrils share a common C-terminal fold and overlay between K28 and A42, but their overall fibril structures differ (Figure 6.12 A). The aggregation of AβUpp(1-42)$_{\Delta 19-24}$ into structurally distinct polymorphs in mice and *in vitro* is likely related to cofactors that are present in the mouse brain, but absent in the *in vitro* preparation. Interestingly, the Uppsala fold of Aβ from tgUppSwe mouse brain shows some similarity to human type II filaments, that were found mostly in individuals with fAD (Figure 6.12 B). Murine AβUpp(1-42)$_{\Delta 19-24}$ fibrils and type II filaments share the same overall S-fold, and show an identical protofilament interface. Prior to the mutation site, side chain orientations differ, but the structures are almost identical between G25 and A42.

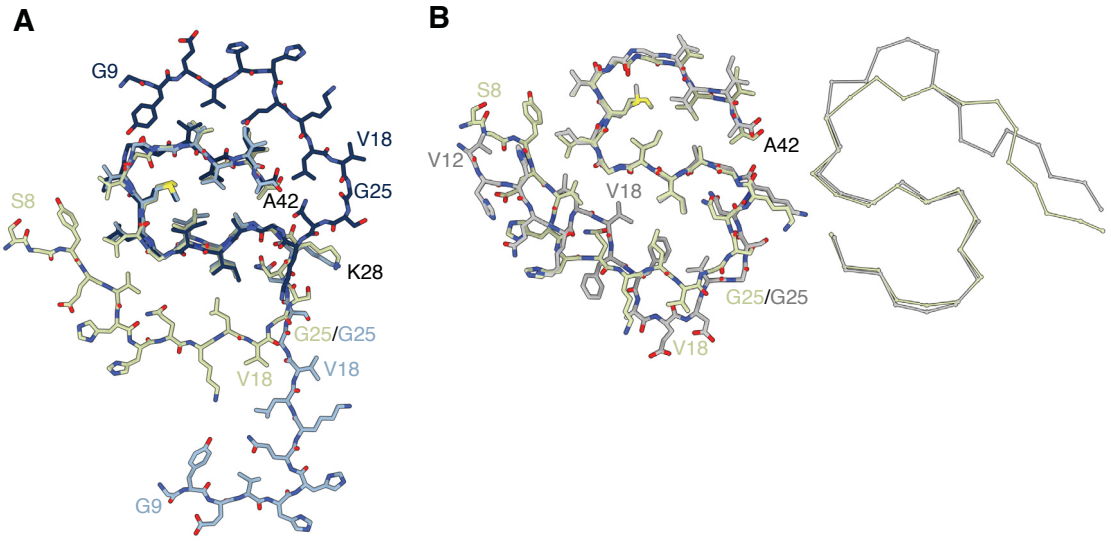

Figure 6.12.: Comparison of protofilaments and fibrils of AβUpp(1-42)$_{\Delta 19-24}$. (A) Comparison of the cryo-EM structures of murine AβUpp(1-42)$_{\Delta 19-24}$ protofilaments (green) with the cryo-EM structure of *in vitro* AβUpp(1-42)$_{\Delta 19-24}$ polymorph 1 (light blue) and polymorph 2 (dark blue) protofilaments. (B) Comparison of the cryo-EM structures of murine AβUpp(1-42)$_{\Delta 19-24}$ fibrils (green) with the cryo-EM structure of human brain Type II Aβ42 fibrils (gray, PDB 7Q4M).

6.1.3. Cryo-EM of a human AβUpp(1-42)$_{\Delta 19-24}$ sample

In contrast to the Aβ fibril sample obtained from tg-UppSwe mice, where all amyloid fibrils observed were Aβ fibrils, the immunogold negative stain EM images of the AβUpp(1-42)$_{\Delta 19-24}$ fibril sample purified from human brain tissue of an individual with the Uppsala mutation show a second population of fibrils (Figure 6.13). Analogous to the murine sample, the monoclonal Aβ antibody Nab228 was used as primary antibody. However, in the human fibril sample, the vast majority of fibrils is not labelled with gold, meaning that they were not recognised by the primary anti-Aβ antibody. The presence of tau fibrils in purified Aβ fibril samples has been previously reported for the sarkosyl extraction method [285]. The unlabelled fibrils are therefore likely to be tau fibrils. Furthermore, Aβ fibrils, which can be identified by the bound gold particles, are often observed within large fibril clusters (Figure 6.13 B).

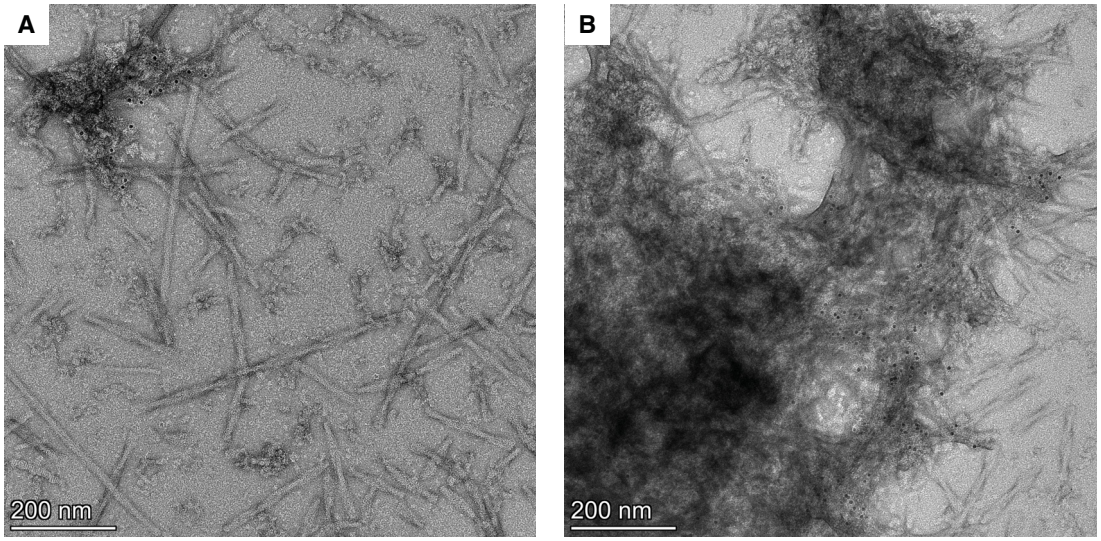

Figure 6.13.: Immunogold negative-stain EM image of the purified Aβ fibrils from brain tissue of an individual with the Uppsala mutation. The Aβ directed antibody Nab228 was used as primary antibody. (A) Unlabelled fibrils are most likely Tau fibrils. (B) Aβ fibrils tend to accumulate into fibril clusters.

In line with these findings, we also observed the presence of thicker isolated fibrils as well as fibril clusters on the acquired cryo-EM images (Figure 6.14 A). In addition, a rather thick and decorated fibril with a width of ~260 Å and a crossover distance of ~780 Å could be observed on some micrographs (Figure 6.14 B). The decoration, which creates a strong contrast on the cryo-EM image, has a diameter of ~60 - 80 Å. Due to the strong clustering of the fibrils as well as low contrast, fibrils were picked manually, however, it was not possible to distinguish between different polymorphs or amyloid fibril species. Accordingly, 2D classification at a larger box size of 1200 pix downscaled to 300 pix was performed to separate different fibril polymorphs. Representative 2D class averages are shown in Figure 6.15. From the 2D classification at a larger box size (Figure 6.15), the manual picked fibril particle set could be clustered manually into four different subsets. The first and dominant fibril type (Figure 6.15, orange arrow) has a diameter of ~18 nm, a crossover distance of ~750 Å, as well as a visible fuzzy coat that surrounds the fibril. The second fibril appears to be straight in the 2D class averages at a larger box size (Figure 6.15, burgundy arrow). This fibril has a diameter of ~6.5 nm.

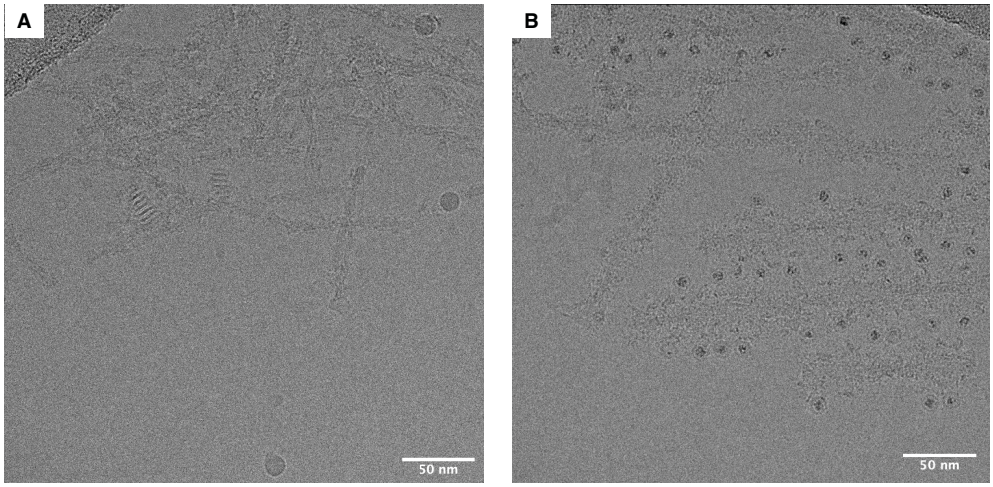

Figure 6.14.: Exemplary cryo-EM micrographs of fibrils extracted from brain tissue of an individual with the Uppsala mutation. (A) Human *ex vivo* fibrils tend to cluster. (B) On some images, decorated fibrils could be observed.

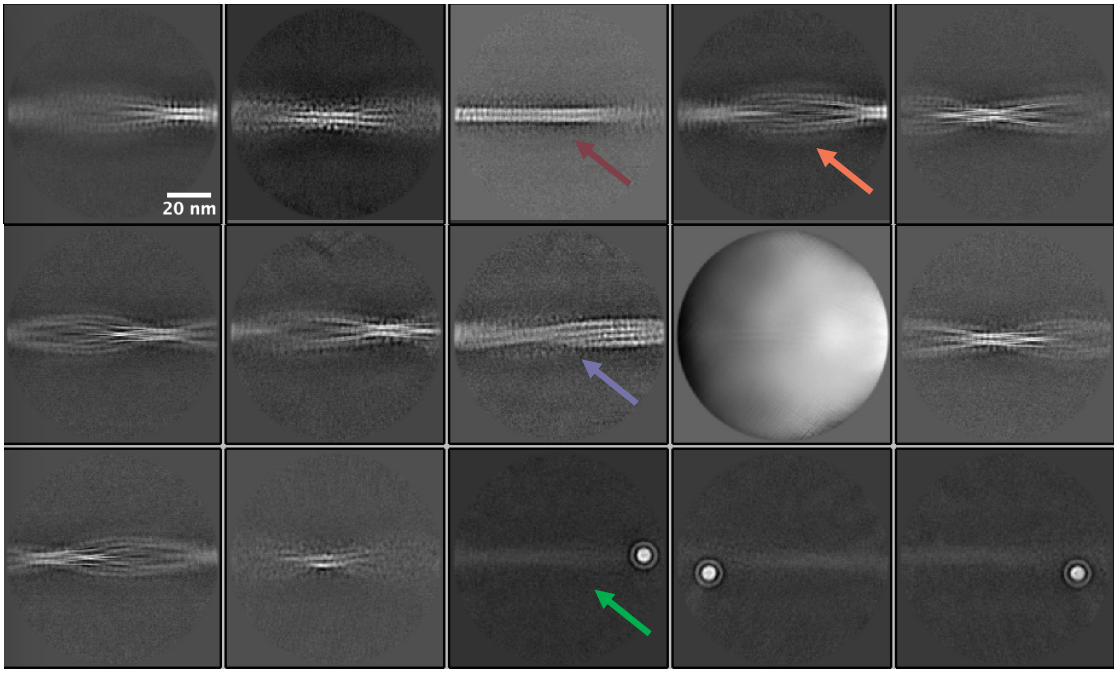

Figure 6.15.: Representative 2D class averages of fibrils extracted from the brain tissue of an individual with the Uppsala mutation. Four different fibril types could be observed indicated by the coloured arrows: symmetric and comparable thick fibrils (orange), straight fibrils (burgundy), asymmetric fibrils (lavender), and decorated fibrils (green). The scale bar in the upper left class applies to all classes.

The third fibril seems to be asymmetric in the displayed 2D class averages (Figure 6.15, lavender arrow). It has a crossover distance of ~680 Å and a width of ~13 nm. Finally, in the fourth type of 2D class averages, a faint fibril density can be observed together with a bright white spot (Figure 6.15, green arrow). The spot, that clearly dominated the alignment, has a diameter of ~65 Å. This corresponds to the diameter of the fibril decoration visible in Figure 6.14 B. The subsequent 2D classification of the four different subgroups at smaller box sizes shows more structural details (Figure 6.16).

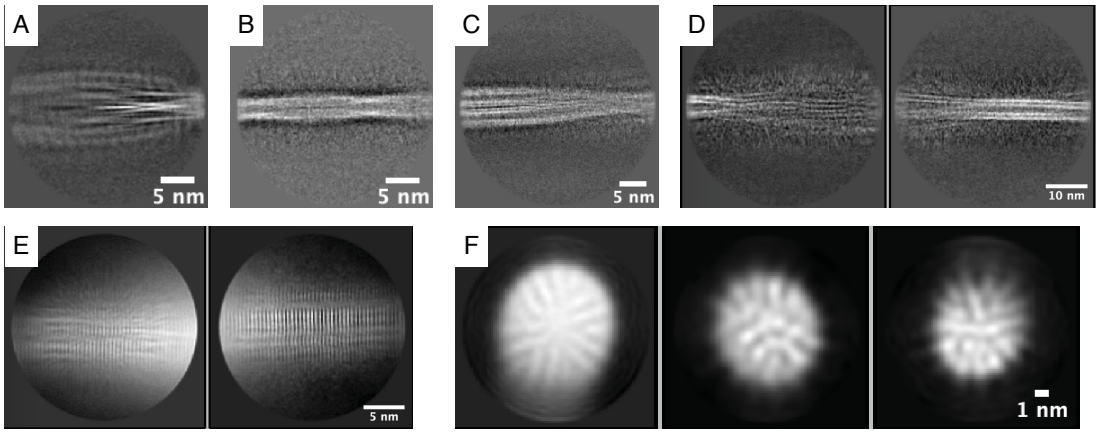

Figure 6.16.: 2D classification of the four fibril subsets in a human Uppsala mutation case cryo-EM dataset. (A) Representative 2D class average of the first fibril at a box size of 600 pix (downscaled to 300 pix). (B) Representative 2D class average of the second fibril at a box size of 600 pix (downscaled to 300 pix). (C) Representative 2D class average of the third fibril at a box size of 756 pix (downscaled to 378 pix). (D) Representative 2D class average of the fourth fibril at a box size of 600 pix (downscaled to 300 pix). (E) Representative 2D class average of the fourth fibril at a box size of 300 pix. (F) Representative 2D class average of the decoration on the fourth fibril at a box size of 168 pix.

Tau paired helical filaments purified from human AβUpp(1-42)$_{\Delta 19-24}$ brain tissue 2D class averages as displayed in Figure 6.16 A identify the dominant fibril, accounting for 92.5% of all reconstructed fibrils, as a tau paired helical filament (PHF) whose structure was previously described by Fitzpatrick et al. [262]. Nevertheless, an initial model was generated *de novo* from multiple 2D class averages at a box size of 600 pix downscaled to a pixel size of 1.616 Å/pix using the

`relion_helix_inimodel2d` command [267] to ensure an unbiased reconstruction process (Figure 6.17).

Despite the limited resolution of the 2D class averages used for the generation of the initial model (Figure 6.17 A), the resulting 3D reconstruction already achieves sufficient resolution to distinguish between the two protofilaments and even identify the protofilament fold (Figure 6.17 B-D). Subsequent refinement results in a 3D reconstruction of the PHF tau filament at a resolution of 3.3 Å (based on the gold-standard FSC 0.143 criterion; Figure 6.18 A,B, and Figure 6.19). The atomic model of PHF tau filaments from a sporadic AD brain (PDB 5O3L) was refined into the reconstructed density map of PHF tau filaments extracted from human brain tissue of an individual with the Uppsala mutation (Figure 6.18 B). An overlay of the sAD PHF structure and the PHF structure from a Uppsala mutation case is shown in Figure 6.18 C.

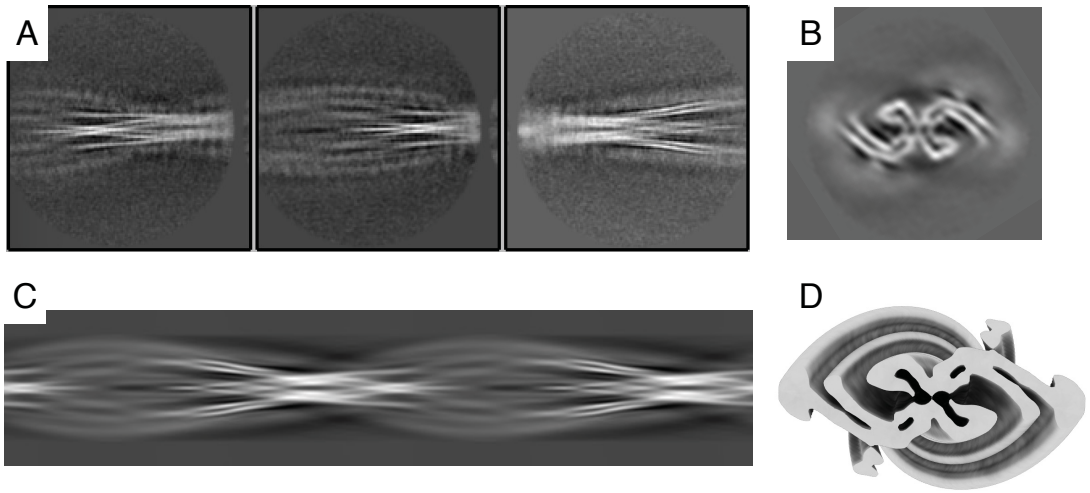

Figure 6.17.: *De novo* initial model of a PHF tau filament observed in a human Uppsala mutation case cryo-EM dataset generated from multiple smaller 2D class averages. (A) Three representative 2D class averages out of 15 2D class averages that were used to generate the initial model. (B) Cross-section of the initial model. (C) The 2D projection of the generated initial model covering 360° of rotation along the helical axis. (D) The 3D map of the computed initial model.

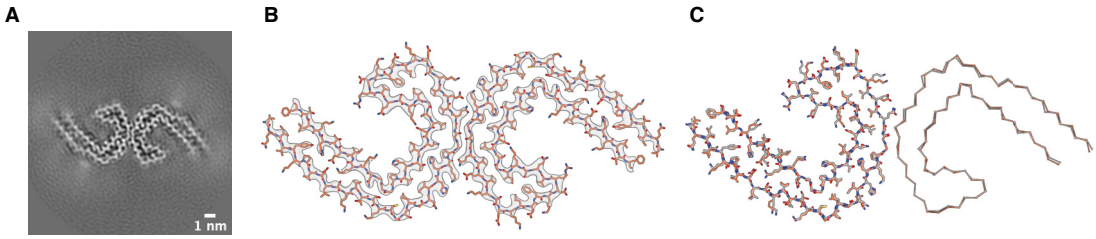

Figure 6.18.: PHF tau filaments purified from brain tissue of an individual with the Uppsala mutation. (A) Projection of the reconstructed density including approximately one β-rung. (B) Reconstructed cryo-EM density map (gray) and the atomic model of PHF tau filaments (orange). (C) Comparison of PHF tau filaments purified from human Uppsala mutation brain tissue (orange) and from sAD brain tissue (gray, PDB 5O3L).

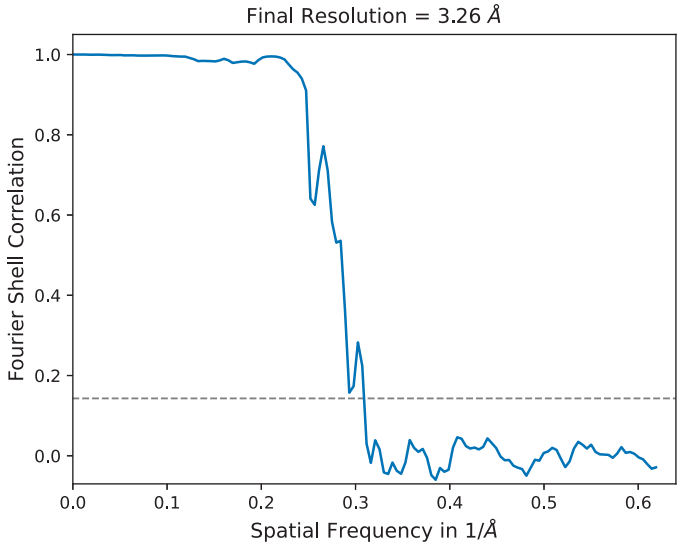

Figure 6.19.: FSC curve from the gold-standard refinement of the cryo-EM map of PHF tau filaments from an Uppsala mutation case yields a resolution of 3.26 Å (using the 0.143 criterion).

Tau straight helical filaments purified from human AβUpp(1-42)$_{\Delta 19-24}$ brain tissue The third fibril (Figure 6.15, lavender arrow, and Figure 6.16 C) accounts for 3.4% of all reconstructed fibrils in the dataset. An initial model was generated *de novo* from one larger box 2D class average (756 pix, downscaled to 378 pix) using the `relion_helix_inimodel2d` command (Figure 6.20).

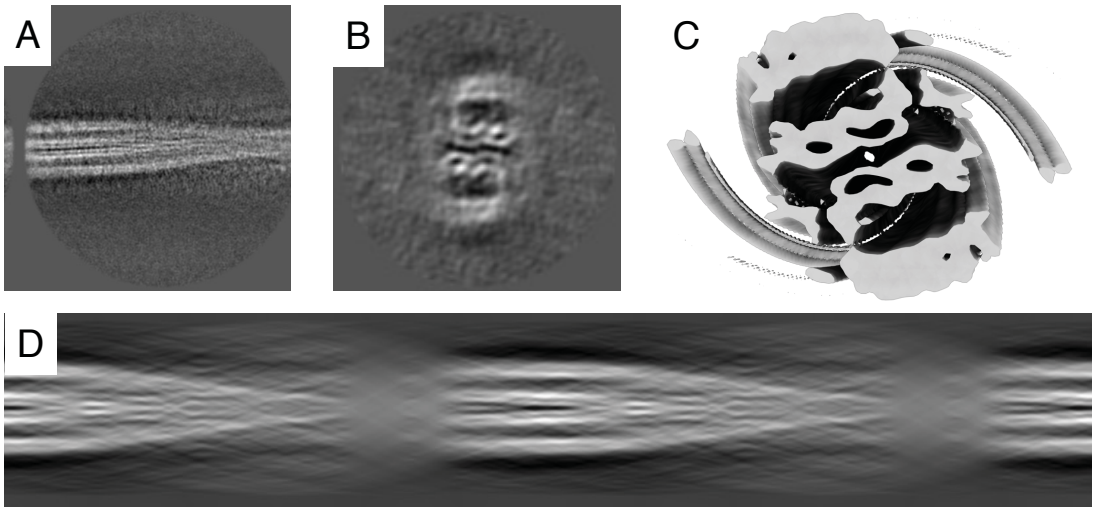

Figure 6.20.: *De novo* initial model of the third fibril observed in a human Uppsala mutation case cryo-EM dataset generated from one larger 2D class average. (A) 2D class average used to generate the initial model. (B) Cross-section of the initial model. (C) The 3D map of the computed initial model. (D) The 2D projection of the generated initial model covering 360° of rotation along the helical axis.

To generate a reasonable 3D initial model *de novo* from only one large 2D class, the 2D class must cover at least a 180° rotation along the helical axis, i.e., one complete crossover. However, most likely due to the limited number of fibril segments and downscaling to a pixel size of 3.232 Å/pix, 2D classification of larger box fibril segments resulted in blurry edges in the 2D class averages (Figure 6.21).

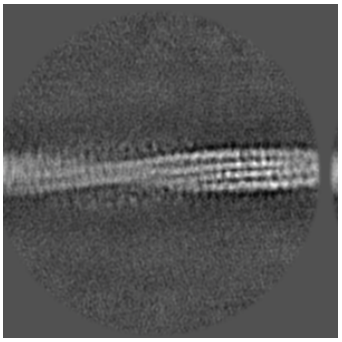

Figure 6.21.: 2D class average of the third fibril observed in a human Uppsala mutation case cryo-EM dataset at a box size of 1200 pix (downscaled to 300 pix).

2D classification at a slightly smaller box size of 756pix (downscaled to 378 pix;

Figure 6.20 A), only resulted in a single 2D class of sufficient resolution. However, this 2D class average does not show one complete crossover. Consequently, the generated initial model is of limited quality due to the missing information. Nevertheless, the refinement of the initial model resulted in a higher resolution reconstruction than the refinement starting from a featureless cylinder. A projection of the resulting final 3D reconstruction of the third fibril is displayed in Figure 6.22 A.

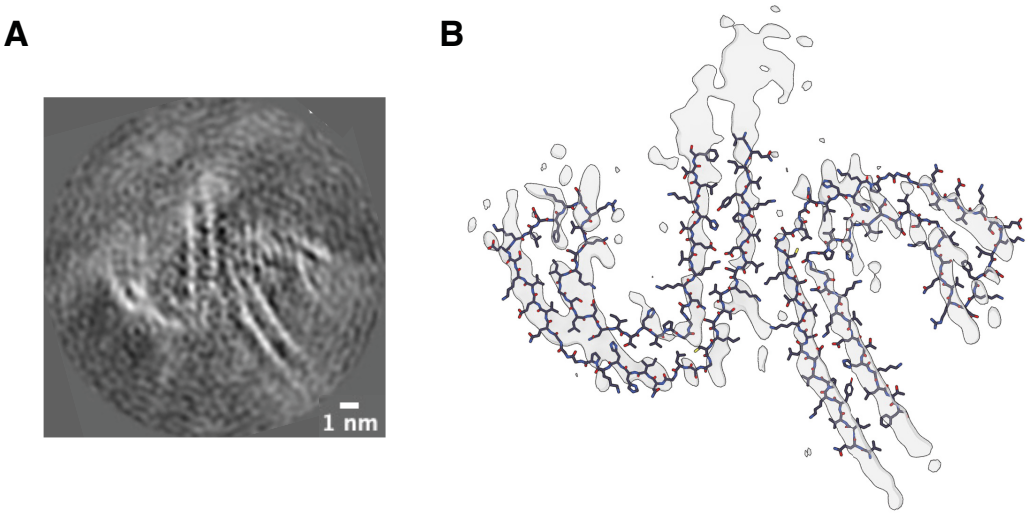

Figure 6.22.: Reconstruction of a tau straight filament (SF) purified from brain tissue of an individual with the Uppsala mutation. (A) Projection of the reconstructed density including approximately one β-rung. (B) Reconstructed cryo-EM density map (gray) and the atomic model of SF tau filaments from sAD brain tissue (blue, PDB 5O3T).

The computed 3D density map of the third fibril reaches a resolution of 4.9 Å (based on the gold-standard FSC 0.143 criterion; Figure 6.23). Although the computed 3D map is only of medium resolution, the third fibril can be identified as a SF tau filament, whose structure was previously described by Fitzpatrick et al. [262]. An overlay of the atomic model of SF tau filaments purified from sAD brain tissue (PDB 5O3T) and the reconstructed cryo-EM map of SF tau filaments purified from brain tissue of an individual with the Uppsala mutation is shown in Figure 6.22 B.

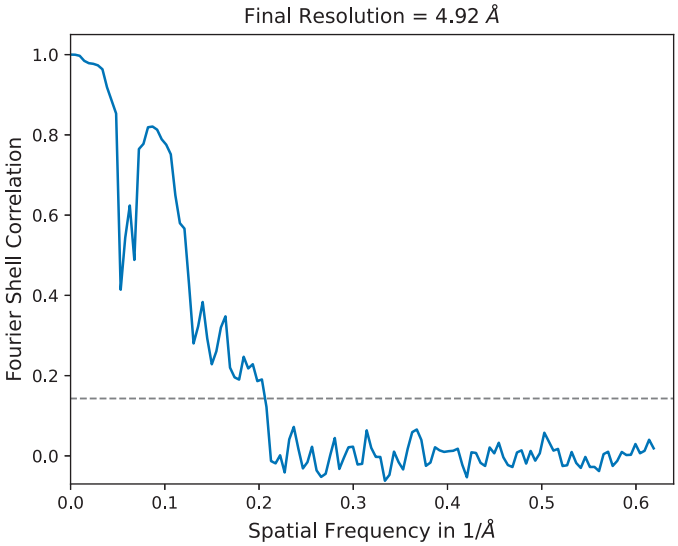

Figure 6.23.: FSC curve from the gold-standard refinement of the cryo-EM map of SF tau filaments from an Uppsala mutation case yields a resolution of 4.92 Å (using the 0.143 criterion).

Decorated fibrils purified from human AβUpp(1-42)$_{\Delta 19-24}$ brain tissue Additionally, a decorated fibril could be observed on some of the acquired cryo-EM images of AβUpp(1-42)$_{\Delta 19-24}$ fibrils purified from the brain tissue of an individual with the Uppsala mutation (Figure 6.14 B). At larger box 2D class averages (box size 1200 pix, downscaled to 300 pix), the alignment is dominated by the decoration and only a faint fibril density can be observed (Figure 6.15, green arrow). At a smaller box size of 600 pix, downscaled to 300 pix (Figure 6.16 D), a fibril surrounded by fuzzy density becomes visible. At a box size of 300 pix, it can be confirmed that the fibril is indeed an amyloid fibril, as the cross-β pattern that is characteristic for amyloid fibrils becomes visible (Figure 6.16 E). Moreover, the 2D class shown on the left in Figure 6.16 D shows some similarity to the 2D class of PHF tau filaments shown in 6.16 A. Unfortunately, the attempt to determine the 3D structure of the decorated fibril using 57,183 available fibril segments was not successful. Moreover, 2D class averages of the fibril decoration (Figure 6.16 F) show only few features, so that their identification is not possible.

Aβ fibrils purified from human AβUpp(1-42)$_{\Delta 19-24}$ brain tissue In an initial 2D classification at a large box (1200 pix, downscaled to 300 pix), a rather thin fibril was observed, accounting for 4.1% of all reconstructed fibrils (Figure 6.15, burgundy arrow). At a box size of 1200 pix, this fibril appears straight, but in a 2D classification at a slightly smaller box size of 600 pix (downscaled to 300 pix), it becomes apparent that the fibril is not straight, but has a pronounced twist with a crossover distance of 260 Å (Figure 6.16 B). An initial model was generated *de novo* from a single 2D class (box size 600 pix, downscaled to 300 pix) of the fibril spanning an entire crossover using the `relion_helix_inimodel2d` command (Figure 6.24). The 2D class average used to compute the initial model is comparatively noisy due to the limited number of fibril segments included in this 2D class average (4271 particles; Figure 6.24 A). Consequently, the resulting initial model is only of low resolution and does not show any structural features (Figure 6.24 B-D).

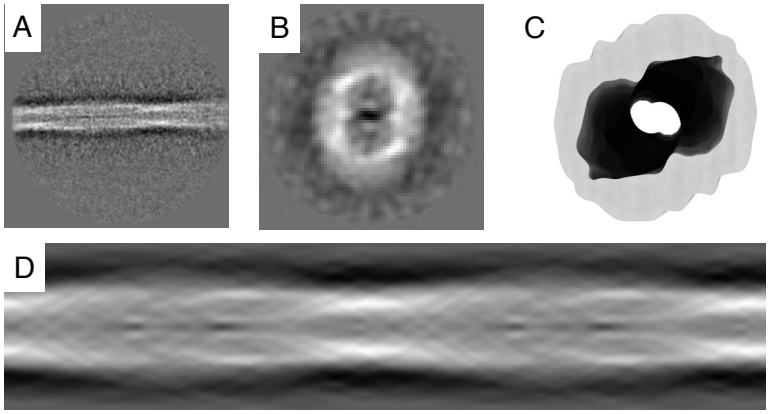

Figure 6.24.: *De novo* initial model of the second fibril observed in a human Uppsala mutation case cryo-EM dataset generated from one larger 2D class average. (A) 2D class average used to generate the initial model. (B) Cross-section of the initial model. (C) The 3D map of the computed initial model. (D) The 2D projection of the generated initial model covering 360° of rotation along the helical axis.

Although the initial model lacks higher-resolution structural features, iterative 3D refinement and classification eventually led to a 3D reconstruction of the fibril at sufficient resolution to reveal the overall fibril structure. The fibril consists of two identical extended S-shaped protofilaments (Figure 6.25 A). From the projection

displayed in Figure 6.25 A the fibril seems to be identical to human wild-type type I Aβ filaments, mostly observed in sAD cases, whose structure was previously described by Yang et al. [261].

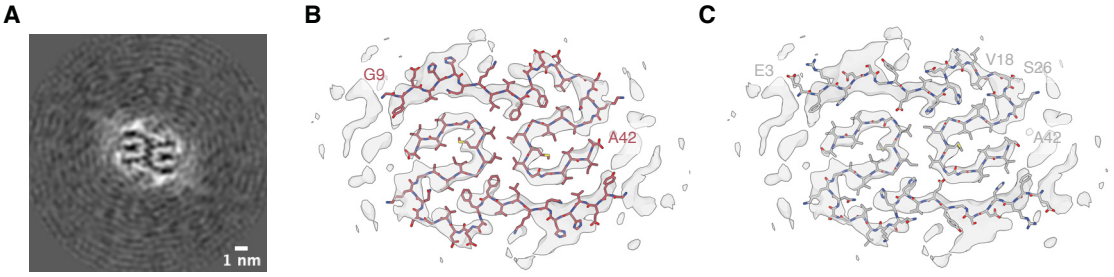

Figure 6.25.: Aβ fibril purified from brain tissue of an individual with the Uppsala mutation. (A) Projection of the reconstructed density including approximately one β-rung. (B) Reconstructed cryo-EM density map (gray) and the atomic model of type I Aβ42 filaments (burgundy, PDB 7Q4B). (C) Reconstructed cryo-EM density map (gray) and the atomic model of type I filaments mutated to the AβUpp(1-42)$_{\Delta 19-24}$ sequence (gray).

Unfortunately, likely due to the limited number of fibril segments (5023 particle images) a high resolution reconstruction was not possible. The final map reaches a global resolution of 5.9 Å (based on the gold-standard FSC 0.143 criterion; Figure 6.26). The local resolution of the map is slightly higher in some parts of the map (Figure 6.27), but the map does not show separated β-strands at a resolution of 5.9 Å. Moreover, side chains are only visible in higher resolution areas of the map and the main chain density shows some unexpected breaks.

At this resolution, it cannot be ruled out with complete certainty that the reconstructed fibril is made of AβUpp(1-42)$_{\Delta 19-24}$, but it is very unlikely that the deletion of six amino acids would result in an Aβ fibril fold identical to the fold of wild-type Aβ42. Figure 6.25 B shows the reconstructed density map with the atomic model of previously described type I Aβ42 filaments. Although side chain densities are not well visible, the atomic model of type I filaments seems to fit well into the reconstructed density map. Nevertheless, it should be noted that the deletion of six amino acids leads to an atomic model that fits the density almost equally well (Figure 6.25 C). For example, the 5.9 Å density map indeed shows some side chain density at residues F19 and F20 in wild-type Aβ42. However, the deletion shifts the sequence through the density map in a way that the same

position is occupied by H13 and H14 in case of the mutated sequence. The same holds true for Y10 in the wild-type Aβ42 sequence for which a bulky density is visible in the density map. This same position, however, is occupied by F4 in the mutated sequence.

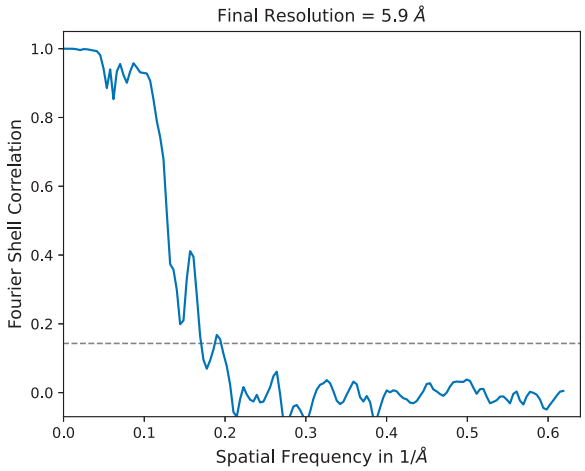

Figure 6.26.: FSC curve from the gold-standard refinement of the cryo-EM map of Aβ fibrils from an Uppsala mutation case yields a resolution of 5.9 Å (using the 0.143 criterion).

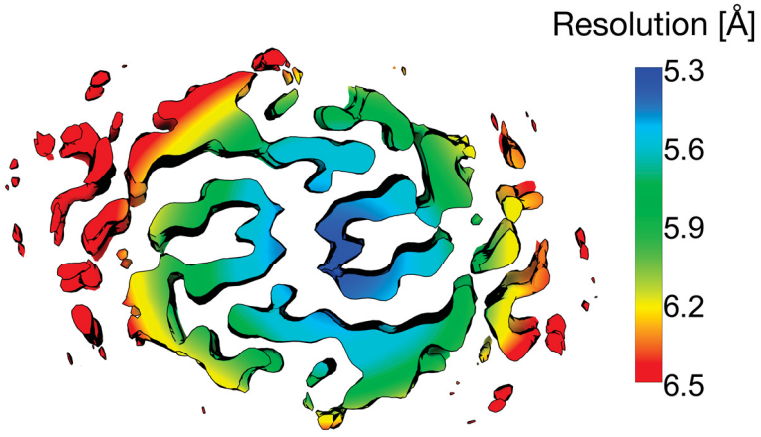

Figure 6.27.: Local resolution plot for Aβ fibrils purified from a human case with the Uppsala mutation.

6.1.4. Summary and Discussion

AβUpp(1-42)$_{\Delta 19-24}$ fibrillised into unique structural polymorphs *in vitro*. The structure of the two dominant polymorphs were determined by cryo-EM. Both polymorphs consist of two identical protofilaments that are related by a pseudo 2_1 screw symmetry. The first and most abundant polymorph is made of two extended S-shaped protofilaments with a large inter-protofilament interface. The second polymorph consists of two identical G-shaped protofilaments and, unlike in the first polymorph, the interface between the protofilaments consists of only three amino acids, while the intra-protofilament interface is comparatively large. Both *in vitro* polymorphs are novel and therefore, distinct from other Aβ fibril structures published. However, both polymorphs show a common structural motif that can also be observed in other cryo-EM and NMR structures of wild-type Aβ fibrils: The U-fold of the C-terminal domain from residues K28-A42. Furthermore, structural changes in comparison to other Aβ fibril structures are introduced close to the mutation site at residues F19-V24.

The sample of AβUpp(1-42)$_{\Delta 19-24}$ purified from tg-UppSwe mouse brain tissue only consists of one polymorph. Murine AβUpp(1-42)$_{\Delta 19-24}$ differ from the *in vitro* AβUpp(1-42)$_{\Delta 19-24}$ fibrils. The three polymorphs only overlay in the C-terminal domain between residues K28-A42. Surprisingly, the murine fibril fold of AβUpp(1-42)$_{\Delta 19-24}$ shows some structural similarity to human type II filaments that are mostly observed in fAD cases. Here, both fibrils are made of two extended S-shaped protofilaments. The protofilaments overlay between G25-A42. Between S8/V12 and G25, the chain trace still shows a minor resemblance, but the orientation of side chains is different. Several additional densities are bound to murine AβUpp(1-42)$_{\Delta 19-24}$ fibrils: Two smaller densities within the intra-protofilament interface and a number of densities on the fibril surface. Their nature remains unknown, but given the difficulties to find the *in vitro* fibrillisation condition that results in Aβ fibrils that are identical to those found *in vivo*, it remains of high interest to determine what co-factors potentially influence aggregation.

Different amyloid fibrils could be observed in fibrils purified from the brain tissue of an individual with the Uppsala mutation. The most dominant fibril was identified as PHF tau filament. Additionally, a small population of SF tau fila-

ments could be observed in the dataset. Aβ fibrils could also be detected in the sample, however, a 3D reconstruction only yielded a medium resolution map that did not allow for *de novo* atomic model building. However, the reconstructed Aβ fibril appears to be identical to wild-type type I Aβ42 filaments, which are mostly observed in sAD cases. Therefore, it can be assumed that the reconstructed fibril is indeed composed of Aβ42 instead of AβUpp(1-42)$_{\Delta 19-24}$.

Structural differences between AβUpp(1-42)$_{\Delta 19-24}$ and wild-type Aβ fibrils could potentially explain some observations made in the three mutation carriers. For example, [^{11}C]PiB PET scans of patients with the Uppsala mutation showed only a slightly positive pattern, although a high amyloid load and positive staining of the amyloid plaques with the amyloid die ThS were observed in the postmortem brain tissue [82]. This suggests that structural changes in comparison to the wild-type Aβ fibril structure might inhibit binding of [^{11}C]PiB by blocking preferred binding sites. Little is known about the interaction of PET-tracers with amyloid fibrils, however, a recent study of the binding of [^{18}F]Flutemetamol (FMT), which is another commonly used PET-tracer in AD diagnostics, to Aβ40 fibrils by solid-state NMR spectroscopy proposes three different binding sites: V12-H14, V18-F20 and V39-V40 [310]. Here, the determined binding sites were further investigated via molecular docking simulations using cryo-EM structures of Aβ(1-40) fibrils [251, 253]. The first identified binding site around V12-H14 looks similar in both structures, with one histidine residue solvent-exposed and the adjacent one facing the fibril interior. This conformation leaves space between V12 and H14 for the ligand to bind. In contrast, in both determined *in vitro* AβUpp(1-42)$_{\Delta 19-24}$ fibrils as well as in the murine AβUpp(1-42)$_{\Delta 19-24}$ fibril, both histidine residues are facing outwards and therefore potentially block this first binding site of the PET tracer. However, it should be noted that the same conformation of H12 and H13 can be observed in human wild-type type I filaments, mostly found in sAD patients. The second binding site V18-F20 lies within the deletion region and therefore, is not available in AβUpp(1-42)$_{\Delta 19-24}$ fibrils. The last found binding site between V39 and V40 lies within the previously discussed C-terminal motif. Whereas, this binding site is available in the first *in vitro* AβUpp(1-42)$_{\Delta 19-24}$ polymorph as well as in the murine AβUpp(1-42)$_{\Delta 19-24}$ fibril, it is blocked in the second *in vitro* AβUpp(1-

42)$_{\Delta 19-24}$ polymorph. Although [^{18}F]FMT might bind differently than [^{11}C]PIB, this exemplifies how slight structural changes, like altered side chain orientation, introduced by a mutation can block possible binding positions, and thus, influence PET signals.

Moreover, it was found that AβUpp(1-42)$_{\Delta 19-24}$ is far more prone to aggregate into fibrils than wild-type Aβ(1-42). Amyloid aggregation is a complex and hardly understood process, that is assumed to be a two-step system with a first step of primary nucleation into fibrillar oligomers followed by secondary processes like secondary nucleation of monomers on the surface of fibrils, elongation of fibrils by the addition of monomers to the fibril or fragmentation of existing fibrils [52, 311]. Primary nucleation is sorely dependent on monomer concentration whereas secondary processes are also at least partially dependent on the concentration of existing fibrils [53]. Thus, a first simple explanation might be that faster aggregation into fibrils in case of patients with the Uppsala mutation can be due to a higher monomer concentration induced by alternations in APP processing that boost monomer production. However, it could also be due to a tendency to increase secondary processes such as fibril elongation as well as secondary nucleation. It has been shown that the aggregation kinetics shift to an aggregation process that is dominated by secondary nucleation rather than primary nucleation for the familial Arctic (E22G), Iowa (D23N), Dutch (E22Q), and Italian (E22K) mutation [312, 313]. Secondary nucleation, however, is not well understood on a structural level and thus, it remains unclear whether the structural changes observed in the *in vitro* as well as murine *ex vivo* fibril structure introduced by the Uppsala mutation increase secondary nucleation. Using enhanced sampling MD simulations, it was found that Aβ42 monomers already can fold into a structure that shows similarities to the structure of Aβ42 peptides in fibrils [314]. The monomer was found to already form the characteristic C-terminal structural motif that could be observed in several other published structures and thus, giving a possible explanation for the low free energy barrier for fibril elongation. Assuming AβUpp(1-42)$_{\Delta 19-24}$ monomers already partially form in the C-terminal domain (K28-A42) the free energy barrier might be additionally decreased in comparison to Aβ42 purely based on the number of amino acids that need to further fold in the protofilament fold.

Finally, the formation of large insoluble fibrils out of soluble protein can also

be linked to simple sequence-dependent physicochemical properties such as hydrophobicity, secondary structure propensity and charge [315], which are altered in the AβUpp(1-42)$_{\Delta 19-24}$ in comparison to wild-type Aβ due to the deletion of four hydrophobic as well as two charged amino acids (Figure 6.28).

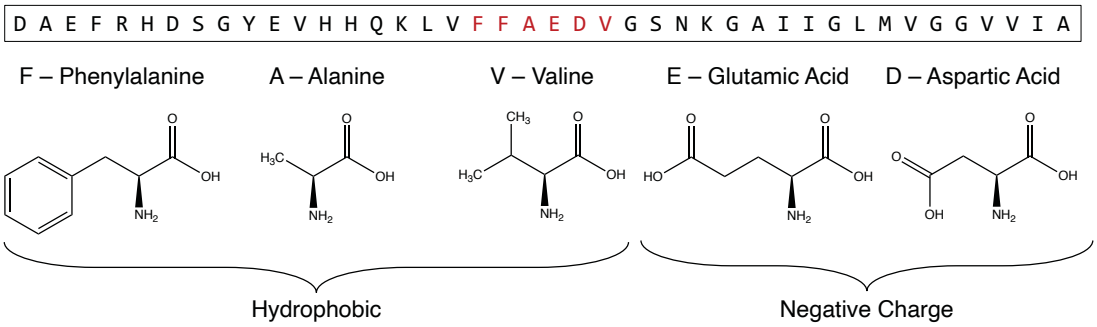

Figure 6.28.: Deleted residues within the Aβ sequence that result in AβUpp(1-42)$_{\Delta 19-24}$.

Within this study, the *in vitro* and *ex vivo* structure of AβUpp(1-42)$_{\Delta 19-24}$ fibrils was investigated. AβUpp(1-42)$_{\Delta 19-24}$ forms unique structural polymorphs *in vitro* that differ from other determined wild-type Aβ fibrils. Murine AβUpp(1-42)$_{\Delta 19-24}$ fibrils show some similarity to human type II filaments, that are mostly observed in fAD patients, but side chain orientations differ between S8/V12 and the mutation site at V18. Finally, Aβ fibrils purified from human brain tissue of an individual with the Uppsala mutation shows an Aβ fibril that is most likely composed of wild-type Aβ given its structural similarity to human type I filaments. Although the structure of human AβUpp(1-42)$_{\Delta 19-24}$ fibrils likely remains unknown, the observations made might guide future experiments. Either AβUpp(1-42)$_{\Delta 19-24}$ does not form fibrils *in vivo* or AβUpp(1-42)$_{\Delta 19-24}$ fibrils tend to aggregate in such a way that the sarkosyl-based extraction protocol used is insufficient to resolve the fibril clusters well enough to enable high-resolution structure determination by cryo-EM.

6.2. Methods

6.2.1. Synthetic AβUpp(1-42)$_{\Delta 19-24}$ fibrils

For this project, 125 µg lyophilized and HFIP treated AβUpp(1-42)$_{\Delta 19\text{-}24}$ (~300 µM monomer concentration) were dissolved in 100 µL HPLC buffer (30% AcN, 0.1% TFA).

Atomic Force Microscopy For AFM imaging, AβUpp(1-42)$_{\Delta 19-24}$ fibrils from ~300 µM monomer concentration were diluted 1:30 in buffer (30% AcN, 0.1% TFA). Afterwards, 5 µL of the diluted sample solution was applied to a freshly cleaved muscovite mica and dried with a stream of N_2 gas. Imaging was performed in intermittent contact mode (AC mode) in a Nano Wizard 3 atomic force microscope (JPK, Berlin) using a silicon cantilever (OMCL-AC160TS, Olympus) with a typical tip radius of 9 ± 2 nm. The images were processed using Gwyddion (version 2.61) [316].

Negative Stain EM For negative stain EM, 3 µL of the AβUpp(1-42)$_{\Delta 19-24}$ sample were applied onto a glow-discharged 300 mesh carbon-coated copper grid (EM Sciences, ECF300-Cu). The sample was incubated on the grid for 2 min and excess liquid was blotted off with filter paper. Afterwards, 3 µL of 2% (w/v) UrAc were applied onto the grid and incubated for 1 min. The UrAc was removed with filter paper and the grid was air-dried. TEM images were acquired using a ThermoFisher Scientific Talos 120C at an accelerating voltage of 120 kV. Images were collected on a 4k x 4k Ceta 16M CMOS camera using EPU data collection software.

Cryo-EM Image Acquisition and Data Preprocessing For cryo-EM imaging, 2 µL of the AβUpp(1-42)$_{\Delta 19-24}$ sample at 300 µM monomer concentration was applied to holey carbon grids (Quantifoil 1.2/1.3, 300 mesh), blotted with filter paper for 5 s and plunge frozen in liquid ethane using a ThermoFisher Scientific Vitrobot Mark IV, set at 95% humidity and 4°C temperature. Data acquisition was performed on a ThermoFisher Scientific Talos Arctica microscope operating at 200 kV with a field emission gun using a Gatan Bioquantum K3 direct electron

detector in counting mode with a Gatan Bio-quantum energy filter with a slit width of 20 eV. The automated collection was directed by EPU data collection software. A total of 3954 movies of 40 frames was recorded during 6.25 s exposures at a 100,000-fold nominal magnification resulting in a pixel size of 0.816 Å on the specimen, and a total dose of approximately 50 $e^-/Å^2$. Defocus values ranged from -1.5 to -3.5 µm. Further details can be found in Table 6.1.

For helical reconstruction of both polymorphs gain-corrected movie frames were aligned and summed into single micrographs using Warp [218]. CTF estimation was performed using CTFFIND4.1 [209]. Structure determination of both polymorphs was performed using helical reconstruction in RELION-3.1 [223, 272].

	Polymorph 1	Polymorph 2
Data collection		
Microscope	Talos Arctica	Talos Arctica
Voltage [kV]	200	200
Detector	K3	K3
Energy filter slit width [eV]	20	20
Magnification	100,000	100,000
Pixel size [Å]	0.816	0.816
Defocus range [µm]	-1.5 to -3.5	-1.5 to -3.5
Exposure time [s]	6.25	6.25
Number of frames	40	40
Total dose [$e^-/Å^2$]	50	50
Reconstruction		
Micrographs	3,954	3,954
Box width [pix]	270	270
Initial particle images [no.]	138,644	517,971
Final particle images [no.]	67,117	45,248
Symmetry imposed	C1	C1
Helical rise [Å]	2.37	2.39
Helical twist [°]	-178.391	179.381
Map resolution [Å]	3.3	3.7
FSC threshold	0.143	0.143

Table 6.1.: Cryo-EM data collection and structure determination statistics of *in vitro* AβUpp(1-42)$_{\Delta 19-24}$ fibrils.

Helical Reconstruction of Polymorph 1 Fibrils were selected manually from the micrograph, resulting in 8,344 fibrils. In total 138,644 fibril segments were extracted from micrographs with a CTF fit resolution better than 5 Å (3149 micrographs) at an inter-box distance of 19 Å and a box size of 270 pix. Reference-free 2D class averaging was performed to discard suboptimal particle images. With a crossover distance of 260 Å measured on the micrographs and an assumed helical rise of about 2.35 Å, an initial helical twist of -178.35° was estimated. Using these parameters, an initial 3D reference was generated *de novo* from 2D class averages of a subset of all picked particles (49,439) at a box size of 320 pix [267]. This initial reference was lowpass filtered to 40 Å and used for 3D refinement. Optimization of twist and rise yielded refined helical parameters of -178.39° and 2.37 Å. After iterative 2D and 3D classification, 67,117 particle images were selected for 3D auto-refinement. During post-processing the map was masked with a soft mask and the final resolution of 3.3 Å was calculated from Fourier shell correlations at 0.143 between the two independently refined half-maps. The map was sharpened using VISDEM [304]. Further image processing statistics are shown in Table 6.1.

Helical Reconstruction of Polymorph 2 Fibrils were selected automatically using crYOLOs filament picker [219, 317]. CrYOLO was trained on 86 polymorph 2 fibrils that were selected manually on 50 images. In total 44,404 fibrils were picked, and 402,403 fibril segments were extracted in RELION using a box size of 270 pix and an inter-box distance of 19 Å. Following reference-free 2D class averaging of all automatically selected particle images, 286,566 particle images could be assigned to polymorph 2. It might be interesting to note, that the network was thus quite successfully trained on identifying and picking only type II filaments. Only 29% of all picked filaments were false positives. An exemplary crYOLO picking result is shown in Figure 6.29.

For further processing only those particles (59,583) with an estimated CTF fit resolution better than 4 Å were used. Like for PM1, reference-free 2D class averaging was performed to discard suboptimal particle images. Determination of the helical twist was ambiguous due to a large flexibility in the helical twist. Measured crossover distances varied between ~350 Å and ~675 Å. This translates to a variability in the helical twist between 178.78° and 179.3°. Using an initial

guess of the helical twist (179.05°), 3D classification using a previously determined low-resolution reconstruction ([82]) lowpass filtered to 20 Å as initial reference with an optimization of helical twist and rise was performed to generate more homogeneous particle subsets. Further optimization of the helical rise and helical twist during 3D refinement converged to a helical twist of 179.38° and a helical rise of 2.39 Å. A final particle set of 45,248 particle images was selected for 3D auto-refinement. During post-processing the map was masked with a soft mask and the final resolution of 3.7 Å was calculated from Fourier shell correlations at 0.143 between the two independently refined half-maps. The map was sharpened using VISDEM. Further image processing statistics are shown in Table 6.1.

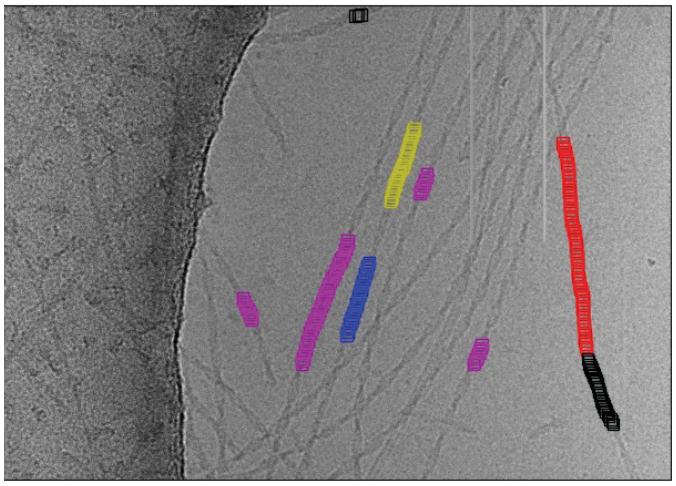

Figure 6.29.: Representative crYOLO picking result for *in vitro* AβUpp(1-42)$_{\Delta 19-24}$ polymorph 2. For training of the network 86 polymorph 2 fibrils were manually selected on 50 images. The automatically picked fibril segments are boxed (the colours are arbitrary). Only a few false-positive fibrils were detected. In addition, no false-negative fibrils are present in this image.

Model Building and Refinement Atomic models for both polymorphs were built *de novo* from the sharpened and symmetrized cryo-EM maps using COOT [318]. The handedness of both maps was determined from AFM imaging as well as model building. Polymorph 2 fibrils were clearly left-handed judging from AFM images. Determination of the handedness of polymorph 1 was not straight forward since it could not be determined from AFM images due to the short crossover distance of only 260 Å. Thus, the handedness was determined to be right-handed based on a

better visual fit of the atomic model into the right-handed map. Building of the initial polyalanine atomic model was started at the well resolved C-Terminus for both filament types. Side chains were added after manual optimization of the polyalanine chain. Side chain rotamers were refined manually monitoring Ramachandran outliers and clash scores using MolProbity [319]. Afterwards, both models were refined using an iterative procedure of automatic refinement in PHENIX [320] followed by manual refinement in COOT using ten symmetry-related monomeric subunits. Hydrogens were added to both structures using `phenix.reduce` [321]. Graphical analysis and visualization were performed using ChimeraX [305]. Refinement statistics are shown in 6.2.

	Polymorph 1	Polymorph 2
Initial model [PDB code]	de novo	de novo
Model Composition		
Chains	10	10
Non-hydrogen atoms	1,990	1,990
Protein residues	280	280
RMS deviations		
Bond lenghts [Å]	0.003	0.007
Bond angles [°]	0.543	0.877
Validation		
MolProbity score	1.85	2.07
Clashscore	11.89	16.75
Poor rotamers [%]	0	0
Ramachandran plot		
Favored [%]	96.15	95.00
Allowed [%]	3.85	5.00
Outliers [%]	0	0

Table 6.2.: Model building statistics of *in vitro* AβUpp(1-42)$_{\Delta 19-24}$ fibrils.

6.2.2. Murine AβUpp(1-42)$_{\Delta 19-24}$ fibrils

Negative Stain EM 2 µL of the final sarkosyl insoluble pellet were applied onto a glow-discharged 300 mesh carbon-coated copper grid (EM Sciences, ECF300-Cu). The sample was incubated for 2 min and excess liquid was blotted off with filter paper. The sample was then washed once with dH_2O. 2 µL of 1% (w/v)

UrAc were applied on the top of the grid, following a 1 min incubation. The UrAc was removed with filter paper and the grid was air-dried. TEM images were acquired using a ThermoFisher Scientific Talos 120C at an acceleration voltage of 120 kV. Images were collected on a 4k x 4k Ceta 16M CMOS camera using Thermo Scientific Velox Software.

Immunogold negative stain EM Immunogold negative-stain grids for EM were prepared following [299]. In brief, 2 µL of the final pellet were placed on a glow-discharged 300 mesh carbon-coated copper grid (EM Sciences, ECF300-CU) for 2 min. The sample was washed once with dH_2O and placed in blocking buffer for 15 min, following incubation with Nab228 (Sigma-Aldrich) primary antibody diluted in blocking buffer at a concentration of 2 µg/mL for 1.5 h. Afterwards, the grid was washed with washing buffer and was incubated with 6 nm gold-conjugated anti-mouse secondary antibody (diluted 1:20 in blocking buffer, Abcam) for 1 h. The grid was washed five times with washing buffer and three times with dH_2O before staining with 1% (w/v) UrAc for 1 min. The sample was air-dried, and EM Images were acquired as described above. Immunogold negative stain EM confirmed that the purified fibrils were indeed Aβ fibrils.

Cryo-EM Image Acquisition and Data Preprocessing For cryo-EM imaging, 2 µL of Aβ fibrils extracted from one single mouse brain were applied to holey carbon grids (Quantifoil 1.2/1.3, 300 mesh), blotted with filter paper for 6 s and plunge frozen in liquid ethane using a ThermoFisher Scientific Vitrobot Mark IV, set at 95% humidity and 4°C temperature. Data acquisition was performed on a ThermoFisher Scientific Titan Krios G4 operating at 300 kV using a Falcon IV detector in counting mode. The automated collection was directed by EPU data collection software. Further details are given in Table 6.3.

Gain-corrected movie frames were aligned and summed into single micrographs on-the-fly using Warp. CTF estimation was performed using CTFFIND4.1.

	Murine Aβ fibrils
Data collection	
Microscope	Krios G4
Voltage [kV]	300
Detector	Falcon IV
Magnification	96,000
Pixel size [Å]	0.808
Defocus range [µm]	-0.5 to -2.5
Exposure time [s]	4.31
Number of frames	40
Total dose [e^-/Å^2]	40
Reconstruction	
Micrographs	11,991
Box width [pix]	300
Initial particle images [no.]	1,271,423
Final particle images [no.]	329,437
Symmetry imposed	C1
Helical rise [Å]	2.35549
Helical twist [°]	178.411
Map resolution [Å]	3.2
FSC threshold	0.143

Table 6.3.: Cryo-EM data collection and structure determination statistics of murine AβUpp(1-42)$_{\Delta 19-24}$ fibrils.

Helical Reconstruction Helical reconstruction was performed using the helical reconstruction methods in RELION 3.1. Fibrils were picked automatically using crYOLO. Reference-free 2D classification at a box size of 800 pix, downscaled to 200 pix, was performed to get an overview on polymorph distribution and to discard false positives from autopicking as well as low quality particle images. Afterwards, fibril segments were re-extracted at 300 pix boxsize and the original pixel size of 0.808 Å/pix. 2D classification was performed to discard low quality particle images. A featureless cylinder with a diameter of 140 Å was low-pass filtered to 40 Å and used as initial 3D reference. Iterative 3D classification and 3D refinement with refinement of the helical parameters was performed to yield a higher resolution reconstruction. 3D auto-refinement and subsequent post-processing was performed to compute the final map and to calculate the resolution according to

gold-standard Fourier Shell Correlations at 0.143 applying a soft-edged solvent mask. Additional information can be found in Table 6.3.

Model Building An atomic model was built *de novo* into an intermediate cryo-EM reconstruction by Gunnar Schröder using COOT and PHENIX. This intermediate model was then refined into the final high-resolution cryo-EM reconstruction using an iterative procedure of refinement in PHENIX and manual modeling in COOT. Side chain rotamers were refined manually monitoring Ramachandran outliers and clash scores using MolProbity. ChimeraX was used for molecular graphics and analyses. Additional information can be found in Table 6.4.

	Murine Aβ fibrils
Initial model [PDB code]	de novo
Model Composition	
Chains	10
Non-hydrogen atoms	2050
Protein residues	290
RMS deviations	
Bond lenghts [Å]	0.007
Bond angles [°]	0.970
Validation	
MolProbity score	2.04
Clashscore	5.24
Poor rotamers [%]	0
Ramachandran plot	
Favored [%]	77.78
Allowed [%]	22.22
Outliers [%]	0

Table 6.4.: Model building statistics of murine AβUpp(1-42)$_{\Delta 19-24}$ fibrils.

6.2.3. Human AβUpp(1-42)$_{\Delta 19-24}$ fibrils

Immunogold negative stain EM Immunogold negative-stain grids for EM were prepared following [299]. In brief, 3 µL of the final pellet were placed on a glow-discharged 300 mesh carbon-coated copper grid (EM Sciences, ECF300-CU) for 2 min. The sample was washed once with dH_2O and placed in blocking buffer

for 15 min, following incubation with Nab228 (Sigma-Aldrich) primary antibody diluted in blocking buffer at a concentration of 2 µg/mL for 1.5 h. Furthermore, the grid was washed with washing buffer and was incubated with 6 nm gold-conjugated anti-mouse secondary antibody (diluted 1:20 in blocking buffer, Abcam) for 1 h. The grid was washed five times with washing buffer and three times with dH_2O before staining with 1% (w/v) UrAc for 1 min. The sample was air-dried, and EM Images were acquired as described above. Immunogold negative stain EM confirmed that some of the purified fibrils were indeed Aβ fibrils.

Cryo-EM Image Acquisition and Data Preprocessing Two datasets were collected on human brain extracted AβUpp(1-42)$_{\Delta 19-24}$ fibrils. For the first cryo-EM data acquisition, 2 µL of Aβ fibrils were applied to holey carbon grids (Quantifoil 1.2/1.3, 300 mesh), blotted with filter paper for 6 s and plunge frozen in liquid ethane using a ThermoFisher Scientific Vitrobot Mark IV, set at 95% humidity and 4°C temperature. Data acquisition was performed on a ThermoFisher Scientific Talos Arctica microscope operating at 200 kV using a Gatan Bioquantum K3 detector in counting mode with a Gatan Bio-quantum energy filter with a slid width of 20 eV. The automated collection was directed by EPU data collection software. Since the first dataset was not of sufficient quality, a second dataset was recorded. Inspection of the micrographs during data collection of the first dataset revealed several areas of very thick ice on the grid likely due to clumped fibrils. Therefore, prior to the second cryo-EM data acquisition the remaining sample of the previously used extraction (~6 µL leftover) was washed and sonicated prior to plunging to disentangle fibril clusters: The sample was centrifuged at 5000 x g for 6 min (4°C), the supernatant was removed and the remaining pellet was resuspended in resuspension buffer. The sample was vortexed for 2 s and again centrifuged at 5000 x g for 6 min (4°C). The sample was transferred to a 500 µL LoBind reaction tube and sonicated in pulses for 3 min (10 s on, 20 s off) in an ultrasonic water bath. 2 µL of sonicated Aβ fibrils were applied to holey carbon grids (Quantifoil 1.2/1.3, 300 mesh), blotted with filter paper for 6 s and plunge frozen in liquid ethane using a ThermoFisher Scientific Vitrobot Mark IV, set at 95% humidity and 4°C temperature. Data acquisition was performed on a ThermoFisher Scientific Titan Krios G4 operating at 300 kV using a Falcon IV detector

in counting mode. The automated collection was directed by EPU data collection software. Further details are given in Table 6.5.

Gain-corrected movie frames were aligned and summed into single micrographs on-the-fly using Warp. CTF estimation was performed using CTFFIND4.1.

	First Dataset	Second Dataset
Data collection		
Microscope	Talos Arctica	Titan Krios
Voltage [kV]	200	300
Detector	K3	Falcon IV
Energy filter slit width [eV]	20	N/A
Magnification	100,000	96,000
Pixel size [Å]	0.816	0.808
Defocus range [µm]	-0.5 to -2.5	-0.75 to -2.5
Exposure time [s]	5	3.55
Number of frames	35	40
Total dose [$e^-/Å^2$]	35.23	40

Table 6.5.: Cryo-EM data collection statistics of human AβUpp(1-42)$_{\Delta 19-24}$ fibrils.

Helical Reconstruction Helical reconstruction was performed using the helical reconstruction methods in RELION. Fibrils were picked automatically on the first dataset using filament picking procedures in crYOLO and manually on the second dataset. Reference-free 2D classification was performed to discard low quality particle images. The first dataset did only show PHF tau filaments and false positives from autopicking in the initial 2D classification (Figure 6.30). Therefore, image processing was stopped and the sample preparation prior to vitrification was adjusted and the second dataset was collected.

Due to clustering of the fibrils on the recorded micrographs, fibrils were picked manually on the second dataset. Fibril segments were extracted at a box size of 1200 pix, downscaled to 300 pix. Reference-free 2D classification was performed to separate different polymorphs. The particle set was split into four subsets that were processed individually. Particles of all subsets were re-extracted at an image processing box size 256, 270, or 300 pix. For PHF tau filaments, SF tau filaments, and Aβ fibrils, an initial model was computed *de novo* from one or multiple 2D class averages using the `relion_helix_inimodel2d` command. The initial 3D

references were low-pass filtered to 6 - 8 Å depending on their quality. Iterative 3D classification and 3D refinement with a refinement of the helical parameters was performed for each fibril to yield a higher resolution reconstruction. 3D auto-refinement and subsequent post-processing were performed to compute the final maps and to calculate the resolutions according to gold-standard FSC at 0.143 applying a soft-edged solvent mask. Additional information can be found in Table 6.6.

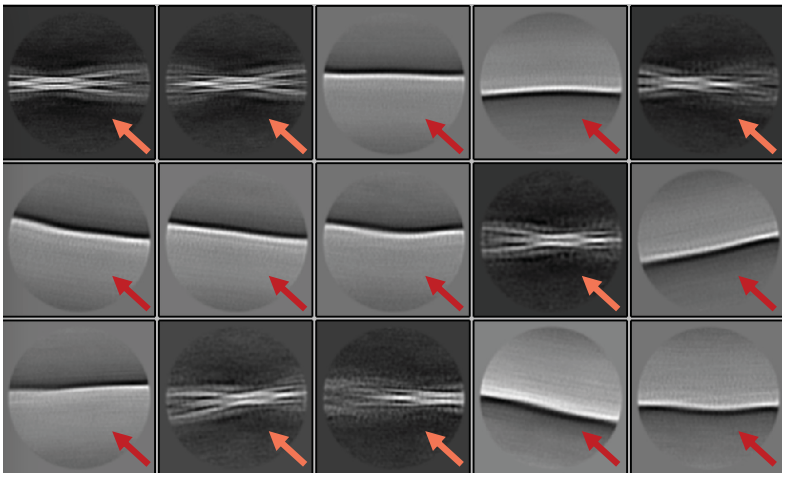

Figure 6.30.: Initial 2D classification of automatically picked fibrils on micrographs of the first dataset of fibrils purified from human brain tissue of an individual with the Uppsala mutation shows only PHF tau filaments (orange). In addition, there are many 2D class averages containing false positives from the crYOLO picking (red). Fibril segments were extracted at a box size of 800 pix, downscaled to 200 pix.

	Aβ	Tau PHF	Tau SF
Micrographs	17,910	17,910	17,910
Box width [pix]	300	270	256
Initial particle images [no.]	515,788	515,788	515,788
Final particle images	5023	112,719	4127
Symmetry imposed	C1	C1	C1
Helical rise [Å]	2.45	2.39	4.75
Helical twist [°]	178.352	179.434	-0.98
Map resolution [Å]	5.9	3.3	4.9
FSC threshold	0.143	0.143	0.143

Table 6.6.: Structure determination statistics of human AβUpp(1-42)$_{\Delta 19-24}$ fibrils.

Automatic picking of the fibril decoration To compute the 2D class averages of the fibril decoration shown in Figure 6.16 F, particles were picked automatically using crYOLO [219]. For this, the model used for picking was trained on 450 particles that were picked manually on 30 micrographs. Automatic particle picking with a model trained on the data resulted in 182,680 picked particles that were subsequently extracted at a box size of 168 pix.

Model Building Atomic modelling was only possible for the high-resolution cryo-EM reconstruction of PHF tau filaments. Here, a previously published cryo-EM structure of PHF tau filaments (PDB 5O3L) [262] was fitted into the reconstructed cryo-EM map using ChimeraX and used as initial model. This model was refined into the density map using an iterative procedure of automatic refinement in PHENIX and manual modeling in COOT. Side chain rotamers were refined manually monitoring Ramachandran outliers and clash scores using MolProbity. ChimeraX was used for molecular graphics and analyses. Additional information can be found in Table 6.7.

	Tau PHF
Initial model [PDB code]	5O3L
Model Composition	
Chains	10
Non-hydrogen atoms	5570
Protein residues	730
RMS deviations	
Bond lenghts [Å]	0.004
Bond angles [°]	0.817
Validation	
MolProbity score	2.41
Clashscore	18.40
Poor rotamers [%]	0
Ramachandran plot	
Favored [%]	85.92
Allowed [%]	14.08
Outliers [%]	0

Table 6.7.: Model building statistics of PHF tau filaments purified from the brain tissue of an individual with the Uppsala mutation.

For SF tau filaments and Aβ fibrils, the achieved resolutions of 4.9 Å and 5.9 Å, respectively, were too low to enable atomic modelling.

6.3. Contribution

I performed negative stain EM screening, cryo-EM grid preparation, data acquisition, image processing and model building for the structural studies of *in vitro* AβUpp(1-42)$_{\Delta 19\text{-}24}$ fibrils. I performed TEM screening of negative stain grids (prepared by Fernanda Salome Peralta Reyes and myself) and immunogold negative stain grids (prepared by Fernanda Salome Peralta Reyes and myself) of murine AβUpp(1-42)$_{\Delta 19\text{-}24}$ fibrils, that were previously extracted from mouse brain tissue by Fernanda Salome Peralta Reyes. I performed sample vitrification, cryo-EM data acquisition and image processing for murine AβUpp(1-42)$_{\Delta 19\text{-}24}$ fibrils. I refined the atomic model of murine AβUpp(1-42)$_{\Delta 19\text{-}24}$ fibrils, that was initially built by Gunnar Schröder. Additionally, I performed TEM screening of negative stain grids (prepared by Fernanda Salome Peralta Reyes and myself) and immunogold negative stain grids (prepared by Fernanda Salome Peralta Reyes and myself) of human AβUpp(1-42)$_{\Delta 19\text{-}24}$ fibrils, that were previously extracted from human brain by Fernanda Salome Peralta Reyes. I performed sample vitrification and collected two cryo-EM datasets of human AβUpp(1-42)$_{\Delta 19\text{-}24}$ fibrils and performed image processing. I built the atomic model of PHF tau filaments.

7. The cryo-EM structures of *in vitro* A2T Aβ(1-42) fibrils

Multiple mutations within the APP gene are linked to early-onset fAD [71]. However, one familial mutation, the Icelandic A673T mutation (A2T in the Aβ sequence), which occurs mainly in the Icelandic and Scandinavian populations, is associated with a protection against amyloid pathology and Alzheimer's disease [83]. Since the A2T variant is associated with minimal amyloid deposition, it is interesting to investigate whether the A2T variant of Aβ42 forms fibrils *in vitro*, and if so, to study their structure by cryo-EM and compare them with other structures.

For this project, synthetic peptide was purchased from Bachem, purified by RP-HPLC and fibrillised under low pH condition as previously described [252]. Sample purification was kindly supported by Lothar Gremer. Afterwards, cryo-EM data was collected and the structure of the two most abundant polymorphs was solved to high-resolution.

7.1. Results and Discussion

To assess the quality of the synthetic A2T Aβ42 peptide and to confirm that it indeed contains mutated Aβ, an analytical RP-HPLC run was performed on A2T Aβ42 as well as a wild-type Aβ42 sample (Figure 7.1 A). The main peak of the A2T variant of Aβ is visible at a retention time of 16.8 min (Figure 7.1 A, blue), while the main peak of the wild-type sample is visible at a retention time of 17 min (Figure 7.1 A, orange). A shorter retention time was to be expected, since the mutation of the hydrophobic A2 to the hydrophilic T2 results in the A2T variant of Aβ being more polar than wild-type Aβ and thus passing more quickly through the non-polar stationary phase (RP-HPLC).

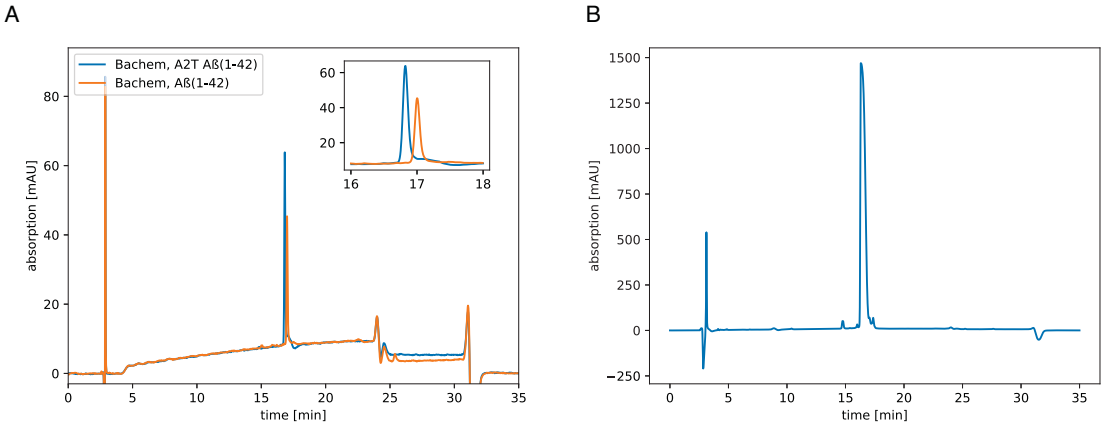

Figure 7.1.: Chromatogram of A2T Aβ42. (A) Chromatogram of an analytical RP-HPLC run of A2T Aβ42 (orange) and wild-type Aβ42 (blue). (B) Chromatogram of the preparative RP-HPLC run of A2T Aβ42.

After confirming that the synthetic peptide indeed is mutated Aβ42, the synthetic peptide was purified in a preparative RP-HPLC run and brought into fibrillisation conditions. The recorded chromatogram is shown in Figure 7.1 B. The main peak at a retention time of 16.31 min was collected.

Cryo-EM screening of the A2T Aβ42 sample after 38 days of incubation reveals that A2T Aβ42 forms long and well-ordered fibrils *in vitro* (Figure 7.2). Moreover, the screening already reveals a high fibril concentration as well as the presence of different fibril polymorphs in the sample (Figure 7.2 B).

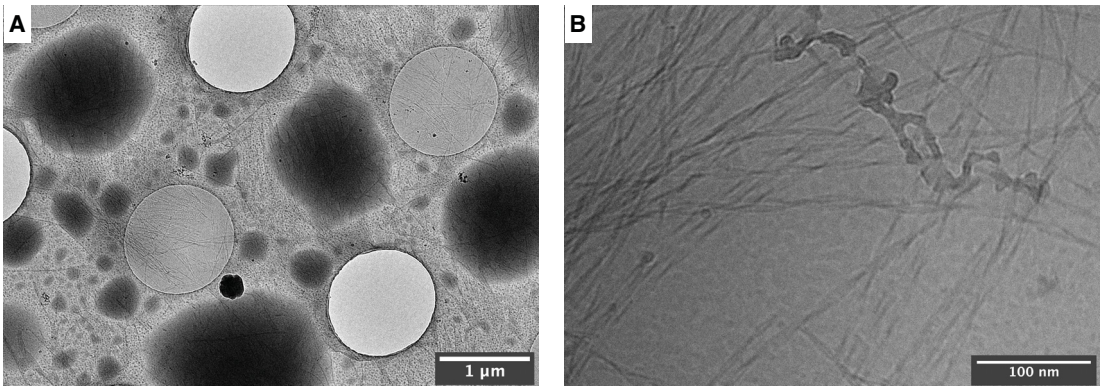

Figure 7.2.: Cryo-EM screening of the *in vitro* A2T Aβ42 fibril sample in a Talos Arctica. (A) At 5600x magnification. (B) At 100,000x magnification.

However, the fibrils tend to clump on the grid, especially on the carbon film, probably due to a too high blot-force or time and/or insufficient glow discharging. Furthermore, most holes are empty and only a few contain fibrils embedded in thin ice.

Negative stain EM screening of the sample confirms the polymorphism of the A2T Aβ42 sample (Figure 7.3).

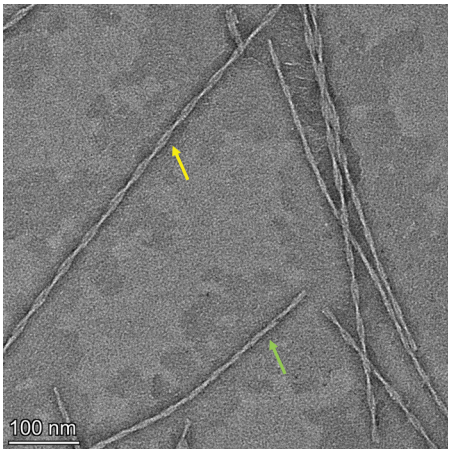

Figure 7.3.: Negative stain EM screening of the *in vitro* A2T Aβ42 fibril sample after 43 days of incubation. Coloured arrows indicate different polymorphs.

After adjusting the blotting conditions, the overall quality of the grid improved, in particular a high fibril concentration was achieved without the formation of fibril clusters and empty holes on the grid (Figure 7.4).

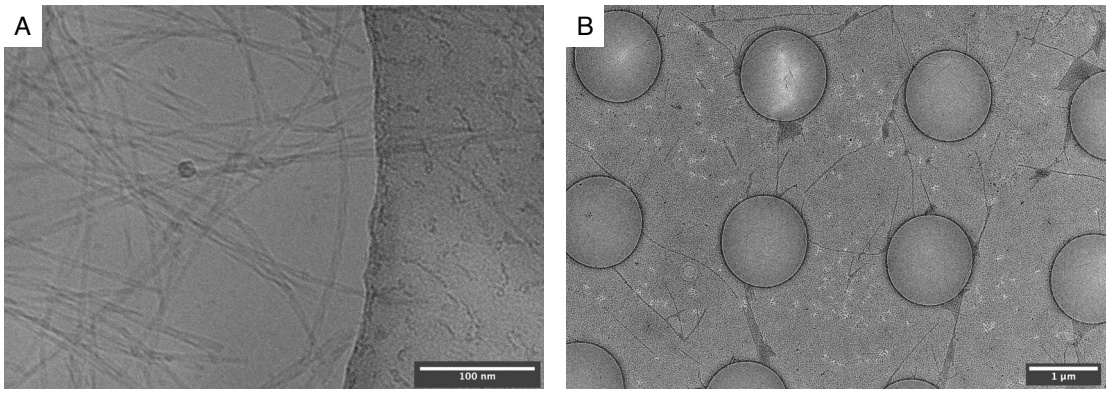

Figure 7.4.: Cryo-EM screening of the *in vitro* A2T Aβ42 fibril sample prior to data collection. (A) At 100,000x magnification. (B) At 5,600x magnification.

Reference-free 2D class averaging of the manually picked fibrils reveals the presence of three polymorphs in the sample (Figure 7.5). The first polymorph (PM1) accounts for 50% of all fibrils in the dataset, has a diameter of 7 nm and a crossover distance of ~460 Å (Figure 7.5 A, B, G). The second polymorph (PM2) has a slightly larger diameter of 9 nm, a crossover distance of ~520 Å and accounts for 43% of all fibrils in the dataset (Figure 7.5 C, D, G). The third polymorph (PM3) with a diameter of 11 nm accounts for the remaining 7% (Figure 7.5 E, F, G). 2D class averages of the separated fibril segments at smaller box sizes, already show the amyloid-typical cross-β pattern (Figure 7.5 B, D, F).

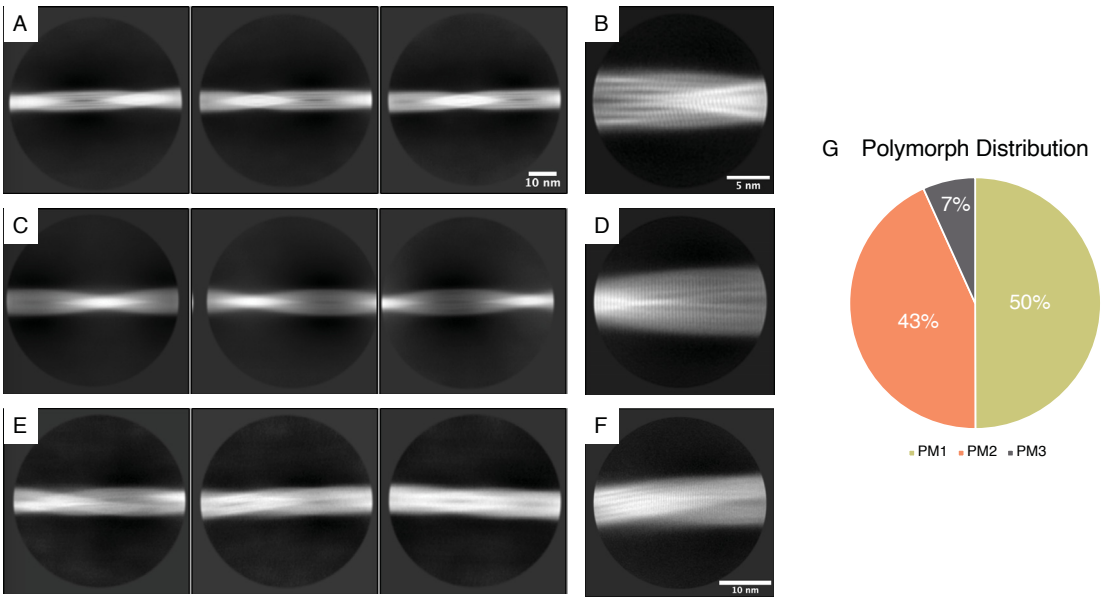

Figure 7.5.: Reference-free 2D class averaging of A2T Aβ42 fibrils. (A), (B) PM1. (C), (D) PM2. (E), (F) PM3. (G) Distribution of polymorphs in the dataset. For 2D class averages shown in (A), (C), (E) fibril segments were extracted at a box size of 810 pix (downscaled to 270 pix). The scalebar in (A) applies to panels (C), and (E) as well. For 2D class averages shown in (B), (D) fibril segments were extracted at a box size of 270 pix. The scalebar in (B) applies to (D) as well. For the 2D class average shown in (F) fibril segments were extracted at a box size of 448 pix.

7.1.1. Cryo-EM Structure of PM1

The first and most abundant polymorph, PM1, was solved to a resolution of

3.9 Å (based on the gold-standard FSC 0.143 criterion; Figure 7.6).

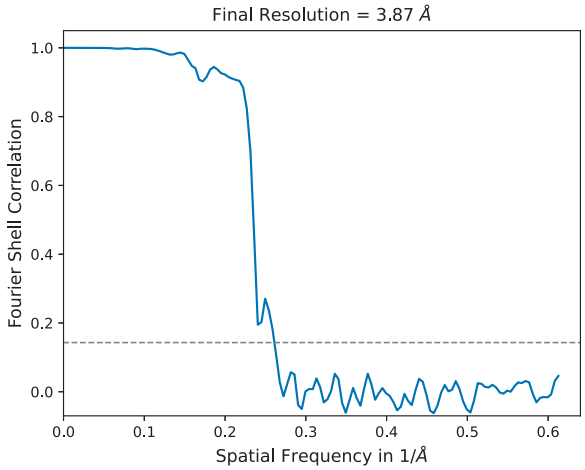

Figure 7.6.: FSC curve from the gold-standard refinement of the cryo-EM map of A2T Aβ42 PM1 yields a resolution of 3.9 Å (using the 0.143 criterion).

PM1 is made of two identical LS-shaped protofilaments that are related by a C2 symmetry with a refined helical rise of 4.8 Å and a helical twist of -2° (Figure 7.7). The ordered L-shaped N-terminus consists of residues D1 to Q15 and, accordingly, residues K16-A42 form the S-shaped domain (Figure 7.7 D, E). Each protofilament comprises one β-sheet extending from residues H13 - A24 (Figure 7.7 A). However, it should be noted that the individual layers are not fully resolved (Figure 7.7 C), which likely influences the β-sheet assignment, as the quality of the assignment is directly related to the quality of the cryo-EM map. The LS-shaped protofilament fold is stabilised by three hydrophobic cluster involving the following residues: (i) F4, L34, and V36, (ii) L17, F19, A21, V24, and I31, and (iii) A30, I32, M35, V40, and A42. The two latter contribute to the S-shape of the C-terminal domain. The kink in the N-terminal L-shape is stabilized by a hydrogen bond between S8 and E11 or a salt bridge between H6 and E11.

The protofilament interface is formed by a salt bridge between D1 and K28 of the opposing protofilament and hydrophobic interactions between the C-termini of both protofilaments involving residues I41 and V39.

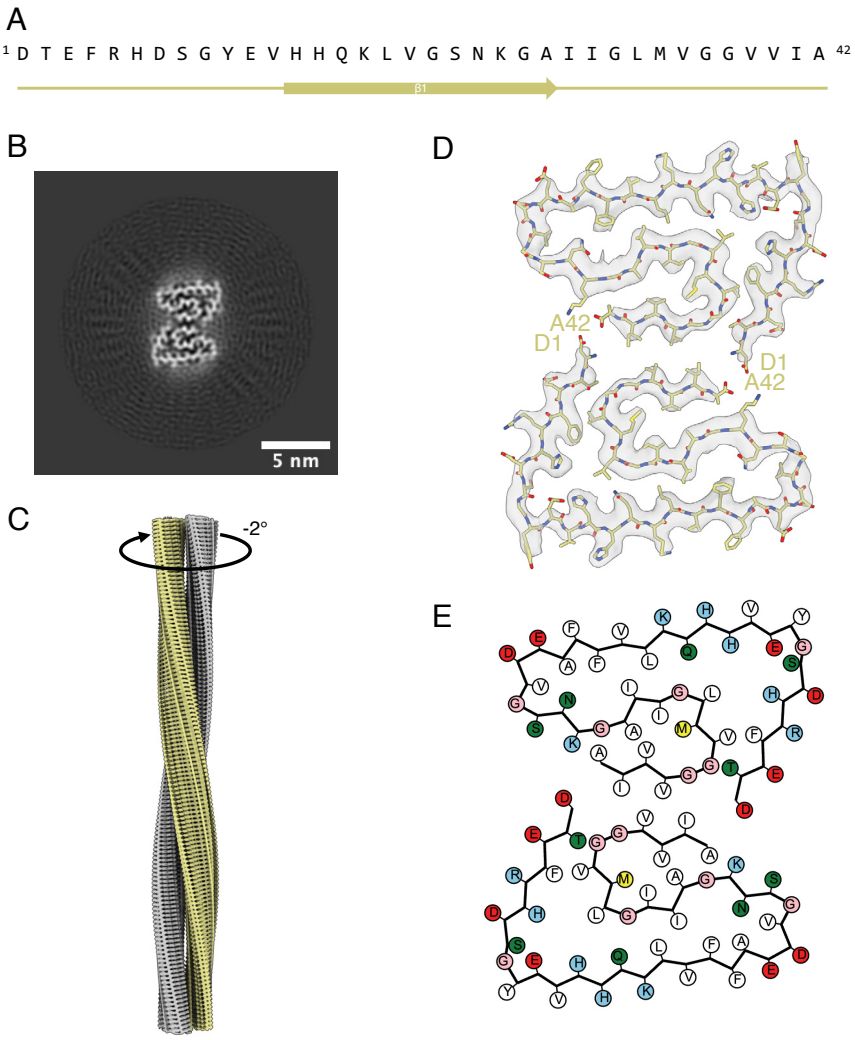

Figure 7.7.: Cryo-EM structure of A2T Aβ42 PM1. (A) Amino acid sequence of A2T Aβ42. Solid lines indicate for which part of the sequence the atomic model was built. Arrows indicate β-strands. (B) Projection of the reconstructed density including approximately one β-rung. (C) Reconstructed cryo-EM density along the helical axis with a label denoting the helical twist. (D) The cryo-EM density map (in transparent gray) with the atomic model (light green). (E) A schematic of the fold, produced with atom2svg.py [309] (red: acidic side chain; blue: basic side chain; green: hydrophilic side chain; white: hydrophobic side chain; pink: glycine; yellow: sulfur containing).

Interestingly, the PM1 fold of A2T Aβ42 is identical to the fold of wild-type Aβ42 fibrils formed under the same fibrillisation conditions [252] (Figure 7.8 A). This is indeed surprising, as Gremer et al. in their 2017 Science publication pos-

tulated: *"A2T (Icelandic) might be protective against Alzheimer's disease, because threonine is more polar than alanine and could destabilize the fibril by disrupting the hydrophobic cluster* Ala^2, Val^{36}, Phe^4, *and* Leu^{34}*"* [252].

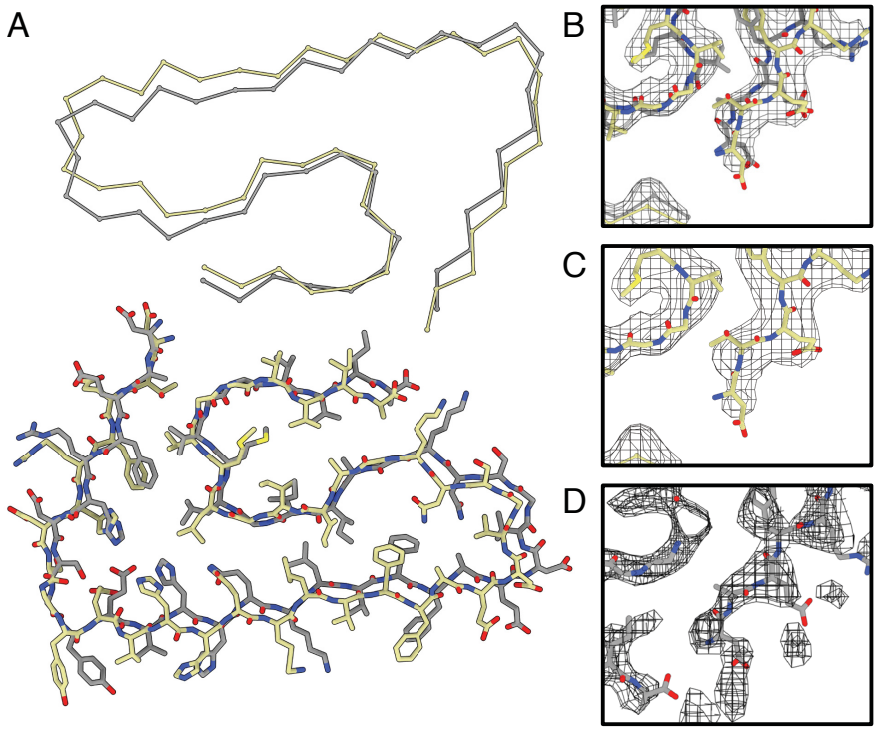

Figure 7.8.: Comparison of the cryo-EM structure of A2T Aβ42 PM1 with the cryo-EM structure of wild-type Aβ42 (PDB 5OQV (Model; as displayed in A, B, D) and EMD 3851 (Map; as displayed in D)) formed under the same fibrillisation conditions. (A) Overlay of the atomic model of A2T Aβ42 PM1 (green) and the atomic model of wild-type Aβ42 (gray). (B) Structure of the D1 - R5 part of A2T Aβ42 PM1 (green) and wild-type Aβ42 (gray) overlaid on the corresponding part of the density map of A2T Aβ42 PM1. (C) Structure of the D1 - R5 part of A2T Aβ42 PM1 (green) overlaid on the corresponding part of the density map of A2T Aβ42 PM1. (D) Structure of the D1 - R5 part of wild-type Aβ42 (gray) overlaid on the corresponding part of the density map of wild-type Aβ42.

A direct comparison of the A2T Aβ42 model and map with the wild-type Aβ42 model and map shows not only that the A2T Aβ42 model actually fits the A2T Aβ42 map better than the wild-type Aβ42 model (Figure 7.8 B), but also that the A2T Aβ42 map indeed has a larger visible side-chain density at position 2 in comparison to the wild-type Aβ42 map (Figure 7.8 C, D).

7.1.2. Cryo-EM Structure of PM2

PM2 consists of the same LS-shaped protofilaments that were observed in PM1, but the two protofilaments are arranged differently (Figure 7.9).

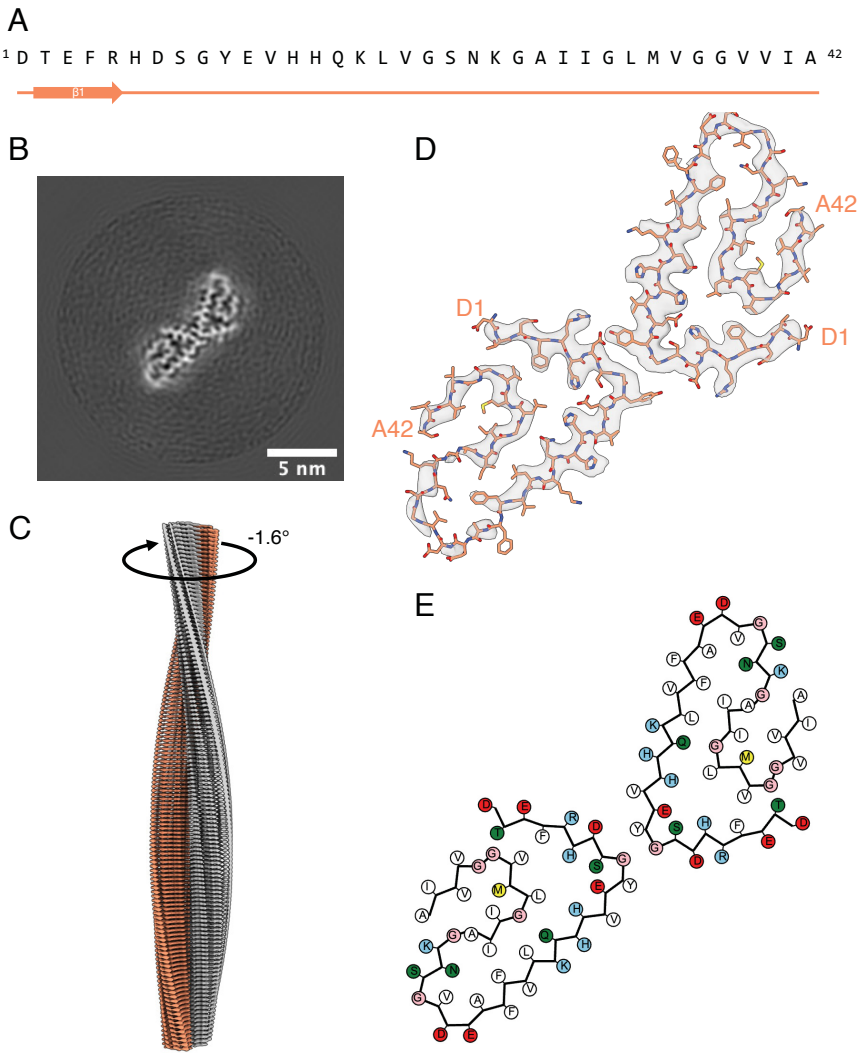

Figure 7.9.: Cryo-EM structure of A2T Aβ42 PM2. (A) Amino acid sequence of A2T Aβ42. Solid lines indicate for which part of the sequence the atomic model was built. Arrows indicate β-strands. (B) Projection of the reconstructed density including approximately one β-rung. (C) Reconstructed cryo-EM density along the helical axis with a label denoting the helical twist. (D) The cryo-EM density map (in transparent gray) with the atomic model (orange). (E) A schematic of the fold, produced with atom2svg.py [309] (red: acidic side chain; blue: basic side chain; green: hydrophilic side chain; white: hydrophobic side chain; pink: glycine; yellow: sulfur containing).

The asymmetric PM2 fibril, that was solved to a resolution of 3.7 Å (based on the gold-standard FSC 0.143 criterion; Figure 7.10) has a refined helical twist of -1.6° and a rise of 4.75 Å (Figure 7.9 B). We observed only one β-sheet in each protofilament on a secondary structure level, extending from residues T2 - R5. However, as mentioned for PM1, the accuracy of the β-sheet assignment is directly linked to the map quality and can therefore be incorrect.

As previously described, the LS-fold of one protofilament is mainly stabilized by three hydrophobic clusters (compare Chapter 7.1.1) (Figure 7.9 D, E). However, in contrast to PM1, where the interface between the two protofilaments is formed by interactions between the C-termini and a salt bridge between D1 and K28, in PM2 fibrils, the two LS-shaped protofilaments are connected via hydrogen bonds between D7 and Y10.

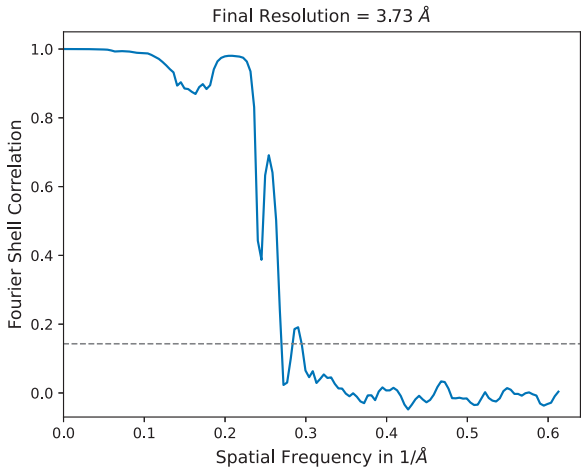

Figure 7.10.: FSC curve from the gold-standard refinement of the cryo-EM map of A2T Aβ42 PM2 yields a resolution of 3.7 Å (using the 0.143 criterion).

The cryo-EM map as shown in Figure 7.9 is the output map of the last 3D refinement step prior to 3D auto-refinement and post-processing, since the quality of the reconstruction unexpectedly degraded during 3D auto-refinement. Figure 7.11 shows the map as displayed in Figure 7.9 and the unsharpened post-processed map at different contour levels.

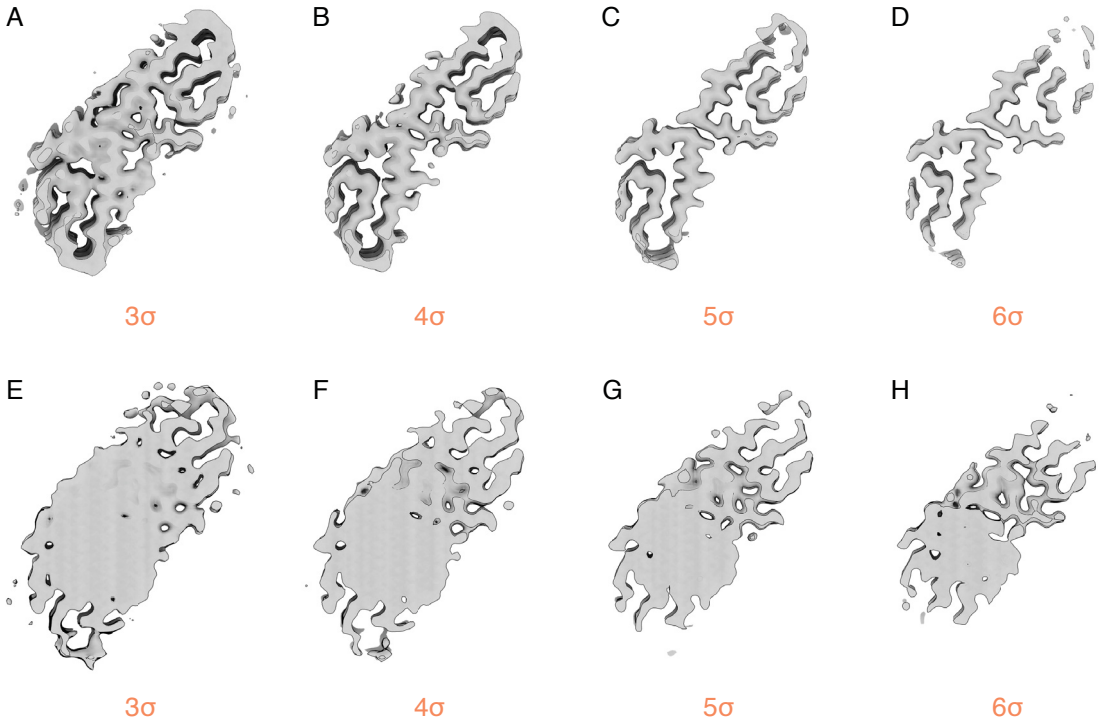

Figure 7.11.: Reconstruction of A2T Aβ42 PM2 at different processing steps and contour levels. (A)-(D) Reconstruction prior to 3D auto-refinement and post processing at 3σ (A), 4σ (B), 5σ (C), and 6σ (D). (E)-(H) Unsharpened post-processed map at 3σ (E), 4σ (F), 5σ (G), and 6σ (H).

The global resolution indicated during post-processing and stated above (Figure 7.10) may therefore not necessarily reflect the actual resolution of the map displayed in Figure 7.9.

7.1.3. Cryo-EM Structure of PM3

The least prevalent polymorph in the dataset, PM3, consists of three identical protofilaments A1, A2, and A3 (Figure 7.12 A).

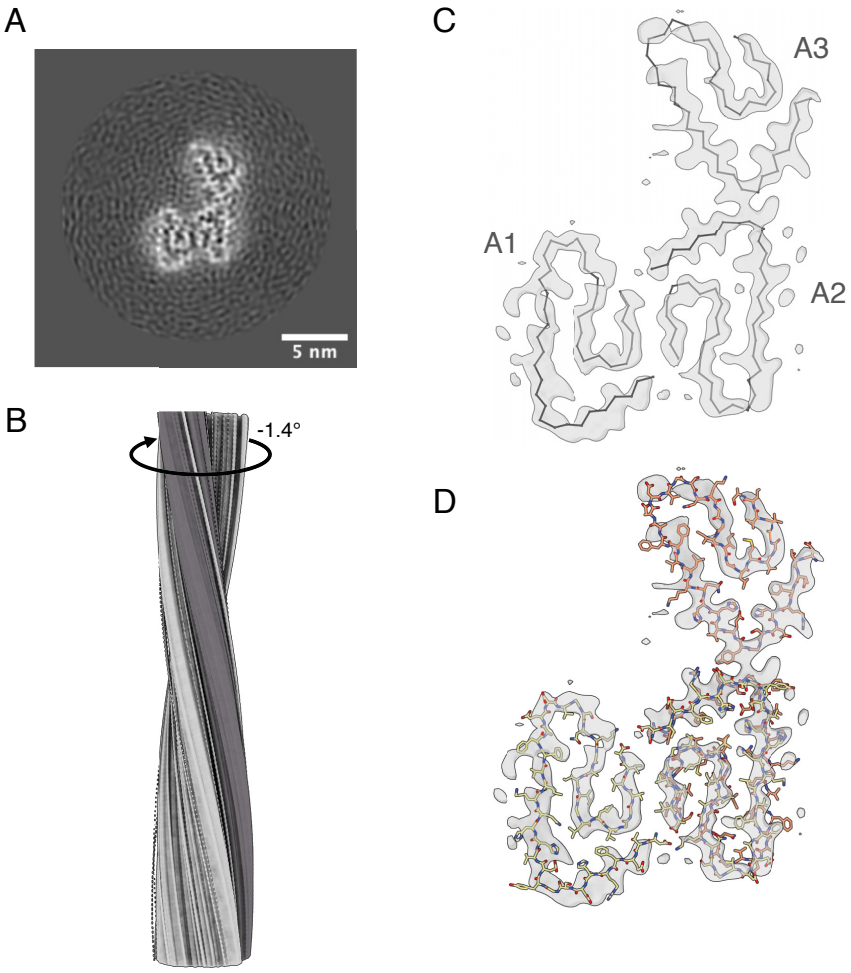

Figure 7.12.: Cryo-EM structure of A2T Aβ42 PM3. (A) Projection of the reconstructed density including approximately one β-rung. (B) Reconstructed cryo-EM density along the helical axis with a label denoting the helical twist. (C) The cryo-EM density map (in transparent gray) with the tentative backbone (purple). (D) The cryo-EM density map (in transparent gray) with the atomic model of PM1 (green) and the atomic model of PM2 (orange).

PM3 fibrils were solved to a resolution of 5.4 Å (based on the gold-standard FSC 0.143 criterion; Figure 7.13) with refined helical parameters of -1.36° (twist) and 4.73 Å (rise) (Figure 7.12 B).

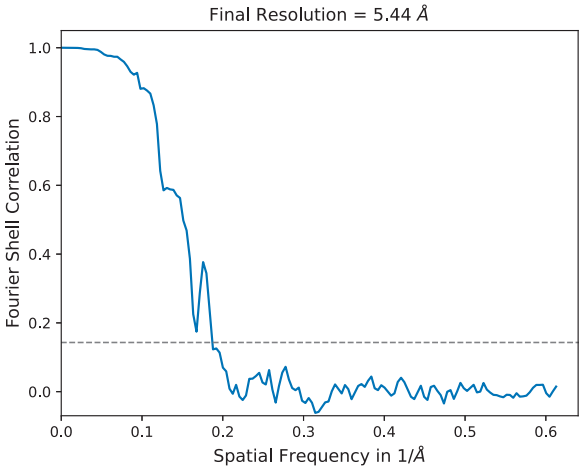

Figure 7.13.: FSC curve from the gold-standard refinement of the cryo-EM map of A2T Aβ42 PM3 yields a resolution of 5.4 Å (using the 0.143 criterion).

The three PM3 protofilaments are connected by two different interfaces, both of which are found individually in PM1 and PM2 fibrils (Figure 7.12 C). In PM3 fibrils, protofilaments A1 and A2 are connected by their C-termini and by a salt bridge between D1 and K28 and therefore, the A1-A2 protofilament pair is identical to PM1 fibrils (Figure 7.12 D). Protofilaments A2 and A3 are connected by hydrogen bonds between D7 and Y10, an interface also found in PM2 fibrils. The 5.4 Å resolution map only allowed for preliminary backbone tracing (Figure 7.12 C), *de novo* atomic model building was not possible due to the lack of layer separation (Figure 7.12 B).

7.1.4. Discussion

Three polymorphs could be observed in the sample of *in vitro* Aβ42 fibrils with the Icelandic A2T mutation. Interestingly, the most abundant PM1 fibrils are identical to the structure of previously described wild-type Aβ42 fibrils formed under the same fibrillisation conditions. This is particularly surprising because the mutation weakens a hydrophobic cluster that was thought to contribute significantly to the stability of the fibril [252]. The PM2 fibril fold shows an alternative conformation that was almost equally favoured. The connection of the two LS-shaped protofilaments through a novel interface mediated by hydrogen bonds between D7 and Y10

has not been described before. Both interfaces are present in the least abundant PM3 fibrils, that are made of three identical protofilaments.

It has previously been reported that the protective Icelandic APP mutation influences APP processing, by decreasing β-secretase cleavage resulting in a reduced production of Aβ40 and Aβ42 [83]. Moreover, A2T Aβ has been reported to be less prone to aggregate in comparison to wild-type Aβ [322, 323]. Especially the latter observation is interesting considering that A2T Aβ forms fibrils at a high concentration *in vitro* after 38 days of incubation. Thus, the mutation itself does not prevent fibril formation, at least *in vitro*. The fact that the A2T mutation protects against Alzheimer's disease is an important argument supporting the amyloid cascade hypothesis and therefore, further investigations of the aggregation behaviour of A2T Aβ *in vivo* remains a target of future research.

7.2. Methods

7.2.1. Sample Purification

The sample was analyzed and purified by RP-HPLC. RP-HPLC is a molecular biology technique that can be used to separate different molecules based on their hydrophobicity [324]. The non-polar stationary phase reduces the retardation time of the polar mobile phase. Prior to RP-HPLC analyses, 1 mg synthetic peptide (Bachem, 4104329, Lot 2002 1000018466, molecular weight 4544.13 Da (220.064 nmol)) was dissolved in 660 µL H_2O, 0.1% TFA resulting in a monomer concentration of 333.43 µM. Afterwards, 2 µL of this solution were diluted in 33 µL H_2O, 0.1% TFA. 20 µL of this solution were used for analytical RP-HPLC. Then, the remaining 658 µL were used for a preparative RP-HPLC run. The main peak after a retardation time of 16.32 min was collected in the mobile phase (RP-HPLC buffer: 30% AcN, 0.1% TFA). For the analytical as well as preparative RP-HPLC run, a ZORBAX 300SB-C8 (4.6 x 250 mm, 5 micron) column was used on a 1260/1290 Infinity system from Agilent Technologies, California. A 1000 µL sample loop and a flow rate of 4 mL/min was used. The purified sample was stored in the elution buffer (30% AcN, 0.1% TFA) at room temperature under dark and quiescent conditions for several days.

7.2.2. EM sample screening

After 38 days of incubation 200 µL sample were taken from the bottom of the Falcon tube, transferred to a LoBind reaction tube and centrifuged at 18,000 x *g* for 60 min. The supernatant (180 µL) was removed and the remaining 20 µL were used for further analyses. For cryo-EM screening, 2.5µL sample was applied to holey carbon grids (Quantifoil 1.2/1.3, 300 mesh), blotted with filter paper for 5s and plunge frozen in liquid ethane using a ThermoFisher Scientific Vitrobot Mark IV, set at 95% humidity and 4°C temperature. Since multiple fibril clusters were observed on the cryo-EM grid, the sample was afterwards screened by negative stain EM. For this, 3 µL sample was applied onto a glow-discharged 300 mesh carbon-coated copper grid (EM Sciences, ECF300-Cu). The sample was incubated on the grids for 2 min and excess buffer was carefully blotted off with filter paper. 3 µL of sodium silicotungstate (SST) stain were applied on the top of the grid, following a 1 min incubation. The excess stain was blotted off with filter paper and the grid was air dried. TEM images were acquired using a ThermoFisher Scientific Talos 120C at an acceleration voltage of 120 kV. Images were collected on a 4k x 4k Ceta 16M CMOS camera using Thermo Scientific Velox Software.

7.2.3. Cryo-EM Image Acquisition and Data Preprocessing

For cryo-EM imaging, 2.5 µL of the A2T Aβ42 fibril sample was applied to holey carbon grids (Quantifoil 1.2/1.3, 300 mesh), blotted with filter paper for 3-5 s at varying blot forces and plunge frozen after 1 s wait time in liquid ethane using a ThermoFisher Scientific Vitrobot Mark IV, set at 90% humidity and 4°C temperature. To avoid empty holes as well as fibril clusters on the grid, four grids were prepared at different blotting conditions ((i) -10 blot force, 3 s blot time; (ii) -10 blot force, 5 s blot time; (iii) -5 blot force, 3 s blot time; (iv) -5 blot force, 4 s blot time). Data acquisition (Grid at blotting condition (iii)) was performed on a ThermoFisher Scientific Talos Arctica microscope operating at 200 kV using a Gatan Bioquantum K3 detector in counting mode with a Gatan Bio-quantum energy filter with a slid width of 20 eV. The automated collection was directed by EPU data collection software. Further details are given in Table 7.1.

Data collection	
Microscope	Talos Arctica
Voltage [kV]	200
Detector	K3
Energy filter slit width [eV]	20
Magnification	100,000
Pixel size [Å]	0.816
Defocus range [µm]	-0.5 to -2.5
Exposure time [s]	1.5
Number of frames	35
Total dose [e^-/Å^2]	27

Table 7.1.: Cryo-EM data collection statistics of *in vitro* A2T Aβ(1-42) fibrils.

Prior to helical reconstruction, gain-corrected movie frames were aligned and summed into single micrographs on-the-fly using Warp [218]. CTF estimation was performed using CTFFIND4.1 [209].

7.2.4. Helical Reconstruction

Helical reconstruction was performed using the helical reconstruction methods in RELION [223, 272]. Fibrils were picked manually and polymorphs were separated during reference-free 2D classification at a box size of 810 pix (downscaled to 270 pix). For PM1, and PM2, fibril segments were afterwards re-extracted at the original pixel size at a box size of 270 pix. PM3 particles were initially re-extracted at a box size of 448 pix and prior to 3D auto-refinement re-extracted at a box size of 300 pix. For all polymorphs, an initial model was generated *de novo* from one larger box 2D class average (PM1: 540 pix, downscaled to 270 pix; PM2: 640 pix, downscaled to 320 pix; PM3: 896 pix, downscaled to 448 pix) using the `relion_helix_inimodel2d` command [267]. The reconstructed *de novo* generated initial models were low-pass filtered to 10 Å. For all polymorphs, 3D classification was used to obtain a homogeneous high-quality subset of fibril segments. 3D auto-refinement and subsequent post-processing was performed for all three polymorphs to compute the final maps and to calculate the resolution according to gold-standard Fourier Shell Correlations at 0.143 applying a soft-edged solvent mask. For PM2, the post-processed map did not yield sufficient

resolution and accordingly, the map of the last 3D refinement instead of the post-processed map was used for model building. The PM2 map was sharpened using VISDEM [304]. Additional image processing information can be found in Table 7.2.

	PM1	PM2	PM3
Micrographs	4,465	4,465	4,465
Box width [pix]	270	270	300
Initial particle images [no.]	137,326	118,944	18,557
Final particle images	102,633	61,066	10,390
Symmetry imposed	C2	C1	C1
Helical rise [Å]	4.80	4.75	4.73
Helical twist [°]	-2.0	-1.59	-1.36
Map resolution [Å]	3.87	3.73	5.44
FSC threshold	0.143	0.143	0.143
Applied B-factor [Å^2]	-183	N/A	-256

Table 7.2.: Image Processing statistics of A2TAβ42 fibrils.

7.2.5. Model Building and Refinement

Atomic model building was only possible for PM1 and PM2 reconstructions. Here, a previously published cryo-EM structure of wild-type Aβ42 fibrils (PDB 5OQV) [252] was fitted into the reconstructed cryo-EM map using ChimeraX [305] and used as initial model. For the asymmetric PM2, two protofilaments were individually fitted into the map. Hydrogens were removed from the model using `phenix.reduce` [321]. A multi layer model was built by applying helical symmetry using the ChimeraX `sym` command. The models were refined into the density map using an iterative procedure of automatic refinement in Phenix [320] and manual modeling in COOT [318]. Side chain rotamers were refined manually monitoring Ramachandran outliers and clash scores using MolProbity [319]. ChimeraX [305] was used for molecular graphics and analyses. Additional information can be found in Table 7.3.

	Polymorph 1	Polymorph 2
Initial model [PDB code]	5OQV	5OQV
Model Composition		
Chains	10	10
Non-hydrogen atoms	3,210	3,200
Protein residues	420	420
RMS deviations		
Bond lenghts [Å]	0.010	0.009
Bond angles [°]	1.987	1.654
Validation		
MolProbity score	2.84	3.14
Clashscore	46.43	69.84
Poor rotamers [%]	0	0
Ramachandran plot		
Favored [%]	82.5	71.5
Allowed [%]	17.5	28.5
Outliers [%]	0	0

Table 7.3.: Model building statistics of A2TAβ42 fibrils.

7.3. Contribution

For this project, I participated in RP-HPLC sample purification (which was performed together with Lothar Gremer). I prepared cryo-EM and negative stain EM grids and performed sample screening by cryo-EM and negative stain EM. I prepared the cryo-EM grids and collected the cryo-EM dataset. I performed image processing and atomic model building.

8. Conclusion and Outlook

Aβ and its aggregation into amyloid fibrils, that eventually accumulate into extracellular amyloid plaques, are a hallmark of AD, a disease that severely impacts the lives of those affected and their relatives through the degeneration of memory and cognitive abilities. In order to develop a cure for the disease it is therefore of great importance to not only identify the causing agents but also investigate their structure on a molecular level.

Chapter 3 provides an overview of the structures of Aβ fibrils presented in Manuscript I, purified from various transgenic mouse models commonly used in Alzheimer's disease research. Novel Aβ polymorphs were observed in APP/PS1, ARTE10 and tg-SwDI mice. In contrast, previously described human type II filaments [261], which are mostly found in familial AD cases, were observed in tg-APP$_{Swe}$, APP23 and ARTE10 mice. Tg-APP$_{ArcSwe}$ mice display an Aβ fibril fold highly similar to human type I Aβ fibrils mostly observed in sporadic AD cases [261]. In summary, this study shows that the fold of Aβ fibrils is different in the different mouse models. Furthermore, it is discussed that tg-APP$_{ArcSwe}$ is the only known mouse model that contains Aβ fibrils that resemble human type I Aβ fibrils mainly observed in sporadic AD patients. This finding is particularly interesting since tg-APP$_{ArcSwe}$ mice were used in the clinical trial of lecanemab, an Alzheimer's drug that was approved by the FDA in the US in 2023. This observation is a good example of the potential of such structural studies for drug development. Often, drugs must first show their efficacy in animal models before they are tested in humans. However, if the molecular target of the therapeutic is different in mice than in humans, wrong conclusions can be drawn. Therefore, the integration of structural investigations of the molecular target of a therapeutic into the drug development pipeline could potentially increase the success rate of clinical trials.

To study certain molecular aspects of Alzheimer's disease, such as the aggregation of Aβ into amyloid fibrils, which is the focus of this thesis, suitable laboratory model systems are as important as suitable animal models. However, the conditions leading to the aggregation of synthetic or recombinant Aβ into fibrils identical to those observed in humans are not yet known. In Chapter 4 the cryo-EM structures of six *in vitro* Aβ42 fibril polymorphs aggregated at neutral pH are presented. The observed fibrils present novel Aβ polymorphs and therefore, differ from other *in vitro* and *ex vivo* fibril structures. And although the aggregation conditions used in this study do not result in a suitable model system in terms of structural identity with human brain extracted Aβ fibrils, it does show polymorphs that could represent an intermediate conformation eventually leading to the formation of a fibril identical to another polymorph observed. Consequently, it is possible that the cryo-EM data set collected after 21 h incubation captures fibril formation or secondary nucleation. The influence of incubation time on fibril structure and the distribution of the different polymorphs will be an interesting topic for future studies.

Early-onset familial AD is, among other things, caused by mutations in the APP gene. Some of these mutations are located in the Aβ sequence and therefore result in the deposition of mutated Aβ in affected patients. One example is the Uppsala APP mutation, in which the deletion of six amino acids leads to a rapidly progressing form of early-onset AD. The cryo-EM structures of *in vitro* and *ex vivo* AβUpp(1-42)$_{\Delta 19-24}$ are presented in Chapter 5 and 6. *In vitro* AβUpp(1-42)$_{\Delta 19-24}$ aggregates into unique fibril polymorphs. The two most abundant polymorphs for which structure determination was possible display novel folds of Aβ and consequently differ from other Aβ fibrils and especially from wild-type Aβ fibrils formed under the same fibrillisation conditions. In addition, the *ex vivo* cryo-EM structure of AβUpp(1-42)$_{\Delta 19-24}$ fibrils purified from tg-mouse brain tissue was presented. Tg-UppSwe mice contain only one polymorph, and interestingly, despite the deletion of six amino acids in the Aβ sequence, this polymorph shows some structural similarity to human type II filaments found mainly in familial AD cases. Finally, a cryo-EM dataset of Aβ fibrils purified from human brain tissue

was collected. The structure of Tau PHF and SF filaments as well as Aβ fibrils could be determined. However, the structure of SF filaments and Aβ fibrils was only solved to a resolution of 4.9 Å and 5.9 Å, respectively. Consequently, the identification of individual side chains in the Aβ-fibril reconstruction was not possible. Nevertheless, the fact that this fibril appears to be identical to human type I Aβ wild-type fibrils suggests that the observed fibril is not made of AβUpp(1-42)$_{\Delta 19-24}$ but wild-type Aβ. This is particularly interesting because the mass spectrometry data presented in Publication II suggest that the majority of Aβ is actually mutant Aβ. This finding may indicate that the reconstructed Aβ fibril is post-translationally modified Aβ42 with a higher molecular weight than unmodified wild-type Aβ42. Moreover, one reason for the absence of AβUpp(1-42)$_{\Delta 19-24}$ fibrils in the recorded dataset could be that the mutant Aβ fibrils clump together even more than wild-type Aβ fibrils. In future attempts to determine the structure of AβUpp(1-42)$_{\Delta 19-24}$ fibrils, the protocol should therefore be adapted so that the fibril clumps are broken up more strongly either chemically or mechanically.

Like the Uppsala mutation, most APP mutations are pathogenic and are associated with early-onset familial AD. An exception to this is the A673T or Icelandic mutation, the only known APP mutation that protects against AD. Within this thesis, the Icelandic mutation was further investigated and the results are presented in Chapter 7. First, synthetic A2T Aβ42 was purified and transferred into fibrillisation conditions. And indeed, as shown in Chapter 7, amyloid fibrils could be observed in the sample after several days of incubation. The cryo-EM structure of all polymorphs present in the sample, three in total, was determined. Interestingly, the most abundant polymorph is identical to wild-type Aβ42 fibrils formed under the same fibrillisation conditions. This is particularly remarkable as it was previously speculated that the reason for the protective properties of the A2T mutation was that the threonine would break up a hydrophobic cluster that was thought to be essential for the stability of the polymorph [252]. The fact that a mutation in APP leading to the production of mutant Aβ results in a protection against AD is one important argument for Aβ playing a role in the early stages of AD. This makes A2T an interesting target for structural investigations. However, it remains to be seen whether A2T Aβ also forms fibrils under the same yet un-

known conditions under which synthetic or recombinant wild-type Aβ aggregates into fibrils identical to those in humans.

In summary, structural studies of Aβ fibrils both *in vitro* and *ex vivo*, as presented in this work, are key to identifying suitable laboratory and animal models to study specific aspects of the disease pathogenesis and to develop novel therapeutics.

9. Materials

9.1. List of Devices

Table 9.1 lists the devices used for this work.

Device	Model	Manufacturer
Glow discharge cleaning system	easiGlow	Pelco
High performance liquid chromatography system	1260/1290 Infinity Series	Agilent Technologies, CA
Minifuge	3-1810	neoLab
Plunge freezing device	Vitrobot Mark IV	Thermo Fisher Scientific
Scales	N/A	Kern ABJ
Table top centrifuge	5417R, 5415R	Eppendorf
Ultra-centrifuge (TLA55)	Optima MAX-XP	Beckmann Coulter
Ultrasound bath	Sonorex	Bandeli
Vortex mixer	Vortex Genie 2	Scientific Industries SI

Table 9.1.: Devices

9.2. List of Microscopes

Table 9.2 lists the microscopes used for this work.

Technique	Microscope Name	Manufacturer	Camera	Manufacturer
Atomic force microscopy	NanoWizard 3	JPK instruments		Navitar
Cryogenic electron microscopy	Talos Arctica G2	TFS	K3 (including energy filter BioContinuum GIF)	Gatan
Cryogenic electron microscopy	Titan Krios G4	TFS	K3 (including energy filter BioContinuum GIF) / Falcon IV	Gatan / TFS
Cryogenic electron microscopy	Titan Krios 1	TFS	K3	Gatan
Transmission electron microscopy	Talos L120C	TFS	4k × 4k Ceta 16M camera CMOS	TFS

Table 9.2.: Microscopes.

9.3. List of Computer Programs

Table 9.3 lists the computer programs used for this work.

Program	Version	Source
Agilent ChemStation Method and Run Control	N/A	Agilent Technology
Agilent ChemStation DataAnalysis	N/A	Agilent Technology
ChemDraw	21.0.0	PerkinElmer
Chimera	1.15	UCSF ([325])
ChimeraX	1.2.5 / 1.6	UCSF ([305])
coot	0.8.9.2 EL	MRC-LMB ([234, 318])
crYOLO	1.8.4	MPI-Dortmund ([219, 277, 317])
CTFFIND	4.1	The Grigorieff Lab([209])
EMAN2	2.99.33	BCM ([326])
EPU (ERC-3 Arctica)	2.12.1.2782REL	TFS
EPU (ERC-3 Krios)	3.2.0	TFS
Gwyddion	2.61	gwyddion.net ([316])
Microsoft Office	2023	Microsoft
phenix	1.19.2-4158-000	phenix-online.org ([239, 320])
RELION	3.1.0	MRC-LMB ([223, 225, 272])
Velox	2.9.0	TFS
VISDEM	1.0	SimTK (DireX) ([304])
Warp (ERC-3 Arctica)	v110 BETA	MPI Göttingen ([218])
Warp (ERC-3 Krios)	v110Beta	MPI Göttingen ([218])

Table 9.3.: Computer Programs.

9.4. Synthetic Aβ material

Table 9.4 lists the synthetic Aβ material used for this work.

Peptide	Provider
Aβ(1-42)	Bachem, Switzerland
Aβ(1-42)A2T	Bachem, Switzerland
AβUpp(1-42)$_{\Delta 19\text{-}24}$	Martin Ingelsson, Uppsala University, Sweden

Table 9.4.: Synthetic Aβ material.

9.5. Antibodies

Table 9.5 lists the antibodies used for this work.

Antibody Name	Manufacturer
Mouse Nab228	Sigma-Aldrich
Anti-mouse secondary gold-conjugated antibody (6 nm)	abcam
Anti-human secondary gold-conjugated antibody (10 nm)	abcam

Table 9.5.: Antibodies

9.6. Consumables and microscopy material

Table 9.6 lists the general laboratory consumables used for this work.

Consumable	Description	Manufacturer
HPLC column	ZORBAC 300SB-C8, StableBond Analytical 4.6 x 250mm, 5-Micron	Agilent
Parafilm	Parafilm M, 4 IN. x 125 FT.	Pechiney Plastic Packaging
Reaction tube 0.5 mL protein LoBind	Protein LoBind 0.5 mL	Eppendorf
Reaction tube 1.5 mL protein LoBind	Protein LoBind 1.5 mL	Eppendorf
Reaction tube 1.5 mL	Reagiergefäß 1.5 mL	Sarstedt
Ultracentrifugation reaction tube 1.5 mL	Microfuge Tube Polypropylene	Beckman Coulter

Table 9.6.: General Laboratory consumables

Table 9.7 lists the AFM consumables used for this work.

Consumable	Description	Manufacturer
Cantilever	OMCL-AC160TS, tip radius 9 ± 2 nm	Olympus
Cantilever Holder	Fixed-Spring cantilever holder	JPK
Mica	Glimmer, "V1", 10mm	Plano
Glue	Plus sofortfest, 2 component glue	UHU
Microscope slide	ground edges, frosted, VWR Catalog No: 631-1553	VWR
Razor blade	N/A	Herkenrath Solingen

Table 9.7.: Consumables and material for AFM

Table 9.8 lists the (cryo-) EM consumables used for this work.

Consumable	Description	Manufacturer
Grids UltraAuFoil®	R1.2/1.3	Quantifoil
Grids Quantifoil®	R1.2/1.3	Quantifoil
Grids negative stain	300 mesh carbon-coated copper grid ECF300-Cu	EM Sciences
Tweezer N5	N5 - Inox - B	Dumont, CH
Tweezer N5-AC	N5 AC-PO	Dumont, CH
Tweezer N1	N1 - Dumoxel - H	Dumont, CH

Table 9.8.: Consumables and material for (cryo-) EM

Bibliography

[1] Mara Zielinski, Christine Röder and Gunnar F. Schröder. 'Challenges in sample preparation and structure determination of amyloids by cryo-EM'. In: *Journal of Biological Chemistry* 297 (2 Aug. 2021), p. 100938. ISSN: 00219258. DOI: 10.1016/j.jbc.2021.100938.

[2] Christian B. Anfinsen. 'Principles that Govern the Folding of Protein Chains'. In: *Science* 181 (4096 July 1973), pp. 223–230. ISSN: 0036-8075. DOI: 10.1126/science.181.4096.223.

[3] Fabrizio Chiti and Christopher M Dobson. 'Protein Misfolding, Functional Amyloid, and Human Disease'. In: *Annual Review of Biochemistry* 75 (1 2006), pp. 333–366. ISSN: 0066-4154. DOI: 10.1146/annurev.biochem.75.101304.123901. URL: http://www.annualreviews.org/doi/10.1146/annurev.biochem.75.101304.123901.

[4] M Sunde et al. 'Common core structure of amyloid fibrils by synchrotron X-ray diffraction.' In: *Journal of molecular biology* 273 (3 Oct. 1997), pp. 729–739. ISSN: 0022-2836 (Print). DOI: 10.1006/jmbi.1997.1348.

[5] Alan S Cohen. *General introduction and a brief history of the amyloid fibril*. Ed. by J Marrink and M H Van Rijswijk. 1986.

[6] Rud Virchow. 'Ueber eine im Gehirn und Rückenmark des Menschen aufgefundene Substanz mit der chemischen Reaction der Cellulose'. In: *Archiv für Pathologische Anatomie und Physiologie und für Klinische Medicin* (1854). ISSN: 09456317. DOI: 10.1007/BF01930815.

[7] Rud Virchow. ‘Weitere Mittheilungen über das Vorkommen der pflanzlichen Cellulose beim Menschen’. In: *Archiv für Pathologische Anatomie und Physiologie und für Klinische Medicin* (1854). ISSN: 09456317. DOI: 10.1007/BF01881064.

[8] N. Friedreich and A. Kekulé. ‘Zur Amyloidfrage’. In: *Archiv für Pathologische Anatomie und Physiologie und für Klinische Medicin* 16 (1-2 Jan. 1859), pp. 50–65. ISSN: 0945-6317. DOI: 10.1007/BF01945246.

[9] A T Petkova et al. ‘A structural model for Alzheimer’s β-amyloid fibrils based on experimental constraints from solid state NMR’. In: *Proceedings of the National Academy of Sciences* 99 (2002), pp. 16742–16747. DOI: 10.1073/pnas.262663499.

[10] A J Geddes et al. ‘"Cross-β" conformation in proteins’. In: *Journal of Molecular Biology* (1968). ISSN: 00222836. DOI: 10.1016/0022-2836(68)90014-4.

[11] Holde Putchler, Faye Sweat and M. Levine. ‘On The Binding of Congo Red by Amyloid’. In: *Journal of Histochemistry and Cytochemistry* 10 (3 May 1962), pp. 355–364. ISSN: 0022-1554. DOI: 10.1177/10.3.355.

[12] Hans -Peter Missmahl and Marga Hartwig. ‘Polarisationsoptische Untersuchungen an der Amyloidsubstanz’. In: *Virchows Archiv für Pathologische Anatomie und Physiologie und für Klinische Medizin* 324 (4 1953), pp. 489–508. ISSN: 0945-6317. DOI: 10.1007/BF00954791.

[13] P S Vassar and C F Culling. ‘Fluorescent stains, with special reference to amyloid and connective tissues.’ In: *Archives of pathology* 68 (Nov. 1959), pp. 487–98. ISSN: 0363-0153.

[14] Matthew G. Iadanza et al. ‘A new era for understanding amyloid structures and disease’. In: *Nature Reviews Molecular Cell Biology* 19 (12 Dec. 2018), pp. 755–773. ISSN: 1471-0072. DOI: 10.1038/s41580-018-0060-8.

[15] Jean D. Sipe et al. ‘Amyloid fibril proteins and amyloidosis: chemical identification and clinical classification International Society of Amyloidosis 2016 Nomenclature Guidelines’.
In: *Amyloid* 23 (4 Oct. 2016), pp. 209–213. ISSN: 1350-6129.
DOI: 10.1080/13506129.2016.1257986.

[16] M. Paul Murphy and Harry LeVine.
‘Alzheimer’s Disease and the Amyloid-β Peptide’.
In: *Journal of Alzheimer’s Disease* 19 (1 Jan. 2010), pp. 311–323.
ISSN: 18758908. DOI: 10.3233/JAD-2010-1221.

[17] L. Stefanis. ‘α-Synuclein in Parkinson’s Disease’. In: *Cold Spring Harbor Perspectives in Medicine* 2 (2 Feb. 2012), a009399–a009399.
ISSN: 2157-1422. DOI: 10.1101/cshperspect.a009399.

[18] Mihael H. Polymeropoulos et al. ‘Mutation in the α-Synuclein Gene Identified in Families with Parkinson’s Disease’.
In: *Science* 276 (5321 June 1997), pp. 2045–2047. ISSN: 0036-8075.
DOI: 10.1126/science.276.5321.2045.

[19] Per Westermark, Arne Andersson and Gunilla T. Westermark.
‘Islet Amyloid Polypeptide, Islet Amyloid, and Diabetes Mellitus’.
In: *Physiological Reviews* 91 (3 July 2011), pp. 795–826. ISSN: 0031-9333.
DOI: 10.1152/physrev.00042.2009.

[20] Kelty R. Baker and Lawrence Rice.
‘The Amyloidoses: Clinical Features, Diagnosis and Treatment’.
In: *Methodist DeBakey Cardiovascular Journal* 8 (3 July 2012), p. 3.
ISSN: 1947-6108. DOI: 10.14797/mdcj-8-3-3.

[21] Douglas M. Fowler et al. ‘Functional amyloid – from bacteria to humans’.
In: *Trends in Biochemical Sciences* 32 (5 May 2007), pp. 217–224.
ISSN: 09680004. DOI: 10.1016/j.tibs.2007.03.003.

[22] Douglas M Fowler et al.
‘Functional Amyloid Formation within Mammalian Tissue’.
In: *PLoS Biology* 4 (1 Nov. 2005), e6. ISSN: 1545-7885.
DOI: 10.1371/journal.pbio.0040006.

[23] Chi L.L. Pham, Ann H. Kwan and Margaret Sunde.
'Functional amyloid: widespread in Nature, diverse in purpose'.
In: *Essays in Biochemistry* 56 (Aug. 2014), pp. 207–219. ISSN: 0071-1365.
DOI: 10.1042/bse0560207.

[24] Antoine Loquet, Sven J. Saupe and Diego Romero.
'Functional Amyloids in Health and Disease'.
In: *Journal of Molecular Biology* 430 (20 Oct. 2018), pp. 3629–3630.
ISSN: 00222836. DOI: 10.1016/j.jmb.2018.07.024.

[25] World Health Organization. *Dementia*. URL:
https://www.who.int/news-room/fact-sheets/detail/dementia.

[26] statista. *Anzahl der Demenzkranken in Deutschland nach Alter und Geschlecht im Jahr 2021*. URL: https://de.statista.com/statistik/daten/studie/246028/umfrage/anzahl-der-demenzkranken-in-deutschland-nach-alter-und-geschlecht/.

[27] Alzheimer's Disease International. *Dementia statistics*.
URL: https://www.alzint.org/about/dementia-facts-figures/dementia-statistics/.

[28] Henry Brodaty et al. 'The World of Dementia Beyond 2020'. In: *Journal of the American Geriatrics Society* 59 (5 May 2011), pp. 923–927.
ISSN: 00028614. DOI: 10.1111/j.1532-5415.2011.03365.x.

[29] Youssef H. El-Hayek et al. 'Tip of the Iceberg: Assessing the Global Socioeconomic Costs of Alzheimer's Disease and Related Dementias and Strategic Implications for Stakeholders'.
In: *Journal of Alzheimer's Disease* 70 (2 July 2019), pp. 323–341.
ISSN: 13872877. DOI: 10.3233/JAD-190426.

[30] David S. Knopman et al. 'Alzheimer disease'.
In: *Nature Reviews Disease Primers* 7 (1 May 2021), p. 33.
ISSN: 2056-676X. DOI: 10.1038/s41572-021-00269-y.

[31] Alois Alzheimer. 'Über eine eigenartige Erkrankung der Hirnrinde'.
In: *Allgemeine Zeitschrift fur Psychiatrie und Psychisch-gerichtliche Medizin* (1907).

[32] Alzheimer Forschung Initiative e.V. (AFI).
Die Geschichte der Alzheimer-Krankheit. URL: https://www.alzheimer-forschung.de/alzheimer/wasistalzheimer/geschichte-der-alzheimer-krankheit/.

[33] Andreas Charidimou et al.
'Emerging concepts in sporadic cerebral amyloid angiopathy'.
In: *Brain* 140 (7 July 2017), pp. 1829–1850. ISSN: 0006-8950.
DOI: 10.1093/brain/awx047.

[34] Charles Duyckaerts, Benoît Delatour and Marie-Claude Potier.
'Classification and basic pathology of Alzheimer disease'.
In: *Acta Neuropathologica* 118 (1 July 2009), pp. 5–36. ISSN: 0001-6322.
DOI: 10.1007/s00401-009-0532-1.

[35] Jesús Avila et al.
'Role of Tau Protein in Both Physiological and Pathological Conditions'.
In: *Physiological Reviews* 84 (2 Apr. 2004), pp. 361–384. ISSN: 0031-9333.
DOI: 10.1152/physrev.00024.2003.

[36] Michael S. Wolfe. 'The Role of Tau in Neurodegenerative Diseases and Its Potential as a Therapeutic Target'. In: *Scientifica* 2012 (2012), pp. 1–20.
ISSN: 2090-908X. DOI: 10.6064/2012/796024.

[37] Richard J. O'Brien and Philip C. Wong.
'Amyloid Precursor Protein Processing and Alzheimer's Disease'.
In: *Annual Review of Neuroscience* 34 (1 July 2011), pp. 185–204.
ISSN: 0147-006X. DOI: 10.1146/annurev-neuro-061010-113613.

[38] Susann Ludewig and Martin Korte.
'Novel Insights into the Physiological Function of the APP (Gene) Family and Its Proteolytic Fragments in Synaptic Plasticity'.
In: *Frontiers in Molecular Neuroscience* 9 (Jan. 2017). ISSN: 1662-5099.
DOI: 10.3389/fnmol.2016.00161.

[39] Ulrike C. Müller, Thomas Deller and Martin Korte. 'Not just amyloid: physiological functions of the amyloid precursor protein family'.

In: *Nature Reviews Neuroscience* 18 (5 May 2017), pp. 281–298. ISSN: 1471-003X. DOI: 10.1038/nrn.2017.29.

[40] C. Haass et al. 'Trafficking and Proteolytic Processing of APP'. In: *Cold Spring Harbor Perspectives in Medicine* 2 (5 May 2012), a006270–a006270. ISSN: 2157-1422. DOI: 10.1101/cshperspect.a006270.

[41] Jing Zhao et al. 'Targeting Amyloidogenic Processing of APP in Alzheimer's Disease'. In: *Frontiers in Molecular Neuroscience* 13 (Aug. 2020). ISSN: 1662-5099. DOI: 10.3389/fnmol.2020.00137.

[42] Patricia Regina Manzine et al. 'ADAM10 in Alzheimer's disease: Pharmacological modulation by natural compounds and its role as a peripheral marker'. In: *Biomedicine and Pharmacotherapy* 113 (May 2019), p. 108661. ISSN: 07533322. DOI: 10.1016/j.biopha.2019.108661.

[43] Justin M. Long and David M. Holtzman. 'Alzheimer Disease: An Update on Pathobiology and Treatment Strategies'. In: *Cell* 179 (2 Oct. 2019), pp. 312–339. ISSN: 00928674. DOI: 10.1016/j.cell.2019.09.001.

[44] Harald Hampel et al. 'The Amyloid-β Pathway in Alzheimer's Disease'. In: *Molecular Psychiatry* 26 (10 Oct. 2021), pp. 5481–5503. ISSN: 1359-4184. DOI: 10.1038/s41380-021-01249-0.

[45] J. Trambauer et al. 'Chapter Six - Analyzing Amyloid-β Peptide Modulation Profiles and Binding Sites of γ-Secretase Modulators'. In: *Enzymology at the Membrane Interface: Intramembrane Proteases*. Ed. by Michael H. Gelb. Vol. 584. Methods in Enzymology. Academic Press, 2017, pp. 157–183. DOI: https://doi.org/10.1016/bs.mie.2016.10.013. URL: https://www.sciencedirect.com/science/article/pii/S0076687916303767.

[46] Raymond J. Kelleher and Jie Shen. 'Presenilin-1 mutations and Alzheimer's disease'. In: *Proceedings of the*

National Academy of Sciences 114 (4 Jan. 2017), pp. 629–631. ISSN: 0027-8424. DOI: 10.1073/pnas.1619574114.

[47] Eleanor Drummond et al. 'Proteomic differences in amyloid plaques in rapidly progressive and sporadic Alzheimer's disease'. In: *Acta Neuropathologica* 133 (6 June 2017), pp. 933–954. ISSN: 0001-6322. DOI: 10.1007/s00401-017-1691-0.

[48] A. Serrano-Pozo et al. 'Neuropathological Alterations in Alzheimer Disease'. In: *Cold Spring Harbor Perspectives in Medicine* 1 (1 Sept. 2011), a006189–a006189. ISSN: 2157-1422. DOI: 10.1101/cshperspect.a006189.

[49] David Eisenberg and Mathias Jucker. 'The Amyloid State of Proteins in Human Diseases'. In: *Cell* 148 (6 Mar. 2012), pp. 1188–1203. ISSN: 00928674. DOI: 10.1016/j.cell.2012.02.022.

[50] Jiyong Lee et al. 'Amyloid-β forms fibrils by nucleated conformational conversion of oligomers'. In: *Nature Chemical Biology* 7 (9 Sept. 2011), pp. 602–609. ISSN: 1552-4450. DOI: 10.1038/nchembio.624.

[51] Joseph T. Jarrett and Peter T. Lansbury. 'Seeding "one-dimensional crystallization" of amyloid: A pathogenic mechanism in Alzheimer's disease and scrapie?' In: *Cell* 73 (6 June 1993), pp. 1055–1058. ISSN: 00928674. DOI: 10.1016/0092-8674(93)90635-4.

[52] Mattias Törnquist et al. 'Secondary nucleation in amyloid formation'. In: *Chemical Communications* 54 (63 2018), pp. 8667–8684. ISSN: 1359-7345. DOI: 10.1039/C8CC02204F.

[53] Samuel I. A. Cohen et al. 'Proliferation of amyloid-β42 aggregates occurs through a secondary nucleation mechanism'. In: *Proceedings of the National Academy of Sciences* 110 (24 June 2013), pp. 9758–9763. ISSN: 0027-8424. DOI: 10.1073/pnas.1218402110.

[54] Rundong Hu et al. ‘Cross-Seeding Interaction between β-Amyloid and Human Islet Amyloid Polypeptide’.
In: *ACS Chemical Neuroscience* 6 (10 Oct. 2015), pp. 1759–1768.
ISSN: 1948-7193. DOI: 10.1021/acschemneuro.5b00192.

[55] Ruina Liang, Yao Tian and John H. Viles.
‘Cross-seeding of WT amyloid-β with Arctic but not Italian familial mutants accelerates fibril formation in Alzheimer’s disease’.
In: *Journal of Biological Chemistry* 298 (7 July 2022), p. 102071.
ISSN: 00219258. DOI: 10.1016/j.jbc.2022.102071.

[56] Ziao Fu et al.
‘Mechanism of Nucleated Conformational Conversion of Aβ42’.
In: *Biochemistry* 54 (27 July 2015), pp. 4197–4207. ISSN: 0006-2960.
DOI: 10.1021/acs.biochem.5b00467.

[57] Filip Hasecke et al. ‘Origin of metastable oligomers and their effects on amyloid fibril self-assembly’.
In: *Chemical Science* 9 (27 2018), pp. 5937–5948. ISSN: 2041-6520.
DOI: 10.1039/C8SC01479E.

[58] Eric Y Hayden and David B Teplow.
‘Amyloid β-protein oligomers and Alzheimer’s disease’.
In: *Alzheimer’s Research and Therapy* 5 (6 2013), p. 60. ISSN: 1758-9193.
DOI: 10.1186/alzrt226.

[59] A.J Modler et al. ‘Assembly of Amyloid Protofibrils via Critical Oligomers—A Novel Pathway of Amyloid Formation’.
In: *Journal of Molecular Biology* 325 (1 Jan. 2003), pp. 135–148.
ISSN: 00222836. DOI: 10.1016/S0022-2836(02)01175-0.

[60] Kenjiro Ono and Mayumi Tsuji. ‘Protofibrils of Amyloid-β are Important Targets of a Disease-Modifying Approach for Alzheimer’s Disease’.
In: *International Journal of Molecular Sciences* 21 (3 Jan. 2020), p. 952.
ISSN: 1422-0067. DOI: 10.3390/ijms21030952.

[61] Marie P. Schützmann et al. 'Endo-lysosomal Aβ concentration and pH trigger formation of Aβ oligomers that potently induce Tau missorting'. In: *Nature Communications* 12 (1 July 2021), p. 4634. ISSN: 2041-1723. DOI: 10.1038/s41467-021-24900-4.

[62] Sebastian Treusch, Douglas M. Cyr and Susan Lindquist. 'Amyloid deposits: Protection against toxic protein species?' In: *Cell Cycle* 8 (11 June 2009), pp. 1668–1674. ISSN: 1538-4101. DOI: 10.4161/cc.8.11.8503.

[63] Alexander J. Dear et al. 'Identification of on- and off-pathway oligomers in amyloid fibril formation'. In: *Chemical Science* 11 (24 2020), pp. 6236–6247. ISSN: 2041-6520. DOI: 10.1039/C9SC06501F.

[64] S. Zraika et al. 'Toxic oligomers and islet beta cell death: guilty by association or convicted by circumstantial evidence?' In: *Diabetologia* 53 (6 June 2010), pp. 1046–1056. ISSN: 0012-186X. DOI: 10.1007/s00125-010-1671-6.

[65] Monica Bucciantini et al. 'Inherent toxicity of aggregates implies a common mechanism for protein misfolding diseases'. In: *Nature* 416 (6880 Apr. 2002), pp. 507–511. ISSN: 0028-0836. DOI: 10.1038/416507a.

[66] Kenjiro Ono, Margaret M. Condron and David B. Teplow. 'Structure–neurotoxicity relationships of amyloid β-protein oligomers'. In: *Proceedings of the National Academy of Sciences* 106 (35 Sept. 2009), pp. 14745–14750. ISSN: 0027-8424. DOI: 10.1073/pnas.0905127106.

[67] Erika N. Cline et al. 'The Amyloid-β Oligomer Hypothesis: Beginning of the Third Decade'. In: *Journal of Alzheimer's Disease* 64 (s1 June 2018), S567–S610. ISSN: 13872877. DOI: 10.3233/JAD-179941.

[68] Iryna Benilova, Eric Karran and Bart De Strooper. 'The toxic Aβ oligomer and Alzheimer's disease: an emperor in need of clothes'.

In: *Nature Neuroscience* 15 (3 Mar. 2012), pp. 349–357. ISSN: 1097-6256. DOI: 10.1038/nn.3028.

[69] Jitin Bali et al. 'Role of genes linked to sporadic Alzheimer's disease risk in the production of β-amyloid peptides'. In: *Proceedings of the National Academy of Sciences* 109 (38 Sept. 2012), pp. 15307–15311. ISSN: 0027-8424. DOI: 10.1073/pnas.1201632109.

[70] George A. Edwards III et al. 'Modifiable Risk Factors for Alzheimer's Disease'. In: *Frontiers in Aging Neuroscience* 11 (June 2019). ISSN: 1663-4365. DOI: 10.3389/fnagi.2019.00146.

[71] Irene Piaceri. 'Genetics of familial and sporadic Alzheimer s disease'. In: *Frontiers in Bioscience* E5 (1 2013), E605. ISSN: 1945-0494. DOI: 10.2741/E605.

[72] Philip B. Verghese et al. 'ApoE influences amyloid-β (Aβ) clearance despite minimal apoE/Aβ association in physiological conditions'. In: *Proceedings of the National Academy of Sciences* 110 (19 May 2013). ISSN: 0027-8424. DOI: 10.1073/pnas.1220484110.

[73] G. William Rebeck et al. 'Apolipoprotein E in sporadic Alzheimer's disease: Allelic variation and receptor interactions'. In: *Neuron* 11 (4 Oct. 1993), pp. 575–580. ISSN: 08966273. DOI: 10.1016/0896-6273(93)90070-8.

[74] Allen D. Roses M.D. 'Apolipoprotein E alleles as risk factors in Alzheimer's disease'. In: *Annual Review of Medicine* 47 (1 Feb. 1996), pp. 387–400. ISSN: 0066-4219. DOI: 10.1146/annurev.med.47.1.387.

[75] Stylianos E. Antonarakis et al. 'Down syndrome'. In: *Nature Reviews Disease Primers* 6 (1 Feb. 2020), p. 9. ISSN: 2056-676X. DOI: 10.1038/s41572-019-0143-7.

[76] Ahmad Salehi, J Wesson Ashford and Elliott J Mufson.
'The Link between Alzheimer's Disease and Down Syndrome. A Historical Perspective.' In: *Current Alzheimer research* 13 (1 2016), pp. 2–6.
ISSN: 1875-5828. DOI: 10.2174/1567205012999151021102914.

[77] Frances K. Wiseman et al. 'A genetic cause of Alzheimer disease: mechanistic insights from Down syndrome'.
In: *Nature Reviews Neuroscience* 16 (9 Sept. 2015), pp. 564–574.
ISSN: 1471-003X. DOI: 10.1038/nrn3983.

[78] David R. Borchelt et al. 'Familial Alzheimer's Disease–Linked Presenilin 1 Variants Elevate Aβ1–42/1–40 Ratio In Vitro and In Vivo'.
In: *Neuron* 17 (5 Nov. 1996), pp. 1005–1013. ISSN: 08966273.
DOI: 10.1016/S0896-6273(00)80230-5.

[79] Christopher Bi, Stephanie Bi and Bin Li.
'Processing of Mutant β-Amyloid Precursor Protein and the Clinicopathological Features of Familial Alzheimer's Disease'.
In: *Aging and disease* 10 (2 2019), p. 383. ISSN: 2152-5250.
DOI: 10.14336/AD.2018.0425.

[80] ALZFORUM - NETWORKING FOR A CURE. *Mutations APP*.
URL: https://www.alzforum.org/mutations/app.

[81] Mike Mullan et al. 'A pathogenic mutation for probable Alzheimer's disease in the APP gene at the N–terminus of β–amyloid'.
In: *Nature Genetics* 1 (5 Aug. 1992), pp. 345–347. ISSN: 1061-4036.
DOI: 10.1038/ng0892-345.

[82] María Pagnon de la Vega et al. 'The *Uppsala APP* deletion causes early onset autosomal dominant Alzheimer's disease by altering APP processing and increasing amyloid β fibril formation'.
In: *Science Translational Medicine* 13 (606 Aug. 2021). ISSN: 1946-6234.
DOI: 10.1126/scitranslmed.abc6184.

[83] Thorlakur Jonsson et al. 'A mutation in APP protects against Alzheimer's disease and age-related cognitive decline'.

In: *Nature* 488 (7409 Aug. 2012), pp. 96–99. ISSN: 0028-0836. DOI: 10.1038/nature11283.

[84] Lydia Hendriks et al. 'Presenile dementia and cerebral haemorrhage linked to a mutation at codon 692 of the β-amyloid precursor protein gene'. In: *Nature Genetics* 1 (3 June 1992), pp. 218–221. ISSN: 1061-4036. DOI: 10.1038/ng0692-218.

[85] Chris De Jonghe et al. 'Flemish and Dutch Mutations in Amyloid β Precursor Protein Have Different Effects on Amyloid β Secretion'. In: *Neurobiology of Disease* 5 (4 Oct. 1998), pp. 281–286. ISSN: 09699961. DOI: 10.1006/nbdi.1998.0202.

[86] Kazuma Murakami et al. 'Synthesis, aggregation, neurotoxicity, and secondary structure of various Aβ1–42 mutants of familial Alzheimer's disease at positions 21–23'. In: *Biochemical and Biophysical Research Communications* 294 (1 May 2002), pp. 5–10. ISSN: 0006291X. DOI: 10.1016/S0006-291X(02)00430-8.

[87] C. Van Broeckhoven et al. 'Amyloid β Protein Precursor Gene and Hereditary Cerebral Hemorrhage with Amyloidosis (Dutch)'. In: *Science* 248 (4959 June 1990), pp. 1120–1122. ISSN: 0036-8075. DOI: 10.1126/science.1971458.

[88] Efrat Levy et al. 'Mutation of the Alzheimer's Disease Amyloid Gene in Hereditary Cerebral Hemorrhage, Dutch Type'. In: *Science* 248 (4959 June 1990), pp. 1124–1126. ISSN: 0036-8075. DOI: 10.1126/science.2111584.

[89] Orso Bugiani et al. 'Hereditary Cerebral Hemorrhage With Amyloidosis Associated With the E693K Mutation of APP'. In: *Archives of Neurology* 67 (8 Aug. 2010). ISSN: 0003-9942. DOI: 10.1001/archneurol.2010.178.

[90] Camilla Nilsberth et al. 'The 'Arctic' APP mutation (E693G) causes Alzheimer's disease by enhanced β protofibril formation'. In: *Nature Neuroscience* 4 (9 Sept. 2001), pp. 887–893. ISSN: 1097-6256. DOI: 10.1038/nn0901-887.

[91] Thomas Wisniewski, Jorge Ghiso and Blas Frangione.
'Peptides homologous to the amyloid protein of Alzheimer's disease containing a glutamine for glutamic acid substitution have accelerated amyloid fibril formation'. In: *Biochemical and Biophysical Research Communications* 179 (3 Sept. 1991), pp. 1247–1254. ISSN: 0006291X. DOI: 10.1016/0006-291X(91)91706-I.

[92] Takami Tomiyama et al. 'A new amyloid β variant favoring oligomerization in Alzheimer's-type dementia'.
In: *Annals of Neurology* 63 (3 Mar. 2008), pp. 377–387. ISSN: 03645134. DOI: 10.1002/ana.21321.

[93] Thomas J. Grabowski et al. 'Novel amyloid precursor protein mutation in an Iowa family with dementia and severe cerebral amyloid angiopathy'.
In: *Annals of Neurology* 49 (6 June 2001), pp. 697–705. ISSN: 0364-5134. DOI: 10.1002/ana.1009.

[94] William E. Van Nostrand et al.
'Pathogenic Effects of D23N Iowa Mutant Amyloid β-Protein'.
In: *Journal of Biological Chemistry* 276 (35 Aug. 2001), pp. 32860–32866. ISSN: 00219258. DOI: 10.1074/jbc.M104135200.

[95] John A. Hardy and Gerald A. Higgins.
'Alzheimer's Disease: The Amyloid Cascade Hypothesis'.
In: *Science* 256 (5054 Apr. 1992), pp. 184–185. ISSN: 0036-8075. DOI: 10.1126/science.1566067.

[96] Roberta Ricciarelli and Ernesto Fedele. 'The Amyloid Cascade Hypothesis in Alzheimer's Disease: It's Time to Change Our Mind.'
In: *Current neuropharmacology* 15 (6 2017), pp. 926–935. ISSN: 1875-6190. DOI: 10.2174/1570159X15666170116143743.

[97] Kristin R Wildsmith et al.
'Evidence for impaired amyloid β clearance in Alzheimer's disease'.
In: *Alzheimer's Research and Therapy* 5 (4 2013), p. 33. ISSN: 1758-9193. DOI: 10.1186/alzrt187.

[98] Robert Katzman et al.
'Clinical, pathological, and neurochemical changes in dementia: A subgroup with preserved mental status and numerous neocortical plaques'.
In: *Annals of Neurology* 23 (2 Feb. 1988), pp. 138–144. ISSN: 0364-5134. DOI: 10.1002/ana.410230206.

[99] Howard Jay Aizenstein et al. 'Frequent Amyloid Deposition Without Significant Cognitive Impairment Among the Elderly'.
In: *Archives of Neurology* 65 (11 Nov. 2008), p. 1509. ISSN: 0003-9942. DOI: 10.1001/archneur.65.11.1509.

[100] Marina D. Kirkitadze, Gal Bitan and David B. Teplow.
'Paradigm shifts in Alzheimer's disease and other neurodegenerative disorders: The emerging role of oligomeric assemblies'.
In: *Journal of Neuroscience Research* 69 (5 Sept. 2002), pp. 567–577. ISSN: 0360-4012. DOI: 10.1002/jnr.10328.

[101] Pei-Pei Liu et al. 'History and progress of hypotheses and clinical trials for Alzheimer's disease'.
In: *Signal Transduction and Targeted Therapy* 4 (1 Aug. 2019), p. 29. ISSN: 2059-3635. DOI: 10.1038/s41392-019-0063-8.

[102] Dennis J Selkoe and John Hardy.
'The amyloid hypothesis of Alzheimer's disease at 25 years'.
In: *EMBO Molecular Medicine* 8 (6 June 2016), pp. 595–608. ISSN: 1757-4676. DOI: 10.15252/emmm.201606210.

[103] Anne C. Conibear. 'Deciphering protein post-translational modifications using chemical biology tools'.
In: *Nature Reviews Chemistry* 4 (12 Oct. 2020), pp. 674–695. ISSN: 2397-3358. DOI: 10.1038/s41570-020-00223-8.

[104] Shahin Ramazi and Javad Zahiri. 'Post-translational modifications in proteins: resources, tools and prediction methods'.
In: *Database* 2021 (Apr. 2021). ISSN: 1758-0463. DOI: 10.1093/database/baab012.

[105] Madhu Ramesh, Pushparathinam Gopinath and Thimmaiah Govindaraju. 'Role of Post-translational Modifications in Alzheimer's Disease'. In: *ChemBioChem* 21 (8 Apr. 2020), pp. 1052–1079. ISSN: 1439-4227. DOI: 10.1002/cbic.201900573.

[106] Andrea Renee Kelley, Stephan B.H. Bach and George Perry. 'Analysis of post-translational modifications in Alzheimer's disease by mass spectrometry'. In: *Biochimica et Biophysica Acta (BBA) - Molecular Basis of Disease* 1865 (8 Aug. 2019), pp. 2040–2047. ISSN: 09254439. DOI: 10.1016/j.bbadis.2018.11.002.

[107] Tamta Arakhamia et al. 'Posttranslational Modifications Mediate the Structural Diversity of Tauopathy Strains'. In: *Cell* 184 (25 Dec. 2021), pp. 6207–6210. ISSN: 00928674. DOI: 10.1016/j.cell.2021.11.029.

[108] Wenjuan Zhang et al. 'Novel tau filament fold in corticobasal degeneration'. In: *Nature* 580 (7802 Apr. 2020), pp. 283–287. ISSN: 0028-0836. DOI: 10.1038/s41586-020-2043-0.

[109] Kun Zhao et al. 'Parkinson's disease-related phosphorylation at Tyr39 rearranges α-synuclein amyloid fibril structure revealed by cryo-EM'. In: *Proceedings of the National Academy of Sciences* 117 (33 Aug. 2020), pp. 20305–20315. ISSN: 0027-8424. DOI: 10.1073/pnas.1922741117.

[110] Lynn Radamaker et al. 'Role of mutations and post-translational modifications in systemic AL amyloidosis studied by cryo-EM'. In: *Nature Communications* 12 (1 Nov. 2021), p. 6434. ISSN: 2041-1723. DOI: 10.1038/s41467-021-26553-9.

[111] Jeffrey Cummings et al. 'Alzheimer's disease drug development pipeline: 2022'. In: *Alzheimer's and Dementia: Translational Research and Clinical Interventions* 8 (1 Jan. 2022). ISSN: 2352-8737. DOI: 10.1002/trc2.12295.

[112] Arun K. Ghosh and Heather L. Osswald.
'BACE1 (β-secretase) inhibitors for the treatment of Alzheimer's disease'.
In: *Chem. Soc. Rev.* 43 (19 Apr. 2014), pp. 6765–6813. ISSN: 0306-0012.
DOI: 10.1039/C3CS60460H.

[113] Harald Hampel et al. 'The β-Secretase BACE1 in Alzheimer's Disease'.
In: *Biological Psychiatry* 89 (8 Apr. 2021), pp. 745–756. ISSN: 00063223.
DOI: 10.1016/j.biopsych.2020.02.001.

[114] Donna M Barten et al. 'Gamma-Secretase Inhibitors for Alzheimer's Disease: balancing efficacy and toxicity'.
In: *Drugs in R and D* 7 (2 2006), pp. 87–97. ISSN: 1174-5886.
DOI: 10.2165/00126839-200607020-00003.

[115] Todd E. Golde et al. 'γ-Secretase inhibitors and modulators'.
In: *Biochimica et Biophysica Acta (BBA) - Biomembranes* 1828 (12 Dec. 2013), pp. 2898–2907. ISSN: 00052736.
DOI: 10.1016/j.bbamem.2013.06.005.

[116] Christopher H. van Dyck. 'Anti-Amyloid-β Monoclonal Antibodies for Alzheimer's Disease: Pitfalls and Promise'.
In: *Biological Psychiatry* 83 (4 Feb. 2018), pp. 311–319. ISSN: 00063223.
DOI: 10.1016/j.biopsych.2017.08.010.

[117] Linda Söderberg et al. 'Lecanemab, Aducanumab, and Gantenerumab — Binding Profiles to Different Forms of Amyloid-Beta Might Explain Efficacy and Side Effects in Clinical Trials for Alzheimer's Disease'.
In: *Neurotherapeutics* (Oct. 2022). ISSN: 1933-7213.
DOI: 10.1007/s13311-022-01308-6.

[118] Jeff Sevigny et al.
'The antibody aducanumab reduces Aβ plaques in Alzheimer's disease'.
In: *Nature* 537 (7618 Sept. 2016), pp. 50–56. ISSN: 0028-0836.
DOI: 10.1038/nature19323.

[119] Mark A. Mintun et al. 'Donanemab in Early Alzheimer's Disease'.
In: *New England Journal of Medicine* 384 (18 May 2021), pp. 1691–1704.
ISSN: 0028-4793. DOI: 10.1056/NEJMoa2100708.

[120] Bernd Bohrmann et al. 'Gantenerumab: A Novel Human Anti-Aβ Antibody Demonstrates Sustained Cerebral Amyloid-β Binding and Elicits Cell-Mediated Removal of Human Amyloid-β'. In: *Journal of Alzheimer's Disease* 28 (1 Jan. 2012), pp. 49–69. ISSN: 18758908. DOI: 10.3233/JAD-2011-110977.

[121] Hillevi Englund et al. 'Sensitive ELISA detection of amyloid-β protofibrils in biological samples'. In: *Journal of Neurochemistry* 0 (0 July 2007). ISSN: 0022-3042. DOI: 10.1111/j.1471-4159.2007.04759.x.

[122] Howard D. Larkin. 'Lecanemab Gains FDA Approval for Early Alzheimer Disease'. In: *JAMA* 329 (5 Feb. 2023), p. 363. ISSN: 0098-7484. DOI: 10.1001/jama.2022.24490.

[123] Dag Sehlin et al. 'Antibody-based PET imaging of amyloid beta in mouse models of Alzheimer's disease'. In: *Nature Communications* 7 (1 Feb. 2016), p. 10759. ISSN: 2041-1723. DOI: 10.1038/ncomms10759.

[124] Andrew M. Stern et al. 'Abundant Aβ fibrils in ultracentrifugal supernatants of aqueous extracts from Alzheimer's disease brains'. In: *Neuron* 111 (May 2023), pp. 1–9. ISSN: 08966273. DOI: 10.1016/j.neuron.2023.04.007.

[125] F. M. LaFerla and K. N. Green. 'Animal Models of Alzheimer Disease'. In: *Cold Spring Harbor Perspectives in Medicine* 2 (11 Nov. 2012), a006320–a006320. ISSN: 2157-1422. DOI: 10.1101/cshperspect.a006320.

[126] Eleanor Drummond and Thomas Wisniewski. 'Alzheimer's disease: experimental models and reality'. In: *Acta Neuropathologica* 133 (2 Feb. 2017), pp. 155–175. ISSN: 0001-6322. DOI: 10.1007/s00401-016-1662-x.

[127] Hiroki Sasaguri et al. 'APP mouse models for Alzheimer's disease preclinical studies'.

In: *The EMBO Journal* 36 (17 Sept. 2017), pp. 2473–2487.
ISSN: 0261-4189. DOI: 10.15252/embj.201797397.

[128] National Institute of General Medical Sciences. *Structural Biology.*
URL: https://nigms.nih.gov/education/fact-sheets/Documents/fact-sheet-structural-biology.pdf.

[129] Nature. *Structure determination.*
URL: https://www.nature.com/subjects/structure-determination.

[130] Nature. *NMR spectroscopy.*
URL: https://www.nature.com/subjects/nmr-spectroscopy.

[131] Nature. *X-ray crystallography.*
URL: https://www.nature.com/subjects/x-ray-crystallography.

[132] NobelPrize.org. *The Nobel Prize in Chemistry 2017.* URL:
https://www.nobelprize.org/prizes/chemistry/2017/summary/.

[133] Y. Zhang et al.
'Could Egg White Lysozyme be Solved by Single Particle Cryo-EM?'
In: *Journal of Chemical Information and Modeling* 60 (5 May 2020), pp. 2605–2613. ISSN: 1549-9596. DOI: 10.1021/acs.jcim.9b01176.

[134] NobelPrize.org. *The Nobel Prize in Physics 1929.*
URL: https://www.nobelprize.org/prizes/physics/1929/summary/.

[135] M. Knoll and E. Ruska. 'Das Elektronenmikroskop'.
In: *Zeitschrift für Physik* 78 (5-6 May 1932), pp. 318–339.
ISSN: 1434-6001. DOI: 10.1007/BF01342199.

[136] E. Abbe. 'Beiträge zur Theorie des Mikroskops und der mikroskopischen Wahrnehmung'.
In: *Archiv für Mikroskopische Anatomie* 9 (1 Dec. 1873), pp. 413–468.
ISSN: 0176-7364. DOI: 10.1007/BF02956173.

[137] Ernst Ruska.
'The development of the electron microscope and of electron microscopy'.
In: *Bioscience Reports* 7 (8 Aug. 1987), pp. 607–629. ISSN: 0144-8463.
DOI: 10.1007/BF01127674.

[138] NobelPrize.org. *The Nobel Prize in Physics 1986*.
URL: https://www.nobelprize.org/prizes/physics/1986/summary/.

[139] Catherine M. Oikonomou and Grant J. Jensen.
'The development of cryo-EM and how it has advanced microbiology'.
In: *Nature Microbiology* 2 (12 Nov. 2017), pp. 1577–1579. ISSN: 2058-5276.
DOI: 10.1038/s41564-017-0073-7.

[140] Eva Nogales. 'The development of cryo-EM into a mainstream structural biology technique'. In: *Nature Methods* 13 (1 Jan. 2016), pp. 24–27.
ISSN: 1548-7091. DOI: 10.1038/nmeth.3694.

[141] R. C. Williams and R. W. G. Wyckoff.
'Shadowed Electron Micrographs of Bacteria'.
In: *Experimental Biology and Medicine* 59 (2 June 1945), pp. 265–270.
ISSN: 1535-3702. DOI: 10.3181/00379727-59-15053.

[142] S Brenner and R W Horne. 'A negative staining method for high resolution electron microscopy of viruses'.
In: *BBA - Biochimica et Biophysica Acta* (1959). ISSN: 00063002.
DOI: 10.1016/0006-3002(59)90237-9.

[143] D. J. De Rosier and A. Klug. 'Reconstruction of three dimensional structures from electron micrographs'. In: *Nature* (1968). ISSN: 00280836.
DOI: 10.1038/217130a0.

[144] D. J. DeRosier and P. B. Moore. 'Reconstruction of three-dimensional images from electron micrographs of structures with helical symmetry'.
In: *Journal of Molecular Biology* (1970). ISSN: 00222836.
DOI: 10.1016/0022-2836(70)90036-7.

[145] Charlotte A. Scarff et al. 'Variations on Negative Stain Electron Microscopy Methods: Tools for Tackling Challenging Systems'.
In: *Journal of Visualized Experiments* (132 Feb. 2018). ISSN: 1940-087X.
DOI: 10.3791/57199.

[146] J. Dubochet and A.W. McDowall. 'VITRIFICATION OF PURE WATER FOR ELECTRON MICROSCOPY'.
In: *Journal of Microscopy* 124 (3 Dec. 1981), pp. 3–4. ISSN: 00222720. DOI: 10.1111/j.1365-2818.1981.tb02483.x.

[147] Jacques Dubochet et al. 'Cryo-electron microscopy of vitrified specimens'.
In: *Quarterly Reviews of Biophysics* 21 (2 May 1988), pp. 129–228. ISSN: 0033-5835. DOI: 10.1017/S0033583500004297.

[148] R. Henderson et al. 'Model for the structure of bacteriorhodopsin based on high-resolution electron cryo-microscopy'.
In: *Journal of Molecular Biology* 213 (4 June 1990), pp. 899–929. ISSN: 00222836. DOI: 10.1016/S0022-2836(05)80271-2.

[149] O. L. Krivanek and P. E. Mooney. 'Applications of slow-scan CCD cameras in transmission electron microscopy.'
In: *Ultramicroscopy* 49 (1-4 1993), pp. 95–108.

[150] Nguyen-Huu Xuong et al. 'First use of a high-sensitivity active pixel sensor array as a detector for electron microscopy'. In: 2004. DOI: 10.1117/12.526021.

[151] A R Faruqi and R Henderson.
Electronic detectors for electron microscopy. 2007. DOI: 10.1016/j.sbi.2007.08.014.

[152] G McMullan, A R Faruqi and R Henderson. *Direct Electron Detectors*. 2016. DOI: 10.1016/bs.mie.2016.05.056.

[153] Joachim Frank, Adriana Verschoor and Miloslav Boublik. 'Computer Averaging of Electron Micrographs of 40S Ribosomal Subunits'.
In: *Science* 214 (4527 Dec. 1981), pp. 1353–1355. ISSN: 0036-8075. DOI: 10.1126/science.7313694.

[154] Joachim Frank.
Three-Dimensional Electron Microscopy of Macromolecular Assemblies. 2010. DOI: 10.1093/acprof:oso/9780195182187.001.0001.

[155] Pawel A. Penczek, Robert A. Grassucci and Joachim Frank.
'The ribosome at improved resolution: New techniques for merging and orientation refinement in 3D cryo-electron microscopy of biological particles'. In: *Ultramicroscopy* 53 (3 Mar. 1994), pp. 251–270. ISSN: 03043991. DOI: 10.1016/0304-3991(94)90038-8.

[156] Marin Van Heel. 'Angular reconstitution: A posteriori assignment of projection directions for 3D reconstruction'.
In: *Ultramicroscopy* 21 (2 Jan. 1987), pp. 111–123. ISSN: 03043991. DOI: 10.1016/0304-3991(87)90078-7.

[157] EMDataResource. *EM software*.
URL: https://www.emdataresource.org/emsoftware.html.

[158] David B. Williams and C. Barry Carter.
Transmission Electron Microscopy. Springer US, 2009.
ISBN: 978-0-387-76500-6. DOI: 10.1007/978-0-387-76501-3.

[159] Linda E. Franken et al.
'A Technical Introduction to Transmission Electron Microscopy for Soft-Matter: Imaging, Possibilities, Choices, and Technical Developments'.
In: *Small* 16 (14 Apr. 2020), p. 1906198. ISSN: 1613-6810.
DOI: 10.1002/smll.201906198.

[160] Caltech. *Getting Started in Cryo-EM*.
URL: https://cryo-em-course.caltech.edu.

[161] G. McMullan et al. 'Comparison of optimal performance at 300keV of three direct electron detectors for use in low dose electron microscopy'.
In: *Ultramicroscopy* 147 (Dec. 2014), pp. 156–163. ISSN: 03043991.
DOI: 10.1016/j.ultramic.2014.08.002.

[162] Yifan Cheng et al.
'A Primer to Single-Particle Cryo-Electron Microscopy'.
In: *Cell* 161 (3 Apr. 2015), pp. 438–449. ISSN: 00928674.
DOI: 10.1016/j.cell.2015.03.050.

[163] J. Ryan Feathers, Katherine A. Spoth and J. Christopher Fromme. 'Experimental evaluation of super-resolution imaging and magnification choice in single-particle cryo-EM'.
In: *Journal of Structural Biology: X* 5 (2021), p. 100047. ISSN: 25901524. DOI: 10.1016/j.yjsbx.2021.100047.

[164] P.A. Thuman-Commike and W. Chiu. 'Reconstruction principles of icosahedral virus structure determination using electron cryomicroscopy'.
In: *Micron* 31 (6 Dec. 2000), pp. 687–711. ISSN: 09684328. DOI: 10.1016/S0968-4328(99)00077-3.

[165] Thermo Fisher Scientific.
Requirements for Preparation of Cryo-EM Samples.
URL: https://assets.thermofisher.com/TFS-Assets/MSD/Product-Information/cryo-EM-High-Level-Sample-Prep-2018.pdf.

[166] L.A. Passmore and C.J. Russo.
Specimen Preparation for High-Resolution Cryo-EM. 2016.
DOI: 10.1016/bs.mie.2016.04.011.

[167] B. Carragher et al. 'Current outcomes when optimizing 'standard' sample preparation for single-particle cryo-EM'.
In: *Journal of Microscopy* 276 (1 Oct. 2019), pp. 39–45. ISSN: 0022-2720. DOI: 10.1111/jmi.12834.

[168] Giulia Weissenberger, Rene J. M. Henderikx and Peter J. Peters. 'Understanding the invisible hands of sample preparation for cryo-EM'.
In: *Nature Methods* 18 (5 May 2021), pp. 463–471. ISSN: 1548-7091. DOI: 10.1038/s41592-021-01130-6.

[169] Theresa Gewering et al. 'Know your detergents: A case study on detergent background in negative stain electron microscopy'.
In: *Journal of Structural Biology* 203 (3 Sept. 2018), pp. 242–246. ISSN: 10478477. DOI: 10.1016/j.jsb.2018.05.008.

[170] Katerina Naydenova, Peipei Jia and Christopher J. Russo. 'Cryo-EM with sub–1 Å specimen movement'.

In: *Science* 370 (6513 Oct. 2020), pp. 223–226. ISSN: 0036-8075.
DOI: 10.1126/science.abb7927.

[171] Christopher J. Russo and Lori A. Passmore.
'Ultrastable gold substrates: Properties of a support for high-resolution electron cryomicroscopy of biological specimens'.
In: *Journal of Structural Biology* 193 (1 Jan. 2016), pp. 33–44.
ISSN: 10478477. DOI: 10.1016/j.jsb.2015.11.006.

[172] Kenneth A. Taylor and Robert M. Glaeser.
'Electron Diffraction of Frozen, Hydrated Protein Crystals'.
In: *Science* 186 (4168 Dec. 1974), pp. 1036–1037. ISSN: 0036-8075.
DOI: 10.1126/science.186.4168.1036.

[173] J. Dubochet et al.
'Electron microscopy of frozen water and aqueous solutions'.
In: *Journal of Microscopy* 128 (3 Dec. 1982), pp. 219–237. ISSN: 00222720.
DOI: 10.1111/j.1365-2818.1982.tb04625.x.

[174] Peter M. Frederik and D.H.W. Hubert.
Cryoelectron Microscopy of Liposomes. 2005.
DOI: 10.1016/S0076-6879(05)91024-0.

[175] Dimitrios Kontziampasis et al.
'A cryo-EM grid preparation device for time-resolved structural studies'.
In: *IUCrJ* 6 (6 Nov. 2019), pp. 1024–1031. ISSN: 2052-2525.
DOI: 10.1107/S2052252519011345.

[176] Xiangsong Feng et al. 'A Fast and Effective Microfluidic Spraying-Plunging Method for High-Resolution Single-Particle Cryo-EM'.
In: *Structure* 25 (4 Apr. 2017), 663–670.e3. ISSN: 09692126.
DOI: 10.1016/j.str.2017.02.005.

[177] Stefan A. Arnold et al.
'Blotting-free and lossless cryo-electron microscopy grid preparation from nanoliter-sized protein samples and single-cell extracts'.
In: *Journal of Structural Biology* 197 (3 Mar. 2017), pp. 220–226.
ISSN: 10478477. DOI: 10.1016/j.jsb.2016.11.002.

[178] Michele C. Darrow et al. ‘Chameleon: Next Generation Sample Preparation for CryoEM based on Spotiton’.
In: *Microscopy and Microanalysis* 25 (S2 Aug. 2019), pp. 994–995.
ISSN: 1431-9276. DOI: 10.1017/S1431927619005701.

[179] Raimond B. G. Ravelli et al. ‘Cryo-EM structures from sub-nl volumes using pin-printing and jet vitrification’.
In: *Nature Communications* 11 (1 May 2020), p. 2563. ISSN: 2041-1723.
DOI: 10.1038/s41467-020-16392-5.

[180] Dariush Ashtiani et al. ‘Delivery of femtolitre droplets using surface acoustic wave based atomisation for cryo-EM grid preparation’.
In: *Journal of Structural Biology* 203 (2 Aug. 2018), pp. 94–101.
ISSN: 10478477. DOI: 10.1016/j.jsb.2018.03.012.

[181] Claudio Schmidli et al. ‘Microfluidic protein isolation and sample preparation for high-resolution cryo-EM’. In: *Proceedings of the National Academy of Sciences* 116 (30 July 2019), pp. 15007–15012.
ISSN: 0027-8424. DOI: 10.1073/pnas.1907214116.

[182] Stefan T Huber et al. ‘Nanofluidic chips for cryo-EM structure determination from picoliter sample volumes’. In: *eLife* 11 (Jan. 2022).
ISSN: 2050-084X. DOI: 10.7554/eLife.72629.

[183] David P. Klebl et al.
‘Sample deposition onto cryo-EM grids: from sprays to jets and back’.
In: *Acta Crystallographica Section D Structural Biology* 76 (4 Apr. 2020), pp. 340–349. ISSN: 2059-7983. DOI: 10.1107/S2059798320002958.

[184] Hui Wei et al.
‘Self-Blotting Nanowire Grids for Cryo-EM Sample Preparation’.
In: *Microscopy and Microanalysis* 23 (S1 July 2017), pp. 848–849.
ISSN: 1431-9276. DOI: 10.1017/S1431927617004901.

[185] John L. Rubinstein et al.
‘Shake-it-off: a simple ultrasonic cryo-EM specimen-preparation device’.
In: *Acta Crystallographica Section D Structural Biology* 75 (12 Dec. 2019), pp. 1063–1070. ISSN: 2059-7983. DOI: 10.1107/S2059798319014372.

[186] Tilak Jain et al. ‘Spotiton: A prototype for an integrated inkjet dispense and vitrification system for cryo-TEM’.
In: *Journal of Structural Biology* 179 (1 July 2012), pp. 68–75.
ISSN: 10478477. DOI: 10.1016/j.jsb.2012.04.020.

[187] Bo Chen et al.
‘Structural Dynamics of Ribosome Subunit Association Studied by Mixing-Spraying Time-Resolved Cryogenic Electron Microscopy’.
In: *Structure* 23 (6 June 2015), pp. 1097–1105. ISSN: 09692126.
DOI: 10.1016/j.str.2015.04.007.

[188] Yong Zi Tan and John L. Rubinstein.
‘Through-grid wicking enables high-speed cryoEM specimen preparation’.
In: *Acta Crystallographica Section D Structural Biology* 76 (11 Nov. 2020), pp. 1092–1103. ISSN: 2059-7983. DOI: 10.1107/S2059798320012474.

[189] Sandip Kaledhonkar et al.
Time-Resolved Cryo-electron Microscopy Using a Microfluidic Chip. 2018.
DOI: 10.1007/978-1-4939-7759-8_4.

[190] Venkata P. Dandey et al. ‘Time-resolved cryo-EM using Spotiton’.
In: *Nature Methods* 17 (9 Sept. 2020), pp. 897–900. ISSN: 1548-7091.
DOI: 10.1038/s41592-020-0925-6.

[191] Ivan Razinkov et al. ‘A new method for vitrifying samples for cryoEM’.
In: *Journal of Structural Biology* 195 (2 Aug. 2016), pp. 190–198.
ISSN: 10478477. DOI: 10.1016/j.jsb.2016.06.001.

[192] Talya S. Levitz et al. ‘Approaches to Using the Chameleon: Robust, Automated, Fast-Plunge cryoEM Specimen Preparation’.
In: *Frontiers in Molecular Biosciences* 9 (June 2022). ISSN: 2296-889X.
DOI: 10.3389/fmolb.2022.903148.

[193] Talya S. Levitz et al.
‘Effects of chameleon dispense-to-plunge speed on particle concentration, complex formation, and final resolution: A case study using the Neisseria gonorrhoeae ribonucleotide reductase inactive complex’.

In: *Journal of Structural Biology* 214 (1 Mar. 2022), p. 107825. ISSN: 10478477. DOI: 10.1016/j.jsb.2021.107825.

[194] David P. Klebl et al. 'Need for Speed: Examining Protein Behavior during CryoEM Grid Preparation at Different Timescales'. In: *Structure* 28 (11 Nov. 2020), 1238–1248.e4. ISSN: 09692126. DOI: 10.1016/j.str.2020.07.018.

[195] Hui Wei et al. 'Optimizing "self-wicking" nanowire grids'. In: *Journal of Structural Biology* 202 (2 May 2018), pp. 170–174. ISSN: 10478477. DOI: 10.1016/j.jsb.2018.01.001.

[196] Hui Wei et al. 'Spotiton and Chameleon Vitrification robots'. In: *Microscopy and Microanalysis* 25 (S2 Aug. 2019), pp. 1010–1011. ISSN: 1431-9276. DOI: 10.1017/S1431927619005786.

[197] Venkata P. Dandey et al. 'Spotiton: New features and applications'. In: *Journal of Structural Biology* 202 (2 May 2018), pp. 161–169. ISSN: 10478477. DOI: 10.1016/j.jsb.2018.01.002.

[198] Giulia Weissenberger et al. 'VitroJet: Bridging the Gap in Sample Prep'. In: *Microscopy and Microanalysis* 26 (S2 Aug. 2020), pp. 328–328. ISSN: 1431-9276. DOI: 10.1017/S1431927620014257.

[199] Thermo Fisher Scientific. *Smart EPU Software*. URL: https://www.thermofisher.com/de/de/home/electron-microscopy/products/software-em-3d-vis/epu-software.html.

[200] David N. Mastronarde. 'Automated electron microscope tomography using robust prediction of specimen movements'. In: *Journal of Structural Biology* 152 (1 Oct. 2005), pp. 36–51. ISSN: 10478477. DOI: 10.1016/j.jsb.2005.07.007.

[201] Quanfu Fan et al. 'CryoRL: Reinforcement Learning Enables Efficient Cryo-EM Data Collection'. In: *arXiv preprint* (2022).

[202] Huihui Kuang et al. 'Smart Leginon: Fully Automated Cryo-EM Grid Screening for CryoEM using Leginon and Ptolemy'. In: *Microscopy and Microanalysis* 28 (S1 Aug. 2022), pp. 1266–1268. ISSN: 1435-8115. DOI: 10.1017/S1431927622005232.

[203] Axel F. Brilot et al.
'Beam-induced motion of vitrified specimen on holey carbon film'.
In: *Journal of Structural Biology* 177 (3 Mar. 2012), pp. 630–637.
ISSN: 10478477. DOI: 10.1016/j.jsb.2012.02.003.

[204] Melody G. Campbell et al. 'Movies of Ice-Embedded Particles Enhance Resolution in Electron Cryo-Microscopy'.
In: *Structure* 20 (11 Nov. 2012), pp. 1823–1828. ISSN: 09692126.
DOI: 10.1016/j.str.2012.08.026.

[205] Sjors HW Scheres.
'Beam-induced motion correction for sub-megadalton cryo-EM particles'.
In: *eLife* 3 (Aug. 2014). ISSN: 2050-084X. DOI: 10.7554/eLife.03665.

[206] Xueming Li et al. 'Electron counting and beam-induced motion correction enable near-atomic-resolution single-particle cryo-EM'.
In: *Nature Methods* 10 (6 June 2013), pp. 584–590. ISSN: 1548-7091.
DOI: 10.1038/nmeth.2472.

[207] Xiao-chen Bai et al. 'Ribosome structures to near-atomic resolution from thirty thousand cryo-EM particles'. In: *eLife* 2 (Feb. 2013).
ISSN: 2050-084X. DOI: 10.7554/eLife.00461.

[208] Shawn Q Zheng et al. 'MotionCor2: anisotropic correction of beam-induced motion for improved cryo-electron microscopy'.
In: *Nature Methods* 14 (4 Apr. 2017), pp. 331–332. ISSN: 1548-7091.
DOI: 10.1038/nmeth.4193.

[209] Alexis Rohou and Nikolaus Grigorieff. 'CTFFIND4: Fast and accurate defocus estimation from electron micrographs'.
In: *Journal of Structural Biology* 192 (2 Nov. 2015), pp. 216–221.
ISSN: 10478477. DOI: 10.1016/j.jsb.2015.08.008.

[210] Kai Zhang. 'Gctf: Real-time CTF determination and correction'.
In: *Journal of Structural Biology* 193 (1 Jan. 2016), pp. 1–12.
ISSN: 10478477. DOI: 10.1016/j.jsb.2015.11.003.

[211] N Volkmann. 'An approach to automated particle picking from electron micrographs based on reduced representation templates'.
In: *Journal of Structural Biology* 145 (1-2 Jan. 2004), pp. 152–156.
ISSN: 10478477. DOI: 10.1016/j.jsb.2003.11.026.

[212] Z Huang. 'Application of template matching technique to particle detection in electron micrographs'.
In: *Journal of Structural Biology* 145 (1-2 Jan. 2004), pp. 29–40.
ISSN: 10478477. DOI: 10.1016/j.jsb.2003.11.004.

[213] A Roseman. 'FindEM—a fast, efficient program for automatic selection of particles from electron micrographs'.
In: *Journal of Structural Biology* 145 (1-2 Jan. 2004), pp. 91–99.
ISSN: 10478477. DOI: 10.1016/j.jsb.2003.11.007.

[214] Sjors H.W. Scheres.
'Semi-automated selection of cryo-EM particles in RELION-1.3'.
In: *Journal of Structural Biology* 189 (2 Feb. 2015), pp. 114–122.
ISSN: 10478477. DOI: 10.1016/j.jsb.2014.11.010.

[215] Yanan Zhu, Qi Ouyang and Youdong Mao.
'A deep convolutional neural network approach to single-particle recognition in cryo-electron microscopy'.
In: *BMC Bioinformatics* 18 (1 Dec. 2017), p. 348. ISSN: 1471-2105.
DOI: 10.1186/s12859-017-1757-y.

[216] Feng Wang et al. 'DeepPicker: A deep learning approach for fully automated particle picking in cryo-EM'.
In: *Journal of Structural Biology* 195 (3 Sept. 2016), pp. 325–336.
ISSN: 10478477. DOI: 10.1016/j.jsb.2016.07.006.

[217] Tristan Bepler et al. 'Positive-unlabeled convolutional neural networks for particle picking in cryo-electron micrographs'.
In: *Nature Methods* 16 (11 Nov. 2019), pp. 1153–1160. ISSN: 1548-7091.
DOI: 10.1038/s41592-019-0575-8.

[218] Dimitry Tegunov and Patrick Cramer.
'Real-time cryo-electron microscopy data preprocessing with Warp'.
In: *Nature Methods* 16 (11 Nov. 2019), pp. 1146–1152. ISSN: 1548-7091.
DOI: 10.1038/s41592-019-0580-y.

[219] Thorsten Wagner et al. 'SPHIRE-crYOLO is a fast and accurate fully automated particle picker for cryo-EM'.
In: *Communications Biology* 2 (1 June 2019), p. 218. ISSN: 2399-3642.
DOI: 10.1038/s42003-019-0437-z.

[220] Pamela A Thuman-Commike. 'Single particle macromolecular structure determination via electron microscopy'.
In: *FEBS Letters* 505 (2 Sept. 2001), pp. 199–205. ISSN: 00145793.
DOI: 10.1016/S0014-5793(01)02804-6.

[221] Jacqueline L. S. Milne et al.
'Cryo-electron microscopy - a primer for the non-microscopist'.
In: *FEBS Journal* 280 (1 Jan. 2013), pp. 28–45. ISSN: 1742464X.
DOI: 10.1111/febs.12078.

[222] Fred J. Sigworth. 'Principles of cryo-EM single-particle image processing'.
In: *Microscopy* 65 (1 Feb. 2016), pp. 57–67. ISSN: 2050-5698.
DOI: 10.1093/jmicro/dfv370.

[223] Jasenko Zivanov et al. 'New tools for automated high-resolution cryo-EM structure determination in RELION-3'. In: *eLife* 7 (Nov. 2018).
ISSN: 2050-084X. DOI: 10.7554/eLife.42166.

[224] EMDB Electron Microscopy Data Bank.
Statistics - EMDB software for image reconstruction distribution.
URL: https://www.ebi.ac.uk/emdb/statistics/emdb_software_image_reconstruction.

[225] Sjors H.W. Scheres. 'RELION: Implementation of a Bayesian approach to cryo-EM structure determination'.
In: *Journal of Structural Biology* 180 (3 Dec. 2012), pp. 519–530.
ISSN: 10478477. DOI: 10.1016/j.jsb.2012.09.006.

[226] Ali Punjani et al. ‘cryoSPARC: algorithms for rapid unsupervised cryo-EM structure determination’.
In: *Nature Methods* 14 (3 Mar. 2017), pp. 290–296. ISSN: 1548-7091. DOI: 10.1038/nmeth.4169.

[227] Marin van Heel and Michael Schatz.
‘Fourier shell correlation threshold criteria’.
In: *Journal of Structural Biology* 151 (3 Sept. 2005), pp. 250–262. ISSN: 10478477. DOI: 10.1016/j.jsb.2005.05.009.

[228] Peter B. Rosenthal and Richard Henderson.
‘Optimal Determination of Particle Orientation, Absolute Hand, and Contrast Loss in Single-particle Electron Cryomicroscopy’.
In: *Journal of Molecular Biology* 333 (4 Oct. 2003), pp. 721–745. ISSN: 00222836. DOI: 10.1016/j.jmb.2003.07.013.

[229] Sjors H W Scheres and Shaoxia Chen.
‘Prevention of overfitting in cryo-EM structure determination’.
In: *Nature Methods* 9 (9 Sept. 2012), pp. 853–854. ISSN: 1548-7091. DOI: 10.1038/nmeth.2115.

[230] Roland Beckmann et al. ‘Alignment of Conduits for the Nascent Polypeptide Chain in the Ribosome-Sec61 Complex’.
In: *Science* 278 (5346 Dec. 1997), pp. 2123–2126. ISSN: 0036-8075. DOI: 10.1126/science.278.5346.2123.

[231] B. Böttcher, S. A. Wynne and R. A. Crowther. ‘Determination of the fold of the core protein of hepatitis B virus by electron cryomicroscopy’.
In: *Nature* 386 (6620 Mar. 1997), pp. 88–91. ISSN: 0028-0836. DOI: 10.1038/386088a0.

[232] Alp Kucukelbir, Fred J Sigworth and Hemant D Tagare.
‘Quantifying the local resolution of cryo-EM density maps’.
In: *Nature Methods* 11 (1 Jan. 2014), pp. 63–65. ISSN: 1548-7091. DOI: 10.1038/nmeth.2727.

[233] F. DiMaio and W. Chiu. *Tools for Model Building and Optimization into Near-Atomic Resolution Electron Cryo-Microscopy Density Maps*. 2016. DOI: 10.1016/bs.mie.2016.06.003.

[234] Paul Emsley and Kevin Cowtan.
'Coot : model-building tools for molecular graphics'.
In: *Acta Crystallographica Section D Biological Crystallography* 60 (12 Dec. 2004), pp. 2126–2132. ISSN: 0907-4449.
DOI: 10.1107/S0907444904019158.

[235] Thomas C. Terwilliger et al. 'Cryo-EM map interpretation and protein model-building using iterative map segmentation'.
In: *Protein Science* 29 (1 Jan. 2020), pp. 87–99. ISSN: 0961-8368.
DOI: 10.1002/pro.3740.

[236] Genki Terashi and Daisuke Kihara.
'De novo main-chain modeling for EM maps using MAINMAST'.
In: *Nature Communications* 9 (1 Apr. 2018), p. 1618. ISSN: 2041-1723.
DOI: 10.1038/s41467-018-04053-7.

[237] Muyuan Chen et al.
'De Novo modeling in cryo-EM density maps with Pathwalking'.
In: *Journal of Structural Biology* 196 (3 Dec. 2016), pp. 289–298.
ISSN: 10478477. DOI: 10.1016/j.jsb.2016.06.004.

[238] Jonas Pfab, Nhut Minh Phan and Dong Si.
'DeepTracer for fast de novo cryo-EM protein structure modeling and special studies on CoV-related complexes'.
In: *Proceedings of the National Academy of Sciences* 118 (2 Jan. 2021).
ISSN: 0027-8424. DOI: 10.1073/pnas.2017525118.

[239] Pavel V. Afonine et al. 'New tools for the analysis and validation of cryo-EM maps and atomic models'. In: *Acta Crystallographica Section D Structural Biology* 74 (9 Sept. 2018), pp. 814–840. ISSN: 2059-7983.
DOI: 10.1107/S2059798318009324.

[240] Roma N. Rambaran and Louise C. Serpell. 'Amyloid fibrils'. In: *Prion* 2 (3 July 2008), pp. 112–117. ISSN: 1933-6896. DOI: 10.4161/pri.2.3.7488.

[241] Roland Riek and David S. Eisenberg. 'The activities of amyloids from a structural perspective'. In: *Nature* 539 (7628 Nov. 2016), pp. 227–235. ISSN: 0028-0836. DOI: 10.1038/nature20416.

[242] Jed J W Wiltzius et al. 'Molecular mechanisms for protein-encoded inheritance'. In: *Nature Structural and Molecular Biology* 16 (9 Sept. 2009), pp. 973–978. ISSN: 1545-9993. DOI: 10.1038/nsmb.1643.

[243] Anthony W. P. Fitzpatrick et al. 'Atomic structure and hierarchical assembly of a cross-β amyloid fibril'. In: *Proceedings of the National Academy of Sciences* 110 (14 Apr. 2013), pp. 5468–5473. ISSN: 0027-8424. DOI: 10.1073/pnas.1219476110.

[244] Lynn Radamaker et al. 'Cryo-EM reveals structural breaks in a patient-derived amyloid fibril from systemic AL amyloidosis'. In: *Nature Communications* 12 (1 Feb. 2021), p. 875. ISSN: 2041-1723. DOI: 10.1038/s41467-021-21126-2.

[245] Andrei T. Alexandrescu. 'Amide Proton Solvent Protection in Amylin Fibrils Probed by Quenched Hydrogen Exchange NMR'. In: *PLoS ONE* 8 (2 Feb. 2013), e56467. ISSN: 1932-6203. DOI: 10.1371/journal.pone.0056467.

[246] Qin Cao et al. 'Cryo-EM structure and inhibitor design of human IAPP (amylin) fibrils'. In: *Nature Structural and Molecular Biology* 27 (7 July 2020), pp. 653–659. ISSN: 1545-9993. DOI: 10.1038/s41594-020-0435-3.

[247] Rodrigo Gallardo et al. 'Fibril structures of diabetes-related amylin variants reveal a basis for surface-templated assembly'. In: *Nature Structural and Molecular Biology* 27 (11 Nov. 2020), pp. 1048–1056. ISSN: 1545-9993. DOI: 10.1038/s41594-020-0496-3.

[248] Franziska Weirich et al. 'Structural Characterization of Fibrils from Recombinant Human Islet Amyloid Polypeptide by Solid-State NMR: The Central FGAILS Segment Is Part of the β-Sheet Core'.
In: *PLOS ONE* 11 (9 Sept. 2016), e0161243. ISSN: 1932-6203.
DOI: 10.1371/journal.pone.0161243.

[249] Christine Röder et al. 'Cryo-EM structure of islet amyloid polypeptide fibrils reveals similarities with amyloid-β fibrils'.
In: *Nature Structural and Molecular Biology* 27 (7 July 2020), pp. 660–667.
ISSN: 1545-9993. DOI: 10.1038/s41594-020-0442-4.

[250] Benjamin Falcon et al. 'Tau filaments from multiple cases of sporadic and inherited Alzheimer's disease adopt a common fold'.
In: *Acta Neuropathologica* 136 (5 Nov. 2018), pp. 699–708.
ISSN: 0001-6322. DOI: 10.1007/s00401-018-1914-z.

[251] Marius Kollmer et al. 'Cryo-EM structure and polymorphism of Aβ amyloid fibrils purified from Alzheimer's brain tissue.'
In: *Nature communications* 10 (1 Oct. 2019), p. 4760.
ISSN: 2041-1723 (Electronic). DOI: 10.1038/s41467-019-12683-8.

[252] Lothar Gremer et al.
'Fibril structure of amyloid-β(1–42) by cryo–electron microscopy'.
In: *Science* 358 (6359 2017), pp. 116–119. ISSN: 10959203.
DOI: 10.1126/science.aao2825.

[253] Linda Cerofolini et al.
'Mixing Aβ(1-40) and Aβ(1-42) peptides generates unique amyloid fibrils'.
In: *Chemical Communications* 56 (62 2020), pp. 8830–8833.
ISSN: 1359-7345. DOI: 10.1039/D0CC02463E.

[254] Michael T. Colvin et al.
'Atomic Resolution Structure of Monomorphic Aβ42 Amyloid Fibrils'.
In: *Journal of the American Chemical Society* 138 (30 Aug. 2016),
pp. 9663–9674. ISSN: 0002-7863. DOI: 10.1021/jacs.6b05129.

[255] Marielle Aulikki Wälti et al.
'Atomic-resolution structure of a disease-relevant Aβ(1-42) amyloid fibril'.
In: *Proceedings of the National Academy of Sciences* 113 (34 Aug. 2016).
ISSN: 0027-8424. DOI: 10.1073/pnas.1600749113.

[256] Anant K. Paravastu et al. 'Molecular structural basis for polymorphism in Alzheimer's β-amyloid fibrils'. In: *Proceedings of the National Academy of Sciences* 105 (47 Nov. 2008), pp. 18349–18354. ISSN: 0027-8424.
DOI: 10.1073/pnas.0806270105.

[257] Yiling Xiao et al. 'Aβ(1-42) fibril structure illuminates self-recognition and replication of amyloid in Alzheimer's disease'. In: *Nature Structural and Molecular Biology* 22 (6 June 2015), pp. 499–505. ISSN: 1545-9993.
DOI: 10.1038/nsmb.2991.

[258] Dieter Willbold et al. 'Amyloid-type Protein Aggregation and Prion-like Properties of Amyloids'.
In: *Chemical Reviews* 121 (13 July 2021), pp. 8285–8307. ISSN: 0009-2665.
DOI: 10.1021/acs.chemrev.1c00196.

[259] Ujjayini Ghosh et al. 'Molecular structure of a prevalent amyloid-β fibril polymorph from Alzheimer's disease brain tissue'.
In: *Proceedings of the National Academy of Sciences of the United States of America* 118 (4 2021).
DOI: https://doi.org/10.1073/pnas.2023089118.

[260] Myungwoon Lee et al.
'Structures of brain-derived 42-residue amyloid-β fibril polymorphs with unusual molecular conformations and intermolecular interactions'.
In: *Proceedings of the National Academy of Sciences* 120 (11 Mar. 2023).
ISSN: 0027-8424. DOI: 10.1073/pnas.2218831120.

[261] Yang Yang et al.
'Cryo-EM structures of amyloid-β 42 filaments from human brains'.
In: *Science* 375 (6577 Jan. 2022), pp. 167–172. ISSN: 0036-8075.
DOI: 10.1126/science.abm7285.

[262] Anthony W. P. Fitzpatrick et al.
'Cryo-EM structures of tau filaments from Alzheimer's disease'.
In: *Nature* 547 (7662 July 2017), pp. 185–190. ISSN: 0028-0836.
DOI: 10.1038/nature23002.

[263] Benjamin Falcon et al.
'Structures of filaments from Pick's disease reveal a novel tau protein fold'.
In: *Nature* 561 (7721 Sept. 2018), pp. 137–140. ISSN: 0028-0836.
DOI: 10.1038/s41586-018-0454-y.

[264] Benjamin Falcon et al. 'Novel tau filament fold in chronic traumatic encephalopathy encloses hydrophobic molecules'.
In: *Nature* 568 (7752 Apr. 2019), pp. 420–423. ISSN: 0028-0836.
DOI: 10.1038/s41586-019-1026-5.

[265] Yang Shi et al. 'Structure-based classification of tauopathies'.
In: *Nature* 598 (7880 Oct. 2021), pp. 359–363. ISSN: 0028-0836.
DOI: 10.1038/s41586-021-03911-7.

[266] Ruben Diaz, William J Rice and David L Stokes.
Fourier-bessel reconstruction of helical assemblies. 2010.
DOI: 10.1016/S0076-6879(10)82005-1.

[267] Sjors H W Scheres. 'Amyloid structure determination in RELION-3.1'.
In: *Acta Crystallographica Section D: Structural Biology* (2020).
ISSN: 20597983. DOI: 10.1107/S2059798319016577.

[268] Kyle L Morris and Louise C Serpell.
'X-ray fibre diffraction studies of amyloid fibrils'.
In: *Methods in Molecular Biology* (2012). ISSN: 10643745.
DOI: 10.1007/978-1-61779-551-0_9.

[269] Edward H Egelman. 'A robust algorithm for the reconstruction of helical filaments using single-particle methods'. In: *Ultramicroscopy* (2000).
ISSN: 03043991. DOI: 10.1016/S0304-3991(00)00062-0.

[270] Elmar Behrmann et al.
'Real-space processing of helical filaments in SPARX'.
In: *Journal of Structural Biology* 177 (2 Feb. 2012), pp. 302–313.
ISSN: 10478477. DOI: 10.1016/j.jsb.2011.12.020.

[271] Ambroise Desfosses et al.
'SPRING – An image processing package for single-particle based helical reconstruction from electron cryomicrographs'.
In: *Journal of Structural Biology* 185 (1 Jan. 2014), pp. 15–26.
ISSN: 10478477. DOI: 10.1016/j.jsb.2013.11.003.

[272] Shaoda He and Sjors H.W. Scheres. 'Helical reconstruction in RELION'.
In: *Journal of Structural Biology* 198 (3 June 2017), pp. 163–176.
ISSN: 10478477. DOI: 10.1016/j.jsb.2017.02.003.

[273] Alexis Rohou and Nikolaus Grigorieff. 'Frealix: Model-based refinement of helical filament structures from electron micrographs'.
In: *Journal of Structural Biology* 186 (2 May 2014), pp. 234–244.
ISSN: 10478477. DOI: 10.1016/j.jsb.2014.03.012.

[274] Kent R. Thurber, Yi Yin and Robert Tycko.
'Automated picking of amyloid fibrils from cryo-EM images for helical reconstruction with RELION'.
In: *Journal of Structural Biology* 213 (2 June 2021), p. 107736.
ISSN: 10478477. DOI: 10.1016/j.jsb.2021.107736.

[275] Stefan T. Huber, Tanja Kuhm and Carsten Sachse.
'Automated tracing of helical assemblies from electron cryo-micrographs'.
In: *Journal of Structural Biology* 202 (1 Apr. 2018), pp. 1–12.
ISSN: 10478477. DOI: 10.1016/j.jsb.2017.11.013.

[276] Sofia Lövestam and Sjors H. W. Scheres.
'High-throughput cryo-EM structure determination of amyloids'.
In: *Faraday Discussions* 240 (2022), pp. 243–260. ISSN: 1359-6640.
DOI: 10.1039/D2FD00034B.

[277] Thorsten Wagner and Stefan Raunser.
'The evolution of SPHIRE-crYOLO particle picking and its application in automated cryo-EM processing workflows'.
In: *Communications Biology* 3 (1 Feb. 2020), p. 61. ISSN: 2399-3642.
DOI: 10.1038/s42003-020-0790-y.

[278] Sorin Luca et al. 'Peptide Conformation and Supramolecular Organization in Amylin Fibrils: Constraints from Solid-State NMR'.
In: *Biochemistry* 46 (2007), pp. 13505–13522. DOI: 10.1021/bi701427q.

[279] Hélène Van Melckebeke et al.
'Atomic-Resolution Three-Dimensional Structure of HET-s(218-289) Amyloid Fibrils by Solid-State NMR Spectroscopy'. In: *Journal of the American Chemical Society* 132 (Oct. 2010), pp. 13765–13775.
DOI: 10.1021/ja104213j.

[280] Alexander Wlodawer and Zbigniew Dauter.
''Atomic resolution': a badly abused term in structural biology'.
In: *Acta Crystallographica Section D Structural Biology* 73 (4 Apr. 2017), pp. 379–380. ISSN: 2059-7983. DOI: 10.1107/S205979831700225X.

[281] Takanori Nakane et al. 'Single-particle cryo-EM at atomic resolution'.
In: *Nature* 587 (7832 Nov. 2020), pp. 152–156. ISSN: 0028-0836.
DOI: 10.1038/s41586-020-2829-0.

[282] Ka Man Yip et al.
'Atomic-resolution protein structure determination by cryo-EM'.
In: *Nature* 587 (7832 Nov. 2020), pp. 157–161. ISSN: 0028-0836.
DOI: 10.1038/s41586-020-2833-4.

[283] Sofia Lövestam et al.
'Assembly of recombinant tau into filaments identical to those of Alzheimer's disease and chronic traumatic encephalopathy'.
In: *eLife* 11 (Mar. 2022). ISSN: 2050-084X. DOI: 10.7554/eLife.76494.

[284] Conny Leistner et al. 'The in-tissue molecular architecture of β-amyloid pathology in the mammalian brain'.

In: *Nature Communications* 14 (1 May 2023), p. 2833. ISSN: 2041-1723. DOI: 10.1038/s41467-023-38495-5.

[285] Yang Yang et al. 'Cryo-EM structures of amyloid-β filaments with the Arctic mutation (E22G) from human and mouse brains'. In: *Acta Neuropathologica* 145 (3 Mar. 2023), pp. 325–333. ISSN: 0001-6322. DOI: 10.1007/s00401-022-02533-1.

[286] Anne K. Schütz et al. 'Atomic-Resolution Three-Dimensional Structure of Amyloid β Fibrils Bearing the Osaka Mutation'. In: *Angewandte Chemie International Edition* 54 (1 Jan. 2015), pp. 331–335. ISSN: 1433-7851. DOI: 10.1002/anie.201408598.

[287] Mara Zielinski et al. 'Cryo-EM of Aβ fibrils from mouse models find $tg - APP_{ArcSwe}$ fibrils resemble those found in patients with sporadic Alzheimer's disease'. In: *Nature Neuroscience* 26 (12 Dec. 2023), pp. 2073–2080. ISSN: 1097-6256. DOI: 10.1038/s41593-023-01484-4.

[288] M. Scholl et al. 'Low PiB PET retention in presence of pathologic CSF biomarkers in Arctic APP mutation carriers'. In: *Neurology* 79 (3 July 2012), pp. 229–236. ISSN: 0028-3878. DOI: 10.1212/WNL.0b013e31825fdf18.

[289] Hannu Kalimo et al. 'The Arctic AβPP mutation leads to Alzheimer's disease pathology with highly variable topographic deposition of differentially truncated Aβ.' In: *Acta neuropathologica communications* 1 (Sept. 2013), p. 60. ISSN: 2051-5960. DOI: 10.1186/2051-5960-1-60.

[290] Ola Philipson et al. 'The Arctic amyloid-β precursor protein (AβPP) mutation results in distinct plaques and accumulation of N- and C-truncated Aβ.' In: *Neurobiology of aging* 33 (5 May 2012), 1010.e1–13. ISSN: 1558-1497. DOI: 10.1016/j.neurobiolaging.2011.10.022.

[291] Antje Willuweit et al. ‘Comparison of the Amyloid Load in the Brains of Two Transgenic Alzheimer’s Disease Mouse Models Quantified by Florbetaben Positron Emission Tomography’.
In: *Frontiers in Neuroscience* 15 (Oct. 2021). ISSN: 1662-453X.
DOI: 10.3389/fnins.2021.699926.

[292] Judianne Davis et al.
‘Early-onset and Robust Cerebral Microvascular Accumulation of Amyloid β-Protein in Transgenic Mice Expressing Low Levels of a Vasculotropic Dutch/Iowa Mutant Form of Amyloid β-Protein Precursor’.
In: *Journal of Biological Chemistry* 279 (19 May 2004), pp. 20296–20306.
ISSN: 00219258. DOI: 10.1074/jbc.M312946200.

[293] Jianting Miao et al.
‘Cerebral Microvascular Amyloid β Protein Deposition Induces Vascular Degeneration and Neuroinflammation in Transgenic Mice Expressing Human Vasculotropic Mutant Amyloid β Precursor Protein’.
In: *The American Journal of Pathology* 167 (2 Aug. 2005), pp. 505–515.
ISSN: 00029440. DOI: 10.1016/S0002-9440(10)62993-8.

[294] Gerhard Leinenga, Wee Kiat Koh and Jürgen Götz. ‘A comparative study of the effects of Aducanumab and scanning ultrasound on amyloid plaques and behavior in the APP23 mouse model of Alzheimer disease’.
In: *Alzheimer’s Research and Therapy* 13 (1 Dec. 2021), p. 76.
ISSN: 1758-9193. DOI: 10.1186/s13195-021-00809-4.

[295] Veronika Logovinsky et al. ‘Safety and tolerability of BAN2401 - a clinical study in Alzheimer’s disease with a protofibril selective Aβ antibody’.
In: *Alzheimer’s Research and Therapy* 8 (1 Dec. 2016), p. 14.
ISSN: 1758-9193. DOI: 10.1186/s13195-016-0181-2.

[296] Chad J. Swanson et al. ‘A randomized, double-blind, phase 2b proof-of-concept clinical trial in early Alzheimer’s disease with lecanemab, an anti-Aβ protofibril antibody’.
In: *Alzheimer’s Research and Therapy* 13 (1 Dec. 2021), p. 80.
ISSN: 1758-9193. DOI: 10.1186/s13195-021-00813-8.

[297] Christopher H. van Dyck et al. ‘Lecanemab in Early Alzheimer’s Disease’. In: *New England Journal of Medicine* 388 (1 Jan. 2023), pp. 9–21. ISSN: 0028-4793. DOI: 10.1056/NEJMoa2212948.

[298] Silvio R. Meier et al. ‘11C-PiB and 124 I-Antibody PET Provide Differing Estimates of Brain Amyloid-β After Therapeutic Intervention’. In: *Journal of Nuclear Medicine* 63 (2 Feb. 2022), pp. 302–309. ISSN: 0161-5505. DOI: 10.2967/jnumed.121.262083.

[299] Neetu M. Gulati et al. ‘Immunoelectron Microscopy of Viral Antigens’. In: *Current Protocols in Microbiology* 53 (1 June 2019). ISSN: 1934-8525. DOI: 10.1002/cpmc.86.

[300] S J Ryu et al. ‘On the role of major vault protein in the resistance of senescent human diploid fibroblasts to apoptosis’. In: *Cell Death and Differentiation* 15 (11 Nov. 2008), pp. 1673–1680. ISSN: 1350-9047. DOI: 10.1038/cdd.2008.96.

[301] Pablo Guerra et al. ‘Symmetry disruption commits vault particles to disassembly’. In: *Science Advances* 8 (6 Feb. 2022). ISSN: 2375-2548. DOI: 10.1126/sciadv.abj7795.

[302] Yazan M. Abbas et al. ‘Structure of V-ATPase from the mammalian brain’. In: *Science* 367 (6483 Mar. 2020), pp. 1240–1246. ISSN: 0036-8075. DOI: 10.1126/science.aaz2924.

[303] Michael P. Collins and Michael Forgac. ‘Regulation of V-ATPase Assembly in Nutrient Sensing and Function of V-ATPases in Breast Cancer Metastasis’. In: *Frontiers in Physiology* 9 (July 2018). ISSN: 1664-042X. DOI: 10.3389/fphys.2018.00902.

[304] M. Spiegel, A.K. Duraisamy and G.F. Schröder. ‘Improving the visualization of cryo-EM density reconstructions’. In: *Journal of Structural Biology* 191 (2 Aug. 2015), pp. 207–213. ISSN: 10478477. DOI: 10.1016/j.jsb.2015.06.007.

[305] Eric F. Pettersen et al. ‘UCSF ChimeraX : Structure visualization for researchers, educators, and developers’.
In: *Protein Science* 30 (1 Jan. 2021), pp. 70–82. ISSN: 0961-8368.
DOI: 10.1002/pro.3943.

[306] Christine Röder.
‘A Glimpse into the Polymorphic Landscape of Amyloids - Structural Investigation of Amyloid Fibrils by Cryo-Electron Microscopy’.
PhD thesis. Heinrich Heine Universität Düsseldorf, May 2021.

[307] Matthias Schmidt et al.
‘Peptide dimer structure in an Aβ(1–42) fibril visualized with cryo-EM’.
In: *Proceedings of the National Academy of Sciences* 112 (38 Sept. 2015), pp. 11858–11863. ISSN: 0027-8424. DOI: 10.1073/pnas.1503455112.

[308] María Pagnon de la Vega. ‘Characterization of the novel "Uppsala mutation" causing a familial from of early onset Alzheimer’s disease’.
PhD thesis. Uppsala Universitet, 2021.

[309] Takanori Nakane. *atom2svg*. Version 200213. Oct. 2020.
DOI: 10.5281/zenodo.4090925.
URL: https://doi.org/10.5281/zenodo.4090925.

[310] Pu Duan et al.
‘Binding Sites of a Positron Emission Tomography Imaging Agent in Alzheimer’s β-Amyloid Fibrils Studied Using ^{19}F Solid-State NMR’.
In: *Journal of the American Chemical Society* 144 (3 Jan. 2022), pp. 1416–1430. ISSN: 0002-7863. DOI: 10.1021/jacs.1c12056.

[311] Sara Linse.
‘Mechanism of amyloid protein aggregation and the role of inhibitors’.
In: *Pure and Applied Chemistry* 91 (2 Feb. 2019), pp. 211–229.
ISSN: 1365-3075. DOI: 10.1515/pac-2018-1017.

[312] Benedetta Bolognesi et al.
‘Single Point Mutations Induce a Switch in the Molecular Mechanism of the Aggregation of the Alzheimer’s Disease Associated Aβ_{42} Peptide’.

In: *ACS Chemical Biology* 9 (2 Feb. 2014), pp. 378–382. ISSN: 1554-8929. DOI: 10.1021/cb400616y.

[313] Xiaoting Yang et al. 'On the role of sidechain size and charge in the aggregation of Aβ42 with familial mutations'.
In: *Proceedings of the National Academy of Sciences* 115 (26 June 2018). ISSN: 0027-8424. DOI: 10.1073/pnas.1803539115.

[314] Bogdan Barz, Alexander K. Buell and Soumav Nath.
'Compact fibril-like structure of amyloid β-peptide (1–42) monomers'.
In: *Chemical Communications* 57 (7 2021), pp. 947–950. ISSN: 1359-7345. DOI: 10.1039/D0CC06607A.

[315] Fabrizio Chiti et al. 'Rationalization of the effects of mutations on peptide andprotein aggregation rates'.
In: *Nature* 424 (6950 Aug. 2003), pp. 805–808. ISSN: 0028-0836. DOI: 10.1038/nature01891.

[316] David Nečas and Petr Klapetek.
'Gwyddion: an open-source software for SPM data analysis'.
In: *Open Physics* 10.1 (Jan. 2012). DOI: 10.2478/s11534-011-0096-2. URL: https://doi.org/10.2478/s11534-011-0096-2.

[317] Thorsten Wagner et al. 'Two particle-picking procedures for filamentous proteins: SPHIRE-crYOLO filament mode and SPHIRE-STRIPER'.
In: *Acta Crystallographica Section D Structural Biology* 76 (7 July 2020), pp. 613–620. ISSN: 2059-7983. DOI: 10.1107/S2059798320007342.

[318] Ana Casañal, Bernhard Lohkamp and Paul Emsley.
'Current developments in Coot for macromolecular model building of Electron Cryo-microscopy and Crystallographic Data'.
In: *Protein Science* 29 (4 Apr. 2020), pp. 1055–1064. ISSN: 0961-8368. DOI: 10.1002/pro.3791.

[319] Christopher J. Williams et al. 'MolProbity: More and better reference data for improved all-atom structure validation'.
In: *Protein Science* 27 (1 Jan. 2018), pp. 293–315. ISSN: 09618368. DOI: 10.1002/pro.3330.

[320] Pavel V. Afonine et al.
'Real-space refinement in PHENIX for cryo-EM and crystallography'.
In: *Acta Crystallographica Section D Structural Biology* 74 (6 June 2018), pp. 531–544. ISSN: 2059-7983. DOI: 10.1107/S2059798318006551.

[321] J.Michael Word et al. 'Asparagine and glutamine: using hydrogen atom contacts in the choice of side-chain amide orientation'.
In: *Journal of Molecular Biology* 285 (4 Jan. 1999), pp. 1735–1747.
ISSN: 00222836. DOI: 10.1006/jmbi.1998.2401.

[322] Iryna Benilova et al.
'The Alzheimer Disease Protective Mutation A2T Modulates Kinetic and Thermodynamic Properties of Amyloid-β (Aβ) Aggregation'.
In: *Journal of Biological Chemistry* 289 (45 Nov. 2014), pp. 30977–30989.
ISSN: 00219258. DOI: 10.1074/jbc.M114.599027.

[323] Janice A. Maloney et al. 'Molecular Mechanisms of Alzheimer Disease Protection by the A673T Allele of Amyloid Precursor Protein'.
In: *Journal of Biological Chemistry* 289 (45 Nov. 2014), pp. 30990–31000.
ISSN: 00219258. DOI: 10.1074/jbc.M114.589069.

[324] Marie-Isabel Aguilar.
'Reversed-Phase High-Performance Liquid Chromatography'. In:
HPLC of Peptides and Proteins: Methods and Protocols.
Ed. by Marie-Isabel Aguilar. Totowa, NJ: Springer New York, 2004, pp. 9–22. ISBN: 978-1-59259-742-0. DOI: 10.1385/1-59259-742-4:9.
URL: https://doi.org/10.1385/1-59259-742-4:9.

[325] Eric F. Pettersen et al. 'UCSF Chimera. A visualization system for exploratory research and analysis'.
In: *Journal of Computational Chemistry* 25 (13 Oct. 2004), pp. 1605–1612.
ISSN: 0192-8651. DOI: 10.1002/jcc.20084.

[326] Guang Tang et al.
'EMAN2: An extensible image processing suite for electron microscopy'.
In: *Journal of Structural Biology* 157 (1 Jan. 2007), pp. 38–46.
ISSN: 10478477. DOI: 10.1016/j.jsb.2006.05.009.

[327] C M Wischik et al. ‘Structural characterization of the core of the paired helical filament of Alzheimer disease.’ In: *Proceedings of the National Academy of Sciences* 85 (13 July 1988), pp. 4884–4888. ISSN: 0027-8424. DOI: 10.1073/pnas.85.13.4884.

Acknowledgements

First of all, I would like to thank my supervisor Gunnar Schröder. Thank you for your trust and continuous support throughout all projects. I have learned so much during my time in your group. And since the group itself was also one reason for me to stay for my PhD, I would also like to thank you for creating such a positive working atmosphere. Thank you for making my PhD such a great experience.

Many thanks to Carsten Sachse for giving scientific advice throughout my PhD and for co-supervising my thesis.

I had the pleasure of working with great scientists during my PhD and therefore, I would like to thank all collaboration partners who have trusted me with their research and all who have enriched my work so much. In particular I would like to thank Fernanda Salome Peralta Reyes, Lothar Gremer, Dieter Willbold, Raimond Ravelli, María Pagnon de la Vega, Dag Sehlin, and Martin Ingelsson.

I'd also like to express my gratitude to all those who donated their brains for research.

Moreover, I'd like to acknowledge the IBI-7, especially the secretariat staff, who helped me a lot with all administrative tasks.

Special thanks to my Schröderlab peers: Christine, Luisa, Simon, James, Karunakar, Benedikt, José, and Janus. Thank you for your support and for the productive (or sometimes less productive, but refreshing) coffee and frisbee breaks.

I'm also thankful for the support of my cryo-EM colleagues at the Sachselab.

Special thanks to Julio Ortiz, Thomas Heidler, Pia Sundermeyer, Saba Shahzad, and Daniel Mann for the support and the microscopy training.

Lastly, I'd also like to thank Eileen for being such a great and supportive friend on this physics journey from the very beginning. Thank you Dominic for being there for me during this time, truly understanding my situation and always encouraging me. Thank you for your open ear, even if it probably involuntarily turned you into a little Alzheimer's expert. Finally, words cannot express my gratitude to my parents and my family, who always supported me. Thank you for being my safe haven.

Reprint Permissions

Publication I

Reprinted from *"Challenges in sample preparation and structure determination of amyloids by cryo-EM"*, Zielinski, M., Röder, C., Schröder, G.F. **Journal of Biological Chemistry** 297.2 (2021).

Publication II

Reprinted from *"The Uppsala APP deletion causes early onset autosomal dominant Alzheimers disease by altering APP processing and increasing amyloid β fibril formation"*, Pagnon de la Vega, M., Giedraitis, V., Michno, W., Kilander, L., Güner, G., Zielinski, M., Löwenmark, M, Brundin, R.M., Danfors, T., Söderberg, L., Alafuzoff, I., Nilsson, L.N.G., Erlandsson, A., Willbold, D. Müller, S.A., Schröder, G.F., Hanrieder, J., Lichtenthaler, S.F., Lannfelt, L., Sehlin, D., Ingelsson, M., **Science translational medicine**, 13.606 (2021). DOI: https://doi.org/10.1126/scitranslmed.abc6184

List of Figures

List of Tables

List of Abbreviations

2D two dimensional.

3D three dimensional.

Aβ Amyloid-β.

AcN acetonitrile.

AD Alzheimer's Disease.

ADAM10 A Disintegrin And Metalloprotease 10.

AFM atomic force microscopy.

AICD APP intracellular domain.

APOE Apolipoprotein E.

APP amyloid precursor protein.

C_c Chromatic Aberration.

C_s Spherical Aberration.

CAA cerebral amyloid angiopathy.

CCD Charged-Coupled Device.

CMOS Complementary metal-oxide-semiconductor.

CNN Convolutional neural network.

cryo-EM Cryogenic Electron Microscopy.

CSF cerebrospinal fluid.

CT Computed Tomography.

CTE chronic traumatic encephalopathy.

CTF Contrast Transfer Function.

DED Direct Electron Detector.

DQE Detective Quantum Efficiency.

EM Electron Microscopy.

EMDB Electron Microscopy Data Bank.

EOAD early-onset AD.

fAD familial AD.

FDA US Food and Drug Administration.

FEG Field Emission Gun.

FMT Flutemetamol.

FSC Fourier Shell Correlation.

FT Fourier Transform.

IDPs intrinsically disordered proteins.

IHRSR iterative helical real-space reconstruction.

LOAD late-onset AD.

mAb monoclonal antibodies.

MAP microtubule-associated protein.

NFTs neurofibrillary tangles.

NMR Nuclear Magnetic Resonance.

PD Parkinson's Disease.

PEN presenilin enhancer.

PET positron emission tomography.

PHF paired helical filament.

PIB Pittsburgh Compound B.

PSEN presenilin.

PSF Point Spread Function.

PTMs Post Translational Modifications.

RP-HPLC reversed phase-high performance liquid chromatography.

sAD sporadic AD.

SF straight filament.

SNR Signal-to-Noise Ratio.

SPR Single Particle Reconstruction.

SST sodium silicotungstate.

T2D Type II Diabetes.

TEM Transmission Electron Microscopy.

TFA trifluoroacetic acid.

ThT Thioflavin T.

UrAc uranyl acetate.

WHO World Health Organisation.

A. Publication I

JBC REVIEWS

Challenges in sample preparation and structure determination of amyloids by cryo-EM

Received for publication, February 3, 2021, and in revised form, June 28, 2021 Published, Papers in Press, July 3, 2021,
https://doi.org/10.1016/j.jbc.2021.100938

Mara Zielinski[1,‡], **Christine Röder**[1,2,‡], **and Gunnar F. Schröder**[1,3,*]

From the [1]*Institute of Biological Information Processing, Structural Biochemistry (IBI-7) and JuStruct, Jülich Center for Structural Biology, Forschungszentrum Jülich, Jülich, Germany;* [2]*Institut für Physikalische Biologie,* [3]*Physics Department, Heinrich-Heine-Universität Düsseldorf, Düsseldorf, Germany*

Edited by Paul Fraser

Amyloids share a common architecture but play disparate biological roles in processes ranging from bacterial defense mechanisms to protein misfolding diseases. Their structures are highly polymorphic, which makes them difficult to study by X-ray diffraction or NMR spectroscopy. Our understanding of amyloid structures is due in large part to recent advances in the field of cryo-EM, which allows for determining the polymorphs separately. In this review, we highlight the main stepping stones leading to the substantial number of high-resolution amyloid fibril structures known today as well as recent developments regarding automation and software in cryo-EM. We discuss that sample preparation should move closer to physiological conditions to understand how amyloid aggregation and disease are linked. We further highlight new approaches to address heterogeneity and polymorphism of amyloid fibrils in EM image processing and give an outlook to the upcoming challenges in researching the structural biology of amyloids.

History of amyloid research

For a long time, the sole imperative in protein research was the Anfinsen dogma, which states that the fold of a protein is dictated by its primary sequence (1). Today, we suspect that all proteins may adopt another generic fold that is independent from their primary sequence—the amyloid fold (2, 3) (Fig. 1). The amyloid fold is characterized by the aggregation of proteins into stacks of β-sheets resulting in fibrils that exhibit a so-called cross-β pattern (2–5). In the 19th century, the term amyloid was coined by Rudolf Virchow, by whom it was selected in reference to the Greek word for starch that Virchow considered the main building block of amyloid (6–8). A couple of years later, amyloid deposits were realized to be proteinaceous (6, 9). Until now, the findings that amyloids exhibit enhanced birefringence through Congo Red staining (6, 10, 11) and that they share the common cross-β pattern are considered the main characteristics of the amyloid fold. Currently, more than 50 amyloids (2, 12, 13) are linked to protein misfolding diseases such as Alzheimer's disease (AD) (14), Parkinson's disease (15, 16), and type II diabetes (T2D) (17), which have therefore been combined under the term amyloidoses (18). The proteins involved in these diseases often are intrinsically disordered proteins such as amyloid β (Aβ) (from AD) or amylin (from T2D), or at least contain a considerable fraction of disordered regions. Moreover, there are non–disease-related amyloidogenic proteins (19) such as the src-homology domain 3 that is known to form amyloids only *in vitro* (20). In addition, it has been observed that metabolites such as phenylalanine assemble into disease-causing amyloid-like aggregates (21). Functional amyloids that are mostly found in fungi or bacteria, where they often work as a defense mechanism against other species, have been identified, too (22–25). Considering the ubiquity of amyloids, it is of great interest to understand why such a variety of proteins is able to adopt the fibrillar fold, either functional or pathogenic. Although amyloid structures share a common overall architecture, the mechanism of protein aggregation from an intrinsically disordered protein or globular fold into amyloid is not yet understood. While some amyloidogenic proteins adopt the amyloid fold only when exposed to extreme conditions such as very low pH, increased temperature, and shaking (20, 26–28), others seem to undergo proteolytic truncations (29–32) before aggregation, and then again, there is a variety of proteins where a coincidental increase in local concentration seems to boost the misfolding reaction (33). Figure 1 visualizes different amyloid species and their putative misfolding pathways leading to either fibrils (on-pathway) or other aggregates (off-pathway). Following the on-pathway, disordered monomers aggregate into fibrillar oligomers that act as the precursor for maturation into fibrils (Fig. 1, lower part). These mature fibrils might then deposit together with other cellular components into insoluble plaques, which we can observe in diseased patients (34, 35). The off-pathway (Fig. 1, upper part), on the other hand, is considered to favor formation of amyloid oligomers that might aggregate into curvilinear fibrils (36–38). The biological relevance of these kind of aggregates remains elusive. However, in recent years, evidence accumulated that amyloid oligomers, especially those following the off-pathway, instead of amyloid fibrils represent the pathogenic species in amyloidoses (39–42). However, the role of on- and

‡ These authors contributed equally to this work.
* For correspondence: Gunnar F. Schröder, gu.schroeder@fz-juelich.de.

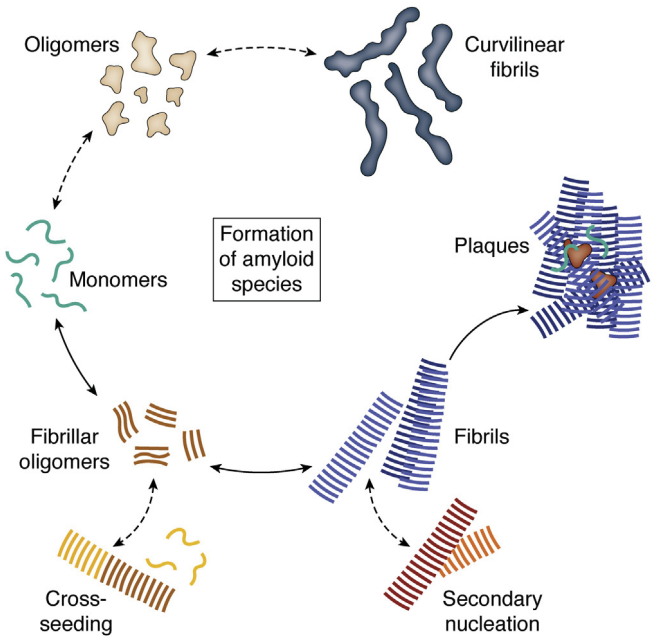

Figure 1. Formation of structurally different amyloid species. Starting from monomeric proteins (*green*), monomers can follow the on-pathway and aggregate into fibrillar oligomers (*brown*). Fibrillar oligomers will over time grow into mature fibrils (*blue*) that might, together with other species and molecules, deposit as plaques. Mature fibrils can undergo secondary nucleation during which monomers attach to a mature fibril and form a new fibril. In addition, fibrillar oligomers could seed formation of fibrils with monomers of a different protein (*yellow*), referred to as cross-seeding. Monomers might also follow the off-pathway and fold into oligomers (*beige*) and further into curvilinear fibrils (*dark blue*).

off-pathway oligomers and amyloid fibrils in the aggregation mechanism and in pathology is not yet explained sufficiently (43–45). Accordingly, the understanding of amyloid fibril formation and their structures still is of high importance, for example, to increase our knowledge about amyloidoses as well as exploiting potential applications for functional amyloids.

Notably, amyloid fibrils have many faces in that under the same conditions, the very same protein might aggregate into structurally different fibrils. This phenomenon is known as polymorphism. Polymorphism in amyloid fibrils can be found on at least two structural levels (Fig. 2*B*). First, protofilament polymorphism, which is mainly described on the secondary structure level of amyloids, namely their β-sheet conformation. Protofilament polymorphism can be subdivided into packing polymorphism (one monomer or protofilament exhibits different β-sheet bending) or segmental polymorphism (different sequence segments of the same peptide are part of the cross-β structure) (46, 47) (Fig. 2*C*). The second level of polymorphism might be described as ultrastructural polymorphism in which protofilaments assemble through different and/or multiple interfaces (Fig. 2*D*). Ultrastructural polymorphism is mainly based on the intermolecular interactions of mature fibrils or protofilaments (48). It can also encompass the defining parameters of amyloid fibrils such as rise, twist, width, and cross-over distance (Fig. 2*A*). While it was assumed that monomer structure can change within one fibril, it was recently described by Radamaker *et al.* (49) that these structural switches can occur multiple times within one fibril. These findings add even more complexity to the topic of amyloid fibril polymorphism.

Structure determination of amyloid fibrils

Although there have been many insights regarding both the diversity of amyloid fibrils and their commonly shared architecture, structural details on the atomic level remained hidden for a long time. The first high-resolution atomic structures of amyloid fibrils were published in the 2000s by means of solid-state NMR spectroscopy assisted by X-ray fiber diffraction and transmission electron microscopy (4, 50, 51). NMR and X-ray diffraction are established tools for protein structure determination, but when it comes to amyloid structures, they both show drawbacks. NMR requires high sample load and isotopic enrichment that often is expensive. Owing to the repetitive nature of amyloid fibrils, NMR signals are usually strong. But because amyloid fibril samples tend to be polymorphic, with NMR, it is hard to differentiate between less-populated polymorph species.

Amyloid crystals consist of small and untwisted fragments from amyloidogenic proteins (52) because crystallization of mature amyloid fibrils (Fig. 2*A*) is impossible. Hence, together with the start of the "resolution revolution" in cryo-EM, a new era began for our understanding of the structural features of amyloidogenic proteins in general and amyloid fibrils in particular. In 2017, the first high-resolution fibril structures of two of the main disease-related amyloids, tau and Aβ1-42, were solved by Fitzpatrick *et al.* (53) and Gremer *et al.* (54) using cryo-EM. With resolutions of 3.4, 3.5 Å (tau) and 4.0 Å (Aβ1-42), atomic model building with cryo-EM data became possible for the first time. Since then, over 70 amyloid cryo-EM structures have been published, most of which reach resolutions of 3 to 4 Å. This resolution allows for distinction of different folds within one sample and often also for atomic model building. However, higher resolutions will be important for identifying posttranslational modifications or cofactors and for a better understanding of, for example, secondary nucleation mechanisms. The atomic resolution barrier, for which the threshold is considered to be 1.2 Å (55), has already been broken in 2020 for large globular protein complexes by single-particle cryo-EM (56, 57). In the field of amyloid research, the highest resolution achieved so far is 2.3 Å (58). However, we are optimistic that the rapid progress in the field of sample preparation and structure determination of amyloid fibrils by cryo-EM will allow us to break the atomic resolution barrier in the future.

Development of cryo-EM

Cryo-EM is based on transmission electron microscopy, which has been developed in the late 1960s. Biological samples first came into play with the development of negative stain EM (59) that led to the first 3D structure of the extended tail of the T4 bacteriophage (60, 61). To no surprise, this sample exhibits helical symmetry because helical samples have two intrinsic

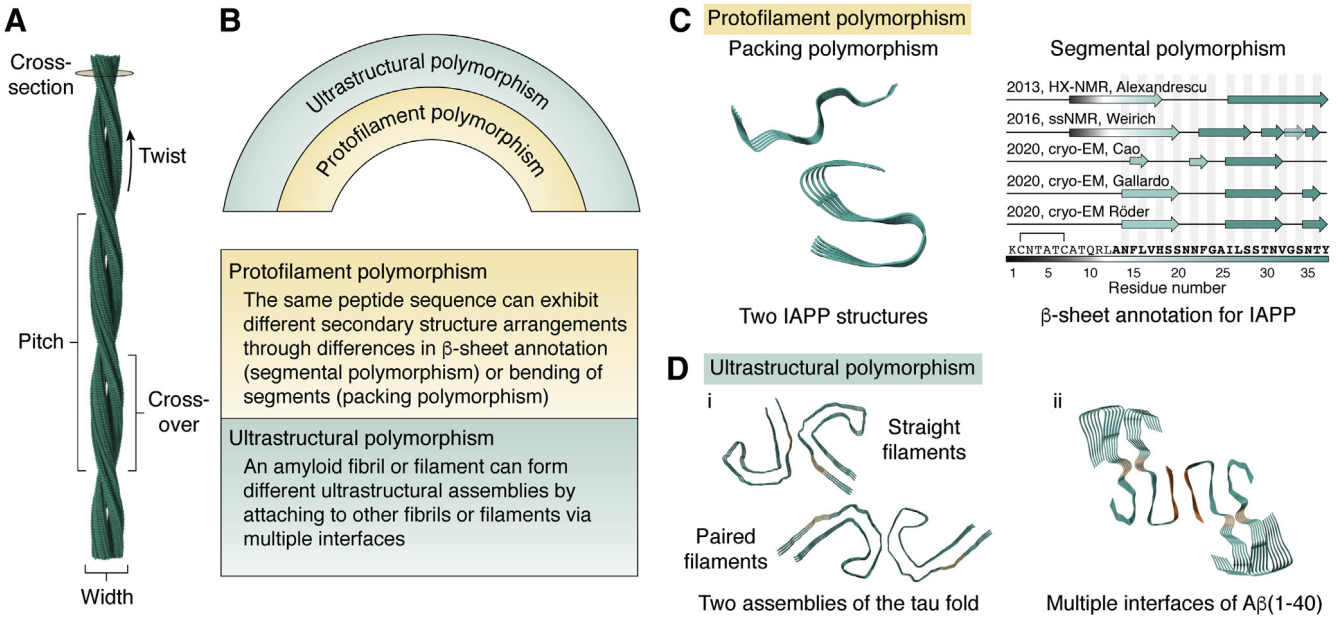

Figure 2. Polymorphism in amyloids. *A*, an amyloid fibril is characterized by the helical parameters twist and rise as well as characteristic measures such as the pitch, crossover, and width. The cross-section usually is shown to display molecular arrangement and polymorphism. *B*, two levels of polymorphism can be distinguished in amyloid fibrils that can occur in different compositions: protofilament polymorphism, which can be subdivided into segmental or packing polymorphism, and ultrastructural polymorphism. *C*, examples for protofilament polymorphism. Packing polymorphism is displayed by the example of islet amyloid polypeptide structures whose segments bend differently depending on pH. Segmental polymorphism has also been revealed for islet amyloid polypeptide as the assignment of β-sheets is different (87–89, 195, 196). *D*, examples of ultrastructural polymorphism. i, the general tau fold can exhibit different interfaces resulting in straight (*left*) or paired (*right*) helical filaments. ii, Aβ(1–40) reveals multiple interfaces (*beige* and *orange*) that result in double fibrils (47). Structures shown: 6Y1A (87), 6VW2 (88) (*C*); 6HRF, 6HRE (197) (*D*(i)); 6SHS (92) (*D*(ii)).

advantages over globular proteins: first, all necessary information is sufficiently provided by one single image, and second, the repeating asymmetrical units in a helical filament show fixed relative orientations. Relative orientations can be deduced from the helical symmetry parameters twist and rise (Fig. 2*A*) (62). Thus, the level of noise can be significantly decreased by averaging over many asymmetrical units (63, 64). For amyloid fibrils, the cross-β arrangement highly facilitates the determination of helical symmetry (65). However, the alignment along the helical axis is almost exclusively based on the 4.7 Å (meridian) signal caused by the cross-β pattern (stacking of several β-sheets along the fibril axis) and a 10 Å (equatorial) signal due to the horizontal interstrand distances within a molecule (66). The predominance of the 4.7 Å signal and the lack of larger structural features may complicate the high-resolution structure determination of amyloid fibrils (65).

Cryo-EM enables the imaging of radiation-sensitive samples under cryogenic conditions, which reduce radiation damage resulting from the interaction of the sample with high-energy electrons. The discovery of the advantages of samples frozen in vitreous ice (67, 68) together with the development of practical applications (69) drastically advanced the field of cryo-EM in general. But still, for years, cryo-EM has been mockingly referred to as "blobology" because the obtained resolutions have been rather low and the process itself was slow. In short, the development of direct electron detectors (70–72) as a replacement for photographic film or charged coupled device cameras led to a big leap in the field. The advancement of cryo-EM into a powerful and widely used tool in structural biology has also substantially been shaped by progress in computation. Because of their inherent advantages described above, helical structures were among the first to be described by cryo-EM (73–75). However, the computational development that made cryo-EM broadly applicable was the single-particle reconstruction, which is based on the groundwork of Joachim Frank (76). Together with a technique referred to as (Box 1) "projection matching" developed by Frank and Penczek (77) and the reconstitution method by Marin van Heel (78), which made sample tilting redundant, these techniques built the basis for today's software packages (https://www.emdataresource.org/emsoftware.html). According to Electron Microscopy Data Bank statistics, RELION (79) that implements a (Box 1) Bayesian approach to structure determination is the most used software contributing to nearly 50% of all released maps (https://www.ebi.ac.uk/pdbe/emdb/statistics_software.html/). In the field of helical reconstruction, major breakthroughs were the application of Fourier–Bessel principles to compute 3D models (60) and the development of the (Box 1) iterative helical real-space reconstruction method (80), which forms the basis of all popular reconstruction programs that are in use today.

In this review, we will focus on the combined growth of the cryo-EM and the amyloid field, especially in regard to computational or technical challenges and advances on amyloid fibril reconstruction (Fig. 3). We aim at clarifying the challenges we see in sample preparation of amyloid fibrils for cryo-EM and what (computational) difficulties are faced during

Box 1.

Glossary

Template matching

Template matching is an image-processing technique that can be used to find images similar to a template by maximizing the cross-correlation between the template and all images.

Convolutional neural network

Convolutional neural networks (CNNs) are a category of artificial neural networks mostly used in the field of image analysis; however, they can also be used for other data analysis tasks as well as classification problems. A CNN, which is inspired by biological processes, is specialized to pick or detect and interpret patterns.

Sliding-window approach

The sliding-window approach is often used in the implementation of a CNN. Here, the image is processed by sliding a rectangular window over the whole image to pass different portions of it through a CNN.

Projection matching

Projection images of an initial reference model are compared with the experimental EM images of the protein, and orientations are assigned based on the highest cross-correlation between projection images and experimental image.

Fourier–Bessel Inversion

The analysis of the helical symmetry as well as the calculation of a 3D reconstruction are conducted in Fourier space. The approach is based on Klug's theory of diffraction patterns of helical structures (192) and Cochran's interpretation of helical filaments as curled-up 2D lattices in Fourier space (193).

Single-particle approach to helical reconstruction

The single-particle approach to helical reconstruction provides an alternative to Fourier–Bessel inversion. The image of a helical protein is divided into equally sized overlapping segments that are treated as individual images, analogous to single particles. Relative orientations of segments are determined by projection matching.

Iterative helical real-space reconstruction algorithm

The algorithm (80) uses the single-particle approach to helical reconstruction and iteratively carries out the steps of projection matching. In-between iterations, the helical symmetry is imposed onto the reconstructed volume that is used as a reference in the next iteration. This way, the density map is optimized in every iteration.

Bayesian approach to structure determination

An image does not get assigned a single orientation but an entire distribution of weighted orientations (the likelihood function). In the Bayesian formalism, this likelihood can be combined with prior knowledge about parameters (*e.g.*, a range of orientations that we think is relevant). This procedure leads to a more robust optimization and allows for a more formal treatment of prior knowledge and errors (64, 194).

reconstruction. In addition, we are taking a closer look at recent technical advances in both sample preparation as well as 3D reconstruction. Finally, we conclude with future developments that might help moving the field of amyloid structure research forward. This review aims to make researchers in the field of amyloid aggregation as well as cryo-EM scientists aware of the intricacies and challenges in cryo-EM structure determination of amyloids and encourage method developers to help with new tools. For further information on amyloids in general, we would like to refer to recent excellent reviews by Iadanza *et al.* (13) and Ke *et al.* (52).

Main text

Sample preparation for amyloids moves closer to in vivo *conditions*

For cryo-EM, the sample protein does not have to be isotope-labeled (NMR) or crystallized and treated with special crystallization screening solutions (X-Ray) to prepare a usable sample. However, also for cryo-EM, the sample preparation needs to be optimized to find conditions that not only lead to thin ice and a favorable particle distribution but also result in stable and homogeneous proteins or protein complexes. This is also true for amyloid fibrils, for which a major challenge during sample preparation is to ensure the formation of individual, well separated but sufficiently concentrated single fibrils.

In general, sufficient protein stability can be very difficult to achieve for globular proteins and membrane proteins in particular. In contrast, the mature amyloid fibril state is considered very stable (81–83). But the understanding of the fibril formation process is elusive and buffer conditions including but not limited to pH, salt concentration, temperature, and pressure are believed to have a strong impact on aggregation pathways of amyloids into either rigid, mature fibrils or curvilinear (proto-)fibrils and oligomers (84) (Fig. 1). In addition, small differences in the buffer system or introduction of physical forces (*e.g.*, beads) might change aggregation kinetics (27, 85, 86) or induce the formation of ultrastructrual polymorphs (87–89).

However, which polymorphs actually appear *in vivo* and are disease-relevant remains an important question (Fig. 3*E* left). Consequently, one approach is to work with *ex vivo* samples that are extracted from tissue (90, 91) (Fig. 3*A*). But purification from cells or organs is challenging especially because of amyloid properties such as the lack of known specific binding partners that could be used for purification. Amyloid species tend to clump, which makes them usually very inhomogeneous in size and hard to separate from other cell components. Moreover, amyloid fibrils can be found as single fibrils of different lengths or as fibril bundles of different mass, for example, Aβ plaques in AD. *In vivo*, there often are several species of one amyloidogenic precursor protein (*e.g.*, Aβ1-42, Aβ1-40, Aβ2-42, etc., in AD (92)) in an inhomogeneous, polymorphic mixture. While polymorphs can already be quite difficult to be distinguished on micrographs, differences in the monomer length might be even more difficult to distinguish if they do not form very different polymorphs. In addition, amyloid formation *in vivo* might result in structural bias because the distinct, probably patient-dependent, environment could lead to preferred formation of one polymorph over another. Structural bias could be introduced as well through harsh extraction conditions that could potentially alter at least the solvent-exposed parts of a fibril. In 2016, Annamalai *et al.* (93) described ultrastructural features of patient-derived fibrils. Although the number of high-resolution *ex vivo* structures has

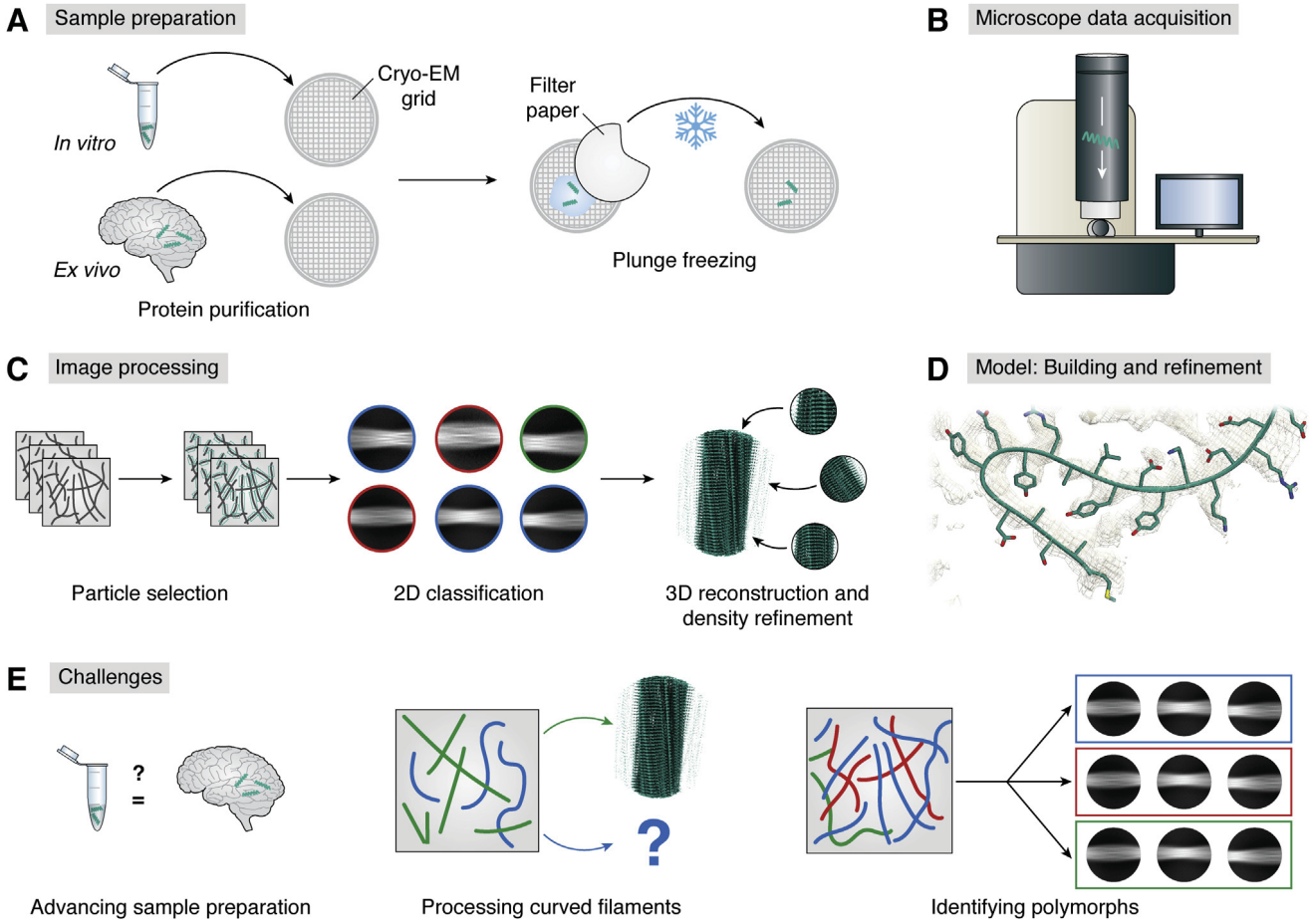

Figure 3. Cryo-EM workflow. *A*, followed by protein purification, the purified sample in the solution is applied onto the cryo-EM grid (sample carrier), and excess buffer is blotted off using filter paper (*white shape*). In a subsequent step, the sample is plunge-frozen in a thin layer of vitreous ice. *B*, a dataset is collected after screening and assessment of the vitrified cryo-EM grids at a cryo-electron microscope equipped with a direct electron detector. *C*, image processing of the acquired data involves several steps, major ones being particle selection, 2D classification, as well as 3D reconstruction and refinement of the density map. Amyloid fibrils are selected from the preprocessed (*e.g.*, motion-corrected and contrast transfer function-estimated) micrographs. In the following step of particle extraction, selected fibrils are segmented into so-called particle images. Subsequently, in 2D classification, particles that show similar views of the protein are grouped together, thereby improving the signal-to-noise ratio. Two-dimensional classes that show invalid or contaminated data are removed from the dataset. In a next step, particles from 2D classes are used to calculate 3D density maps. *D*, as soon as a high-resolution reconstruction is obtained, an atomic model can be built and refined. *E*, challenges in amyloid structure determination: advanced sample preparation approaches (*left*), processing curved filaments (*center*), and identification of polymorphs as part of the automated particle selection process (*right*).

been continuously growing since (53, 58, 92, 94–99), it remains challenging to use tissue-extracted amyloid fibril material for use in cryo-EM. As a workaround, patient-extracted tissues have been used to seed fibril growth for subsequent structural studies (90, 100, 101). Here, monomers of the amyloidogenic proteins are added in excess to homogenized tissue to amplify the existing *ex vivo* fibrils. This procedure is based on the assumption that the existing aggregates in the tissue will seed the growth of aggregates, fibrils in particular, of the same polymorph (101–103). The observed amplified sample is thus not directly taken from human tissue but is a more indirect representation of *in vivo* structures than *ex vivo* structures.

Interestingly, none of the few known *ex vivo* fibril structures have been observed either *in vitro* or in amplified patient-derived samples, yet (99, 104). Nonetheless, *in vitro* structures have broadened our understanding of amyloid architecture in general and revealed common structural features such as the amyloid key, which has been observed *in vitro* and *in vivo* and they furthermore help interpret aggregation kinetics (105, 106). Moreover, *in vitro* structures provided valuable insights regarding the improvement of fibril preparation and fibril reconstruction. Although the example of an amyloid key shows general overarching patterns, the transferability of *in vitro* data to the mechanisms and structures forming in organisms remains unclear. Hence, one future goal is to enable the *in vitro* production of disease-relevant amyloid aggregates (not necessarily restricted to fibrils), which are needed to study the molecular disease mechanism and facilitate drug development, by reproducing *in vivo* findings in the test tube. Notably, several of the *ex vivo* structures show incorporation of small molecules, which very likely are important for stabilizing the observed polymorph. Reproducing the *ex vivo* polymorphs would therefore require to identify these cosolutes and add them to *in vitro* fibrillization assays. Without better knowledge of the *in vivo* fibrillization conditions, it will therefore be very difficult to form the polymorphs

that are, for example, involved in disease progression, in *in vitro* experiments.

The same holds true for amyloids consisting of more than one protein. Until now, amyloid fibril structures have been exclusively determined from a single sort of protein, although coaggregation (107) of different amyloidogenic proteins has been described.

Amyloid fibrils could benefit from novel vitrification tools

Plunge-freezing (Fig. 3*A*) was first established as a manual technique (68, 69). Later, automated and commercial plunging tools were developed (*e.g.*, the Vitrobot (108)), with the goal to achieve reproducibly good ice thickness, less contaminations, and homogeneous vitrification of the sample. Newer developments of grid preparation devices mostly aim to replace the blotting step, which is hard to control precisely, leads to nonuniform ice thickness, and adds significantly to the lack of proper reproducibility (109).

For amyloid fibrils, we often observe that sample concentrations on the grid vary drastically between replicates of the same origin concentration, which might be caused by blotting. Blotting could affect helical structures more than single particles because an attachment of one part of a filament to the blotting paper could potentially remove a whole network of filaments from the grid. Furthermore, the large hydrodynamic forces exert considerable stress that could affect filaments and fibrils. And again, this stress can be expected to affect filaments much more than individual globular protein complexes because filaments extend over longer distances. For example, the filament variability (such as filament twist) and also the subunit conformation of F-actin have been shown to be susceptible to forces on the filament (110–112). How much these hydrodynamic forces affect the structure of amyloid fibrils remains to be studied.

The Chameleon system (introduced under the name Spotiton (113–116)) transfers a drop of picolitre volume onto the EM grid automatically. The use of such a small sample volume makes the step of blotting unnecessary, which could be of advantage for sample preparation of amyloid fibrils as explained above. Similarly, the cryoWriter (117–119) only needs some nanolitres of sample and uses a microcapillary to apply the sample to the grid while the grid is moving (hence "writer"). An IR laser controls for the perfect film thickness before plunge-freezing automatically (120). During the process, the cryoWriter does not create aerosols during the application step, which is important for amyloid samples, where there are hints toward the transmissibility of disease *via* protein samples. Experiments with mice showed that Aβ pathology can be transferred from human tissue samples through intracerebral inoculation of pathogenic amyloid (121). The study was based on former findings of initial evidence for Aβ transmission *via* neurosurgery (122, 123). On the other hand, retrospective studies show no increased risk for AD from blood transfusions in-between humans (124, 125). However, because the infectiousness of amyloid samples is unclear, precautions should be taken when handling these samples.

Comparable with the process of 3D printing, the VitroJet (126, 127) "prints" the sample solution onto the EM grid in a layer thin enough to make the blotting step obsolete. Instead of plunge-freezing, the cryogen is sprayed onto the grid directly, which shall ensure faster and more homogenous vitrification that would be advantageous for all kinds of samples.

An affordable DIY grid preparation device has been introduced by Rubinstein *et al.* (128) with the Shakeit-off. It is based on a simple USB ultrasonic humidifier that sprinkles the sample across a self-wicking nanogrid (129, 130) before subsequent vitrification. Owing to the undirected spreading of the sample and the production of aerosols, the system would need further adaptation to shield the user from the spread of hazardous samples.

Some of the grid preparation devices mentioned above and their ability to improve the distribution within the air–water interface have been analyzed by Klebl *et al.* (131). Other techniques (108, 115, 118, 127, 128) and sprayer designs (132) proposed in the last years are yet not widely used and thus will have to prove their practicality on amyloid samples in the future. It would also be an additional benefit if the next generation of plunge-freezing devices were able to orientate or align filaments on the grid because identical orientations of fibrils would facilitate particle picking and subsequent 3D reconstruction.

Automated (pre-)processing is on the rise for filaments

Because of the variety of cryo-EM software and complexity of settings, structure determination with cryo-EM data is highly dependent on individual skills and expert knowledge (133). Automated (pre-)processing, including all steps between data acquisition and 3D reconstruction (Fig. 3, *B* and *C*), might help making the technique more widely accessible (134). Commonly used software packages that include automated preprocessing steps are, for example, cryoSPARC (135), SPHIRE (136), and RELION 3.1 (79).

Amyloid fibril reconstructions are challenging and usually require extensive manual work. One reason for this is that the 4.7 Å-spaced cross-β pattern is very dominant and creates many false local optima during the simultaneous determination of particle orientation and helical symmetry parameters. For example, the directions of fibrils, described by the psi angle, usually converge rather slowly. Furthermore, because the fibril twist is energetically not strongly restrained, variations in helical symmetry can occur between different fibrils and even along a single fibril. In addition, the data often show different polymorphs with only small structural differences that are difficult to sort out (100).

Particle selection from electron micrographs lays the groundwork for a high-resolution reconstruction. Manual picking of particles is still considered the most accurate way of particle selection although it is very time consuming, especially for large datasets. There are various software tools that implement an algorithm for (semi-) automated particle selection mostly based on (Box 1) template matching (137–140) or (Box 1) convolutional neural networks (CNNs) (141–145).

Typically, in a first step, a small subset of the entire dataset needs to be picked manually either to train the CNN or to generate template images. Subsequently, automated particle picking of the entire dataset can be performed. For data with grid-like topology, CNN-based methods are lately the best choice for pattern recognition and object detection. While most tools that implement CNNs are based on the so-called (Box 1) sliding-window approach, crYOLO (143) implements the deep-learning object detection system You Only Look Once (YOLO) (146). In contrast to the computationally expensive sliding-window approach, the YOLO algorithm speeds up calculations to six micrographs per second on one graphics processing unit. In the future, this might be supported by the automated particle-diameter estimation by Li *et al.* (134), a single-particle tool that performs automatic particle-diameter estimation and supersedes the training need for crYOLO by determination of the correct box size for picking through a trial-and-error approach. Automatic picking of amyloid fibrils remains challenging because of the need of avoiding the selection of crossings and overlaps of fibrils as well as the start- and end-point of a fibril not necessarily being visible on the image frame. Recently, filament selection has been implemented in crYOLO (147), and it may open the door for the transition from time-consuming manual particle selection to automated selection also in the field of amyloid fibril structure determination.

Recently, Thurber *et al.* (148) presented FibrilFinder, an approach to fully automated particle selection without requiring prepicking of the dataset. Although the algorithm avoids picking fibrils on carbon, it cannot detect intersections of fibrils. Subsequent use of their program FibrilFixer, which can be applied after particle extraction, discards particle images that show fibril intersections. The latter one could also be a helpful stand-alone tool after manual particle selection. Here, picking intersections is usually avoided, and as a result, one fibril is split into several smaller fibril segments, causing a loss of information about angular correlations. Recovering this information could facilitate image alignment. Both FibrilFinder and FibrilFixer are directly compatible with RELION-3.1, making them easy to integrate into the image processing workflow.

MicHelixTrace (149), which is available in the SPRING (150) software suite, locates helical filaments on micrographs by using a 2D class average as the reference image. The detection of filament positions on the micrographs is based on a cross-correlation map that is generated by the determination of the rotation and translation of small, straight fibril segments relative to the reference image. Moreover, the program determines the persistence length of each filament, which may be used to characterize mechanical properties and assess the potential for the reconstruction to reach high resolution.

In the last few years, major steps in the field of automated (pre-)processing have improved the workflow. For globular proteins, automated selection often is not only faster but possibly even more precise than manual particle selection. Similarly, automation tools already assist in the preprocessing of amyloid reconstruction; however, it is not yet expedient to perform entirely automated processing. At least at the current stage, where, for example, automated selection of helical filaments still suffers from inaccuracies such as insufficient identification of different polymorphs, manual inspection of the results is indispensable.

New tools facilitate initial model generation

As mentioned above, the search for orientation and helical symmetry parameters suffers from many false local optima (151). Determination of a robust initial estimate of the 3D structure greatly facilitates subsequent density refinement and image classification (Fig. 3*C*). RELION 3.1 offers a novel approach to calculate an initial 3D model *de novo* (65). The model can be calculated either from one 2D reference-free class average that shows an entire crossover or from several class averages that, given some additional information, can be combined to calculate an initial 3D density. Another method to produce an initial model by combining several 2D class averages was presented by Ghosh *et al.* (101) in their structural study of an Aβ polymorph from AD brain tissue. Moreover, introducing additional orientation parameter regularization avoids local optima. Ghosh *et al.* (101) used a modified version of the software package RELION 3.0 beta (79) for 3D reconstruction.With their modifications, angular restraints between neighboring segments from the same fibril were introduced to make the image alignment during 3D reconstruction in RELION 3.0 more robust and consistent. In addition, a method to increase the precision of the 2D alignment before moving to the step of 3D reconstruction was introduced.

Curvature of amyloid fibrils remains a challenge in 3D reconstruction

Amyloid fibrils tend to be flexible and therefore rarely appear as straight filaments on electron micrographs. Especially, long fibrils tend to be entangled in a fibril network and have a higher chance of interacting with surfaces. They are more susceptible to hydrodynamic forces and therefore cannot as easily relax into a straight conformation as short fibrils. However, for classical helical reconstruction, it is necessary to use the straight parts of a fibril because the applied helical symmetry ignores bending, which can limit the resolution (Fig. 3*E* center). The resolution could also be further improved when releasing the symmetry altogether during the refinement and treat segments of the fibrils as single, independent particles (152). If the fibrils are strongly curved, the total amount of usable data could be limited because strongly curved regions of the fibrils need to be excluded from processing. To include bent filaments, Ohashi *et al.* (153) introduced a novel soft-body model for 3D reconstruction instead of the classical rigid body. Through introduction of hidden parameters, which define the curvature of a fibril, it allows for optimization of 3D reconstruction based on Bayesian inference.

Amyloid structure determination requires polymorph identification

The morphological composition of an amyloid fibril sample is a valuable information which shows the structural diversity of an amyloidogenic protein and its sensitivity to environmental conditions. As of now, the image processing (Fig. 3*C*) of different polymorphs is performed separately comparable with the processing of different protein conformations. As a consequence, the application of tools for automatic particle selection on highly heterogeneous datasets of amyloid fibrils is severely limited because even the most accurate algorithms still fail to distinguish between different polymorphs (Fig. 3*E* right). Thus, fibril characteristics such as the fibril diameter and the cross-over distance (Fig. 2*A*) are usually determined manually, for example, from 2D classes (154) or micrographs. Interestingly, two different monomer folds, which were observed within one fibril polymorph, could be separated in 3D classification for a sample from amyloid light-chain amyloidosis (49). However, the separation of different morphologies by hand is a laborious and error-prone task. But, manual polymorph selection can be facilitated by gold nanoparticles that have been shown to attach to the surface of a large variety of amyloid fibrils and hence can be used for fibril characterization (155). With their small size and high electron density, these gold nanoparticles make helical characteristics such as pitch and crossovers well visible in electron micrographs and hence allow for easy differentiation between polymorphs (Fig. 2).

An alternative and less-laborious approach to manual selection is the automated detection of cross-overs in images of amyloid fibrils, which can be achieved by applying conventional computer vision techniques combined with machine learning approaches (156). This method enables the statistical analysis of the sample and thus gives insights into its morphological composition. However, it is yet not possible to incorporate automatic crossover detection into the processing workflow in a way that datasets can be separated into subsets of different polymorphs automatically. The latter can be achieved by applying Clustering of Helical Polymers (CHEP) (157, 158), an algorithm which clusters polymorphs into homogeneous groups, each representing one polymorph through its conformation, composition, and/or helical symmetry. The polymorph separation is achieved by the combination of 2D classification results and information about the association of a particle image to the originate fibril. Hence, automated particle selection for amyloid fibrils may be facilitated by CHEP, separating the original dataset into homogeneous subdatasets. In addition, the method can likewise be used for statistical analysis of the morphological composition of the sample. Moreover, by applying CHEP to amyloid datasets, the final resolution might increase because for low-contrast micrographs, the manual separation of one dataset into homogeneous subsets is difficult. Here, errors are likely to be introduced because of incorrect picking, which inevitably causes a decrease in the final resolution of the reconstruction. Hence, to be able to compute a high-resolution reconstruction, it is of major importance to detect different polymorphs with high precision. Especially, for small structural differences between different polymoprhs, it is therefore desirable to develop tools that can either assist in manual identification or enable the use of automatic selection tools, which until now lack sensitivity to select different polymorphs separately.

Outlook

Time-resolved cryo-EM for understanding amyloid formation

After the ground-breaking work by Nigel Unwin (159) that introduced time-resolved cryo-EM, recent developments further pushed time-resolution to the order of milliseconds by mixing reactants with microfluidics devices (160, 161). For vitrification, the chameleon system has recently been modified to prepare samples for time-resolved cryo-EM (162). However, amyloid aggregation is a rather slow process and usually occurs on the time scale of minutes up to weeks and would therefore not even require sophisticated sample preparation methods. It is usually possible to simply prepare grids at many time points during the aggregation process, thereby creating snapshots of the structural evolution of different aggregates and polymorphs. Such a time-dependent analysis of amyloid formation has, however, not been extensively exploited so far. Observing the time evolution of the distribution of aggregating amyloids as, for example, a shift in the oligomer to fibril ratio over the course of minutes to days or appearance of different polymorphs with different kinetics and potential transient aggregates would be very insightful to understand the aggregation pathways and aggregation mechanisms and how different species are connected. Even negative-stain EM could yield valuable information on the structural landscape at low resolution. The main challenge is, however, the structural heterogeneity, which makes it difficult to identify specific polymorphs and to separate them during the image processing, in particular for polymorphs that are only weakly populated.

Heterogeneous amyloid aggregates will be future cryo-EM targets

Since 2017, the number of high-resolution structures of amyloid fibrils has increased rapidly, while at the same time the amyloid field has made great progress in describing the formation of different amyloids. It is common agreement that amyloids form through several pathways that include monomeric self-assembly (163–165), secondary nucleation (166), and (cross-)seeding (167) (Fig. 1). While the amyloid structures we know to date are based on monomeric self-assembly or homonuclear seeding, other pathways are much more difficult to observe because of their comparably low occurrence. Although cryo-EM experiments could show secondary nucleation on an ultrastructural level (168), high-resolution details of this process are still lacking. First insights might be given by an interesting cryo-EM structure of amylin comprising two identical and one different protofilament that has recently been described and possibly is showing secondary nucleation (89). On the other hand, cryo-electron tomography (cryo-ET) in combination with cryo-focused ion beam milling

can give much more insight into irregular and heterogeneous aggregates, especially in a cellular environment as, for example, described by Bäuerlein *et al.* (169) who visualized polyglutamine inclusions from Huntington's disease in neurons. In addition, cryo-ET might also shed some light on amyloid fibrils that do not show any apparent twist (170). A missing twist could be an inherent property of a fibril but also an artifact from a close contact or attachment to the air–water interface (171). Structures of amyloid fibrils without twist (100, 106) lack helical symmetry and therefore cannot be solved using standard helical reconstruction techniques.

Interestingly, there have been indications that certain amyloidoses may trigger each other's progression as, for example, for T2D and Parkinson's disease (172, 173) or AD (174). Hence, the cross-seeding ability of the respective disease-associated proteins has been examined and confirmed (175–177). Structural data on this phenomenon would be of high impact and could potentially be observed using cryo-ET.

Recent interest in structure determination of oligomeric amyloid species

In recent years, the toxic oligomer hypothesis (41, 178–180), which states that small, soluble oligomers are the most toxic amyloid species, has gained popularity. These soluble oligomers are therefore high up on the list of potential drug targets for several neurodegenerative diseases. There is therefore a strong interest in determining structures of amyloid oligomers for rational drug development to either prevent oligomer formation or disassemble them (181, 182), develop diagnostic tools based on oligomers (183), or evaluate the failing of previous drug candidates targeting oligomeric states (184, 185). It is of great interest to understand how monomers fold into oligomers and what the structural difference is between oligomers that are on-pathway toward fibril formation and those oligomers that do not further evolve into fibrils (36, 186, 187) (Fig. 1). However, because oligomers are structurally highly heterogeneous with a high variability in size and shape, it is challenging to determine their structure, but it might be possible to study them by cryo-EM. *In situ* structure determination by cryo-ET allows the analysis of aggregation processes of heterogenous samples and rare species in their cellular context by examining, for example, cellular sections. It is currently applied for amyloids (169, 188), and we assume it will play an important role in oligomer research in the future, if it improved in resolution. On the other hand, single-particle cryo-EM already delivers high-resolution structures, and *in vitro* oligomeric species such as the dimAβ construct, a toxic Aβ oligomer that forms homogeneously and reproducibly out of Aβ dimers (189), could work in favor of cryo-EM measurements. For visualization of small proteins, the usage of fragment antigen binding has been established (190) and applied for amyloid fibrils already (191). Likewise, fragment antigen binding could enhance the visibility of small oligomeric species in cryo-EM datasets by increasing the total complex size and introducing a reoccurring feature for alignment.

Summary

The last years have shown that amyloid fibrils can be very well studied by cryo-EM even to high-resolution, which has provided exciting new insight into the architecture of amyloid fibrils. We have shown that cryo-EM of amyloid fibrils benefit from several recent technological advances. The apparent discrepancy of *ex vivo* and *in vitro* structures shows that we have not yet sufficiently understood how to mimick the physiological conditions for fibril formation *in vitro*, which remains an important next question to be answered. Finally, the structure of other aggregates such as toxic oligomers will hopefully soon complement our picture of amyloids.

Author contributions—M. Z., C. R., and G. F. S. conceptualization; M. Z. and C. R. writing–original draft; M. Z., C. R., and G. F. S. writing–review and editing; G. F. S. supervision.

Conflict of interest—The authors declare that they have no conflicts of interest with the contents of this article.

Abbreviations—The abbreviations used are: Aβ, amyloid β; AD, Alzheimer's disease; CHEP, Clustering of Helical Polymers; CNNs, convolutional neural networks; cryo-ET, cryo-electron tomography; T2D, type II diabetes; YOLO, You Only Look Once.

References

1. Anfinsen, C. B. (1973) Principles that govern the folding of protein chains. *Science* **181**, 223–230
2. Chiti, F., and Dobson, C. M. (2006) Protein misfolding, functional amyloid, and human disease. *Annu. Rev. Biochem.* **75**, 333–366
3. Sunde, M., Serpell, L. C., Bartlam, M., Fraser, P. E., Pepys, M. B., and Blake, C. C. (1997) Common core structure of amyloid fibrils by synchrotron X-ray diffraction. *J. Mol. Biol.* **273**, 729–739
4. Petkova, A. T., Ishii, Y., Balbach, J. J., Antzutkin, O. N., Leapman, R. D., Delaglio, F., and Tycko, R. (2002) A structural model for Alzheimer's β-amyloid fibrils based on experimental constraints from solid state NMR. *Proc. Natl. Acad. Sci. U. S. A.* **99**, 16742–16747
5. Geddes, A. J., Parker, K. D., Atkins, E. D. T., and Beighton, E. (1968) "Cross-β" conformation in proteins. *J. Mol. Biol.* **32**, 343–344. IN23, 345-358
6. Cohen, A. S. (1986) General introduction and a brief history of the amyloid fibril. In: Marrink, J., Van Rijswijk, M. H., eds. *Amyloidosis*, Nijhoff, Dordrecht, The Netherlands: 3–19
7. Virchow, R. (1854) Weitere Mittheilungen über das Vorkommen der pflanzlichen Cellulose beim Menschen. *Arch. Pathol. Anat. Physiol. Klin. Med.* **6**, 268–271
8. Virchow, R. (1854) Ueber eine im Gehirn und Rückenmark des Menschen aufgefundene Substanz mit der chemischen Reaction der Cellulose. *Arch. Pathol. Anat. Physiol. Klin. Med.* **6**, 135–138
9. Friedreich, N., and Kekulé, A. (1859) Zur Amyloidfrage. *Arch. Pathol. Anat. Physiol. Klin. Med.* **16**, 50–65
10. Missmahl, H. P., and Hartwig, M. (1953) Polarisationsoptische untersuchungen an der amyloid substance. *Virchows Arch. Pathol. Anat.* **324**, 489–508
11. Puchtler, H., Sweat, F., and Levine, M. (1962) On the binding of Congo red by amyloid. *J. Histochem. Cytochem.* **10**, 355–364
12. Sipe, J. D., Benson, M. D., Buxbaum, J. N., Ikeda, S. I., Merlini, G., Saraiva, M. J. M., and Westermark, P. (2016) Amyloid fibril proteins and amyloidosis: Chemical identification and clinical classification International Society of Amyloidosis 2016 Nomenclature Guidelines. *Amyloid* **23**, 209–213

13. Iadanza, M. G., Jackson, M. P., Hewitt, E. W., Ranson, N. A., and Radford, S. E. (2018) A new era for understanding amyloid structures and disease. *Nat. Rev. Mol. Cell Biol.* **19**, 755–773
14. Murphy, M. P., and Levine, H. (2010) Alzheimer's disease and the amyloid-β peptide. *J. Alzheimers Dis.* **19**, 311–323
15. Polymeropoulos, M. H., Lavedan, C., Leroy, E., Ide, S. E., Dehejia, A., Dutra, A., Pike, B., Root, H., Rubenstein, J., Boyer, R., Stenroos, E. S., Chandrasekharappa, S., Athanassiadou, A., Papapetropoulos, T., Johnson, W. G., *et al.* (1997) Mutation in the α-synuclein gene identified in families with Parkinson's disease. *Science* **276**, 2045–2047
16. Stefanis, L. (2012) α-Synuclein in Parkinson's disease. *Cold Spring Harb. Perspect. Med.* **2**, a009399
17. Johnson, K. H., O'Brien, T. D., Betsholtz, C., and Westermark, P. (1989) Islet amyloid, islet-amyloid polypeptide, and diabetes mellitus. *N. Engl. J. Med.* **321**, 513–518
18. Baker, K. R., and Rice, L. (2012) The amyloidoses: Clinical features, diagnosis and treatment. *Methodist Debakey Cardiovasc. J.* **8**, 3–7
19. Astbury, W. T., and Street, A. (1931) X-ray studies of the structure of hair, wool, and related fibres.- I. General. *Philos. Trans. R. Soc. A* **230**, 75–101
20. Guijarro, J. I., Sunde, M., Jones, J. A., Campbell, I. D., and Dobson, C. M. (1998) Amyloid fibril formation by an SH3 domain. *Proc. Natl. Acad. Sci. U. S. A.* **95**, 4224–4228
21. Adler-Abramovich, L., Vaks, L., Carny, O., Trudler, D., Magno, A., Caflisch, A., Frenkel, D., and Gazit, E. (2012) Phenylalanine assembly into toxic fibrils suggests amyloid etiology in phenylketonuria. *Nat. Chem. Biol.* **8**, 701–706
22. Loquet, A., Saupe, S. J., and Romero, D. (2018) Functional amyloids in health and disease. *J. Mol. Biol.* **430**, 3629–3630
23. Fowler, D. M., Koulov, A. V., Alory-Jost, C., Marks, M. S., Balch, W. E., and Kelly, J. W. (2006) Functional amyloid formation within mammalian tissue. *PLoS Biol.* **4**, 0100–0107
24. Fowler, D. M., Koulov, A. V., Balch, W. E., and Kelly, J. W. (2007) Functional amyloid - from bacteria to humans. *Trends Biochem. Sci.* **32**, 217–224
25. Pham, C. L. L., Kwan, A. H., and Sunde, M. (2014) Functional amyloid: Widespread in nature, diverse in purpose. *Essays Biochem.* **56**, 207–219
26. Zurdo, J., Guijarro, J. I., Jiménez, J. L., Saibil, H. R., and Dobson, C. M. (2001) Dependence on solution conditions of aggregation and amyloid formation by an SH3 domain. *J. Mol. Biol.* **311**, 325–340
27. Vettore, N., and Buell, A. K. (2019) Thermodynamics of amyloid fibril formation from chemical depolymerization. *Phys. Chem. Chem. Phys.* **21**, 26184–26194
28. Ow, S.-Y., and Dunstan, D. E. (2013) The effect of concentration, temperature and stirring on hen egg white lysozyme amyloid formation. *Soft Matter* **9**, 9692–9701
29. Annamalai, K., Liberta, F., Vielberg, M.-T., Close, W., Lilie, H., Gührs, K.-H., Schierhorn, A., Koehler, R., Schmidt, A., Haupt, C., Hegenbart, U., Schönland, S., Schmidt, M., Groll, M., and Fändrich, M. (2017) Common fibril structures imply systemically conserved protein misfolding pathways *in vivo*. *Angew. Chem. Int. Ed. Engl.* **56**, 7510–7514
30. Picotti, P., De Franceschi, G., Frare, E., Spolaore, B., Zambonin, M., Chiti, F., de Laureto, P. P., and Fontana, A. (2007) Amyloid fibril formation and disaggregation of fragment 1-29 of apomyoglobin: Insights into the effect of pH on protein fibrillogenesis. *J. Mol. Biol.* **367**, 1237–1245
31. Page, L. J., Ji, Y. S., Huff, M. E., Lim, H. J., Venable, J., Yates, J., Kelly, J. W., and Balch, W. E. (2005) Metalloendoprotease cleavage triggers gelsolin amyloidogenesis. *EMBO J.* **24**, 4124–4132
32. Li, G. H., Arora, P. D., Chen, Y., Mcculloch, C. A., and Liu, P. (2012) Multifunctional roles of gelsolin in health and diseases. *Med. Res. Rev.* **32**, 999–1025
33. Lomakin, A., Chung, D. S., Benedek, G. B., Kirschner, D. A., and Teplow, D. B. (1996) On the nucleation and growth of amyloid beta-protein fibrils: Detection of nuclei and quantitation of rate constants. *Proc. Natl. Acad. Sci. U. S. A.* **93**, 1125–1129
34. Serrano-Pozo, A., Frosch, M. P., Masliah, E., and Hyman, B. T. (2011) Neuropathological alterations in Alzheimer disease. *Cold Spring Harb. Perspect. Med.* **1**, a006189
35. Drummond, E., Nayak, S., Faustin, A., Pires, G., Hickman, R. A., Askenazi, M., Cohen, M., Haldiman, T., Kim, C., Han, X., Shao, Y., Safar, J. G., Ueberheide, B., and Wisniewski, T. (2017) Proteomic differences in amyloid plaques in rapidly progressive and sporadic Alzheimer's disease. *Acta Neuropathol.* **133**, 933–954
36. Hasecke, F., Miti, T., Perez, C., Barton, J., Schölzel, D., Gremer, L., Grüning, C. S. R., Matthews, G., Meisl, G., Knowles, T. P. J., Willbold, D., Neudecker, P., Heise, H., Ullah, G., Hoyer, W., *et al.* (2018) Origin of metastable oligomers and their effects on amyloid fibril self-assembly. *Chem. Sci.* **9**, 5937–5948
37. Modler, A. J., Gast, K., Lutsch, G., and Damaschun, G. (2003) Assembly of amyloid protofibrils via critical oligomers - a novel pathway of amyloid formation. *J. Mol. Biol.* **325**, 135–148
38. Ehrnhoefer, D. E., Bieschke, J., Boeddrich, A., Herbst, M., Masino, L., Lurz, R., Engemann, S., Pastore, A., and Wanker, E. E. (2008) EGCG redirects amyloidogenic polypeptides into unstructured, off-pathway oligomers. *Nat. Struct. Mol. Biol.* **15**, 558–566
39. Ono, K., Condron, M. M., and Teplow, D. B. (2009) Structure-neurotoxicity relationships of amyloid β-protein oligomers. *Proc. Natl. Acad. Sci. U. S. A.* **106**, 14745–14750
40. Bucciantini, M., Giannoni, E., Chiti, F., Baroni, F., Formigli, L., Zurdo, J., Taddei, N., Ramponi, G., Dobson, C. M., and Stefani, M. (2002) Inherent toxicity of aggregates implies a common mechanism for protein misfolding diseases. *Nature* **416**, 507–511
41. Benilova, I., Karran, E., and De Strooper, B. (2012) The toxic Aβ oligomer and Alzheimer's disease: An emperor in need of clothes. *Nat. Neurosci.* **15**, 349–357
42. Cline, E. N., Bicca, M. A., Viola, K. L., and Klein, W. L. (2018) The amyloid-β oligomer hypothesis: Beginning of the third decade. *J. Alzheimers Dis.* **64**, S567–S610
43. Treusch, S., Cyr, D. M., and Lindquist, S. (2009) Amyloid deposits: Protection against toxic protein species? *Cell Cycle* **8**, 1668–1674
44. Zraika, S., Hull, R. L., Verchere, C. B., Clark, A., Potter, K. J., Fraser, P. E., Raleigh, D. P., and Kahn, S. E. (2010) Toxic oligomers and islet beta cell death: Guilty by association or convicted by circumstantial evidence? *Diabetologia* **53**, 1046–1056
45. Dear, A. J., Meisl, G., Šarić, A., Michaels, T. C. T., Kjaergaard, M., Linse, S., and Knowles, T. P. J. (2020) Identification of on- and off-pathway oligomers in amyloid fibril formation. *Chem. Sci.* **11**, 6236–6247
46. Wiltzius, J. J. W., Landau, M., Nelson, R., Sawaya, M. R., Apostol, M. I., Goldschmidt, L., Soriaga, A. B., Cascio, D., Rajashankar, K., and Eisenberg, D. (2009) Molecular mechanisms for protein-encoded inheritance. *Nat. Struct. Mol. Biol.* **16**, 973–978
47. Riek, R., and Eisenberg, D. S. (2016) The activities of amyloids from a structural perspective. *Nature* **539**, 227–235
48. Fitzpatrick, A. W. P., Debelouchina, G. T., Bayro, M. J., Clare, D. K., Caporini, M. A., Bajaj, V. S., Jaroniec, C. P., Wang, L., Ladizhansky, V., Müller, S. A., MacPhee, C. E., Waudby, C. A., Mott, H. R., De Simone, A., Knowles, T. P. J., *et al.* (2013) Atomic structure and hierarchical assembly of a cross-β amyloid fibril. *Proc. Natl. Acad. Sci. U. S. A.* **110**, 5468–5473
49. Radamaker, L., Baur, J., Huhn, S., Haupt, C., Hegenbart, U., Schönland, S., Bansal, A., Schmidt, M., and Fändrich, M. (2021) Cryo-EM reveals structural breaks in a patient-derived amyloid fibril from systemic AL amyloidosis. *Nat. Commun.* **12**, 875
50. Luca, S., Yau, W.-M., Leapman, R., and Tycko, R. (2007) Peptide conformation and supramolecular organization in amylin fibrils: Constraints from solid-state NMR. *Biochemistry* **46**, 13505–13522
51. Van Melckebeke, H., Wasmer, C., Lange, A., Ab, E., Loquet, A., Böckmann, A., and Meier, B. H. (2010) Atomic-resolution three-dimensional structure of HET-s(218-289) amyloid fibrils by solid-state nmr spectroscopy. *J. Am. Chem. Soc.* **132**, 13765–13775
52. Ke, P. C., Zhou, R., Serpell, L. C., Riek, R., Knowles, T. P. J., Lashuel, H. A., Gazit, E., Hamley, I. W., Davis, T. P., Fändrich, M., Otzen, D. E., Chapman, M. R., Dobson, C. M., Eisenberg, D. S., and Mezzenga, R. (2020) Half a century of amyloids: Past, present and future. *Chem. Soc. Rev.* **49**, 5473–5509
53. Fitzpatrick, A. W. P., Falcon, B., He, S., Murzin, A. G., Murshudov, G., Garringer, H. J., Crowther, R. A., Ghetti, B., Goedert, M., and Scheres, S.

H. W. (2017) Cryo-EM structures of tau filaments from Alzheimer's disease. *Nature* **547**, 185–190
54. Gremer, L., Schölzel, D., Schenk, C., Reinartz, E., Labahn, J., Ravelli, R. B. G., Tusche, M., Lopez-Iglesias, C., Hoyer, W., Heise, H., Willbold, D., and Schröder, G. F. (2017) Fibril structure of amyloid-β(1–42) by cryo–electron microscopy. *Science* **358**, 116–119
55. Wlodawer, A., and Dauter, Z. (2017) 'Atomic resolution': A badly abused term in structural biology. *Acta Crystallogr. D Struct. Biol.* **73**, 379–380
56. Yip, K. M., Fischer, N., Paknia, E., Chari, A., and Stark, H. (2020) Atomic-resolution protein structure determination by cryo-EM. *Nature* **587**, 157–161
57. Nakane, T., Kotecha, A., Sente, A., McMullan, G., Masiulis, S., Brown, P. M. G. E., Grigoras, I. T., Malinauskaite, L., Malinauskas, T., Miehling, J., Uchański, T., Yu, L., Karia, D., Pechnikova, E. V., de Jong, E., *et al.* (2020) Single-particle cryo-EM at atomic resolution. *Nature* **587**, 152–156
58. Falcon, B., Zivanov, J., Zhang, W., Murzin, A. G., Garringer, H. J., Vidal, R., Crowther, R. A., Newell, K. L., Ghetti, B., Goedert, M., and Scheres, S. H. W. (2019) Novel tau filament fold in chronic traumatic encephalopathy encloses hydrophobic molecules. *Nature* **568**, 420–423
59. Brenner, S., and Horne, R. W. (1959) A negative staining method for high resolution electron microscopy of viruses. *Biochim. Biophys. Acta* **34**, 103–110
60. De Rosier, D. J., and Klug, A. (1968) Reconstruction of three dimensional structures from electron micrographs. *Nature* **217**, 130–134
61. DeRosier, D. J., and Moore, P. B. (1970) Reconstruction of three-dimensional images from electron micrographs of structures with helical symmetry. *J. Mol. Biol.* **52**, 355–369
62. Diaz, R., Rice, W. J., and Stokes, D. L. (2010) Fourier-Bessel reconstruction of helical assemblies. *Methods Enzymol* **482**, 131–165
63. He, S. (2018) *Helical Reconstruction in RELION*. Ph.D. thesis, University of Cambridge
64. He, S., and Scheres, S. H. W. (2017) Helical reconstruction in RELION. *J. Struct. Biol.* **198**, 163–176
65. Scheres, S. H. W. (2020) Amyloid structure determination in RELION-3.1. *Acta Crystallogr. D Struct. Biol.* **76**, 94–101
66. Morris, K. L., and Serpell, L. C. (2012) X-ray fibre diffraction studies of amyloid fibrils. *Methods Mol. Biol.* **849**, 121–135
67. Taylor, K. A., and Glaeser, R. M. (1976) Electron microscopy of frozen hydrated biological specimens. *J. Ultrasruct. Res.* **55**, 448–456
68. Taylor, K. A., and Glaeser, R. M. (1974) Electron diffraction of frozen, hydrated protein crystals. *Science* **186**, 1036–1037
69. Dubochet, J., Lepault, J., Freeman, R., Berriman, J. A., and Homo, J.-C. (1982) Electron microscopy of frozen water and aqueous solutions. *J. Microsc.* https://doi.org/10.1111/j.1365-2818.1982.tb04625.x
70. Xuong, N.-H., Milazzo, A.-C., LeBlanc, P., Duttweiler, F., Bouwer, J., Peltier, S., Ellisman, M., Denes, P., Bieser, F., Matis, H. S., Wieman, H., and Kleinfelder, S. (2004) First use of a high-sensitivity active pixel sensor array as a detector for electron microscopy. In **, 5301**. *Sensors and Camera Systems for Scientific, Industrial, and Digital Photography Applications V*, International Society for Optics and Photonics, Bellingham, Washington: 242–249
71. Faruqi, A. R., and Henderson, R. (2007) Electronic detectors for electron microscopy. *Curr. Opin. Struct. Biol.* **17**, 549–555
72. McMullan, G., Faruqi, A. R., and Henderson, R. (2016) Direct electron detectors. *Methods Enzymol.* **579**, 1–17
73. Böttcher, B., Wynne, S. A., and Crowther, R. A. (1997) Determination of the fold of the core protein of hepatitis B virus by electron cryomicroscopy. *Nature* **386**, 88–91
74. Zhang, X., Settembre, E., Xu, C., Dormitzer, P. R., Bellamy, R., Harrison, S. C., and Grigorieff, N. (2008) Near-atomic resolution using electron cryomicroscopy and single-particle reconstruction. *Proc. Natl. Acad. Sci. U. S. A.* **105**, 1867–1872
75. Yu, X., Jin, L., and Zhou, Z. H. (2008) 3.88 Å structure of cytoplasmic polyhedrosis virus by cryo-electron microscopy. *Nature* **453**, 415–419
76. Frank, J. (2006) *Three-dimensional electron microscopy of macromolecular assemblies: visualization of biological molecules in their native state*. Oxford university press, Oxford, United Kingdom
77. Penczek, P. A., Grassucci, R. A., and Frank, J. (1994) The ribosome at improved resolution: New techniques for merging and orientation refinement in 3D cryo-electron microscopy of biological particles. *Ultramicroscopy* **53**, 251–270
78. Van Heel, M. (1987) Angular reconstitution: *A posteriori* assignment of projection directions for 3D reconstruction. *Ultramicroscopy* **21**, 111–123
79. Zivanov, J., Nakane, T., Forsberg, B. O., Kimanius, D., Hagen, W. J. H., Lindahl, E., and Scheres, S. H. W. (2018) New tools for automated high-resolution cryo-EM structure determination in RELION-3. *Elife* **7**, 1–22
80. Egelman, E. H. (2000) A robust algorithm for the reconstruction of helical filaments using single-particle methods. *Ultramicroscopy* **85**, 225–234
81. Knowles, T. P., Fitzpatrick, A. W., Meehan, S., Mott, H. R., Vendruscolo, M., Dobson, C. M., and Welland, M. E. (2007) Role of intermolecular forces in defining material properties of protein nanofibrils. *Science* **318**, 1900–1903
82. Makin, O. S., Atkins, E., Sikorski, P., Johansson, J., and Serpell, L. C. (2005) Molecular basis for amyloid fibril formation and stability. *Proc. Natl. Acad. Sci. U. S. A.* **102**, 315–320
83. Hirota-Nakaoka, N., Hasegawa, K., Naiki, H., and Goto, Y. (2003) Dissolution of beta2-microglobulin amyloid fibrils by dimethylsulfoxide. *J. Biochem.* **134**, 159–164
84. Miti, T., Mulaj, M., Schmit, J. D., and Muschol, M. (2015) Stable, metastable, and kinetically trapped amyloid aggregate phases. *Biomacromolecules* **16**, 326–335
85. Buell, A. K., Galvagnion, C., Gaspar, R., Sparr, E., Vendruscolo, M., Knowles, T. P. J., Linse, S., and Dobson, C. M. (2014) Solution conditions determine the relative importance of nucleation and growth processes in α-synuclein aggregation. *Proc. Natl. Acad. Sci. U. S. A.* **111**, 7671–7676
86. Peduzzo, A., Linse, S., and Buell, A. K. (2020) The properties of α-synuclein secondary nuclei are dominated by the solution conditions rather than the seed fibril strain. *ACS Chem. Neurosci.* **11**, 909–918
87. Röder, C., Kupreichyk, T., Gremer, L., Schäfer, L. U., Pothula, K. R., Ravelli, R. B. G., Willbold, D., Hoyer, W., and Schröder, G. F. (2020) Cryo-EM structure of islet amyloid polypeptide fibrils reveals similarities with amyloid-β fibrils. *Nat. Struct. Mol. Biol.* **27**, 660–667
88. Cao, Q., Boyer, D. R., Sawaya, M. R., Ge, P., and Eisenberg, D. S. (2020) Cryo-EM structure and inhibitor design of human IAPP (amylin) fibrils. *Nat. Struct. Mol. Biol.* **27**, 653–659
89. Gallardo, R., Iadanza, M. G., Xu, Y., Heath, G. R., Foster, R., Radford, S. E., and Ranson, N. A. (2020) Fibril structures of diabetes-related amylin variants reveal a basis for surface-templated assembly. *Nat. Struct. Mol. Biol.* **27**, 1048–1056
90. Paravastu, A. K., Qahwash, I., Leapman, R. D., Meredith, S. C., and Tycko, R. (2009) Seeded growth of β-amyloid fibrils from Alzheimer's brain-derived fibrils produces a distinct fibril structure. *Proc. Natl. Acad. Sci. U. S. A.* **106**, 7443–7448
91. Lu, J. X., Qiang, W., Yau, W. M., Schwieters, C. D., Meredith, S. C., and Tycko, R. (2013) Molecular structure of β-amyloid fibrils in Alzheimer's disease brain tissue. *Cell* **154**, 1257–1268
92. Kollmer, M., Close, W., Funk, L., Rasmussen, J., Bsoul, A., Schierhorn, A., Schmidt, M., Sigurdson, C. J., Jucker, M., and Fändrich, M. (2019) Cryo-EM structure and polymorphism of Aβ amyloid fibrils purified from Alzheimer's brain tissue. *Nat. Commun.* **10**, 4760
93. Annamalai, K., Gührs, K. H., Koehler, R., Schmidt, M., Michel, H., Loos, C., Gaffney, P. M., Sigurdson, C. J., Hegenbart, U., Schönland, S., and Fändrich, M. (2016) Polymorphism of amyloid fibrils *in vivo*. *Angew. Chem. Int. Ed. Engl.* **55**, 4822–4825
94. Schmidt, M., Wiese, S., Adak, V., Engler, J., Agarwal, S., Fritz, G., Westermark, P., Zacharias, M., and Fändrich, M. (2019) Cryo-EM structure of a transthyretin-derived amyloid fibril from a patient with hereditary ATTR amyloidosis. *Nat. Commun.* **10**, 5008
95. Arakhamia, T., Lee, C. E., Carlomagno, Y., Duong, D. M., Kundinger, S. R., Wang, K., Williams, D., DeTure, M., Dickson, D. W., Cook, C. N., Seyfried, N. T., Petrucelli, L., and Fitzpatrick, A. W. P. (2020) Post-translational modifications mediate the structural diversity of tauopathy strains. *Cell* **180**, 633–644.e12

96. Falcon, B., Zhang, W., Murzin, A. G., Murshudov, G., Garringer, H. J., Vidal, R., Crowther, R. A., Ghetti, B., Scheres, S. H. W., and Goedert, M. (2018) Structures of filaments from Pick's disease reveal a novel tau protein fold. *Nature* **561**, 137–140
97. Zhang, W., Tarutani, A., Newell, K. L., Murzin, A. G., Matsubara, T., Falcon, B., Vidal, R., Garringer, H. J., Shi, Y., Ikeuchi, T., Murayama, S., Ghetti, B., Hasegawa, M., Goedert, M., and Scheres, S. H. W. (2020) Novel tau filament fold in corticobasal degeneration. *Nature* **580**, 283–287
98. Swuec, P., Lavatelli, F., Tasaki, M., Paissoni, C., Rognoni, P., Maritan, M., Brambilla, F., Milani, P., Mauri, P., Camilloni, C., Palladini, G., Merlini, G., Ricagno, S., and Bolognesi, M. (2019) Cryo-EM structure of cardiac amyloid fibrils from an immunoglobulin light chain AL amyloidosis patient. *Nat. Commun.* **10**, 1269
99. Bansal, A., Schmidt, M., Rennegarbe, M., Haupt, C., Liberta, F., Stecher, S., Puscalau-girtu, I., Biedermann, A., and Fändrich, M. (2021) AA amyloid fibrils from diseased tissue are structurally different from *in vitro* formed SAA fibrils. *Nat. Commun.* **12**, 1013
100. Schweighauser, M., Shi, Y., Tarutani, A., Kametani, F., Murzin, A. G., Ghetti, B., Matsubara, T., Tomita, T., Ando, T., Hasegawa, K., Murayama, S., Yoshida, M., Hasegawa, M., Scheres, S. H. W., and Goedert, M. (2020) Structures of α-synuclein filaments from multiple system atrophy. *Nature* **585**, 464–469
101. Ghosh, U., Thurber, K. R., Yau, W.-M., and Tycko, R. (2021) Molecular structure of a prevalent amyloid-β fibril polymorph from Alzheimer's disease brain tissue. *Proc. Natl. Acad. Sci. U. S. A.* **118**, e2023089118
102. Saborio, G. P., Permanne, B., and Soto, C. (2001) Sensitive detection of pathological prion protein by cyclic amplification of protein misfolding. *Nature* **411**, 810–813
103. Strohäker, T., Jung, B. C., Liou, S. H., Fernandez, C. O., Riedel, D., Becker, S., Halliday, G. M., Bennati, M., Kim, W. S., Lee, S. J., and Zweckstetter, M. (2019) Structural heterogeneity of α-synuclein fibrils amplified from patient brain extracts. *Nat. Commun.* **10**, 1–12
104. Lövestam, S., Schweighauser, M., Matsubara, T., Murayama, S., Tomita, T., Ando, T., Hasegawa, K., Yoshida, M., Tarutani, A., Hasegawa, M., Goedert, M., and Scheres, S. H. W. (2021) Seeded assembly *in vitro* does not replicate the structures of α-synuclein filaments from multiple system atrophy. *FEBS Open Bio* **11**, 999–1013
105. Liberta, F., Loerch, S., Rennegarbe, M., Schierhorn, A., Westermark, P., Westermark, G. T., Grigorieff, N., Fandrich, M., and Schmidt, M. (2019) Cryo-EM structure of an amyloid fibril from systemic amyloidosis. *Nat. Commun.* **10**, 1104
106. Röder, C., Vettore, N., Mangels, L. N., Gremer, L., Ravelli, R. B. G., Willbold, D., Hoyer, W., Buell, A. K., and Schröder, G. F. (2019) Atomic structure of PI3-kinase SH3 amyloid fibrils by cryo-electron microscopy. *Nat. Commun.* **10**, 3754
107. Hu, R., Zhang, M., Chen, H., Jiang, B., and Zheng, J. (2015) Cross-seeding interaction between β-amyloid and human islet amyloid polypeptide. *ACS Chem. Neurosci.* **6**, 1759–1768
108. Frederik, P. M., and Hubert, D. H. W. (2005) Cryoelectron microscopy of liposomes. *Methods Enzymol.* **391**, 431–448
109. Armstrong, M., Han, B.-G., Gomez, S., Turner, J., Fletcher, D. A., and Glaeser, R. M. (2020) Microscale fluid behavior during cryo-EM sample blotting. *Biophys. J.* **118**, 708–719
110. Egelman, E. H. (2020) Cryo-EM: Ice is nice, but good ice can be hard to find. *Biophys. J.* **118**, 1238–1239
111. Galkin, V. E., Orlova, A., Vos, M. R., Schröder, G. F., and Egelman, E. H. (2015) Near-atomic resolution for one state of F-actin. *Structure* **23**, 173–182
112. Galkin, V. E., Orlova, A., and Egelman, E. H. (2012) Actin filaments as tension sensors. *Curr. Biol.* **22**, R96–R101
113. Dandey, V. P., Wei, H., Zhang, Z., Eng, E. T., Noble, A., Rice, W. J., Raczkowski, A., Carragher, B., and Potter, C. S. (2017) Spotiton: A new method for vitrifying samples for cryo-EM. *Acta Crystallogr. A Found. Adv.* **73**, C1295
114. Wei, H., Dandey, V. P., Kopylov, M., Eng, E. T., Kahn, P., Potter, C. S., and Carragher, B. (2019) Spotiton and chameleon vitrification robots. *Microsc. Microanal.* **25**, 1010–1011
115. Jain, T., Sheehan, P., Crum, J., Carragher, B., and Potter, C. S. (2012) Spotiton: A prototype for an integrated inkjet dispense and vitrification system for cryo-TEM. *J. Struct. Biol.* **179**, 68–75
116. Dandey, V. P., Wei, H., Zhang, Z., Tan, Y. Z., Acharya, P., Eng, E. T., Rice, W. J., Kahn, P. A., Potter, C. S., and Carragher, B. (2018) Spotiton: New features and applications. *J. Struct. Biol.* **202**, 161–169
117. Arnold, S. A., Albiez, S., Bieri, A., Syntychaki, A., Adaixo, R., McLeod, R. A., Goldie, K. N., Stahlberg, H., and Braun, T. (2017) Blotting-free and lossless cryo-electron microscopy grid preparation from nanoliter-sized protein samples and single-cell extracts. *J. Struct. Biol.* **197**, 220–226
118. Arnold, S. A., Albiez, S., Opara, N., Chami, M., Schmidli, C., Bieri, A., Padeste, C., Stahlberg, H., and Braun, T. (2016) Total sample conditioning and preparation of nanoliter volumes for electron microscopy. *ACS Nano* **10**, 4981–4988
119. Schmidli, C., Albiez, S., Rima, L., Righetto, R., Mohammed, I., Oliva, P., Kovacik, L., Stahlberg, H., and Braun, T. (2019) Microfluidic protein isolation and sample preparation for high-resolution cryo-EM. *Proc. Natl. Acad. Sci. U. S. A.* **116**, 15007–15012
120. Ramakrishnan, C., Bieri, A., Sauter, N., Roizard, S., Ringler, P., Müller, S. A., Goldie, K. N., Enimanev, K., Stahlberg, H., Rinn, B., and Braun, T. (2014) OpenBEB: Open biological experiment browser for correlative measurements. *BMC Bioinformatics* **15**, 84
121. Purro, S. A., Farrow, M. A., Linehan, J., Nazari, T., Thomas, D. X., Chen, Z., Mengel, D., Saito, T., Saido, T., Rudge, P., Brandner, S., Walsh, D. M., and Collinge, J. (2018) Transmission of amyloid-β protein pathology from cadaveric pituitary growth hormone. *Nature* **564**, 415–419
122. Jaunmuktane, Z., Quaegebeur, A., Taipa, R., Viana-Baptista, M., Barbosa, R., Koriath, C., Sciot, R., Mead, S., and Brandner, S. (2018) Evidence of amyloid-β cerebral amyloid angiopathy transmission through neurosurgery. *Acta Neuropathol.* **135**, 671–679
123. Kovacs, G. G., Lutz, M. I., Ricken, G., Ströbel, T., Höftberger, R., Preusser, M., Regelsberger, G., Hönigschnabl, S., Reiner, A., Fischer, P., Budka, H., and Hainfellner, J. A. (2016) Dura mater is a potential source of Aβ seeds. *Acta Neuropathol.* **131**, 911–923
124. Edgren, G., Hjalgrim, H., Rostgaard, K., Lambert, P., Wikman, A., Norda, R., Titlestad, K. E., Erikstrup, C., Ullum, H., Melbye, M., Busch, M. P., and Nyrén, O. (2016) Transmission of neurodegenerative disorders through blood transfusion: A cohort study. *Ann. Intern. Med.* **165**, 316–324
125. Bu, X. L., Li, W. W., and Wang, Y. J. (2019) Is Alzheimer's disease transmissible in humans? *Neurosci. Bull.* **35**, 1113–1115
126. Weissenberger, G., Nijpels, F., Henderikx, R., Beulen, B., Ravelli, R., and Peters, P. (2020) VitroJet: Bridging the gap in sample prep. *Microsc. Microanal.* **26**, 1–2
127. Ravelli, R. B. G., Nijpels, F. J. T., Henderikx, R. J. M., Weissenberger, G., Thewessem, S., Gijsbers, A., Beulen, B. W. A. M. M., López-Iglesias, C., and Peters, P. J. (2020) Cryo-EM structures from sub-nl volumes using pin-printing and jet vitrification. *Nat. Commun.* **11**, 2563
128. Rubinstein, J. L., Guo, H., Ripstein, Z. A., Haydaroglu, A., Au, A., Yip, C. M., Trani, J. M. D., Benlekbira, S., and Kwoka, T. (2019) Shake-it-off: A simple ultrasonic cryo-EM specimen-preparation device Rubinstein John L. *Acta Crystallogr. D Struct. Biol.* **75**, 1063–1070
129. Wei, H., Dandey, V., Zhang, Z., Raczkowski, A., Carragher, B., and Potter, C. S. (2017) Self-blotting nanowire grids for cryo-EM sample preparation. *Microsc. Microanal.* **23**, 848–849
130. Wei, H., Dandey, V. P., Zhang, Z., Raczkowski, A., Rice, W. J., Carragher, B., and Potter, C. S. (2018) Optimizing "self-wicking" nanowire grids. *J. Struct. Biol.* **202**, 170–174
131. Klebl, D. P., Gravett, M. S. C., Kontziampasis, D., Wright, D. J., Bon, R. S., Monteiro, D. C. F., Trebbin, M., Sobott, F., White, H. D., Darrow, M. C., Thompson, R. F., and Muench, S. P. (2020) Need for speed: Examining protein behavior during CryoEM grid preparation at different timescales. *Structure* **28**, 1238–1248.e4
132. Klebl, D. P., Monteiro, D. C. F., Kontziampasis, D., Kopf, F., Sobott, F., White, H. D., Trebbin, M., and Muench, S. P. (2020) Sample deposition onto cryo-EM grids: From sprays to jets and back. *Acta Crystallogr. D Struct. Biol.* **76**, 340–349
133. Lawson, C. L., and Chiu, W. (2018) Comparing cryo-EM structures. *J. Struct. Biol.* **204**, 523–526

134. Li, Y., Cash, J. N., Tesmer, J. J. G., and Cianfrocco, M. A. (2020) High-throughput cryo-EM enabled by user-free preprocessing routines. *Structure* **28**, 858–869.e3
135. Punjani, A., Rubinstein, J. L., Fleet, D. J., and Brubaker, M. A. (2017) CryoSPARC: Algorithms for rapid unsupervised cryo-EM structure determination. *Nat. Methods* **14**, 290–296
136. Moriya, T., Saur, M., Stabrin, M., Merino, F., Voicu, H., Huang, Z., Penczek, P. A., Raunser, S., and Gatsogiannis, C. (2017) High-resolution single particle analysis from electron cryo-microscopy images using SPHIRE. *J. Vis. Exp.* **2017**, 1–11
137. Volkmann, N. (2004) An approach to automated particle picking from electron micrographs based on reduced representation templates. *J. Struct. Biol.* **145**, 152–156
138. Huang, Z., and Penczek, P. A. (2004) Application of template matching technique to particle detection in electron micrographs. *J. Struct. Biol.* **145**, 29–40
139. Roseman, A. M. (2004) FindEM—a fast, efficient program for automatic selection of particles from electron micrographs. *J. Struct. Biol.* **145**, 91–99
140. Scheres, S. H. W. (2015) Semi-automated selection of cryo-EM particles in RELION-1.3. *J. Struct. Biol.* **189**, 114–122
141. Zhu, Y., Ouyang, Q., and Mao, Y. (2017) A deep convolutional neural network approach to single-particle recognition in cryo-electron microscopy. *BMC Bioinformatics* **348**, 1–10
142. Tegunov, D., and Cramer, P. (2019) Real-time cryo-electron microscopy data preprocessing with Warp. *Nat. Methods* **16**, 1146–1152
143. Wagner, T., Merino, F., Stabrin, M., Moriya, T., Antoni, C., Apelbaum, A., Hagel, P., Sitsel, O., Raisch, T., Prumbaum, D., Quentin, D., Roderer, D., Tacke, S., Siebolds, B., Schubert, E., *et al.* (2019) SPHIRE-crYOLO is a fast and accurate fully automated particle picker for cryo-EM. *Commun. Biol.* **2**, 1–13
144. Wang, F., Gong, H., Liu, G., Li, M., Yan, C., Xia, T., Li, X., and Zeng, J. (2016) DeepPicker: A deep learning approach for fully automated particle picking in cryo-EM. *J. Struct. Biol.* **195**, 325–336
145. Bepler, T., Morin, A., Rapp, M., Brasch, J., Shapiro, L., Noble, A. J., and Berger, B. (2019) Positive-unlabeled convolutional neural networks for particle picking in cryo-electron micrographs. *Nat. Methods* **16**, 1153–1160
146. Redmon, J., Divvala, S., Girshick, R., and Farhadi, A. (2016) You only look once: Unified, real-time object detection. *Proc. IEEE Comput. Soc. Conf. Comput. Vis. Pattern Recognit.*, 779–788
147. Wagner, T., and Raunser, S. (2020) The evolution of SPHIRE-crYOLO particle picking and its application in automated cryo-EM processing workflows. *Commun. Biol.* **3**, 1–5
148. Thurber, K. R., Yin, Y., and Tycko, R. (2021) Automated picking of amyloid fibrils from cryo-EM images for helical reconstruction with RELION. *J. Struct. Biol.* **213**, 107736
149. Huber, S. T., Kuhm, T., and Sachse, C. (2018) Automated tracing of helical assemblies from electron cryo-micrographs. *J. Struct. Biol.* **202**, 1–12
150. Desfosses, A., Ciuffa, R., Gutsche, I., and Sachse, C. (2014) SPRING - an image processing package for single-particle based helical reconstruction from electron cryomicrographs. *J. Struct. Biol.* **185**, 15–26
151. Egelman, E. H. (2010) Reconstruction of helical filaments and tubes. *Methods Enzymol* **482**, 167–183
152. Von Der Ecken, J., Heissler, S. M., Pathan-Chhatbar, S., Manstein, D. J., and Raunser, S. (2016) Cryo-EM structure of a human cytoplasmic actomyosin complex at near-atomic resolution. *Nature* **534**, 724–728
153. Ohashi, M., Maeda, S. I., and Sato, C. (2019) Bayesian inference for three-dimensional helical reconstruction using a soft-body model. *Phys. Rev. E* **100**, 042411
154. Glynn, C., Sawaya, M. R., Ge, P., Gallagher-Jones, M., Short, C. W., Bowman, R., Apostol, M., Zhou, Z. H., Eisenberg, D. S., and Rodriguez, J. A. (2020) Cryo-EM structure of a human prion fibril with a hydrophobic, protease-resistant core. *Nat. Struct. Mol. Biol.* **27**, 417–423
155. Cendrowska, U., Silva, P. J., Ait-Bouziad, N., Müller, M., Guven, Z. P., Vieweg, S., Chiki, A., Radamaker, L., Kumar, S. T., Fändrich, M., Tavanti, F., Menziani, M. C., Alexander-Katz, A., Stellacci, F., and Lashuel, H. A. (2020) Unraveling the complexity of amyloid polymorphism using gold nanoparticles and cryo-EM. *Proc. Natl. Acad. Sci. U. S. A.* **117**, 6866–6874
156. Weber, M., Bäuerle, A., Schmidt, M., Neumann, M., Fändrich, M., Ropinski, T., and Schmidt, V. (2020) Automatic identification of crossovers in cryo-EM images of murine amyloid protein A fibrils with machine learning. *J. Microsc.* **277**, 12–22
157. Pothula, K. R., Smyrnova, D., and Schröder, G. F. (2019) Clustering cryo-EM images of helical protein polymers for helical reconstructions. *Ultramicroscopy* **203**, 132–138
158. Pothula, K. R., Geraets, J. A., Ferber, I. I., and Schröder, G. F. (2021) Clustering polymorphs of tau and IAPP fibrils with the CHEP algorithm. *Prog. Biophys. Mol. Biol.* **160**, 16–25
159. Berriman, J., and Unwin, N. (1994) Analysis of transient structures by cryo-microscopy combined with rapid mixing of spray droplets. *Ultramicroscopy* **56**, 241–252
160. Kontziampasis, D., Klebl, D. P., Iadanza, M. G., Scarff, C. A., Kopf, F., Sobott, F., Monteiro, D. C. F., Trebbin, M., Muench, S. P., and White, H. D. (2019) A cryo-EM grid preparation device for time-resolved structural studies. *IUCrJ* **6**, 1024–1031
161. Mäeots, M. E., Lee, B., Nans, A., Jeong, S. G., Esfahani, M. M. N., Ding, S., Smith, D. J., Lee, C. S., Lee, S. S., Peter, M., and Enchev, R. I. (2020) Modular microfluidics enables kinetic insight from time-resolved cryo-EM. *Nat. Commun.* **11**, 3465
162. Dandey, V. P., Budell, W. C., Wei, H., Bobe, D., Maruthi, K., Kopylov, M., Eng, E. T., Kahn, P. A., Hinshaw, J. E., Kundu, N., Nimigean, C. M., Fan, C., Sukomon, N., Darst, S. A., Saecker, R. M., *et al.* (2020) Time-resolved cryo-EM using Spotiton. *Nat. Methods* **17**, 897–900
163. Eisenberg, D., and Jucker, M. (2012) The amyloid state of proteins in human diseases. *Cell* **148**, 1188–1203
164. Campioni, S., Carret, G., Jordens, S., Nicoud, L., Mezzenga, R., and Riek, R. (2014) The presence of an air-water interface affects formation and elongation of α-synuclein fibrils. *J. Am. Chem. Soc.* **136**, 2866–2875
165. Galvagnion, C., Buell, A. K., Meisl, G., Michaels, T. C. T., Vendruscolo, M., Knowles, T. P. J., and Dobson, C. M. (2015) Lipid vesicles trigger α-synuclein aggregation by stimulating primary nucleation. *Nat. Chem. Biol.* **11**, 229–234
166. Törnquist, M., Michaels, T. C. T., Sanagavarapu, K., Yang, X., Meisl, G., Cohen, S. I. A., Knowles, T. P. J., and Linse, S. (2018) Secondary nucleation in amyloid formation. *Chem. Commun.* **54**, 8667–8684
167. Jarrett, J. T., and Lansbury, P. T. (1993) Seeding "one-dimensional crystallization" of amyloid: A pathogenic mechanism in Alzheimer's disease and scrapie? *Cell* **73**, 1055–1058
168. Törnquist, M., Cukalevski, R., Weininger, U., Meisl, G., Knowles, T. P. J., Leiding, T., Malmendal, A., Akke, M., and Linse, S. (2020) Ultrastructural evidence for self-replication of Alzheimer-associated Aβ42 amyloid along the sides of fibrils. *Proc. Natl. Acad. Sci. U. S. A.* **117**, 11265–11273
169. Bäuerlein, F. J. B., Saha, I., Mishra, A., Kalemanov, M., Martínez-Sánchez, A., Klein, R., Dudanova, I., Hipp, M. S., Hartl, F. U., Baumeister, W., and Fernández-Busnadiego, R. (2017) *In situ* architecture and cellular interactions of PolyQ inclusions. *Cell* **171**, 179–187.e10
170. Li, D., and Liu, C. (2020) Structural diversity of amyloid fibrils and advances in their structure determination. *Biochemistry* **59**, 639–646
171. Gorbenko, G., Trusova, V., Girych, M., Adachi, E., Mizuguchi, C., Akaji, K., and Saito, H. (2015) FRET evidence for untwisting of amyloid fibrils on the surface of model membranes. *Soft Matter* **11**, 6223–6234
172. Xu, Q., Park, Y., Huang, X., Hollenbeck, A., Blair, A., Schatzkin, A., and Chen, H. (2011) Diabetes and risk of Parkinson's disease. *Diabetes Care* **34**, 910–915
173. Santiago, J. A., and Potashkin, J. A. (2014) System-based approaches to decode the molecular links in Parkinson's disease and diabetes. *Neurobiol. Dis.* **72**, 84–91
174. Morales, R., Moreno-Gonzalez, I., and Soto, C. (2013) Cross-seeding of misfolded proteins: Implications for etiology and pathogenesis of protein misfolding diseases. *PLoS Pathog.* **9**, e1003537

175. Horvath, I., and Wittung-Stafshede, P. (2016) Cross-talk between amyloidogenic proteins in type-2 diabetes and Parkinson's disease. *Proc. Natl. Acad. Sci. U. S. A.* **113**, 12473–12477
176. Moreno-Gonzalez, I., Edwards, G., Salvadores, N., Shahnawaz, M., Diaz-Espinoza, R., and Soto, C. (2017) Molecular interaction between type 2 diabetes and Alzheimer's disease through cross-seeding of protein misfolding. *Mol. Psychiatry* **9**, 1327–1334
177. Zhang, Y., Zhang, M., Liu, Y., Zhang, D., Tang, Y., Ren, B., and Zheng, J. (2021) Dual amyloid cross-seeding reveals steric zipper-facilitated fibrillization and pathological links between protein misfolding diseases. *J. Mater. Chem. B* **9**, 3300–3316
178. Alam, P., Bousset, L., Melki, R., and Otzen, D. E. (2019) α-Synuclein oligomers and fibrils: A spectrum of species, a spectrum of toxicities. *J. Neurochem.* **150**, 522–534
179. Haataja, L., Gurlo, T., Huang, C. J., and Butler, P. C. (2008) Islet amyloid in type 2 diabetes, and the toxic oligomer hypothesis. *Endocr. Rev.* **29**, 303–316
180. Michaels, T. C. T., Šarić, A., Curk, S., Bernfur, K., Arosio, P., Meisl, G., Dear, A. J., Cohen, S. I. A., Dobson, C. M., Vendruscolo, M., Linse, S., and Knowles, T. P. J. (2020) Dynamics of oligomer populations formed during the aggregation of Alzheimer's Aβ42 peptide. *Nat. Chem.* **12**, 445–451
181. Li, S., and Selkoe, D. J. (2020) A mechanistic hypothesis for the impairment of synaptic plasticity by soluble Aβ oligomers from Alzheimer's brain. *J. Neurochem.* **154**, 583–597
182. van Groen, T., Schemmert, S., Brener, O., Gremer, L., Ziehm, T., Tusche, M., Nagel-Steger, L., Kadish, I., Schartmann, E., Elfgen, A., Jürgens, D., Willuweit, A., Kutzsche, J., and Willbold, D. (2017) The Aβ oligomer eliminating D-enantiomeric peptide RD2 improves cognition without changing plaque pathology. *Sci. Rep.* **7**, 16275
183. Schuster, J., and Funke, S. A. (2016) Methods for the specific detection and quantitation of amyloid-β oligomers in cerebrospinal fluid. *J. Alzheimers Dis.* **53**, 53–67
184. Mehta, D., Jackson, R., Paul, G., Shi, J., and Sabbagh, M. (2017) Why do trials for Alzheimer's disease drugs keep failing? A discontinued drug perspective for 2010-2015. *Expert Opin. Investig. Drugs* **26**, 735–739
185. Oxford, A. E., Stewart, E. S., and Rohn, T. T. (2020) Clinical trials in Alzheimer's disease: A hurdle in the path of remedy. *Int. J. Alzheimers Dis.* **2020**, 5380346
186. Michaels, T. C. T., Šarić, A., Habchi, J., Chia, S., Meisl, G., Vendruscolo, M., Dobson, C. M., and Knowles, T. P. J. (2018) Chemical kinetics for bridging molecular mechanisms and macroscopic measurements of amyloid fibril formation. *Annu. Rev. Phys. Chem.* **69**, 273–298
187. Dear, A. J., Michaels, T. C. T., Meisl, G., Klenerman, D., Wu, S., Perrett, S., Linse, S., Dobson, C. M., and Knowles, T. P. J. (2020) Kinetic diversity of amyloid oligomers. *Proc. Natl. Acad. Sci. U. S. A.* **117**, 12087–12094
188. Guo, Q., Lehmer, C., Martínez-Sánchez, A., Rudack, T., Beck, F., Hartmann, H., Pérez-Berlanga, M., Frottin, F., Hipp, M. S., Hartl, F. U., Edbauer, D., Baumeister, W., and Fernández-Busnadiego, R. (2018) *In situ* structure of neuronal C9orf72 poly-GA aggregates reveals proteasome recruitment. *Cell* **172**, 696–705.e12
189. [preprint] Schützmann, M. P., Hasecke, F., Bachmann, S., Zielinski, M., Hänsch, S., Schröder, G. F., Zempel, H., and Hoyer, W. (2020) Endo-lysosomal Aβ concentration and pH enable formation of Aβ oligomers that potently induce tau missorting. *bioRxiv*. https://doi.org/10.1101/2020.06.28.175885
190. Wu, S., Avila-Sakar, A., Kim, J., Booth, D. S., Greenberg, C. H., Rossi, A., Liao, M., Li, X., Alian, A., Griner, S. L., Juge, N., Yu, Y., Mergel, C. M., Chaparro-Riggers, J., Strop, P., *et al*. (2012) Fabs enable single particle cryoEM studies of small proteins. *Structure* **20**, 582–592
191. Schmidt, M., Rohou, A., Lasker, K., Yadav, J. K., Schiene-Fischer, C., Fändrich, M., Grigorieff, N., and Petsko, G. A. (2015) Peptide dimer structure in an Aβ(1-42) fibril visualized with cryo-EM. *Proc. Natl. Acad. Sci. U. S. A.* **112**, 11858–11863
192. Klug, A., Crick, F. H. C., and Wyckoff, H. W. (1958) Diffraction by helical structures. *Acta Crystallogr.* **11**, 199–213
193. Cochran, W., Crick, F. H., and Vand, V. (1952) The structure of synthetic polypeptides. I. The transform of atoms on a helix. *Acta Crystallogr.* **5**, 581–586
194. Scheres, S. H. W. (2012) RELION: Implementation of a bayesian approach to cryo-EM structure determination. *J. Struct. Biol.* **180**, 519–530
195. Alexandrescu, A. T. (2013) Amide proton solvent protection in amylin fibrils probed by quenched hydrogen exchange NMR. *PLoS One* **8**, e56467
196. Weirich, F., Gremer, L., Mirecka, E. A., Schiefer, S., Hoyer, W., and Heise, H. (2016) Structural characterization of fibrils from recombinant human islet amyloid polypeptide by solid-state NMR: The central FGAILS segment is part of the β-sheet core. *PLoS One* **11**, e0161243
197. Falcon, B., Zhang, W., Schweighauser, M., Murzin, A. G., Vidal, R., Garringer, H. J., Ghetti, B., Scheres, S. H. W., and Goedert, M. (2018) Tau filaments from multiple cases of sporadic and inherited Alzheimer's disease adopt a common fold. *Acta Neuropathol.* **136**, 699–708

B. Manuscript I

Cryo-EM Structures of Amyloid-β Fibrils from Alzheimer's Disease Mouse Models

Mara Zielinski[1,2‡], Fernanda S. Peralta Reyes[3‡], Lothar Gremer[1,2,3§], Sarah Schemmert[1], Benedikt Frieg[1,2], Antje Willuweit[4], Lili Donner[5], Margitta Elvers[5], Lars N. G. Nilsson[6], Stina Syvänen[7], Dag Sehlin[7], Martin Ingelsson[7,8,9], Dieter Willbold[1,2,3§], Gunnar F. Schröder[1,2,10§]

[1]Institute of Biological Information Processing, Structural Biochemistry (IBI-7), Forschungszentrum Jülich, Jülich, Germany

[2]JuStruct, Jülich Center for Structural Biology, Forschungszentrum Jülich, Jülich, Germany

[3]Institut für Physikalische Biologie, Heinrich Heine University Düsseldorf, Düsseldorf, Germany

[4]Institute of Neuroscience and Medicine, Medical Imaging Physics (INM-4), Forschungszentrum Jülich GmbH, Jülich, Germany

[5]Department of Vascular- and Endovascular Surgery, University Hospital Düsseldorf, Heinrich-Heine University, Düsseldorf, Germany

[6]Department of Pharmacology, Institute of Clinical Medicine, University of Oslo and Oslo University Hospital, Oslo, Norway

[7]Department of Public Health and Caring Sciences, Molecular Geriatrics, Rudbeck Laboratory, Uppsala University, Uppsala, Sweden

[8]Krembil Brain Institute, University Health Network, Toronto, Ontario, Canada

[9]Department of Medicine and Tanz Centre for Research in Neurodegenerative Diseases, University of Toronto, Toronto, Ontario, Canada

[10]Physics Department, Heinrich Heine University Düsseldorf, Düsseldorf, Germany.

[§]corresponding authors.

[‡]these authors contributed equally

Abstract

The development of novel drugs for Alzheimer's disease has proven difficult, with a high failure rate in clinical trials. Typically, transgenic mice displaying amyloid-β peptide brain pathology are used to develop therapeutic options and to test their efficacy in preclinical studies. However, the properties of Aβ in such mice have not been systematically compared to Aβ from the patient brains. Here, we determined the structures of nine *ex vivo* Aβ fibrils from six different mouse models by cryo-EM. We found novel Aβ fibril structures in the APP/PS1, ARTE10, and tg-SwDI models, whereas the human familial type II fibril fold was found in the ARTE10, tg-APP_{Swe}, and APP23 models. The tg-APP_{ArcSwe} mice showed an Aβ fibril whose structure resembles the human sporadic type I fibril. These structural elucidations are key to the selection of adequate mouse models for the development of novel plaque-targeting therapeutics and PET imaging tracers.

One Sentence Summary

Cryo-EM structures of Aβ fibrils extracted from brains of mouse models used for Alzheimer's disease preclinical research are presented.

Main Text

Alzheimer's disease (AD) is the most common form of dementia and is neuropathologically defined by the presence of extracellular plaques containing amyloid-β (Aβ) in the brain parenchyma and intraneuronal neurofibrillary tangles containing phosphorylated tau [1]–[4]. In the amyloidogenic pathway, Aβ is sequentially cleaved from the amyloid precursor protein (APP) by β- and ɣ-secretases [5], [6]. Typically, depending on ɣ-secretase cleavage, monomers between 37 and 43 residues in length are generated, however, the most abundant peptides are 40 (Aβ40) and 42 (Aβ42) residues in length [7]. These monomers tend to aggregate into insoluble fibrils, the structure of which has been extensively studied *in vitro* by cryogenic-electron microscopy (cryo-EM) and solid-state nuclear magnetic resonance (NMR) spectroscopy, revealing a spectrum of different polymorphs [8]–[14]. However, these fibrils are structurally different from both Aβ40 and Aβ42 fibrils derived from AD brain tissue by seeded growth [15], [16] as well as Aβ40 and Aβ42 fibrils extracted from AD meninges [17] and parenchyma [18], respectively. Yang and colleagues determined two human fibril polymorphs: 'type I filaments', which are mostly associated with sporadic AD (sAD) and 'type II filaments' observed in familial AD (fAD) and other neurodegenerative disorders [18]. Animal models are an important tool to study the pathogenesis of AD and to conduct preclinical testing of novel therapeutics [19]. Commonly used animal models are transgenic mice that mimic different clinical characteristics of the disease [20]. The structures of Aβ fibrils extracted from two different mouse models, the knock-in APP^{NL-G-F} and the knock-in APP^{NL-F}, were recently determined by cryo-EM [18], [21], [22]. While the APP^{NL-F} Aβ42 fibril resembles the human type II Aβ42 fold, the fold of the APP^{NL-G-F} Aβ42(E22G) fibrils differs from fibrils extracted from human brain.

To date, there is no cure for AD, but aggregated Aβ is a common target for drug development [23]. One of the most successful treatments so far is the Aβ-directed antibody lecanemab which was developed primarily against intermediately sized soluble Aβ aggregates, in particular, Aβ oligomers and protofibrils [24], [25]. The structure of these Aβ aggregates remains elusive, but a recent study [26] showed interactions between lecanemab and Aβ fibrils that were present in "ultracentrifugal supernatants of aqueous extracts from AD brains". Nevertheless, developing

novel drugs for AD has been challenging, with a drug development failure rate of almost 100% [27]. Structural differences between human and murine Aβ fibrils may explain why positron emission tomography (PET) imaging tracers fail to detect Aβ deposits in some patients (e.g., patients with the Arctic mutation) [28]. Additionally, it might help to understand why fibril-targeting drug candidates show efficacy when tested in mouse models but then fail to show the desired effect in clinical trials.

Here, we extracted Aβ fibrils from the brains of six different mouse models based on a previously described sarkosyl extraction method [18] and determined their structure by cryo-EM (**Fig. 1, Fig. S1, Fig. S2, Fig. S3, Table S1**). The investigated mouse models, APP/PS1, ARTE10, tg-SwDI, tg-APP_{Swe}, APP23, and tg-APP_{ArcSwe} are all commonly used lines in AD research and drug development.

Murine type III Aβ fibrils from APP/PS1 and ARTE10 mouse brains

For the APP/PS1 mice, we observed only one fibril type made of two identical LS-shaped protofilaments related by a C2 symmetry (**Fig. 1 and Fig. 2, A and B**). This fibril type, which we call the murine type III Aβ fold in the following, was also found in ARTE10 mouse brain (**Fig 2C**) and accounts for 4% of all reconstructed ARTE10 fibrils (**Table S2**). Murine type III fibrils were determined to a resolution of 3.5 Å and 3.3 Å for APP/PS1 mice and ARTE10 mice, respectively (**Table S3 and Fig. S4, A and B**). For APP/PS1 murine type III Aβ42 fibrils, atomic model building was possible for the ordered core from residues G9-A42 (**Fig. 2, A and B**). Interestingly, in contrast to ARTE10 murine type II, the reconstructed density of ARTE10 murine type III suggests that the fibril is composed of Aβ40 rather than Aβ42. Accordingly, an atomic model was built from residue G9-V40 (**Fig. 2, A and C**). The N-terminal L-turn involves residues Y10-F19 and is mainly stabilized by one hydrophobic cluster composed of Y10, V12, L17, F10, L34 and V36 (**Fig. 2, B and C and Fig. S5, A and B**). The S-turn, which involves residues F20-V40/A42, is stabilized by two hydrophobic clusters: in the first half of the S-turn between F20-K28 involving A21, V24 and I31 and the C-terminal second half of the S-turn involving A30, I32, M35, V40 (and A42). The protofilament interface involving residues D23-K28 of murine type III fibrils is stabilized by symmetric salt bridges between D23 and K28 of the opposing subunits.

Interestingly, similarities can be observed between murine type III fibrils and human Arctic (E693G, E22G in Aβ) Aβ filaments [21] (**Fig. 3A**). The human Arctic Aβ filament shows two distinct protofilaments A and B, with each being present twice in the four-protofilament fibril. The main chain trace of murine type III fibrils resembles one protofilament A-B pair of human Arctic Aβ-filaments. The structures including side chain orientations are identical between E22/G22 and the C-terminus of Aβ, leading to the same solvent exposed residues. Moreover, in both cases the interface is stabilized by salt bridges between D23 and K28. The largest deviation between the two structures can be found in the orientation of the side chains in the N-terminal part up to the single point mutation site (E22G).

Novel Aβ folds from tg-SwDI mouse brain

For tg-SwDI mice, which harbor the Dutch (E22Q) and Iowa (D23N) mutations within the Aβ sequence, we observed three different polymorphs (**Fig. 1 and Fig. 2, A, E, F, and G**). The most dominant polymorph, which we call DI1, accounts for 41% of all fibrils and reveals a symmetric dimer (**Fig. 2, A and E and Table S2**). The other two polymorphs, labeled DI2 and DI3, consist

of a single protofilament and account for 32% and 27%, respectively (**Fig. 2, A, F, and G and Table S2**).

The 3.3 Å map of DI1 was used to build an atomic model of the ordered core between D1 and V36 (**Fig. 2, A and E and Table S3 and Fig. S4D**). The two S-shaped protofilaments of DI1 are connected via the extended N-terminus (**Fig. 2E**). A hydrogen bond between D1 and S26 and a salt bridge between E3 and K28 of the opposing protofilament stabilize the interface between the two subunits. A hydrogen bond between Q15 and N23 stabilizes the first half of the S-turn. This turn is further stabilized by a hydrogen bond between Y10 and a backbone oxygen at $N23^{i-1}$ in the adjacent layer within the same protofilament (denoted by the index i-1)**.**

For DI2 fibrils an atomic model of residues D1-V39 could be built into the 4.2 Å map (**Fig. 2, A and F and Table S3 and Fig. S4E**). Except for the N-terminus, the fold is similar to the fold of DI1 fibrils (**Fig. 2, E and F and Fig. S6A**). The N-terminus is fixed in its position by a salt bridge between D1 and $K28^{i+2}$ as well as a hydrogen bond between E3 and $S26^{i+2}$. The second β-sheet found in DI1 is also present in DI2 (**Fig. 2A**).

For DI3, the atomic model consists of A2-G33 (**Fig.2, A and G**). The overall DI3 fold differs from the DI1 fold and aligns only in residues V24-G33 with the DI2 fold (**Fig. 2, E, F, and G and Fig. S6A**). Therefore, secondary structure assignments differ from DI1 and DI2, showing two β-sheets in the N-terminal domain (**Fig. 2A**). The fold of DI3 fibrils is mainly stabilized by a salt bridge between E11 and $K28^{i+1}$ and a hydrogen bond between E11 and $S26^{i+1}$. The C-terminal kink in the structure around K28 is stabilized by a hydrogen bond between N27 and the carbonyl group at G29. Additionally, a hydrophobic cluster around V18, A21 and V24 stabilizes the overall fold (**Fig. S5F**).

Aβ fibrils extracted from tg-SwDI mouse brain are structurally different from Aβ fibrils extracted from human and APP^{NL-F} mouse brain tissue [18]. However, DI1 fibrils show some structural similarities to Aβ40 fibrils extracted from the meninges of human AD brain (**Fig. 3B**) [17] and from APP^{NL-G-F} mouse [21], [22] (**Fig. S6B**). Remarkably, unlike in most other known Aβ structures, the N-terminus in human Aβ40, APP^{NL-G-F} as well as in DI1, DI2 and DI3 fibrils is ordered. Here, the extended N-terminal arm of DI1 overlays with the N-terminus of the human Aβ40 fibril between residues D1 and Y10 and with the murine Arctic Aβ filament between E3 and S8. Moreover, the orientation of these side chains is identical in all structures, suggesting the same degree of solvent-accessibility of the N-terminus.

Finally, in contrast to wild-type (WT) Aβ42 fibrils, in which negatively charged and solvent exposed residues E22 and D23 induce a kink in the main chain, in DI1 and DI2 fibrils mutant residues Q22 and N23 are interior, in extended conformation (**Fig. 2, E and F**).

Murine type II Aβ Fibrils from ARTE10, tg-APP_{Swe}, and APP23 mouse brains

Aβ fibrils extracted from ARTE10, tg-APP_{Swe}, and APP23 mouse brains are composed of Aβ42 and identical to previously described type II filaments extracted from human brain tissue of familial AD [18], therefore here they are referred to as murine type II (**Fig. 1 and Fig.2, A, D, H, and I and Fig. 3C**).

The residues V12-A42 form the ordered core of all three murine type II fibrils, whereas N-terminal residues D1-E11 are likely flexible and therefore not resolved in the high-resolution cryo-EM structure (**Fig.2, A, D, H, and I**). Murine type II fibrils are made of two S-shaped protofilaments, which are related by a C2 symmetry in all three models. Each monomeric subunit is stabilized by

two hydrophobic clusters around residues (i) L17, V18, F20, V24, N27, I31, and L34 and (ii) A30, I32, M35, V40, and A42 (**Fig.2, A, D, H, and I and Fig. S5, C, G, and H**). The interface between the two protofilaments is rather small, involving only two symmetric hydrogen bonds between K28 and A42 of the opposing subunit.

Additionally, as previously discussed by Yang et al. [18], murine models that resemble the type II filament fold overlap in their S-shaped domain partially with seeded Aβ40 fibrils extracted from cortical tissue of an AD patient [15] (**Fig. S6C**).

Aβ Fibrils from tg-APP$_{ArcSwe}$ mouse brain

The sample of Aβ fibrils with the Arctic mutation (E693G, E22G in Aβ) extracted from tg-APP$_{ArcSwe}$ mouse brain tissue consisted of at least three different polymorphs. Structure determination was possible for the most abundant polymorph (**Table S2 and Table S3**), which we call the murine$_{Arc}$ type I Aβ fibril in the following, with a crossover distance of ~950 Å and a diameter of 90 nm (**Fig. 1**). Murine$_{Arc}$ type I Aβ fibrils consist of two identical S-shaped protofilaments that are related by a pseudo-2_1 symmetry (**Fig. 2J**). The 3 Å-resolution map of murine$_{Arc}$ type I Aβ fibrils allowed for atomic model building of the ordered core from G9-V40, in agreement with an observed predominance of Arctic Aβ40 fibrils in the sample (**Fig. 2, A and J and Table S3 and Fig. S4I**) [25], [29]. The S-shaped domain is formed by the residues F19-V40, with an associated extended N-terminal arm of G9-V18 that interacts with the C-terminus of the opposing protofilament. The S-shape is stabilized by two hydrophobic clusters around (i) F19, F18, V24, and I31 and (ii) A30, I32, M35, and V40 (**Fig. 2J and Fig. S5I**). The interface between the two protofilaments consists mainly of hydrophobic interactions involving the side chains of Y10, V12, Q15, L17, V36, and V39 at the contact point of the N-terminus of one protofilament and the C-terminus of the opposing protofilament. The fibril center harbors a hydrophobic cavity between the two C-terminal domains of both protofilaments, where two isolated symmetric densities can be observed indicating the presence of additional hydrophobic molecules of unknown identity in the interface.

Murine$_{Arc}$ type I Aβ40 fibrils resemble human type I Aβ42 filaments found in sAD patients for the most part (**Fig. 3D**) [18]. In detail, the solvent-accessible surface is almost identical to human type I Aβ42 filaments, but the C-terminus is slightly shifted, likely caused by the bound molecules in the hydrophobic fibril cavity. Aβ filaments from APP^{NL-G-F} knock-in mice also carry the Arctic mutation [21], [22], and although APP^{NL-G-F} Aβ filaments and murine$_{Arc}$ type I Aβ40 fibrils share a common substructure between residues L17-V36, the overall fold and the resulting arrangement of the two protofilaments differs (**Fig. S6D**). Additionally, and in contrast to APP^{NL-G-F} Aβ filaments, in which the mutant residue G22 is hidden in the protofilament interface, the G22 in murine$_{Arc}$ type I Aβ fibrils is exposed to solvents similarly to E22 in human type I filaments. To date, there is no other murine model known that contains predominantly Aβ fibrils that mimic the human type I fold.

The only *in vitro* preparation that resembles the Aβ40 murine$_{Arc}$ type I fold to a large extent is the NMR structure of Aβ40 fibrils with the Osaka mutation (E693Δ, E22Δ in Aβ) [30] (**Fig. S6E**). In both cases, the mutation (or deletion) of the acidic residue E22 in Aβ40 results in fibrils highly similar to sAD fibrils. Additionally, it was previously shown that Aβ42 fibrils that also harbor the Arctic mutation extracted from knock-in APP^{NL-G-F} mice brain do not resemble human type I filaments [21], [22]. As discussed for murine type II fibrils, the murine$_{Arc}$ type I fibrils also partially overlap with the cryo-EM structure of brain homogenate seeded Aβ40 [15] (**Fig. S6C**).

Additional densities in murine Aβ fibrils

We have observed additional densities on the surface of all murine fibrils. Strong, localized densities can be observed close to K16 in murine type III, DI1, DI2, DI3, and murine type II Aβ fibrils (**Fig.1 and Fig. 2 and Fig. S7, A, B, and C**). Moreover, murine type III fibrils show a smaller density close to F20 and E22 (**Fig. 7D**) and in DI3 fibrils, an additional density can be found next to Y10. Similar densities bound to K16 were previously described for APP^{NL-G-F} mice but not for AD patients [18], [21]. The observed additional density might be related to bound co-factors or post-translational modifications such as ubiquitination, as it was previously described for tau filaments [31]. Weak, micelle-like density of unknown origin bound to the fibril surface is visible in tg-SwDI Aβ fibrils (**Fig.1 and Fig. S7B**), reminiscent of previously described densities on the surface of alpha-synuclein fibrils [32].

Discussion

Here we extracted Aβ fibrils from six different transgenic mouse models and determined their structure using cryo-EM.

We observed novel Aβ fibril folds in brain extracts from three mouse models (APP/PS1, ARTE10, and tg-SwDI). Although murine type III Aβ fibrils extracted from APP/PS1 and ARTE10 mice showed some similarities to the human Arctic Aβ filament [21], their fold has not yet been observed in AD patients. The tg-SwDI model harbors a triple mutation [33], [34] that cannot be found in patients, however, these have been observed individually in early-onset AD families. DI1, DI2, and DI3 fibril structures differ from human type I and type II filaments [18] and, consequently, tg-SwDI might not be an appropriate model for neither sAD nor fAD. However, tg-SwDI is also used to study cerebral amyloid angiopathy (CAA) and indeed, the N-terminus of DI1 fibrils is identical to that of a previously described human Aβ40 polymorph obtained from vascular deposits in the brain meninges associated with CAA [17]. Therefore, tg-SwDI mice could indeed be appropriate to study CAA.

Additionally, Aβ fibrils from three mouse models (ARTE10, tg-APP_{Swe}, and APP23) resemble the human fAD type II filament fold and are therefore, together with the previously described knock-in APP^{NL-F} model [18], possible candidates for therapeutic research focused on fAD. For example, the APP23 line underwent treatment with different aducanumab analogs, showing positive results such as reduction of total plaque area and improvement in spatial memory [35] Therefore, preclinical testing with aducanumab might have been predictive for efficacy in fAD, but not well tested for sAD.

Aβ fibrils extracted from tg-APP_{ArcSwe} mouse are almost identical to human type I filaments [18] and are therefore here referred to as $murine_{Arc}$ type I fibrils. Human type I filaments are mainly found in sporadic AD, which accounts for more than 95% of all such cases [36]. However, in contrast to human type I filaments, which are composed of wildtype Aβ42, $murine_{Arc}$ type I fibrils consist of the E22G variant of Aβ40. Moreover, $murine_{Arc}$ type I fibrils show two additional densities in the protofilament interface. The Arctic mutation is also present in knock-in APP^{NL-G-F} mice, but their Aβ(E22G) fibril structure differs from $murine_{Arc}$ type I fibrils and human type I filaments [18], [21], [22]. In therapeutic research, tg-APP_{ArcSwe} mice were treated with the mAb158 monoclonal antibody promoting protofibril clearance [37]–[39]. A humanized version of the mAb158 antibody, named as BAN2401 but most commonly known as lecanemab, showed deceleration of cognitive decline and reduction of amyloid plaque burden in the brain of AD

patients [40]–[43]. So far, our murine$_{Arc}$ type I structure is the only fibril structure that resembles the human type I filament fold and therefore, tg-APP$_{ArcSwe}$ might be a valuable model to predict which drug candidate will show efficacy in sAD. The structural similarity between murine$_{Arc}$ type I filaments and human sporadic type I filaments might explain the clinical success of lecanemab [43], especially considering that it binds not only to intermediately sized soluble aggregates, but also to "diffusible Aβ fibrils" whose structure is identical to that of Aβ fibrils found in insoluble plaques [25], [26], [40].

[^{11}C] Pittsburgh compound B (PiB) and later developed fluorine-18 (^{18}F) radiolabeled analogues are commonly used PET tracers to detect AD pathology in the living brain. A positive PET scan has served as an inclusion criterion in clinical studies of antibodies such as aducanumab and lecanemab and further, a reduction in the PET signal intensity has been interpreted as successful removal of brain amyloid plaque, and thus, included as a secondary endpoint in the clinical trials. Interestingly, it was observed that patients with the human Arctic mutation are "PET-negative" [28] in spite of having massive Aβ-deposition *post mortem* [44], [45]. However, in line with our result showing that the murine$_{Arc}$ type I structure found in the tg-APP$_{ArcSwe}$ model resembles the human type I filament fold found in human sAD, PET imaging performed in the tg-APP$_{ArcSwe}$ mouse model with [^{11}C]PiB visualizes amyloid pathology [25]. Likewise, [^{11}C]PiB also works effectively in the ARTE10, tg-APP$_{Swe}$, and APP23 mouse models, that show an Aβ fibril fold similar to human type II filaments, as long as the studied mice exhibit high total brain Aβ levels. Yet, [^{11}C]PiB does not work effectively in every mouse model, as is the case for the APP/PS1 model and interestingly, that model contains murine type III fibrils which are similar to those of human Arctic brain which is also PiB-negative [28]. Thus, it is believed that the ability of [^{11}C] PiB to detect pathology depends on differences in the structure of amyloid plaques and Aβ fibrils therein [46]–[49]. For example, it has been shown that the tg-APP$_{ArcSwe}$ model exhibits higher [^{11}C]PiB binding that the APP^{NL-G-F} model [50], whose purified Aβ structures differ from human type I and type II filaments. Furthermore, a recent study that used the ^{18}F-labeled amyloid PET tracer florbetaben (FBB) to directly compare the APP/PS1 and the ARTE10 mouse models showed that the ARTE10 mice are more suitable for amyloid-PET due to their congophilic dense-cored plaques and overall higher plaque load compared to the APP/PS1 mouse model [49].

Therapeutic approaches that succeeded in animals and failed to produce positive outcomes in humans may have overlooked the possibility that animal models might not contain the relevant molecular drug targets for sAD as they do not necessarily present the same folds and surfaces. Considering that most of AD patients have a sporadic background, one can infer that this might be one important reason why the failure rate of clinical trials has been so high [27]. Structural studies of Aβ fibrils from animal models and their comparison to human Aβ fibrils, as presented in this work, reveal the molecular targets, and may help us identify the most adequate animal model for the development of novel AD treatments and PET tracers targeting amyloid deposits.

References

[1] J. M. Long and D. M. Holtzman, "Alzheimer Disease: An Update on Pathobiology and Treatment Strategies," *Cell*, vol. 179, no. 2, pp. 312–339, Oct. 2019, doi: 10.1016/j.cell.2019.09.001.

[2] P. Scheltens *et al.*, "Alzheimer's disease," *The Lancet*, vol. 388, no. 10043, pp. 505–517, Jul. 2016, doi: 10.1016/S0140-6736(15)01124-1.

[3] P. T. Nelson *et al.*, "Correlation of Alzheimer Disease Neuropathologic Changes With Cognitive Status: A Review of the Literature," *J Neuropathol Exp Neurol*, vol. 71, no. 5, pp. 362–381, May 2012, doi: 10.1097/NEN.0b013e31825018f7.

[4] F. Chiti and C. M. Dobson, "Protein Misfolding, Amyloid Formation, and Human Disease: A Summary of Progress Over the Last Decade," *Annu Rev Biochem*, vol. 86, no. 1, pp. 27–68, Jun. 2017, doi: 10.1146/annurev-biochem-061516-045115.

[5] G. Chen *et al.*, "Amyloid beta: structure, biology and structure-based therapeutic development," *Acta Pharmacol Sin*, vol. 38, no. 9, pp. 1205–1235, Sep. 2017, doi: 10.1038/aps.2017.28.

[6] J. A. Hardy and G. A. Higgins, "Alzheimer's Disease: The Amyloid Cascade Hypothesis," *Science (1979)*, vol. 256, no. 5054, pp. 184–185, Apr. 1992, doi: 10.1126/science.1566067.

[7] C. Zhang *et al.*, "Amyloid-β Production Via Cleavage of Amyloid-β Protein Precursor is Modulated by Cell Density," *Journal of Alzheimer's Disease*, vol. 22, no. 2, pp. 683–694, Oct. 2010, doi: 10.3233/JAD-2010-100816.

[8] L. Gremer *et al.*, "Fibril structure of amyloid-β(1–42) by cryo–electron microscopy," *Science (1979)*, vol. 358, no. 6359, pp. 116–119, 2017, doi: 10.1126/science.aao2825.

[9] L. Cerofolini *et al.*, "Mixing Aβ(1–40) and Aβ(1–42) peptides generates unique amyloid fibrils," *Chemical Communications*, vol. 56, no. 62, pp. 8830–8833, 2020, doi: 10.1039/D0CC02463E.

[10] M. T. Colvin *et al.*, "Atomic Resolution Structure of Monomorphic Aβ42 Amyloid Fibrils," *J Am Chem Soc*, vol. 138, no. 30, pp. 9663–9674, Aug. 2016, doi: 10.1021/jacs.6b05129.

[11] M. A. Wälti *et al.*, "Atomic-resolution structure of a disease-relevant Aβ(1–42) amyloid fibril," *Proceedings of the National Academy of Sciences*, vol. 113, no. 34, Aug. 2016, doi: 10.1073/pnas.1600749113.

[12] A. K. Paravastu, R. D. Leapman, W.-M. Yau, and R. Tycko, "Molecular structural basis for polymorphism in Alzheimer's β-amyloid fibrils," *Proceedings of the National Academy of Sciences*, vol. 105, no. 47, pp. 18349–18354, Nov. 2008, doi: 10.1073/pnas.0806270105.

[13] Y. Xiao *et al.*, "Aβ(1–42) fibril structure illuminates self-recognition and replication of amyloid in Alzheimer's disease," *Nat Struct Mol Biol*, vol. 22, no. 6, pp. 499–505, Jun. 2015, doi: 10.1038/nsmb.2991.

[14] D. Willbold, B. Strodel, G. F. Schröder, W. Hoyer, and H. Heise, "Amyloid-type Protein Aggregation and Prion-like Properties of Amyloids," *Chem Rev*, vol. 121, no. 13, pp. 8285–8307, Jul. 2021, doi: 10.1021/acs.chemrev.1c00196.

[15] U. Ghosh, K. R. Thurber, W.-M. Yau, and R. Tycko, "Molecular structure of a prevalent amyloid-β fibril polymorph from Alzheimer's disease brain tissue," *Proc Natl Acad Sci U S A*, vol. 118, no. 4, 2021, doi: https://doi.org/10.1073/pnas.2023089118.

[16] M. Lee, W.-M. Yau, J. M. Louis, and R. Tycko, "Structures of brain-derived 42-residue amyloid-β fibril polymorphs with unusual molecular conformations and intermolecular interactions," *Proceedings of the National Academy of Sciences*, vol. 120, no. 11, Mar. 2023, doi: 10.1073/pnas.2218831120.

[17] M. Kollmer *et al.*, "Cryo-EM structure and polymorphism of Aβ amyloid fibrils purified from Alzheimer's brain tissue," *Nat Commun*, vol. 10, no. 1, p. 4760, Dec. 2019, doi: 10.1038/s41467-019-12683-8.

[18] Y. Yang *et al.*, "Cryo-EM structures of amyloid-β 42 filaments from human brains," *Science (1979)*, vol. 375, no. 6577, pp. 167–172, Jan. 2022, doi: 10.1126/science.abm7285.

[19] F. M. LaFerla and K. N. Green, "Animal Models of Alzheimer Disease," *Cold Spring Harb Perspect Med*, vol. 2, no. 11, pp. a006320–a006320, Nov. 2012, doi: 10.1101/cshperspect.a006320.

[20] E. Drummond and T. Wisniewski, "Alzheimer's disease: experimental models and reality," *Acta Neuropathol*, vol. 133, no. 2, pp. 155–175, Feb. 2017, doi: 10.1007/s00401-016-1662-x.

[21] Y. Yang *et al.*, "Cryo-EM structures of amyloid-β filaments with the Arctic mutation (E22G) from human and mouse brains," *Acta Neuropathol*, vol. 145, no. 3, pp. 325–333, Mar. 2023, doi: 10.1007/s00401-022-02533-1.

[22] C. Leistner *et al.*, "The in-tissue molecular architecture of β-amyloid in the mammalian brain," *bioRxiv*, p. 2022.11.08.515609, Jan. 2022, doi: 10.1101/2022.11.08.515609.

[23] J. Cummings *et al.*, "Alzheimer's disease drug development pipeline: 2022," *Alzheimer's & Dementia: Translational Research & Clinical Interventions*, vol. 8, no. 1, Jan. 2022, doi: 10.1002/trc2.12295.

[24] H. Englund *et al.*, "Sensitive ELISA detection of amyloid-β protofibrils in biological samples," *J Neurochem*, vol 103, no. 1, p. 334-45, 2007

[25] D. Sehlin, X. T. Fang, L. Cato, G. Antoni, L. Lannfelt, and S. Syvänen, "Antibody-based PET imaging of amyloid beta in mouse models of Alzheimer's disease," *Nat Commun*, vol. 7, no. 1, p. 10759, Feb. 2016, doi: 10.1038/ncomms10759.

[26] A. M. Stern *et al.*, "Abundant Aβ fibrils in ultracentrifugal supernatants of aqueous extracts from Alzheimer's disease brains," *bioRxiv*, Oct. 2022.

[27] J. L. Cummings, T. Morstorf, and K. Zhong, "Alzheimer's disease drug-development pipeline: few candidates, frequent failures," *Alzheimers Res Ther*, vol. 6, no. 4, p. 37, 2014, doi: 10.1186/alzrt269.

[28] M. Scholl *et al.*, "Low PiB PET retention in presence of pathologic CSF biomarkers in Arctic APP mutation carriers," *Neurology*, vol. 79, no. 3, pp. 229–236, Jul. 2012, doi: 10.1212/WNL.0b013e31825fdf18.

[29] O. Philipson *et al.*, "A highly insoluble state of Aβ similar to that of Alzheimer's disease brain is found in Arctic APP transgenic mice," *Neurobiol Aging*, vol. 30, no. 9, pp. 1393–1405, Sep. 2009, doi: 10.1016/j.neurobiolaging.2007.11.022.

[30] A. K. Schütz *et al.*, "Atomic-Resolution Three-Dimensional Structure of Amyloid β Fibrils Bearing the Osaka Mutation," *Angewandte Chemie International Edition*, vol. 54, no. 1, pp. 331–335, Jan. 2015, doi: 10.1002/anie.201408598.

[31] T. Arakhamia *et al.*, "Posttranslational Modifications Mediate the Structural Diversity of Tauopathy Strains," *Cell*, vol. 184, no. 25, pp. 6207–6210, Dec. 2021, doi: 10.1016/j.cell.2021.11.029.

[32] B. Frieg *et al.*, "The 3D structure of lipidic fibrils of α-synuclein," *Nat Commun*, vol. 13, no. 1, p. 6810, Nov. 2022, doi: 10.1038/s41467-022-34552-7.

[33] J. Davis *et al.*, "Early-onset and Robust Cerebral Microvascular Accumulation of Amyloid β-Protein in Transgenic Mice Expressing Low Levels of a Vasculotropic Dutch/Iowa Mutant Form of Amyloid β-Protein Precursor," *Journal of Biological Chemistry*, vol. 279, no. 19, pp. 20296–20306, May 2004, doi: 10.1074/jbc.M312946200.

[34] J. Miao, F. Xu, J. Davis, I. Otte-Höller, M. M. Verbeek, and W. E. Van Nostrand, "Cerebral Microvascular Amyloid β Protein Deposition Induces Vascular Degeneration and Neuroinflammation in Transgenic Mice Expressing Human Vasculotropic Mutant Amyloid β Precursor Protein," *Am J Pathol*, vol. 167, no. 2, pp. 505–515, Aug. 2005, doi: 10.1016/S0002-9440(10)62993-8.

[35] G. Leinenga, W. K. Koh, and J. Götz, "A comparative study of the effects of Aducanumab and scanning ultrasound on amyloid plaques and behavior in the APP23 mouse model of Alzheimer disease," *Alzheimers Res Ther*, vol. 13, no. 1, p. 76, Dec. 2021, doi: 10.1186/s13195-021-00809-4.

[36] J. Bali, A. H. Gheinani, S. Zurbriggen, and L. Rajendran, "Role of genes linked to sporadic Alzheimer's disease risk in the production of β-amyloid peptides," *Proceedings of the National Academy of Sciences*, vol. 109, no. 38, pp. 15307–15311, Sep. 2012, doi: 10.1073/pnas.1201632109.

[37] A. Lord *et al.*, "An amyloid-β protofibril-selective antibody prevents amyloid formation in a mouse model of Alzheimer's disease," *Neurobiol Dis*, vol. 36, no. 3, pp. 425–434, Dec. 2009, doi: 10.1016/j.nbd.2009.08.007.

[38] S. Tucker *et al.*, "The Murine Version of BAN2401 (mAb158) Selectively Reduces Amyloid-β Protofibrils in Brain and Cerebrospinal Fluid of tg-ArcSwe Mice," *Journal of Alzheimer's Disease*, vol. 43, no. 2, pp. 575–588, Nov. 2014, doi: 10.3233/JAD-140741.

[39] S. Syvänen *et al.*, "Efficient clearance of Aβ protofibrils in AβPP-transgenic mice treated with a brain-penetrating bifunctional antibody," *Alzheimers Res Ther*, vol. 10, no. 1, p. 49, Dec. 2018, doi: 10.1186/s13195-018-0377-8.

[40] L. Söderberg *et al.*, "Lecanemab, Aducanumab, and Gantenerumab — Binding Profiles to Different Forms of Amyloid-Beta Might Explain Efficacy and Side Effects in Clinical Trials for Alzheimer's Disease," *Neurotherapeutics*, Oct. 2022, doi: 10.1007/s13311-022-01308-6.

[41] V. Logovinsky *et al.*, "Safety and tolerability of BAN2401 - a clinical study in Alzheimer's disease with a protofibril selective Aβ antibody," *Alzheimers Res Ther*, vol. 8, no. 1, p. 14, Dec. 2016, doi: 10.1186/s13195-016-0181-2.

[42] C. J. Swanson *et al.*, "A randomized, double-blind, phase 2b proof-of-concept clinical trial in early Alzheimer's disease with lecanemab, an anti-Aβ protofibril antibody," *Alzheimers Res Ther*, vol. 13, no. 1, p. 80, Dec. 2021, doi: 10.1186/s13195-021-00813-8.

[43] C. H. van Dyck *et al.*, "Lecanemab in Early Alzheimer's Disease," *New England Journal of Medicine*, vol. 388, no. 1, pp. 9–21, Jan. 2023, doi: 10.1056/NEJMoa2212948.

[44] H. Kalimo *et al.*, "The Arctic AβPP mutation leads to Alzheimer's disease pathology with highly variable topographic deposition of differentially truncated Aβ.," *Acta Neuropathol Commun*, vol. 1, p. 60, Sep. 2013, doi: 10.1186/2051-5960-1-60.

[45] O. Philipson *et al.*, "The Arctic amyloid-β precursor protein (AβPP) mutation results in distinct plaques and accumulation of N- and C-truncated Aβ.," *Neurobiol Aging*, vol. 33, no. 5, pp. 1010.e1–13, May 2012, doi: 10.1016/j.neurobiolaging.2011.10.022.

[46] A. Snellman *et al.*, "Longitudinal Amyloid Imaging in Mouse Brain with 11C-PIB: Comparison of APP23, Tg2576, and APPswe-PS1dE9 Mouse Models of Alzheimer Disease," *Journal of Nuclear Medicine*, vol. 54, no. 8, pp. 1434–1441, Aug. 2013, doi: 10.2967/jnumed.112.110163.

[47] A. Snellman *et al.*, "In vivo PET imaging of beta-amyloid deposition in mouse models of Alzheimer's disease with a high specific activity PET imaging agent [18F]flutemetamol," *EJNMMI Res*, vol. 4, no. 1, p. 37, Dec. 2014, doi: 10.1186/s13550-014-0037-3.

[48] B. H. Yousefi *et al.*, "FIBT versus florbetaben and PiB: a preclinical comparison study with amyloid-PET in transgenic mice," *EJNMMI Res*, vol. 5, no. 1, p. 20, Dec. 2015, doi: 10.1186/s13550-015-0090-6.

[49] A. Willuweit *et al.*, "Comparison of the Amyloid Load in the Brains of Two Transgenic Alzheimer's Disease Mouse Models Quantified by Florbetaben Positron Emission Tomography," *Front Neurosci*, vol. 15, Oct. 2021, doi: 10.3389/fnins.2021.699926.

[50] S. R. Meier *et al.*, "11C-PiB and 124 I-Antibody PET Provide Differing Estimates of Brain Amyloid-β After Therapeutic Intervention," *Journal of Nuclear Medicine*, vol. 63, no. 2, pp. 302–309, Feb. 2022, doi: 10.2967/jnumed.121.262083.

[51] Takanori Nakane, "atom2svg." 2020. Accessed: May 01, 2022. [Online]. Available: https://zenodo.org/record/4090925#.YqNEES-21iM

[52] J. L. Jankowsky *et al.*, "Mutant presenilins specifically elevate the levels of the 42 residue β-amyloid peptide in vivo: evidence for augmentation of a 42-specific γ secretase," *Hum Mol Genet*, vol. 13, no. 2, pp. 159–170, Jan. 2004, doi: 10.1093/hmg/ddh019.

[53] C. Janus, A. Y. Flores, G. Xu, and D. R. Borchelt, "Behavioral abnormalities in APPSwe/PS1dE9 mouse model of AD-like pathology: comparative analysis across multiple behavioral domains," *Neurobiol Aging*, vol. 36, no. 9, pp. 2519–2532, Sep. 2015, doi: 10.1016/j.neurobiolaging.2015.05.010.

[54] M. Garcia-Alloza *et al.*, "Characterization of amyloid deposition in the APPswe/PS1dE9 mouse model of Alzheimer disease," *Neurobiol Dis*, vol. 24, no. 3, pp. 516–524, Dec. 2006, doi: 10.1016/j.nbd.2006.08.017.

[55] A. Willuweit *et al.*, "Early-Onset and Robust Amyloid Pathology in a New Homozygous Mouse Model of Alzheimer's Disease," *PLoS One*, vol. 4, no. 11, p. e7931, Nov. 2009, doi: 10.1371/journal.pone.0007931.

[56] F. Xu *et al.*, "Early-onset subicular microvascular amyloid and neuroinflammation correlate with behavioral deficits in vasculotropic mutant amyloid β-protein precursor transgenic mice," *Neuroscience*, vol. 146, no. 1, pp. 98–107, Apr. 2007, doi: 10.1016/j.neuroscience.2007.01.043.

[57] J. Davis *et al.*, "Early-onset and Robust Cerebral Microvascular Accumulation of Amyloid β-Protein in Transgenic Mice Expressing Low Levels of a Vasculotropic Dutch/Iowa Mutant Form

of Amyloid β-Protein Precursor," *Journal of Biological Chemistry*, vol. 279, no. 19, pp. 20296–20306, May 2004, doi: 10.1074/jbc.M312946200.

[58] A. Lord, H. Kalimo, C. Eckman, X.-Q. Zhang, L. Lannfelt, and L. N. G. Nilsson, "The Arctic Alzheimer mutation facilitates early intraneuronal Aβ aggregation and senile plaque formation in transgenic mice," *Neurobiol Aging*, vol. 27, no. 1, pp. 67–77, Jan. 2006, doi: 10.1016/j.neurobiolaging.2004.12.007.

[59] S. Lillehaug, G. H. Syverstad, L. N. G. Nilsson, J. G. Bjaalie, T. B. Leergaard, and R. Torp, "Brainwide distribution and variance of amyloid-beta deposits in tg-ArcSwe mice," *Neurobiol Aging*, vol. 35, no. 3, pp. 556–564, Mar. 2014, doi: 10.1016/j.neurobiolaging.2013.09.013.

[60] W. Michno *et al.*, "Pyroglutamation of amyloid-βx-42 (Aβx-42) followed by Aβ1–40 deposition underlies plaque polymorphism in progressing Alzheimer's disease pathology," *Journal of Biological Chemistry*, vol. 294, no. 17, pp. 6719–6732, Apr. 2019, doi: 10.1074/jbc.RA118.006604.

[61] N. M. Gulati, U. Torian, J. R. Gallagher, and A. K. Harris, "Immunoelectron Microscopy of Viral Antigens," *Curr Protoc Microbiol*, vol. 53, no. 1, Jun. 2019, doi: 10.1002/cpmc.86.

[62] D. Tegunov and P. Cramer, "Real-time cryo-electron microscopy data preprocessing with Warp," *Nat Methods*, vol. 16, no. 11, pp. 1146–1152, Nov. 2019, doi: 10.1038/s41592-019-0580-y.

[63] A. Rohou and N. Grigorieff, "CTFFIND4: Fast and accurate defocus estimation from electron micrographs," *J Struct Biol*, vol. 192, no. 2, pp. 216–221, Nov. 2015, doi: 10.1016/j.jsb.2015.08.008.

[64] S. He and S. H. W. Scheres, "Helical reconstruction in RELION," *J Struct Biol*, vol. 198, no. 3, pp. 163–176, 2017, doi: 10.1016/j.jsb.2017.02.003.

[65] J. Zivanov *et al.*, "New tools for automated high-resolution cryo-EM structure determination in RELION-3," *Elife*, vol. 7, Nov. 2018, doi: 10.7554/eLife.42166.

[66] T. Wagner, L. Lusnig, S. Pospich, M. Stabrin, F. Schönfeld, and S. Raunser, "Two particle-picking procedures for filamentous proteins: SPHIRE-crYOLO filament mode and SPHIRE-STRIPER," *Acta Crystallogr D Struct Biol*, vol. 76, no. 7, pp. 613–620, Jul. 2020, doi: 10.1107/S2059798320007342.

[67] T. Wagner *et al.*, "SPHIRE-crYOLO is a fast and accurate fully automated particle picker for cryo-EM," *Commun Biol*, vol. 2, no. 1, p. 218, Jun. 2019, doi: 10.1038/s42003-019-0437-z.

[68] X. Bai, E. Rajendra, G. Yang, Y. Shi, and S. H. Scheres, "Sampling the conformational space of the catalytic subunit of human γ-secretase," *Elife*, vol. 4, Dec. 2015, doi: 10.7554/eLife.11182.

[69] S. H. W. Scheres, "Amyloid structure determination in RELION-3.1," *Acta Crystallogr D Struct Biol*, 2020, doi: 10.1107/S2059798319016577.

[70] M. Spiegel, A. K. Duraisamy, and G. F. Schröder, "Improving the visualization of cryo-EM density reconstructions," *J Struct Biol*, vol. 191, no. 2, pp. 207–213, Aug. 2015, doi: 10.1016/j.jsb.2015.06.007.

[71] A. Casañal, B. Lohkamp, and P. Emsley, "Current developments in Coot for macromolecular model building of Electron Cryo-microscopy and Crystallographic Data," *Protein Science*, vol. 29, no. 4, pp. 1055–1064, Apr. 2020, doi: 10.1002/pro.3791.

[72] C. J. Williams *et al.*, "MolProbity: More and better reference data for improved all-atom structure validation," *Protein Science*, vol. 27, no. 1, pp. 293–315, Jan. 2018, doi: 10.1002/pro.3330.

[73] P. V. Afonine *et al.*, "Real-space refinement in PHENIX for cryo-EM and crystallography," *Acta Crystallogr D Struct Biol*, vol. 74, no. 6, pp. 531–544, Jun. 2018, doi: 10.1107/S2059798318006551.

[74] T. I. Croll, "ISOLDE: a physically realistic environment for model building into low-resolution electron-density maps," *Acta Crystallogr D Struct Biol*, vol. 74, no. 6, pp. 519–530, Jun. 2018, doi: 10.1107/S2059798318002425.

[75] E. F. Pettersen *et al.*, "UCSF ChimeraX : Structure visualization for researchers, educators, and developers," *Protein Science*, vol. 30, no. 1, pp. 70–82, Jan. 2021, doi: 10.1002/pro.3943.

Acknowledgments

Acknowledgments: MZ and GFS. gratefully acknowledge the electron microscopy training, imaging and access time granted by the life science EM facility of the Ernst-Ruska Centre at Forschungszentrum Jülich. MZ, BF and GFS. are grateful for the computing time provided by Forschungszentrum Jülich on the supercomputer JURECA/JURECA-DC at Jülich Supercomputing Center (JSC). The ARTE10 mouse line was a generous gift from Taconic Biosciences Inc. GFS acknowledges support from Alzheimer Forschung Initiative e.V. SaS received funding from the German Federal Ministry for Education and Research (project number 16LW028). MI has received grants from the Swedish Research Council (2021-02793). SS and DS acknowledge funding from the Swedish Research council (2021-01083 and 2021-03524), Alzheimerfonden and Hjärnfonden. D.W. was supported by ‘‘Portfolio Drug Research’’ of the ‘‘Impuls und Vernetzungs-Fonds der Helmholtzgemeinschaft.’’

Author Contributions:

Conceptualization: LG, GFS
Organisation of breeding and characterization of mouse tissue: SaS, SS, DS, MI, LD, ME, AW, LNGN
Extraction of Aβ fibrils: FSPR
Immunogold labelling: MZ, FSPR
Cryo-EM grid preparation and data collection: MZ
Image processing, reconstruction, and model building: MZ, BF, GFS
Visualization: MZ, FSPR
Supervision: LG, DW, GFS
Writing - original draft: MZ, FSPR, LG, GFS
Writing - review & editing: All Authors

Competing interests: LNGN is on the scientific advisory board and receives a research grant from BioArctic. MI is a paid consultant to BioArctic. D.W. is a founder and shareholder of the company Priavoid and member of its supervisory board. D.W. is co-inventor of patents related to the compound RD2. D.W. is a founder and shareholder of attyloid. D.W. is member of attyloid's supervisory board. These had no influence on the interpretation of the data. All other authors declare no competing interests.

Data and materials availability:

Cryo-EM maps have been deposited to the Electron Microscopy Data Bank (EMDB) and to the Protein Data Bank (PDB) under the following accession numbers: EMD-16944 (PDB ID: 8OL3) for murine type III Aβ42 fibrils from APP/PS1, EMD-16960 (PDB ID: 8OLO) for murine type III Aβ40 fibrils from ARTE10, EMD-16949 (PDB ID: 8OL5) for murine type II Aβ42 fibrils from ARTE10, EMD-16959 (PDB ID: 8OLN) for DI1 Aβ fibrils from tg-SwDI, EMD-16957 (PDB ID: 8OLG) for DI2 Aβ fibrils from tg-SwDI, EMD-16961 (PDB ID: 8OLQ) for DI3 Aβ fibrils from tg-SwDI, EMD-16952 (PDB ID: 8OL6) for murine type II Aβ42 fibrils from tg-APP_{Swe}, EMD-16942 (PDB ID: 8OL2) for murine type II Aβ42 fibrils from APP23, and EMD-16953 (PDB ID: 8OL7) for $murine_{Arc}$ type I Aβ40 fibrils from tg-APP_{ArcSwe}.

Main Figures

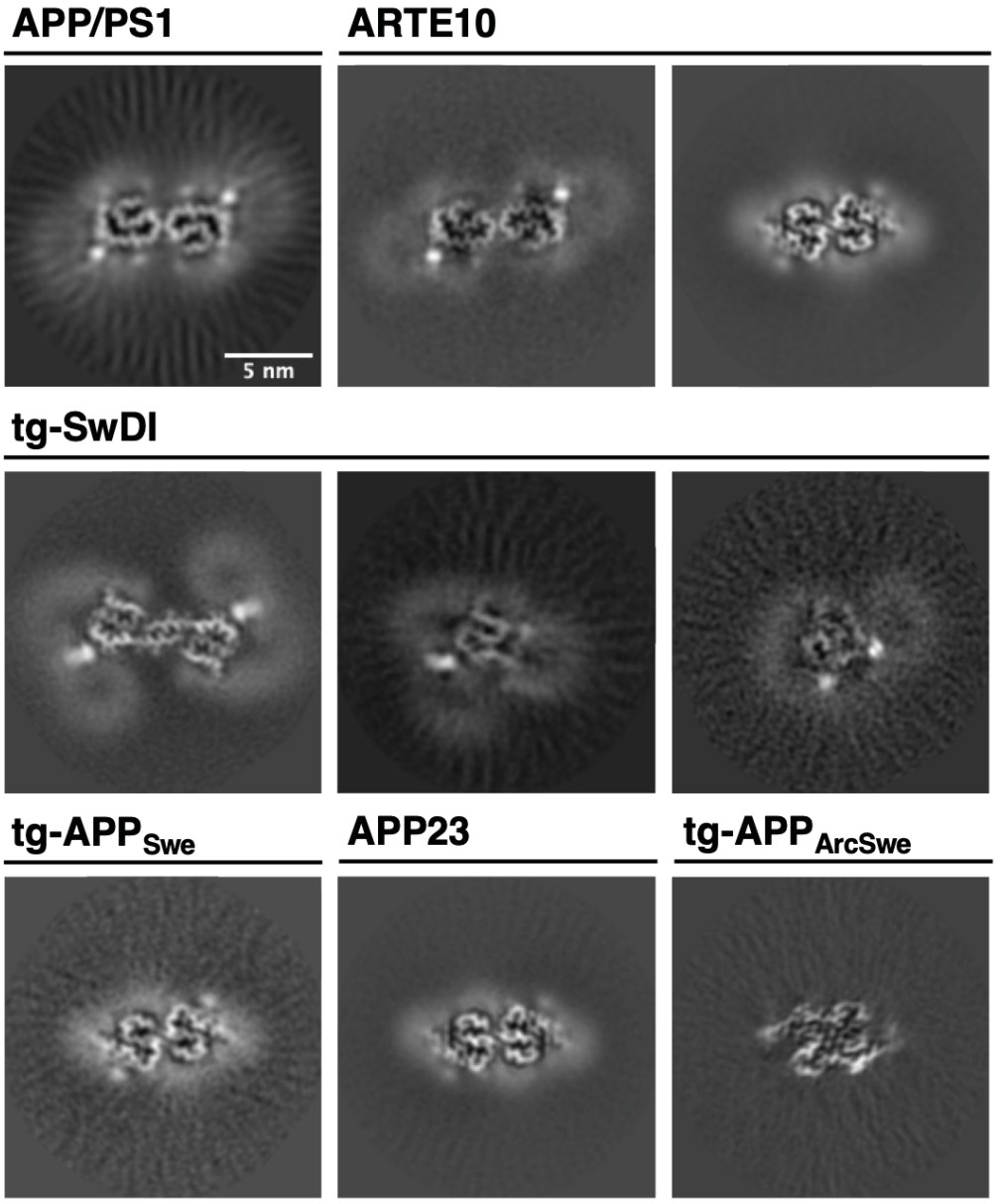

Figure 1: Cryo-EM reconstructions of Aβ fibrils extracted from APP/PS1, ARTE10, tg-SwDI, tg-APP_{Swe}, APP23, and tg-APP_{ArcSwe} mouse brain tissue. For every reconstructed fibril, a cross-section through the reconstructed density map is shown. The scale bar in the top left panel applies to all shown panels. From upper left to lower right: murine type III (APP/PS1), murine type III (ARTE10), murine type II (ARTE10), DI1, DI2, DI3, murine type II (tg-APP_{Swe}), murine type II (APP23) and $murine_{Arc}$ type I.

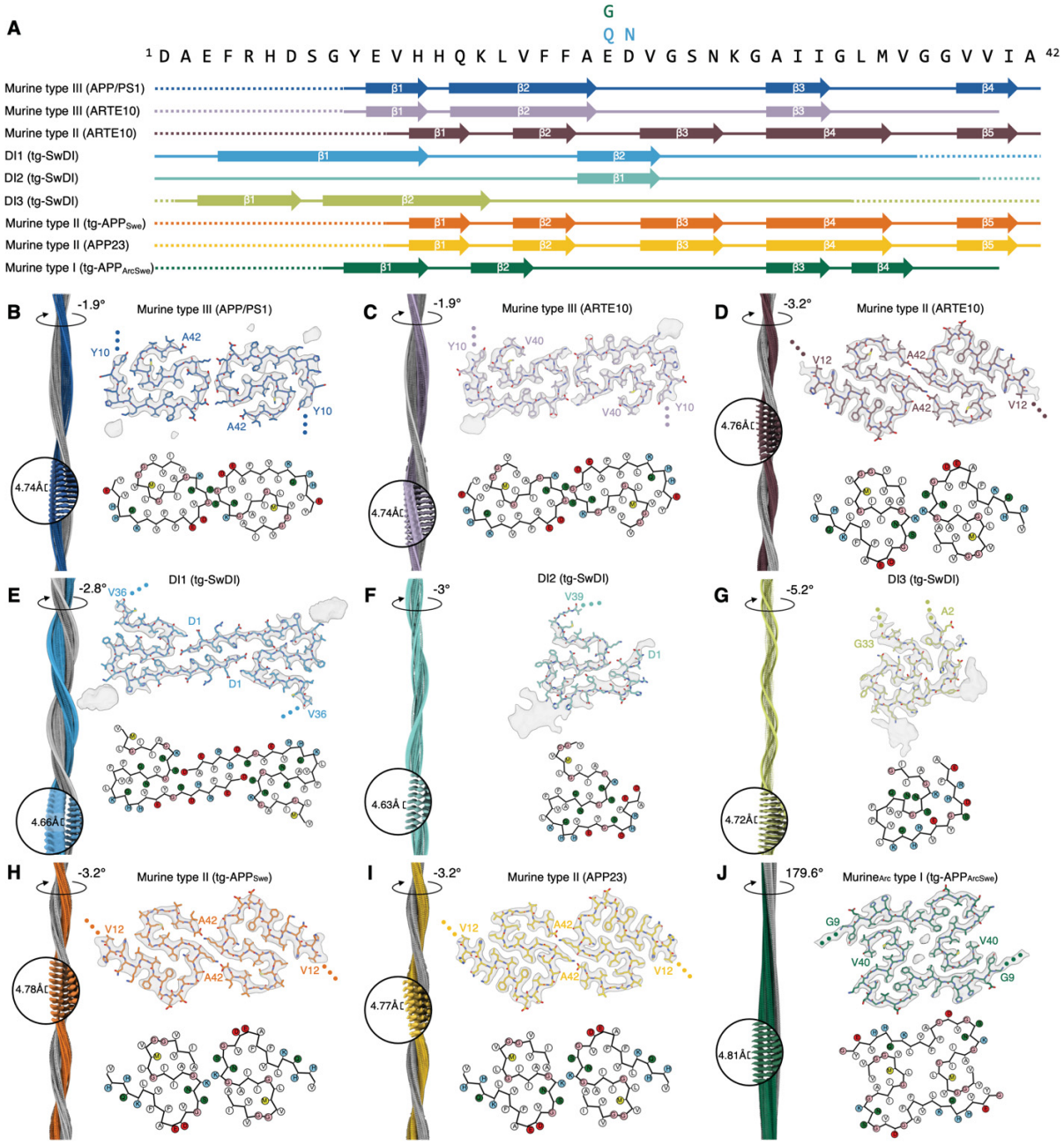

Figure 2: Overview of all murine Aβ fibril structures. (A) Amino acid sequence of Aβ42. The sequence contains the following mutations for tg-SwDI: E22Q and D23N; and for tg-APP$_{ArcSwe}$: E22G. Solid lines indicate for which part of the sequence atomic model building was possible (accordingly, dotted lines represent parts of the sequence that were not modelled). Arrows indicate β-strands. Panels (B-J) consist of: the reconstructed cryo-EM density along the helical axis and a close-up with labels denoting the helical twist and rise (left); the cryo-EM density map (in transparent gray) with the corresponding atomic model (top right); a schematic of the fold, produced with atom2svg.py [51] (red: acidic side chain; blue: basic side chain; green: hydrophilic side chain; white: hydrophobic side chain; pink: glycine; yellow: sulfur containing) (bottom right). Cryo-EM structure of (B) murine type III Aβ42 fibrils from APP/PS1 mouse brain, (C) murine

type III Aβ40 fibrils from ARTE10 mouse brain, (D) murine type II Aβ42 fibrils from ARTE10 mouse brain, (E) DI1 Aβ fibrils from tg-SwDI mouse brain, (F) DI2 Aβ fibrils from tg-SwDI mouse brain, (G) DI3 Aβ fibrils from tg-SwDI mouse brain, (H) murine type II Aβ42 fibrils from tg-APP_{Swe} mouse brain, (I) murine type II Aβ42 fibrils from APP23 mouse brain, and (J) murine$_{Arc}$ type I Aβ40 fibrils from tg-APP_{ArcSwe} mouse brain.

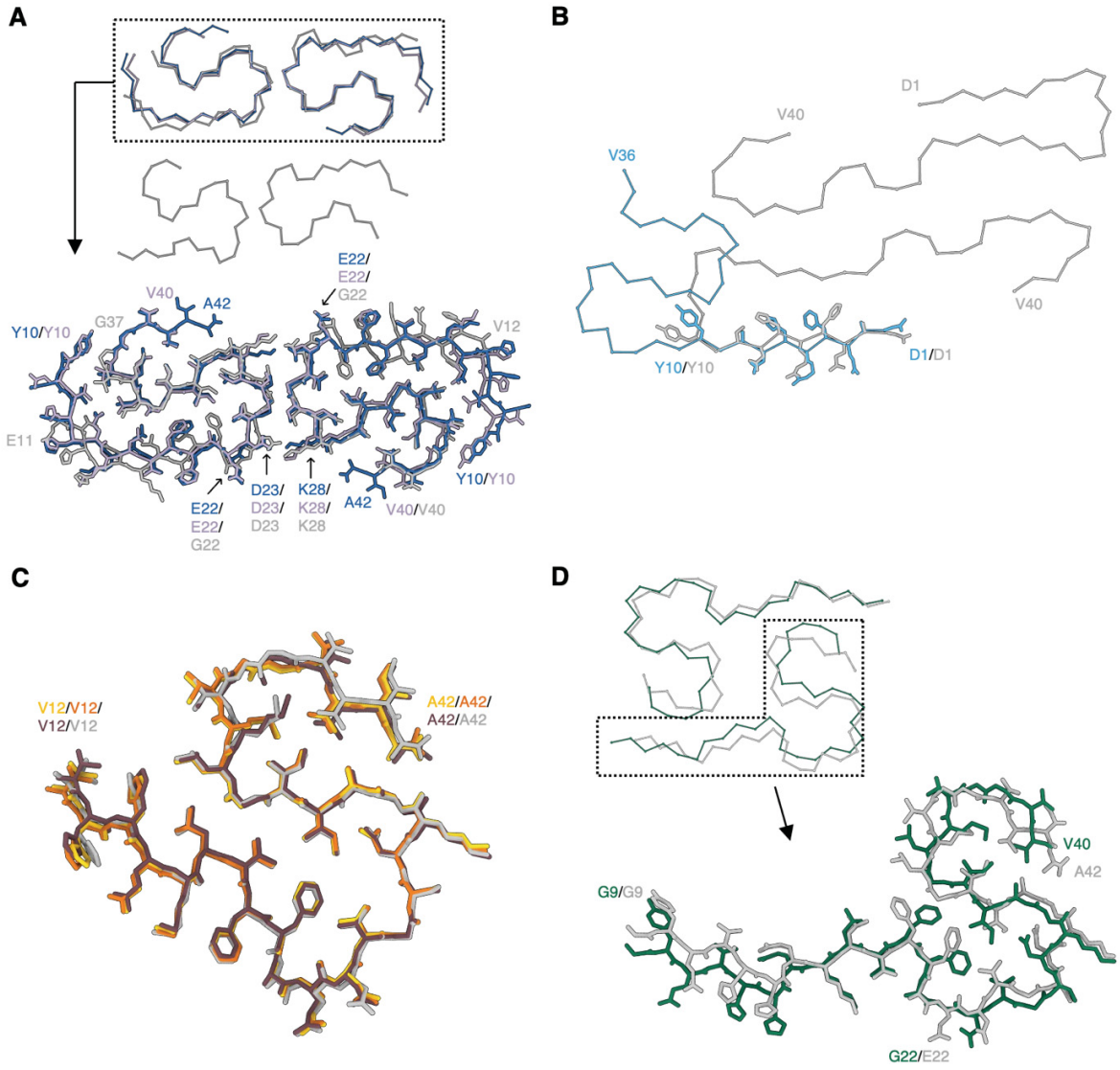

Figure 3: Comparison of brain-derived murine Aβ fibrils to brain-derived human extracted Aβ fibrils. (A) Comparison of murine type III Aβ fibrils (blue: APP/PS1; lavender: ARTE10) with the cryo-EM structure of human brain extracted Aß filaments with the E693G (E22G) mutation (gray, PDB code: 8BG0), (B) Comparison of the DI1 Aβ fibril (light blue) with the cryo-EM structure of Aβ40 fibrils extracted from the meninges of human AD brain tissue (gray, PDB code: 6SHS), (C) Comparison of the APP23 (yellow), tg-APP$_{Swe}$ (orange) and ARTE10 (burgundy) Aβ42 fibril fold with human type II Aβ42 filaments (gray, PDB code: 7Q4M), (D) Comparison of the murine$_{Arc}$ type I (green) Aβ40 fibril fold with human type I Aβ42 filament fold (gray, PDB code: 7Q4B).

Supplementary materials and methods

Materials and Methods

Animals

In the present study, the following mouse lines were used for experimentation including immunohistochemistry, negative stain sample screening, immunogold negative stain, and cryo-EM:

APP/PS1 (APPswe/PSEN1dE) (heterozygous; n=4 (male = 3; female = 1); age: 27–33 months old) on a C57BL/6;C3H background (strain name B6.Cg-Tg(APPswe,PSEN1dE9)85Dbo/Mmjax) are well described in terms of their behavioral and pathological characteristics [52]–[54]. Depending on the used protocol, APP/PS1 mice develop (contextual and spatial) cognitive deficits by seven months of age. Aβ plaques can be detected by six months of age in hippocampus and cortex, followed by a pronounced gliosis. Abundant Aβ plaques and gliosis are prominent with twelve months of age. Four heterozygous APP/PS1 mice brains were used in this study.

ARTE10 (homozygous; n= 1 (female); age= 24 months old) mouse on a C57Bl/6 background (strain name B6.CBA-Tg(Thy1-PSEN1*M146V,-APP*Swe)10Arte) was a generous gift from Taconic Biosciences Inc. (Germantown, NY, USA). The mice express APPswe (APP KM670/671NL) and PS1-M146V under Thy1.1 regulatory sequences, which leads to the development of a progressive plaque pathology and CAA starting around the age of 3 months [55].

Tg-SwDI mice (heterozygous; n = 4 (all male); age: 26–29 months old) on a C57BL/6 background (strain name C57BL/6-Tg(Thy1-APPSwDutIowa)BWevn/Mmjax) were first introduced by Davis et al. in 2004 as a model to study cerebral amyloid angiopathy (CAA) in AD [56], [57]. Cognitive deficits and Aβ plaques with associated gliosis can be detected by three months of age, increasing, and manifesting with age.

APP23 mice (heterozygous; n= 2 (all male); age= 21 months old) are on a C56BL/6 background (strain name B6.Cg-Tg(Thy1-APP)3Somm/J) and have a 7-fold overexpression of mutant human APP_{751} bearing the pathogenic Swedish mutation. Aβ deposit starting at six months of age and increase in size and number with age [52]. APP23 mice also develop CAA [53].

Tg-APP_{ArcSwe} (heterozygous; n= 1 (male); age= 18 months old) and tg-APP_{Swe} (heterozygous; n= 2 (all male); age= 22 months old) are maintained on a C57BL/6 background [58]. Tg-APP_{ArcSwe} mice harbor the Swedish and the Arctic APP mutations and develop plaque pathology starting at

around 6 months of age, while Tg-APP$_{Swe}$ mice that harbor the Swedish mutation have a later onset of plaque pathology starting at 10–12 months of age and then increasing with rapidly with age.

APP/PS1, ARTE10, tg-SwDI, APP23 experiments were performed in accordance with the German Law on the protection of animals (TierSchG §§7–9). Breeding of APP/PS1 mice was approved by a local ethics committee [Landesamt für Natur, Umwelt und Verbraucherschutz Nordrhein-Westfalen (LANUV), North Rhine-Westphalia, Germany, Az: 84-02.04.2014.362] before start of the study. APP/PS1 and tg-SwDI mice were (and can be) purchased by the Jackson Lab (JAX MMRRC Stock# 034829 or JAX MMRRC Stock# 034843).The tg-APP$_{ArcSwe}$ and tg-APP$_{Swe}$ mice were bred under the ethical permit 5.8.18-20401/20 approved by the Uppsala County Animal Ethics board. All mice were kept and bred under controlled conditions with 12/12 h light/dark cycle, 54% humidity, a temperature of 22°C as well as food and water *ad libitum.*

Brain tissue characterization

Brain tissue from the tg-APP$_{Swe}$, tg-APP$_{ArcSwe}$, and the ARTE10 mouse models has been extensively characterized in previous studies [29], [49], [55], [58]–[60].

The remaining APP/PS1, tg-SwDI and APP23 mouse lines were immunohistochemically stained as follows: In brief, after cervical dislocation, the brains were snap frozen in isopentane and cut in 20 µm sagittal sections with a microtome. Afterwards, the sections were fixed with 4% paraformaldehyde (PFA) in TRIS-buffered saline (TBS) for 10 min at room temperature (RT). The sections were washed three times with 1% Triton in TBS (TBST) for 5 min and further incubated in 70% formic acid for 5 min at RT for antigen retrieval. The sections were again washed with TBST before incubation with primary antibody overnight at 4°C in a humidified chamber (6E10 (BioLegend, Alexa Fluor 594 anti-β-Amyloid, 803018) and 4G8 (BioLegend, 800708, both diluted 1:500 in TBST with 1% bovine serum albumin (BSA)). The day after, the tissue sections were washed with TBST before incubation with the secondary antibody (only 4G8, goat anti-mouse antibody, Alexa Fluor 488, Invitrogen, diluted 1:300 in TBST and 1% BSA) for 1 h at RT. For cell nuclei staining, the sections were washed again with TBST before incubation with DAPI ((4′,6-Diamidin-2-phenylindol) (Merck, Germany)) for 5 min. Subsequently, the sections were washed three times with TBST before mounting (Fluoromount Aqueous Mounting Medium, Sigma-Aldrich, St. Louis, USA). Images were taken with a LMD6000 microscope (Leica Camera, Germany) with a DFC310 FX camera (Leica Camera, Germany).

Extraction of Aβ Fibrils

Aβ fibril extraction was essentially based on a published procedure [18]. In brief, non-fixed mouse brain tissue was snap frozen in -80°C cold isopentane and stored at -80°C previous to experimentation. Between 0.4 and 0.6 g of brain tissue was thawed and manually homogenized in 20-times volume (w/v) of extraction buffer (10 mM Tris-HCl, pH 7.5, 0.8 M NaCl, 10% sucrose, 1 mM EGTA) by applying 300 strokes using a Dounce glass tissue grinder. Subsequently, 10% sarkosyl diluted in $_{d}H_2O$ (Sigma-Aldrich) was added to the homogenate to a final sarkosyl concentration of 2% and was thoroughly mixed 30-times by pipetting up and down. After 1h incubation at 37°C, the homogenate was centrifuged at 10.000 x g for 10 min at 4°C and the

resulting supernatant was further ultracentrifuged at 100.000 x g for 60 min at 4°C (Beckman Coulter Optima MAX-XP, TLA55 fixed-angle rotor). After removal of the supernatant, extraction buffer (1 ml/g original tissue mass) was added to the pellet and mixed, followed by 5.000 x g centrifugation for 5 min at 4°C. The supernatant was then diluted 3-fold in dilution buffer (50 mM Tris-HCl, pH 7.5, 0.15 M NaCl, 10% sucrose, 0.2% sarkosyl) and ultracentrifuged at 100.000 x g for 30 min at 4°C. The resulting supernatant was discarded and resuspension buffer (20 mM Tris-HCl, pH 7.4, 50 mM NaCl) was added (100 µl/g original tissue mass) to the sarkosyl insoluble Aβ fibril rich pellet. The pellet was used for further negative staining, immunogold labelling and cryo-EM analysis.

We noticed that the fibril extraction protocol was sensitive to changes in temperature, sarkosyl concentration and frequency of homogenization, therefore, the procedure was optimized accordingly.

Negative stain Electron Microscopy

2 µl of the final sarkosyl insoluble fraction, consisting of a homogeneous mixture of the final pellet after fibril extraction and resuspension buffer, were applied onto a glow-discharged 300 mesh carbon-coated copper grid (EM Sciences, ECF300-Cu). The sample was incubated for 2 min and carefully blotted off with filter paper. The sample was then washed once with $_{d}$H2O and blotted off immediately. 2 µl of 1% (w/v) uranyl acetate (UrAc) were applied on the top of the grid, following a 1 min incubation. The UrAc was removed with filter paper and the grid was air-dried. TEM images were acquired using a ThermoFisher Scientific Talos 120C at an acceleration voltage of 120 kV. Images were collected on a 4k x 4k Ceta 16M CEMOS camera using Thermo Scientific Velox Software.

Immunogold negative stain Electron Microscopy

Immunogold negative-stain grids for electron microscopy were prepared following [61]. In brief, 3 µl of the final pellet containing the extracted Aβ fibrils were placed on a glow-discharged 300 mesh carbon-coated copper grid (EM Sciences, ECF300-CU) for 2 min. The sample was washed once with $_{d}$H20 and placed in blocking buffer for 15 min, following incubation with Nab228 (Sigma-Aldrich) primary antibody diluted in blocking buffer at a concentration of 2 µg/ml for 1-2 h. Furthermore, the grid was washed with washing buffer and was incubated with 6 nm gold-conjugated anti-mouse secondary antibody (diluted 1:20 in blocking buffer, Abcam) for 1 h. The grid was washed five times with washing buffer and three times with $_{d}$H20 before staining with 1% (w/v) uranyl acetate for 1 min. The sample was air-dried, and EM Images were acquired as described above. Immunogold negative stain EM confirmed that the purified fibrils were indeed Aβ fibrils (**Fig. S2**).

Cryo-EM Image Acquisition and Data Preprocessing

For cryo-EM imaging, 2-3 µL of Aβ fibril sample from a single mouse brain was applied to holey carbon grids (Quantifoil 1.2/1.3, 300 mesh), blotted with filter paper for 3-5 s and plunge frozen in liquid ethane using a ThermoFisher Scientific Vitrobot Mark IV, set at 95% humidity and 4°C temperature. Data acquisition was performed on a ThermoFisher Scientific Talos Arctica microscope operating at 200 kV using a Gatan Bioquantum K3 detector in counting mode with a

Gatan Bio-quantum energy filter with a slid width of 20 eV, and on a ThermoFisher Scientific Titan Krios G4 operating at 300 kV using a Falcon 4 detector in counting mode. The automated collection was directed by EPU data collection software. Further details are given in **Table S1**.

For helical reconstruction of all datasets, gain-corrected movie frames were aligned and summed into single micrographs on-the-fly using Warp [62]. CTF estimation was performed using CTFFIND4.1 [63].

Helical Reconstruction

Helical reconstruction was performed using the helical reconstruction methods in RELION [64], [65]. For all datasets, fibrils were picked automatically using crYOLO [66], [67]. Reference-free 2D classification was performed to separate different polymorphs and to discard low quality particle images.

In the recorded dataset of tg-APP$_{ArcSwe}$ at least three polymorphs could be identified and 2D class averages suggest that all polymorphs have a pronounced unstructured region. Indeed, even after multiple 3D classification and refinement runs, we only obtained class averages revealing unstructured regions at the fibril periphery. Therefore, we performed a masked classification with residual signal subtraction [68] and removed the unstructured regions from the reconstruction.

For ARTE10 murine type II, ARTE10 murine type III, DI2, DI3, tg-APP$_{Swe}$ murine type II, APP23 murine type II and murine$_{Arc}$ type I, a featureless cylinder was used as initial 3D reference. For APP/PS1 murine type III and DI1, an initial 3D reference was computed *de novo* from multiple 2D class averages assuming a helical rise of 4.75 Å and a twist value calculated from the crossover-distance of each fibril observed from larger box 2D class averages [69]. Cylinders were initially low-pass filtered to 40 Å, reconstructed *de novo* initial models were low-pass filtered to 8-10 Å depending on their quality. 3D classification was used to obtain a homogeneous high-quality subset of particles for each fibril type. 3D auto-refinement and subsequent post-processing was performed to fibril the final maps and to calculate the resolution according to gold-standard Fourier Shell Correlations at 0.143 applying a soft-edged solvent mask. For APP/PS1 murine type III, ARTE10 murine type III, DI1, DI2 and tg-APP$_{Swe}$ murine type II fibrils VISDEM sharpening [70] was used instead of automatic B-factor sharpening. Additional image processing information can be found in **Table S3.**

Statistics on the distribution of different polymorphs are given in **Table S2**. The term "unassigned" refers to particles that were noisy, heterogenous, and could not be used for further structure determination. Additionally, it should be noted that given statistics on polymorph distribution are based on an initial 2D classification of automatically picked particles and therefore, might be influenced by inaccurate 2D classification.

Model Building and Refinement

For APP/PS1 murine type III fibrils and all tg-SwDI polymorphs, atomic models were built *de novo* into the computed high-resolution cryo-EM reconstructions using COOT [71]. Side chain rotamers were refined manually monitoring Ramachandran outliers and clash scores using MolProbity [72]. All models were refined using an iterative procedure of refinement in PHENIX [73] and manual modeling in COOT and ISOLDE [74].

For ARTE10 murine type III fibrils, the atomic model of APP/PS1 murine type III filaments was fitted into the density and refined using COOT, ISOLDE and PHENIX.

For ARTE10, tg-APP$_{Swe}$, and APP23 murine type II fibrils, an atomic model of previously determined human type II Aβ filaments ([18], PDB code: 7Q4M) was fitted into the density maps and refined using COOT and PHENIX.

For tg-APP$_{ArcSwe}$ fibrils, an atomic model of previously determined human type I Aβ filaments ([18], PDB code: 7Q4B) was fitted into the density maps and refined using COOT and PHENIX.

ChimeraX [75] was used for molecular graphics and analyses. Additional information on final models can be found in **Table S4**.

Supplementary Tables

Table S1: Statistics of Data Acquisition

	APP/PS1	**ARTE10**	**tg-SwDI**	**tg-APP$_{Swe}$**	**APP23**	**tg-APP$_{ArcSwe}$**
Microscope	Talos Arctica	Titan Krios	Titan Krios	Titan Krios	Titan Krios	Titan Krios
Detector	K3	Falcon IV	Falcon IV	Falcon IV	Falcon IV	Falcon IV
Energy filter slit width (e^-V)	20	N/A	N/A	N/A	N/A	N/A
Magnification	100,000	96,000	96,000	96,000	96,000	96,000
Voltage (kV)	200	300	300	300	300	300
Pixel Size (Å)	0.816	0.808	0.808	0.808	0.808	0.808
Total electron exposure (e^-/Å^2)	30.28	40	40.1	40.35	40.31	40.35
Defocus range (μm)	[-0.5, -2.5]	[-0.5, -2.5]	[-0.5, -2.5]	[-0.5, -2.5]	[-0.5, -2.5]	[-0.5, -2.5]
Micrographs collected	3674	9521	25662	9370	11622	17577

Table S2: Distribution of polymorphs in extracted Aβ fibril samples from different mouse models. The term "unassigned" refers to particles that were noisy, heterogenous, and could not be used for structure determination.

Mouse Model	**Distribution**
APP/PS1	murine type III: 100%
ARTE10	murine type II: 49%; murine type III: 8%; unassigned: 43%
tg-SwDI	DI1: 41%; DI2: 32%; DI3: 27%
tg-APP$_{Swe}$	murine type II: 15%; unassigned: 85%
APP23	murine type II: 42%; unassigned: 58%
tg-APP$_{ArcSwe}$	murine$_{Arc}$ type I: 38%; unassigned: 62%

Table S3: Statistics on Image Processing

	APP/PS1 murine type III	**ARTE10 murine type III**	**ARTE10 murine type II**	**tg-SwDI DI1**	**tg-SwDI DI2**	**tg-SwDI DI3**	**tg-APP$_{Swe}$ murine type II**	**APP23 murine type II**	**tg-APP$_{ArcSwe}$ murine$_{Arc}$ type I**
Final Segments (no.)	171,432	10,369	226,920	54,018	37,937	10,869	12,100	119,710	19,036
Symmetry imposed	C2	C2	C2	C2	C1	C1	C2	C2	C1
Helical rise (Å)	4.74	4.74	4.76	4.66	4.63	4.72	4.78	4.77	2.41
Helical twist (°)	-1.89	-1.91	-3.21	-2.78	-2.95	-5.24	-3.17	-3.23	179.56
Map resolution (Å)	3.5	3.5	3.4	3.3	4.2	4.0	3.8	3.0	3.0
Map Sharpening B-factor	N/A	N/A	-126.1	N/A	N/A	-90.1	N/A	-106.5	-80.1

Table S4: Statistics on Model Building and Refinement

	APP/PS1 murine type III	**ARTE10 murine type III**	**ARTE10 murine type II**	**tg-SwDI DI1**	**tg-SwDI DI2**	**tg-SwDI DI3**	**tg-APP$_{Swe}$ murine type II**	**APP23 murine type II**	**tg-APP$_{ArcSwe}$ murine$_{Arc}$ type I**
Initial Model (PDB code)	*de novo*	*de novo*	7Q4M	*de novo*	*de novo*	*de novo*	7Q4M	7Q4M	7Q4B
Model composition									
Chains	10	10	10	10	5	5	10	10	10
Non-hydrogen atoms	2470	2330	2260	2830	1490	1260	2260	2260	2320
Protein residues	330	310	310	360	195	160	310	310	320
RMS deviations									
Bond lengths (Å)	0.008	0.005	0.003	0.002	0.002	0.002	0.004	0.004	0.006
Bond angles (°)	0.67	0.87	0.438	0.48	0.41	0.49	0.560	0.455	0.811
Validation									
MolProbity score	1.41	1.96	0.96	2.34	2.14	1.16	1.66	2.21	1.74
Clashscore	7.46	9.87	2.0	10.8	9.6	3.7	8.0	9.6	10.1
Ramachandran plot									
Outliers (%)	0	0	0	0	0	0	0	0	0
Allowed (%)	0	6.9	0	8.82	13.51	0	3.45	3.45	3.33
Favored (%)	100	93.1	100	91.18	86.49	100.00	96.55	96.55	96.67

Supplementary Figures

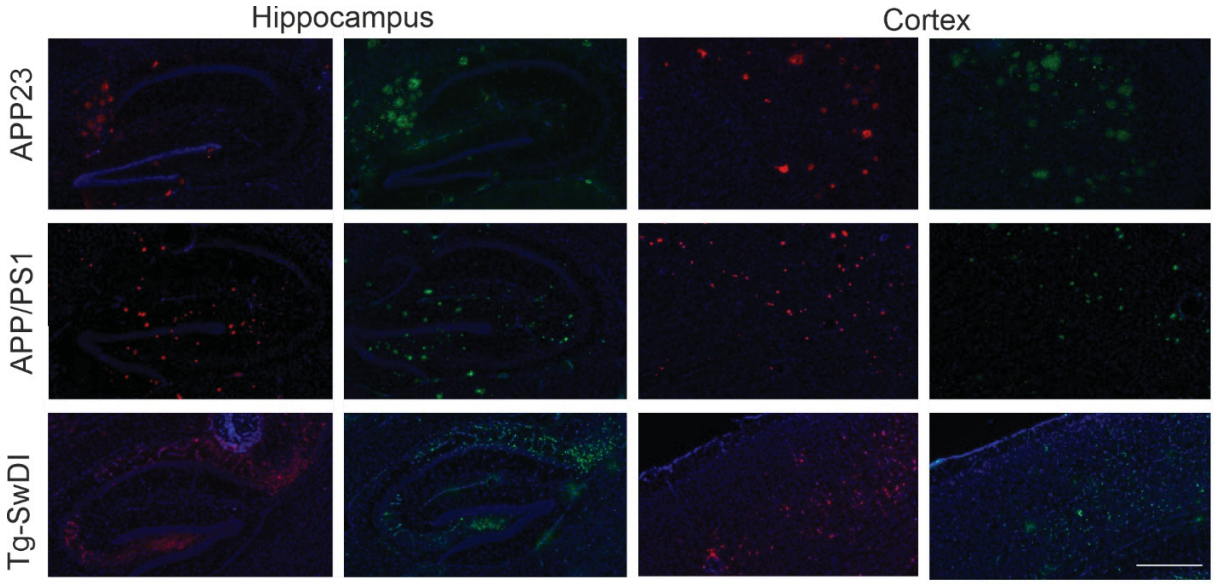

Figure S1: Immunohistochemical staining showing Aβ plaques in the hippocampus (left images) and cortex (right images) of APP23 (upper panel), APP/PS1 (middle panel) and tg-SwDI mice (lower panel). Two different stainings were conducted (6E10 labelled in red and 4G8 labelled in green). Nuclear staining was done with DAPI (blue). Scale bar= 500 µm.

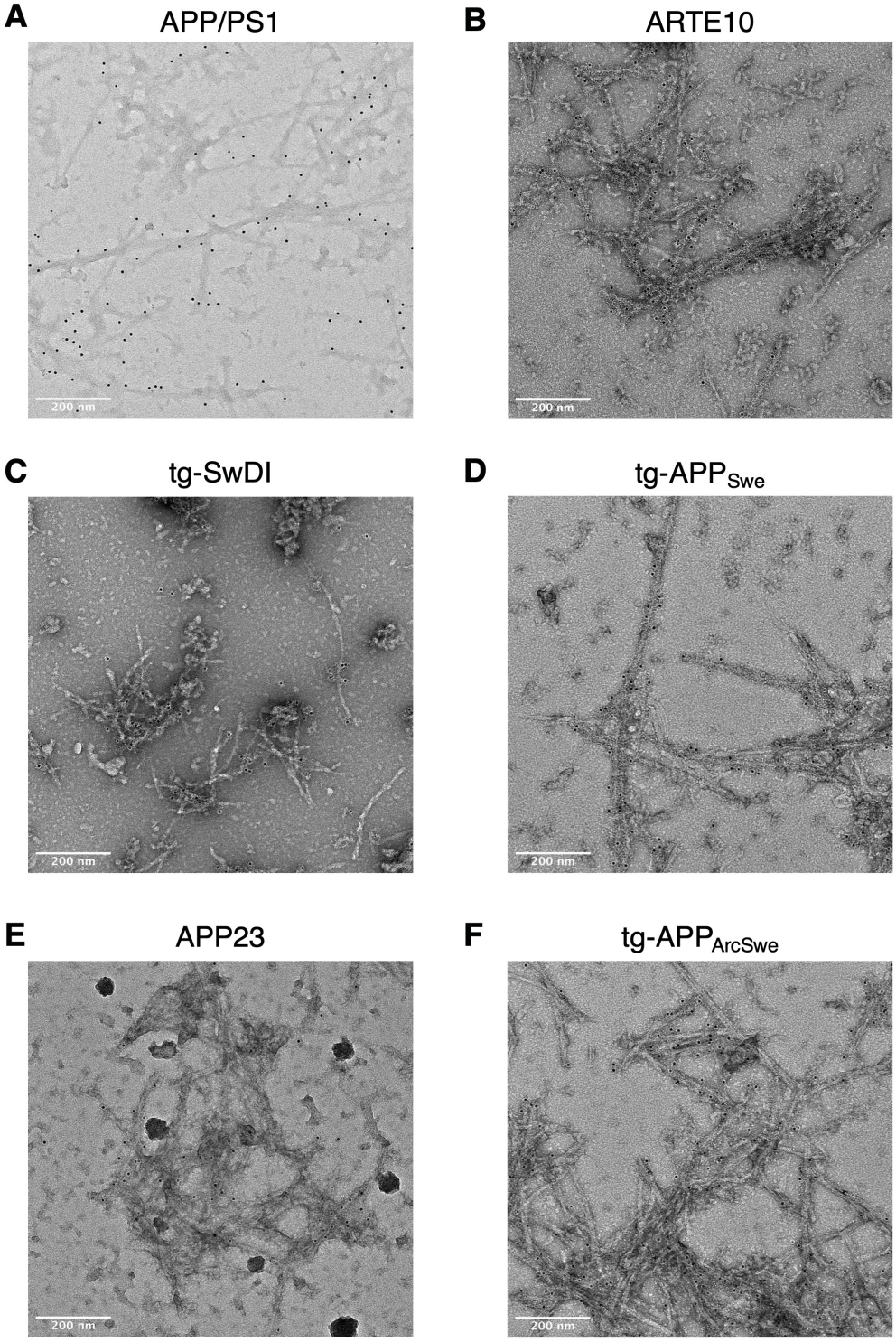

Figure S2: Immunogold labelling of the purified Aβ fibrils from (A) APP/PS1, (B) ARTE10, (C) tg-SwDI, (D) tg-APP_{Swe}, (E) APP23 and (F) tg-APP_{ArcSwe} mouse models. NAB228 was used as primary antibody. A goat anti-mouse gold-conjugated antibody with a gold particle diameter of 6nm was used as secondary antibody.

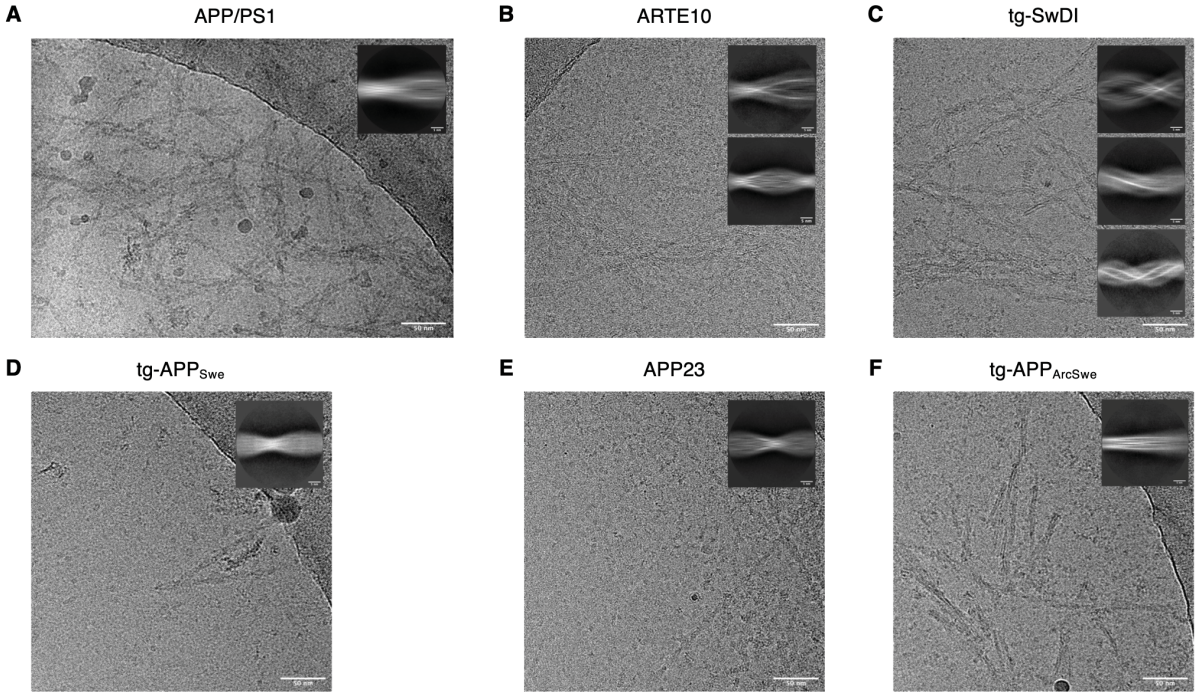

Figure S3: One exemplary Micrograph and 2D class of (A) APP/PS1, (B) ARTE10, (C) tg-SwDI, (D) tg-APP_{Swe}, (E) APP23 and (F) tg-APP_{ArcSwe}.

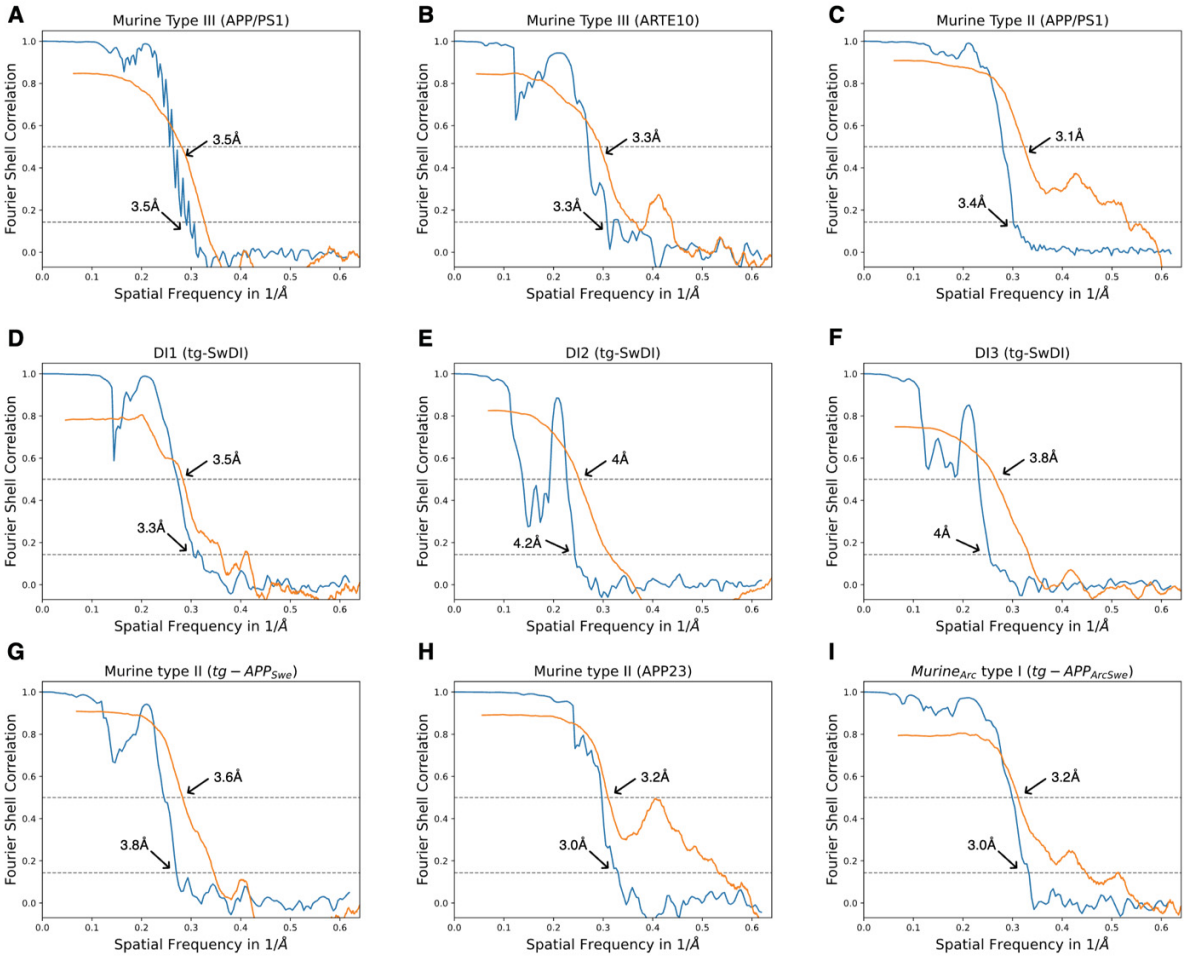

Figure S4: FSC curves for cryo-EM maps and structures of (A) APP/PS1 murine type III, (B) ARTE10 murine type III, (C) ARTE 10 murine type II, (D) DI1, (E) DI2, (F) DI3, (G) tg-APP$_{Swe}$ murine type II, (H) APP23 murine type II, and (I) tg-APP$_{ArcSwe}$ murine$_{Arc}$ type I fibrils. FSC curves for two independently refined half maps are shown in blue; FSC curves for the refined atomic model against the final cryo-EM map in orange.

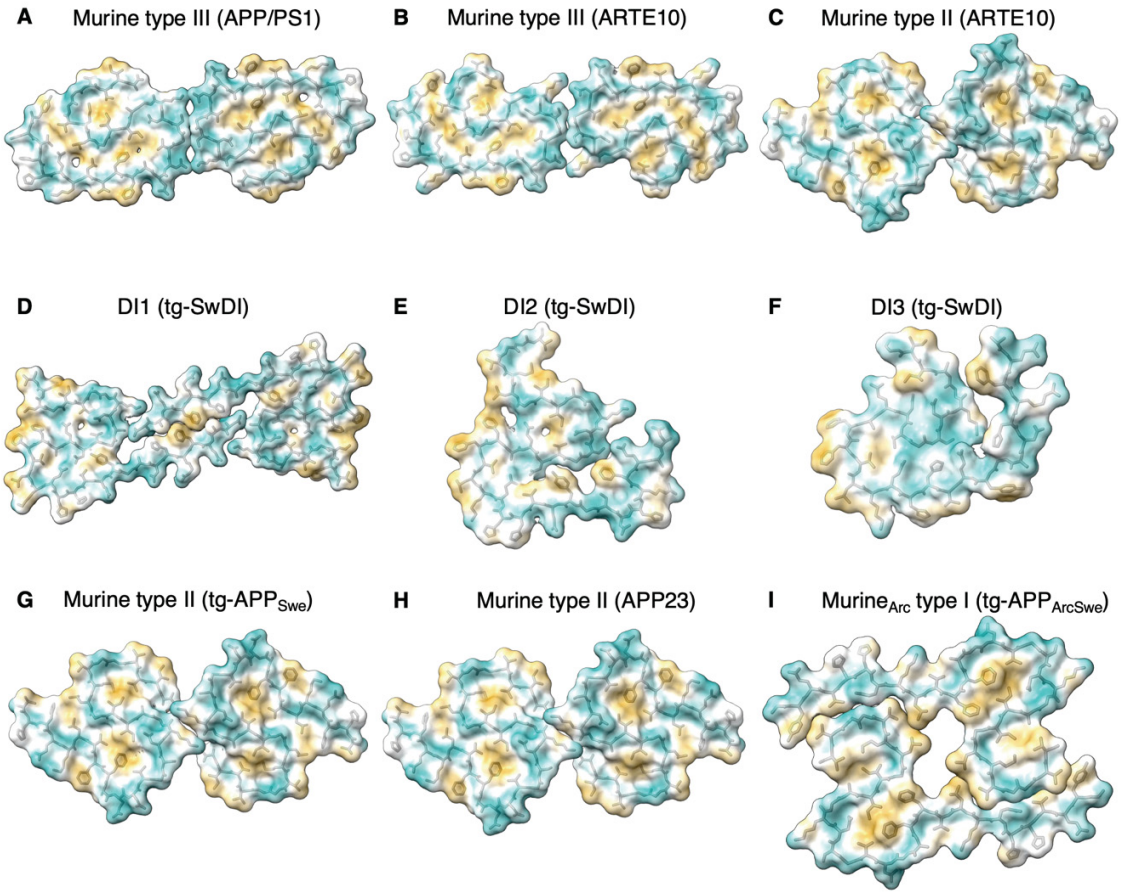

Figure S5: Molecular lipophilicity potential (MLP) maps for (A) APP/PS1 murine type III, (B) ARTE10 murine type III, (C) ARTE10 murine type II, (D) DI1, (E) DI2, (F) DI3, (G) tg-APP_{Swe} murine type III, (H) APP23 murine type III, and (J) $murine_{Arc}$ type I. Coloring on the surface ranging from cyan (most hydrophilic) to white to yellow (most lipophilic/hydrophobic).

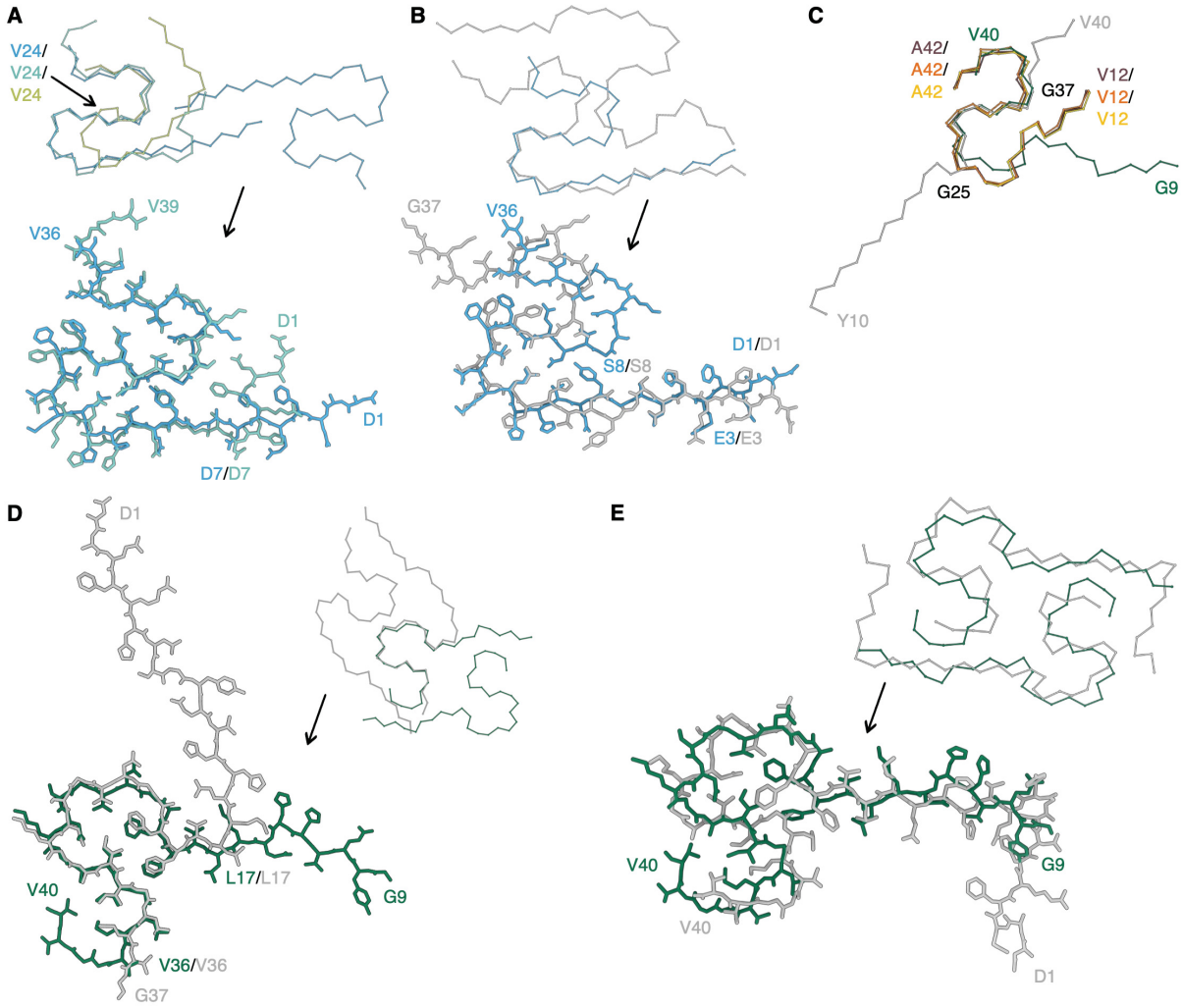

Figure S6: Comparison of murine Aβ fibrils with other structures. (A) Comparison of the main chain trace of DI1 (light blue) with DI2 (teal) and DI3 (light green) (top) and comparison of DI1 and DI2 (bottom). (B) Comparison of DI1 (light blue) and murine Aβ42(E22G) filaments extracted from knock-in APP^{NL-G-F} mice (gray, PDB code: 8BG9). (C) Comparison of APP23 murine type II (yellow), tg-APP_{Swe} murine type II (orange), ARTE10 murine type II (burgundy), tg-APP_{ArcSwe} $murine_{Arc}$ type I (green) fibrils with the cryo-EM structure of Aβ40 fibrils seeded from brain homogenates from cortical tissue of an AD patient (gray, PDB code: 6W0O). (D) Comparison of tg-APP_{ArcSwe} (green) and murine Aβ42(E22G) filaments extracted from knock-in APP^{NL-G-F} mice (gray, PDB code: 8BG9). (E) Comparison of tg-APP_{ArcSwe} (green) with an NMR structure of recombinant Aβ40 E22Δ fibrils (gray, PDB code: 2MVX).

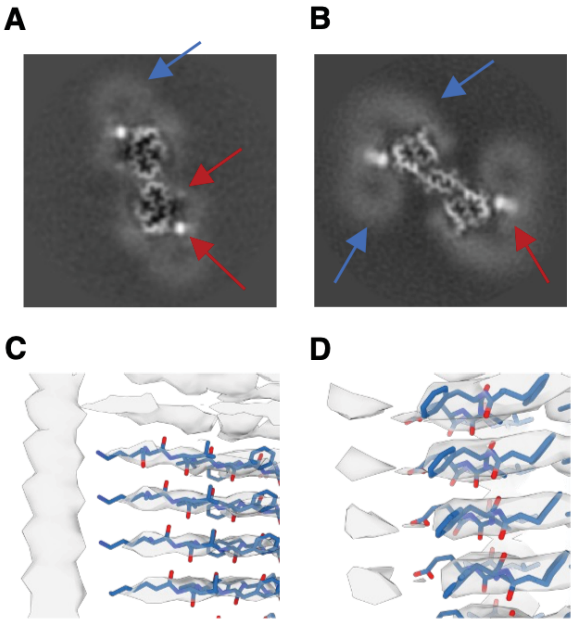

Figure S7: Additional densities bound to murine Aβ fibrils. (A,B) Reconstruction of Aβ fibrils extracted from (A) APP/PS1 and (B) tg-SwDI mice brain. Red arrows indicate localized, strong density, blue arrows indicate micelle-like, weak densities. (C,D) show extra densities close to (C) Lys16 and (D) Phe20/Glu22 in APP/PS1 murine type III Aβ fibrils.

C. Publication II

ALZHEIMER'S DISEASE

The *Uppsala APP* deletion causes early onset autosomal dominant Alzheimer's disease by altering APP processing and increasing amyloid β fibril formation

María Pagnon de la Vega[1], Vilmantas Giedraitis[1], Wojciech Michno[2,3], Lena Kilander[1], Gökhan Güner[4], Mara Zielinski[5], Malin Löwenmark[1], RoseMarie Brundin[1], Torsten Danfors[6], Linda Söderberg[7], Irina Alafuzoff[8], Lars N.G. Nilsson[9], Anna Erlandsson[1], Dieter Willbold[5,10,11], Stephan A. Müller[4], Gunnar F. Schröder[5,12], Jörg Hanrieder[2,13], Stefan F. Lichtenthaler[4,14], Lars Lannfelt[1], Dag Sehlin[1†], Martin Ingelsson[1*†]

Point mutations in the amyloid precursor protein gene (*APP*) cause familial Alzheimer's disease (AD) by increasing generation or altering conformation of amyloid β (Aβ). Here, we describe the *Uppsala APP* mutation (Δ690–695), the first reported deletion causing autosomal dominant AD. Affected individuals have an age at symptom onset in their early forties and suffer from a rapidly progressing disease course. Symptoms and biomarkers are typical of AD, with the exception of normal cerebrospinal fluid (CSF) Aβ42 and only slightly pathological amyloid–positron emission tomography signals. Mass spectrometry and Western blot analyses of patient CSF and media from experimental cell cultures indicate that the *Uppsala APP* mutation alters APP processing by increasing β-secretase cleavage and affecting α-secretase cleavage. Furthermore, in vitro aggregation studies and analyses of patient brain tissue samples indicate that the longer form of mutated Aβ, AβUpp1–42$_{\Delta 19–24}$, accelerates the formation of fibrils with unique polymorphs and their deposition into amyloid plaques in the affected brain.

INTRODUCTION

Alzheimer's disease (AD) is neuropathologically characterized by a progressive deposition of amyloid β (Aβ) in parenchyma and blood vessels of the cerebrum (*1*). Upon sequential cleavage of the amyloid precursor protein (APP) by β- and γ-secretases, Aβ peptides of 38 to 43 amino acids are generated. If instead α-secretase cleavage occurs, then no Aβ is formed [reviewed in (*2*)].

Increased generation of the more amyloidogenic Aβ42 is seen for several of the *APP* mutations positioned in vicinity of the γ-secretase cleavage site (*3*–*14*), whereas the *Swedish* mutation close to the β-secretase cleavage site results in increased production of both Aβ42 and Aβ40, as demonstrated in plasma and fibroblasts from mutation carriers (*15*–*17*). Pathogenic *APP* mutations within the Aβ sequence have been described to result in various disease phenotypes. Patients with the *Dutch* (E693Q) and *Italian* (E693K) mutations display amyloid accumulation in cerebral blood vessel walls and intracerebral hemorrhage (*18*, *19*), whereas carriers of the *Flemish* (A692G) and *Iowa* (D694N) mutations suffer from both intracerebral hemorrhage and progressive dementia (*20*, *21*). The *Arctic* mutation (E693G) leads to an increased formation of protofibrils (*22*) and other large Aβ oligomers with particularly neurotoxic properties (*23*). Clinical examinations and neuropathological analyses confirmed that carriers of the *Arctic* mutation have an AD phenotype (*24*), although their brains almost only display diffuse parenchymal Aβ deposits (*24*–*26*). The only protective *APP* variant described to date, the *Icelandic* mutation (A673T), has been shown to decrease β-secretase cleavage resulting in reduced Aβ production (*27*) and aggregation (*28*, *29*).

For the only identified disease-causing *APP* deletion (E693Δ), resulting in a recessive form of familial AD, an increased intraneuronal presence of toxic Aβ oligomers was suggested as an underlying pathogenic feature. A decreased inhibition of both β- and γ-secretase, with increased enzymatic activities and relative resistance to degradation of mutant Aβ by neprilysin and insulin-degrading enzyme, has been proposed as other effects of this deletion (*30*).

Here, we report a pathogenic *APP* deletion (690–695Δ) that causes a dominantly inherited form of early onset dementia in three mutation carriers of a family originating from the city of Uppsala, Sweden. Clinical and neuropathological examinations are compatible with AD, and experimental studies indicate that the phenotype is caused by pathological alterations of the β- and α-secretase cleavage of APP, which result in increased Aβ production in combination with a very rapid aggregation of the longer Aβ mutant (AβUpp1–42$_{\Delta 19–24}$) into unique polymorphic structures.

[1]Department of Public Health and Caring Sciences, Geriatrics, Uppsala University, 75185 Uppsala, Sweden. [2]Department of Psychiatry and Neurochemistry, University of Gothenburg, 43180 Gothenburg, Sweden. [3]Department of Neuroscience, Physiology and Pharmacology, University College London, WC1E 6BT London, UK. [4]German Center for Neurodegenerative Diseases (DZNE) and Neuroproteomics, School of Medicine, Klinikum rechts der Isar, Technical University of Munich, 81377 Munich, Germany. [5]Institute of Biological Information Processing, Structural Biochemistry (IBI-7) and JuStruct, Jülich Center for Structural Biology, Forschungszentrum Jülich, 52425 Jülich, Germany. [6]Department of Surgical Sciences, Radiology, Uppsala University, 75185 Uppsala, Sweden. [7]BioArctic AB, 11251 Stockholm, Sweden. [8]Department of Immunology, Genetics and Pathology, Clinical and Experimental Pathology, Uppsala University, 75185 Uppsala, Sweden. [9]Department of Pharmacology, University of Oslo and Oslo University Hospital, 0316 Oslo, Norway. [10]Institut für Physikalische Biologie, Heinrich-Heine-Universität Düsseldorf, 40225 Düsseldorf, Germany. [11]Research Center for Molecular Mechanisms of Aging and Age-Related Diseases, Moscow Institute of Physics and Technology, State University, 141701 Dolgoprudny, Russia. [12]Physics Department, Heinrich-Heine-Universität Düsseldorf, 40225 Düsseldorf, Germany. [13]Department of Neurodegenerative Disease, Queen Square Institute of Neurology, University College London, WC1N 3BG London, UK. [14]Munich Cluster for Systems Neurology (SyNergy), 81377 Munich, Germany.
*Corresponding author. Email: martin.ingelsson@pubcare.uu.se
†These authors contributed equally to this work.

RESULTS

Epidemiological and clinical features of the *Uppsala APP* mutation family

The *Uppsala APP* mutation was detected in two siblings and their cousin, who were all referred to the Memory Disorder Unit, Uppsala University Hospital (for pedigree, see Fig. 1A). The ages of symptom onset were 43 years (sibling 1), 40 years (sibling 2), and 41 years (cousin). All three patients had a manifest cognitive impairment and scored 20 to 22 points on the Mini-Mental State Examination (MMSE) at the time of referral, with word finding difficulties, dyscalculia, apraxia, and visuospatial/executive impairment as major symptoms. Sibling 1 developed myoclonus and had a rapid disease progression with severe anxiety and behavioral disturbances. Death occurred 6 years after onset, at the age of 49. At the initial neuropsychological evaluation, sibling 2 had normal scores on episodic memory tests but featured severe dyscalculia and problems with the clock drawing test. At the 4-year follow-up examination, this patient had become increasingly affected by apathy and mutism. The cousin of the two siblings displayed impaired episodic memory, language, and executive functions as dominant symptoms.

One parent of the two siblings had been referred for assessment more than 20 years earlier after having refused to see a physician for several years. This patient had symptom onset at about 47 years of age, and the diagnosis of AD was supported by a computerized tomography (CT) scan, showing cortical and central atrophy at the age of 54. Death occurred at the age of 60. One of the parents of the cousin had onset of symptoms at about 45 years of age and was subsequently also diagnosed with AD. This patient became aggressive and spent several years at a geropsychiatric ward before death occurred about 15 years later. In addition, one of the siblings' grandparents developed dementia with onset at about 40 years of age and died at the age of 51 (Fig. 1A).

All three cases underwent lumbar puncture and subsequent cerebrospinal fluid (CSF) analyses. CSF concentrations of Aβ42 were within the normal range of non-AD controls, whereas concentrations of total tau (t-tau) and phospho-tau (p-tau) were pathologically elevated (table S1).

Brain imaging

The two siblings and their cousin underwent CT brain examinations at the time of diagnosis. The scan of sibling 1, who was in a more advanced disease stage at the initial visit, showed medial temporal lobe atrophy (MTA) grade 2 together with a moderate frontoparietal lobe atrophy. Sibling 2 and his cousin had a moderate global cortical and central atrophy, whereas the temporal lobes were well preserved (MTA grades 0 to 1) (Fig. 1B). Moreover, the siblings and their cousin underwent fluorodeoxyglucose positron emission tomography [^{18}F]FDG-PET, which showed a decreased uptake mainly

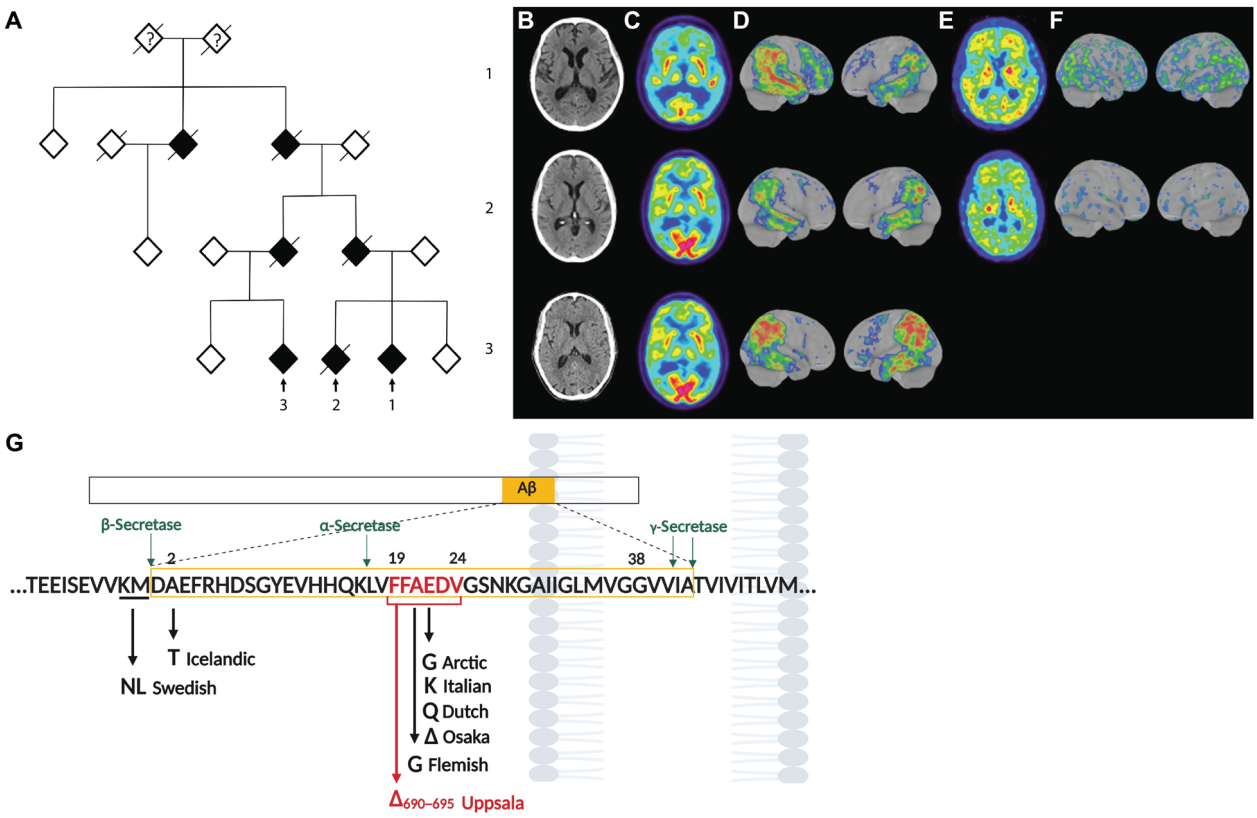

Fig. 1. Epidemiological and clinical features of the *Uppsala APP* mutation family. Pedigree of the *Uppsala APP* mutation family (**A**). Filled symbols are affected family members. Slashed symbols are deceased individuals. Index cases are indicated by arrows. Several healthy individuals in the latest generation have been omitted on purpose. CT and PET images of the three affected patients (sibling 1, sibling 2, and cousin 3, from top to bottom rows). Axial CT (**B**), [^{18}F]FDG-PET (**C** and **D**), and [^{11}C]PIB-PET images (**E** and **F**). Three-dimensional surface projection showing areas with pathological cortical tracer uptake (D and F). For (C) and (D), the color scale represents decreased tracer uptake with *z* score between 0 (blue) and −7 (red). For (E) and (F), the color scale represents increased tracer uptake with *z* scores between 0 (blue) and 8 (red). The location of the *Uppsala APP* mutation and its relation to other intra-Aβ *APP* mutations (**G**).

in the temporal and parietal lobes (Fig. 1, C and D). Two of them also underwent amyloid-PET using Pittsburgh compound B ([^{11}C]PIB), which demonstrated a pathological pattern but only with a slightly increased accumulation of [^{11}C]PIB in cortical areas (Fig. 1, E and F).

Genetic analyses reveal the *Uppsala APP* mutation

In the three affected cases (two siblings and their cousin), we identified an 18–base pair deletion in exon 17, which leads to the loss of six amino acids (690–695Δ) within Aβ. It should be noted that this deletion spans over the region that is affected by previously identified intra-Aβ mutations (Fig. 1G). In addition, we have analyzed more than 500 DNA samples from Swedish patients with AD, older unaffected family members, and from older healthy control subjects, all of which were negative for this genetic alteration. Furthermore, the two siblings were analyzed for the apolipoprotein E gene (*APOE*) and found to be *APOE ε3* homozygotes (table S1).

The *Uppsala APP* mutation leads to mainly AβUpp1–42$_{Δ19–24}$ pathology

One brain of an *Uppsala APP* mutation carrier (sibling 1) has come to autopsy. The weight of the brain was 1480 g, and the right hemisphere was subjected to routine analyses. On gross inspection, dilated ventricles were evident. Microscopically, a pronounced gliosis was seen in limbic and in neocortical areas (Fig. 2A and fig. S1). Moreover, there was a widespread tau pathology, corresponding to Braak stage VI, as visualized with the AT8 anti-tau antibody (Fig. 2, B and C).

Aβ plaques were abundant and widespread, corresponding to Thal stage 5. Tissue sections from occipital (Fig. 2), temporal, and parietal (fig. S1) neocortices were analyzed by immunohistochemistry with a panel of different monoclonal anti-Aβ antibodies and by thioflavin S (ThS) staining. Antibodies directed toward the Aβ C terminus revealed abundant Aβ42 staining, whereas Aβ40 staining was much less intense in all cortical areas investigated (Fig. 2, D to G, and fig. S1). With the 6F/3D antibody, binding to Aβ amino acids 8 to 17 (*25*), abundant pathology was observed in several neocortical regions (Fig. 2H), and a similar pattern could be observed with ThS (Fig. 2I).

Furthermore, brain tissues from fresh-frozen frontal, temporal, and occipital neocortex as well as cerebellum of the mutation carrier, 11 sporadic AD (sAD), and 9 non-neurological control brains (table S2) were homogenized and sequentially extracted with tris-buffered saline (TBS) and formic acid (FA) for analysis with MSD electrochemiluminescence-based Aβ immunoassay (Meso Scale Discovery) and enzyme-linked immunosorbent assay (ELISA). Compared to sAD and control samples, the *Uppsala APP* mutation brain displayed lower concentrations of Aβ40, whereas concentrations of Aβ42 were elevated, especially in the FA fraction (Fig. 3A), which corresponds to insoluble Aβ deposits, but also in the TBS fraction, representing more soluble Aβ, including aggregates (Fig. 3B). In contrast to elevated Aβ42 in the FA fraction of all investigated brain regions, concentrations of TBS soluble oligomers were lower in the *Uppsala APP* mutation brain compared to sAD, when analyzed with an ELISA that detects soluble Aβ aggregates of all sizes (Fig. 3C). Furthermore, when analyzed with an ELISA that preferentially recognizes larger oligomers and protofibrils (*31*), the *Uppsala APP* mutation brain displayed low concentrations, comparable to those in the controls, whereas the amounts of such Aβ species in sAD brains were elevated (Fig. 3D).

The composition of amyloid plaques from temporal neocortex was further analyzed by luminescent conjugated oligothiophene (LCO) staining and matrix-assisted laser desorption/ionization (MALDI) imaging mass spectrometry (IMS). Similar to those that were positive for ThS, plaques stained with the LCOs q-FTAA and h-FTAA (Fig. 3E) showed a distinct core surrounded by a diffuse halo of fibrillar Aβ (Fig. 3F). The MALDI-IMS analyses suggested that the plaques mainly consist of AβUpp42$_{Δ19–24}$, either in its full-length version or as N-terminally truncated peptides, which mainly start at positions 3 (pyroglutamate), 4, 5, or 8. The contribution by AβUpp1–40$_{Δ19–24}$, Aβwt1–40, and Aβwt1–42 to the formation of amyloid plaques in the *Uppsala APP* mutation brain seemed to be minor (Fig. 3, G and H). These results, as well as the peptide sequence identity, were confirmed by immunoprecipitation (IP) and MS analyses of pooled material from 50 individually laser-microdissected plaques, identified with LCO staining (table S3).

To investigate the contribution of AβUpp and Aβwt in CSF from *Uppsala APP* mutation cases and thereby understand why Aβ1–42

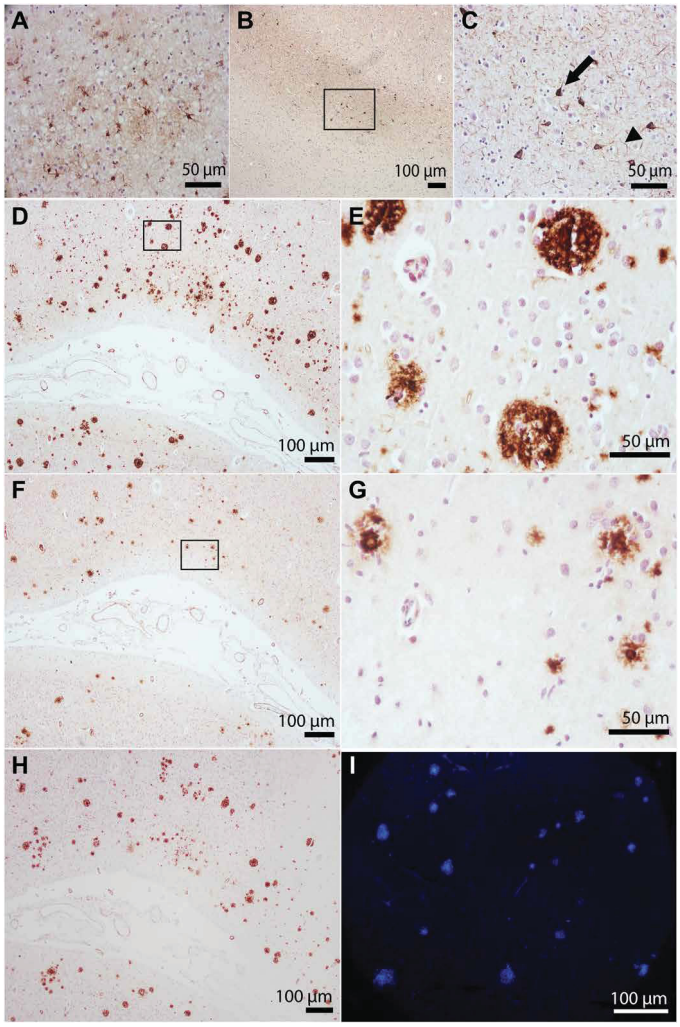

Fig. 2. Pronounced Aβ and tau pathology in the *Uppsala APP* mutation carrier brain. Immunohistochemistry of tissue sections from the *Uppsala APP* mutation brain, against GFAP (glial fibrillary acidic protein) (anti-GFAP) (**A**), tau (AT8) (**B** and **C**), Aβ42 (anti-Aβ42) (**D** and **E**), Aβ40 (anti-Aβ40) (**F** and **G**), and total Aβ (6F/3D) (**H**). Staining of amyloid plaques with ThS (**I**). (A) Temporal cortex; (B to I) occipital cortex. Squares in (B), (D), and (F): Regions displayed in the higher-magnification images (C, E, and G). Arrow in (C) points to a tangle; arrowhead points to a dystrophic neurite.

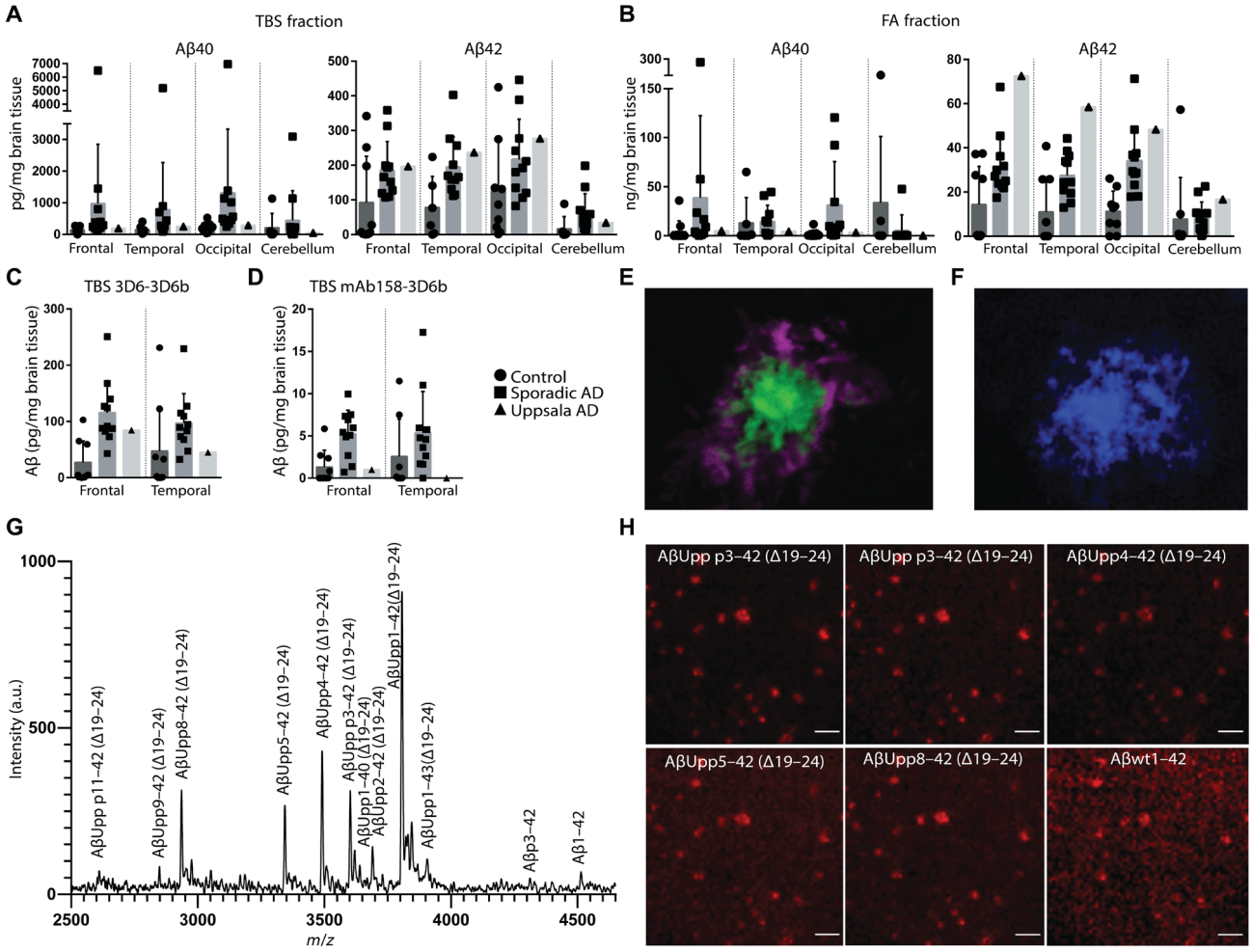

Fig. 3. Plaques in the *Uppsala APP* mutation brain mainly consist of AβUpp42$_{Δ19–24}$. Electrochemiluminescence (MSD) immunoassay (**A** and **B**) and ELISA (**C** and **D**) analyses of human brain extracts. Concentrations of Aβ40 and Aβ42 in the TBS (A) and FA (B) fractions. Concentrations of TBS soluble Aβ aggregates (C) and large Aβ oligomers (D). Staining of Aβ plaques on fresh-frozen temporal neocortical tissue of the *Uppsala APP* mutation brain with the luminescent conjugated oligothiophenes (LCOs) q-FTAA (green) and h-FTAA (purple) (**E**) and with ThS (blue) (**F**). MALDI-IMS spectrum (**G**) and images of plaques from the *Uppsala APP* mutation brain (**H**). Error bars represent SD. For controls, $n = 9$; for sporadic AD (sAD), $n = 11$. Because $n = 1$ for the Uppsala AD group, no statistical analysis was performed. a.u., arbitrary units; *m/z*, mass/charge ratio.

CSF concentrations were within the normal range in these patients, we performed IP-MS analyses using 6E10 (Aβ amino acids 5 to 10) and antibodies targeting the Aβ40 and Aβ42 C terminus for IP. CSF from the three mutation carriers (sibling 1, sibling 2, and cousin) was analyzed and compared to CSF from 11 sAD cases and 10 healthy control subjects (Fig. 4A) (demographic information; table S1). Mutation carriers displayed higher CSF amounts of Aβ1–40, Aβ1–42, and total Aβ (sum of all detected Aβ variants) as compared to sAD cases and control subjects (Fig. 4B). The amounts of Aβwt1–40 in CSF, produced from their nonmutated *APP* allele, were lower in patients with the *Uppsala APP* mutation than in sAD cases and control subjects, whereas Aβwt1–42 was not different in patients with the mutations compared to controls (Fig. 4C). The *Uppsala APP* mutation carriers displayed a relative increase of both AβUpp1–40$_{Δ19–24}$ and AβUpp1–42$_{Δ19–24}$ (Fig. 4D). Thus, the expression of Aβ from the mutated allele probably accounts for the unexpectedly high Aβ1–42 CSF concentrations in the routine analysis of patients with the *Uppsala APP* mutation. These measurements were performed with an immunoassay that should detect Aβwt1–42 and AβUpp1–42$_{Δ19–24}$ equally well. However, a comparison of Aβ1–42 measurements performed with the routine immunoassay and IP-MS (fig. S2A) showed that whereas values from control and sAD samples correlated well between the two methods, those from the three *Uppsala APP* mutation cases did not (fig. S2B). Ion spectra from AβUpp1–42$_{Δ19–24}$ and AβUpp1–40$_{Δ19–24}$ are shown in fig. S3.

The *Uppsala APP* mutation alters APP processing, resulting in increased Aβ production

To study the potential effects of the *Uppsala APP* mutation on APP processing, conditioned media of human embryonic kidney (HEK) 293 cells transfected with *APP* carrying the *Uppsala* mutation (*APPUpp*) or wild-type *APP* (*APPwt*) were analyzed with MSD immunoassays to determine sAPPα and sAPPβ concentrations of soluble APP fragments resulting from α- and β-cleavage, as well as in Aβ40 and Aβ42. Only background amounts of sAPPα were detected in media from the *APPUpp* culture, whereas high concentrations were found in media

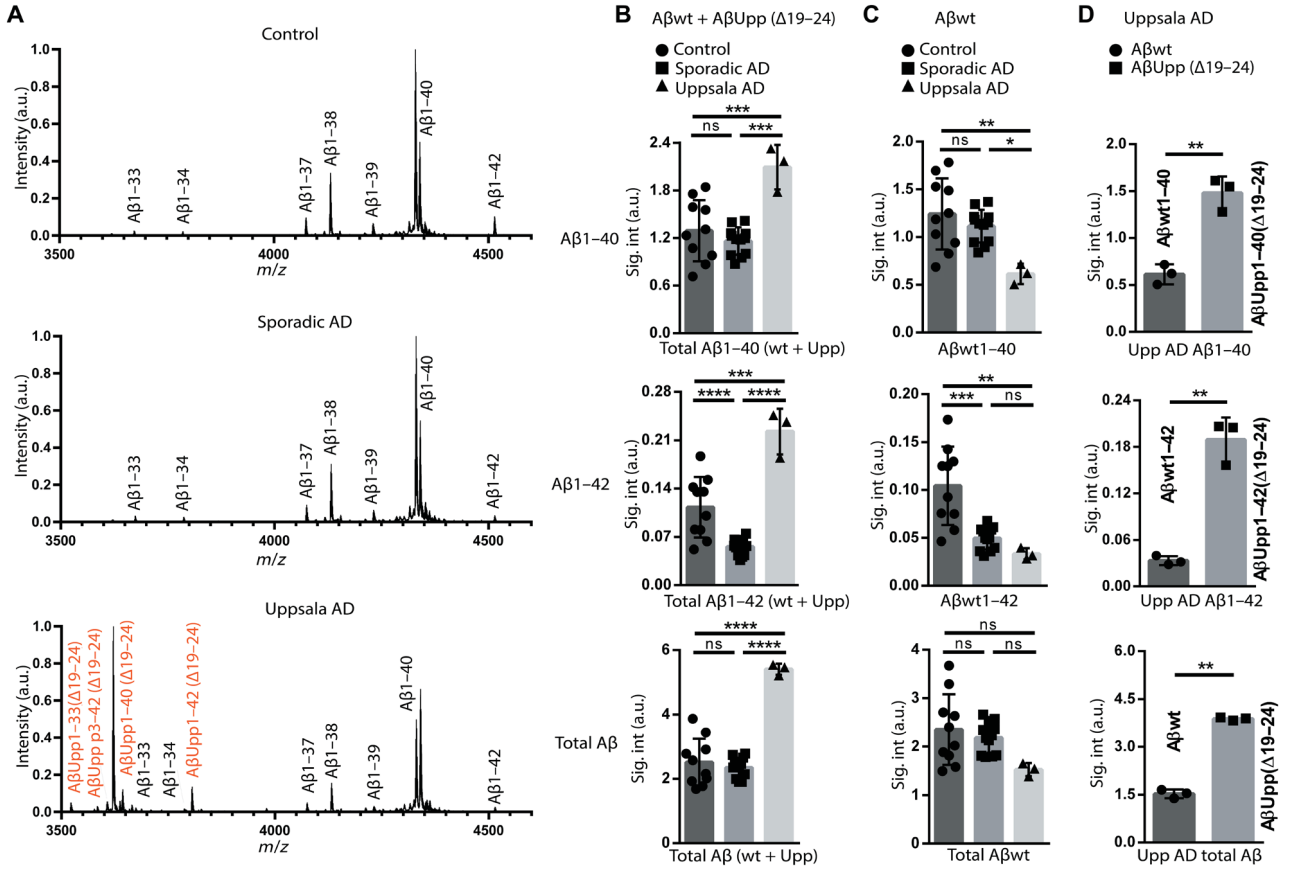

Fig. 4. *Uppsala APP* mutation carriers present increased concentration of Aβ in CSF. IP-MS analyses of CSF from 10 healthy controls, 11 sAD cases, and the 3 *Uppsala APP* mutation patients (**A**). IP-MS–based quantitation of CSF Aβ1–40, Aβ1–42, and total Aβ concentrations in CSF (**B** to **D**). All data are represented as group means, and error bars represent SD. The arbitrary units in the *y* axes represent ratios of intact mass peak area of individual Aβ peptide signals normalized to the spiked Aβ1–40 internal standard. For control CSF, $n = 10$; for sAD, $n = 11$; for Uppsala CSF, $n = 3$. Analyses of individual peptide signals and comparisons between the groups were performed by one-way ANOVA in (B) ($P = 0.0002$, $P < 0.0001$, and $P < 0.0001$ for Aβ1–40, Aβ1–42, and total Aβ, respectively) and (C) ($P = 0.0069$, $P = 0.0001$, and $P = 0.0767$ for Aβ1–40, Aβ1–42, and total Aβ, respectively) followed by Tukey's post hoc test. For (D), paired *t* test was performed ($P = 0.0029$, $P = 0.0081$, and $P = 0.0007$ for Aβ1–40, Aβ1–42, and total Aβ, respectively). Nonsignificant (ns), $^{*}P < 0.05$, $^{**}P < 0.01$, $^{***}P < 0.001$, and $^{****}P < 0.0001$.

from *APPwt*-expressing cells (Fig. 5A). In contrast, concentrations of sAPPβ were higher in media from *APPUpp* than *APPwt* cells (Fig. 5B), which was also reflected in a higher concentration of both Aβ40 and Aβ42 (Fig. 5C).

To study whether the *Uppsala APP* mutation causes an ablation of α-secretase cleavage or whether the cleavage site is shifted toward the N terminus due to the six–amino acid deletion, Western blot was performed on the same cell media as used for the MSD analyses. Total soluble APP (detected with 22C11, binding to an N-terminal epitope of APP) was similar in cell media from *APPUpp*- and *APPwt*-transfected cells. Similar to the MSD analyses, no sAPPα could be detected in the media from the *APPUpp* culture when probing with 6E10 (directed against Aβ amino acids 5 to 10 and usually present on sAPPα) ($P = 0.0004$) or 2B3 (specific for the C-terminal end of sAPPα) ($P = 0.0045$). However, when detected with mAb1C3 that binds to Aβ amino acids 3 to 8, which is closer to the APP N terminus than 6E10 (fig. S4), a faint sAPPα band was observed ($P = 0.0291$) (Fig. 5, D and E).

Next, the same cell media were analyzed with two different Aβ sandwich ELISAs: Aβ1–40 (using Aβ N-terminal–specific antibody 3D6 for detection) and Aβx–40 (using 6E10 for detection). Because the MSD and Western blot–based results suggested an additional cleavage site in *APPUpp* resulting in mAb1C3-positive sAPP fragment, we expected that the C-terminal side of this cleavage site would be detectable with the Aβx–40 ELISA (Fig. 5F). Cell media from the *APPUpp* culture showed a significantly higher ($P = 0.0016$) Aβx–40/Aβ1–40 ratio compared to *APPwt*-transfected cells, indicating that, in addition to Aβ, an extra N-truncated Aβ fragment was present in the *APPUpp* cell media (Fig. 5G).

To confirm that the reduction of sAPPα in *APPUpp* cell media was α-secretase cleavage specific, we performed Western blot with the same constructs as in the other cell culture–based experiments. When probing with the sAPPα-specific antibody 14D6, sAPPα was found to be reduced ($P < 0.0001$) in *APPUpp* compared to *APPwt* cell media. Moreover, upon treatment with the metalloprotease inhibitor GI254023X that blocks a disintegrin and metalloproteinase 10 (ADAM10), the major α-secretase (*32*) (Fig. 5, H and I), sAPPα was decreased in media from both cell cultures. In addition, and in line with the MSD results (Fig. 5B), sAPPβ was increased ($P < 0.01$) in media from *APPUpp*-transfected cells (Fig. 5, H and I). A mild reduction in total sAPP was observed (Fig. 5, H and I). Moreover, we performed Western blot on the cell lysates using a

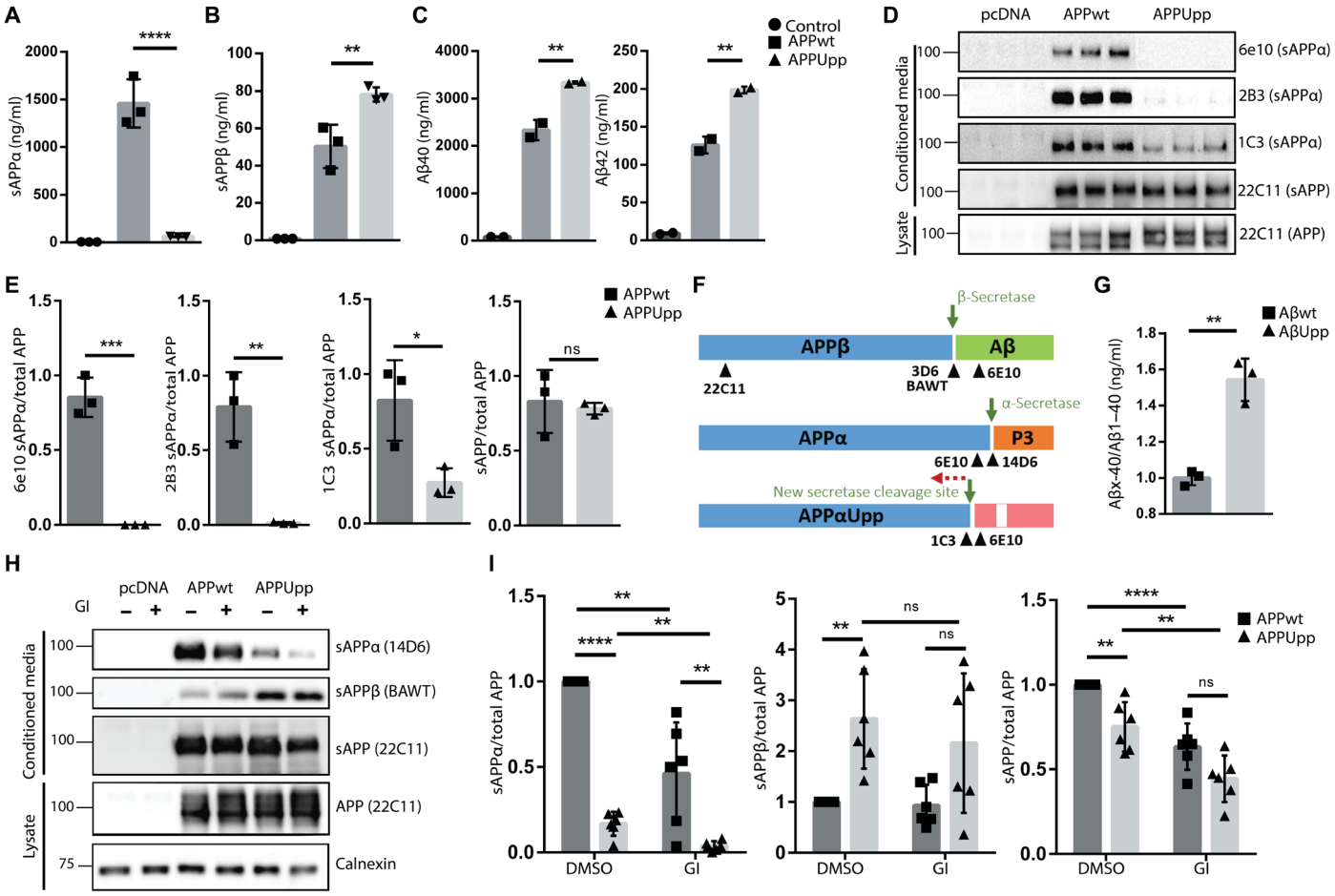

Fig. 5. The *Uppsala APP* mutation alters APP processing. Electrochemiluminescence immunoassay (MSD) analyses of sAPPα (**A**), sAPPβ (**B**), and Aβ40 and Aβ42 (**C**) in conditioned media from HEK293 cells transfected with *APPUpp* as compared to *APPwt* ($n = 3$, $N = 1$). Western blot of *APPUpp* conditioned media, with the sAPPα antibody 2B3 (C terminus), 6E10 (Aβ5–10), and mAb1C3 (Aβ3–8) ($n = 3$, $N = 3$) (**D**). Results from (D) quantified as a ratio of sAPPα (detected with 6E10, 2B3, or 1C3) or total sAPP (detected with 22C11) in cell medium over total APP in cell lysate (**E**). Schematic image indicating β- and α-cleavage sites of APPwt and APPUpp, with antibody binding epitopes indicated (**F**). Ratio of Aβx–40 and Aβ1–40 in *APPwt* and *APPUpp* medium quantified by ELISA ($n = 3$, $N = 3$) (**G**). Western blot analyses of media and lysates from HEK293 cells transiently transfected with *APPwt* or *APPUpp*, with or without the ADAM10-preferring inhibitor GI254023X (GI) using specific antibodies for α- and β-APP ($n = 6$, $N = 4$) (**H**). Results from (H) quantified as a ratio of sAPPα, sAPPβ, or total sAPP in cell medium over total APP in cell lysate (**I**). Statistical significance was determined by one-way ANOVA (A to C) [for (A) and (B), $P < 0.0001$; for (C), Aβ40 and Aβ42, $P = 0.0003$] followed by Tukey's post hoc test, two-tailed unpaired *t* test [$P = 0.004$, 0.0045, 0.0291, and 0.7167 (E) and $P = 0.0016$ (G)], and multiple *t* test (H). All data are represented as group means, and error bars represent SD. *$P < 0.05$, **$P < 0.01$, ***$P < 0.001$, and ****$P < 0.0001$. All results were normalized to total APP. DMSO, dimethyl sulfoxide.

γ-secretase inhibitor [difluorophenylacetyl-alanyl-phenylglycine-t-butyl-ester (DAPT)] to detect C-terminal fragments (CTFs) resulting from α- and β-secretase cleavage of APP and found a slight reduction in CTFα and a more prominent increase in 6E10-postive CTFs (fig. S5).

In addition to the Western blot analyses, we applied MS to investigate the altered APP processing. With respect to *APP*-transfected cells, subjected to IP with 6E10, anti-Aβ40, and anti-Aβ42, the most prominent forms of Aβ were Aβ1–40 and Aβ17–40 in media from *APPwt*-transfected cells (Fig. 6A), whereas AβUpp1–40$_{\Delta 19-24}$ and AβUpp5–40$_{\Delta 19-24}$ were the dominating species in media from *APPUpp*-transfected cells (Fig. 6B), suggesting a new major cleavage of *APPUpp* between amino acids 4 and 5 in the Aβ sequence.

Furthermore, affinity-purified sAPP was digested with the protease LysN, which cleaves proteins at the N-terminal side of lysines, followed by liquid chromatography–tandem MS analyses of peptides that are specific for the cleavage sites of α-secretase and β-secretase. Two different peptides in the N-terminal part of APP, upstream of the α-secretase and β-secretase cleavage sites, respectively, could then be found at similar concentrations in *APPUpp* and *APPwt* cell media (Fig. 6, C and D). Analysis of the α-secretase cleavage site–specific peptide KMDAEFRHDSGYEVHHQK (595–612 in wt hAPP695) showed that cleavage at this site was not significantly reduced ($P = 0.10$) in *APPUpp* compared to *APPWt* media (Fig. 6E). In contrast, the intensity of the β-secretase cleavage site–specific peptide KTEEISEVKM(ox) (587–596 in wt hAPP695) was strongly increased in *APPUpp* in comparison to *APPwt* media ($P < 0.001$), indicating increased cleavage by beta-site APP cleaving enzyme 1 (BACE1), the major β-secretase (Fig. 6F). Moreover, the semi-specific peptide (N terminus specific for LysN, C terminus unspecific) KMDAEFRHDSGY (595–606 in wt hAPP695) was identified. It ends at amino acid 10 of the Aβ sequence (same as the β′-secretase cleavage site) and was found to have a much higher intensity in media from *APPUpp*

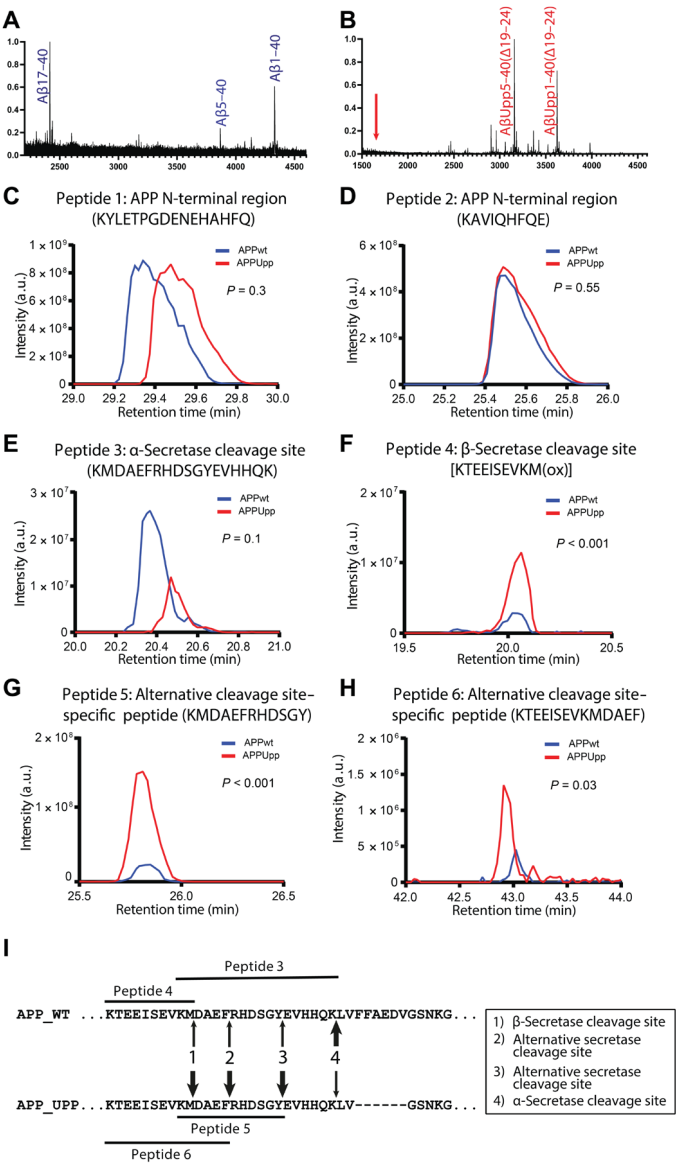

Fig. 6. The *Uppsala APP* mutation increases β-secretase cleavage and alters α-secretase cleavage. MS spectra of the *APPwt*-transfected (**A**) and *APPUpp*-transfected (**B**) HEK293 cells that showed the most prominent peptides present in cell media from cells transfected with either *APPUpp* or *APPwt*. The absence of Upp17–40$_{\Delta 19–24}$ is indicated by the red arrow (B). Extracted ion chromatograms of different peptides of APP (blue, *APPwt*; red, *APPUpp*). Chromatogram of the N-terminal APP peptides, peptide 1, KYLETPGDENEHAHFQ (302–317 in wt hAPP695) (**C**) and peptide 2, KAVIQHFQE (354–362 in wt hAPP695) (**D**). Shifts in retention times between *APPwt* and *APPUpp* were within the normal range of shifts between runs. Chromatogram of the α-secretase cleavage site–specific peptide 3, KMDAEFRHDSGYEVHHQK (595–612 in wt hAPP695, containing one missed LysN cleavage site) (**E**). Chromatogram of the β-cleavage site–specific peptide 4, KTEEISEVKM(ox) (587–596 in wt hAPP695, also containing one missed LysN cleavage site) (**F**). Chromatogram of the semi-specific peptides (N terminus specific for LysN, C terminus unspecific), peptide 5, KMDAEFRHDSGY (595–606 in wt hAPP695) (**G**) and peptide 6, KTEEISEVKMDAEF (587–600 in wt hAPP695) (**H**). (**I**) Cleavage sites of α- and β-secretase are indicated for the sequences of *APPwt* and *APPUpp*. Thick arrows indicate increased and thin arrows indicate decreased cleavage of the two APP sequences.

compared to *APPwt* cells ($P < 0.001$) (Fig. 6G). In addition, a peptide generated upon cleavage between amino acids 4 and 5 of the Aβ sequence, KTEEISEVKMDAEF (587–600 in wt hAPP695), was strongly increased in *APPUpp* media ($P = 0.03$) (Fig. 6H). These MS-based results thus demonstrate activity at two major cleavages sites within the N-terminal part of the Aβ domain of APPUpp. The effects on APP processing revealed by MS analyses are summarized in Fig. 6I. MS sequencing results are shown in fig. S6.

AβUpp1–42$_{\Delta 19–24}$ is prone to form amyloid fibrils in vitro and displays a unique structural polymorphism

To investigate the aggregation behavior of AβUpp, we performed in vitro aggregation experiments. Monomeric Aβ was extracted from solubilized lyophilized synthetic AβUpp1–42$_{\Delta 19–24}$, Aβwt1–42, and AβArc1–42 peptides with high-performance liquid chromatography–size exclusion chromatography (SEC) and analyzed with three different methods upon aggregation at 37°C without shaking.

First, we analyzed fibril formation with the thioflavin T assay (ThT), which revealed that AβUpp1–42$_{\Delta 19–24}$ fibrillizes very rapidly, reaching half of its maximum ThT signal after 0.93 hours, compared to 8.3 hours for Aβwt1–42 and 1.3 hours for AβArc1–42$_{E22G}$. AβUpp1–42$_{\Delta 19–24}$ thus aggregated significantly faster than Aβwt1–42 ($P < 0.0001$) and with a similar rate as AβArc1–42$_{E22G}$, albeit apparently with a somewhat less prominent lag phase (Fig. 7A). The AβUpp1–40$_{\Delta 19–24}$ peptide did not display any fibril formation and was therefore not included in the analysis. Next, we applied an ELISA that selectively measures soluble Aβ oligomers/protofibrils (*33*) and found that the concentration of such Aβ species decreased for AβUpp1–42$_{\Delta 19–24}$, whereas they increased with time for Aβwt1–42 and AβArc1–42 (Fig. 7B). In the same samples (isolated at 1 and 8 hours), the distribution of protofibrillar and monomeric Aβ was qualitatively visualized with SEC. Before SEC analysis, fibrillar Aβ was pelleted with centrifugation, and hence, fibril formation was also indirectly monitored as a decreased size of the protofibril and monomer peaks. Overall, SEC largely confirmed the results from the ThT assay and ELISA, with a prominent decrease of monomeric AβUpp1–42$_{\Delta 19–24}$ over time (from 1 to 8 hours). In addition, similar to the ThT assay and ELISA data and in contrast to Aβwt1–42 and AβArc1–42, no increase in the protofibril peak could be observed over time for AβUpp1–42$_{\Delta 19–24}$ (Fig. 7C).

To further investigate the structural polymorphism of Aβ formed as a result of the *Uppsala APP* mutation, AβUpp1–42$_{\Delta 19–24}$ was fibrillized under a low-pH condition that has previously been shown to yield slow-growing and well-ordered Aβwt1–42 fibrils (*34*). Electron microscopy (EM) imaging of negatively stained fibrils revealed the presence of long and well-ordered fibrils with at least four different polymorphs (Fig. 7D). For higher-resolution examination of these fibrils, cryo-EM experiments were performed. For the two most dominant polymorphs, we obtained three-dimensional density reconstructions at resolutions of 5.7 and 5.1 Å for polymorphs 1 and 2, respectively (Fig. 7D). Both fibrils were found to consist of two symmetric protofilaments. The density allowed for building a tentative backbone trace, but because no side-chain density was visible, the amino acid sequence and also the N- and C-termini could not be assigned to the backbone trace. For both polymorphs, all 36 residues could be accommodated by the density and thus seem to be part of the folded AβUpp1–42$_{\Delta 19–24}$ fibril.

Polymorph 1 (Fig. 7D, middle) resembles an Aβwt1–42 fibril structure that has been earlier described (*35*) and possibly shares the

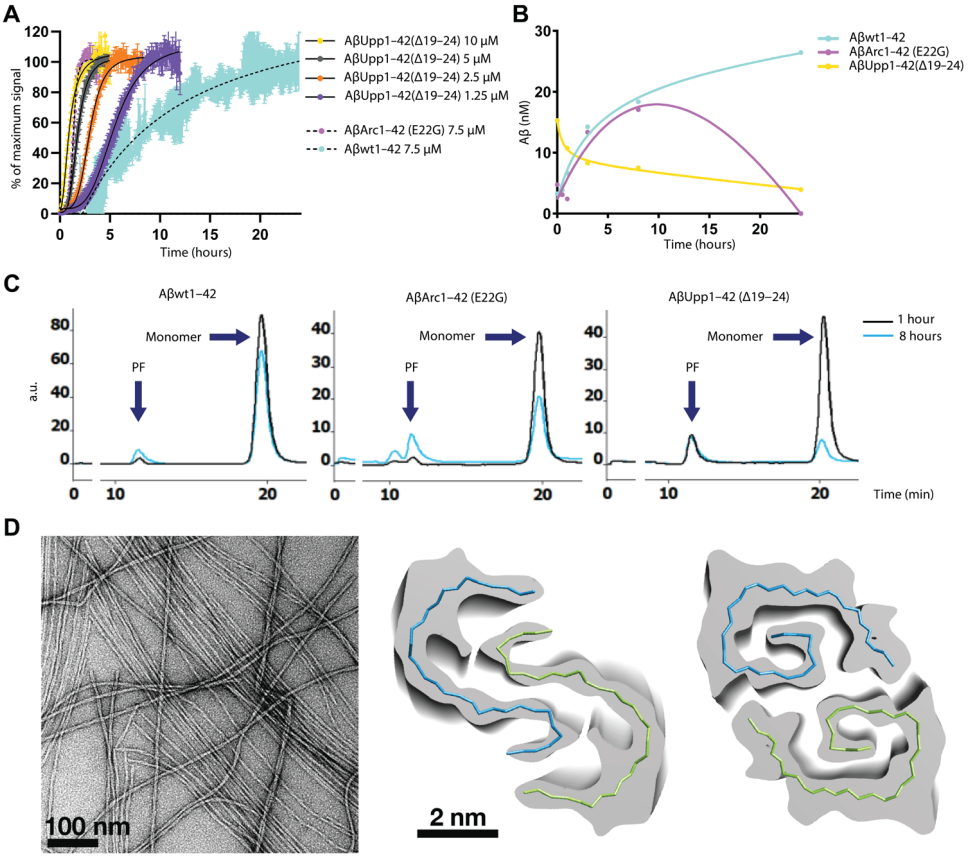

Fig. 7. The *Uppsala APP* mutation accelerates the formation of fibrils. ThT assay of different AβUpp1–42$_{Δ19–24}$, AβArc1–42$_{E22G}$, and Aβwt1–42 (**A**). Concentrations of soluble Aβ oligomers/protofibrils for incubated AβUpp1–42$_{Δ19–24}$, AβArc1–42$_{E22G}$, and Aβwt1–42 samples, as measured by ELISA (**B**) and SEC (**C**). Negative stain EM image of AβUpp1–42$_{Δ19–24}$ fibrils formed at low pH resulted in long, well-ordered fibrils (**D**) (left). Cryo-EM reconstructions (D) (middle and right). For ThT, four replicates of each peptide were aggregating simultaneously ($n = 4$) for each of the three experiments ($N = 3$). Error bars represent SD of the replicates, and black and dashed lines represent curves fitted to the ThT data points. For ELISA, from the same monomeric fraction used for ThT, two replicates ($n = 2$) for each experiment ($N = 3$). SEC was performed one time ($N = 1$). PF, protofibrils.

same protofilament interface in the fibril core (fig. S7). Polymorph 2 has a vague similarity to the previously described Aβwt1–42 structure (*34*), where the prominent salt bridge between the N-terminal Asp^{1} and Lys^{28} residues could also be present in AβUpp1–42$_{Δ19–24}$ fibrils (fig. S7). However, the C-terminal protofilament interface in the core of the fibril is instead very similar to the interface in two solid-state nuclear magnetic resonance structures of Aβwt1–42 (fig. S8) (*36*, *37*).

DISCUSSION

We here describe the *Uppsala APP* mutation, an *APP* deletion causing a dominantly inherited form of AD. This pathogenic deletion, resulting in a loss of six amino acids in the mid-region of Aβ, was found in three affected family members and not in 500 other subjects, including older nonaffected family members, older healthy controls, and sAD cases.

Most of the AD-causing *APP* mutations lead to symptom onset between 40 and 65 years (*38*), although cases with an even earlier onset have been reported for some mutations (*7*, *9*, *12*). The clinical effects of the *Uppsala APP* mutation are severe, insofar that mutation carriers develop symptoms already in their early forties and have an aggressive disease course. The clinical picture involves severe dementia, characterized by widespread parietotemporal lobe involvement, leading to death from dementia-related illnesses within 5 to 11 years. These clinical characteristics are thus similar to AD in general and to what has been reported for other familial disease variants.

In terms of structural brain imaging, the CT scans displayed the expected symmetrical pattern of global cortical atrophy and mild MTA. As for PET, investigations with the [^{18}F]FDG ligand showed a disease-characteristic hypometabolism of posterior parietal and temporal lobes, whereas analysis with [^{11}C]PIB, which selectively binds to amyloid plaques, only showed a slightly positive pattern. Analyses of postmortem brain tissue from one of the affected cases resulted in several important observations. First, the pathological picture was compatible with AD, including abundant deposition of extracellular Aβ-positive plaques and intracellular tau-positive tangles and neurites accompanied by pronounced gliosis. The regional distribution of Aβ aggregates was extended from neocortex to cerebellum, corresponding to Thal phase 5, and p-tau pathology was observed from locus coeruleus to neocortex, corresponding to Braak stage VI. Second, upon a more detailed examination of tissues from different cortical areas, it became evident that the Aβ pathology of the *Uppsala APP* mutation carriers mainly consists of Aβ42. This observation was corroborated by MALDI-IMS analyses of Aβ plaques from the temporal cortex, which in addition suggested that almost only mutated Aβ was present, either in its full-length version or as N-terminally truncated forms. Third, Aβ plaques were positive for staining with the amyloid dye ThS, which is structurally similar to PIB, raising the question why patients were only slightly [^{11}C]PIB-PET positive, despite high total Aβ concentrations in the postmortem brain tissue analysis. The PET results are displayed as a standard uptake value ratio (SUVR), which is a ratio of the PET signal in the region of interest to the signal from a reference region, in this case the cerebellum. Hence, a low SUVR could have been explained by a high reference region signal, but this interpretation could be ruled out as ThS staining of cerebellum in the patient with *Uppsala APP* revealed a low amyloid burden in this brain region. Although amyloid plaques generally reach the plateau phase rather early in the disease course, we cannot rule out that the time between the scan and the postmortem analyses could explain these differences in patients with *Uppsala APP*. Subtle changes in the fibrillar structure of AβUpp$_{Δ19–24}$ could be another potential explanation for the low PIB retention signal seen for the patients with *Uppsala APP*.

Biochemical analyses of AD CSF biomarkers revealed the expected pathological increase of t-tau and p-tau, whereas, unlike other *APP* mutation cases (*39*), concentrations of Aβ42 were normal for all three *Uppsala APP* mutation carriers investigated. The IP-MS–based CSF analyses suggest an explanation for this unexpected finding, as they demonstrated that the amounts of AβUpp1–$40_{\Delta 19–24}$ and, especially, AβUpp1–$42_{\Delta 19–24}$ produced by the mutated allele were substantially higher than Aβwt1–40 and Aβwt1–42 generated from the nonmutated allele. Thus, an increased generation of Aβ from the allele with the *Uppsala APP* mutation seems to result in higher total CSF concentrations of Aβ1–40 and Aβ1–42 as compared to both sAD cases and controls. Comparison of the IP-MS and routine ELISA-based CSF Aβ data revealed a good correlation for all control and sAD samples, whereas for the *Uppsala APP* mutation carriers, IP-MS–generated CSF Aβ concentrations were relatively higher. The ELISA measurement displayed normal concentrations of Aβ1–42 in CSF from *Uppsala APP* mutation cases, which is higher than in sAD cases, but in the same range as control subjects. We speculate that this discrepancy may be related to a difference in conformation between $AβUpp_{\Delta 19–24}$ and Aβwt. Whereas ELISA detection of Aβ1–42 relies on the simultaneous binding of the assay antibodies to the C and N terminus of Aβ, the IP-MS method is only dependent on one antibody-Aβ interaction at a time, which could facilitate its detection of $AβUpp_{\Delta 19–24}$. We therefore believe that the IP-MS results in this case better reflect the true amounts of Aβ1–42 in CSF, which, in turn, suggests a substantially increased production of Aβ in the brain of *Uppsala APP* mutation carriers.

We next performed cell-based experiments to seek a molecular explanation for the difference in Aβ production from the mutant and wild-type alleles in the mutation carriers. The MSD and Western blot–based analyses of cell media from *APP*-transfected cells, together with analyses of CTF fragments with the 2C11 (C-terminal APP) and 6E10 (Aβ5–10) antibodies on the same cell model, demonstrated an increased production of sAPPβ accompanied by a higher concentration of Aβ in medium from cells transfected with *APPUpp*. The MS analyses of the same cell culture media confirmed an increased β-secretase cleavage, thereby providing an explanation to the elevated amounts of $AβUpp_{\Delta 19–24}$ observed with IP-MS in CSF from the *Uppsala APP* mutation carriers. The detection of an increase in both Aβ and sAPPβ by different methods confirms that the increased CSF $AβUpp_{\Delta 19–24}$ detected by IP-MS was not a method-related artifact.

Because the N-terminal start of the *Uppsala APP* mutation is located only two amino acids from the α-secretase cleavage site, and this enzyme is dependent on the distance from the membrane and not exclusively on a determined cleavage site (*40*–*42*), we reasoned that the mutation may also affect α-secretase activity and/or the location of the cleavage site itself. In line with this, we could demonstrate that α-secretase–related APP processing is indeed altered by the *Uppsala APP* mutation. MSD and Western blot analyses of conditioned media from HEK293 cells transfected with *APPUpp* suggested a strongly decreased α-secretase cleavage at position Aβ16–17. This was further strengthened by analysis of corresponding CTF fragments with the C-terminal APP (2C11) antibody in the same cell model. Moreover, with enzyme inhibition experiments, we could demonstrate that the decreased cleavage indeed was specific to α-secretase. Furthermore, Western blot analysis revealed an additional APP fragment that was faintly detected with mAb1C3 (which binds to Aβ amino acids 3 to 8), but not with 6E10 (which binds to Aβ amino acids 5 to 10) or 2B3 (which binds to an epitope near the C-terminal end of APPα) antibodies, suggesting possible alternative cleavage sites.

To identify the alternative cleavage sites, IP-MS analyses of sAPP fragments secreted in media from *APPUpp*- or *APPwt*-transfected cells were performed and indicated that the mutation results in a new major cleavage site located 12 amino acids N-terminally of the conventional α-secretase cleavage site, between amino acids 4 and 5 of the Aβ sequence. This site was also detected with MS analysis of LysN-digested peptides from media of *APPUpp*-transfected cells. The resulting peptide, AβUpp5–$40_{\Delta 19–24}$, was present in media from *APPUpp* cells to a similar extent as Aβwt17–40 (also known as p3) was in media from *APPwt* cells. Furthermore, AβUpp5–$40_{\Delta 19–24}$ was identified by IP-MS in CSF from *Uppsala APP* mutation carriers, albeit less abundantly than in media from *APPUpp*-transfected HEK293 cells, a cell type that usually has a much higher activity of α-secretase than β-secretase as we could observe with the MSD analyses of the cell culture media. In addition, AβUpp5–$42_{\Delta 19–24}$, likely resulting from the same enzymatic cleavage, was detected by MALDI-IMS in the brain, suggesting that it coaggregates with AβUpp1–$42_{\Delta 19–24}$ into plaques.

Whereas AβUpp5–$40_{\Delta 19–24}$ seems to be consistently present as a result of the *Uppsala APP* mutation, it is at this point unclear whether it is generated as a result of cleavage at an alternative α-secretase site or by some other protease. Several additional proteolytic cleavages of APP may occur within or just outside of the Aβ sequence, for example, by BACE2 or proteases referred to as δ- and η-secretases or by alternative β-secretases, such as meprin-b (*43*–*51*). We speculate, however, that AβUpp5–$40_{\Delta 19–24}$ could be an alternative version of p3 resulting from a shifted α-secretase cleavage, which coaggregates with AβUpp1–$42_{\Delta 19–24}$ to form plaques and thereby contribute to the pathogenesis in mutation carriers. As additional support of its potential pathogenic significance, Aβwt5–42 has, in a previous study, been found to have similar toxicity as Aβwt1–42 but with an even higher propensity to aggregate (*52*). Furthermore, two previous studies have shown that treatment with a BACE1 inhibitor resulted in increased concentrations of Aβ5–40/42 (*53*, *54*), indicating that the cleavage of APPwt between Aβ4 and Aβ5 is indeed independent of β-secretase. Irrespective of the nature of the secretases involved, our data, together with these previous observations, thus suggest that both the β-secretase and the new cleavage site N-terminally of the α-secretase cleavage site are altered by *APPUpp*.

An additional major cleavage site between amino acids 10 and 11 of the Aβ sequence was found to be increased in *APPUpp* compared to *APPwt* cell media. Accordingly, Aβ11–$40_{\Delta 19–24}$ and Aβ11–$42_{\Delta 19–24}$ were identified in CSF from patients with the *Uppsala APP* mutation and in *APPUpp* cell media. Moreover, Aβp11–$42_{\Delta 19–24}$ was abundant in the plaques of the mutation carrier brain, likely as a consequence of increased cleavage at this site. This additional cleavage occurs at the β′ cleavage site, and it is, at this point, uncertain whether the observed activity with the *Uppsala APP* mutation is due to a general increase of BACE1 activity that affects both β-secretase sites in *APPUpp* or whether it represents an additional shifted α-secretase cleavage site resulting from the deletion of six amino acids in the *APPUpp* sequence.

Thus, the *Uppsala APP* mutation seems to abolish the non–amyloid-generating pathway of APP processing, which may further contribute to the pathogenesis in affected individuals. However, to confirm the responsible protease(s) of the additional cleavage sites, further experimental studies using different protease inhibitors are needed.

To investigate the inherent properties of Aβ, we next performed in vitro studies that examined the aggregation behavior of the mutated peptides. Upon analyzing results generated by the ThT assay, it became evident that AβUpp1–$42_{\Delta 19–24}$ was forming bona fide fibrils very rapidly. With respect to oligomers or protofibrils, both Aβwt1–42 and AβArc1–42 formed such intermediately sized soluble aggregates that increased with time, which is in line with what has been proposed as the pathogenic mechanism for the *Arctic* mutation (*22*). However, AβUpp1–$42_{\Delta 19–24}$ oligomer/protofibril concentrations decreased over time, probably because the in vitro fibril formation was so rapid and complete that intermediate species were immediately fibrillized. This theory may be supported by the finding that, compared to sAD cases, TBS extracts of the *Uppsala APP* mutation carrier brain displayed lower concentrations of oligomers/protofibrils, especially larger variants, which may suggest that $A\beta Upp_{\Delta 19–24}$ aggregates into smaller-sized oligomers that rapidly fibrillize and deposit into plaques. Despite this, oligomers/protofibrils of Aβ are likely to be of relevance for the pathogenesis of AD caused by the *Uppsala APP* mutation.

Structural analyses of two different polymorphs of the *Uppsala APP* mutation revealed that they share some features of previously published Aβ1–42 fibril structures but generally differ from all Aβ fibril structures that have been described to date. Further studies will be required to determine the effects of these structural polymorphs with respect to how they interact with amyloid dyes, such as PIB, and how they may contribute to the formation of toxic Aβ oligomers. Such oligomer formation could be driven by secondary nucleation, which has previously been reported to depend on the structure of the fibrillar surface where such a process is believed to occur (*55*).

To the best of our knowledge, the only previously described intra-Aβ *APP* deletion is the *Osaka* mutation (*30*). Whereas this mutation has been reported to have a recessive character, the *Uppsala APP* mutation is inherited in a dominant manner. Overall, AβUpp1–$42_{\Delta 19–24}$ seems to be forming amyloid fibrils much more aggressively than the corresponding form of $A\beta_{Osaka}$. For example, an *Osaka APP* mutation knock-in mouse model was reported to display brain pathology only when the inserted gene was homozygously expressed (*56*). In the *Osaka APP* mutation mouse model, a reduced α-secretase cleavage could be observed, similar to what we report here for the *Uppsala APP* mutation (*57*).

Taken together, we have identified an *APP* mutation, which is an intra-Aβ deletion causing dominantly inherited AD. The loss of six amino acids results in an increase of the Aβ promoting β-secretase cleavage, leading to an elevated generation of $A\beta Upp_{\Delta 19–24}$ with a concomitant suppression of the regular α-secretase cleavage. Thus, the non–amyloid-generating pathway is seemingly abolished with the mutation. Instead, two other Aβ species, AβUpp5–$40/42_{\Delta 19–24}$ and AβUpp11–$40/42_{\Delta 19–24}$, are formed, possibly as a result of a shift of the α-secretase cleavage site, and these may contribute to disease development in mutation carriers. The facts that Aβwt5–42 has previously been reported as pathogenic and that AβUpp5–$42_{\Delta 19–24}$ was found to be present in plaques from the investigated *Uppsala APP* mutation brain support that, at least, this species may be contributing to the pathogenesis. Moreover, the mutation also renders unique properties to AβUpp1–$42_{\Delta 19–24}$, which accelerates its fibrillization into distinctive polymorphs and promotes plaque deposition in the affected brains. Thus, the combined effect of three putative pathogenic mechanisms by the *Uppsala APP* mutation may well explain why affected carriers develop an aggressive form of disease with a very early age at symptom onset.

Although the study has clearly identified that the *Uppsala APP* mutation causes AD by a combination of three mechanisms, all related to APP, it is based on a limited patient material from *Uppsala APP* mutation carriers (CSF, $n = 3$ and brain, $n = 1$), which limits the statistical power of certain analyses. Therefore, the exact quantitative impact of the mutation on the development of Aβ and downstream pathologies is difficult to assess, because a certain individual variation between patients is to be expected. Furthermore, although we have identified alterations in APP processing, at both the α- and β-cleavage sites, it remains to be confirmed by which enzymes the cleavages occur. Future studies will also be needed to elucidate the impact of each of the three disease mechanisms presented here, as well as the temporal and structural aspects of the development of Aβ pathology. Some of these future studies could be performed in genetically modified mice carrying the *Uppsala APP* mutation.

MATERIALS AND METHODS

Study design

This study was designed to characterize the clinical and mechanistic features of the herein identified *Uppsala APP* mutation, which results in early onset familial AD. Three members of the "Uppsala family" showing manifest AD symptoms were identified as mutation carriers and subjected to clinical evaluation, structural and amyloid brain imaging, and lumbar puncture for analyses of CSF biomarkers. Furthermore, brain tissue from one of the mutation carriers was analyzed postmortem to assess a range of pathological markers—Aβ, tau, and neuroinflammation—and stage the pathology according to established criteria. Brain tissue was also analyzed with MALDI imaging and immunoassays to investigate the nature of Aβ pathology in comparison with groups of sAD brains ($n = 11$) and neurologically normal control brains ($n = 9$). To study the mechanistic properties of the *Uppsala APP* mutation, MS and immunoassays were used to analyze Aβ and APP fragments resulting from APP processing. Such studies were performed in (i) CSF from the three *Uppsala APP* mutation carriers in comparison with CSF from sAD ($n = 10$) and control ($n = 10$) and (ii) medium and lysate from cell cultures transfected with APP harboring the *Uppsala APP* mutation in comparison with wild-type APP. Last, the aggregation behavior and structure of Aβ aggregates were studied with ThT aggregation assay and cryo-EM. Sample sizes for brain tissue and CSF studies were determined to achieve a statistical power of 80%, based on group differences and variability from previous experience of measurements of Aβ concentrations. Researchers were blinded to sample identity where possible. Selection of the brain tissue and CSF samples is stated in the Supplementary Materials. Figure legends contain the sample sizes, replicate information, and statistical tests used.

Statistics

Statistical analyses were performed using GraphPad Prism (versions 6 and 7). Differences between two groups were evaluated for significance with two-tailed Student's *t* test and multiple *t* test when comparing two treatments. Comparisons of three or more groups on a single dataset were performed by one-way analysis of variance (ANOVA), followed by Tukey's post hoc test. A *P* value threshold of 0.05 was used for the assessment of statistical significance. Values are shown as means ± SD. Individual subject-level data are reported in data files S1 and S2.

SUPPLEMENTARY MATERIALS

stm.sciencemag.org/cgi/content/full/13/606/eabc6184/DC1
Materials and Methods
Figs. S1 to S8
Tables S1 to S3
Data files S1 and S2
References (*58*–*75*)

View/request a protocol for this paper from *Bio-protocol*.

REFERENCES AND NOTES

1. B. T. Hyman, C. H. Phelps, T. G. Beach, E. H. Bigio, N. J. Cairns, M. C. Carrillo, D. W. Dickson, C. Duyckaerts, M. P. Frosch, E. Masliah, S. S. Mirra, P. T. Nelson, J. A. Schneider, D. R. Thal, B. Thies, J. Q. Trojanowski, H. V. Vinters, T. J. Montine, National Institute on Aging-Alzheimer's Association guidelines for the neuropathologic assessment of Alzheimer's disease. *Alzheimers Dement.* **8**, 1–13 (2012).
2. D. J. Selkoe, J. Hardy, The amyloid hypothesis of Alzheimer's disease at 25 years. *EMBO Mol. Med.* **8**, 595–608 (2016).
3. A. Goate, M. C. Chartier-Harlin, M. Mullan, J. Brown, F. Crawford, L. Fidani, L. Giuffra, A. Haynes, N. Irving, L. James, R. Mant, P. Newton, K. Rooke, P. Roques, C. Talbot, M. Pericak-Vance, A. Roses, R. Williamson, M. Rossor, M. Owen, J. Hardy, Segregation of a missense mutation in the amyloid precursor protein gene with familial Alzheimer's disease. *Nature* **349**, 704–706 (1991).
4. J. Murrell, M. Farlow, B. Ghetti, M. D. Benson, A mutation in the amyloid precursor protein associated with hereditary Alzheimer's disease. *Science* **254**, 97–99 (1991).
5. M.-C. Chartier-Harlin, F. Crawfort, H. Houlden, A. Warren, D. Hughes, L. Fidani, A. Goate, M. Rossor, P. Roques, J. Hardy, M. Mullan, Early-onset Alzheimer's disease caused by mutations at codon 717 of the β-amyloid precursor protein gene. *Nature* **353**, 844–846 (1991).
6. C. Eckman, N. Mehta, R. Crook, J. Perez-Tur, G. Prihar, E. Pfeiffer, N. Graff-Radford, P. Hinder, D. Yager, B. Zenk, L. Refolo, C. Prada, S. Younkin, M. Hutton, J. Hardy, A new pathogenic mutation in the APP gene (I716V) increases the relative proportion of Aβ42(43). *Hum. Mol. Genet.* **6**, 2087–2089 (1997).
7. J. R. Murrell, A. M. Hake, K. A. Quaid, M. R. Farlow, B. Ghetti, Early-onset Alzheimer disease caused by a new mutation (V717L) in the amyloid precursor protein gene. *Arch. Neurol.* **57**, 885–887 (2000).
8. J. B. Kwok, Q. X. Li, M. Hallupp, S. Whyte, D. Ames, K. Beyreuther, C. L. Masters, P. R. Schofield, Novel Leu723Pro amyloid precursor protein mutation increases amyloid β42(43) peptide levels and induces apoptosis. *Ann. Neurol.* **47**, 249–253 (2000).
9. S. Kumar-Singh, C. De Jonghe, M. Cruts, R. Kleinert, R. Wang, M. Mercken, B. De Strooper, H. Vanderstichele, A. Löfgren, I. Vanderhoeven, H. Backhovens, E. Vanmechelen, P. Kroisel, C. Van Broeckhoven, Nonfibrillar diffuse amyloid deposition due to a γ_{42}-secretase site mutation points to an essential role for N-truncated $A\beta_{42}$ in Alzheimer's disease. *Hum. Mol. Genet.* **9**, 2589–2598 (2000).
10. M. Cruts, B. Dermaut, R. Rademakers, M. Van den Broeck, F. Stögbauer, C. Van Broeckhoven, Novel APP mutation V715A associated with presenile Alzheimer's disease in a German family. *J. Neurol.* **250**, 1374–1375 (2003).
11. J. Theuns, E. Marjaux, M. Vandenbulcke, K. Van Laere, S. Kumar-Singh, G. Bormans, N. Brouwers, M. Van den Broeck, K. Vennekens, E. Corsmit, M. Cruts, B. De Strooper, C. Van Broeckhoven, R. Vandenberghe, Alzheimer dementia caused by a novel mutation located in the APP C-terminal intracytosolic fragment. *Hum. Mutat.* **27**, 888–896 (2006).
12. R. J. Guerreiro, M. Baquero, R. Blesa, M. Boada, J. M. Bras, M. J. Bullido, A. Calado, R. Crook, C. Ferreira, A. Frank, T. Gomez-Isla, I. Hernandez, A. Lleo, A. Machado, P. Martinez-Lage, J. Masdeu, L. Molina-Porcel, J. L. Molinuevo, P. Pastor, J. Perez-Tur, R. Relvas, C. R. Oliveira, M. H. Ribeiro, E. Rogaeva, A. Sa, L. Samaranch, R. Sanchez-Valle, I. Santana, L. Tarraga, F. Valdivieso, A. Singleton, J. Hardy, J. Clarimon, Genetic screening of Alzheimer's disease genes in Iberian and African samples yields novel mutations in presenilins and APP. *Neurobiol. Aging* **31**, 725–731 (2010).
13. Q. Wang, J. Jia, W. Qin, L. Wu, D. Li, Q. Wang, H. Li, A novel AβPP M722K mutation affects amyloid-β secretion and tau phosphorylation and may cause early-onset familial Alzheimer's disease in Chinese individuals. *J. Alzheimers Dis.* **47**, 157–165 (2015).
14. S. Hsu, B. A. Gordon, R. Hornbeck, J. B. Norton, D. Levitch, A. Louden, E. Ziegemeier, R. Laforce Jr., J. Chhatwal, G. S. Day, E. McDade, J. C. Morris, A. M. Fagan, T. L. S. Benzinger, A. M. Goate, C. Cruchaga, R. J. Bateman; Dominantly Inherited Alzheimer Network (DIAN), C. M. Karch, Discovery and validation of autosomal dominant Alzheimer's disease mutations. *Alzheimers Res. Ther.* **10**, 67 (2018).
15. M. Citron, C. Vigo-Pelfrey, D. B. Teplow, C. Miller, D. Schenk, J. Johnston, B. Winblad, N. Venizelos, L. Lannfelt, D. J. Selkoe, Excessive production of amyloid beta-protein by peripheral cells of symptomatic and presymptomatic patients carrying the Swedish familial Alzheimer disease mutation. *Proc. Natl. Acad. Sci. U.S.A.* **91**, 11993–11997 (1994).
16. J. A. Johnston, R. F. Cowburn, S. Norgren, B. Wiehager, N. Venizelos, B. Winblad, C. Vigo-Pelfrey, D. Schenk, L. Lannfelt, C. O'Neill, Increased β-amyloid release and levels of amyloid precursor protein (APP) in fibroblast cell lines from family members with the Swedish Alzheimer's disease APP670/671 mutation. *FEBS Lett.* **354**, 274–278 (1994).
17. D. Scheuner, C. Eckman, M. Jensen, X. Song, M. Citron, N. Suzuki, T. D. Bird, J. Hardy, M. Hutton, W. Kukull, E. Larson, E. Levy-Lahad, M. Viitanen, E. Peskind, P. Poorkaj, G. Schellenberg, R. Tanzi, W. Wasco, L. Lannfelt, D. Selkoe, S. Younkin, Secreted amyloid β–protein similar to that in the senile plaques of Alzheimer's disease is increased in vivo by the presenilin 1 and 2 and *APP* mutations linked to familial Alzheimer's disease. *Nat. Med.* **2**, 864–870 (1996).
18. E. Levy, M. D. Carman, I. J. Fernandez-Madrid, M. D. Power, I. Lieberburg, S. G. van Duinen, G. T. Bots, W. Luyendijk, B. Frangione, Mutation of the Alzheimer's disease amyloid gene in hereditary cerebral hemorrhage, Dutch type. *Science* **248**, 1124–1126 (1990).
19. O. Bugiani, G. Giaccone, G. Rossi, M. Mangieri, R. Capobianco, M. Morbin, G. Mazzoleni, C. Cupidi, G. Marcon, A. Giovagnoli, A. Bizzi, G. Di Fede, G. Puoti, F. Carella, A. Salmaggi, A. Romorini, G. M. Patruno, M. Magoni, A. Padovani, F. Tagliavini, Hereditary cerebral hemorrhage with amyloidosis associated with the E693K mutation of APP. *Arch. Neurol.* **67**, 987–995 (2010).
20. L. Hendriks, C. M. van Duijn, P. Cras, M. Cruts, W. Van Hul, F. Van Harskamp, A. Warren, M. G. McInnis, S. E. Antonarakis, J.-J. Martin, A. Hofman, C. Van Broeckhoven, Presenile dementia and cerebral haemorrhage linked to a mutation at codon 692 of the β–amyloid precursor protein gene. *Nat. Genet.* **1**, 218–221 (1992).
21. T. J. Grabowski, H. S. Cho, J. P. Vonsattel, G. W. Rebeck, S. M. Greenberg, Novel amyloid precursor protein mutation in an Iowa family with dementia and severe cerebral amyloid angiopathy. *Ann. Neurol.* **49**, 697–705 (2001).
22. C. Nilsberth, A. Westlind-Danielsson, C. B. Eckman, M. M. Condron, K. Axelman, C. Forsell, C. Stenh, J. Luthman, D. B. Teplow, S. G. Younkin, J. Näslund, L. Lannfelt, The 'Arctic' APP mutation (E693G) causes Alzheimer's disease by enhanced Aβ protofibril formation. *Nat. Neurosci.* **4**, 887–893 (2001).
23. A.-S. Johansson, F. Berglind-Dehlin, G. Karlsson, K. Edwards, P. Gellerfors, L. Lannfelt, Physiochemical characterization of the Alzheimer's disease-related peptides Aβ1–42Arctic and Aβ1–42wt. *FEBS J.* **273**, 2618–2630 (2006).
24. H. Basun, N. Bogdanovic, M. Ingelsson, O. Almkvist, J. Naslund, K. Axelman, T. D. Bird, D. Nochlin, G. D. Schellenberg, L. O. Wahlund, L. Lannfelt, Clinical and neuropathological features of the arctic APP gene mutation causing early-onset Alzheimer disease. *Arch. Neurol.* **65**, 499–505 (2008).
25. O. Philipson, A. Lord, M. Lalowski, R. Soliymani, M. Baumann, J. Thyberg, N. Bogdanovic, T. Olofsson, L. O. Tjernberg, M. Ingelsson, L. Lannfelt, H. Kalimo, L. N. Nilsson, The Arctic amyloid-β precursor protein (AβPP) mutation results in distinct plaques and accumulation of N- and C-truncated Aβ. *Neurobiol. Aging* **33**, 1010.e1–1010.e1011013 (2012).
26. H. Kalimo, M. Lalowski, N. Bogdanovic, O. Philipson, T. D. Bird, D. Nochlin, G. D. Schellenberg, R. Brundin, T. Olofsson, R. Soliymani, M. Baumann, O. Wirths, T. A. Bayer, L. N. Nilsson, H. Basun, L. Lannfelt, M. Ingelsson, The Arctic AβPP mutation leads to Alzheimer's disease pathology with highly variable topographic deposition of differentially truncated Aβ. *Acta Neuropathol. Commun.* **1**, 60 (2013).
27. T. Jonsson, J. K. Atwal, S. Steinberg, J. Snaedal, P. V. Jonsson, S. Bjornsson, H. Stefansson, P. Sulem, D. Gudbjartsson, J. Maloney, K. Hoyte, A. Gustafson, Y. Liu, Y. Lu, T. Bhangale, R. R. Graham, J. Huttenlocher, G. Bjornsdottir, O. A. Andreassen, E. G. Jonsson, A. Palotie, T. W. Behrens, O. T. Magnusson, A. Kong, U. Thorsteinsdottir, R. J. Watts, K. Stefansson, A mutation in APP protects against Alzheimer's disease and age-related cognitive decline. *Nature* **488**, 96–99 (2012).
28. J. A. Maloney, T. Bainbridge, A. Gustafson, S. Zhang, R. Kyauk, P. Steiner, M. van der Brug, Y. Liu, J. A. Ernst, R. J. Watts, J. K. Atwal, Molecular mechanisms of Alzheimer disease protection by the A673T allele of amyloid precursor protein. *J. Biol. Chem.* **289**, 30990–31000 (2014).
29. I. Benilova, R. Gallardo, A. A. Ungureanu, V. Castillo Cano, A. Snellinx, M. Ramakers, C. Bartic, F. Rousseau, J. Schymkowitz, B. De Strooper, The Alzheimer disease protective mutation A2T modulates kinetic and thermodynamic properties of amyloid-β (Aβ) aggregation. *J. Biol. Chem.* **289**, 30977–30989 (2014).
30. K. Nishitsuji, T. Tomiyama, K. Ishibashi, K. Ito, R. Teraoka, M. P. Lambert, W. L. Klein, H. Mori, The E693Delta mutation in amyloid precursor protein increases intracellular accumulation of amyloid beta oligomers and causes endoplasmic reticulum stress-induced apoptosis in cultured cells. *Am. J. Pathol.* **174**, 957–969 (2009).
31. S. Abu Hamdeh, E. R. Waara, C. Moller, L. Soderberg, H. Basun, I. Alafuzoff, L. Hillered, L. Lannfelt, M. Ingelsson, N. Marklund, Rapid amyloid-β oligomer and protofibril accumulation in traumatic brain injury. *Brain Pathol.* **28**, 451–462 (2018).
32. P. H. Kuhn, H. Wang, B. Dislich, A. Colombo, U. Zeitschel, J. W. Ellwart, E. Kremmer, S. Rossner, S. F. Lichtenthaler, ADAM10 is the physiologically relevant, constitutive alpha-secretase of the amyloid precursor protein in primary neurons. *EMBO J.* **29**, 3020–3032 (2010).

33. H. Englund, D. Sehlin, A. S. Johansson, L. N. Nilsson, P. Gellerfors, S. Paulie, L. Lannfelt, F. E. Pettersson, Sensitive ELISA detection of amyloid-beta protofibrils in biological samples. *J. Neurochem.* **103**, 334–345 (2007).
34. L. Gremer, D. Schölzel, C. Schenk, E. Reinartz, J. Labahn, R. B. G. Ravelli, M. Tusche, C. Lopez-Iglesias, W. Hoyer, H. Heise, D. Willbold, G. F. Schröder, Fibril structure of amyloid-β(1–42) by cryo–electron microscopy. *Science* **358**, 116–119 (2017).
35. M. Schmidt, A. Rohou, K. Lasker, J. K. Yadav, C. Schiene-Fischer, M. Fandrich, N. Grigorieff, Peptide dimer structure in an Aβ(1–42) fibril visualized with cryo-EM. *Proc. Natl. Acad. Sci. U.S.A.* **112**, 11858–11863 (2015).
36. M. T. Colvin, R. Silvers, Q. Z. Ni, T. V. Can, I. Sergeyev, M. Rosay, K. J. Donovan, B. Michael, J. Wall, S. Linse, R. G. Griffin, Atomic resolution structure of monomorphic Aβ42 amyloid fibrils. *J. Am. Chem. Soc.* **138**, 9663–9674 (2016).
37. M. A. Walti, F. Ravotti, H. Arai, C. G. Glabe, J. S. Wall, A. Bockmann, P. Guntert, B. H. Meier, R. Riek, Atomic-resolution structure of a disease-relevant Aβ(1–42) amyloid fibril. *Proc. Natl. Acad. Sci. U.S.A.* **113**, E4976–E4984 (2016).
38. N. S. Ryan, M. N. Rossor, Correlating familial Alzheimer's disease gene mutations with clinical phenotype. *Biomark. Med.* **4**, 99–112 (2010).
39. R. J. Bateman, C. Xiong, T. L. Benzinger, A. M. Fagan, A. Goate, N. C. Fox, D. S. Marcus, N. J. Cairns, X. Xie, T. M. Blazey, D. M. Holtzman, A. Santacruz, V. Buckles, A. Oliver, K. Moulder, P. S. Aisen, B. Ghetti, W. E. Klunk, E. McDade, R. N. Martins, C. L. Masters, R. Mayeux, J. M. Ringman, M. N. Rossor, P. R. Schofield, R. A. Sperling, S. Salloway, J. C. Morris; Dominantly Inherited Alzheimer Network, Clinical and biomarker changes in dominantly inherited Alzheimer's disease. *N. Engl. J. Med.* **367**, 795–804 (2012).
40. S. S. Sisodia, Beta-amyloid precursor protein cleavage by a membrane-bound protease. *Proc. Natl. Acad. Sci. U.S.A.* **89**, 6075–6079 (1992).
41. P. Saftig, S. F. Lichtenthaler, The alpha secretase ADAM10: A metalloprotease with multiple functions in the brain. *Prog. Neurobiol.* **135**, 1–20 (2015).
42. S. F. Lichtenthaler, M. K. Lemberg, R. Fluhrer, Proteolytic ectodomain shedding of membrane proteins in mammals-hardware, concepts, and recent developments. *EMBO J.* **37**, e99456 (2018).
43. M. Farzan, C. E. Schnitzler, N. Vasilieva, D. Leung, H. Choe, BACE2, a beta -secretase homolog, cleaves at the beta site and within the amyloid-beta region of the amyloid-beta precursor protein. *Proc. Natl. Acad. Sci. U.S.A.* **97**, 9712–9717 (2000).
44. E. Portelius, G. Brinkmalm, A. J. Tran, H. Zetterberg, A. Westman-Brinkmalm, K. Blennow, Identification of novel APP/Abeta isoforms in human cerebrospinal fluid. *Neurodegener Dis* **6**, 87–94 (2009).
45. J. Bien, T. Jefferson, M. Causevic, T. Jumpertz, L. Munter, G. Multhaup, S. Weggen, C. Becker-Pauly, C. U. Pietrzik, The metalloprotease meprin β generates amino terminal-truncated amyloid β peptide species. *J. Biol. Chem.* **287**, 33304–33313 (2012).
46. E. Portelius, M. Olsson, G. Brinkmalm, U. Rüetschi, N. Mattsson, U. Andreasson, J. Gobom, A. Brinkmalm, M. Hölttä, K. Blennow, H. Zetterberg, Mass spectrometric characterization of amyloid-β species in the 7PA2 cell model of Alzheimer's disease. *J. Alzheimers Dis.* **33**, 85–93 (2013).
47. A. T. Welzel, J. E. Maggio, G. M. Shankar, D. E. Walker, B. L. Ostaszewski, S. Li, I. Klyubin, M. J. Rowan, P. Seubert, D. M. Walsh, D. J. Selkoe, Secreted amyloid β-proteins in a cell culture model include N-terminally extended peptides that impair synaptic plasticity. *Biochemistry* **53**, 3908–3921 (2014).
48. N. Kaneko, R. Yamamoto, T. A. Sato, K. Tanaka, Identification and quantification of amyloid beta-related peptides in human plasma using matrix-assisted laser desorption/ionization time-of-flight mass spectrometry. *Proc. Jpn. Acad. Ser. B Phys. Biol. Sci.* **90**, 104–117 (2014).
49. M. Willem, S. Tahirovic, M. A. Busche, S. V. Ovsepian, M. Chafai, S. Kootar, D. Hornburg, L. D. Evans, S. Moore, A. Daria, H. Hampel, V. Muller, C. Giudici, B. Nuscher, A. Wenninger-Weinzierl, E. Kremmer, M. T. Heneka, D. R. Thal, V. Giedraitis, L. Lannfelt, U. Müller, F. J. Livesey, F. Meissner, J. Herms, A. Konnerth, H. Marie, C. Haass, η-Secretase processing of APP inhibits neuronal activity in the hippocampus. *Nature* **526**, 443–447 (2015).
50. Z. Zhang, M. Song, X. Liu, S. S. Kang, D. M. Duong, N. T. Seyfried, X. Cao, L. Cheng, Y. E. Sun, S. Ping Yu, J. Jia, A. I. Levey, K. Ye, Delta-secretase cleaves amyloid precursor protein and regulates the pathogenesis in Alzheimer's disease. *Nat. Commun.* **6**, 8762 (2015).
51. K. Baranger, Y. Marchalant, A. E. Bonnet, N. Crouzin, A. Carrete, J. M. Paumier, N. A. Py, A. Bernard, C. Bauer, E. Charrat, K. Moschke, M. Seiki, M. Vignes, S. F. Lichtenthaler, F. Checler, M. Khrestchatisky, S. Rivera, MT5-MMP is a new pro-amyloidogenic proteinase that promotes amyloid pathology and cognitive decline in a transgenic mouse model of Alzheimer's disease. *Cell. Mol. Life Sci.* **73**, 217–236 (2016).
52. T. Weiffert, G. Meisl, P. Flagmeier, S. De, C. J. R. Dunning, B. Frohm, H. Zetterberg, K. Blennow, E. Portelius, D. Klenerman, C. M. Dobson, T. P. J. Knowles, S. Linse, Increased secondary nucleation underlies accelerated aggregation of the four-residue N-terminally truncated Aβ42 species Aβ5–42. *ACS Chem. Neurosci.* **10**, 2374–2384 (2019).
53. N. Mattsson, L. Rajendran, H. Zetterberg, M. Gustavsson, U. Andreasson, M. Olsson, G. Brinkmalm, J. Lundkvist, L. H. Jacobson, L. Perrot, U. Neumann, H. Borghys, M. Mercken, D. Dhuyvetter, F. Jeppsson, K. Blennow, E. Portelius, BACE1 inhibition induces a specific cerebrospinal fluid β-amyloid pattern that identifies drug effects in the central nervous system. *PLOS ONE* **7**, e31084 (2012).
54. E. Portelius, R. A. Dean, U. Andreasson, N. Mattsson, A. Westerlund, M. Olsson, R. B. Demattos, M. M. Racke, H. Zetterberg, P. C. May, K. Blennow, β-site amyloid precursor protein-cleaving enzyme 1(BACE1) inhibitor treatment induces Aβ5-X peptides through alternative amyloid precursor protein cleavage. *Alzheimers Res. Ther.* **6**, 75 (2014).
55. S. Linse, Monomer-dependent secondary nucleation in amyloid formation. *Biophys. Rev.* **9**, 329–338 (2017).
56. T. Umeda, T. Kimura, K. Yoshida, K. Takao, Y. Fujita, S. Matsuyama, A. Sakai, M. Yamashita, Y. Yamashita, K. Ohnishi, M. Suzuki, H. Takuma, T. Miyakawa, A. Takashima, T. Morita, H. Mori, T. Tomiyama, Mutation-induced loss of APP function causes GABAergic depletion in recessive familial Alzheimer's disease: Analysis of Osaka mutation-knockin mice. *Acta Neuropathol. Commun.* **5**, 59 (2017).
57. L. Kulic, J. McAfoose, T. Welt, C. Tackenberg, C. Spani, F. Wirth, V. Finder, U. Konietzko, M. Giese, A. Eckert, K. Noriaki, T. Shimizu, K. Murakami, K. Irie, S. Rasool, C. Glabe, C. Hock, R. M. Nitsch, Early accumulation of intracellular fibrillar oligomers and late congophilic amyloid angiopathy in mice expressing the Osaka intra-Aβ APP mutation. *Transl. Psychiatry* **2**, e183 (2012).
58. G. McKhann, D. Drachman, M. Folstein, R. Katzman, D. Price, E. M. Stadlan, Clinical diagnosis of Alzheimer's disease: Report of the NINCDS-ADRDA Work Group under the auspices of department of health and human services task force on Alzheimer's disease. *Neurology* **34**, 939–944 (1984).
59. C. E. Teunissen, A. Petzold, J. L. Bennett, F. S. Berven, L. Brundin, M. Comabella, D. Franciotta, J. L. Frederiksen, J. O. Fleming, R. Furlan, R. Q. Hintzen, S. G. Hughes, M. H. Johnson, E. Krasulova, J. Kuhle, M. C. Magnone, C. Rajda, K. Rejdak, H. K. Schmidt, V. van Pesch, E. Waubant, C. Wolf, G. Giovannoni, B. Hemmer, H. Tumani, F. Deisenhammer, A consensus protocol for the standardization of cerebrospinal fluid collection and biobanking. *Neurology* **73**, 1914–1922 (2009).
60. A. Elobeid, S. Libard, M. Leino, S. N. Popova, I. Alafuzoff, Altered proteins in the aging brain. *J. Neuropathol. Exp. Neurol.* **75**, 316–325 (2016).
61. O. Philipson, P. Hammarström, K. P. Nilsson, E. Portelius, T. Olofsson, M. Ingelsson, B. T. Hyman, K. Blennow, L. Lannfelt, H. Kalimo, L. N. Nilsson, A highly insoluble state of Abeta similar to that of Alzheimer's disease brain is found in Arctic APP transgenic mice. *Neurobiol. Aging* **30**, 1393–1405 (2009).
62. W. Michno, S. Nystrom, P. Wehrli, T. Lashley, G. Brinkmalm, L. Guerard, S. Syvanen, D. Sehlin, I. Kaya, D. Brinet, K. P. R. Nilsson, P. Hammarstrom, K. Blennow, H. Zetterberg, J. Hanrieder, Pyroglutamation of amyloid-βx-42 (Aβx-42) followed by Aβ1–40 deposition underlies plaque polymorphism in progressing Alzheimer's disease pathology. *J. Biol. Chem.* **294**, 6719–6732 (2019).
63. T. Klingstedt, A. Aslund, R. A. Simon, L. B. Johansson, J. J. Mason, S. Nyström, P. Hammarström, K. P. Nilsson, Synthesis of a library of oligothiophenes and their utilization as fluorescent ligands for spectral assignment of protein aggregates. *Org. Biomol. Chem.* **9**, 8356–8370 (2011).
64. J. Rasmussen, J. Mahler, N. Beschorner, S. A. Kaeser, L. M. Hasler, F. Baumann, S. Nystrom, E. Portelius, K. Blennow, T. Lashley, N. C. Fox, D. Sepulveda-Falla, M. Glatzel, A. L. Oblak, B. Ghetti, K. P. R. Nilsson, P. Hammarstrom, M. Staufenbiel, L. C. Walker, M. Jucker, Amyloid polymorphisms constitute distinct clouds of conformational variants in different etiological subtypes of Alzheimer's disease. *Proc. Natl. Acad. Sci. U.S.A.* **114**, 13018–13023 (2017).
65. E. Portelius, A. Westman-Brinkmalm, H. Zetterberg, K. Blennow, Determination of beta-amyloid peptide signatures in cerebrospinal fluid using immunoprecipitation-mass spectrometry. *J. Proteome Res.* **5**, 1010–1016 (2006).
66. E. Portelius, A. J. Tran, U. Andreasson, R. Persson, G. Brinkmalm, H. Zetterberg, K. Blennow, A. Westman-Brinkmalm, Characterization of amyloid beta peptides in cerebrospinal fluid by an automated immunoprecipitation procedure followed by mass spectrometry. *J. Proteome Res.* **6**, 4433–4439 (2007).
67. G. Brinkmalm, E. Portelius, A. Ohrfelt, N. Mattsson, R. Persson, M. K. Gustavsson, C. H. Vite, J. Gobom, J. E. Mansson, J. Nilsson, A. Halim, G. Larson, U. Ruetschi, H. Zetterberg, K. Blennow, A. Brinkmalm, An online nano-LC-ESI-FTICR-MS method for comprehensive characterization of endogenous fragments from amyloid β and amyloid precursor protein in human and cat cerebrospinal fluid. *J. Mass Spectrom.* **47**, 591–603 (2012).
68. A. Ludwig, C. Hundhausen, M. H. Lambert, N. Broadway, R. C. Andrews, D. M. Bickett, M. A. Leesnitzer, J. D. Becherer, Metalloproteinase inhibitors for the disintegrin-like metalloproteinases ADAM10 and ADAM17 that differentially block constitutive and phorbol ester-inducible shedding of cell surface molecules. *Comb. Chem. High Throughput Screen.* **8**, 161–171 (2005).
69. A. Colombo, H. Wang, P. H. Kuhn, R. Page, E. Kremmer, P. J. Dempsey, H. C. Crawford, S. F. Lichtenthaler, Constitutive α- and β-secretase cleavages of the amyloid precursor protein are partially coupled in neurons, but not in frequently used cell lines. *Neurobiol. Dis.* **49**, 137–147 (2013).

70. P. H. Kuhn, K. Koroniak, S. Hogl, A. Colombo, U. Zeitschel, M. Willem, C. Volbracht, U. Schepers, A. Imhof, A. Hoffmeister, C. Haass, S. Rossner, S. Brase, S. F. Lichtenthaler, Secretome protein enrichment identifies physiological BACE1 protease substrates in neurons. *EMBO J.* **31**, 3157–3168 (2012).
71. C. Höfling, M. Morawski, U. Zeitschel, E. R. Zanier, K. Moschke, A. Serdaroglu, F. Canneva, S. von Horsten, M. G. De Simoni, G. Forloni, C. Jäger, E. Kremmer, S. Roßner, S. F. Lichtenthaler, P.-H. Kuhn, Differential transgene expression patterns in Alzheimer mouse models revealed by novel human amyloid precursor protein-specific antibodies. *Aging Cell* **15**, 953–963 (2016).
72. C. S. Hughes, S. Foehr, D. A. Garfield, E. E. Furlong, L. M. Steinmetz, J. Krijgsveld, Ultrasensitive proteome analysis using paramagnetic bead technology. *Mol. Syst. Biol.* **10**, 757 (2014).
73. J. Cox, M. Y. Hein, C. A. Luber, I. Paron, N. Nagaraj, M. Mann, Accurate proteome-wide label-free quantification by delayed normalization and maximal peptide ratio extraction, termed MaxLFQ. *Mol. Cell. Proteomics* **13**, 2513–2526 (2014).
74. J. Zivanov, T. Nakane, B. O. Forsberg, D. Kimanius, W. J. Hagen, E. Lindahl, S. H. Scheres, New tools for automated high-resolution cryo-EM structure determination in RELION-3. *eLife* **7**, e42166 (2018).
75. A. Rohou, N. Grigorieff, CTFFIND4: Fast and accurate defocus estimation from electron micrographs. *J. Struct. Biol.* **192**, 216–221 (2015).

Acknowledgments: We thank C. Röder and L. Gremer for help with sample preparation for cryo-EM, discussions, and advice. We also thank P. Hammarström and P. Nilsson for providing fluorophores q-FTAA and h-FTAA. We also thank the Uppsala Genome Center for the help with targeted exome sequencing, L. Streubel-Gallasch for statistical advice, H. Zetterberg for assistance with CSF ELISA measurements, and J. Watts for critical proofreading of the manuscript. Last, Fig. 1G was made in part using Biorender. **Funding:** This work was supported by the Swedish Research Council (#2016-02120 to L.L. and #2018-02181 to J.H.); the Swedish Alzheimer Foundation (to L.L. and J.H.); the Swedish Brain Foundation (to L.L.); Åke Wibergs Stiftelse (to J.H.); Åhlén Stiftelsen (to J.H.); the German Research Foundation within the framework of the Munich Cluster for Systems Neurology (EXC 2145 SyNergy, project ID 390857198) and the research unit FOR2290, the BMBF within project CLINSPECT-M, and by JPco-fuND2 2019 Personalized Medicine for Neurodegenerative Diseases 01ED2002B (to S.F.L.). **Author contributions:** M.P.d.l.V., V.G., L.L., D.S., and M.I. designed the study. L.L. obtained the funding. These authors performed the experiments: M.P.d.l.V. (genetic analyses, immunostainings, ELISAs, ThS staining, cell transfection, Western blot, Meso Scale electrochemiluminescence, and ThT assay), V.G. (genetic analyses and plasmid designs), W.M. (MALDI imaging, MS, and LCO stainings), G.G. (cell transfection and immunoblotting with protease inhibitors and CTF fragments), M.Z. (transmission electron microscopy), L.S. (SEC), and S.A.M. (MS for APPUpp cleavage site determination of transfected cell culture). M.P.d.l.V., V.G., W.M., T.D., L.S., I.A., L.N.G.N., A.E., D.W., G.F.S., J.H., S.F.L., L.L., D.S., and M.I. analyzed the data. L.K., R.B., M.L., and M.I. contributed to sample collection. M.P.d.l.V., V.G., D.S., and M.I. wrote the first draft of the paper. All authors contributed to the final version of the paper. **Competing interests:** L.N.G.N. has received an honorarium from BioArctic AB and has a research collaboration with this company, outside the submitted work. L.L. is a cofounder of BioArctic AB. M.I. is a paid consultant for BioArctic AB. **Data and materials availability:** All data associated with this study are present in the paper or the Supplementary Materials. Materials in this study will be made available by contacting the corresponding author and completion of a material transfer agreement. Exon 17 nucleotide sequence for Uppsala mutation was submitted to GenBank (MW892394). Density maps of the AβUpp1–42$_{\Delta 19–24}$ obtained by cryo-EM were deposited in the EMDB for polymorph 1 (EMD-12592) and for polymorph 2 (EMD-12593).

Submitted 5 May 2020
Resubmitted 5 February 2021
Accepted 22 June 2021
Published 11 August 2021
10.1126/scitranslmed.abc6184

Citation: M. Pagnon de la Vega, V. Giedraitis, W. Michno, L. Kilander, G. Güner, M. Zielinski, M. Löwenmark, R. Brundin, T. Danfors, L. Söderberg, I. Alafuzoff, L. N. Nilsson, A. Erlandsson, D. Willbold, S. A. Müller, G. F. Schröder, J. Hanrieder, S. F. Lichtenthaler, L. Lannfelt, D. Sehlin, M. Ingelsson, The *Uppsala APP* deletion causes early onset autosomal dominant Alzheimer's disease by altering APP processing and increasing amyloid β fibril formation. *Sci. Transl. Med.* **13**, eabc6184 (2021).

Science Translational Medicine

The *Uppsala APP* deletion causes early onset autosomal dominant Alzheimer's disease by altering APP processing and increasing amyloid β fibril formation

María Pagnon de la Vega, Vilmantas Giedraitis, Wojciech Michno, Lena Kilander, Gökhan Güner, Mara Zielinski, Malin Löwenmark, RoseMarie Brundin, Torsten Danfors, Linda Söderberg, Irina Alafuzoff, Lars N.G. Nilsson, Anna Erlandsson, Dieter Willbold, Stephan A. Müller, Gunnar F. Schröder, Jörg Hanrieder, Stefan F. Lichtenthaler, Lars Lannfelt, Dag Sehlin and Martin Ingelsson

Sci Transl Med **13**, eabc6184.
DOI: 10.1126/scitranslmed.abc6184

APP from Sweden

The amyloid precursor protein (*APP*) gene encodes amyloid precursor protein, whose proteolysis gives rise to A β peptides. Mutations in *APP* cause familial Alzheimer's disease (AD). In this study, Pagnon de la Vega *et al.* describe a pathogenic APP deletion causing a dominant form of AD. This mutation, called the *Uppsala APP* mutation, results in early onset, fast-progressing AD. At molecular level, the Uppsala *APP* mutation alters the protein processing, resulting in increased A β production and rapid aggregation. The results contribute to elucidate the molecular mechanisms regulating AD development and to understand the impact of *APP* mutations on disease pathophysiology.

Science Translational Medicine
AAAS

Supplementary Materials for

The *Uppsala APP* deletion causes early onset autosomal dominant Alzheimer's disease by altering APP processing and increasing amyloid β fibril formation

María Pagnon de la Vega *et al*.

Corresponding author: Martin Ingelsson, martin.ingelsson@pubcare.uu.se

Sci. Transl. Med. **13**, eabc6184 (2021)
DOI: 10.1126/scitranslmed.abc6184

The PDF file includes:

Other Supplementary Material for this manuscript includes the following:

Data files S1 and S2

Materials and Methods

Human subjects and ethical considerations

The Regional Ethical Review Board in Uppsala, Sweden and the Swedish Ethical Review Authority had approved of all parts of the study (2005-244, Ö 48-2005, 2005-103, 2011-044, 2013-187, 2020-03703). The CSF samples were obtained from the Uppsala Biobank and the *post mortem* brain tissues were obtained from the Uppsala Biobank and the Netherlands Brain Bank (NBB, Amsterdam, the Netherlands), respectively. Written informed consent had been given from all participants or from their direct next-of-kin.

The control CSF samples were selected from our cohort of individuals who had been recruited via advertisements in the local newspaper and undergone lumbar puncture preceded by an examination to rule out cognitive dysfunction. The clinical AD diagnosis of patients with dementia was performed according to NINCDS-ADRDA criteria (*58*). Disease-specific neuropathology was confirmed in all *post mortem* AD cases using recommended histopathological protocols and formalin-fixed specimens.

Positron emission tomography and computed tomography (PET/CT)

All imaging investigations were performed at Uppsala University Hospital PET Centre and radiology department. For the two siblings, PET imaging was performed on a General Electric healthcare (GE) Discovery ST PET/CT system. A 10-minute scan was acquired 50 min post injection of 3.5 MBq FDG/kg. For [^{11}C]PIB, a 20-minute scan was acquired between 40 and 60 minutes after injection of 3 MBq [^{11}C]PIB/kg. Images were reconstructed using the included scanner software with ordered subset expectation maximization (OSEM), applying all the appropriate corrections for random scatter etc. and a 5 mm Gaussian post- filter. Attenuation correction was based on a low-dose CT.

For the last subject [^{18}F]FDG-PET imaging was done on a GE Discovery MI PET/CT system using the same parameters as above but with a 5-minute scan instead of 10 due to improved camera sensitivity.

Post processing of PET images was done using CortexID (CortexID suite v 2.1, Ext. 2. General Electric Company). Standard uptake value ratios (SUVR) were calculated using a global reference for [^{18}F]FDG and the cerebellum gray matter for [^{11}C]PIB. Image interpretation was based on both visual examination and semi quantitative measurements.

A standard clinical routine CT without contrast enhancement and with visual interpretation was performed on all subjects at the department of radiology.

Lumbar puncture and CSF analyses

Samples were collected according to the recommended consensus protocol for CSF collection and biobanking (*59*). The concentrations of Aβ42, t-tau and p-tau in CSF were measured at the Clinical Neurochemistry Laboratory, University of Gothenburg, Mölndal, Sweden. The

measurements were performed by board-certified laboratory technicians, who were blinded to clinical data, using two immunoassays with identical set-up of antibodies (Lumipulse automated assay for one of the mutation carriers (cousin) and INNOTEST ELISA for the rest of the samples; Fujirebio) and procedures accredited by the Swedish Board of Accreditation and Conformity Assessment.

Cerebrospinal fluid samples from ten sporadic AD (sAD) cases and three patients with the *Uppsala APP* mutation with similar pathology stage, and ten controls (older than 78) were analyzed. The information about the patients can be found in table S1.

Genetic analyses

DNA was extracted from blood samples of older family members. In addition, DNA was available from 273 subjects with sAD and 262 healthy controls. The presence of an intra-Aβ 18 nucleotide deletion was identified in two of the index cases by targeted exome sequencing. All selected exons, including at least 25 nucleotides surrounding exons, were amplified using AmpliSeq sequence enrichment method followed by IonTorrent sequencing (Life Technologies). Sequenced gene regions were aligned to the human reference genome (assembly hg19). Targeted exome sequencing was also used to infer the *APOE* genotypes.

For the screening of other samples (older family members, Swedish patients with AD, and older healthy control subjects), a DNA fragment containing the mutation site was amplified by PCR and analyzed on an agarose gel (3%). Polymerase chain reaction (PCR) was performed in a standard buffer to a final volume of 15 µl containing 30 ng genomic DNA and 0.2 µM of each primer (CATCCAAATGTCCCCTGCAT and GCACCTTTGTTTGAACCCAC) and 0.45U GoTaq DNA polymerase (Promega). The following amplification protocol was used: denaturation for 2 min at 95°C followed by 35 cycles of 94°C for 30 s, 58°C for 30 s and 72°C for 30 s. Two PCR fragments were observed in DNA samples from individuals with the mutation, whereas in subjects without the mutation only one band was found. In order to confirm results from the first PCR, a second PCR was performed with a common forward primer (CATCCAAATGTCCCCTGCAT) and a reverse primer either specific to the mutation site (ACCTTTGTTTGAACCCACCTT), or to wild type *APP* (TTGAACCCACATCTTCTGCAA).

Immunohistochemistry and Thioflavin S staining of human brain tissues

Paraformaldehyde fixed and paraffinized tissue blocks from temporal, parietal and occipital cortices were sectioned at 7 µm. Next, the sections were deparaffinized and treated with 80% formic acid or 50 mM citrate buffer for 1 h (*60*). To stain amyloid plaques, we used different Aβ antibodies – 6F/3D, binding to Aβ amino acids 8-17 (*61*), anti-Aβ40 and anti-Aβ42 (Agrisera, Umeå, Sweden), whereas for p-tau slides were incubated with the AT8 antibody (Thermo Fisher). Vector NovaRED Peroxidase (HRP) substrate Kit (Vector Laboratories) was used for detection. For ThS staining, paraffinized sections were pretreated in a 2:1 chloroform/absolute ethanol solution for 10 minutes, followed by incubation in 1:1 mixture chloroform/absolute ethanol. Thereafter, the sections were incubated in 95% and 7% ethanol, 3 minutes in each, quickly rinsed in water and incubated

in 0.1% ThS for 5 minutes. Finally, they were briefly washed in 80% ethanol and water, dehydrated in ethanol, cleared in xylenes and mounted with DPX.

MSD Electrochemiluminescence immunoassay and ELISA of human brain extracts

Approximately 200 mg of superior frontal, superior occipital, medial temporal gyrus of the *Uppsala APP* brain, eleven sAD brains and nine control brains (for three of them no temporal gyrus) were homogenized in TBS using the Precellys Evolution homogenizer (Bertin Instruments, Montigny-le-Bretonneux, France) and centrifuged for 1 h at 16 000 x g. The supernatant was collected and the pellet re-homogenized in formic acid (FA) and centrifuged 1 h at 16 000 x g as described above. The V-PLEX Aβ Peptide Panel 1 (6E10) electrochemiluminescence assay (Meso Scale Discovery), was used to detect Aβ40, Aβ42 and Aβ38 in TBS and FA supernatants from the human brain homogenates (following the manufacturer's recommended protocols). Statistical analyses were performed using GraphPad Prism (version 6), bars on the figures shows standard deviation (SD) values. The experiment was performed one time with duplicates of each sample.

The 3D6 antibody, which selectively recognizes the N-terminal end of Aβ, and the mAb158, which selectively recognizes Aβ protofibrils (*33*), were combined in sandwich ELISAs to detect soluble Aβ aggregates of different sizes in the TBS extracts (*31*).

Ninety-six well plates were coated with 1 µg/ml of 3D6 or 2 µg/ml of mAb158 in PBS. Plates were blocked with 1% BSA in PBS and a standard series of synthetic Aβ protofibrils was applied for quantification. The TBS fractions were incubated overnight at 4^{o}C and added to the respective plates. Biotinylated 3D6 (0.5 µg/ml) was added as secondary antibody in both ELISAs and signals were detected with streptavidin-conjugated horseradish peroxidase (SA-HRP; Mabtech AB) and K Blue Aqueous TMB substrate (Neogen Corp.). Plates were developed and read with a spectrophotometer (Magellan infinite 2000Pro) at 450 nm. The experiment was performed 3 times with duplicates of each sample.

The information about the patients are provided in table S1.

MALDI imaging MS and LCO staining of Aβ peptides in *Uppsala APP* mutation human Brain

For MALDI imaging, fresh frozen tissue blocks were cut into 12-µm-thick sections on a cryostat microtome (Leica CM 1520, Leica Biosystems) at -18 °C. The tissue was thaw-mounted on conductive indium tin oxide glass slides (Bruker Daltonics) and analyzed as previously described (*62*). Briefly, a series of sequential washes of 100% EtOH (60 s), 70% EtOH (30 s), Carnoy's fluid (6:3:1 EtOH/chloroform/acetic acid) (110 s), 100% EtOH (15 s), H_2O with 0.2% TFA (60 s), and 100% EtOH (15 s) was carried out. Next, the tissue was subjected to formic acid vapor for 20 min. 2.5-Dihydroxyacetophenone was used as matrix compound and applied using a TM Sprayer (HTX Technologies). A matrix solution of 15 mg/ml 2.5-dihydroxyacetophenone (DHAP) in 70% acetonitrile, 2% acetic acid, 2% TFA was sprayed onto the tissue sections using the following instrumental parameters: nitrogen flow (10 p.s.i.), spray temperature (75 °C), nozzle height (40 mm), eight passes with offsets and

rotations, spray velocity (1000 mm/min), and isocratic flow of 100 µl/min using 70% acetonitrile as pushing solvent.

MALDI IMS was performed at 25 µm spatial resolution on a Bruker UltrafleXtreme MALDI ToF/ToF instrument equipped with a SmartBeam II Nd:YAG/355-nm laser as previously described (*62*). For verification of Aβ peptide distribution *in situ*, image data were reconstructed, normalized to the total ion current, and visualized using Flex Imaging version 3.0 software (Bruker Daltonics).

To verify the identity of the Aβ peptides observed with MALDI imaging MS, laser microdissection pressure catapulting (LMPC) and immunoprecipitation mass spectrometry analysis (IP-MS) of single plaques were performed. Here, consecutive sections (12µm) were collected on 0.17 PEN membrane slides (Zeiss/P.A.L.M., Microlaser Technologies) and stored at −80 °C.

Prior to laser microdissection, the sections were stained with the LCO fluorophores q-FTAA and h-FTAA (*63*) were used to identify all Aβ plaques present in the tissue. First, the sections were thawed in a desiccator and fixed at −20 °C for 10 min using 95% ethanol. The sections were double-stained with q-FTAA and h-FTAA (2.4 µm q-FTAA and 0.77 µm h-FTAA in PBS) similar to a protocol previously described (*62, 64*) and incubated for 30 min at room temperature in the dark, rinsed with milliQ water and finally dried through desiccation.

LMPC isolation of Aβ plaques was done using a PALM Microbeam LMPC microscope (Zeiss) equipped with a 355-nm pulsed UV laser. A total of 200-250 Aβ plaques were collected in Adhesive Cap 500 opaque tubes (Zeiss) and stored at −20 °C prior to extraction. Prior to IP, 70% formic acid solution (FA) containing 5 mM EDTA was added to the laser microdissected plaques. The plaques were sonicated for 5 min and incubated for 1 h at 24 °C. Following FA hydrolysis, the samples were neutralized to pH 7 using 0.5 M Tris.

Aβ immunoprecipitation, Aβ quantification and mass spectrometry of brain tissue and CSF

Amyloid-β peptides in the LMPC isolated extracts, CSF of control subjects, sAD cases and patients with the *Uppsala APP* mutation, were purified through immunoprecipitation using Aβ-specific antibodies (6E10 and Aβ C-terminal antibodies 12F4 and 11A50, BioLegend), coupled to magnetic Dynabeads M-280 sheep anti-mouse (Invitrogen) using a modified version of previously developed procedure (*44, 62, 65, 66*). Here, in order to ensure reliable quantification a synthetic Aβ1-40 containing stable isotope ^{15}N, ^{13}C labeled Arginine (R) was used as internal standard (Caslo) and spiked into the CSF sample prior to extraction. Following antibody-bead conjugation and incubation with the samples, three sequential washes were performed using 0.025% Tween-20 in PBS, PBS and 50nM ammonium hydrogen carbonate, 10 seconds each. Elution from the beads was done over the course of 4 minutes using 0.5% formic acid with the recovery of ~80%. The supernatant was collected and dried through lyophilization. Mass spectrometric analysis of the samples was performed using a MALDI ToF/ToF UltrafleXtreme instrument (Bruker Daltonics). The instrument was

operated on positive reflector mode, and 10 000 shot were collected for each spectrum over a mass range of 500-5000Da, at 1 kHz laser speed and random walk activated (*62, 67*).

To further verify the sequence identity of the observed peptides, LC-MS/MS analysis was performed as described previously (*67*). Briefly, liquid chromatography separation of amyloid peptides was performed with an UltiMate 3000 binary pump, column oven, and autosampler system (Thermo Scientific) using a C18 reversed phase column and an alkaline mobile phase system. MS analysis of the eluting peptides was carried out using a Q Exactive quadrupole–Orbitrap hybrid mass spectrometer equipped with a heated electrospray ionization source (HESI-II) (Thermo Scientific) and operated in data-dependent mode. Here acquisition was performed with 1 μscan/acquisition with the resolution set to 70.000 and target values of 1×10^6 for both for MS and MS/MS. The precursor isolation width was 3 *m*/*z* units, and ions were fragmented by higher-energy collision-induced dissociation (HE-CID) at a normalized collision energy of 25.

For statistical analyses, individual mass spectra were exported as csv files from FlexAnalysis (version 3.0, Bruker Daltonics) and imported into Origin (version 8.1 OriginLab). Bin borders were used for area under curve (AUC) peak integration within each bin using an in-house developed R script. Individual peptide signals of CSF were normalized with the isotopically labelled Aβ1-40 internal standard. Aβ peptide pattern in brain lysates was performed without internal standard, for qualitative profiling. The mass spectrometry analysis of brain lysates was otherwise performed as for CSF.

Processing of raw LC-MS/MS data obtained for Aβ peptide verification, was performed using Xcalibur 2.2 Quanbrowser (Thermo Scientific). Spectra were deconvoluted using Mascot Distiller before submission to database search using the Mascot search engine (both Matrix Science) (*62, 67*). The MS/MS spectra were searched toward an in-house generated database containing unmodified and mutant human *APP* sequences using the following search parameters: Type of search: MSMS Ion search; precursor mass ± 20 ppm; fragment mass ± 0.05 Da; no fixed modifications; variable modifications: deamidation (NQ), Glu->pyro-Glu (N-term E), oxidation (M); instrument:Distiller CID. Only peptides with ion score >100 were considered.

Cell culture and transfection

Human embryonic kidney 293 (HEK293) cells were cultured in Dulbecco's modified Eagle's medium (DMEM, Invitrogen) supplemented with 10% fetal bovine serum (FBS), 1% PeSt and 4 mM of glutamax. Human 695 amino acid long *wt* or *Uppsala APP* was cloned into a pcDNA3.4-TOPO vector (Thermo Fisher Scientific) and transfected into cells with polyethylenimine (PEI). For establishing a stable cell line, transfected cells were split 24 h post transfection into new 9 cm dishes with the following dilutions: 1:10, and 1:5. For selection G418 (Geneticin) was used (400 μg/mL; according to the antibiotic kill curve). After selection cells were cultured in maintenance medium (10% FBS, 2 mM glutamax, 200 μg/mL G418).

The medium was changed 24 h before collection (maintenance medium) and cells were lysed (20 mM Tris pH 7.5, 0.5 % Triton-X-100, 0.5 % deoxycholic acid, 150 mM NaCl, 10 mM EDTA, 30 mM NaPyroP). To normalize with the total amount of protein, lysates and media were analyzed with Pierce BCA Protein Assay Kit (Thermo Fisher).

Electrochemiluminescence of transfected cell culture samples

An sAPPα/sAPPβ ELISA kit (MSD) based on electrochemiluminescence, was used to quantify sAPPα and sAPPβ in cell media from HEK293 cells transfected with wild-type *APP* (*APPwt*) and *Uppsala APP* (*APPUpp*) (following the manufacturer's recommended protocol). V-PLEX Aβ Peptide Panel 1 (6E10) was used to quantify Aβ in the same cell media. Samples were loaded by total protein concentration in lysates, determined by Pierce BCA Protein Assay Kit. Results were normalized by total sAPP determined by WB of the cell culture samples and statistical analyses were performed using GraphPad Prism (version 6). The experiment was performed once with duplicates of samples from three biological replicates (n=3).

Western blot of transfected cell culture samples

Western blot was performed to analyze APP and APP fragments resulting from α- or β-secretase cleavage. Media from the HEK293 transfected cells with the different versions of APP containing ~7 µg of total protein (determined by Pierce BCA Protein Assay Kit) was diluted in PBS. Samples were denatured in BOLT LDS buffer (Invitrogen) mixed with reducing agent (Invitrogen), boiled at 70^{o}C for 10 min and loaded in a 4-20% Tris-glycine Bolt gel (Invitrogen). The proteins were transferred by electrophoresis to a nitrocellulose membrane (Invitrogen) and the membrane was blocked with 6% skim milk in PBS-T (0.1% Tween-20) for 45 min. After blocking, the membrane was incubated overnight at 4^{o}C with primary antibody (1 µg/ml 6E10, binding to amino acid 5-10 of Aβ; 3 µg/ml Anti-human APPα 2B3 (IBL-International), binding to the C-terminal part of APPα (targeted to DAEFRHDSGYEVHHQK); 2 µg/ml 1C3 (*33*), binding to amino acids 3-8 of Aβ and 0.5 µg/ml 22C11 (eBioscience from Thermo Fisher Scientific), binding to the N-terminal part of APP in PBST (0.1% Tween-20, 0.05% BSA) and washed with PBST (0.1% Tween-20), followed by incubation with anti-mouse IgG/IgM-HRP (0.8 µg/mL) in PBST (0.1% Tween-20, 0.05% BSA). The membrane was exposed to Amersham ECL Western Blotting detection reagents (GE Healthcare) for 2 min and the ECL signal was detected in ChemiDoc XRS+ with Image Lab software (Bio-Rad).

Aβ1-40 and Aβx-40 sandwich ELISA of transfected cell culture sample

Ninety-six well plates were coated with 1 µg/ml of anti-Aβ40 (Agrisera) in PBS. Plates were blocked with 1% BSA in PBS and standard series of synthetic Aβwt1-40 was applied. A total of 60 µg of total protein in HEK 293 media diluted according to BCA normalization were added to the plate in ELISA buffer. For the two different ELISA, respective biotinylated 3D6 (binding to amino acid 1-5 of Aβ) or 6E10 (binding to amino acid 5-10 of Aβ) antibodies (1 µg/ml) were added as detecting antibody and signals were detected with streptavidin-conjugated horseradish peroxidase (SA-HRP; Mabtech AB) and K Blue Aqueous TMB substrate (Neogen Corp.). Plates were developed and read with a spectrophotometer

(Magellan infinite 2000Pro) at 450 nm. Results were expressed as a ratio and statistical analyses were performed using GraphPad Prism (version 6, San Diego, CA).

Immunoblotting with protease inhibitors treatment of transfected cell culture samples

2.5x 10^5 HEK293 cells were seeded on pre-coated 24 well plates and transfected with indicated constructs with Lipofectamine 2000 according to the manufacturer's instructions (Thermo Fisher). Cells were incubated overnight in 500 µL DMEM (Gibco, 31966047) with 10% FCS, containing either 5 µM of the α-secretase-preferring inhibitor GI254023X (Sigma, SML0789) (*68*), 1 µM of the γ-secretase inhibitor DAPT in the case of CTF fragments, or vehicle DMSO. In measurements for secreted APP species, the conditioned media were collected and centrifuged for 1 h at 100,000 g and stored at -20 ^{o}C. Cells were lysed with STET (150 mM NaCl, 50 mM Tris (pH 7.5), 2 mM EDTA, 1% Triton X-100) buffer containing 1x protease inhibitor (Sigma, P8340). Five µg of the lysate and the corresponding equal volume of conditioned media were loaded on 10% SDS-PAGE gels. Antibodies used for immunoblotting: 22C11 (APP N-terminus), 14D6 (specific for human APPsα in culture media) (*69*), BAWT (specific for human sAPPβ) (*32, 69, 70*), 2C11 (specific for human C-terminal APP) (*69, 70*), 6E10 (binding to amino acid 5-10 of Aβ) and calnexin (Enzo, ADI-SPA-860). Image J was used for quantification and all the results were normalized by total APP, which was normalized by loading control protein calnexin.

Mass Spectrometry of *APPUpp* and *APPwt* transfected cell culture media

Cell media from the transfected HEK293 cells, were purified through immunoprecipitation and followed the same MS protocol as for CSF and human brain extracts explained above in the section "Aβ immunoprecipitation, Aβ quantification and mass spectrometry of brain tissue and CSF".

Mass Spectrometry for APP-Upp cleavage site determination of transfected cell culture samples

5x10^6 HEK293 cells were seeded on 10 cm dishes. Two different approaches were used for determining the cleavage site. For specific peptide analysis, cells were transfected with *APPwt or APPUpp*. After one day medium was replaced with fresh 6 ml DMEM + 10% FCS. Two days later the conditioned media were collected and centrifuged. For cleavage site-specific peptide analysis, 1D1 antibody (hAPP40-64) (*71*) as used for immunoprecipitation of secreted sAPP from conditioned media. Elution was done by 0.5% formic acid in ddH2O. Eluate was neutralized by ammonium bicarbonate and processed by SP3 protocol (*72*) and digested by LysN (Promega, VA1180). The generated peptides were analyzed on an Easy nLC1200 (Thermo Scientific) coupled to Q-Exactive HF Mass Spectrometer (Thermo Scientific). Peptides were separated with a binary gradient of water (A) and acetonitrile (B) containing 0.1% formic acid at 50°C column temperature and a flow of 250 nl/min (0 min, 2.4% B; 3:30 min, 4.8% B; 48:30 min, 24% B; 59:30 min, 35.2% B; 64:30 min, 60% B) on a self-packed C18 column (75 µm×30 cm, 1.9 µm C18-AQ 120, Dr. Maisch). Full MS spectra were acquired at a resolution of 120,000. The ten most intense ions were chosen for collision induced dissociation. The dynamic exclusion was set to 6 s.

The data were analyzed with Maxquant software (maxquant.org, Max-Planck Institute Munich) version 1.6.10.43 (*73*). The MS data were searched against a canonical fasta database of *Homo sapiens* from UniProt (download: December 02nd 2019, 74468 entries). LysN was defined as protease. Two missed cleavages and semispecific generated peptides were allowed for the database search. The option first search was used to recalibrate the peptide masses within a window of 20 ppm. For the main search, peptide and peptide fragment mass tolerances were set to 4.5 and 20 ppm, respectively. Carbamidomethylation of cysteine was defined as static modification and acetylation of the protein N-terminus as well as oxidation of methionine were set as variable modifications. The false discovery rate for both peptides and proteins was adjusted to less than 1% using a target and decoy approach (concatenated forward/reverse database). Extracted ion chromatograms for peptides identified for APP were exported with Xcalibur Qual Browser Version 2.2 SP1.48 (Thermo Scientific).

Synthetic peptides

Synthetic peptides of wild type Aβ (Aβ wt) 1-42, *Arctic* Aβ (Aβ Arc) 1-42, and *Uppsala* Aβ (AβUpp) 1-42$_{\Delta 19\text{-}24}$ were purchased (Innovagen AB).

Aβ aggregation experiments

For aggregation experiments, lyophilized synthetic Aβ 1-42 (wt, Arc, Upp) peptides were dissolved in 6 M GuHCl for 30 min and subjected to gel filtration on a Superdex 75 10/300 GL column in degassed 20 mM sodium phosphate buffer, pH 8, with 200 µM EDTA. The center of the monomer peak of each peptide was collected on ice and peptide concentrations were determined by absorbance at 280 nm using ε_{280} = 1440 L·mol^{-1} cm^{-1}. Monomers were then diluted in ThT (10 µM) to a starting concentration of 10 µM and added in quadruplicates into a 96 well plate (black, clear bottom, half area; corning 3881) in different dilution series. To monitor fibrillization at different time-points, fluorescence was measured at 448 nm (excitation) and 485 nm (emission) each 5 minutes during 24 h (overnight) with a Magellan infinite 2000Pro plate reader (Tecan instruments). AβUpp1-42$_{\Delta 19\text{-}24}$ was analyzed at different dilutions (10, 5, 2.5 and 1.25 µM) and compared with Aβwt1-42 and AβUpp1-42$_{E22G}$ (both at 7.5 µM). Aggregation curves are presented as % of maximum ThT signal, using the plateau phase of each curve as maximum. Each curve starts at minimum signal and ends when maximum is reached. A sigmoidal four-parameter curve is fitted to the data points to allow comparisons between data sets.

Aβ protofibril ELISA

The 3D6 antibody, which selectively recognizes the N-terminal end of Aβ, was used in a homogeneous sandwich ELISA to detect and monitor formation of Aβ protofibrils during aggregation of synthetic peptides, without interference from Aβ monomers (*33*).

Ninety-six well plates were coated with 1 µg/ml of 3D6 in PBS. Plates were blocked with 1% BSA in PBS and standard series of synthetic Aβ protofibrils was applied. The monomer fractions in a concentration of 10µM were incubated at different time points (0, 0.5, 1, 3, 8 and 24 h) and added to the respective plates at a final concentration of 10 nM and incubated for 2 h at room temperature. Biotinylated 3D6 (0.5 µg/ml) was added as secondary antibody

and signals were detected with streptavidin-conjugated horseradish peroxidase (SA-HRP; Mabtech AB) and K Blue Aqueous TMB substrate (Neogen Corp.). Plates were developed and read with a spectrophotometer (Magellan infinite 2000Pro) at 450 nm.

Size exclusion chromatography

Monomer in a concentration of 6 µM were incubated at different time-points (t=1 h, t=8 h). Prior to analysis, 6 µM samples were mixed 1:1 with 20 mM sodium phosphate buffer and centrifuged at 16,000 x g for 5 min to remove fibrillized Aβ. For size separation of the Aβ peptides the supernatant was injected (25µl) in Superdex 75, increase 3.2/300 column (GE Healthcare) on a Merck Hitachi D-700 HPLC LaChrom system. The samples were eluted with PBS-Tween, pH 7.4 (50 mM sodium phosphate, 0.15 M NaCl, 0.1% Tween-20, pH 7.4) at a flow rate of 0.08 ml/min and data obtained at 214 nm.

Transmission electron microscopy of low pH fibrils

Synthetic AβUpp1-42Δ19-24 peptides were prepared under the same conditions as previously described (*34*) and incubated in 30% (v/v) acetonitrile (AcN), 0.1% (v/v) trifluoroacetic acid (TFA) at pH 2. Conversion of monomeric AβUpp1-42Δ19-24 to several µm long, unbranched fibrils occurred over several weeks at room temperature under quiescent conditions. Negatively stained fibrils were prepared with 2% uranyl acetate stain solution. For cryo-imaging, fibrils were plunge-frozen on Quantifoil 1.2/1.3 grids. In total 1977 micrographs were recorded on a Tecnai Arctica (200 kV) using a Gatan Bioquantum K3 direct electron detector, yielding a pixel size of 0.839 Å. The image processing was performed using the RELION 3.0.5 software package (*74*). The contrast transfer function (CTF) of the micrographs was estimated using the program CTFFIND4 (*75*). Manual picking of the first and second polymorph resulted in 2052 and 1612 fibrils, respectively. Fibril segments were extracted from the fibril images with 90% overlap resulting in 66651 segments for the first polymorph and 59296 segments for the second polymorph. A box size of 200 pixel was used, which corresponds to 167.8 Å. 2D and 3D classification was performed to clean the dataset. During 3D refinement, only micrographs that contain a signal beyond a resolution of 5 Å were used for further processing steps. Moreover, particle images with a number of samples above 5000 were discarded. 3D reconstructions calculated from the negative stain images were low-pass filtered to 60 Å and were used as an initial model. The resolutions of 5.7 Å for polymorph 1 and 5.1 Å for polymorph 2 were assessed by the Fourier shell correlation (fig. S8). A search for helical symmetry parameters resulted in a helical rise of 2.41 Å and an azimuthal rotation of 178.45° for the first polymorph and in a helical rise of 2.29 Å and an azimuthal rotation of 179.45° for the second polymorph. The resulting helical pitch is 232 Å for the first polymorph and 375 Å for the second polymorph.

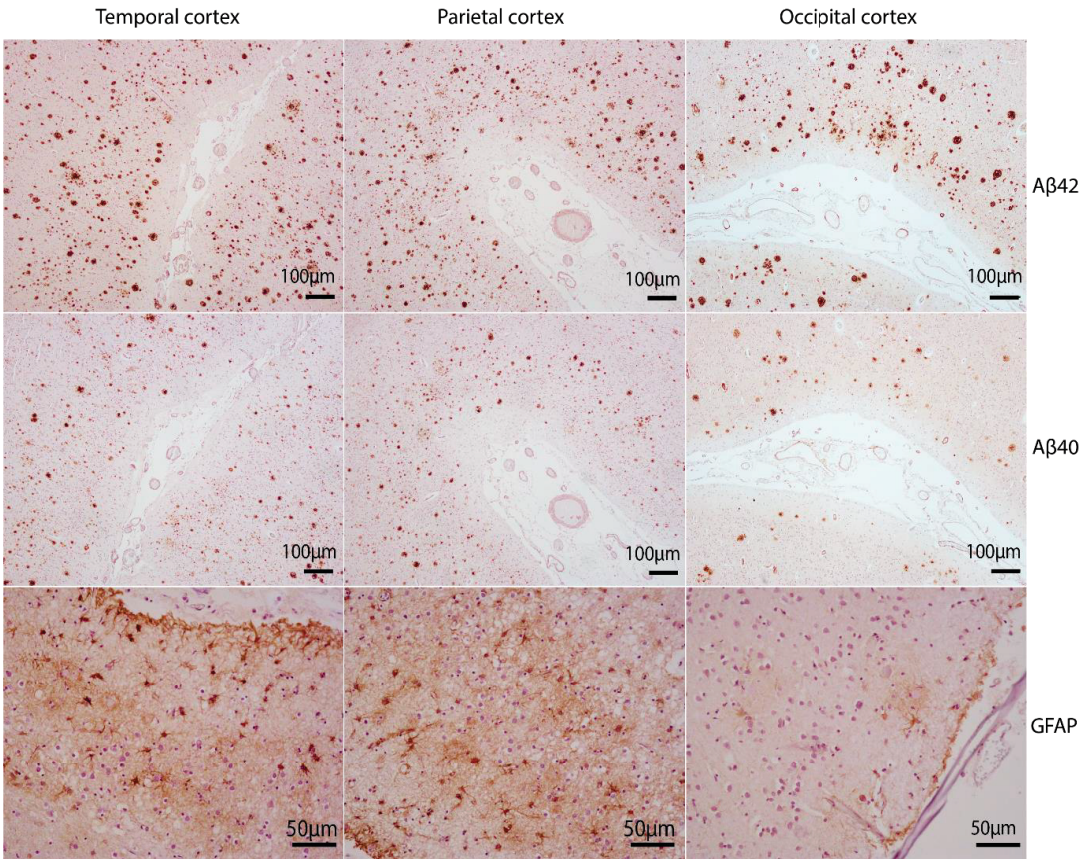

Fig. S1: Immunohistochemistry of different regions of the *Uppsala APP* mutation brain with Aβ40, Aβ42 and GFAP antibodies.

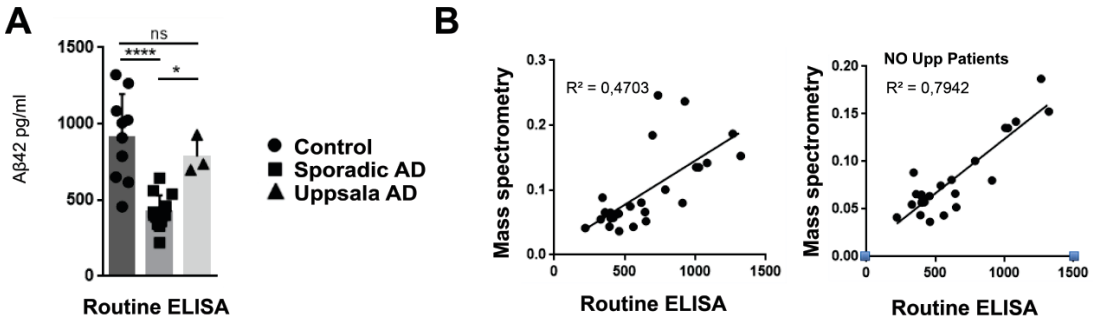

Fig. S2: Aβ42 in CSF measured by two different methods. Electrochemiluminescence-based immunoassay (MSD) and immunoassays (INNOTEST or Lumipulse automated assay, Fujirebio, Ghent, Belgium) (A). Correlation curves of the different methods, routine ELISA and mass spectrometry with and without UppAD samples (B). For control CSF n=10, for sAD n=11, for Uppsala CSF n=3. Comparisons between the groups were performed by one-way ANOVA in A (error bars represent SD).

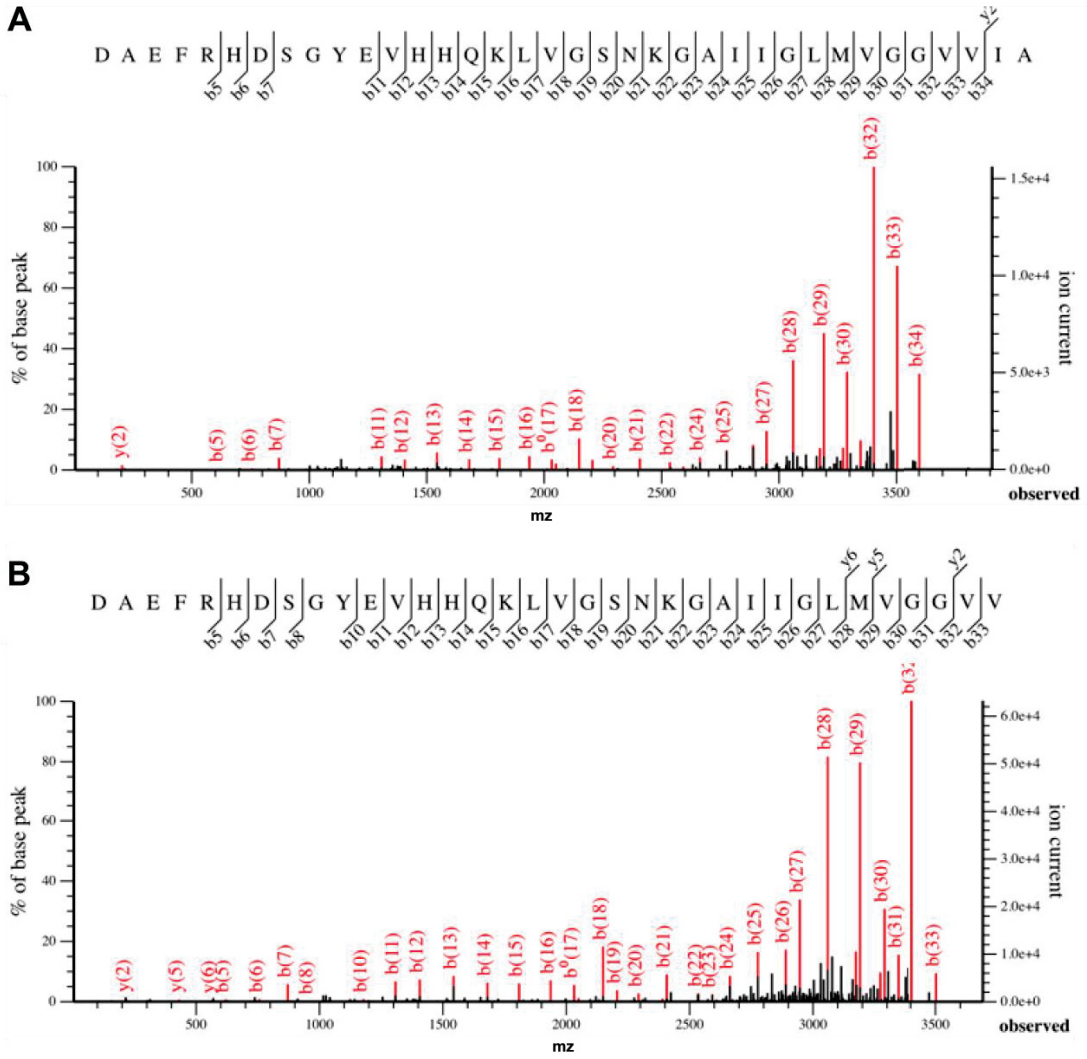

Fig. S3: Sequence verification of Aβ peptides. LC-MS/MS based sequence validation of (A) Aβ1-42$\Delta_{19\text{-}24}$ and (B) Aβ1-40$\Delta_{19\text{-}24}$ extracted from CSF. For each peptide MS/MS fragment mass spectra and matching peptide sequence are shown including annotation of major fragment ions detected. The fragment spectra show dominating b-ions with almost complete sequence coverage allowing unequivocal sequence identification through database search.

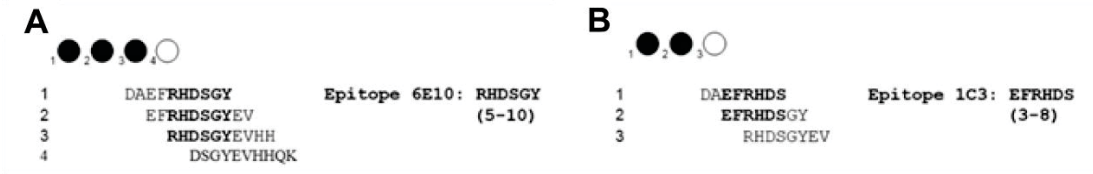

Fig. S4: 6E10 and 1C3 binding epitopes. Antibody binding epitopes of 6E10 (A) and 1C3 (B) were determined by spotting 8-10 amino acid long peptides spanning the N-terminal part of Aβ. Binding (displayed as filled circle) to the 3-4 first spots revealed the antibody's epitope.

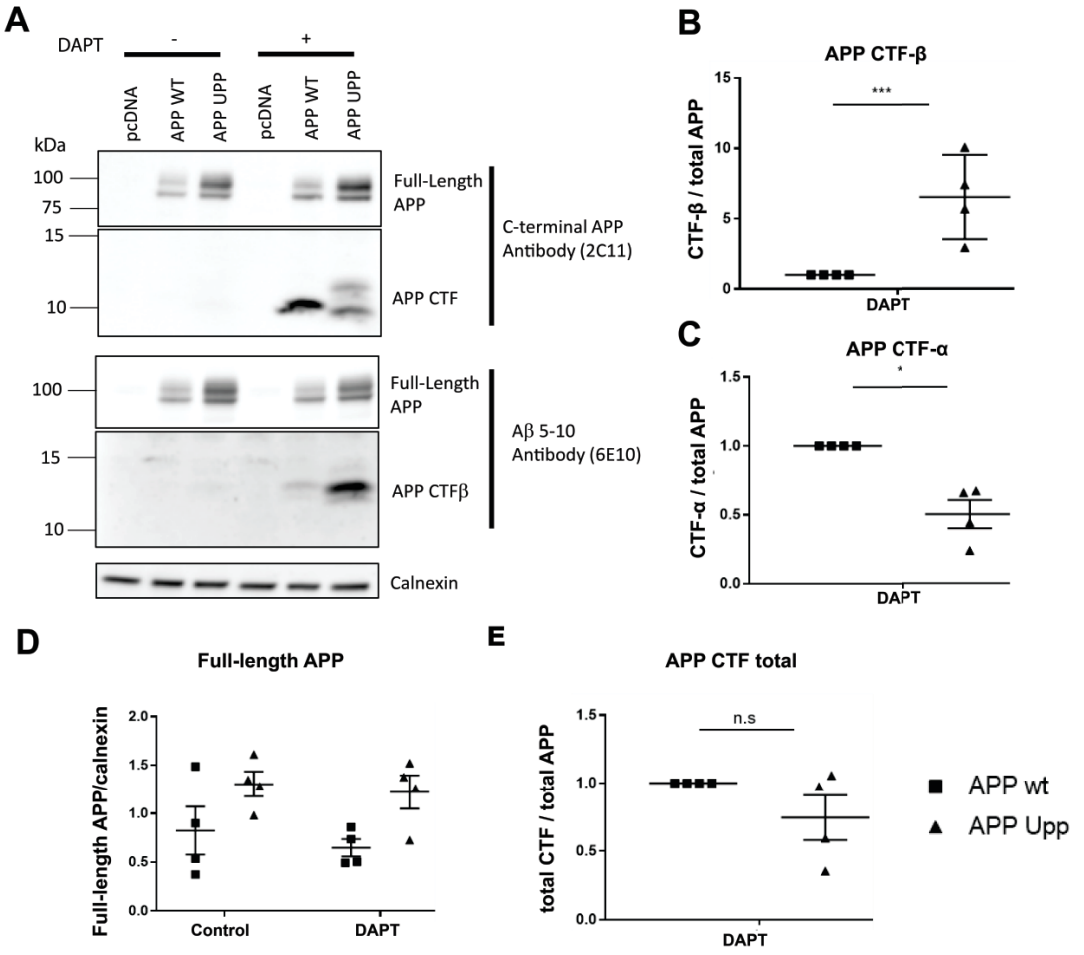

Fig. S5: APP C-terminal fragments (CTFs) in cell lysate from HEK293 cells transfected with *APPwt* and A*PPUpp*. Western blot showing full-length APP and CTFs with 2C11 antibody and full-length APP and CTFβ fragment with 6E10 antibody in the cell lysates of transfected HEK293 cells after treatment with a γ-secretase inhibitor (DAPT) (A).

Quantifications of APP CTF-β (B), CTF-α (C), full-length APP (D) and APP CTF total (E). (n=4, N=4)

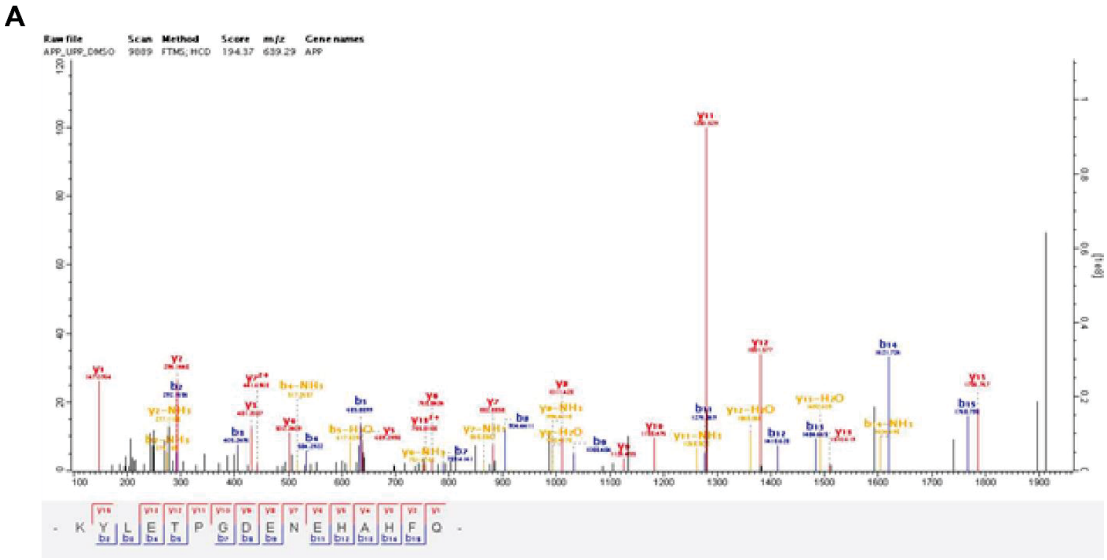

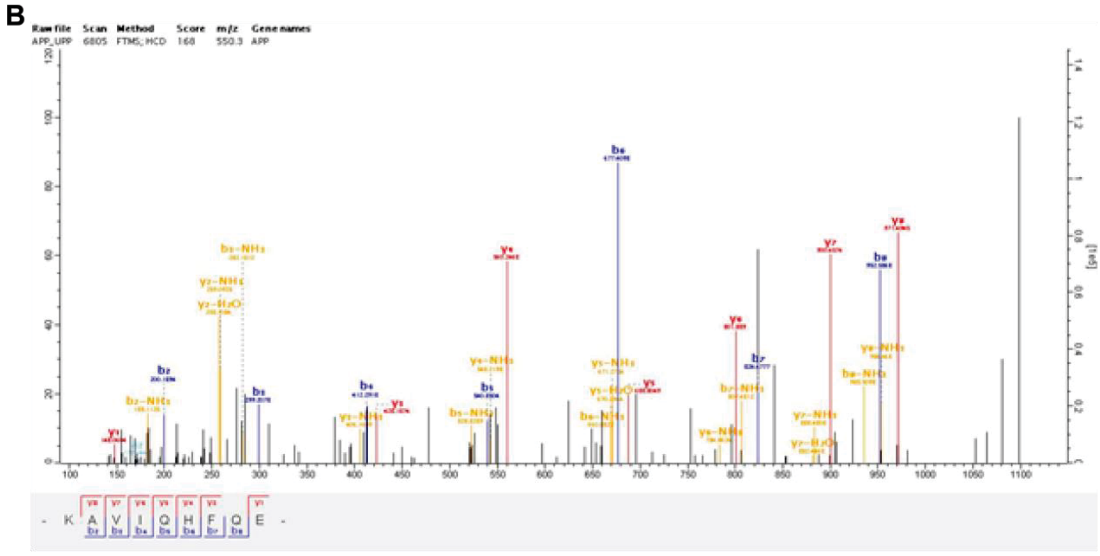

C

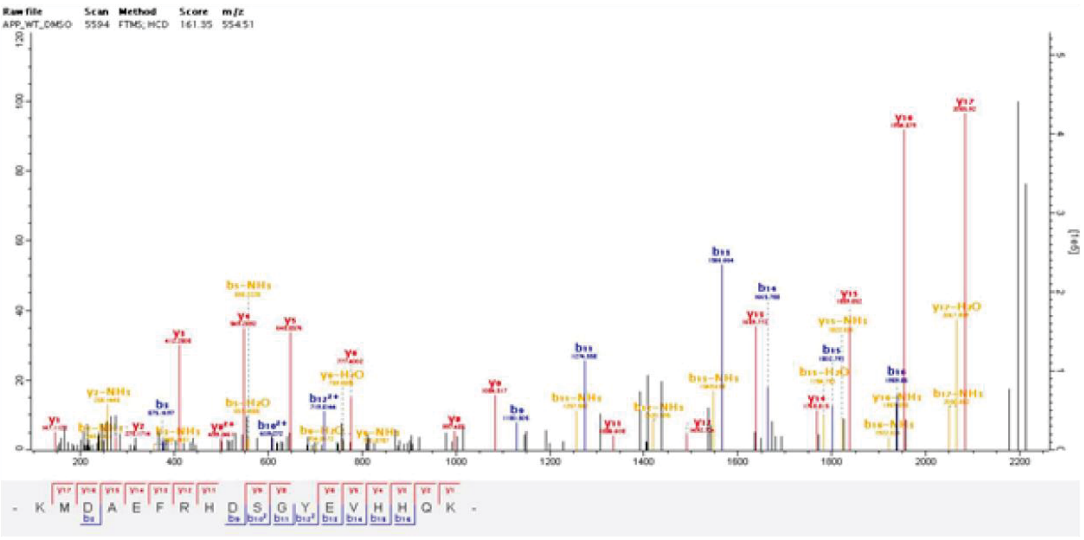
Raw file Scan Method Score m/z
APP_WT_DMSO 5594 FTMS; HCD 161.35 554.51
- K M D A E F R H D S G Y E V H H Q K -

D

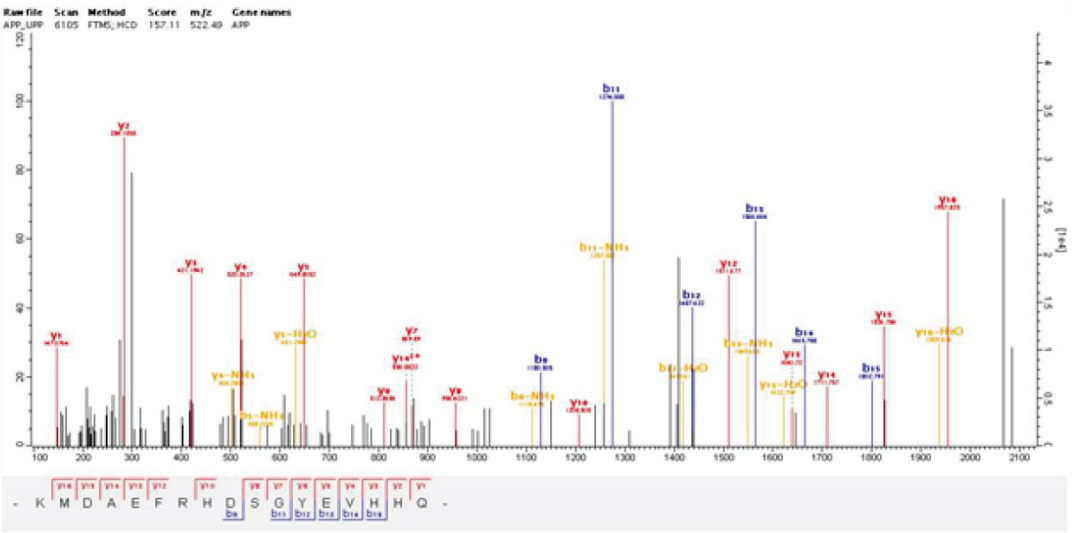
Raw file Scan Method Score m/z Gene names
APP_UPP 6105 FTMS; HCD 157.11 522.49 APP
- K M D A E F R H D S G Y E V H H Q -

E

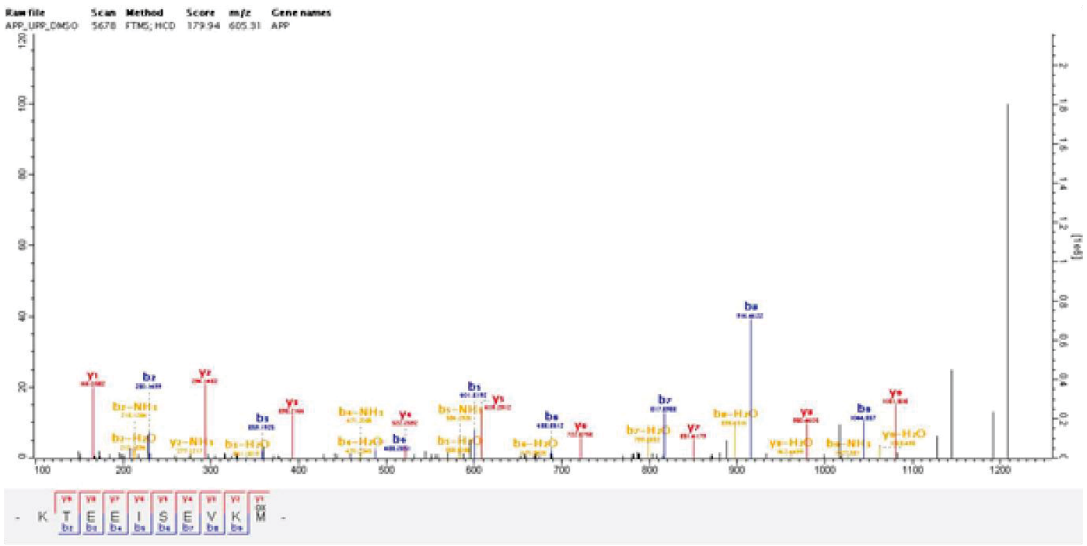
Raw file Scan Method Score m/z Gene names
APP_UPR_DMSO 5678 FTMS; HCD 179.94 605.31 APP
- K T E E I S E V K M -

F

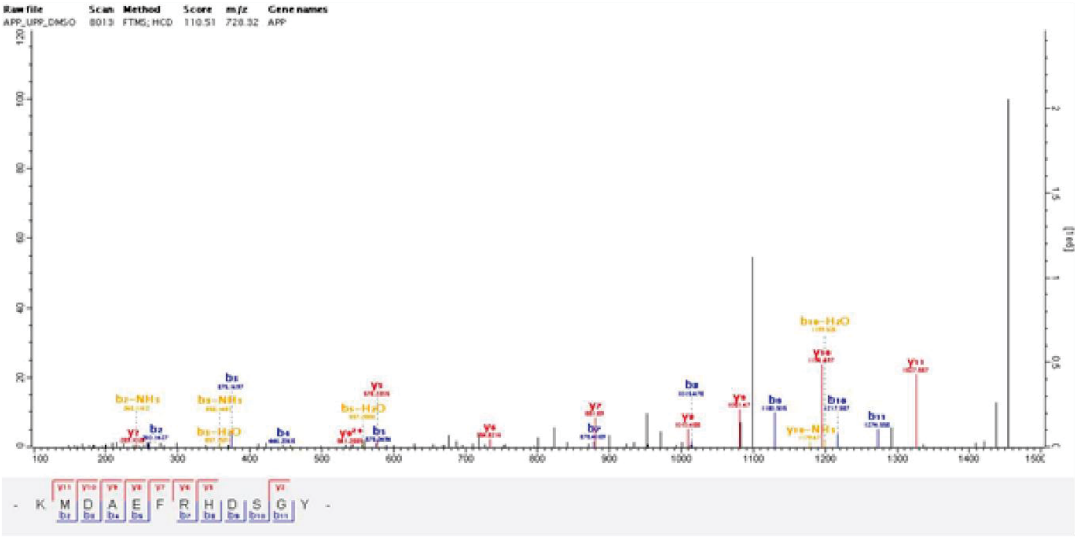
Raw file Scan Method Score m/z Gene names
APP_UPR_DMSO 8013 FTMS; HCD 110.51 720.32 APP
- K M D A E F R H D S G Y -

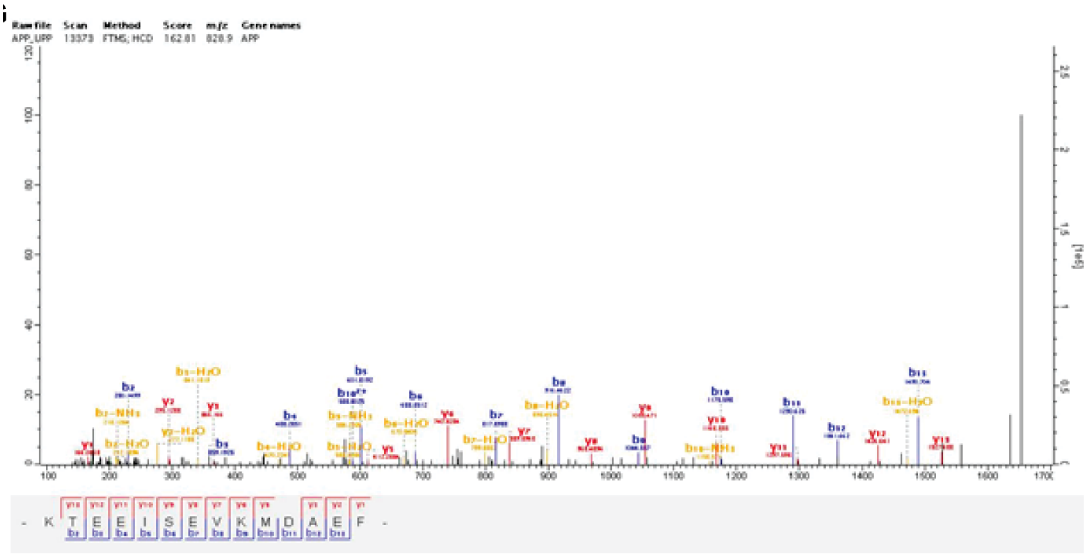

Fig. S6: Fragment ion spectra of selected APP derived peptides from Figure 6. Representative fragment ion spectra of the peptides from Fig. 6: A) KYLETPGDENEHAHFQ; B) KAVIQHFQE; C) KMDAEFRHDSGYEVHHQK; D) KMDAEFRHDSGYEVHHQ; E) KTEEISEVKM(ox); F) KMDAEFRHDSGY; G) KTEEISEVKMDAEF.

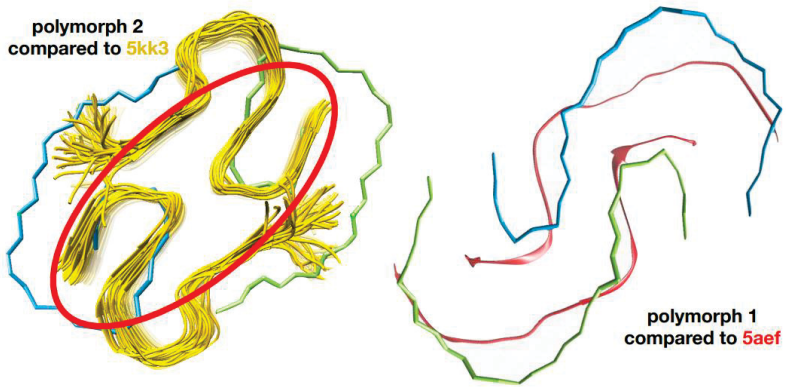

Fig. S7: Comparison of Aβ1-42Δ_{19-24} most common polymorphs with existing Aβ fibril structures.

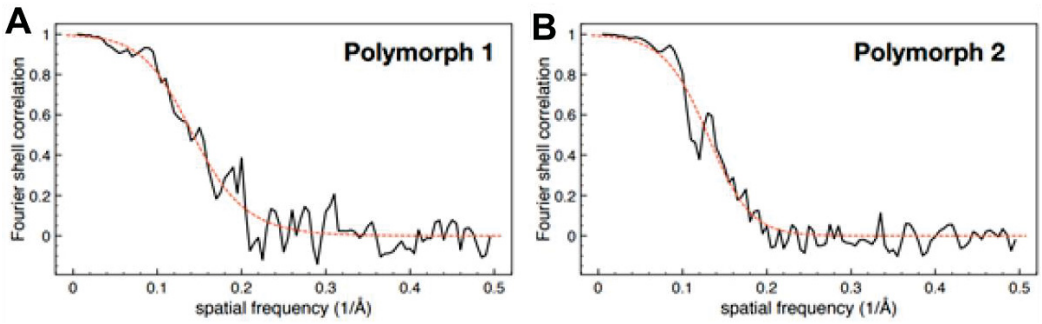

Fig. S8: Fourier shell correlation (FSC) of both polymorphs. Fourier shell correlation (FSC) curves for the 3D reconstruction of A polymorph 1 and B polymorph 2. The curves are fitted with the model $1/[1+\exp(x-A)/B)]^C$ (red), to obtain a more reliable resolution estimate.

Table S1: CSF samples from the Uppsala BioBank (UBB), patient information.

CSF samples	Biobank	Age	Diagnosis	Aβ1-42 (pg/ml)	T-tau (pg/ml)	P-tau (pg/ml)	ApoE
1	UBB	45	UppAD	926	1420	129	33
2	UBB	43	UppAD	736	1220	142	33
3	UBB	44	UppAD	696	512	79	
4	UBB	74	sAD	539	703	94	
5	UBB	74	sAD	644	1330	147	
6	UBB	76	sAD	399	977	92	
7	UBB	80	sAD	342	1300	110	
8	UBB	87	sAD	460	960	129	
9	UBB	81	sAD	329	812	111	
10	UBB	82	sAD	401	1010	109	
11	UBB	74	sAD	391	949	87	
12	UBB	80	sAD	560	850	93	
13	UBB	73	sAD	399	792	85	
14	UBB	76	sAD	420	1100	128	
15	UBB	77	sAD	360	890	130	
16	UBB	78	sAD	220	840	123	
17	UBB	78	Control	1026	657	45	
18	UBB	78	Control	1322	510	64	
19	UBB	78	Control	1266	542	67	
20	UBB	78	Control	650	228	36	
21	UBB	85	Control	788	368	44	
22	UBB	86	Control	1084	496	63	
23	UBB	84	Control	909	383	45	
24	UBB	82	Control	617	361	47	
25	UBB	78	Control	457	277	31	
26	UBB	83	Control	1006	348	49	

Age = at sampling

Reference values: Aβ1-42 >550 pg/ml; Aβ42/40 >0.89; t-tau <300 pg/ml; p-tau <60 pg/ml.

Table S2: Brain samples from the Uppsala BioBank (UBB) and Netherlands Brain Bank (NBB), patient information.

Brain samples	Brain bank	Sex	Age	Braak	Thal/ Amyloid	ApoE	Diagnosis	Aβ1-42 (pg/mg brain tissue- Frontal cortex)
1	UBB	M	49	VI	5	33	UppAD	72665
2	UBB	F	90	V	3		sAD	36179
3	UBB	F	63	VI	5		sAD	45384
4	UBB	M	71	IV	3		sAD	22747
5	UBB	F	88	II	0		Control	18
6	UBB	M	63	0	0		Control	58
7	UBB	M	90	II	0		Control	527
8	NBB	M	56	VI	C	33	AD	17528
9	NBB	M	57	VI	C		AD	67580
10	NBB	M	77	V	C	43	AD	27090
11	NBB	M	79	V	C	43	AD	25003
12	NBB	F	54	VI	C	43	AD	21807
13	NBB	F	68	V	C	33	AD	23810
14	NBB	F	75	V	C	44	AD	31784
15	NBB	F	79	V	C	33	AD	29912
16	NBB	M	71	II	B		Control	27653
17	NBB	M	79	II	B	33	Control	37151
18	NBB	M	80	I	A		Control	25951
19	NBB	F	50	I	0		Control	20
20	NBB	F	73	I	B		Control	37466
21	NBB	F	80	I	A		Control	419

AD = Alzheimer's disease; sAD = sporadic Alzheimer's disease; UppAD = Alzheimer's disease caused by Uppsala mutation; Control = Non-demented control

Table S3: Assignment of observed peaks in human brain tissue using MALDI imaging MS and LC-MS/MS based verification from extracts of individually laser microdissected plaques. Predicted Average Mass for MALDI IMS corresponds to the singly charged species [M+H]+ based on the theoretical molecular mass of the corresponding Aβ peptide. For LC-MS/MS, the Predicted Monoisotopic mass corresponds to the neutral species [M] based on the theoretical molecular mass of the corresponding Aβ peptide. Ox refers to oxidation of methionine (M+16).

	MALDI imaging		LMPC + LCMSMS (arbitrap)	
Peptide Sequence MALDI IMS	**Predicted Average Mass $[M+H]^+$ (m/z)**	**MALDI IMS Average Mass observed $[M+H]^+$ (m/z)**	**Predicted Monoisotopic Mass [M] (m/z)**	**Plaque Extract Monoisotopic Mass [M] (m/z)**
Aβ11pE-$36_{UPPSALA}$	2610.14	2610.38	-	-
Aβ11pE-$36_{UPPSALA}$ (OX)	2626.13	-	2623.4632	2623.4717
Aβ9-$36_{UPPSALA}$	2848.38	2848.64	-	-
Aβ9-$36_{UPPSALA}$ (OX)	2864.37	-	2861.5586	2861.5707
Aβ8-$36_{UPPSALA}$	2935.46	2935.47	-	-
Aβ8-$36_{UPPSALA}$ (OX)	2951.45	2951.43	2948.5906	2948.6066
Aβ7-$36_{UPPSALA}$	3050.55	3050.70	-	-
Aβ7-$36_{UPPSALA}$ (OX)	3066.54	-	3063.6176	3063.6241
Aβ7-$37_{UPPSALA}$	3151.65	-	-	-
Aβ7-$37_{UPPSALA}$ (OX)	3167.65	3167.91	3164.6652	3164.6783
Aβ6-$36_{UPPSALA}$	3187.69	3187.46	-	-
Aβ6-$36_{UPPSALA}$ (OX)	3203.68	-	3200.6765	3200.6731
Aβ5-$36_{UPPSALA}$	3343.87	3343.80	-	-
Aβ5-$36_{UPPSALA}$ (OX)	3359.86	3359.66	3356.7776	3356.7887
Aβ4-$36_{UPPSALA}$	3491.05	3491.15	-	-
Aβ4-$36_{UPPSALA}$ (OX)	3507.04	3507.06	3503.8460	3503.8491
Aβ3pE-$36_{UPPSALA}$	3602.16	3602.02	-	-
Aβ3pE-$36_{UPPSALA}$ (OX)	3618.15	3618.05	3614.8780	3614.8899
Aβ1-$34_{UPPSALA}$	3622.10	3622.19	-	-
Aβ1-$34_{UPPSALA}$ (OX)	3638.09	3638.27	3634.8315	3634.8437
Aβ2-$36_{UPPSALA}$	3691.25	3691.03	-	-
Aβ2-$36_{UPPSALA}$ (OX)	3707.24	3707.28	3703.9257	3703.9328
Aβ3pE-$37_{UPPSALA}$	3703.26	3703.15	-	-
Aβ3pE-$37_{UPPSALA}$ (OX)	3719.25	3719.13	3715.9257	3715.9301
Aβ1-$36_{UPPSALA}$	3806.33	3806.37	-	-
Aβ1-$36_{UPPSALA}$ (OX)	3822.33	3822.01	3818.9526	3818.9488
Aβ1-$37_{UPPSALA}$	3907.44	3907.50	-	-
Aβ1-$37_{UPPSALA}$ (OX)	3923.43	3923.05	3920.0003	3920.0008
Aβ4-42	4199.82	4199.62	-	-
Aβ4-42 (OX)	4215.81	4214.18	4212.1579	4212.1716
Aβ3pE-42	4310.92	4310.98	-	-
Aβ3pE-42 (OX)	4326.91	4326.99	4323.1899	4323.2053
Aβ2-42	4400.01	4400.10	-	-
Aβ2-42 (OX)	4416.00	-	4412.2376	4412.2611
Aβ1-42	4515.10	4514.91	-	-
Aβ1-42 (OX)	4531.09	4530.84	4527.2645	4527.2741

D. Supplementary Material

D.0.1. Cryo-EM Data Collection - sporadic AD6

As part of the Uppsala mutation project (compare Chapter 6), we first trained the process of human brain fibril extraction and structure determination by cryo-EM with sporadic AD brain tissue. As part of this, fibrils were extracted from tissue material taken from the superior parietal gyrus of a male AD patient (AD6, Braak stage 5, amyloid C). The brain tissue was provided by Bettina Kass and Fernanda Salome Peralta Reyes purified fibrils from the brain tissue following a published procedure [261]. The methods for the EM analysis of Aβ fibrils purified from sAD brain tissue are described in the following.

Negative stain EM 2 µL of the purified Aβ fibril sample were applied onto a glow-discharged 300 mesh carbon-coated copper grid (EM Sciences, ECF300-Cu). The sample was incubated for 2 min and excess liquid was blotted off with filter paper. The sample was then washed once in a 15 µL droplet of dH_2O. 2 µL of 1% (w/v) UrAc were applied on the top of the grid, following a 1 min incubation. Excess liquid was removed with filter paper and the grid was air-dried. TEM images were acquired using a ThermoFisher Scientific Talos 120C at an acceleration voltage of 120 kV. Images were collected on a 4k x 4k Ceta 16M CMOS camera using the Thermo Scientific Velox software. Negative stain EM confirmed the presence of fibrils in the sample (Figure D.1).

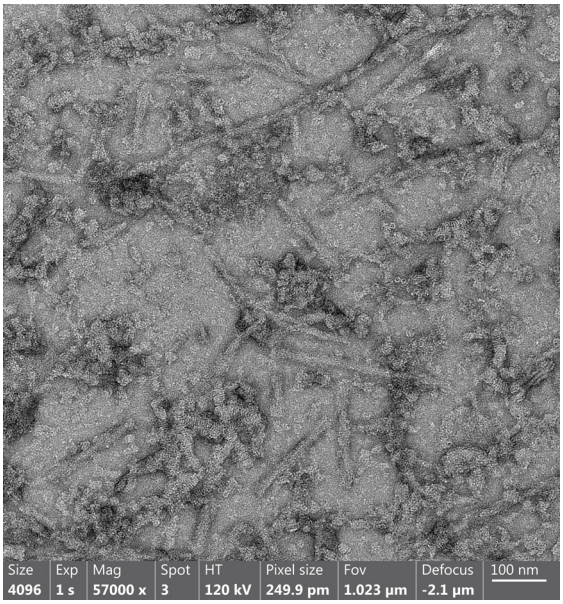

Figure D.1.: Negative stain EM of a sample of Aβ fibrils purified from human sAD brain tissue (AD6).

Immunogold negative stain EM Immunogold negative-stain grids for EM were prepared following [299]. In brief, 2 µL of the sample were placed on a glow-discharged 300 mesh carbon-coated copper grid (EM Sciences, ECF300-Cu) for 2 min. The sample was washed once with dH_2O and placed in blocking buffer for 15 min, following incubation with Nab228 (Sigma-Aldrich) primary antibody diluted in blocking buffer at a concentration of 2 µg/mL for 1.5 h. Afterwards, the grid was washed with washing buffer and was incubated with 6 nm gold-conjugated anti-mouse secondary antibody (diluted 1:20 in blocking buffer, abcam) for 1 h. The grid was washed five times with washing buffer and three times with dH_2O before staining with 1% (w/v) UrAc for 1 min. The sample was air-dried, and EM Images were acquired as described above. Immunogold negative stain EM confirmed that the sample contained Aβ fibrils (Figure D.2). However, Aβ fibrils were mostly located within larger fibril clumps. Moreover, several isolated but unlabelled fibrils could be observed, likely Tau fibrils.

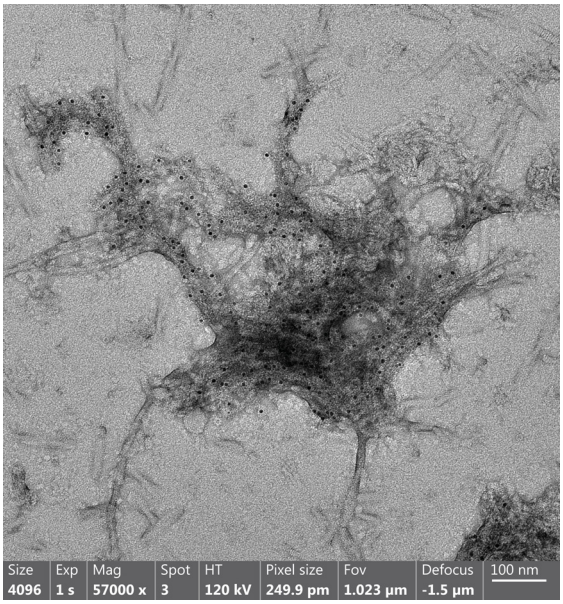

Figure D.2.: Immunogold negative stain EM of a sample of Aβ fibrils purified from human sAD brain tissue (AD6).

Cryo-EM Image Acquisition and Image Processing For cryo-EM imaging, 3 µL of the final sample were applied to holey carbon grids (Quantifoil 1.2/1.3, 300 mesh), blotted with filter paper for 5 s and plunge frozen in liquid ethane using a ThermoFisher Scientific Vitrobot Mark IV, set at 95% humidity and 4°C temperature. Data acquisition was performed on a ThermoFisher Scientific Titan Krios G4 operating at 300 kV using a Falcon IV detector in counting mode. The automated collection was directed by EPU data collection software. Further details are given in Table D.1.

	AD6
Data collection	
Microscope	Krios G4
Voltage [kV]	300
Detector	Falcon IV
Magnification	96,000
Pixel size [Å]	0.808
Defocus range [µm]	-0.5 to -2.5
Exposure time [s]	2.82
Number of frames	40
Total dose [e^-/Å^2]	40.19

Table D.1.: Cryo-EM data collection statistics of Aβfibrils purified from sporadic AD6 brain.

Gain-corrected movie frames were aligned and summed into single micrographs on-the-fly using Warp [218]. CTF estimation was performed using CTFFIND4.1 [209].

To produce the 2D class averages shown in Figure 3.3, particles were picked automatically using crYOLO [277]. 44,108 particles were extracted from the cryo-EM micrographs at a box size of 200 pix prior to 2D classification.

D.0.2. Obtaining isolated fibrils from human brain samples

As described in chapter 6, obtaining isolated Aβ fibrils from human brain material is not straightforward. Several things were tried in an attempt to resolve the fibril clusters to produce a sample suitable for cryo-EM. Two different systems were used for testing: (i) *in vitro* Aβ42 fibrils at neutral pH (the reader is referred to Chapter 4 for details on the sample preparation), and (ii) Aβ fibrils purified by Fernanda Salome Peralta Reyes from sporadic human brain tissue provided by Martin Ingelsson following a previously described extraction protocol [261].

Disentangling *in vitro* Aβ42 fibrils In order to generate an *in vitro* system that mimics the *ex vivo* sample as well as possible in terms of the used buffer system, 30 µL of *in vitro* Aβ42 fibrils were transferred into an ultracentrifugation reaction tube and pelletised in an ultracentrifuge for 30 min at 153,700 x *g*. The supernatant

was removed and the pellet was resuspended in 15 µL buffer. This was done three times in total to generate three equivalent samples.

For the first sample, the pellet was dissolved in 15 µL resuspension buffer (compare [261]) and then sonicated in an ultrasonic water bath for 0 s, 10 s, 30 s, and 1 min in attempt to dissolve the fibril clusters by mechanical forces. After each sonication step, a negative stain EM grid was prepared as described in Chapter 4.2.2 (Figure D.3 A-D).

For the second and third sample, we tried to dissolve the fibril clusters by interrupting chemical interactions such as hydrophobic interactions and salt bridges. In order to destroy potentially clustering hydrophobic interactions, we added isopropyl alcohol to the sample solution. To prepare the resuspension buffer, 15 µL of isopropyl alcohol were added onto 85 µL of resuspension buffer (compare [261]). The pellet was then resuspended in resuspension buffer with 15% isopropyl alcohol. A negative stain EM grid was prepared following the protocol described in Chapter 4.2.2 (Figure D.3 E).

To interrupt salt bridges, the pellet of the third sample was resuspended in 15 µL of a salt containing buffer. The added salt buffer (resuspension buffer with 300 mM NaCl) was prepared by mixing 94 µL of resuspension buffer (compare [261]) with 6 µL of 5M NaCl. A negative stain EM grid was prepared as described in Chapter 4.2.2 (Figure D.3 F).

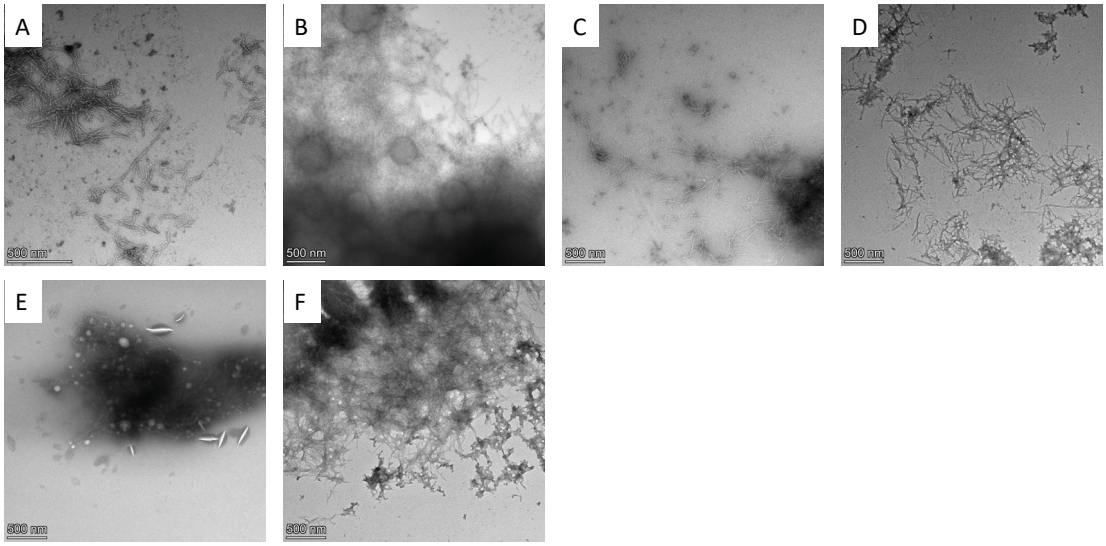

Figure D.3.: Negative stain EM of a processed Aβ42 sample. (A) 0 s sonication. (B) 10 s sonication. (C) 30 s sonication. (D) 1 min sonication. (E) Sample resuspended in isopropyl alcohol containing buffer. (F) Sample resuspended in salt containing buffer.

As seen in Figure D.3, none of the above described methods were successful in disentangling fibrils.

Disentangling human brain extracted fibrils using Pronase and Sonication In addition to clustered Aβ fibrils, all human brain samples also contain a considerable amount of tau fibrils, which not only complicate high-resolution reconstruction but may also affect fibril clustering. It has previously been reported that pronase, a mixture of different proteases, removes the fuzzy coat of tau fibrils while leaving the fibril core intact [327]. Moreover, pronase was also used to prepare the cryo-EM grids of human brain extracted Aβ fibrils [261, 285]. To study the effects of pronase on our purified fibril samples, we mixed 2 µL human brain extracted Aβ fibrils with 1 µL of pronase at a concentration of 0.4 mg/mL in PBS. The pronase solution was prepared by adding 5.375 mL of PBS onto 2.15 mg of Pronase. The sample-pronase mixture was incubated for 30 min. A negative stain EM grid was prepared as described in Chapter 4.2.2. However, since staining with UrAc does not work well for phosphate buffers, after sample incubation on the grid, the grid was washed with dH_2O. For this, the grid was incubated three times in a 10 µL droplet of dH_2O for 3 min. For an alternative procedure to incubate the

sample in pronase, 2 µL of sample was applied onto a glow-discharged 300 mesh carbon-coated copper grid (EM Sciences, ECF300-Cu). The sample was incubated for 2 min and excess liquid was blotted off with filter paper. The grid was then incubated in a 10 µL droplet of Pronase at a concentration of 0.4 mg/mL for 5 min. The grid was afterwards washed with water as described above and stained with UrAc as described in Chapter 4.2.2.

Since sonication of *in vitro* Aβ42 fibrils in an ultracentrifugation reaction tube did not show any effect (Figure D.3 A-D), 3 µL of the *ex vivo* Aβ fibril sample was transferred into a 500 µL LoBind reaction tube and sonicated in an ultrasonic water bath for 10 s.

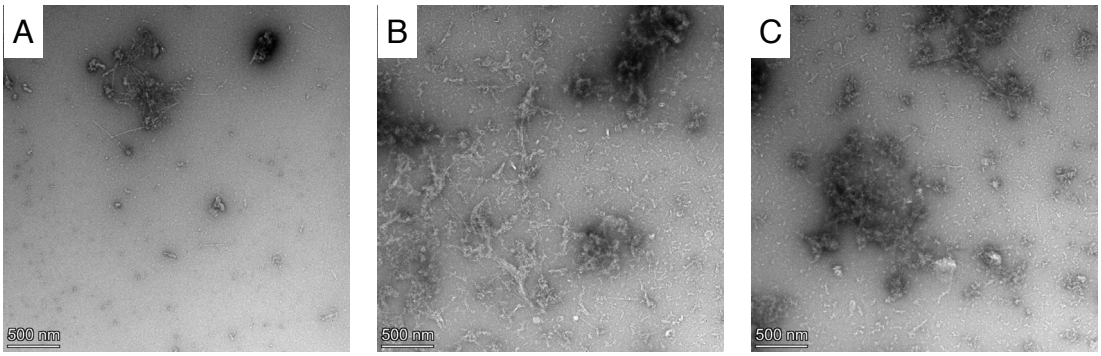

Figure D.4.: Negative stain EM of a processed *ex vivo* Aβ sample. (A) Sample-pronase Mixture incubated for 30 min. (B) Sample incubated in pronase for 5 min. (C) Sample sonicated for 10 s.

From Figure D.4 A it can be seen that incubating the sample with pronase for 30 min not only removes most of the Tau fibrils, but also reduces the level of contamination with other cellular components. However, it appears that pronase treatment also affects the concentration of Aβ fibrils. In contrast, incubation of the grid in a droplet of pronase for 5 min does not seem to remove any fibrils or dissolve any fibril clusters (Figure D.4 B). Finally, sonication of the sample for 10 s also does not seem to decrease the amount of clustering (Figure D.4 C).

Pulse sonication of human brain extracted fibrils Since continuous sonication of the sample does not seem to have much effect on the fibril clusters, pulse sonication was performed in an attempt to enhance the effect. For this, 5 µL of human

brain extracted Aβ fibrils were transferred into a 500 µL LoBind reaction tube. The sample was then sonicated in an ultrasonic water bath for a total of 3 min in pulses of 10 s on and 20 s off. Then, 3 µL of the sample were applied onto a glow-discharged 300 mesh carbon-coated copper grid (EM Sciences, ECF300-Cu). The sample was incubated for 2 min and excess liquid was blotted off with filter paper. Afterwards the sample was washed two times in 15 µL droplets of dH_2O for 1min. Excess liquid was removed and 3 µL of 1% (w/v) UrAc were applied on the top of the grid, following a 1 min incubation. Excess liquid was removed with filter paper and the grid was air-dried. TEM images were recorded as described in Chapter 4.2.2.

Although many fibril clusters are still visible in Figure D.5 A, it seems that pulse sonication has at least detached some fibrils from large clusters (Figure D.5 B).

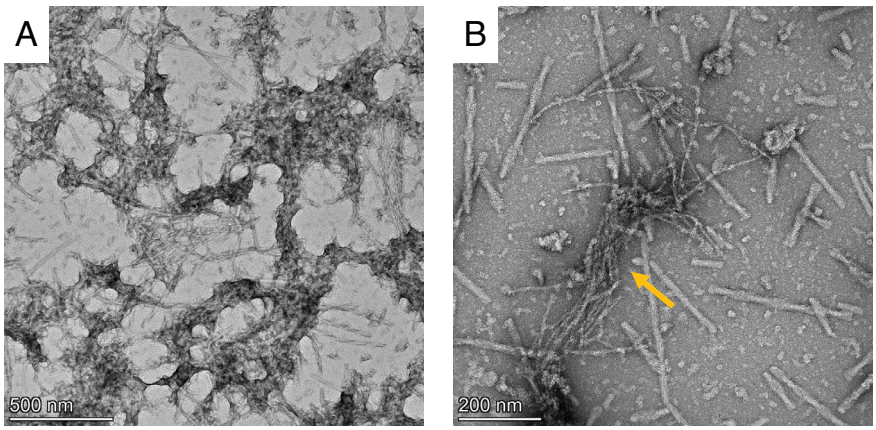

Figure D.5.: Negative stain EM of a pulse sonicated *ex vivo* Aβ sample. (A) At 28,000 x magnification (B) At 57,000 x magnification. The yellow arrow indicates fibrils that are likely Aβ

Pulse sonication in combination with pronase treatment of human brain extracted fibrils To test the effect of combining pulse sonication with pronase treatment, the leftover sample (2 µL) of the pulse sonication experiment (compare D.0.2; *Pulse sonication of human brain extracted fibrils*) was treated with 0.5 µL pronase at a concentration of 0.4 mg/mL. The sample was incubated for 30 min before a negative stain EM grid was prepared as described in Chapter 4.2.2.

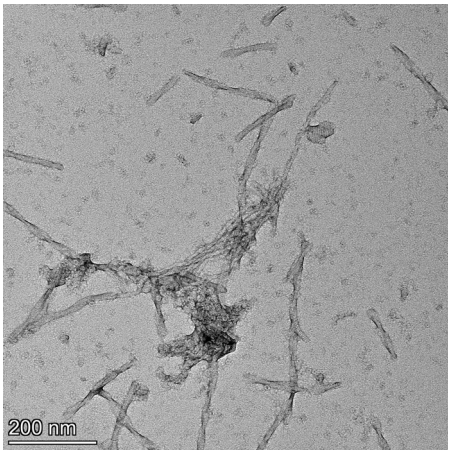

Figure D.6.: Negative stain EM of a pulse sonicated and pronase treated *ex vivo* Aβ fibril sample

As before, the sample contains less impurities after pronase treatment, but the amount of clustering on the grid appears to be identical whether pronase is added or not.

Immunogold negative stain EM of treated human brain extracted fibrils In order to confirm that pulse sonication indeed increases the number of isolated fibrils in the sample, immunogold negative stain EM of a pulse sonicated sample was performed. For this, 3 µL *ex vivo* Aβ fibrils were transferred to a PCR reaction tube and sonicated in an ultrasonic water bath for 3 min, in pulses of 10 s on, 20 s off. The grid was then prepared as described in Chapter D.0.1.

Two additional immunogold negative stain grids of the *ex vivo* Aβ fibrils were prepared, but prior to sample application the sample was treated once with ethanol and once with sarkosyl. For ethanol treatment, 1 µL of 90% ethanol were added onto 2 µL sample solution. For sarkosyl treatment, 0.6 µL of 10% sarkosyl were added onto 2.4 µL sample solution. Both samples were shortly vortexed before they were applied onto the grid.

Unfortunately, the staining is not ideal for assessing the success of pulse sonication, yet fibril clusters can still be seen in Figure D.7 A. Furthermore, both ethanol and sarkosyl treatment of the sample do not seem to dissolve the fibril clusters well (Figure D.7 B, C). The addition of sarkosyl to the sample may have even deteriorated its quality.

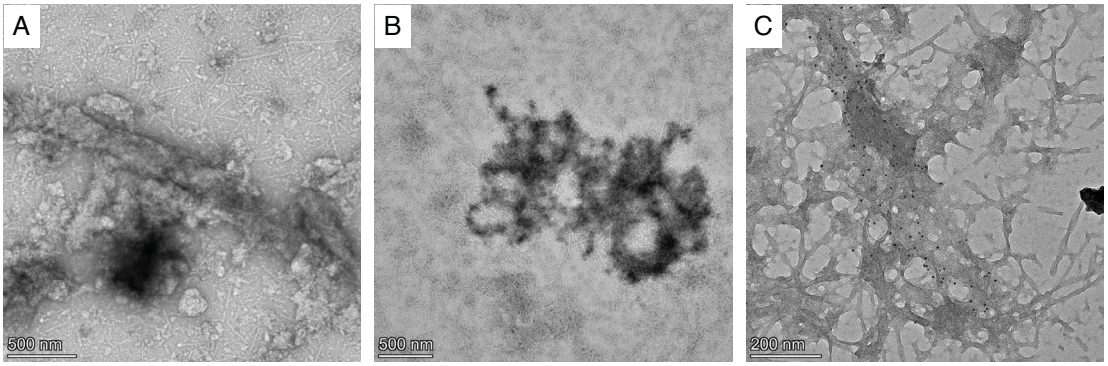

Figure D.7.: Immunogold negative stain EM of (A) a pulse sonicated *ex vivo* Aβ sample, (B) an ethanol treated *ex vivo* Aβ sample, and (C) a sarkosyl treated *ex vivo* Aβ sample.

Sonication and washing of human brain extracted fibrils As the addition of sarkosyl to the sample seems to worsen the sample quality, additional washing steps were added to the sample purification protocol to further decrease the sarkosyl concentration. Prior to washing, 8 µL of the *ex vivo* fibril sample was transferred into a 500 µL LoBind reaction tube and sonicated in an ultrasonic waterbath for 2 min in pulses of 10 s on, 20 s off. To monitor sonication, 2 µL of this sample were applied on a glow-discharged 300 mesh carbon-coated copper grid (EM Sciences, ECF300-Cu) to perform immunogold negative stain EM screening.

The remaining 6 µL were sonicated for two additional pulses (10 s on, 20s off). Again, 2 µL of this sample were applied on a glow-discharged 300 mesh carbon-coated copper grid (EM Sciences, ECF300-Cu) to perform immunogold negative stain EM screening. The remaining sample (~4 µL) was mixed with another 5 µL leftover from a previous sonication step (compare *Pulse sonication of human brain extracted fibrils*) and the sample was centrifuged in an ultracentrifuge reaction tube at 5,000 x *g* and 4°C for 6 min. The supernatant was removed and 6 µL of resuspension buffer were added to the sample. Afterwards, the sample solution was centrifuged again at 5,000 x *g* and 4°C for 6 min. As before, the supernatant was removed and 6 µL resuspension buffer were added to the pellet. A negative stain grid was prepared using 2 µL of sample and two water washes instead of one (compare Chapter 6.2.2).

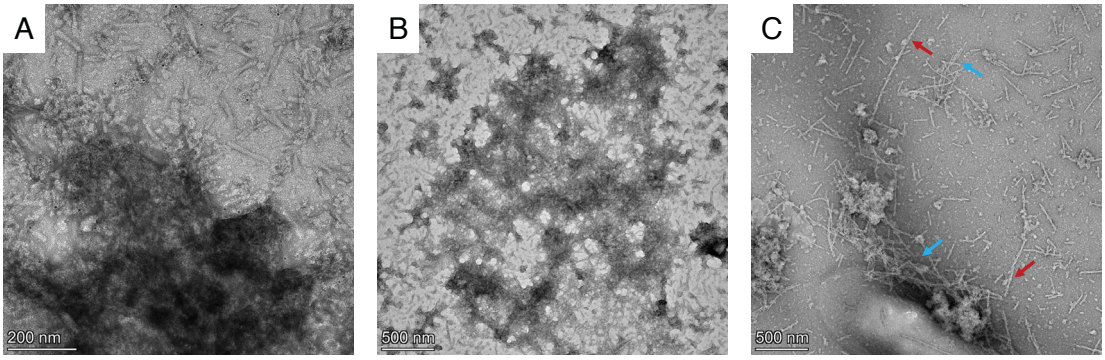

Figure D.8.: Immunogold negative stain EM of (A) a pulse sonicated *ex vivo* Aβ sample (2 min, 4 pulses), (B) a pulse sonicated *ex vivo* Aβ sample (3 min, 6 pulses), and (C) a two times washed *ex vivo* Aβ sample. Red arrows indicate thick fibrils, that are likely Tau fibrils. Blue arrows indicate thin fibrils, that are likely Aβ fibrils.

As seen in Figure D.8 A, B, pulse sonication did not dissolve the fibril clusters after either 2 min or 3 min. Only a few isolated and labelled fibrils can be observed in the images. However, washing the sample twice after sonication seems to remove impurities and lead to more isolated fibrils (Figure D.8 C).

In order to determine whether the order of the two steps (sonication and washing) influences the success of the technique, and furthermore to verify the observation that washing indeed improves sample quality, two further grids were prepared. For the first grid, 6 µL of an *ex vivo* fibril sample were transferred into a 500 µL LoBind reaction tube and sonicated in an ultrasonic water bath for 3 min in pulses of 10 s on, 20 s off. The sample was then centrifuged at 5,000 x g and 4°C for 6 min. The supernatant was removed and 5 µL of resuspension buffer was added onto the pellet. An immunogold negative stain EM grid was prepared as previously described in Chapter D.0.1. For the second grid, the remaining 5 µL of the sample that were used for the first grid were mixed with the supernatant from the previous step and centrifuged in an ultracentrifugation reaction tube at 5,000 x g and 4°C for 6 min. The supernatant was removed and 7 µL of resuspension buffer was added onto the pellet. Afterwards, the sample was centrifuged again at 5,000 x g and 4°C for 6 min, the pellet was resuspended in 7 µL resuspension buffer and transferred to a 500 µL LoBind reaction tube. The sample was then sonicated in an ultrasonic water bath for 3 min in pulses of 10 s on, 20 s off. An immunogold negative stain EM grid was prepared as previously described in Chapter D.0.1.

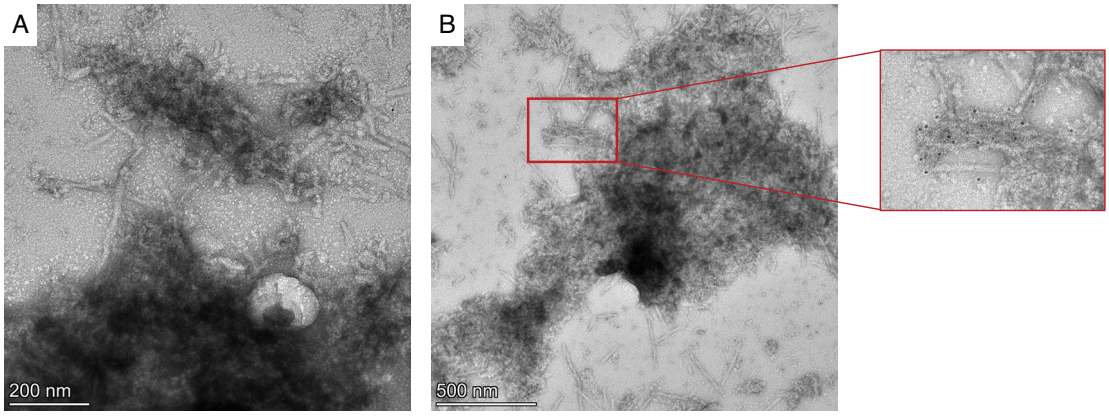

Figure D.9.: Immunogold negative stain EM of (A) a pulse sonicated (3 min, 6 pulses) and then washed *ex vivo* Aβ sample, (B) a washed and then pulse sonicated (3 min, 6 pulses) *ex vivo* Aβ sample.

From the images shown in Figure D.9, it seems that the combination of first washing and subsequent sonication does indeed result in more isolated fibrils, although clumps of fibrils are still clearly visible in this preparation as well.